

Integrated analysis of leaf cell division and growth

Samantha Fox

PhD by Publication

University of East Anglia

John Innes Centre

December 2019

© This copy of the thesis has been supplied on condition that anyone who consults it is understood to recognise that its copyright rests with the author and that use of any information derived therefrom must be in accordance with current UK Copyright Law. In addition, any quotation or extract must include full attribution

1. Abstract

This thesis provides a critical analysis of published work undertaken by the author between 2005 and 2019.

A major challenge in biology is to understand how buds comprising just a few cells can deform through growth to generate complex plant and animal appendages, like leaves or limbs. In this thesis, I bring together my peer-reviewed publications to focus on how the *Arabidopsis* first leaf attains its shape through coordinated patterns of orientated growth and cell division. I highlight innovative approaches used to track leaf growth in multiple cell layers and in different genetic backgrounds. I present maps of leaf development which reveal dynamic, spatiotemporal patterns of orientated tissue growth and cell division. I present models developed through collaborations with computer scientists that provide key insights into how leaf shapes are formed during organ morphogenesis via an underlying biochemical-based polarity system that may also be applicable to more complex shape development. I discuss how the patterns of cell division and cell sizes are correlated and present an integrated model that suggests how cell division and growth can be regulated via a dual control mechanism with cross connections. Prior to the work presented here, no previous model had been proposed to explain leaf shape transformation according to biologically validated observations. In this work I assess the impact of this research to the field of plant developmental biology and suggest that the knowledge gained provides valuable information to the plant science community upon which future studies may be based.

Access Condition and Agreement

Each deposit in UEA Digital Repository is protected by copyright and other intellectual property rights, and duplication or sale of all or part of any of the Data Collections is not permitted, except that material may be duplicated by you for your research use or for educational purposes in electronic or print form. You must obtain permission from the copyright holder, usually the author, for any other use. Exceptions only apply where a deposit may be explicitly provided under a stated licence, such as a Creative Commons licence or Open Government licence.

Electronic or print copies may not be offered, whether for sale or otherwise to anyone, unless explicitly stated under a Creative Commons or Open Government license. Unauthorised reproduction, editing or reformatting for resale purposes is explicitly prohibited (except where approved by the copyright holder themselves) and UEA reserves the right to take immediate 'take down' action on behalf of the copyright and/or rights holder if this Access condition of the UEA Digital Repository is breached. Any material in this database has been supplied on the understanding that it is copyright material and that no quotation from the material may be published without proper acknowledgement.

Table of Contents

1. Abstract.....	2
2. List of figures.....	5
3. List of accompanying material	6
3.1. Key first author papers on which I base the critical analysis of this thesis.....	6
3.2. Supporting papers which demonstrate my wider contribution to plant biology.....	6
4. Acknowledgements.....	8
5. Introduction	9
5.1. The leaf as a model for organ development.....	9
5.2. Leaf morphology and early development.....	9
5.3. Coordination of cell division	10
5.4. Growth can be mathematically described by a tensor field.....	11
5.5. Morphogens.....	12
5.6. The relationship between orientated division and growth	13
5.7. Cell verses organismal control of morphogenesis.....	13
5.8. The role of polarity in oriented growth	14
6. Generation of Leaf Shape Through Early Patterns of Growth and Tissue Polarity.....	16
6.1. Live imaging enabled leaf ontogeny to be studied dynamically.....	16
6.2. Standard growth curves.....	17
6.3. Clonal analysis.....	17
6.4. Leaf excision.....	18
6.5. Models of leaf growth.....	18
7. Spatiotemporal coordination of cell division and growth during organ morphogenesis....	19
7.1. Time-lapse imaging	19
7.2. Tracking growth and divisions	19
7.3. Analysis of cell size using 3D segmentation.....	20
7.4. Analysis of subepidermal cells in wild type	20
7.5. Standard growth curves for spch and fama leaf width.....	21
7.6. Integrated models of growth and cell division	21
8. Supporting papers.....	22

8.1.	Systems biology approach pinpoints minimum requirements for auxin distribution during fruit opening	22
8.2.	Evolution of regulatory interactions controlling floral asymmetry	22
8.3.	Additional collaborations.....	23
9.	General Discussion.....	25
9.1.	Summary of this work.....	25
9.2.	Increase in leaf width and length is exponential at early stages of development	26
9.3.	A proximodistal gradient of growth rates along the leaf midline is present from early stages	27
9.4.	A proximodistal gradient can account for observed growth rates along the midline .	29
9.5.	Areal growth rates in the epidermis exhibit a complex spatiotemporal pattern	30
9.6.	Leaf growth is highly anisotropic	34
9.7.	Leaf shape can be coordinated through tissue polarity	36
9.8.	Leaves are not able to repattern and regenerate following excision.....	38
9.9.	The pattern of clones does not support the hypothesis that cell division is focused at the margin	40
9.10.	Integrating patterns of growth and cell division.....	43
9.11.	The relationship between cell division and growth can be explored in the spch mutant	44
9.12.	A proximal zone of division competence explains the dynamics of cell division	47
9.13.	Dynamics of the competence zone explains the cell cycle arrest front progression ..	53
9.14.	Organ size can be influenced by changes in cell size and/or cell number.....	54
9.15.	Cell size is negatively correlated with cell division	55
9.16.	The relationship between growth and division is decoupled in the subepidermis.....	56
9.17.	An integrated model predicts cells execute division at a threshold area that varies spatiotemporally	59
9.18.	The relationship of cell division plane and orientation of growth.....	61
9.19.	The biological basis of polarity.....	62
10.	Conclusion.....	65
11.	List of abbreviations.....	67
12.	References	68
13.	Appendix 1: letters of support from co-authors.....	79
14.	Annexe 2: Submitted publications	94

2. List of figures

Figure 9-1. Growth analysis of leaf one*	27
Figure 9-2. Leaf growth analysis in 1D*	28
Figure 9-3. Leaf growth analysis in 2D*	31
Figure 9-4. Dynamics of growth in the <i>spch</i> epidermist	33
Figure 9-5. Principal directions of growth*	35
Figure 9-6. 2D models*	37
Figure 9-7. Distal leaf excision*	39
Figure 9-8. Validation of direct tracking using clonal analysis*	42
Figure 9-9. Comparison of wild-type and <i>spch</i> grown in the imaging chamber†	45
Figure 9-10. Comparison of wild-type, <i>spch</i> and <i>fama</i> leaf widthst	47
Figure 9-11. Dynamics of cell division in the <i>spch</i> epidermist	48
Figure 9-12. Dynamics of cell division in the wild-type epidermist	49
Figure 9-13. Assignment of the midline and lamina regions†	51
Figure 9-14. Canvas deformations	52
Figure 9-15. Comparison of epidermal and subepidermal cell areal growth rates†	57
Figure 9-16. Subepidermal cells in <i>spch</i> †	58

* Reproduced with permission from AAAS.

† Reproduced under CC BY 2.0

3. List of accompanying material

This thesis is based on the manuscripts listed below. For this work I coordinated and executed an extensive and complex program of experiments, conducted analysis and collaborated with colleagues to develop hypotheses supported by computational modelling.

In Appendix 1 there are letters of support from some of my co-authors confirming my contribution to the work. In Appendix 2 the original publications are reproduced with the kind permission of the relevant journals.

3.1. Key first author papers on which I base the critical analysis of this thesis

Fox, S.*, Southam, P.* , Pantin, F.* , Kennaway R., Robinson, S., Castorina, G., Sánchez-Corrales, Y., Sablowski, R., Chan, J., Grieneisen, V., Marée, A., Bangham, A., and Coen, E. (2018).

"Spatiotemporal coordination of cell division and growth during organ morphogenesis." PLOS Biology 16(11): e2005952.

Kuchen, E. E.* , **Fox, S.***, Barbier de Reuille, P., Kennaway, R., Bensmihen, S., Avondo, J., Calder, G. M., Southam, P., Robinson, S., Bangham, and A., Coen., E. (2012). "Generation of Leaf Shape Through Early Patterns of Growth and Tissue Polarity." Science 335(6072): 1092.

* Lead authors contributed equally to this work

3.2. Supporting papers which demonstrate my wider contribution to plant biology

Li, X.-R., R. M. A. Vroomans, **S. Fox**, V. A. Grieneisen, L. Østergaard and A. F. M. Marée (2019).

"Systems Biology Approach Pinpoints Minimum Requirements for Auxin Distribution during Fruit Opening." Molecular Plant 12(6): 863-878.

Castorina, G., **S. Fox**, C. Tonelli, M. Galbiati and L. Conti (2016). "A novel role for STOMATAL CARPENTER 1 in stomata patterning." *BMC Plant Biology* 16(1): 172.

Bencivenga, S., A. Serrano-Mislata, M. Bush, **S. Fox** and R. Sablowski (2016). "Control of Oriented Tissue Growth through Repression of Organ Boundary Genes Promotes Stem Morphogenesis." *Dev Cell* 39(2): 198-208.

Patron, N. J., D. Orzaez, S. Marillonnet, H. Warzecha, C. Matthewman, M. Youles, O. Raitskin, A. Leveau, G. Farré, C. Rogers, A. Smith, J. Hibberd, A. A. R. Webb, J. Locke, S. Schornack, J. Ajioka, D. C. Baulcombe, C. Zipfel, S. Kamoun, J. D. G. Jones, H. Kuhn, S. Robatzek, H. P. Van Esse, D. Sanders, G. Oldroyd, C. Martin, R. Field, S. O'Connor, **S. Fox**, B. Wulff, B. Miller, A. Breakspear, G. Radhakrishnan, P.-M. Delaux, D. Loqué, A. Granell, A. Tissier, P. Shih, T. P. Brutnell, W. P. Quick, H. Rischer, P. D. Fraser, A. Aharoni, C. Raines, P. F. South, J.-M. Ané, B. R. Hamberger, J. Langdale, J. Stougaard, H. Bouwmeester, M. Udvardi, J. A. H. Murray, V. Ntoukakis, P. Schäfer, K. Denby, K. J. Edwards, A. Osbourn and J. Haseloff (2015). "Standards for plant synthetic biology: a common syntax for exchange of DNA parts." *New Phytologist* 208(1): 13-19.

Chan, J., G. Calder, **S. Fox** and C. Lloyd (2007). "Cortical microtubule arrays undergo rotary movements in Arabidopsis hypocotyl epidermal cells." *Nature Cell Biology* 9: 171.

Costa, M. M. R., **S. Fox**, A. I. Hanna, C. Baxter and E. Coen (2005). "Evolution of regulatory interactions controlling floral asymmetry." *Development* 132(22): 5093.

Chan, J., G. Calder, **S. Fox** and C. Lloyd (2005). "Localization of the microtubule end binding protein EB1 reveals alternative pathways of spindle development in Arabidopsis suspension cells." *The Plant cell* 17(6): 1737-1748

4. Acknowledgements

This thesis has been a long time in the making. It wouldn't have been possible without the support and collaboration of a large number of colleagues at the John Innes Centre, most notably, my supervisor since 2004, Professor Enrico Coen. Always ready to offer support and guidance, Rico has been the best mentor I could wish for. I am incredibly grateful for the training he has given me to become the scientist I am. Central to this thesis is the combination of experimental biology and modelling. I am hugely grateful to have collaborated closely with many computer scientists and biologists. Foremost in my mind is the late Professor Andrew Bangham. It was a privilege to know and work with him, I know he would be proud to see me reach this milestone. I would also like to thank Erika Kuchen, who has the rare talent of being a great experimentalist and an accomplished modeller. I enjoyed our time working together immensely. My thanks also to Richard Kennaway, Paul Southam, Florent Pantin and Pierre-Barbier de Ruille. I could not have done this work without the expertise of Grant Calder, thanks for the microscopy support, technical innovation and endless patience. To my many colleagues and co-authors, past and present, thank you. Thank you to the John Innes Centre for funding.

Lastly, and most importantly, thanks to all of my family for their love and support, especially mum and dad for always believing in me.

Simon, the last words are for you. What a journey this has been. Thank you for the encouragement, support and love. As one book finishes, another one begins and the adventure continues. I can't wait!

5. Introduction

5.1. The leaf as a model for organ development

Eudicot leaves exhibit a vast array of morphological diversity, from simple ovate shapes, to highly serrated, lobed and compound leaves. When grown under uniform conditions, corresponding leaves of the same species exhibit broadly uniform characteristics and reach a determinate size and shape (Pyke, Marrison et al. 1991, Mündermann, Erasmus et al. 2005). How genes control development to create such complex shapes remains one of the major problems in biology. The *Arabidopsis* leaf provides a good model to study morphogenesis, the biological process whereby shape is acquired. A wide range of genetic material is available through mutants with varying leaf phenotypes. The first leaf is a relatively small, flat structure that is amenable to imaging from an early stage of development and exhibits a transformation from a dome-shaped bud to a simple leaf shape.

5.2. Leaf morphology and early development

Leaves are determinate organs. They arise on the flanks of the shoot apical meristem (SAM) in a regular arrangement, or phyllotaxy, as a bulge of a few cells at the site of an auxin maxima (Reinhardt, Pesce et al. 2003). Leaf initiation provides a new orientation of growth away from the main stem and defines the proximodistal leaf axis. Laminae expand in the orthogonal orientation, from the midrib to the margins, along the mediolateral leaf axis. This occurs concurrently with dorsiventral or adaxial-abaxial axis establishment (Waites and Hudson 1995). Though these anatomical changes have been well described, the question of how undifferentiated cells at the SAM transform into a determinate structure remains the subject of much scientific debate.

Plant growth is symplastic in that the relative positions of cells are constrained by the cell wall with the result that cells do not slide relative to one another (Erickson 1986). Apart from a few specific cases, programmed cell death is not thought to contribute to the shape of plant leaves (Gunawardena, Greenwood et al. 2004). Cell division and cell expansion alone provide

the means by which plant organs are formed. The fact that the leaf surface is contiguous suggests that cell behaviour is coordinated across large areas of the tissue. Shape transformation is assumed to be entirely dependent upon modulation of rates and orientations of local growth (Green, Kennaway et al. 2010). This raises the question of how genes control tissue deformations through coordinated cellular behaviours.

5.3. Coordination of cell division

At initiation, the primordium has been described as a peg-like structure with no blade (Esau 1960). The transition to a flattened blade or lamina is proposed to occur through localised meristematic activity in a strip along two opposite sides of the primordium. This region has been termed the 'marginal meristem' and is thought to play a key role in the formation of a new leaf organ (Avery 1933, Esau 1977). Nevertheless, there is a lack of clarity about what exact role this region may play and where precisely it is located. Classical studies suggest that marginal meristems drive leaf growth from a row of subepidermal and epidermal initials towards the adaxial surface at the very lateral edges (Avery 1933, Esau 1960). These appear as a single cell in each layer in transverse view, and as a band of cells in longitudinal view. Initial cells are proposed to divide periclinally to create cell layers and anticlinally to increase surface area. The intercalary divisions in the derivatives of marginal initials are proposed to continue until the final leaf form is attained (Esau 1960). Later studies raised doubts over the spatial and temporal dynamics stipulated by this hypothesis. It has been suggested that marginal meristems are active for a short duration at the very earliest stages of development and only responsible for organising the regular array of cell layers (Maksymowych and Erickson 1960). A basal 'plate meristem' or 'blastozone' is proposed to coordinate planar growth concurrent with lamina outgrowth (Maksymowych and Erickson 1960, Pyke, Marrison et al. 1991, Hagemann and Gleissberg 1996, Donnelly, Bonetta et al. 1999). One view is that cells could be supplied to this plate meristem from the junction between the leaf blade and petiole (Ichihashi, Kawade et al. 2011). Genetic studies suggest that the juxtaposition of adaxial and abaxial leaf domains at the leaf boundary may play an important role in leaf growth.

In *Antirrhinum*, mutations in *PHANTASTICA* (*phan*) result in the development of needle-like leaves which lack dorsal cell identity and lateral outgrowth (Waites and Hudson 1995). Lateral cell proliferation is predicted to form the lamina via a plate of cells near the ventral boundary of the expression domain. In *Nicotiana sylvestris*, the 'bladeless' mutant (*lam1*), is characterised by leaves that grow to full length but fail to develop laterally. The long, thin cells normally located at the boundary between adaxial and abaxial surfaces are absent (McHale and Marcotrigiano 1998). In *Arabidopsis*, members of the *KANADI* (*KAN*) and *PHABULOSA* (*PHB*)-like gene families function antagonistically to contribute to abaxial-adaxial patterning, together with polar *YABBY* gene expression; overexpression of *KAN2* results in radialized abaxialised leaves (Eshed, Izhaki et al. 2004). Despite these data, the mechanism by which domains of adaxial and abaxial identity could generate lamina outgrowth remains unclear.

To understand the process of leaf morphogenesis, it is essential to evaluate patterns of cell division in the context of a continually expanding and deforming tissue. Through this approach we can unpick the relationship between the regulation of cell division and growth and attempt to uncover the underlying framework for organ development.

5.4. Growth can be mathematically described by a tensor field

There are several ways that the expansion of tissue through growth can be defined, depending on whether rates vary locally (differential growth), whether growth is equal in all directions (isotropic), or whether growth is not equal in all directions (anisotropic). For the purposes of quantifying planar growth, the leaf can be considered as a sheet of tissue in two-dimensions (2D).

Growth tensors are used to describe growth of biological tissues; these capture relative growth rates along orthogonal axes and can be visually represented as ellipses with orthogonal lines (Coen, Kennaway et al. 2017, Whitewoods and Coen 2017). In 2D, a growth tensor captures the rate of growth along two orthogonal axes, the sum of which corresponds to areal growth rate. The orientation of highest magnitude is referred to as the principle, or major orientation of growth. Perpendicular to this is the minor orientation of growth. Growth rates

aligned with any other reference point or orientation, such as the leaf midline, can also be calculated. A growth tensor can be defined for any region of tissue delimited by material points.

5.5. Morphogens

A key principle of development is that undifferentiated cells are provided with unique positional information which is interpreted by cells to give rise to spatial patterns. Morphogen gradients have been proposed to provide such positional information (Wolpert 1969, Wolpert 2011). Morphogens are substances that form concentration gradients, either within a cell or across a field of cells, and elicit cellular responses. In *Drosophila*, the transcription factor Bicoid forms an intracellular gradient across the anterior-posterior axis of the early embryo. The concentration of Bicoid sensed by nuclei determines the effect on target genes in a spatially controlled manner (reviewed by (Christian 2012)). The concentration gradient is diffused across a common cytoplasm (nuclei divide in the absence of cell division) and causes a direct change in gene expression through targeted effects. In a multicellular setting, the mechanism by which cells receive and interpret a morphogen gradient is more complex. Proteins are thought to be locally produced and transported across a field of cells through the extracellular matrix. Cells within the field must have a mechanism to distinguish small differences in morphogen concentration, store and interpret information and translate it into differential gene responses. In the mouse limb, digit/non-digit patterning is predicted to be organised by underlying morphogen gradients (Hiscock and Megason 2015).

The biological basis whereby cell polarities are established and coordinated in plants is less well established. The plant cell wall provides a barrier between cells that is absent in animal cells. Evidence for the role of morphogen gradients in plants is provided indirectly through the observation of polar transport proteins. Currently the best candidate for a plant morphogen is the phytohormone auxin (Bhalerao and Bennett 2003). Determining how auxin could function in plants for tissue patterning would be a breakthrough of great significance.

5.6. The relationship between orientated division and growth

One theory of how morphogens could modulate tissue patterning is by influencing the orientation of local growth (Green, Kennaway et al. 2010). Since the position of cell walls does not change during development, an interpretation is that walls are aligned along the principle direction of growth (Hejnowicz and Romberger 1984). This hypothesis is supported by the observations that the plane of cell division tends to be normal to the growth axis (Hofmeister's rule, reviewed by (Lyndon 1994)). A key question is therefore what the causal relationship is between these processes. A general dogma in plant development is that the orientation of new cell walls inserted at cell division specifies the orientation of growth and thus relates to organ axuality. The analysis of periclinal divisions during leaf initiation highlighted the close relationship between changes in cell division orientation and the onset of a new axis of organ growth (Cunninghame and Lyndon 1986). Nevertheless, a correlation between cell geometry and orientation of division plane does not in itself define causality. It remains unclear through observations of cell plates alone whether division plane orientation is responsible for setting the orientation of growth or responding to it. There are at least three possible hypotheses: 1) the orientation of cell division plane influences the orientation of growth, 2) the orientation of growth influences the orientation of division plane, 3) growth and division orientations are not sequentially linked but coordinated in parallel by some other mechanism. The origin of regulation for each of these possibilities could originate within the cell or alternatively via a supracellular mechanism in which control operates at the organismal level.

5.7. Cell verses organismal control of morphogenesis

Understanding the role of morphogens and polarity in growth has repercussions for our wider understanding of multicellularity and development. According to cell-theory, individual cells function akin to single celled organisms and aggregate together to form a super organism, with regulation controlled by homeostatic properties of each cell. An alternative organismal-based theory is that individual cells arise as a result of subdivisions of the organism, thus the regulation of processes must occur at the level of the organ, or organism, as a whole (Kaplan and Hagemann 1991).

Traditionally, leaf morphogenesis has been studied from the perspective of cell theory. According to this viewpoint, individual cells act as the primary unit of organisation to shape an organ through coordinated patterns of division, growth and geometry. This hypothesis predicts a strict correlation between patterns of cell division and regions exhibiting high growth rates. An alternative possibility is that the processes underlying increase in cell number through the division execution and increase in cell size through cell expansion are separate and under independent regulation (Kaplan and Hagemann 1991).

In this critical analysis I will revisit the cell versus organismal theories to evaluate the insights that may be gleaned through my published works on leaf growth.

5.8. The role of polarity in oriented growth

Growth of individual plant cells results from the loosening of cell wall material and depends on the degree of cell wall extensibility (the ability to irreversibly increase in area) and cell turgor (Cosgrove 2005). Since the physical pressure of turgor is isotropic, growth anisotropy can only arise if some walls have greater extensibility in some orientation relative to others. Cell wall extensibility is proposed to depend on the alignment of cellulose fibres (Baskin 2005). A mechanism for guiding cell wall anisotropy according to an underlying axially could be provided by microtubules that function to align cellulose fibres along tracks (Whitewoods and Coen 2017). Such axially could be defined by the cell itself or relative to a tissue-wide axially system. Since plant cells are connected by the cell wall, the behaviour of individual cells can influence that of others. Thus, a distinction can be made between how a cell would grow in isolation (specified growth) with how a cell grows as part of an interconnected tissue under external mechanical constraints (resultant growth). The resultant pattern of growth tensors across a tissue emerges as a consequence of growth specified according to underlying orthogonal axes, together with rotations that resolve conflicts between neighbouring regions that are specified to grow differently (Whitewoods and Coen 2017).

It is currently unknown how axiality is coordinated within a growing plant tissue. One hypothesis is that the concentration gradient of a morphogen may provide a biochemical-based polarity field from which orientations are specified (Coen, Rolland-Lagan et al. 2004, Green, Kennaway et al. 2010). Alternatively, axiality could be defined according to mechanical signals relative to the principle orientation of stresses (Hamant, Heisler et al. 2008, Hervieux, Dumond et al. 2016). If a cell can sense the principle orientation of stress, then growth may be specified in relation to this. Mechanical stresses result from turgor pressure and conflicts derived through differential growth in which regions growing at different rates influence each other. Local mechanical conflicts influence microtubule behaviour in sepal epidermal cells adjacent to rapidly growing trichomes (Hervieux, Tsugawa et al. 2017). Stress could influence the principle orientations of growth directly, as has been suggested from ablation experiments in which microtubules are seen to realign (Hamant, Heisler et al. 2008), or indirectly by influencing a biochemical polarity field (Heisler, Hamant et al. 2010). While stresses may be involved, the simplest explanation to explore is the hypothesis that genes influence shape through a biochemical-based polarity system. In this thesis I explore insights gained through computer modelling to predict how this could be organised *in planta*.

6. Generation of Leaf Shape Through Early Patterns of Growth and Tissue Polarity

In this chapter I outline my contributions to a paper published in the journal *Science* (Kuchen, Fox et al. 2012), reproduced in Appendix 2 with permission from AAAS. My position as joint first author reflects the role I played throughout the entire program of research over more than five years. Erika Kuchen and I contributed equally to the work. I led the extensive program of experiments as outlined below, compiled figures and co-authored all manuscript text.

6.1. Live imaging enabled leaf ontogeny to be studied dynamically

A major limitation of previous attempts to understand the ontogeny of a leaf is the challenge of validating hypotheses with direct observations of changes happening at the tissue level at the very earliest stages of development. The concept that specific regions of the leaf function as distinct meristems is an enduring one, despite a lack of direct observations of dynamically growing tissues. Rather, supporting evidence has been gathered via the indirect approach of using snapshot images to predict regions undergoing high levels of cell division as an indicator of growth. This association is underpinned by the assumption that cell divisions are directly linked to growth and that identifying the location of cell proliferation explains how leaves are formed. There has been a notable lack of discussion about how growth could be regulated independently from cell division or alternatively, how patterns of cell divisions in specific regions could lead to differential patterns of growth. Live-imaging the leaf surface offers a fresh perspective with which to evaluate pre-existing ideas. Tracking tissue dynamics from the early stages of leaf development enabled the investigation of how growth may be coordinated to shape a leaf.

I employed a novel method to directly track *Arabidopsis* leaf one using time-lapse confocal microscopy to visualise fluorescently-labelled cells. I used an optical-imaging chamber in which multiple seedlings can be maintained for several days (Calder, Hindle et al. 2015).

Leaf primordia were imaged using time-lapse confocal microscopy from 5 days after stratification (DAS), at a width of approximately 100 μm . In this environment, leaves remain relatively flat. Accordingly, growth analysis was carried out in two dimensions (2D), simplifying analysis.

I collaborated with computer scientist Pierre Barbier de Ruille to develop specialist software to track growth and generate quantitative measurements. I manually placed thousands of points at cell vertices on each image frame such that growth tensors could be calculated for each region of the leaf. From these data, I generated measurements of growth rates, anisotropy and principle orientations of growth. I manually determined the location of the petiole-lamina boundary for each image so that growth from different datasets could be compared. I tracked growth at a cellular level from cells lying approximately over the midline.

6.2. Standard growth curves

I generated growth curves for *Arabidopsis* leaf one from seedlings grown in standard conditions on plates. I measured leaf widths and lengths for multiple seedlings from initiation to maturity and used logistic curves to estimate growth rates, the time of leaf initiation and the upper asymptote. From this framework, leaves grown in the chamber could be developmentally staged. These data also provided the context to design clonal analysis experiments such that clones were induced and imaged at a controlled developmental stage.

6.3. Clonal analysis

I used clonal analysis to estimate patterns of growth from *Arabidopsis* plants grown in standard conditions on plates. These data were used to validate the results of live-imaging and assess model predictions in regions of the leaf that are not amenable to live imaging. I generated sectors of Green Fluorescent Protein (GFP) by heat shock at 3 or 6 days after initiation (DAI). After 3 or 6 days of further growth leaves were removed, flattened and the abaxial surface imaged by confocal microscopy. I used a modified version of the Sector

Analysis Toolbox (Green, Kennaway et al. 2010) to analyse clonal patterns by a semi-automatic process with manual input. This generated a virtual composite shape from the mean outlines of individual leaves using Procrustes alignment (Gower 1975), normalising for scale and position. Epidermal clones were segmented using a combination of automatic and manual segmentation, after which each individual clone was warped onto the mean shape. To validate direct tracking using clonal analysis I manually traced cell fates from time-lapse images and compared these to patterns of clones at corresponding developmental stages.

6.4. Leaf excision

I repeated leaf excision experiments described in (Sena, Wang et al. 2009) to determine if an excised young leaf retains the ability to repattern and regenerate. I cut leaves in half approximately perpendicular to the midvein using micro-scissors and found no regeneration. I developed a novel technique to improve the precision of the cut using a laser dissecting microscope. Following laser excision, I transferred seedlings to the optical-imaging chamber to carry out live-imaging of the events immediately following cutting. I found no regeneration. These results undermined previously published reports and supported our model predictions.

6.5. Models of leaf growth

I collaborated with computer scientists to employ a mathematical modelling approach to investigate mechanisms underlying organ shape and account for my experimental observations. The Growing Polarised Tissue (GPT) framework was used to simulate the leaf as a continuous sheet in which regionally expressed factors can interact and propagate (Kennaway, Coen et al. 2011). Polarity is provided by signals that propagate through the tissue and is anchored by polarity 'organisers'. Model simulations were coded and implemented by my co-authors Erika Kuchen and Richard Kennaway. I contributed to the theoretical development and evaluation of models against experimental observations during collaborative group sessions led by Professor Enrico Coen.

7. Spatiotemporal coordination of cell division and growth during organ morphogenesis

In this chapter I outline my contributions to a paper published in the journal *PLOS Biology* ((Fox, Southam et al. 2018) reproduced in Appendix 2, licensed under CC BY 2.0) on which I am joint first author. This publication represents the culmination of a huge body of work undertaken over several years by myself and a talented group of collaborators, including experimentalists and computer scientists. My role as lead experimentalist was to execute the large number of experiments and provide training and day-to-day supervision to PhD students who also contributed to the project. I co-developed hypotheses, produced and compiled all figures, co-authored all text, and carried out additional experiments required by reviewers.

7.1. Time-lapse imaging

I carried out time-lapse confocal imaging using the optical-imaging chamber at various intervals to capture leaf growth from the *speechless (spch)* mutant and wild type. I measured leaf width prior to converting confocal image stacks into single projections using various image processing tools. For the later stages, when the leaf could not be captured in a single scan, I merged multiple overlapping tiled scans to create a single composite image. I created projections of the subepidermal layer using visualisation software to peel off the epidermal surface. Several projections were created for each Z-stack (using different parameters to reveal as many cells as possible in approximately the middle of the cell layer) which I then manually merged together to create a composite image. This approach enabled me to evaluate corresponding regions of multiple cell layers in the same organ.

7.2. Tracking growth and divisions

I quantified growth and division by tracking the displacement of cell vertices and incorporating new cell walls as they appeared. The frequency of cell divisions was not

synchronised; neighbouring cells divided at different times and exhibited variation in the duration of cell cycle. Some cells did not divide at all throughout the experiment. To aid visualisation and characterise the pattern across the tissue, I categorised cells at each time point according to whether they would undergo division (were competent to divide) during the next time interval or at some point during the experiment, or whether they did not divide for the remainder of the tracking experiment. This was visualised using a toolset (Track 'n' R) created by my co-author Florent Pantin. I manually identified the first row of nondividing cells for each tracking experiment and coloured these and corresponding cells in subsequent images to show how these cells were displaced through growth. I identified the location of the petiole-lamina boundary and categorised cells as forming part of the midline or lamina regions by tracking lineages back from a later time point when these features were more easily identifiable.

7.3. Analysis of cell size using 3D segmentation

I carried out segmentation in three dimensions (3D) to validate surface measurements with volumetric data. I collaborated with Professor Robert Sablowski to use modified Python scripts (Serrano-Mislata, Schiessl et al. 2015), to measure the external surfaces and volume of epidermal and subepidermal cells in 3D. I used Fiji macros (Schindelin, Arganda-Carreras et al. 2012) using the 3D Viewer and Point Picker plugins to visualise images and select cells with manual input and quality control. I manually identified corresponding cells in surface projections and plotted projected segmentation-based area against vertex-based area, segmented surface area and cell volumes. I found vertex-based cell area to be a good proxy for 3D cell size. Cell thickness showed relatively little spatial variation, confirming that the major contribution to cell size variation derives from cell area, validating our approach.

7.4. Analysis of subepidermal cells in wild type

To visualise subepidermal cells in wild-type leaves, I grew seedlings on plates in standard conditions before sampling and fixing leaves to preserve tissue structure. I used confocal

microscopy to image through the entire depth of the leaf before creating projections of the subepidermal layer. I determined that subepidermal cells in wild type are broadly similar to those in *spch*.

7.5. Standard growth curves for *spch* and *fama* leaf width

I generated growth curves for *Arabidopsis* leaf one from *spch* and *fama* mutant seedlings grown on plates. I measured leaf widths for multiple seedlings at various DAS and used logistic curves to fit the data. I compared these results to the standard curve of wild-type leaves and showed that leaf widths are reduced in *spch* and *fama*.

7.6. Integrated models of growth and cell division

I collaborated with computer scientists to incorporate models of cell division competence and execution to our previously published models of leaf growth. The GPT framework (Kennaway, Coen et al. 2011) was used to simulate the leaf as a continuous sheet with an additional superimposed layer of virtual cells (v-cells). Models were implemented by co-authors Paul Southam, Florent Pantin and Richard Kennaway.

8. Supporting papers

In this chapter, I summarise my contribution to several publications on which I am a contributing author.

8.1. Systems biology approach pinpoints minimum requirements for auxin distribution during fruit opening

I provided experimental data that helped to determine how auxin minima are generated and maintained in the developing *Arabidopsis* fruit ((Li, Vroomans et al. 2019) reproduced in Appendix 2, licensed under CC BY 2.0). The valve margin is a highly specialised tissue that forms a narrow strip down the entire length of the fruit and is required for fruit opening and seed dispersal. Computer simulations suggested high rates of auxin flux across the valve margin lead to the formation of auxin minima. I employed confocal microscopy to visualise how the auxin efflux carrier PIN3 is localised in the valve margin. A previous study had suggested the existence of apolar localisation of PIN efflux carriers in this location but was unable to detect these (Sorefan, Girin et al. 2009). My images confirmed this prediction and showed how auxin could be transported from the valve margin to the surrounding tissues. I modified the laser dissection technique that I previously developed for the leaf (Kuchen, Fox et al. 2012) to carry out precise ablations in the valve margin. These partial ablations of valve margin tissue confirmed model predictions that leaving any part of the valve margin intact is sufficient to redistribute auxin. My mechanical experiments provided the foundation for a genetic approach that ablated the entire valve margin.

8.2. Evolution of regulatory interactions controlling floral asymmetry

In *Antirrhinum*, the transcription factor CYCLOIDIA (CYC) is key regulator of floral asymmetry. I carried out a detailed analysis of *Arabidopsis* leaves and flowers in which *CYC* is ectopically overexpressed in response to the glucocorticoid inducer dexamethasone (DEX) ((Costa, Fox et al. 2005) reproduced in Appendix 2 with permission). I found petals from

Arabidopsis grown on DEX to be about 1.5 times larger than wild-type petals. Conversely, leaves grown on DEX were dramatically smaller than wild type, as was the overall stature of the plant. I used scanning electron microscopy to reveal the morphology of cells in induced and non-induced leaves and petals. I found that the effect of CYC on petal area was due to increased cell expansion. Conversely, I showed that CYC repressed growth in leaves through reduced cell growth and reduced cell number. We hypothesised that this was likely through early onset of cell division arrest.

8.3. Additional collaborations

I provided a genetic resource to reveal how repression of organ boundary genes promotes morphogenesis of the *Arabidopsis* stem ((Bencivenga, Serrano-Mislata et al. 2016) reproduced in Appendix 2, licensed under CC BY 2.0). I previously used the *Cre-lox* recombination system to generate clones of ectopic GFP to study growth in the *Arabidopsis* leaf (Kuchen, Fox et al. 2012). A limitation of using this plant line is that expression is down-regulated after approximately seven days. Furthermore, clones were not able to be induced in the SAM. Transcriptional gene silencing has previously been associated with multicopy transgenes incorporating the 35S promoter of cauliflower mosaic virus (Al-Kaff, Kreike et al. 2000, Tang, Newton et al. 2006, Daxinger, Hunter et al. 2008). To overcome this, I designed and assembled a new synthetic version of the *lox*-flanked construct using golden gate modular cloning according to the common syntax ((Patron, Orzaez et al. 2015) on which I am named as an author, reproduced in Appendix 2 with permission). I exchanged β -glucuronidase for cyan fluorescent protein such that upon recombination, cells surrounding the GFP clone can be visualised using confocal microscopy. I generated several independent stably transformed plant lines containing a single insertion of the construct. Single copy, hemizygous individuals had greatly reduced gene silencing. I shared this line with Professor Robert Sablowski, who used it to visualise clones in the SAM and confirm the origin of the stem by revealing distinct patterns of oriented cell division and growth in the central and peripheral regions of the rib zone (Bencivenga, Serrano-Mislata et al. 2016).

I developed a transgenic line of *Arabidopsis* that underpinned two highly cited papers that enhance our understanding of microtubule dynamics during plant cell division. I generated

stable transgenic lines of *Arabidopsis* that incorporate a fluorescently tagged microtubule end binding protein AtEB1a-GFP. The AtEB1a-GFP marks the plus ends of microtubules with a comet-like pattern, enabling the transitions of microtubule arrays throughout the division cycle to be analysed in suspension cells ((Chan, Calder et al. 2005) reproduced in Appendix 2 with permission) and in hypocotyls ((Chan, Calder et al. 2007) reproduced in Appendix 2, licensed under CC BY 2.0).

In 2013 I provided training and supervision for a visiting PhD student, Giulia Castorina, for a 4-month placement in the Coen group. I trained Giulia in many techniques, including time lapse imaging and provided advice and guidance for her project. After her departure I continued the collaboration with Giulia and her group leader Lucio Conti, contributing to the overall direction of research and providing critical analysis. My contribution to the overall project, preparation of the manuscript and response to reviewer's comments was recognised with authorship on the published paper ((Castorina, Fox et al. 2016) reproduced in Appendix 2, licensed under CC BY 2.0).

9. General Discussion

9.1. Summary of this work

In this work I present a detailed description of the patterns of cell growth and cell division that underlie the shape transformation of an *Arabidopsis* leaf primordium into a mature leaf. I find that growth occurs in a coordinated pattern which exhibits a broadly proximodistal gradient in growth rates. I quantify the temporal dynamics and show that a global drop in growth rates is evident at later developmental stages. I reveal the pattern of growth anisotropy and show that initial pattern of growth is mainly orientated parallel with the leaf midline. The major orientation of growth subsequently undergoes a switch to drive lateral leaf expansion. I track the execution of cell division and show that a proximal zone of epidermal cell division competence extends with the leaf as it grows, before retracting to the base. I show how patterns of growth rates, cell division and cell sizes are integrated and exhibit distinct relationships in different cell layers, genetic backgrounds and growth conditions.

These dynamic maps of early organ development provided the basis to formulate and evaluate hypotheses of how leaf growth and cell division could be coordinated using computational modelling. The design-build-test iterative process enabled models to be developed to match experimental observations and for model predictions to feed-back and influence experimental design. This Systems Biology approach led to a hypothesis which explains how a leaf shape can arise with patterns of growth and cell division that closely match experimental observations. The integrated model predicts that orientated growth is coordinated by an underlying biochemical-based polarity system and explains how the processes of cell division and cell growth could be coordinated by a dual control mechanism via common regulatory elements with cross connections. In this discussion, I evaluate how these results contribute to the field of research and previously held views of leaf maturation and growth coordination. I contribute to the long-held debate of how organs form from single cells and conclude that aspects of cell theory and organismal theory taken together could account for how complex, multicellular organs are formed.

9.2. Increase in leaf width and length is exponential at early stages of development

Leaf elongation has been described as occurring in several phases according to distinct features; firstly a 'rapid but declining growth rate' concurrent with leaf initiation, followed by exponential growth and finally a decline in growth rates during leaf maturation (Poethig and Sussex 1985). To explore if this hypothesis accurately reflects macroscopic changes at the organ level I measured leaf widths and lengths from multiple individual leaves at different developmental stages from primordium initiation to maturity. Plotting these data revealed that growth in width and length could be best approximated by a logistic function ((Kuchen, Fox et al. 2012) Fig. S1., reproduced here in Figure 9-1). The rate of increase in leaf length and width are exponential at early stages and subsequently drop to zero as length and width plateaus when leaves reach maturity. Leaf widths from seedlings grown in the optical-imaging chamber were evaluated according to this framework and found to be unperturbed for several days. The analysis of epidermal surface growth rates provided the opportunity to develop hypotheses that account for how tissue growth could be coordinated to generate changes at the organ level.

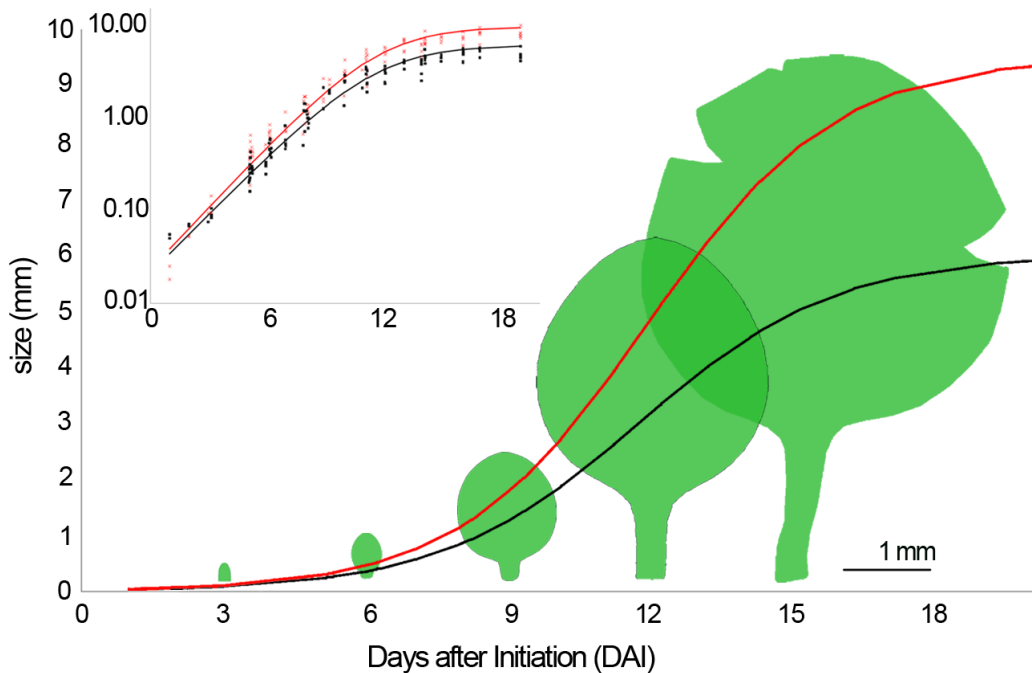


Figure 9-1. Growth analysis of leaf one. Growth curves for leaf width (black) and length (red), with outlines of representative leaves. Inset shows measurements on a logarithmic scale. From Kuchen, Fox et al. 2012.

9.3. A proximodistal gradient of growth rates along the leaf midline is present from early stages

Live imaging revealed a complex and dynamic field of growth tensors throughout early development. As a first step to understanding spatiotemporal dynamics of this pattern, I quantified growth rates parallel to the long axis of the leaf in cells located along the midline. I collaborated with Erika Kuchen to plot these results graphically. We found that growth occurs along the full length of the midline, with rates that varied from the base to tip. Rates were highest at the petiole-lamina boundary and were lowest close to the distal tip. The slope of this gradient changed dynamically, from near-linear at early stages to subsequently flattening out

in proximal regions whilst retaining a steep decline close to the leaf tip ((Kuchen, Fox et al. 2012) Fig. 1., reproduced here in Figure 9-2).

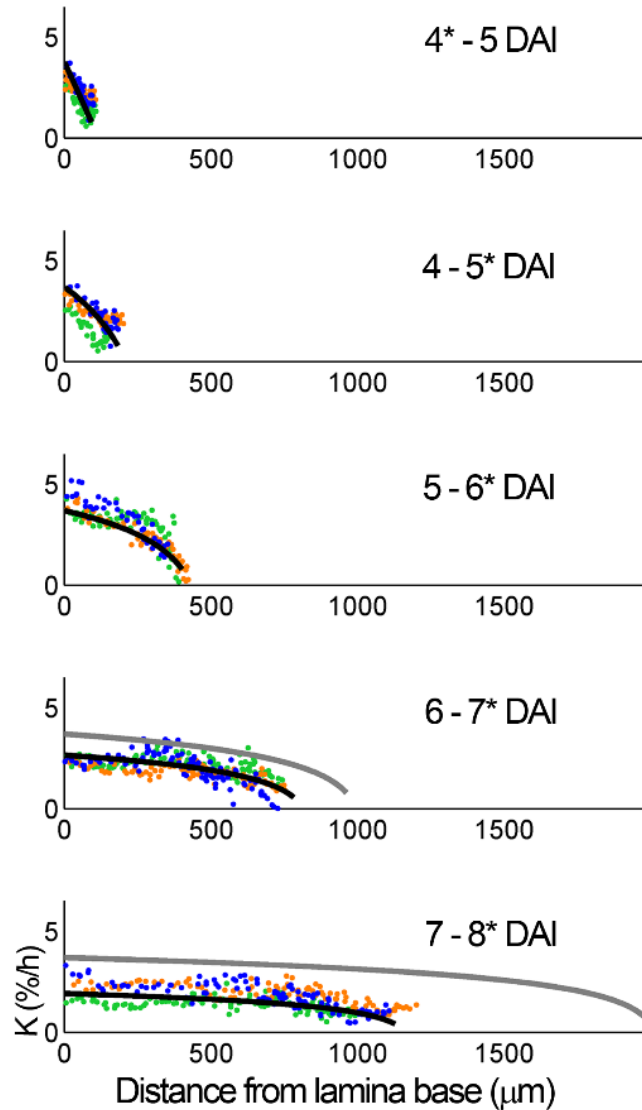


Figure 9-2. Leaf growth analysis in 1D. Midline proximodistal growth rates for three replicates (orange, green, and blue), and 1D models (black and grey lines). Distances from lamina base correspond to those on the day indicated by an asterisk. Adapted from Kuchen, Fox et al. 2012.

The pattern of growth rates described here is broadly consistent with earlier observations by George S. Avery in his classic work of 1933, which sought to define the origin

of leaf tissues in *Nicotiana tabacum* (Avery 1933). The leaf surface was marked with a rectangular network such that changes in the length and width of segments relative to the organ could be calculated. Different regions of the leaf were found to grow at different rates. Greater growth was recorded at the base, marginal and central regions relative to the tip. The observation of slower relative growth at the leaf tip together with a study of tissue structure prompted the idea that leaf maturity occurs basipetally, with the tip maturing earlier than the base. Quantitative analysis was subsequently carried out using the displacement of points that formed the corners of the grid to reveal a gradient in relative areal growth rates (Richards and Kavanagh 1943). A limitation of this approach is that the placing of ink marks on the surface of leaves required the tissue to be large enough to access, thus missing early stages during which the major shape transformation occurs.

Longitudinal elongation of the young primordium has previously been studied indirectly through histological characterisation of tissue sections. Cell divisions were predicted to emanate from a region at the apex, suggesting that a meristematic region is located in this zone (Avery 1933, Esau 1977). It was proposed that the early primordium elongates initially through apical growth up until a leaf length of 2-3 mm, after which a switch occurs and growth proceeds basipetally (Avery 1933). My dynamic quantification of growth parallel to the leaf midline provides no evidence for apical driven growth. In contrast, I find a proximodistal gradient in growth rates from the earliest stages amenable to tracking, around 0.2 mm length. The pattern of differential growth I observe confirms Avery's findings in leaves at later stages and suggests that a basipetal pattern is present from the early stages of development. This raises the question of how this pattern of growth could be coordinated.

9.4. A proximodistal gradient can account for observed growth rates along the midline

Computer modelling was used to explore how the observed pattern of differential growth along the midline could be generated. Models were developed using a limited set of factors including a growth-promoting factor, PGRAD. In a simulation in which an initially linear gradient of PGRAD was fixed to the tissue, the pattern of resultant growth rates was similar to

those observed experimentally. The slope of growth rates changed from a linear drop to exhibiting an extended downward curve at later stages (Figure 9-2). This is because regions with the highest concentration of PGRAD, grow faster and extend more than regions with lower concentrations of PGRAD. Mathematically recapitulating experimental observations in a simplified modelling environment helps to clarify how they might be coordinated biologically. Models are underpinned by the idea that a gradient of a growth-promoting factor is fixed to the tissue and deforms with growth. This suggests that cells may have a mechanism to retain growth rate information and transmit it to their progeny, via a kind of ‘memory’.

Our initial model was not sufficient to capture the observed temporal variation within the growth pattern: growth rates dropped in all regions of the leaf through time. The global drop in growth rates could be accounted for by incorporating a factor that functions to negatively regulate growth rates at the later stages. Thus, a prediction is that a molecular regulator may become active at the later stages of development to negatively influence growth rates via some sort of ‘timer’.

The modelling described here shows how a differential pattern of growth rates could be coordinated in one-dimension (1D) by the graded distribution of a factor. Thus, a mechanism based on long-range signalling could coordinate growth across the tissue: cells exhibit growth rates dependent on the concentration of growth-promoting signal they receive. The model also suggests a degree of cell autonomous control, since the concentration of PGRAD is subsequently ‘remembered’ or maintained by individual cells and their progeny. To explore if such a hypothesis could be extended to account for growth patterns in 2D, I analysed patterns of growth across the leaf surface.

9.5. Areal growth rates in the epidermis exhibit a complex spatiotemporal pattern

Plotting areal growth rates across the surface of the lamina revealed a complex pattern that varied in space and time ((Kuchen, Fox et al. 2012) Fig. 1., reproduced here in Figure 9-3). Areal growth rates were highest towards the lamina base and in lateral regions, and were

generally lower along the midline and towards the tip. These data are broadly consistent with the pattern of growth rates described previously for the tobacco leaf (Avery 1933, Richards and Kavanagh 1943) and Xanthium (Erickson 1966) and provide a new opportunity to explore the role of anisotropic growth in shape formation.

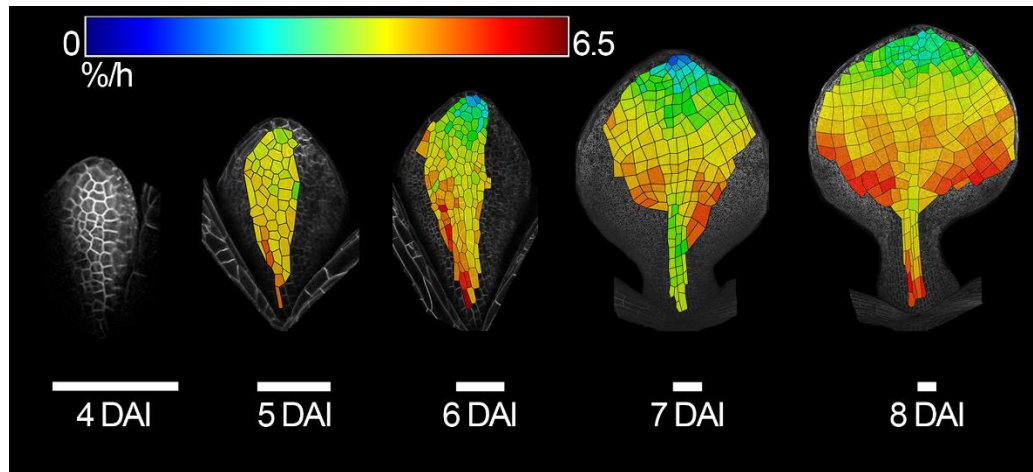


Figure 9-3. Leaf growth analysis in 2D. Areal growth rates (heat map) at the end of each period. Scale bars, 100 μm . Adapted from Kuchen, Fox et al. 2012.

Areal growth rates can be decomposed from growth tensors in each region to reveal the relative contribution of growth in the major and minor orientations. In addition, growth relative to any other orientation can be evaluated mathematically. Decomposing areal growth rates relative to the overall organ axes revealed how the patterns of growth aligned with longitudinal extension of the primordium and lateral expansion of the lamina ((Fox, Southam et al. 2018) Fig. 1., reproduced here in Figure 9-4). Growth rates parallel to the leaf midline for the whole leaf surface amenable to tracking showed a proximodistal pattern similar to that observed for the midline region alone. In contrast, plotting growth in the mediolateral orientation (perpendicular to the midline) revealed that growth rates increase with proximity to the lateral boundaries and decrease towards the leaf midline. These observations may be key to understanding how organ outgrowth is coordinated. The presence of small cells close to the margin has previously been interpreted as evidence for high rates of cell proliferation. This formed the basis of the idea that a meristem coordinates lamina outgrowth through control of

orientated cell division. An alternative hypothesis is that proximodistal and mediolateral leaf expansion could be coordinated through coordinated patterns of orientated growth.

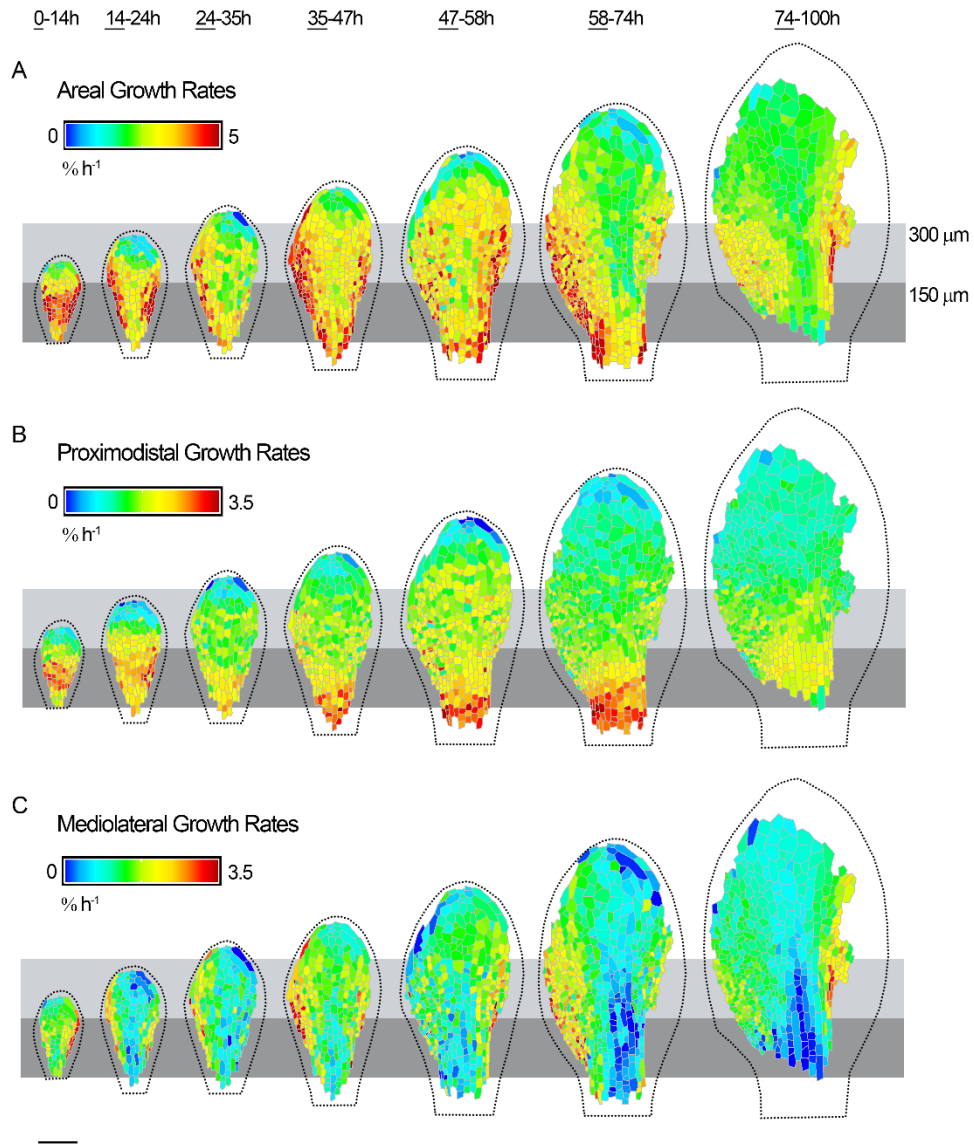


Figure 9-4. Dynamics of growth in the *spch* epidermis. Time-lapse imaging of a *spch* leaf at approximately 12-h intervals over 4 d (0–100 h; last time point in series not shown). Data shown on the first time point (underlined) for each tracking interval. Leaf widths for the first time point (left to right) are 0.15, 0.22, 0.27, 0.31, 0.39, 0.48, and 0.68 mm. (A-C) Cellular growth rates (heat maps) for each tracking interval. (A) Areal growth rates. (B) Growth rates parallel to the midline (proximodistal). (C) Growth rates perpendicular to the midline (mediolateral). Leaf outline indicated by dotted black line. Grey boxes are aligned to the petiole-lamina boundary and extend to 150 or 300 μm. Scale bar, 100 μm. Adapted from Figure 1 of Fox, Southam et al. 2018.

9.6. Leaf growth is highly anisotropic

Despite the limitations of the methodology and mathematical analysis, Avery postulated that differentially distributed growth, which he termed 'localised growth', together with 'polarised growth' (greater growth in one dimension than another, now termed anisotropy) are together responsible for the shape of the organ (Avery 1933). This hypothesis is based on the profound understanding that the patterning of growth itself should be considered in addition to the patterns of cell division. As will be discussed later, many subsequent studies used markers of cell division as a proxy with which to make predictions of how growth of the organ could be coordinated. The growth anisotropy of the tobacco leaf surface was captured by the quantification of relative growth rates to produce the orientations of maximum and minimum growth rates for each segment (Richards and Kavanagh 1943). Although this analysis provided only a crude approximation of leaf growth, it is clear from the figures that major orientation of growth varies across the surface of the lamina, implying a role for growth anisotropy. The contribution of anisotropic growth has been questioned by subsequent reports in *Xanthium* (Erickson 1966) and tobacco (Poethig and Sussex 1985) that concluded leaf growth is largely isotropic.

The role of isotropic growth has recently been explored mathematically through conformal mapping in which local angles are preserved after transformational displacement through growth. One report suggested that around 90% of the overall displacement field of organ growth could be accounted for by conformal transformations (Alim, Armon et al. 2016). Another study suggested conformal leaf growth could be accounted for through differential patterns of isotropic growth coordinated according to a linear gradient of a diffusible signal molecule (Mitchison 2016). These analyses did not fully consider regional and temporal variations in anisotropy that may be more important at earlier stages of development.

My analysis provides a dataset from which a detailed quantification of the spatiotemporal dynamics of the surface relative growth rates could be carried out and from which the contributions of growth in different orientations could be evaluated. Characterisation of the spatiotemporal dynamics of the major orientations of growth in the *Arabidopsis* leaf showed a complex dynamic pattern of anisotropic and isotropic growth

((Kuchen, Fox et al. 2012) Fig. 1., reproduced here in Figure 9-5). I found growth to be highly anisotropic at the earliest stages visualised. The major orientations of growth at this stage are aligned broadly parallel to the proximodistal axis of the leaf. This is consistent with the idea that primordium first elongates preferentially along this direction after organ initiation, prior to lamina outgrowth. Dynamic tracking revealed a nuance to this pattern that had not been previously predicted. Growth orientations converge towards the leaf tip in distal regions. Furthermore, at later stages of development, I observed that lamina regions close to the midline exhibit oblique orientations of growth. Orientations appear to splay out from the midline and angle towards the leaf margin. In some regions of the lamina growth is isotropic. At the latest stage tracked, I observed a switch in orientation with major orientations of growth aligned predominantly with the mediolateral axis of the leaf. Some of these features were also captured by an independent study that quantified growth patterns in three dimensions via the displacement of fluorescent beads (Remmler and Rolland-Lagan 2012). Growth anisotropy was observed from the earliest stages analysed and found to decrease together with growth rates as leaves reached maturity.

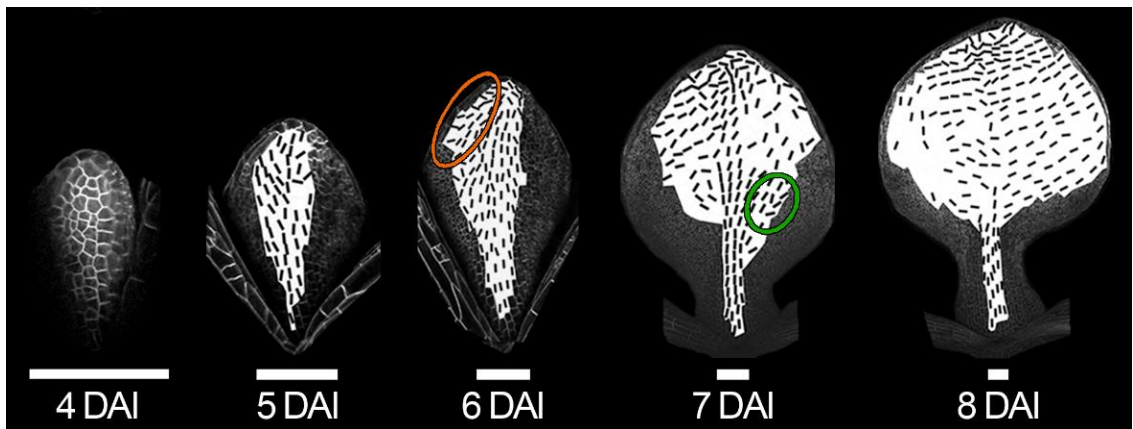


Figure 9-5. Principal directions of growth. Black lines, where anisotropy > 10%) at the end of each period. Scale bars, 100 μ m. Adapted from Kuchen, Fox et al. 2012.

This detailed quantitative analysis serves to resolve previous inconsistencies in the literature and add weight to the importance of growth anisotropy in shaping a leaf. My dynamic description of epidermal leaf growth confirms the extent and character of anisotropic

growth that underpins early leaf development. This raises the question of how such a highly coordinated pattern of anisotropic growth could be coordinated.

9.7. Leaf shape can be coordinated through tissue polarity

The pattern of differential anisotropic growth described here raises the question of how the principle orientations of growth are defined and coordinated *in planta*. A hypothesis to account for how organ shape and tissue polarity could be coordinated by underlying tissue polarity organisers has previously been proposed to account for the shape of the snapdragon (*Antirrhinum*) flower (Green, Kennaway et al. 2010). This theoretical framework has the benefit of abstracting away from cells and considers a continuum of interconnected tissue. Due to experimental constraints, the snapdragon model could not be validated with direct observations of tissue growth patterns. The *Arabidopsis* leaf offered an opportunity to explore if a similar framework may help explain organ formation in an experimental system in which models could be evaluated against quantitative dynamic data.

Models were implemented in 2D using the GPT framework. Local growth orientations are specified parallel and perpendicular to the proximodistal gradient of a factor distributed through the canvas, POLARISER (POL). The distribution of POL is maintained parallel to the midline and is independent of tissue deformations. Growth rates depend on the activity of factors that promote or repress growth and simulate the action of genes. Mechanical constraints also affect growth since the tissue is interconnected, as such neighbouring regions influence the growth of each other. Thus, resultant growth rates do not match exactly to the underlying specified rates. Starting with a canvas shape based on the shape and size of a young primordium, running the model generated shape changes and patterns of growth rates and orientations that broadly match those observed experimentally ((Kuchen, Fox et al. 2012) Fig.1, reproduced here in Figure 9-6 A,C).

It is not clear how such a non-deforming orthogonal pattern of POL could be coordinated biologically. We explored an alternative method of POL propagation in which the polarity field deforms with feedback from geometry and tissue growth. The gradient of POL is generated by the antagonistic effects of production at the base by an identity factor and

degradation everywhere else at a constant rate. Propagation rates of POL were varied such that the initial distribution of POL was fixed to the initial canvas or at the other extreme, continuously deformed with the tissue. Both models generated similar patterns of resultant growth and orientations that matched experimental observations better than the non-deforming model (Figure 9-6 B,D).

The modelling described here suggests a mechanism by which genes can control orientated growth according to an underlying biochemical-based polarity system.

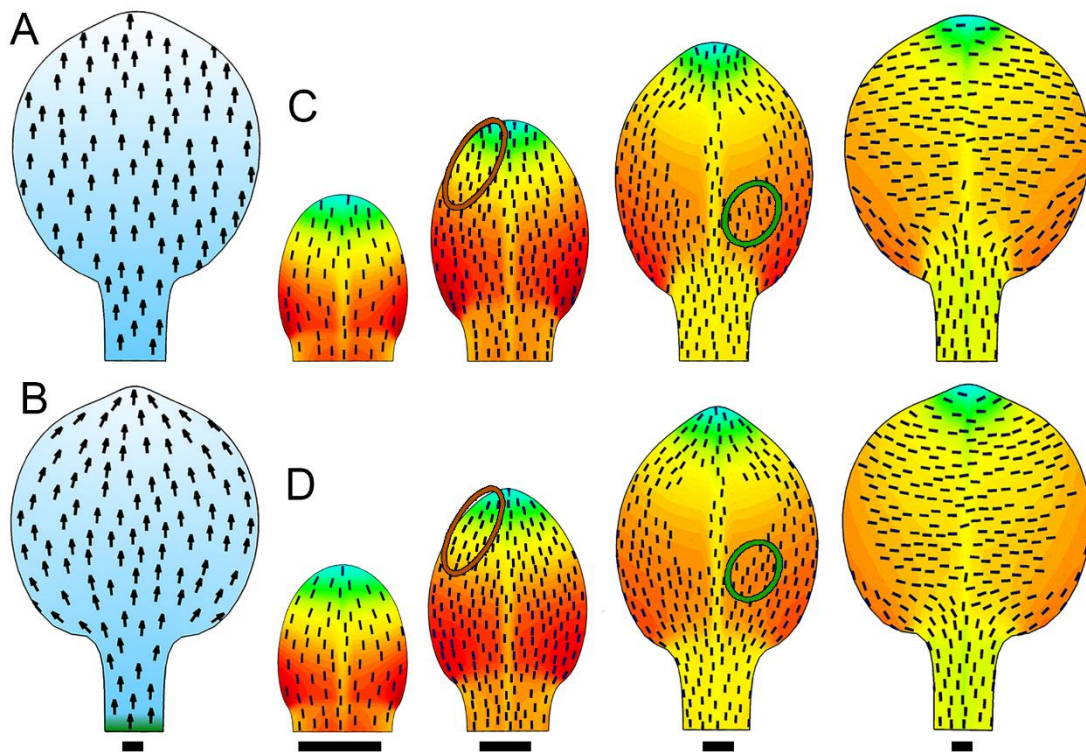


Figure 9-6. 2D models. (A) Resultant shape, POL levels and specified growth orientations (arrows) for nondeforming and (B) deforming (organiser based) models. (C) Resultant shapes, areal growth rates, and directions of growth (black lines, where anisotropy > 5%) for 2D nondeforming and (D) deforming (organiser-based) models. Heat map and staging as in Figure 9-3. Scale bars, 100 μm . Adapted from Kuchen, Fox et al. 2012. Models were generated by Erika Kuchen.

9.8. Leaves are not able to repattern and regenerate following excision

A key feature of the leaf models is that the spatial pattern of growth rates is established early in development. There is no implication that leaves could spontaneously repattern growth and regenerate tissue to reach a predetermined final size. This hypothesis was undermined by a report that suggested young leaves retain the ability to regenerate following distal leaf excision (Sena, Wang et al. 2009).

To explore this possibility, I made precise excisions of young leaf tissue and used live-imaging to monitor any subsequent changes at tissue level. I found no evidence of re-patterning or re-generation. In contrast, I found rates below the point of excision largely unchanged except for narrow regions very close to the site of excision which appeared slightly reduced in growth ((Kuchen, Fox et al. 2012) Fig. 3., reproduced here in Figure 9-7).

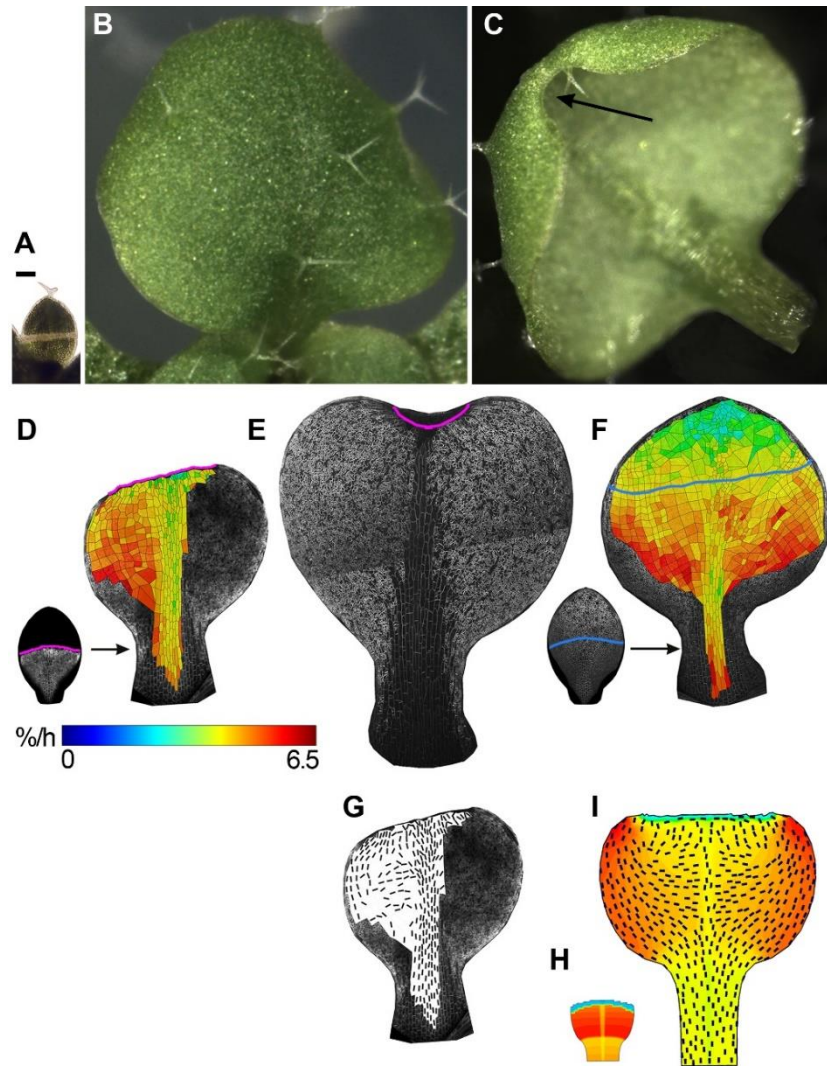


Figure 9-7 Distal leaf excision. (A) Excision of the distal half of leaf 1 lamina at 6 DAI. Distal region was removed after laser cut (pale line). (B) Leaf 1, 6 days after distal excision, viewed from the top and (C) from lower (abaxial) side, showing a curved indentation at the tip (arrow). (D) Leaf 1 cut at 6 DAI (left) and tracked until 9 DAI (right). Areal growth rates (heat map) calculated over the last 24 hours of tracking. Boundary of cut highlighted with magenta line. (E) Leaf after tracking growth for 5 days after distal excision. (F) Tracked uncut leaf with a blue line shown at a similar position to the cut in (D). (G) Principal directions of growth (black lines, where anisotropy >10%) for leaf shown in (D). (H) Excision of the distal half of the canvas and (I) output after growth according to the organizer-based model, showing areal growth rates and resultant directions of growth (black lines, where anisotropy >5%). Scale bar, 100 mm. From Kuchen, Fox et al. 2012. Models in (H) and (I) were generated by Erika Kuchen.

The leaf model was modified to simulate distal leaf excision. Resultant patterns of growth rates and the final organ shape matched well to experimental observations. The model helps to explain how previous results could have been misinterpreted. Excision of a relatively large proportion of the young leaf results in only a small absence of material at later stages because of differential growth rates.

9.9. The pattern of clones does not support the hypothesis that cell division is focused at the margin

Thus far I have discussed how the orientations of growth in the lamina region broadly align with the mediolateral leaf axis at later stages. Furthermore, I have shown that quantifying growth rates confirms earlier predictions that growth is indeed higher in the lamina compared to other regions. These findings appear to support the idea that a region at the margin is important for coordinating lamina outgrowth, yet do not explicitly imply a role for coordinated cell division as has previously been proposed.

The idea that lamina outgrowth is coordinated through orientated cell division at the abaxial-adaxial leaf boundary underpins a model that generates a flat-leaf structure (Hayakawa, Tachikawa et al. 2016). A simulated cross-section of a leaf was generated through mutual inhibition of adaxial-abaxial identities if cells at the margin divide periclinally to maintain flatness. The tissue extends laterally from the margin because after a cell divides, the daughter cell closest to the margin will be next to divide again. A file of related cells was generated maintaining the boundary between cell identities. This model implies that the adaxial-abaxial boundary provides a polarity bias to control the cell division axis. If cell division is restricted to the margin, it should be possible to visualise this by tracing cell lineages.

Clonal analysis has previously been used as a tool to investigate cell lineage and the origin of leaf tissue in tobacco (Poethig and Sussex 1985). The method used to generate clones was based on irradiation to generate a cell-autonomous mutation, visualised by a colour change of the tissue from yellow to dark green. Variation in mutation frequency was linked to cell cycle and thus frequency of cell division. In contrast to what might be expected, no clones

were observed to extend from the margin to the midline. Thus, the orientation and frequency of cell division close to the leaf margin was interpreted to play a minor role on the overall growth of the organ.

Direct tracking should provide unequivocal evidence on the patterns of divisions close to the margin. Unfortunately, the most lateral regions of the leaf, particularly regions close to the leaf base, are not easily visualised in intact seedlings. This is due to the curvature of the leaf rendering these regions too far away and at an oblique angle from the microscope objective. Furthermore, at early stages, primordia are obscured by the petioles of overlying cotyledons. Growth in lateral regions of *Arabidopsis* leaves has been visualised by others using a long working-distance water immersion objective (Vuolo, Kierzkowski et al. 2018). The optical-imaging chamber is a sealed sterile unit, in which multiple seedlings can be visualised through a coverslip. This system is not compatible with water immersion objectives. It is possible that seedlings could have been mounted at a sideways angle with respect to the coverslip, however this proved technically difficult to achieve without damaging other parts of the seedling. As an alternative, I used clonal analysis to estimate patterns of growth across the full surface of the leaf. The expression of GFP is induced via by a 2-component transgenic system mediated by *Cre-lox* recombination (Gallois, Woodward et al. 2002). After a brief heat shock, cells are randomly induced to express GFP cell autonomously, independent of the cell cycle. By limiting the duration of heat shock, the number of induced cells is reduced and a random spread of clones generated. The timing of heat shock and subsequent imaging of flattened leaves was matched to complement the developmental stages captured by live imaging. Since clonal analysis could be carried out on seedlings grown on plates, this approach also had the benefit of providing a qualitative validation of growth parameters generated from plants grown in the chamber.

The size, shape and orientation of induced clones matched well those generated by tracing cell fates from live-imaging data ((Kuchen, Fox et al. 2012) Fig S6, reproduced here in Figure 9-8). Clones appear evenly distributed across the surface with no clear bias in any region. A statistical analysis could be carried out to confirm this. In contrast to what may be expected if division was concentrated at the leaf margin, I found few clones to be in direct

contact with this region. Furthermore, the pattern of clones does not splay out from the margin. My analysis confirms cell division is dispersed across the leaf surface.

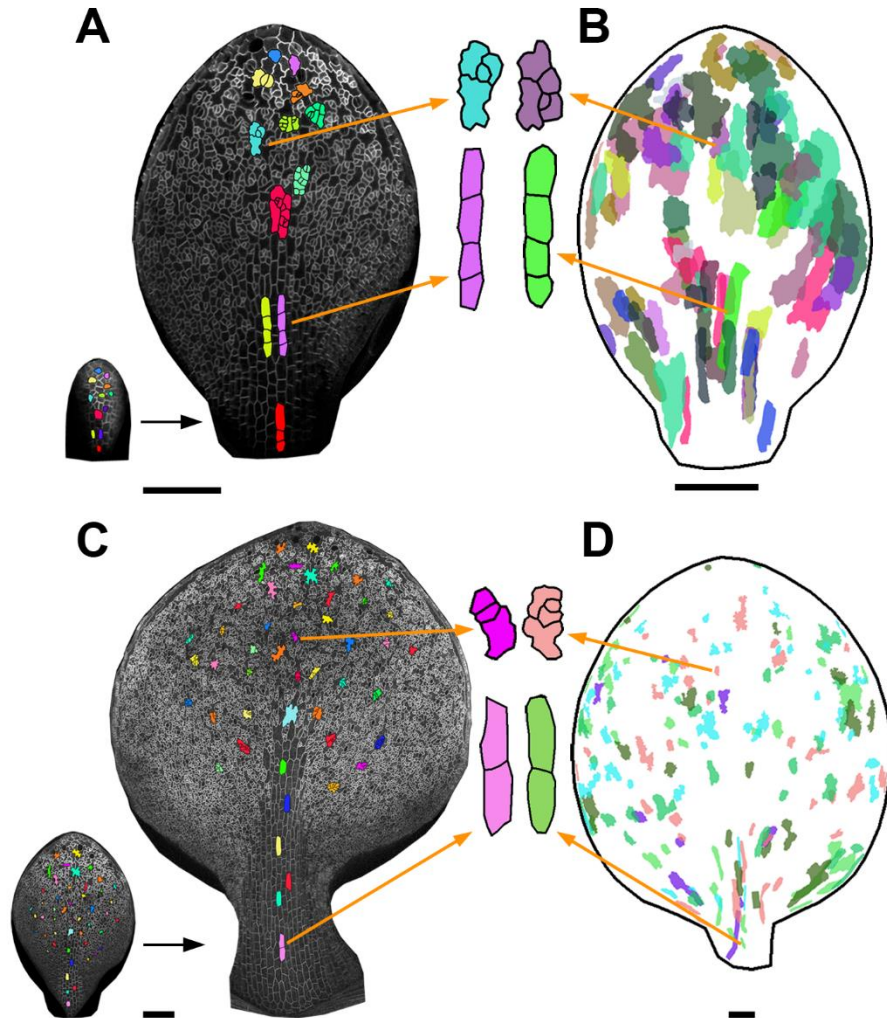


Figure 9-8 Validation of direct tracking using clonal analysis. (A and C) Cell fates from time-lapse imaging: (A) Cells tracked from 4 DAI (small leaf on left) to 6 DAI (right leaf) and (C) from 6 DAI (left leaf) to 8 DAI (right leaf). Examples of tracked clones are shown enlarged. (B and D) Clones induced at 3 DAI (B) or 6 DAI (D) and imaged at comparable developmental stages to (A) and (B) respectively (6 DAI and 9 DAI). Clones from several leaves have been superimposed. Scale bars, 100 μ m. From Kuchen, Fox et al. 2012.

Clonal analysis combined with dynamic patterns of growth captured through live imaging provides a detailed description of the changes taking place throughout the entire epidermal surface during early leaf development. These provide evidence that leaf morphogenesis is coordinated across the surface through orientated patterns of growth and dispersed patterns of cell division. Biologically, tissue grows by the combined processes of cell division and cell expansion. A key question to address is how these processes are integrated within a growing tissue.

9.10. Integrating patterns of growth and cell division

Patterns of cell proliferation have previously been predicted from fixed specimens according to the expression of a molecular marker of cell cycling. Localisation of *cyc1At::GUS* indicated that cell division is not restricted to cells at the boundary between cell surfaces in *Arabidopsis*, as has been predicted (Hayakawa, Tachikawa et al. 2016). Cells ceased cycling in this region long before those of other leaf tissues (Donnelly, Bonetta et al. 1999). Mitotic cells were initially observed throughout the leaf and gradually became restricted towards the leaf base. This finding was linked with patterns of high growth in basal regions (Avery 1933) and supported the idea that patterns of growth could be inferred from regions undergoing cell division. These data lead to the suggestion that cell cycling related to differentiation of specific cell types is superimposed on that of general, proliferative cell divisions. Secondary, differentiating divisions were predicted to occur with a distinct spatial pattern that was maintained for longer than proliferating divisions (Donnelly, Bonetta et al. 1999). These findings align less with the term marginal or plate 'meristem' since no evidence was found for stem cell initials. Instead, the term 'marginal blastozone', has been proposed to better reflect that growth and division may be coordinated in a specific region that is competent for organogenesis (Hagemann and Gleissberg 1996).

By simplifying my analysis to ignore cell division and consider how patterns of anisotropic growth could be coordinated in isolation we were able to generate a model that accounts for leaf morphology through a reductionist approach independent of the unit of the cell. In order to fully understand the process of leaf morphogenesis it was necessary to explore

how patterns of cell division and cell sizes relate to the observed patterns of growth and determine how these features could be integrated to shape a leaf.

9.11. The relationship between cell division and growth can be explored in the *spch* mutant

Analysing patterns of cell proliferation in the epidermal leaf surface through direct tracking or via static images of cells undergoing mitosis is complicated because divisions leading to the differentiation of specialised cell types are interspersed with general proliferating divisions. It has been proposed that general proliferating divisions are the primary contributor to leaf morphogenesis and are coordinated by an independent regulatory pathway to the dispersed differentiating divisions (Donnelly, Bonetta et al. 1999, White 2006).

The abaxial surface of *Arabidopsis* leaf one comprises many stomata which function to facilitate gas exchange. The *speechless* (*spch*) mutant lacks divisions in the stomatal lineage and exhibits a considerably simplified pattern of divisions (MacAlister, Ohashi-Ito et al. 2006). When grown on soil or plates, *spch* plants are small and pale (MacAlister, Ohashi-Ito et al. 2006). In the optical-imaging chamber, in which seedlings are submerged under liquid, leaf one of *spch* is similar in size and shape to WT ((Fox, Southam et al. 2018) S14 Fig., reproduced here in Figure 9-9).

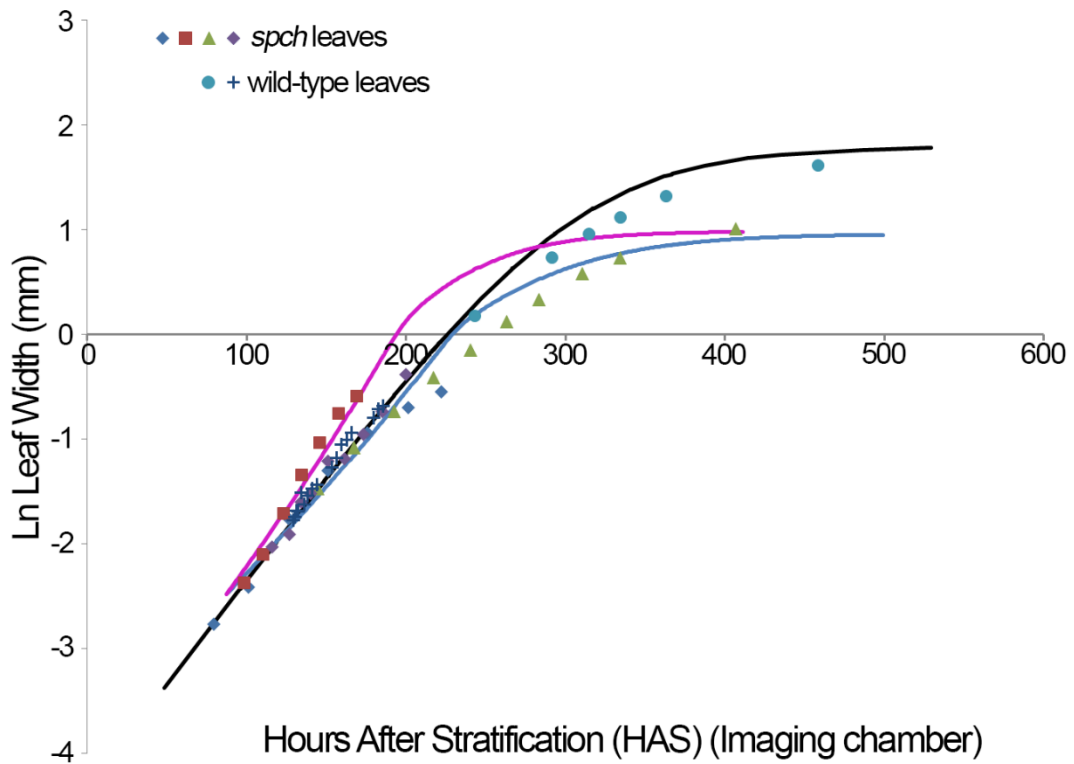


Figure 9-9. Comparison of wild-type and *spch* grown in the imaging chamber. Measurements of leaf 1 from six independent tracking experiments, two wild-type individuals, and four *spch* individuals (colour key). The initial data point from each tracking experiment was normalised to the wildtype logistic curve (solid black line) to enable subsequent growth rates to be compared. Pink line shows output leaf widths for the model. Blue line shows output for the leaf model tuned to match *spch* growth in the chamber at later stages. From S14 Fig. of Fox, Southam et al. 2018.

The finding that environmental conditions can mitigate the *spch* growth defect suggests it is at least partly physiological in nature and due to the lack of functioning stomata rather than changes in the pattern of cell proliferation *per se*. Furthermore, this finding suggests that the size and shape of a mature leaf is at least partially independent of the differentiating divisions that form part of the stomatal lineage. This hypothesis is supported by comparing the phenotype of *spch* leaves to those of the *fama* (basic helix-loop-helix transcription factor bHLH097) mutant. Leaves of *fama* lack functioning stomata yet retain asymmetric divisions in the stomatal lineage (Ohashi-Ito and Bergmann 2006). I found that *fama* mutant leaves attained only slightly larger width to *spch* mutants when grown on plates, consistent with the lack of stomata being the primary cause of reduced growth ((Fox, Southam et al. 2018) S14 Fig., reproduced here in Figure 9-10). Time-lapse imaging of a developing *spch* leaf provided a dataset from which the spatiotemporal patterns of pavement cell divisions and growth rates could be analysed.

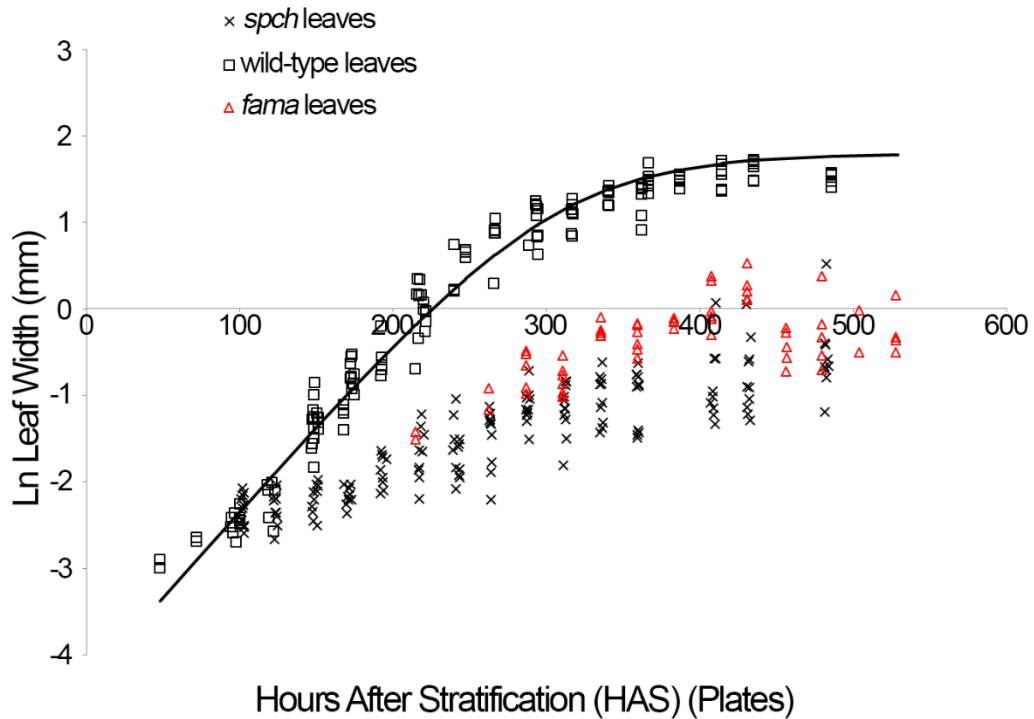


Figure 9-10. Comparison of wild-type, *spch* and *fama* leaf widths. Width measurements of leaf 1 from wild type, *spch* and *fama* seedlings grown on plates. The fitted growth curve of wild type (solid black line) was based on a logistic calculation of leaf widths (open squares). Adapted from S14 Fig. of Fox, Southam et al. 2018.

9.12. A proximal zone of division competence explains the dynamics of cell division

Tracking cell division competence in *spch* revealed a coordinated pattern of division competence in the epidermal layer ((Fox, Southam et al. 2018) Fig. 1., reproduced here in Figure 9-11). Cells were competent to divide in a specific proximal corridor that spans the width of the leaf. The zone of epidermal division competence has a fixed distal limit that extends through growth to a maximum of approximately 300 μm from the petiole-lamina

boundary. The competence zone later retracted to the base of the leaf. Retraction occurred earlier in the midline region than in the lateral lamina.

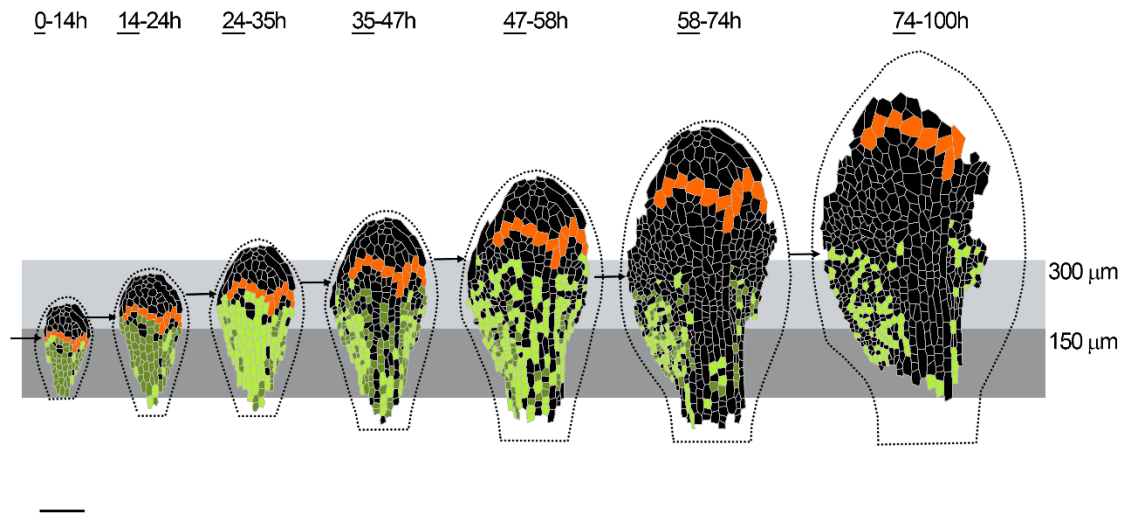


Figure 9-11. Dynamics of cell division in the *spch* epidermis. Time-lapse imaging of a *spch* leaf at approximately 12-h intervals over 4 d (0–100 h; last time point in series not shown). Data shown on the first time point (underlined) for each tracking interval. Leaf widths for the first time point (left to right) are 0.15, 0.22, 0.27, 0.31, 0.39, 0.48, and 0.68 mm. Cells amenable to tracking that were competent to divide (green), and either executed division during the interval (light green) or divided in a later interval (dark green). Cells that did not divide (black, first row in 0–14 h are coloured orange throughout). For the last interval (74–100 h), cell divisions could only be tracked for a subset of cells because of missing data points at 100 h. Leaf outline indicated by dotted black line. Grey boxes are aligned to the petiole-lamina boundary and extend to 150 or 300 μm . Scale bar = 100 μm . Adapted from Figure 1 of Fox, Southam et al. 2018.

Analysis of wild-type leaves confirmed that the dynamics captured in *spch* are applicable to cells that do not form part of the stomatal lineage in wild type (Fox, Southam et al. 2018) Fig.7., reproduced here in Figure 9-12). These spatiotemporal dynamics help clarify previous predictions based on snapshot images and can be used to evaluate the idea that leaf growth is coordinated at the margin.

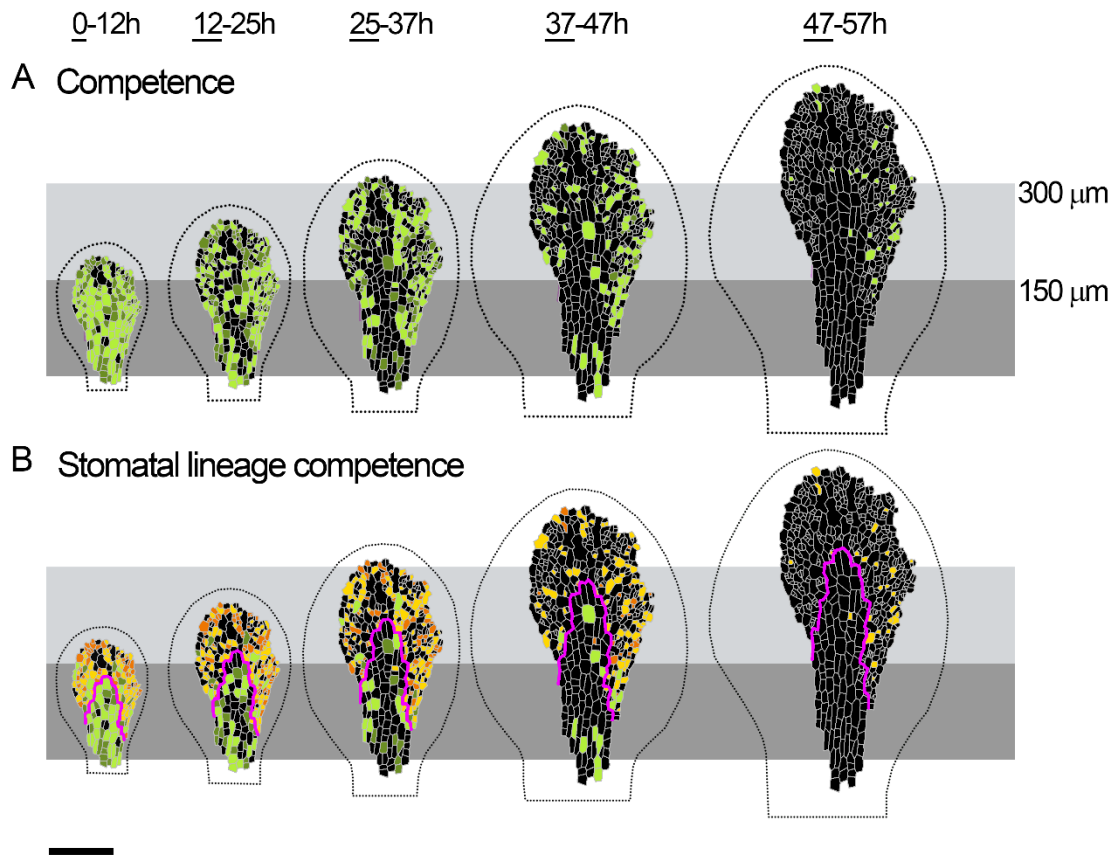


Figure 9-12. Dynamics of cell division in the wild-type epidermis. Cells amenable to tracking from time-lapse imaging of a wild-type leaf at approximately 1-h intervals over 2.5 d (0–57 h, last time point in series not shown). Data are visualised over about 12-h intervals and shown on first time point (underlined) for each interval. Leaf widths for first time point (left to right) are 0.17, 0.23, 0.28, 0.39, and 0.42 mm. (A) Cells amenable to tracking that were competent to divide (green) and either executed division during the interval (light green) or divided in a later interval (dark green). Cells that did not divide (black). (B) Non-stomatal divisions coloured as for (A). Stomatal lineage divisions that executed division during the interval (yellow) or divided in a later interval (orange). Leaf outline indicated by dotted black line. The petiole-lamina boundary was defined as described in Fig 1. Grey boxes are aligned to the petiole-lamina boundary and extend to 150 or 300 μm . Cells within the magenta lines were assigned as being destined to form the midline according to their position and shape in the final image. Scale bars, 100 μm . Adapted from Fig 7 of Fox, Southam et al. 2018.

The smallest leaves tracked were around 100 μm width and 150-175 μm length, appearing as a dome-shape. At this stage, cotyledons obscure the most lateral and basal regions, such that only cells in the middle and tip regions can be visualised. Epidermal cells are similar in size and shape across the surface. Tracking only the cells that are visible in the first time point (excluding those that become visible as the leaf grows and flattens) reveals that their progeny form the central and distal region of the leaf in the final time point ((Fox, Southam et al. 2018) S2 Fig, reproduced here in Figure 9-13). Cells in the central region were classified as forming the midline (within the black outline) based on their elongated shapes. The rest of the leaf tissue must originate from the region between tracked cells and leaf outline in the first image.

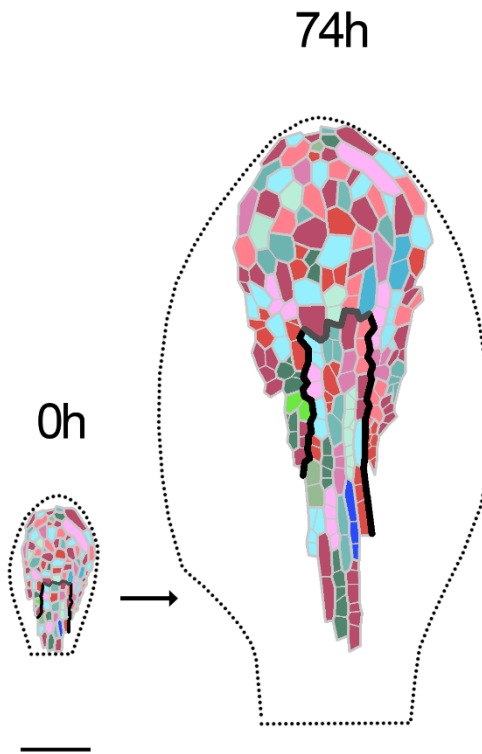


Figure 9-13. Assignment of the midline and lamina regions. Lineages were traced from cells visible at the beginning of the experiment (0 h, left) through to the end (74 h, right) and were assigned an arbitrary colour. Cells in the midline (within the black outline) were identified using the position and shape of clones (cells of the same lineage) in the final image, as was the approximate position of the distal end of the midline (dark grey). Cells outside the midline region were classified as being in the lamina. Scale bar, 100 μm . From S2 Fig. of Fox, Southam et al. 2018.

The displacement of tissue through non-uniform growth is captured by the growth model and can be visualised through the deformation of a regular grid superimposed onto the surface ((Kuchen 2011), reproduced with permission in Figure 9-14). Higher rates of growth in the base region of the leaf, coupled with the restriction on growth in the midline in the mediolateral orientation, result in non-uniform deformation. The highlighted region comprises 39% of the grid in the first time point and 72% in the final time point.

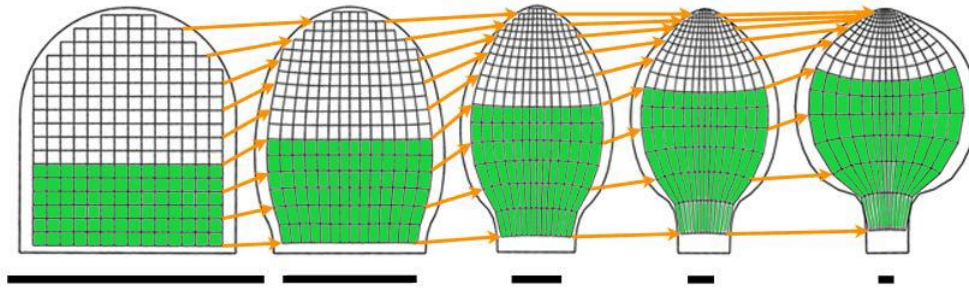


Figure 9-14. Canvas deformations. The canvas non-uniformly deforms with growth as demonstrated by a superimposed grid. Note how the squares are wider towards the margin in the last timepoint. Scale bars 100 μm . Adapted from Kuchen 2011.

The observation that differential orientated growth is associated with lamina outgrowth helps clarify previous hypotheses. I show here that divisions are not restricted to cells at the adaxial-abaxial epidermal boundary. In contrast, divisions are dispersed across the tissue in a pattern that forms a proximal zone of division competence. This pattern is broadly consistent with the idea that division is coordinated in a blastozone. The challenge of understanding thus becomes how changes at the cellular level are integrated to generate the observed patterns at the tissue level. The temporal and spatial dynamics of the zone of division competence provides a unique opportunity to explore how mechanisms underlying the control of cell division and the timing of division arrest contribute to organ growth and how these processes relate to cell expansion.

9.13. Dynamics of the competence zone explains the cell cycle arrest front progression

The dynamics of cell division arrest underpin much of current thinking relating to leaf morphogenesis. Conceptually, if cells continue to divide for longer, the leaf could end up with more cells and reach maturity at a larger size and potentially with an altered shape, assuming cells attain their final size. The timing of cell division arrest is therefore assumed to influence final leaf size and shape, as exhibited by mutants which have larger leaves and an increased number of cells (Nath, Crawford et al. 2003, White 2006, Li, Zheng et al. 2008).

Cell division arrest and the switch to growth by expansion is associated with leaf maturity and presents with a basipetal pattern (Avery 1933, Esau 1977, Donnelly, Bonetta et al. 1999). The conventional view that a wave of cell division arrest emanates at the leaf tip and progresses gradually towards the leaf base (Donnelly, Bonetta et al. 1999, Nath, Crawford et al. 2003, White 2006) has been superseded by the idea that exit from proliferation is not such a gradual process (Andriankaja, Dhondt et al. 2012). The dynamics of cell cycle arrest were characterised through static images in accordance with leaf size to suggest that rather than a basipetal wave, the primary arrest front associated with proliferating divisions remains at a fixed distance from the leaf base before retracting (Kazama, Ichihashi et al. 2010). A computer simulation in 1D reproduced arrest front positioning by assuming that division is regulated by the concentration of a mobile growth factor. The transition from proliferation to expansion has also been mapped using morphological changes to predict whether cells are proliferative or not (Andriankaja, Dhondt et al. 2012). Cells that are small and round were assumed to be more likely to divide than large jigsaw puzzle-shaped cells. The authors suggested that rather than having an absolute fixed distal limit, the proliferation zone increases in absolute size, while decreasing in relative length in proportion to the leaf overall. These complex dynamics may require multiple underlying processes acting antagonistically to regulate cell expansion and proliferation.

A complication of these experimental approaches is that the dynamics of cell-cycle arrest of epidermal proliferative divisions were difficult to discriminate from differentiating

divisions. Tracking divisions in the *spch* background offered a novel opportunity to explore arrest front dynamics.

9.14. Organ size can be influenced by changes in cell size and/or cell number

Live-imaging revealed a proximal zone of cell division competence (Figure 9-11). Cells outside the competence zone continue to grow after they have ceased dividing thus are larger than those in the competence zone. These direct observations confirm some earlier predictions of division patterns based on the notion that small, round cells are more likely to be mitotic (Andriankaja, Dhondt et al. 2012). Cell size reflects the antagonistic processes of growth through expansion which increases cell size and cell division execution which causes a halving in size after each cell cycle (for symmetrical divisions). Cell size thus may be an emergent feature of the interplay of these processes.

The relationship between cell division and growth is difficult to characterise in the context of a continuously deforming and changing environment. Since the processes are so tightly linked, it can be challenging to disentangle cause from effect. In theory, cell division could drive growth, growth could drive division or independent regulation could act upon both processes. Evidence for a sequential control mechanism appears to be supported by mutants in which changes in cell number appear to be compensated for by changes in cell size (reviewed by (Horiguchi and Tsukaya 2011)). This suggests leaves have a mechanism to maintain overall organ size. In other examples, leaves that are reduced in size have smaller, fewer cells (Horiguchi, Ferjani et al. 2006).

Exploring the correlations between growth and cell division dynamically and in multiple cell layers provided evidence that the relationship may not always be so conserved.

9.15. Cell size is negatively correlated with cell division

Analysis of cell surface area in the epidermis revealed a proximodistal gradient in cell size that correlated with growth rates and competence to divide ((Fox, Southam et al. 2018) Fig 4.). Correlations between cell size and growth rates have previously been reported for the *Arabidopsis* shoot apical meristem (SAM), suggesting an inverse relationship between cell size and cell cycle duration whereby smaller cells take longer to divide than larger cells (Jones, 2017). I found a negative correlation between these features; regions of the leaf exhibiting higher growth rates tend to have smaller cell sizes as well as shorter cell cycle durations. This suggests that correlations between cell size and cell division rates are not universal. It also provides evidence that the mechanism underlying cell size homeostasis in the SAM is not compatible with the shape transformation of determinate organs. There was no fixed threshold of growth rates above which cells were competent to divide; the relationship is not constant for different regions or developmental stages ((Fox, Southam et al. 2018) Fig. 3I). This suggests that though cell size alone cannot accurately define whether a cell is competent to divide, the feature can indicate where divisions are likely to occur within a heterogenic region of a leaf.

Thus far I have described growth dynamics in the epidermal cell layer and abstracted behaviours to the whole organ level. This is supported by the general view that the epidermis plays an important role in coordinating growth (Savaldi-Goldstein, Peto et al. 2007). Genetic chimeras provide evidence that the epidermis influences cell division in the mesophyll, suggesting that this cell type drives expansion of the leaf blade (Marcotrigiano 2010). In *Arabidopsis*, *reticulata* mutant leaves have greatly reduced cell density of internal layers yet almost normal leaf shape (González-Bayón, Kinsman et al. 2006). Nevertheless, cell division has been predicted to continue in the subepidermis after division has ceased in the epidermis (Avery 1933, Donnelly, Bonetta et al. 1999). It is unclear whether the observed relationships between cell division and growth are maintained in this different cell type.

Growing plants under liquid growth media in the chamber renders subepidermal cells more amenable to imaging than they would normally be in live specimens. Since the size of

cells is not conserved, analysing tissue dynamics in the subepidermis offered the opportunity to explore the relationship between growth rates and cell division in these distinct layers.

9.16. The relationship between growth and division is decoupled in the subepidermis

Patterns of cell division and cell growth in the epidermis are highly correlated. One hypothesis to explain this is that these processes are regulatory linked. If this is a conserved feature of organ development then we should expect to see similar correlation in other tissue layers.

Adjacent to the abaxial epidermis lies a layer of subepidermal cells. I used 3D image visualisation software to reveal the subepidermal cell layer from *spch* plants grown in the chamber. I compared patterns of cell division competence, cell size and growth rates to those of the adjacent epidermal layer. Areal growth rates were broadly similar in both the epidermal and subepidermal layers, with rates marginally lower in the subepidermis ((Fox, Southam et al. 2018) S9 Fig., reproduced here in Figure 9-15).

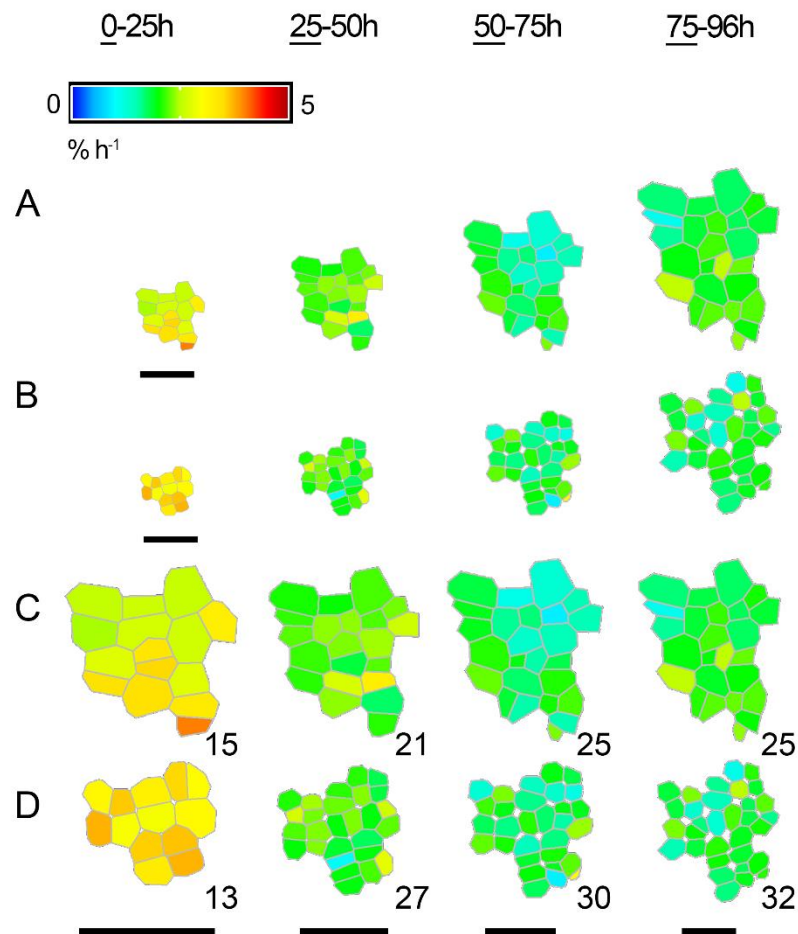


Figure 9-15. Comparison of epidermal and subepidermal cell areal growth rates. Average cell areal growth rates for each tracking interval are shown on the first image of each interval (time point underlined). (A) Epidermis, (B) subepidermis. The patch of cells is also shown at different scales for comparison. (C) Epidermis. (D) Subepidermis, showing increase in number of cells through division compared to the epidermis. Numbers refer to number of cells. Scale bars, 50 μm . From S9 Fig. of Fox, Southam et al. 2018.

This difference in growth rates between layers manifests in the appearance of air spaces between subepidermal cells which become progressively larger over time ((Fox, Southam et al. 2018) Fig. 5., reproduced here in Figure 9-16). This supports the idea that expansion of the leaf is primarily driven by cells in the epidermis.

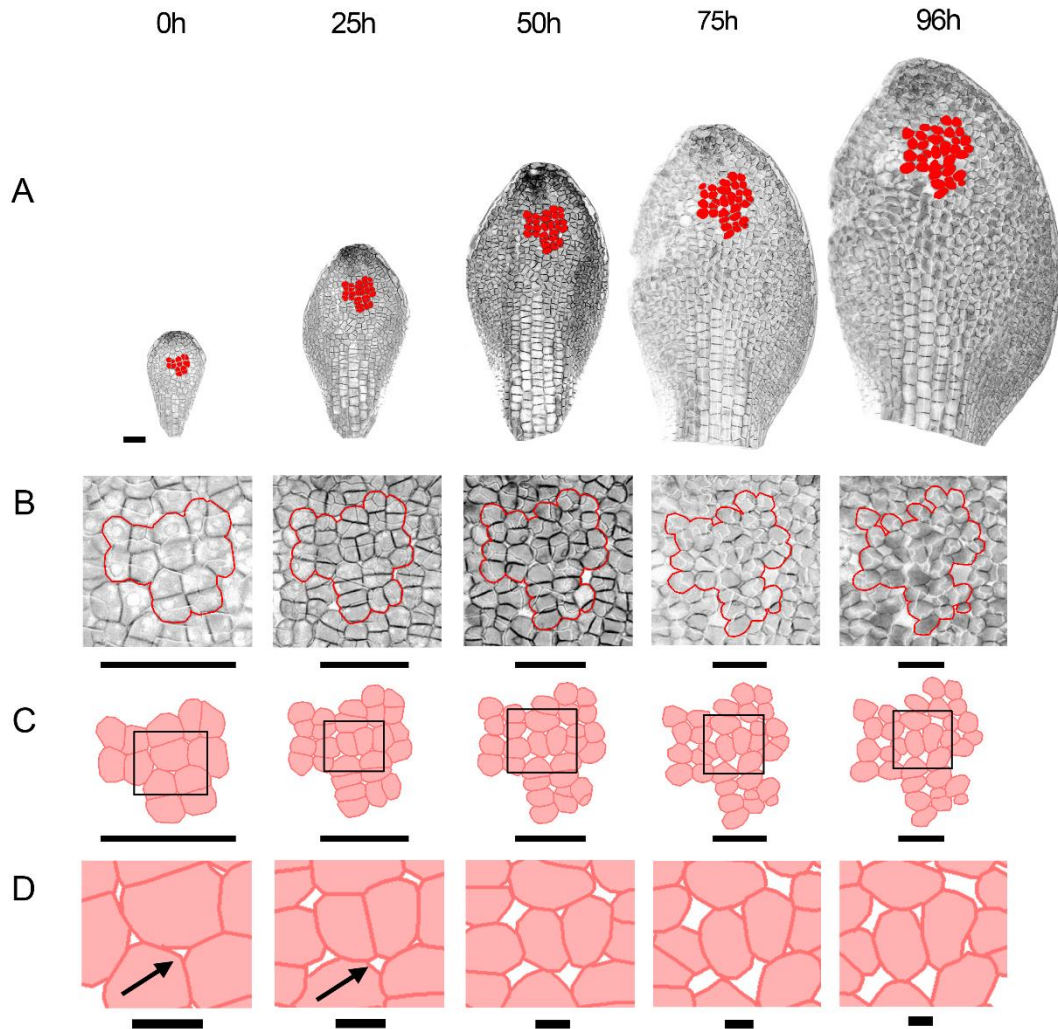


Figure 9-16. Subepidermal cells in *spch*. (A) Projections of the subepidermal layer, imaged approximately every 24 h over 4 d (0–96 h). Leaf widths (left to right) are 0.17, 0.27, 0.39, 0.50, and 0.58 mm. A patch of cells was tracked between intervals (cells coloured red). (B) Enlargement of the patch of cells in (A) (red outline). (C) Cells outlined in (B), showing individual cells (filled pink, outlined red). (D) Enlargement of cells located in the black box of C, showing air spaces (white, examples highlighted with black arrows). Scale bars for A, B, C, 50 μm ; scale bar for D, 10 μm . Adapted from Fig. 5. of Fox, Southam et al. 2018.

Paul Southam generated plots to graphically represent cell sizes in relation to the proximodistal leaf axis. Cell sizes in the distal region of the subepidermis were considerably smaller than the adjacent epidermal cells ((Fox, Southam et al. 2018) Fig. 3AB). This feature can be explained due to an increase in the distal limit of the subepidermal zone of cell division competence, whereby cells continue to divide for longer in the distal region thus reducing cell areas. In contrast to what was observed for the epidermis, we found no difference in the mean growth rates at early stages for competent and non-competent cells in the subepidermis ((Fox, Southam et al. 2018) Fig. 3J). The relationship between growth and division is not conserved in these neighbouring, closely related tissues.

9.17. An integrated model predicts cells execute division at a threshold area that varies spatiotemporally

Understanding how the observed pattern of cell division competence could be generated may help address the question of how cells act as building blocks to shape organs. If the decision-making power lies at the level of the cell, there must be some way for cells to sense overall organ size or developmental age such that division continues until maturity is reached. No evidence for such a mechanism has been identified in plants. An alternative possibility is that competence to divide is regulated at the organismal level. Cells may sense the local concentration of a molecular gradient and execute division according to predetermined thresholds. Concentration gradients thus provide positional information which determines cellular behaviour.

In this work I have discussed the hypothesis developed through computer modelling that indicates that leaf shape may be generated through early patterns of growth and tissue polarity. The information provided by tracking cell proliferation prompted the opportunity to explore how growth could manifest at the cellular level through patterns of division execution and cell expansion.

Computer modelling was used to explore how the observed dynamics in division competence could be regulated. Since the relationship between growth and division was

observed not to be constant, we explored how control of these processes could be achieved independently. For simplicity, a limited number of components was used to represent genetic networks underpinning control of cell division and growth.

The leaf growth model (Kuchen, Fox et al. 2012) was adapted to account for the pattern of division competence by the incorporation of a superimposed layer of polygons to represent virtual cells (v-cells). A proximal mobile factor (PMF) is generated at the petiole-lamina boundary and distributed through the canvas creating a concentration gradient. PMF is not fixed to the tissue, thus the profile gradient does not change in response to deformation of the tissue. Competence to divide is specified by a factor (CDIV) that is expressed when v-cells encounter a concentration threshold of PMF. A second component reflects the observed variation in cell area at time of division execution and ensures cell division is executed at threshold area that varies around a mean. This interaction introduces a cross-dependency between growth and division, since cells grow to reach the threshold size before executing division. Components of the underlying growth regulatory network (PGRAD, and MID) function to modulate the threshold area for division. The pattern of v-cell areas and competence to divide broadly matched those observed in the subepidermis ((Fox, Southam et al. 2018) Fig. 8EF).

A further dependency on CDIV that also requires PGRAD to be above a threshold level accounts for the differences observed in the epidermis and reproduces the extension of the zone of division competence coincident with tissue growth ((Fox, Southam et al. 2018) Fig. 8GH). Earlier retraction of competence in the midline is achieved if MID is inhibited when LATE reaches a threshold value. Thus, the observed patterns of cell division competence and cell areas can be accounted for in different cell layers by varying the interactions controlling cell division.

A key aspect of these models is that components of cell division and cell expansion are regulated independently via a dual control mechanism with cross connections. The cross dependency between cell size and division execution suggests that control of division is influenced cell-autonomously and predicts cells have a geometric size-sensing mechanism. Feedback from cell size to growth could also explain why cells close to the distal tip appear to

have an upper size limit, if maximum cell size checkpoint feeds back to inhibit growth. Cell size reductions in *Arabidopsis* leaves with manipulated cell cyclin components suggest that the relationship between cell size and division frequency can be altered genetically (Kuwabara, Backhaus et al. 2011).

9.18. The relationship of cell division plane and orientation of growth

Throughout leaf growth, new cell walls in the epidermis are aligned perpendicular to the surface, with the consequence that a single layer of cells is maintained (Maksymowych and Erickson 1960). The anticlinal orientation of division plane thus has a major influence on leaf anatomy. In early plant embryogenesis, cell division is highly regulated and correct placement of division plane is essential for normal development (Yoshida, Barbier de Reuille et al. 2014).

The patterning of division planes involves cues from cell geometry and is also influenced by auxin transport and has been assumed to be the driving force behind orientated growth. Recently, a plant-specific family of polar, edge-localized proteins has been identified that interprets global polarity cues to influence cell division orientation and provide a link between cell polarity and organismal axes (Yoshida, van der Schuren et al. 2019).

The angle and positioning of new cell walls in planar cell divisions is closely associated with growth. The role of cell polarity switching in the patterning of stomatal lineages is well documented and involves control of asymmetrical cell division (Robinson, Barbier de Reuille et al. 2011). The orientation of division in proliferating cells also appears highly regulated, cells in the midline preferentially divide perpendicular to the leaf proximodistal axis forming long, thin cells. It is currently unclear whether the placement of division plane specifies the orientation of growth or emerges in response to it.

Maize leaves carrying the *tangled-1* (*tan-1*) mutation, have dramatically altered patterns of cell division, yet relatively normal shape (Smith, Hake et al. 1996). This suggests that the generation of organ shape during development is largely independent of the control of cell division orientation. In contrast, the spatial regulation of orientated cell divisions in

Sarracenia purpurea is key for the formation of the complex pitcher leaves (Fukushima, Fujita et al. 2015).

In our leaf models, division of v-cells is specified according to Errera's rule in which the new wall is positioned along the shortest path through the centre of the v-cell (Errera 1888). The positioning of a division plane is therefore influenced by cell geometry which is in turn a product of growth anisotropy, tissue deformations and frequency of division. The orientation of v-cell division is not specified but emerges as a consequence of underlying regulatory networks. Biologically, division plane orientation may also arise in response to several integrated processes. Recent modelling of complex leaf shapes in 3D support the idea that planes of division are an emergent property rather than the cause of orientated growth (Whitewoods, Gonçalves et al. 2019).

9.19. The biological basis of polarity

The work summarised in this thesis makes the prediction that leaf morphogenesis depends on patterns of orientated growth that are coordinated by an underlying system of tissue cell polarity. This hypothesis was developed using a simplified framework in which growth and division parameters are specified by a distribution of factors through a continuous sheet. Polarity is established by the concentration gradient of a signal that propagates through the tissue and is anchored at the boundary. In a multicellular setting, it is likely that this process depends on more complex signalling mechanisms.

A mechanism of intracellular partitioning has been proposed to account for tissue cell polarity in both plants and animals (Abley, De Reuille et al. 2013). According to this hypothesis, a polarity field is coordinated by a proximal organiser that functions to transmit axial information through the tissue via a molecular signalling mechanism. Cell-cell coupling coordinates cell polarities in the absence of asymmetric cues. Our leaf models incorporate an identity factor which functions as a source of POL. It was not necessary to incorporate a sink of POL, though this does not exclude the possibility that a minus-organiser could be located at the leaf tip. Indeed, the formation of more complex shapes may depend on the spatiotemporal positioning of antagonistic organisers (Lee, Bushell et al. 2019).

It would be interesting to explore if our deforming leaf model could account for leaf shapes that arise through divergent patterns of allometry such as have been reported (Das Gupta and Nath 2015).

Polarised expression of the auxin efflux carrier *PIN1* at the distal end of cells in young primordia suggest that a proximodistal polarity field is present at the early stages of primordium initiation (Scarpella, Marcos et al. 2006). The expression is transient; it is unclear whether polar auxin transport continues through the epidermis at later stages or is fixed at an early stage of development. A role for polar auxin transport in leaf shape formation has been identified at later stages through analysis of *pin1* mutants that lack serrations in the margin (Hay, Barkoulas et al. 2006). Auxin maxima are generated at the tips of serrations that form through feedback between the CUP-SHAPED COTYLEDON2 (*CUC2*) transcription factor and *PIN1* convergence (Bilsborough, Runions et al. 2011). An alternative interpretation of this result is that the underlying proximodistal polarity is modulated in these regions due to spatiotemporally regulated expression of a minus organiser of tissue cell polarity. The auxin importer *LAX1* is expressed at serration tips as well as the distal tips of leaves, while serrations are reduced in mutants which lack the *AUX1/LAX* gene family of auxin importers (Kasprzewska, Carter et al. 2015). Thus, *LAX1* may function as a minus-organiser of tissue polarity.

This idea was explored through analysis of tissue outgrowths in *kanadi1/kanadi2* mutants of *Arabidopsis*. Expression of *LAX1* was observed at the tip of outgrowths and *CUC2* at the base, suggesting that these projections may result from alterations in organiser patterning leading to polarity convergences (Abley, Sauret-Güeto et al. 2016).

An alternative mechanism of integrating local and global growth patterns has recently been explored by combining a previously published model of serration development with a model of planar growth (Kierzkowski, Runions et al. 2019). Cells at the leaf margin provide local anisotropic growth which combines with broadly isotropic growth through the leaf to produce a leaf shape. It is not explicitly outlined how polarity within the model is defined but since *PIN1* transport is incorporated we might assume that auxin transport provides a biochemical basis of polarity. Our models do not depend on such local anisotropies defined at the leaf margin, but these could be incorporated via the spatiotemporal control of organiser activity to generate serrations (Kuchen 2011).

Further evidence for a tissue-wide polarity field is provided through the ectopic expression of the stomatal lineage protein, BREAKING OF ASYMMETRY IN THE STOMATAL LINEAGE (*BASL*). Live imaging revealed coordinated polarised expression of *BASL* across the leaf surface at all developmental stages (Mansfield, Newman et al. 2018). Furthermore, *BASL* was observed to reorient around serrations, mirroring the pattern of *PIN1*. It seems unlikely that the primary function of *BASL* is to provide the molecular basis of tissue-cell polarity, since the native expression pattern is restricted to cells undergoing division in the stomatal lineage. Rather, *BASL* may interact with another, currently unknown, molecule, which may function to transport auxin, or another as-yet unidentified molecule.

Factors predicted within the leaf models may correspond to the function of individual genes or the combined effects of multiple genes. This simplification allows hypotheses to be explored unencumbered by the complexities of genetic networks or limitations of current knowledge. My current research is focused on exploring the genetic basis of polarity through modulation of candidate organiser genes. Preliminary results indicate a role for *CUC2* as a plus organiser of polarity.

10. Conclusion

The overarching theme of this thesis is focused on explaining how organs develop through integrated patterns of orientated growth and cell division. Live imaging provided the novel opportunity to quantify these dynamic processes at the cellular level. Computer modelling provided the framework to formulate hypotheses to account for experimental observations in a dynamically changing system.

The initiation of the lamina has been predicted to occur from a region close to the leaf margin and form part of the 'primary morphogenesis' of a leaf (Dengler and Tsukaya 2001). This idea is underpinned by observations of small cells in the lateral regions and the notion that leaf maturation proceeds from tip to base. By capturing dynamic patterns of cell division and growth I provide quantitative measurements that validate and refine these ideas.

Tracking cell vertices demonstrates how a gradient in growth rates results in a large portion of the lamina originating from a region near the proximal-lateral margin that is initially relatively small. The dynamics of cell division competence explains how this region is spatially and temporally distributed and explains how leaf maturation appears to retract towards the leaf base. Imaging leaf growth from very early stages revealed that cell division occurs in a competence zone that is spatially and temporally regulated. Cell expansion was observed to take place throughout development, concurrent with division. These observations undermine the idea that the leaf transitions through distinct phases of development. In contrast, my analysis demonstrates through observations of different cell layers and genetic backgrounds that different regions exhibit behaviours that vary spatiotemporally.

Computer modelling revealed how observed patterns of division and growth could be regulated via a dual control mechanism with cross connections. This hypothesis helps reconcile the apparent dichotomy between the cellular and organismal-based theories of development. Tissue-wide coordination of growth rates, growth orientations and competence to divide are predicted to be coordinated by long-range signals. The finding that *spch* and wild-type leaves grow at similar rates (in the chamber) yet have different cell sizes suggests that SPCH acts cell autonomously to promote division at smaller sizes and/or shorter cell cycle

durations. Cell-autonomous size sensing also likely contributes to general spacing divisions. It has previously been proposed that coordination of behaviours could emerge if cells possess a mechanism to sense the presence of their neighbours and alter division patterns and cell fates accordingly (Meyerowitz 1996, Marcotrigiano 2001). Our models involve components of both organismal control (through the action of long-range signals) as well as aspects of cell theory (feedback from cell size) with the only requirement of cell-cell communication being the sensing of local concentration gradients. These results support the idea that both theories can be integrated through understanding that the mechanism of plant growth involves cell based machinery as well as global regulation (Fleming 2006). Thus, I show how organ morphogenesis could involve regulation at both the cell and organismal levels.

The work synthesised here represents many years of research underpinned by novel approaches to unlock one of the biggest challenges in biology; understanding how biological shapes are formed. The quality, depth and breadth of data has greatly enhanced our understanding of this process. Instrumental to this has been my role in developing novel approaches. I have supported many other colleagues by sharing my expertise and providing training and advice, particularly in the use of time-lapse imaging and tracking growth. My direct observations of changes at the cellular and tissue level have provided much needed clarity to the field. Though there are still many unknowns, the body of work presented here provides a solid foundation that will support many future investigations.

11. List of abbreviations

AAAS, American association for the advancement of science
BASL, BREAKING OF ASYMMETRY IN THE STOMATAL LINEAGE
CDIV, competence to divide
CUC, CUP-SHAPED COTYLEDON
CYC, CYCLOIDIA
1D, one dimension
3D, three dimensions
DAI, days after initiation
DAS, days after stratification
DEX, dexamethasone
GFP, green fluorescent protein
GPT, growing polarised tissue
KAN, KANADI
LATE, a timing factor
LAX, LIKE AUXIN RESISTANT
MID, a mediolateral factor
PGRAD, a graded proximodistal factor
PMF, proximal mobile factor
POL, factor determining polarity field
PHB, PHABULOSA
PIN, PINFORMED
SPCH, SPEECHLESS
SAM, shoot apical meristem
v-cells, virtual cells

12. References

- Abley, K., P. B. De Reuille, D. Strutt, A. Bangham, P. Prusinkiewicz, A. F. M. Marée, V. A. Grieneisen and E. Coen (2013). "An intracellular partitioning-based framework for tissue cell polarity in plants and animals." Development **140**(10): 2061.
- Abley, K., S. Sauret-Güeto, A. F. M. Marée and E. Coen (2016). "Formation of polarity convergences underlying shoot outgrowths." eLife **5**: e18165.
- Al-Kaff, N. S., M. M. Kreike, S. N. Covey, R. Pitcher, A. M. Page and P. J. Dale (2000). "Plants rendered herbicide-susceptible by cauliflower mosaic virus–elicited suppression of a 35S promoter-regulated transgene." Nature Biotechnology **18**(9): 995-999.
- Alim, K., S. Armon, B. I. Shraiman and A. Boudaoud (2016). "Leaf growth is conformal." Physical Biology **13**(5): 05LT01.
- Andriankaja, M., S. Dhondt, S. De Bodt, H. Vanhaeren, F. Coppens, L. De Milde, P. Muhlenbock, A. Skiryecz, N. Gonzalez, G. T. Beemster and D. Inze (2012). "Exit from proliferation during leaf development in *Arabidopsis thaliana*: a not-so-gradual process." Dev Cell **22**(1): 64-78.
- Avery, G. S. (1933). "Structure and development of the tobacco leaf." American Journal of Botany **20**(9): 565-592.
- Baskin, T. I. (2005). "Anisotropic expansion of the plant cell wall." Annual Review of Cell and Developmental Biology **21**(1): 203-222.
- Bencivenga, S., A. Serrano-Mislata, M. Bush, S. Fox and R. Sablowski (2016). "Control of Oriented Tissue Growth through Repression of Organ Boundary Genes Promotes Stem Morphogenesis." Dev Cell **39**(2): 198-208.
- Bhalerao, R. P. and M. J. Bennett (2003). "The case for morphogens in plants." Nature Cell Biology **5**(11): 939-943.

Bilsborough, G. D., A. Runions, M. Barkoulas, H. W. Jenkins, A. Hasson, C. Galinha, P. Laufs, A. Hay, P. Prusinkiewicz and M. Tsiantis (2011). "Model for the regulation of Arabidopsis thaliana leaf margin development." Proceedings of the National Academy of Sciences **108**(8): 3424.

Calder, G., C. Hindle, J. Chan and P. Shaw (2015). "An optical imaging chamber for viewing living plant cells and tissues at high resolution for extended periods." Plant Methods **11**(1): 22.

Castorina, G., S. Fox, C. Tonelli, M. Galbiati and L. Conti (2016). "A novel role for STOMATAL CARPENTER 1 in stomata patterning." BMC Plant Biology **16**(1): 172.

Chan, J., G. Calder, S. Fox and C. Lloyd (2005). "Localization of the microtubule end binding protein EB1 reveals alternative pathways of spindle development in Arabidopsis suspension cells." The Plant cell **17**(6): 1737-1748.

Chan, J., G. Calder, S. Fox and C. Lloyd (2007). "Cortical microtubule arrays undergo rotary movements in Arabidopsis hypocotyl epidermal cells." Nature Cell Biology **9**: 171.

Christian, J. L. (2012). "Morphogen gradients in development: from form to function." Wiley Interdisciplinary Reviews: Developmental Biology **1**(1): 3-15.

Coen, E., R. Kennaway and C. Whitewoods (2017). "On genes and form." Development **144**(23): 4203.

Coen, E., A.-G. Rolland-Lagan, M. Matthews, J. A. Bangham and P. Prusinkiewicz (2004). "The genetics of geometry." Proceedings of the National Academy of Sciences of the United States of America **101**(14): 4728-4735.

Cosgrove, D. J. (2005). "Growth of the plant cell wall." Nature Reviews Molecular Cell Biology **6**(11): 850-861.

Costa, M. M. R., S. Fox, A. I. Hanna, C. Baxter and E. Coen (2005). "Evolution of regulatory interactions controlling floral asymmetry." Development **132**(22): 5093.

Cunningham, M. E. and R. F. Lyndon (1986). "The Relationship Between the Distribution of Periclinal Cell Divisions in the Shoot Apex and Leaf Initiation." Annals of Botany **57**(6): 737-746.

Das Gupta, M. and U. Nath (2015). "Divergence in Patterns of Leaf Growth Polarity Is Associated with the Expression Divergence of miR396." The Plant Cell **27**(10): 2785.

Daxinger, L., B. Hunter, M. Sheikh, V. Jauvion, V. Gascioli, H. Vaucheret, M. Matzke and I. Furrer (2008). "Unexpected silencing effects from T-DNA tags in Arabidopsis." Trends in Plant Science **13**(1): 4-6.

Dengler, Nancy G. and H. Tsukaya (2001). "Leaf Morphogenesis in Dicotyledons: Current Issues." International Journal of Plant Sciences **162**(3): 459-464.

Donnelly, P. M., D. Bonetta, H. Tsukaya, R. E. Dengler and N. G. Dengler (1999). "Cell Cycling and Cell Enlargement in Developing Leaves of Arabidopsis." Developmental Biology **215**(2): 407-419.

Erickson, R. O. (1966). "Relative Elemental Rates and Anisotropy of Growth in Area: a Computer Programme." Journal of Experimental Botany **17**(2): 390-403.

Erickson, R. O. (1986). "Symplastic growth and symplasmic transport." Plant physiology **82**(4): 1153-1153.

Errera, L. (1888). "Uber Zellformen und Seifenblasen." Bot. Centralbl. **34**: 395-398.

Esau, K. (1960). Anatomy of seed plants, Wiley.

Esau, K. (1977). Anatomy of seed plants, John Wiley & Sons, New York.

Eshed, Y., A. Izhaki, S. F. Baum, S. K. Floyd and J. L. Bowman (2004). "Asymmetric leaf development and blade expansion in Arabidopsis are mediated by KANADI and YABBY activities." Development **131**(12): 2997-3006.

Fleming, A. J. (2006). "The integration of cell proliferation and growth in leaf morphogenesis." Journal of Plant Research **119**(1): 31-36.

Fox, S., P. Southam, F. Pantin, R. Kennaway, S. Robinson, G. Castorina, Y. E. Sánchez-Corrales, R. Sablowski, J. Chan, V. Grieneisen, A. F. M. Marée, J. A. Bangham and E. Coen (2018). "Spatiotemporal coordination of cell division and growth during organ morphogenesis." PLOS Biology **16**(11): e2005952.

Fukushima, K., H. Fujita, T. Yamaguchi, M. Kawaguchi, H. Tsukaya and M. Hasebe (2015). "Oriented cell division shapes carnivorous pitcher leaves of *Sarracenia purpurea*." Nature Communications **6**: 6450.

Gallois, J.-L., C. Woodward, G. V. Reddy and R. Sablowski (2002). "Combined SHOOT MERISTEMLESS and WUSCHEL trigger ectopic organogenesis in *Arabidopsis*." Development **129**(13): 3207.

González-Bayón, R., E. A. Kinsman, V. Quesada, A. Vera, P. Robles, M. R. Ponce, K. A. Pyke and J. L. Micol (2006). "Mutations in the RETICULATA gene dramatically alter internal architecture but have little effect on overall organ shape in *Arabidopsis* leaves." Journal of Experimental Botany **57**(12): 3019-3031.

Gower, J. C. (1975). "Generalized procrustes analysis." Psychometrika **40**(1): 33-51.

Green, A. A., J. R. Kennaway, A. I. Hanna, J. A. Bangham and E. Coen (2010). "Genetic Control of Organ Shape and Tissue Polarity." PLOS Biology **8**(11): e1000537.

Gunawardena, A. H. L. A. N., J. S. Greenwood and N. G. Dengler (2004). "Programmed Cell Death Remodels Lace Plant Leaf Shape during Development." The Plant Cell **16**(1): 60.

Hagemann, W. and S. Gleissberg (1996). "Organogenetic capacity of leaves: The significance of marginal blastozones in angiosperms." Plant Systematics and Evolution **199**(3): 121-152.

Hamant, O., M. G. Heisler, H. Jönsson, P. Krupinski, M. Uyttewaal, P. Bokov, F. Corson, P. Sahlin, A. Boudaoud, E. M. Meyerowitz, Y. Couder and J. Traas (2008). "Developmental Patterning by Mechanical Signals in *Arabidopsis*." Science **322**(5908): 1650.

Hay, A., M. Barkoulas and M. Tsiantis (2006). "ASYMMETRIC LEAVES1 and auxin activities converge to repress *BREVIPEDICELLUS* expression and promote leaf development in *Arabidopsis*." Development **133**(20): 3955.

Hayakawa, Y., M. Tachikawa and A. Mochizuki (2016). "Flat leaf formation realized by cell-division control and mutual recessive gene regulation." Journal of Theoretical Biology **404**: 206-214.

Heisler, M. G., O. Hamant, P. Krupinski, M. Uyttewaal, C. Ohno, H. Jönsson, J. Traas and E. M. Meyerowitz (2010). "Alignment between PIN1 Polarity and Microtubule Orientation in the Shoot Apical Meristem Reveals a Tight Coupling between Morphogenesis and Auxin Transport." PLOS Biology **8**(10): e1000516.

Hejnowicz, Z. and J. A. Romberger (1984). "Growth tensor of plant organs." Journal of Theoretical Biology **110**(1): 93-114.

Hervieux, N., M. Dumond, A. Sapala, A.-L. Routier-Kierzkowska, D. Kierzkowski, Adrienne H. K. Roeder, Richard S. Smith, A. Boudaoud and O. Hamant (2016). "A Mechanical Feedback Restricts Sepal Growth and Shape in *Arabidopsis*." Current Biology **26**(8): 1019-1028.

Hervieux, N., S. Tsugawa, A. Fruleux, M. Dumond, A.-L. Routier-Kierzkowska, T. Komatsuzaki, A. Boudaoud, J. C. Larkin, R. S. Smith, C.-B. Li and O. Hamant (2017). "Mechanical Shielding of Rapidly Growing Cells Buffers Growth Heterogeneity and Contributes to Organ Shape Reproducibility." Current Biology **27**(22): 3468-3479.e3464.

Hiscock, Tom W. and Sean G. Megason (2015). "Orientation of Turing-like Patterns by Morphogen Gradients and Tissue Anisotropies." Cell Systems **1**(6): 408-416.

Horiguchi, G., A. Ferjani, U. Fujikura and H. Tsukaya (2006). "Coordination of cell proliferation and cell expansion in the control of leaf size in *Arabidopsis thaliana*." Journal of Plant Research **119**(1): 37-42.

Horiguchi, G. and H. Tsukaya (2011). "Organ Size Regulation in Plants: Insights from Compensation." Frontiers in Plant Science **2**(24).

Ichihashi, Y., K. Kawade, T. Usami, G. Horiguchi, T. Takahashi and H. Tsukaya (2011). "Key Proliferative Activity in the Junction between the Leaf Blade and Leaf Petiole of *Arabidopsis*." Plant Physiology **157**(3): 1151.

Kaplan, D. R. and W. Hagemann (1991). "The Relationship of Cell and Organism in Vascular Plants Are cells the building blocks of plant form?" BioScience **41**(10): 693-703.

Kasprzewska, A., R. Carter, R. Swarup, M. Bennett, N. Monk, J. K. Hobbs and A. Fleming (2015). "Auxin influx importers modulate serration along the leaf margin." The Plant Journal **83**(4): 705-718.

Kazama, T., Y. Ichihashi, S. Murata and H. Tsukaya (2010). "The Mechanism of Cell Cycle Arrest Front Progression Explained by a KLUH/CYP78A5-dependent Mobile Growth Factor in Developing Leaves of *Arabidopsis thaliana*." Plant and Cell Physiology **51**(6): 1046-1054.

Kennaway, R., E. Coen, A. Green and A. Bangham (2011). "Generation of Diverse Biological Forms through Combinatorial Interactions between Tissue Polarity and Growth." PLOS Computational Biology **7**(6): e1002071.

Kierzkowski, D., A. Runions, F. Vuolo, S. Strauss, R. Lymbouridou, A.-L. Routier-Kierzkowska, D. Wilson-Sánchez, H. Jenke, C. Galinha, G. Mosca, Z. Zhang, C. Canales, R. Dello Ioio, P. Huijser, R. S. Smith and M. Tsiantis (2019). "A Growth-Based Framework for Leaf Shape Development and Diversity." Cell.

Kuchen, E. E. (2011). How organs organise their ontogeny : modelling feedback between polarity, growth and geometry during Arabidopsis leaf development. PhD, University of East Anglia.

Kuchen, E. E., S. Fox, P. Barbier de Reuille, R. Kennaway, S. Bensmihen, J. Avondo, G. M. Calder, P. Southam, S. Robinson, A. Bangham and E. Coen (2012). "Generation of Leaf Shape Through Early Patterns of Growth and Tissue Polarity." Science **335**(6072): 1092.

Kuwabara, A., A. Backhaus, R. Malinowski, M. Bauch, L. Hunt, T. Nagata, N. Monk, G. Sanguinetti and A. Fleming (2011). "A Shift toward Smaller Cell Size via Manipulation of Cell Cycle Gene Expression Acts to Smoothen Arabidopsis Leaf Shape." Plant Physiology **156**(4): 2196.

Lee, K. J. I., C. Bushell, Y. Koide, J. A. Fozard, C. Piao, M. Yu, J. Newman, C. Whitewoods, J. Avondo, R. Kennaway, A. F. M. Marée, M. Cui and E. Coen (2019). "Shaping of a three-dimensional carnivorous trap through modulation of a planar growth mechanism." PLOS Biology **17**(10): e3000427.

Li, X.-R., R. M. A. Vroomans, S. Fox, V. A. Grieneisen, L. Østergaard and A. F. M. Marée (2019). "Systems Biology Approach Pinpoints Minimum Requirements for Auxin Distribution during Fruit Opening." Molecular Plant **12**(6): 863-878.

Li, Y., L. Zheng, F. Corke, C. Smith and M. W. Bevan (2008). "Control of final seed and organ size by the DA1 gene family in Arabidopsis thaliana." Genes & Development **22**(10): 1331-1336.

Lyndon, R. F. (1994). "Tansley Review No. 74 Control of organogenesis at the shoot apex." New Phytologist **128**(1): 1-18.

MacAlister, C. A., K. Ohashi-Ito and D. C. Bergmann (2006). "Transcription factor control of asymmetric cell divisions that establish the stomatal lineage." Nature **445**: 537.

Maksymowych, R. and R. O. Erickson (1960). "Development of the Lamina in Xanthium italicum Represented by the Plastochron Index." American Journal of Botany **47**(6): 451-459.

Mansfield, C., J. L. Newman, T. S. G. Olsson, M. Hartley, J. Chan and E. Coen (2018). "Ectopic BASL Reveals Tissue Cell Polarity throughout Leaf Development in *Arabidopsis thaliana*." Current biology : CB **28**(16): 2638-2646.e2634.

Marcotrigiano, M. (2001). "Genetic Mosaics and the Analysis of Leaf Development." International Journal of Plant Sciences **162**(3): 513-525.

McHale, N. A. and M. Marcotrigiano (1998). "LAM1 is required for dorsoventrality and lateral growth of the leaf blade in *Nicotiana*." Development **125**(21): 4235-4243.

Meyerowitz, E. M. (1996). "Plant development: local control, global patterning." Current Opinion in Genetics & Development **6**(4): 475-479.

Mitchison, G. (2016). "Conformal growth of *Arabidopsis* leaves." Journal of Theoretical Biology **408**: 155-166.

Mündermann, L., Y. Erasmus, B. Lane, E. Coen and P. Prusinkiewicz (2005). "Quantitative Modeling of *Arabidopsis* Development." Plant Physiology **139**(2): 960.

Nath, U., B. C. W. Crawford, R. Carpenter and E. Coen (2003). "Genetic Control of Surface Curvature." Science **299**(5611): 1404.

Ohashi-Ito, K. and D. C. Bergmann (2006). "*Arabidopsis* FAMA controls the final proliferation/differentiation switch during stomatal development." Plant Cell **18**(10): 2493-2505.

Patron, N. J., D. Orzaez, S. Marillonnet, H. Warzecha, C. Matthewman, M. Youles, O. Raitskin, A. Leveau, G. Farré, C. Rogers, A. Smith, J. Hibberd, A. A. R. Webb, J. Locke, S. Schornack, J. Ajioka, D. C. Baulcombe, C. Zipfel, S. Kamoun, J. D. G. Jones, H. Kuhn, S. Robatzek, H. P. Van Esse, D. Sanders, G. Oldroyd, C. Martin, R. Field, S. O'Connor, S. Fox, B. Wulff, B. Miller, A. Breakspear, G. Radhakrishnan, P.-M. Delaux, D. Loqué, A. Granell, A. Tissier, P. Shih, T. P. Brutnell, W. P. Quick, H. Rischer, P. D. Fraser, A. Aharoni, C. Raines, P. F. South, J.-M. Ané, B. R. Hamberger, J. Langdale, J. Stougaard, H. Bouwmeester, M. Udvardi, J. A. H. Murray, V. Ntoukakis, P. Schäfer,

- K. Denby, K. J. Edwards, A. Osbourn and J. Haseloff (2015). "Standards for plant synthetic biology: a common syntax for exchange of DNA parts." New Phytologist **208**(1): 13-19.
- Poethig, R. S. and I. M. Sussex (1985). "The cellular parameters of leaf development in tobacco: a clonal analysis." Planta **165**(2): 170–184.
- Poethig, R. S. and I. M. Sussex (1985). "The developmental morphology and growth dynamics of the tobacco leaf." Planta **165**(2): 158-169.
- Pyke, K. A., J. L. Marrison and A. M. Leech (1991). "Temporal and Spatial Development of the Cells of the Expanding First Leaf of *Arabidopsis thaliana* (L.) Heynh." Journal of Experimental Botany **42**(11): 1407-1416.
- Reinhardt, D., E.-R. Pesce, P. Stieger, T. Mandel, K. Baltensperger, M. Bennett, J. Traas, J. Friml and C. Kuhlemeier (2003). "Regulation of phyllotaxis by polar auxin transport." Nature **426**(6964): 255-260.
- Remmler, L. and A.-G. Rolland-Lagan (2012). "Computational Method for Quantifying Growth Patterns at the Adaxial Leaf Surface in Three Dimensions." Plant Physiology **159**(1): 27.
- Richards, O. W. and A. J. Kavanagh (1943). "The analysis of the relative growth gradients and changing form of growing organisms: Illustrated by the tobacco leaf." The American Naturalist **77**: 385-399.
- Robinson, S., P. Barbier de Reuille, J. Chan, D. Bergmann, P. Prusinkiewicz and E. Coen (2011). "Generation of Spatial Patterns Through Cell Polarity Switching." Science **333**(6048): 1436.
- Savaldi-Goldstein, S., C. Peto and J. Chory (2007). "The epidermis both drives and restricts plant shoot growth." Nature **446**(7132): 199-202.
- Scarpella, E., D. Marcos, J. Friml and T. Berleth (2006). "Control of leaf vascular patterning by polar auxin transport." Genes & development **20**(8): 1015-1027.

Schindelin, J., I. Arganda-Carreras, E. Frise, V. Kaynig, M. Longair, T. Pietzsch, S. Preibisch, C. Rueden, S. Saalfeld, B. Schmid, J. Y. Tinevez, D. J. White, V. Hartenstein, K. Eliceiri, P. Tomancak and A. Cardona (2012). "Fiji: an open-source platform for biological-image analysis." Nat Methods **9**(7): 676-682.

Sena, G., X. Wang, H. Y. Liu, H. Hofhuis and K. D. Birnbaum (2009). "Organ regeneration does not require a functional stem cell niche in plants." Nature **457**(7233): 1150-1153.

Serrano-Mislata, A., K. Schiessl and R. Sablowski (2015). "Active Control of Cell Size Generates Spatial Detail during Plant Organogenesis." Current Biology **25**(22): 2991-2996.

Smith, L. G., S. Hake and A. W. Sylvester (1996). "The tangled-1 mutation alters cell division orientations throughout maize leaf development without altering leaf shape." Development **122**(2): 481.

Sorefan, K., T. Girin, S. J. Liljegren, K. Ljung, P. Robles, C. S. Galván-Ampudia, R. Offringa, J. Friml, M. F. Yanofsky and L. Østergaard (2009). "A regulated auxin minimum is required for seed dispersal in Arabidopsis." Nature **459**(7246): 583-586.

Tang, W., R. J. Newton and D. A. Weidner (2006). "Genetic transformation and gene silencing mediated by multiple copies of a transgene in eastern white pine." Journal of Experimental Botany **58**(3): 545-554.

Vuolo, F., D. Kierzkowski, A. Runions, M. Hajheidari, R. A. Mentink, M. D. Gupta, Z. Zhang, D. Vlad, Y. Wang, A. Pecinka, X. Gan, A. Hay, P. Huijser and M. Tsiantis (2018). "LMI1 homeodomain protein regulates organ proportions by spatial modulation of endoreduplication." Genes & Development.

Waites, R. and A. Hudson (1995). "phantastica: a gene required for dorsoventrality of leaves in *Antirrhinum majus*." Development **121**(7): 2143.

White, D. W. R. (2006). "PEAPOD regulates lamina size and curvature in Arabidopsis." Proceedings of the National Academy of Sciences **103**(35): 13238-13243.

Whitewoods, C. D. and E. Coen (2017). "Growth and Development of Three-Dimensional Plant Form." Current Biology **27**(17): R910-R918.

Whitewoods, C. D., B. Gonçalves, J. Cheng, M. Cui, R. Kennaway, K. Lee, C. Bushell, M. Yu, C. Piao and E. Coen (2019). "Evolution of carnivorous traps from planar leaves through simple shifts in gene expression." Science: eaay5433.

Wolpert, L. (1969). "Positional information and the spatial pattern of cellular differentiation." Journal of Theoretical Biology **25**(1): 1-47.

Wolpert, L. (2011). "Positional information and patterning revisited." Journal of Theoretical Biology **269**(1): 359-365.

Yoshida, S., P. Barbier de Reuille, B. Lane, George W. Bassel, P. Prusinkiewicz, Richard S. Smith and D. Weijers (2014). "Genetic Control of Plant Development by Overriding a Geometric Division Rule." Developmental Cell **29**(1): 75-87.

Yoshida, S., A. van der Schuren, M. van Dop, L. van Galen, S. Saiga, M. Adibi, B. Möller, C. A. ten Hove, P. Marhavy, R. Smith, J. Friml and D. Weijers (2019). "A SOSEKI-based coordinate system interprets global polarity cues in Arabidopsis." Nature Plants **5**(2): 160-166.

13. Appendix 1: letters of support from co-authors

18th December 2019

TO WHOM IT MAY CONCERN

Re: Samantha Fox – PhD by publication candidate

Samantha joined my group as a research assistant in 2004. During that time, she has co-authored three highly cited papers and I am delighted to now support her submission for a PhD by publication to the University of East Anglia.

I can confirm that in respect of the following two papers Sam contributed to the design of investigation and carried out extensive programme of experiments. Most notably, generating live imaging datasets of growing leaves using confocal microscopy, clonal analysis, leaf excision, and tracking growth and division. Sam worked in close collaboration with other colleagues to account for her experimental observations using computational modelling, providing novel insights into how leaf growth is coordinated. Sam contributed to all stages of the research program, development of hypotheses and preparation of manuscripts. In recognition of her leading role, for each of these papers Sam created YouTube videos to communicate our findings to the general public on behalf of the John Innes Centre.

Fox, S., Southam, P.*, Pantin, F.*, Kennaway R., Robinson, S., Castorina, G., Sánchez-Corrales, Y., Sablowski, R., Chan, J., Grieneisen, V., Marée, A., Bangham, A., and Coen, E. (2018). "Spatiotemporal coordination of cell division and growth during organ morphogenesis." PLOS Biology 16(11): e2005952.*

Kuchen, E. E., Fox, S.*, Barbier de Reuille, P., Kennaway, R., Bensmihen, S., Avondo, J., Calder, G. M., Southam, P., Robinson, S., Bangham, and A., Coen., E. (2012). "Generation of Leaf Shape Through Early Patterns of Growth and Tissue Polarity." Science 335(6072): 1092.*

Earlier in her career, Sam contributed to the paper below by supporting a post-doc in the group. Sam carried out a phenotypic analysis of leaves and petals overexpressing *CYCLOIDIA*, contributed in discussion and prepared figures for the manuscript.

Costa, M., Fox, S., Hanna, A.I., Baxter, C., Coen, E (2005) Evolution of regulatory interactions controlling floral asymmetry. Development. DOI: 10.1242/dev.02085EID: 2-s2.0-28844496309

In conclusion, there is no doubt that the work published in the above papers would not have been accepted without Sam's excellent and skillful contributions. I therefore strongly support her in reaching this recognition of her achievements.

Yours Sincerely,

Professor Enrico Coen
Group Leader

John Innes Centre is a company limited by guarantee.
Registered in England No. 511709 Registered Charity No. 223852.

Director, Professor Dale Sanders ScD FRS FRSE
Registered Office
John Innes Centre, Norwich Research Park, Norwich NR4 7UH

John Innes Centre is grant aided by the Biotechnology and Biological Sciences Research Council.

Tel: +44(0)1603 450000 Fax: +44(0)1603 450045

Azone Ltd.
Unit 3
Downham Grove
Wymondham
NR18 0SN

28th November 2019

Re: Letter of support for Samantha Fox – PhD by Publication


To Whom It May Concern

I am writing this letter in support of Samantha Fox as a candidate for a PhD degree at the University of East Anglia. I met Sam for the first time while working as a Senior Research Associate at the John Innes Centre in early 2008. Since then we have worked closely together on a number of successful research projects. Her work and contribution has been instrumental in the development and publication of several high-quality manuscripts, including:

- S. Fox, P. Southam F. Pantin, R. Kennaway, S. Robinson, G. Castorina, et al. (2018) Spatiotemporal coordination of cell division and growth during organ morphogenesis. PLoS Biol 16(11): e2005952. <https://doi.org/10.1371/journal.pbio.2005952>
- S. Fox, E. Kuchen, P. Barbier de Reuille, R. Kennaway, S. Bensmihen, J. Avondo, G. Calder, P. Southam, S. Robinson, A. Bangham and E. Coen, (2012) Generation of Leaf Shape Through Early Patterns of Growth and Tissue Polarity, Science, 335(6071), pp. 1092-1096, DOI: 10.1126/science.1214678

These publications are the culmination of years of collaboration with Sam and speak on their own about the quality of Sam's work. During my time collaborating with Sam, I was always impressed with her dedication, commitment and professionalism. She is an excellent collaborator, scientist and a wonderful personality. Without a doubt, I believe that she is an exceptionally strong candidate for a PhD and I am therefore very happy to write this letter of support.

Yours faithfully



Dr. Paul Southam

Date: 17 December 2019

To Whom it may concern

Re: Samantha Fox – PhD by publication candidate

I have worked with Samantha Fox at the John Innes Centre since 2007. My role has been to design, develop, and support tools for modelling the development of plant tissues, which Samantha and other members of Prof. Coen's group have used in their research.

This has led to publications in *Science* ("Generation of Leaf Shape through Early Patterns of Growth and Tissue Polarity") and *PLoS Biology* ("Spatiotemporal coordination of cell division and growth during organ morphogenesis"). Samantha is a co-senior author on both of these.

Her role in these papers involved evaluating models of leaf growth in *Arabidopsis* (using the software that I developed to run these models), performing image analysis on experimental microscopy data, assessing the correspondence of the models with these results, and writing of the papers.

I am happy to recommend her for a Ph.D.

Yours Sincerely,



Dr Richard Kennaway
Cell and Developmental Biology

John Innes Centre is a company limited by guarantee.
Registered in England No. 511709 Registered Charity No. 223852

*John Innes Centre is grant aided by the Biotechnology and Biological
Sciences Research Council*

Director, Professor Dale Sanders ScD FRS
Registered Office
Norwich Research Park, Norwich, NR4 7UH
Tel: +44(0)1603 450000 Fax: +44(0)1603 450045

Norwich, 2nd December 2019

To Whom it may concern

Re: Samantha Fox – PhD candidate

I am delighted to write this letter in support of Samantha (Sam) Fox and her submission for a PhD by publication to the University of East Anglia. I have known Sam since soon after I started my group at the John Innes Centre in 2005. We have interacted at many occasions over this time and most significantly on a project to understand auxin distribution during the development of the Arabidopsis fruit. This work was recently published with Sam as a co-author (Li *et al.* 2019 *Molecular Plant* 12: 863-878).

Using a combination of genetic studies and mathematical modelling, we focused on a highly specialised tissue in the fruit called the valve margin, which runs in a narrow strip down the entire length of the fruit and which is required for fruit opening and seed dispersal upon maturity. During valve-margin formation, this tissue experiences a timely and spatially restricted decrease in auxin levels to form a so-called 'auxin-minimum'. Counter-intuitively, our modelling simulations suggested this involves high auxin flux across the valve margin. In order to test our hypotheses and computational models, we required highly advanced confocal microscopy skills as well as development of a technique to physically ablate the valve margin cells. Sam delivered both and in addition to confirming the high auxin flux, she also showed how auxin transporters of the PIN family are positioned in the valve margin to facilitate auxin transport out of the valve margin cells. We had hypothesised this PIN positioning in a paper published in *Nature* in 2009, but had been unable to demonstrate it at the time.

In conclusion, there is no doubt that the work published in Li *et al.* (2019) would not have been accepted in *Molecular Plant* without Sam's excellent and skillful contribution. Based on this close collaboration as well as my knowledge of the always extremely high quality of Sam's work, it is hard to imagine a stronger candidate for achieving a PhD by publication. I therefore strongly support her in reaching this hugely deserved recognition.

Yours sincerely



Professor Lars Østergaard
Institute Programme Leader

Phone: +44 1603 450572
Skype name: lars.oest

Erika Kuchen
Catenion GmbH
Münzstr. 18
10178 Berlin

Re: Samantha Fox – PhD candidate

Dear Sir or Madame,

I hereby recommend Samantha Fox for a PhD by publication at the University of East Anglia. I have worked with Samantha for several years from 2007 – 2012 during my PhD at the John Innes Centre and co-authored her publication Fox, Kuchen et al. (2012) *Generation of Leaf Shape Through Early Patterns of Growth and Tissue Polarity*. In this work, we applied time-lapse imaging, clonal analysis and mathematical modelling to understand how growth rate and polarity are coordinated in leaf organ development.

In detail, Samantha was responsible for the initial feasibility assessment of the experimental part of the project including setup and maintenance of the time-lapse confocal microscope and infrastructure and exploration into different leaf growth tracking methods. Following her recommendations, Samantha and I used a microfluidics chamber to grow and continuously image leaves under the microscope over several days. She took the lead in quantifying leaf growth rates from these movies using the custom-made, semi-automated image analysis and tracking software volviewer. In addition, Samantha applied several other snapshot imaging methods to quantify leaf shape and growth rates by clonal analysis. This data was then used to test several hypotheses on the coordination of growth rate and polarity during the early stages of leaf development with a finite element model. Samantha was instrumental in testing the model predictions by independently designing and performing leaf ablation experiments. Together with the lead investigator on this project, Prof Enrico Coen, we co-wrote the manuscript, designed and arranged the figures and prepared the manuscript for publication. Furthermore, Samantha was the main person publicising the work, such as by making a movie for the Science journal website.

During her long career at the John Innes Centre Samantha has become an expert on plant development, plant imaging and specifically growth quantification. I have been very lucky to have benefited so much from her knowledge during our very close collaboration and successful publication of our work, to which we contributed equally. To be awarded a PhD by publication is therefore highly deserved.

Yours faithfully,

Erika Kuchen

Technology Facility
Department of Biology
University of York
Wentworth Way, York
YO10 5DD
United Kingdom

Experimental Officer: Grant Calder
E-mail: grant.calder@york.ac.uk
Telephone: +44 (0)1904 328809

Date: 13/12/2019

To whom it may concern,

Regarding: Samantha Fox –Ph.D. candidate by publication

I am writing this letter of support for Samantha Fox as a candidate for a PhD degree at the University of East Anglia. In my previous role as a Senior Scientist in the Bio-imaging Facility at the John Innes Centre (JIC), I had the pleasure of working with Sam on many microscopy-based projects. Sam has many personal attributes that make her a great scientist and collaborator. Not only is Sam technically gifted but her dedication and perseverance has made it possible for her to develop many new tools used in understanding tissue development in plants e.g. heat inducible clonal analysis. Perhaps Sam's greatest strength is having the vision to adopt of new techniques and apply them to current issues.

Sam's work has led to several high quality publications, notably the Science paper "Generation of Leaf Shape Through Early Patterns of Growth and Tissue Polarity", for which Sam was first author. This ground breaking paper required cutting edge time-lapse optical microscopy and multi-scaled image analysis combined with predictive computer modelling. One of the many issues that had to be overcome was high resolution imaging of a growing leaf, for which cellular expansion and division were tracked over many days. This collaboration led to the development of a new microscope imaging chamber for plant research. Sam was also proactive in the development of the molecular and imaging tools e.g. inducible clonal analysis and laser ablation required for validating the principle rules behind the formation of leaf tissue. Sam's role not only required hands-on experimental and analysis but significant intellectual input into experimental design, conception of theories, talks and manuscript preparation.

Sam is also an excellent ambassador for science and I have always been impressed with her ability to inspire future generations of potential scientists. Sam has delivered high quality research through her career and I believe is an exceptional candidate for a PhD. Therefore, I'm delighted to write this letter of support.

Yours sincerely,

Grant Calder



Date: 11 December 2019

To Whom it may concern

Re: Samantha Fox – PhD by publication candidate

I have known Samantha (Sam) since she joined the JIC in 2000. In 2003, Sam, joined the lab of Clive Lloyd as a research assistant on a short-term contract. I was Sam's direct line manager and supervised her work daily. During that time, Samantha created novel transgenic lines of Arabidopsis that enabled me to visualise the microtubule end binding protein AtEB1a in planta. This was used for two high impact papers on which Sam is named as a contributing author.

Chan, J., Calder, G., Fox, S., & Lloyd, C., (2007) Cortical microtubule arrays undergo rotary movements in Arabidopsis hypocotyl epidermal cells. Nature Cell Biology. DOI: 10.1038/ncb1533EID: 2-s2.0-33947231099

Chan, J., Calder, G., Fox, S. & Lloyd, C. (2005) Localization of the Microtubule End Binding Protein EB1 Reveals Alternative Pathways of Spindle Development in Arabidopsis Suspension Cells. Plant Cell. DOI: 10.1105/tpc.105.032615EID: 2-s2.0-32944461130

Samantha went on to join the group of Enrico Coen in 2004. Sam and I continued to collaborate on the development of the live-imaging technique, and it is partly due to this collaboration that I myself joined the Coen group in 2009. I have since witnessed Sam enhance her skills as a scientist and can confirm that she made leading contributions to a paper on which I was also recognised as an author for providing genetic material.

Fox, S.*, Southam, P.*, Pantin, F.*, Kennaway R., Robinson, S., Castorina, G., Sánchez-Corrales, Y., Sablowski, R., Chan, J., Grieneisen, V., Marée, A., Bangham, A., and Coen, E. (2018). "Spatiotemporal coordination of cell division and growth during organ morphogenesis." PLOS Biology 16(11): e2005952.

I have been impressed with Sam's commitment and quality of work. Sam drove the development of live imaging techniques and generation of reporter lines to enable the filming of growing leaves. This work resulted in Sam making the first ever movies of small primordia developing into mature leaves. Sam also drove the development of key pipelines to track cells and extract their growth and cell division parameters from these data sets. I think her work provides the most comprehensive guide to the behaviour of cells during the early stages of leaf development ever published. This detailed work has been critical for informing and testing computer models, which has led to fundamental breakthroughs in how tissue growth can be coordinated through cell polarity.

Sam has given extremely engaging presentations about leaf development at the JIC and international conferences.

I have no hesitation on supporting Sam for PhD by publication and feel she is very deserving of this degree.

Yours Sincerely,

A handwritten signature in black ink, appearing to be 'J. Chan', with a long horizontal stroke extending to the right.

Dr Jordi Chan
Cell and Developmental Biology

John Innes Centre is a company limited by guarantee.
Registered in England No. 511709 Registered Charity No. 223852

*John Innes Centre is grant aided by the Biotechnology and Biological
Sciences Research Council*

Director, Professor Dale Sanders ScD FRS
Registered Office
Norwich Research Park, Norwich, NR4 7UH
Tel: +44(0)1603 450000 Fax: +44(0)1603 450045



UNIVERSITÀ DEGLI STUDI DI MILANO

DIPARTIMENTO DI SCIENZE AGRARIE E AMBIENTALI
PRODUZIONE. TERRITORIO. AGROENERGIA

Milan, December 09, 2019

To Whom It May Concern:
Re: Samantha Fox - Ph.D. by Publication

To Whom It May Concern:
Re: Samantha Fox - Ph.D. by Publication

I am writing this letter in support of Samantha Fox as a candidate for a PhD by publication at the University of East Anglia.

I met Samantha for the first time at John Innes Centre (Norwich Research Park, Norwich) in April 2013. She supervised the experimental work during my PhD visiting student period in the Enrico Coen Group. I worked closely with Samantha for four months and during that time Sam trained me in the live-imaging tracking technique on the confocal microscope. Since then, I have had the pleasure to collaborate with her in two projects and the results produced two high-quality manuscripts.

I would like to highlight Samantha's contribution to these particular publications:

1. Fox, S., Southam, P., Pantin, F., Kennaway, R., Robinson, S., Castorina, G., ... & Marée, A. F. (2018). Spatiotemporal coordination of cell division and growth during organ morphogenesis. *PLoS biology*, 16(11), e2005952.

Samantha played a key role and worked in conceptualization, data curation, formal analysis, investigation, methodology, resources, validation, visualization, writing the original draft and during review & editing.

2. Castorina, G., Fox, S., Tonelli, C., Galbiati, M., & Conti, L. (2016). A novel role for STOMATAL CARPENTER 1 in stomata patterning. *BMC plant biology*, 16(1), 172.

Samantha wrote the corresponding parts of the methods section, and generally enabled the rest of this work, participating with the manuscripts writing.

These publications speak on their own about the quality of work but I would also like to add that I have been impressed with her dedication and commitment to deliver excellence in her work. I believe she is an exceptionally strong candidate for a PhD and therefore I am very happy to write this letter of support.

Yours sincerely,
Giulia Castorina

Dipartimento di Scienze Agrarie e Ambientali - Produzione, Territorio, Agroenergia
Via G. Celoria, n° 2 - 20133 Milano, Italy
Tel 02 503 16847 - direttore.disaa@unimi.it

To Whom it may concern

Re: Samantha Fox – PhD by publication candidate

I have known Samantha for many years as head of Cell and Developmental Biology at the John Innes Centre. During this time, I have co-authored two highly regarded papers with Sam.

For the following paper published in PLoS Biology, I can confirm that Sam had a leading role in the experimental part of the project and collaborated with computer scientists to develop and test hypotheses about how growth is coordinated in a leaf. Throughout the project Sam presented high quality department seminars at which she communicated progress, shared hypotheses and demonstrated her knowledge and innovative approaches. Sam is well known at the JIC and beyond for her expertise in studying plant growth using dynamic tracking. For this paper, I collaborated with Sam to provide training and support for her to segment cells in 3D images using computational tools that I previously developed and modified for this project.

Fox, S.*, Southam, P.*, Pantin, F.*, Kennaway R., Robinson, S., Castorina, G., Sánchez-Corrales, Y., Sablowski, R., Chan, J., Grieneisen, V., Marée, A., Bangham, A., and Coen, E. (2018). "Spatiotemporal coordination of cell division and growth during organ morphogenesis." PLOS Biology 16(11): e2005952. (* joint first authors)

For the following paper, Sam provided my group with a new transgenic plant line which she had developed to improve clonal analysis in *Arabidopsis*. This provided us with the means to generate marked clones in the shoot apical meristem. We were grateful to Sam for sharing this resource, on which she worked for several months to develop.

Bencivenga, S., Serrano-Mislata, A., Bush, M., Fox, S., Sablowski, R. (2016) Control of Oriented Tissue Growth through Repression of Organ Boundary Genes Promotes Stem Morphogenesis. Developmental Cell. DOI: 10.1016/j.devcel.2016.08.013EID: 2-s2.0-84994480561

Based on the contributions described above, I am delighted to now support Sam's submission for a PhD by publication.

Yours Sincerely,



Professor Robert Sablowski
Head of Cell and Developmental Biology



9th December 2019

To whom it may concern,

I am writing to express my strong support for the application of Samantha Fox for a PhD by publication. I worked with Sam during my PhD. She was responsible for teaching me how to collect and analyse live imaging data. Our work resulted in two co-authored publications. Kuchen and Fox *et al.* 2012 and Fox, Southam and Pantin *et al.* 2018. Both of these papers have at their core time-lapse data from live growing Arabidopsis leaves. Sam performed the majority of these experiments and analysed the data. Sam wrote the corresponding parts of the papers and the majority of the 2018 paper in collaboration with the other authors. Sam is a careful and dedicated scientist who is deserving of a PhD.

I am happy to answer any additional questions

Sincerely,

Dr. Sarah Robinson
Sarah.Robinson@slcu.cam.ac.uk
Career Development Fellow and Royal Society Fellow
The Sainsbury Laboratory Cambridge University

Sainsbury Laboratory Cambridge
University of Cambridge
Bateman Street, Cambridge
CB2 1LR, UK



Earlham Institute
Norwich Research Park,
Norwich,
NR4 7UH, UK

Tel: +44 (0)1603 450001
Fax: +44 (0)1603 450021
www.earlham.ac.uk
enquiries@earlham.ac.uk



Decoding Living Systems

Dr. Nicola J. Patron
Group Leader | Engineering Biology
nicola.patron@earlham.ac.uk

10th December 2019

To whom it may concern,

RE: SAMANTHA FOX – PHD CANDIDATE

I am delighted to write a letter of support for Samantha Fox's submission for a PhD by publication to the University of East Anglia. I first met Sam when she was an MSc student many years ago and was very happy to be reacquainted when I returned to the Norwich Research Park as an Independent Scientist in 2013.

We have interacted on many occasions over this time, particularly as Sam led efforts in the Coen laboratory to adopt novel approaches for the design and assembly of synthetic DNA assemblies. Sam represented the Coen lab on a highly-cited paper that established community standards for interoperable DNA parts for plants (Patron et al, 2015). Sam implemented these tools and techniques to develop a modular 'heat-shock:cre' inducible gene expression system that she applied to the visualisation of clones in plant shoot apical meristems. Following this experimental success, Sam contacted me several times to advance her understanding while she trained other members of her laboratory in the use of modular, hierarchical assembly of complex multigene DNA constructs.

Based on observing Sam's ability to adapt novel methodologies to experimental challenges, as well as her commitment to sharing knowledge and skills to advance plant science, I have no hesitation in supporting Sam's submission for a PhD by publication.

Yours sincerely

A handwritten signature in black ink, appearing to read 'Nicola'.

Dr. Nicola J. Patron
Group Leader | Engineering Biology
<http://nicolajpatron.com>

Director | Earlham BioFoundry
<https://www.earlham.ac.uk/earlham-bio-foundry>

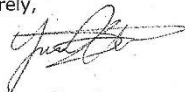
Re: Letter of support for Samantha Fox – candidate for PhD by Publication

I am writing this letter in support of Samantha Fox as a candidate for a PhD degree at the University of East Anglia. I worked with Sam at the John Innes Centre while I was undertaking my PhD from 2009-2013. Sam is an expert in live imaging and trained me in the technique of generating confocal images of growing *Arabidopsis* leaves, which was critical for my own research. I can confirm that Sam provided the experimental contributions that were critical to the success of the publication listed below, including live imaging, image processing and tracking growth and cell division using specialist software.

Fox, S.*, Southam, P.*, Pantin, F.*, Kennaway R., Robinson, S., Castorina, G., Sánchez-Corrales, Y., Sablowski, R., Chan, J., Grieneisen, V., Marée, A., Bangham, A., and Coen, E. (2018). "Spatiotemporal coordination of cell division and growth during organ morphogenesis." PLOS Biology 16(11): e2005952.

This paper represents the culmination of years of research throughout which Sam provided the lead experimentally and managed collaborations with a number of other colleague's expert in different areas such as computational modelling. I have no reservation in recommending Sam for a PhD and I am therefore very happy to write this letter of support.

Yours Sincerely,



Dr Yara Sanchez-Corrales



Campus de Gualtar
4710-057 Braga – P

Universidade do Minho
Escola de Ciências
Departamento de Biologia

17 Dec 2019

To whom it may concern

I worked closely with Samantha Fox whilst I was a Post-doctoral researcher at Prof. Enrico Coen's lab, at the John Innes Centre, between 2004 and 2006. During that period, Sam was involved in the phenotypic analysis of the development of leaves and petals of *Arabidopsis thaliana* plants overexpressing a dexamethasone-inducible protein. She carried out extensive phenotypic analysis using light microscopy and scanning electron microscopy and made quantitative measurements of cell size and number of the plant organs. An excellent output of this collaboration was the publication,

Costa, M., Fox, S., Hanna, A.I., Baxter, C., Coen, E (2005) Evolution of regulatory interactions controlling floral asymmetry. *Development*. DOI: 10.1242/dev.02085EID: 2-s2.0-28844496309,

for which Sam has contributed with many discussions and assisted in the preparation of the manuscript.

Since taking up a position as a Lecturer at the University of Minho (Portugal), I have maintained a close collaboration with the Coen group with frequent visits to the lab, including a 8 month-sabbatical period. It was with a great satisfaction that I have witnessed Sam developing into a highly skilled and respected scientist. Therefore, I am very happy to support her submission for a PhD by publication to the University of East Anglia.

Yours Sincerely,

Maria Manuela Ribeiro Costa
Lecturer at the Biology Department
University of Minho
Braga
Portugal

14. Annexe 2: Submitted publications

RESEARCH ARTICLE

Spatiotemporal coordination of cell division and growth during organ morphogenesis

Samantha Fox¹, Paul Southam¹, Florent Pantin^{1,2}, Richard Kennaway¹, Sarah Robinson¹, Giulia Castorina¹, Yara E. Sánchez-Corrales¹, Robert Sablowski¹, Jordi Chan¹, Verônica Grieneisen³, Athanasius F. M. Marée³, J. Andrew Bangham^{2†}, Enrico Coen^{1*}

1 Department of Cell and Developmental Biology, John Innes Centre, Norwich, England, United Kingdom, **2** School of Computational Sciences, University of East Anglia, Norwich, England, United Kingdom, **3** Department of Computational and Systems Biology, John Innes Centre, Norwich, England, United Kingdom

 These authors contributed equally to this work.

 Deceased.

^{ea} Current address: School of Computational Sciences, University of East Anglia, Norwich, England, United Kingdom

^{eb} Current address: UMR LEPSE, Montpellier SupAgro/INRA, Montpellier, France

^{ec} Current address: Institute of Plant Sciences, University of Bern, Bern, Switzerland

^{ed} Current address: Department of Agricultural and Environmental Sciences—Production, Landscape, Agroenergy, University of Milan, Milan, Italy

^{ee} Current address: MRC-Laboratory of Molecular Biology, Cambridge Biomedical Campus, Francis Crick Avenue, Cambridge, England, United Kingdom

* enrico.coen@jic.ac.uk



 OPEN ACCESS

Citation: Fox S, Southam P, Pantin F, Kennaway R, Robinson S, Castorina G, et al. (2018) Spatiotemporal coordination of cell division and growth during organ morphogenesis. *PLoS Biol* 16 (10): e2005952. <https://doi.org/10.1371/journal.pbio.2005952>

Academic Editor: Mark Estelle, University of California San Diego, United States of America

Received: March 8, 2018

Accepted: September 20, 2018

Published: November 1, 2018

Copyright: © 2018 Fox et al. This is an open access article distributed under the terms of the [Creative Commons Attribution License](https://creativecommons.org/licenses/by/4.0/), which permits unrestricted use, distribution, and reproduction in any medium, provided the original author and source are credited.

Data Availability Statement: Images and models software from this study are available at <https://figshare.com/s/b14c8e6cb1fc5135dd87>. Models and GFTbox modeling software are also available at <http://cmpdartsvr3.cmp.uea.ac.uk/wiki/BanghamLab/index.php/Software>.

Funding: Biotechnology and Biological Sciences Research Council (grant number BB/P013511/1, BB/J004588/1). The funder had no role in study design, data collection and analysis, decision to publish, or preparation of the manuscript.

Abstract

A developing plant organ exhibits complex spatiotemporal patterns of growth, cell division, cell size, cell shape, and organ shape. Explaining these patterns presents a challenge because of their dynamics and cross-correlations, which can make it difficult to disentangle causes from effects. To address these problems, we used live imaging to determine the spatiotemporal patterns of leaf growth and division in different genetic and tissue contexts. In the simplifying background of the *speechless* (*spch*) mutant, which lacks stomatal lineages, the epidermal cell layer exhibits defined patterns of division, cell size, cell shape, and growth along the proximodistal and mediolateral axes. The patterns and correlations are distinctive from those observed in the connected subepidermal layer and also different from the epidermal layer of wild type. Through computational modelling we show that the results can be accounted for by a dual control model in which spatiotemporal control operates on both growth and cell division, with cross-connections between them. The interactions between resulting growth and division patterns lead to a dynamic distributions of cell sizes and shapes within a deforming leaf. By modulating parameters of the model, we illustrate how phenotypes with correlated changes in cell size, cell number, and organ size may be generated. The model thus provides an integrated view of growth and division that can act as a framework for further experimental study.

Biotechnology and Biological Sciences Research Council (grant number BB/M023117/1, BB/F005997/1, and BB/L008920/1). Received by EC. The funder had no role in study design, data collection and analysis, decision to publish, or preparation of the manuscript. ERC (grant number Camomorph, 323028). Received by EC. The funder had no role in study design, data collection and analysis, decision to publish, or preparation of the manuscript. Biotechnology and Biological Sciences Research Council (grant number BB/F005555/1). Received by AB. The funder had no role in study design, data collection and analysis, decision to publish, or preparation of the manuscript. Marie Skłodowska-Curie actions (grant number HEMOTIONAL, 329784). Received by FP. The funder had no role in study design, data collection and analysis, decision to publish, or preparation of the manuscript. Consejo Nacional de Ciencia y Tecnología. Received by YSC. The funder had no role in study design, data collection and analysis, decision to publish, or preparation of the manuscript.

Competing interests: The authors have declared that no competing interests exist.

Abbreviations: \bar{A} , mean threshold cell area for division execution; CD, cumulative difference; CDIV, competence to divide; CER, controlled environment room; *cyc1AT-GUS*, *cyclin1 Arabidopsis thaliana* β -glucuronidase; DAI, day after initiation; HAI, hour after initiation; FAMA, basic helix-loop-helix transcription factor (bHLH097, KLUH, *Arabidopsis* cytochrome P450/CYP78A5; K_{par} , specified growth rate parallel to polarity axis; K_{per} , specified growth rate perpendicular to polarity axis; KRN, growth regulatory network; LAM, a factor distinguishing lamina from petiole; LATE, a timing factor; LOCO-EFA, Lobe-Contribution Elliptic Fourier Analysis; MID, a mediolateral factor; mPS-PI, modified pseudo-Schiff propidium iodide; PGRAD, a graded proximodistal factor; PMF, proximal mobile factor; POL, factor determining polarity field; SDS, Sodium Dodecyl Sulfate; spch, *speechless*; v-cell, virtual cell.

Author summary

Organ morphogenesis involves two coordinated processes: growth of tissue and increase in cell number through cell division. Both processes have been analysed individually in many systems and shown to exhibit complex patterns in space and time. However, it is unclear how these patterns of growth and cell division are coordinated in a growing leaf that is undergoing shape changes. We have addressed this problem using live imaging to track growth and cell division in the developing leaf of the mustard plant *Arabidopsis thaliana*. Using subsequent computational modelling, we propose an integrated model of leaf growth and cell division, which generates dynamic distributions of cell size and shape in different tissue layers, closely matching those observed experimentally. A key aspect of the model is dual control of spatiotemporal patterns of growth and cell division parameters. By modulating parameters in the model, we illustrate how phenotypes may correlate with changes in cell size, cell number, and organ size.

Introduction

The development of an organ from a primordium typically involves two types of processes: increase in cell number through division, and change in tissue shape and size through growth. However, how these processes are coordinated in space and time is unclear. It is possible that spatiotemporal regulation operates through a single control point: either on growth with downstream effects on division, or on division with downstream effects on growth. Alternatively, spatiotemporal regulation could act on both growth and division (dual control), with cross talk between them. Distinguishing between these possibilities is challenging because growth and division typically occur in a context in which the tissue is continually deforming. Moreover, because of the correlations between growth and division it can be hard to distinguish cause from effect [1]. Plant development presents a tractable system for addressing such problems because cell rearrangements make little or no contribution to morphogenesis, simplifying analysis [2].

A growing plant organ can be considered as a deforming mesh of cell walls that yields continuously to cellular turgor pressure [3,4]. In addition to this continuous process of mesh deformation, new walls are introduced through cell division, allowing mesh strength to be maintained and limiting cell size. It is thus convenient to distinguish between the continuous expansion and deformation of the mesh, referred to here as growth, and the more discrete process of introducing new walls causing increasing cell number, cell division [5–8].

The developing *Arabidopsis* leaf has been used as a system for studying cell division control within a growing and deforming tissue. Developmental snapshots of epidermal cells taken at various stages of leaf development reveal a complex pattern of cell sizes and shapes across the leaf, comprising both stomatal and non-stomatal lineages [9]. Cell shape analysis suggests that there is a proximal zone of primary proliferative divisions that is established and then abolished abruptly. Expression analysis of the cell cycle reporter construct *cyclin1 Arabidopsis thaliana* β -glucuronidase (*cyc1AT-GUS*) [10] shows that the proximal proliferative zone extends more distally in the subepidermal as compared with the epidermal layer. Analysis of the intensity of *cyc1AT-GUS*, which combines both epidermal and subepidermal layers, led to a one-dimensional model in which cell division is restricted to a corridor of fixed length in the proximal region of the leaf [11]. The division corridor is specified by a diffusible factor generated at the leaf base, termed mobile growth factor, controlled by expression of *Arabidopsis* cytochrome P450/CYP78A5 (*KLUII*). Two-dimensional models have been proposed based on

growth and cell division being regulated in parallel by a morphogen generated at the leaf base [12,13]. These models assume either a constant cell area at division, or constant cell cycle duration.

The above models represent important advances in understanding the relationships between growth and division, but leave open many questions, such as the relations of divisions to anisotropic growth, variations along both mediolateral and proximodistal axes, variation between cell layers, variation between genotypes with different division patterns, and predictions in relation to mutants that modify organ size, cell numbers, and cell sizes [14].

Addressing these issues can be greatly assisted through the use of live confocal imaging to directly quantify growth and division [15–22]. Local rates and orientations of growth can be estimated by the rate that landmarks, such as cell vertices, are displaced away from each other. Cell division can be monitored by the appearance of new walls within cells. This approach has been used to measure growth rates and orientations for developing *Arabidopsis* leaves and has led to a tissue-level model for its spatiotemporal control [16]. Live tracking has also been used to follow stomatal lineages and inform hypotheses for stomatal division control [23]. It has also been applied during a late stage of wild-type leaf development after most divisions have ceased [24]. However, this approach has yet to be applied across an entire leaf for extended periods to compare different cell layers and genotypes.

Here, we combine tracking and modelling of 2D growth in different layers of the growing *Arabidopsis* leaf to study how growth and division are integrated during organ morphogenesis. We exploit the *speechless* (*spch*) mutant to allow divisions to be followed in the absence of stomatal lineages, and show how the distribution and rates of growth and cell division vary in the epidermal and subepidermal layers along the proximodistal and mediolateral axes and in time. We further compare these findings to those of wild-type leaves grown under similar conditions. Our results reveal spatiotemporal variation in both growth rates and cell properties, including cell sizes, shapes, and patterns of division. By developing an integrated model of growth and division, we show how these observations can be accounted for by a model in which core components of both growth and division are under spatiotemporal control. Varying parameters of this model illustrates how changes in organ size, cell size, and cell number are likely interdependent, providing a framework for evaluating growth and division mutants.

Results

To develop an integrated model of growth and division, we first tracked the epidermis of *spch* mutants, as they exhibit a simplified pattern of cell lineages [23]. Cell division dynamics were monitored by measuring spatiotemporal variation in two components: competence and execution. Competence refers to whether a cell has the potential to divide at some point in the future, whereas execution refers to a cell undergoing division (i.e., being cleaved into two).

A proximal zone of division competence initially extends with tissue growth in the epidermis

Tracking cell vertices on the abaxial epidermis of *spch* seedlings imaged at about 12-h intervals allowed cells at a given developmental stage to be classified into those that would undergo division (competent to divide, green, Fig 1A), and those that did not divide for the remainder of the tracking period (black, Fig 1A). During the first time interval imaged (Fig 1A, 0–14 h), division competence was restricted to the basal half of the leaf, with a distal limit of about 150 μm (all distances are measured relative to the petiole-lamina boundary, Fig 1). To visualise the fate of cells at the distal limit, we identified the first row of nondividing cells (orange) and displayed them in all subsequent images. During the following time intervals, the zone of

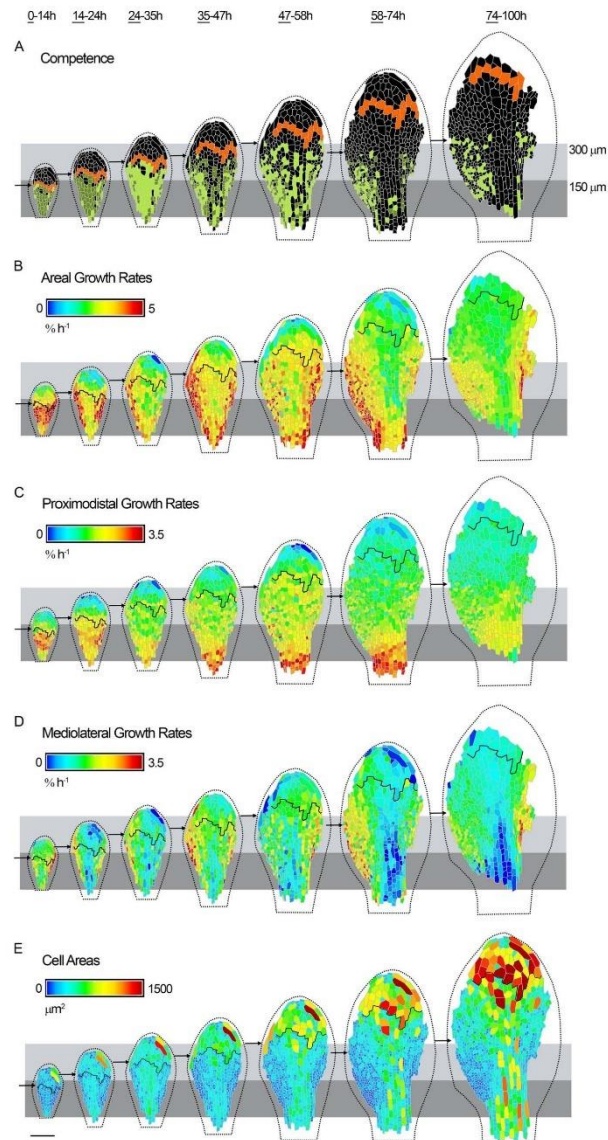


Fig 1. Dynamics of cell division and growth in the *spch* epidermis. Time-lapse imaging of a *spch* leaf at approximately 12-h intervals over 4 d (0–100 h; last time point in series not shown). Data shown on the first time point

(underlined) for each tracking interval. Leaf widths for the first time point (left to right) are 0.15, 0.22, 0.27, 0.31, 0.39, 0.48, and 0.68 mm. (A) Cells amenable to tracking that were competent to divide (green), and either executed division during the interval (light green) or divided in a later interval (dark green). Cells that did not divide (black, first row in 0–14 h are coloured orange throughout). For the last interval (74–100 h), cell divisions could only be tracked for a subset of cells because of missing data points at 100 h. (B–D) Cellular growth rates (heat maps) for each tracking interval. Black line refers to orange cells in (A). (B) Areal growth rates. (C) Growth rates parallel to the midline (proximodistal). (D) Growth rates perpendicular to the midline (mediolateral). (E) Cell areas for the first time point of the interval. Leaf outline indicated by dotted black line. The petiole-lamina boundary was defined by selecting a cell from a later stage of development, where the lamina narrows, and then tracing its lineage back to all stages. Grey boxes are aligned to the petiole-lamina boundary and extend to 150 or 300 μm . Black arrows indicate distal boundary of the zone of division competence. Scale bar = 100 μm . See also S1 Fig, S2 Fig, S3 Fig, S4 Fig, S5 Fig, and S6 Fig. Source data are available from <https://figshare.com/s/b14c8e6cb1fc5135dd87>. *spch*, *speechless*.

<https://doi.org/10.1371/journal.pbio.2005952.g001>

competence extended together with growth of the tissue to a distance of about 300 μm , after which it remained at this position, while orange boundary cells continued to extend further through growth. Fewer competent cells were observed in the midline region at later stages. Thus, the competence zone shows variation along the proximodistal and mediolateral axes of the leaf, initially extending through growth to a distal limit of about 300 μm and disappearing earlier in the midline region.

Execution of division exhibits spatiotemporal variation in the epidermis

To monitor execution of division, we imaged *spch* leaves at shorter intervals (every 2 h). At early stages, cells executed division when they reached an area of about 150 μm^2 (Fig 2A, 0–24 h). At later stages, cells in the proximal lamina (within 150 μm) continued to execute division at about this cell area (mean = 151 \pm 6.5 μm^2 , Fig 2B), while those in the more distal lamina or in the midline region executed divisions at larger cell areas (mean = 203 \pm 9.7 μm^2 or 243.0 \pm 22.4 μm^2 , respectively, Fig 2A, 2B and 2D). Cell cycle duration showed a similar pattern, being lowest within the proximal 150 μm of the lamina (mean = 13.9 \pm 0.8 h) and higher distally (mean = 19.4 \pm 1.8 h) or in the midline region (18.9 \pm 2.1 h, Fig 2C and 2E). Within any given region, there was variation around both the area at time of division execution and the cell cycle duration (Fig 2F and 2G). For example, the area at execution of division within the proximal 150 μm of the lamina had a mean of about 150 μm^2 , with standard deviation of about 40 μm^2 (Fig 2F). The same region had a cell cycle duration with a mean of about 14 h and a standard deviation of about 3 h. Thus, both the area at which cells execute division and cycle duration show variation around a mean, and the mean varies along the proximodistal and mediolateral axes of the leaf. These findings suggest that models in which either cell area at the time of division or cell cycle duration are fixed would be unable to account for the observed data.

Epidermal growth rates exhibit spatiotemporal variation

To determine how cell division competence and execution are related to leaf growth, we measured areal growth rates (relative elemental growth rates [25]) for the different time intervals, using cell vertices as landmarks (Fig 1B). Areal growth rates varied along both the mediolateral and proximodistal axis of the leaf, similar to variations observed for competence and execution of division. The spatiotemporal variation in areal growth rate could be decomposed into growth rates in different orientations. Growth rates parallel to the midline showed a proximodistal gradient, decreasing towards the distal leaf tip (Fig 1C and S1A Fig). By contrast, mediolateral growth was highest in the lateral lamina and declined towards the midline, becoming very low there in later stages (Fig 1D and S1B Fig). The region of higher mediolateral growth may correspond to the marginal meristem [26]. Regions of low mediolateral growth (i.e., the proximal midline) showed elongated cell shapes. Models for leaf growth therefore need to

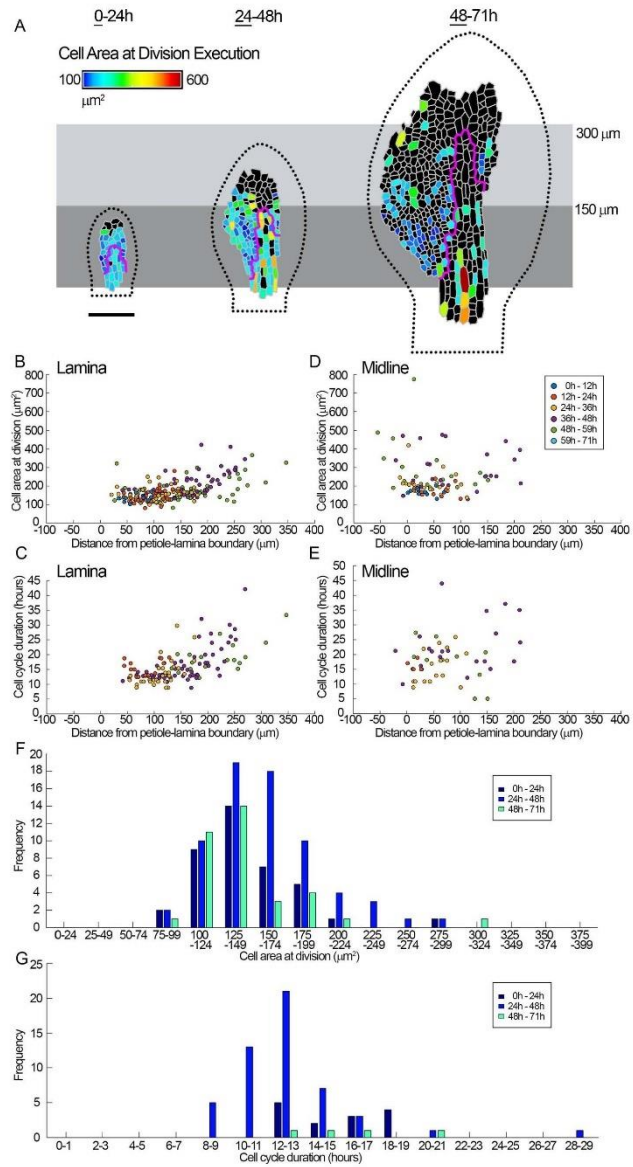


Fig 2. Quantification of cell division execution. Time-lapse imaging of a *spch* leaf imaged at 2-h intervals over 3 d (0–71 h, last time point in series not shown). Leaf widths for the first time point (left to right) are 0.09, 0.21, and 0.36 mm. (A) Cell area at division execution (heat map) for cells amenable to tracking, visualised over 24-h intervals and shown on the first time point of the interval (underlined). Cells that did not divide during the 24-h interval are coloured black. If cells divided more than once in the 24-h interval, the area of the first division is shown. Leaf outline indicated by dotted black line. The petiole-lamina boundary was defined as described in Fig 1. Grey boxes are aligned to the petiole-lamina boundary and extend to 150 or 300 μm . Cells within the magenta line were assigned as being within the midline region. (B–E) Data grouped into intervals of 12 h (inset in D). Means (μ) are shown with + ranges indicating $1.96 \times$ standard error, corresponding to the 95% confidence limit for a normal distribution. (B, D) Area of cells at division execution versus distance from the petiole-lamina boundary. (B) Cells in the lamina ($\mu = 170.8 \pm 7.7 \mu\text{m}^2$), mean cell area of cells within the proximal 150 $\mu\text{m} = 151 \pm 6.5 \mu\text{m}^2$, mean cell area of cells outside the proximal 150 $\mu\text{m} = 203 \pm 9.7 \mu\text{m}^2$. (D) Cells in the midline region ($\mu = 243.0 \pm 22.4 \mu\text{m}^2$). (C, E) Cell cycle duration versus distance from the petiole-lamina boundary. (C) Cells in the lamina ($\mu = 16.2 \pm 1.0$ h). For cells in the proximal 150 μm , $\mu = 13.9 \pm 0.8$ h. For cells outside the proximal 150 μm , $\mu = 19.4 \pm 1.8$ h. (E) Cells in the midline ($\mu = 18.9 \pm 2.1$ h). (F, G) Histograms of cell area at time of division execution, and cell cycle duration, during time intervals of 24 h (as in A). (F) Area at division execution for cells within the proximal 150 μm of the lamina ($\mu = \{145.6, 158.3, 142.6\}$, standard deviation $\sigma = \{36.3, 37.9, 40.1\}$). (G) Cell cycle duration for cells within the proximal 150 μm of the lamina ($\mu = \{15.8, 13.1, 16.7\}$, $\sigma = \{2.5, 3.3, 2.7\}$). Measurements of cell area and cell cycle duration are accurate to within 2 h (the time interval between imaging) of division execution. Scale bar = 100 μm . See also S7 Fig. Source data are available from <https://figshare.com/s/b14c86cb1fc5135dd87>. *spch*, *speechless*.

<https://doi.org/10.1371/journal.pbio.2005952.g002>

account not only for the spatiotemporal pattern of areal growth rates but also the pattern of anisotropy (differential growth in different orientations) and correlated patterns of cell shape.

Cell sizes reflect the combination of growth and division

Cell size should reflect both growth and division: growth increases cell size while division reduces cell size. Cell periclinal areas were estimated from tracked vertices (Fig 1E). Segmenting a sample of cells in 3D showed that these cell areas were a good proxy for cell size, although factors such as leaf curvature introduced some errors (for quantifications see S5 Fig, and ‘Analysis of cell size using 3D segmentation’ in Materials and methods). At the first time point imaged, cell areas were about 100–200 μm^2 throughout most of the leaf primordium (Fig 1E, left). Cells within the proximal 150 μm of the lamina remained small at later stages, reflecting continued divisions. In the proximal 150–300 μm of the lamina, cells were slightly larger, reflecting larger cell areas at division execution. Lamina cells distal to 300 μm progressively enlarged, reflecting the continued growth of these nondividing cells (Fig 1E and Fig 3A). Cells in the midline region were larger on average than those in the proximal lamina, reflecting execution of division at larger cell areas (Fig 1E and Fig 3C). Thus, noncompetent cells increase in area through growth, while those in the competence zone retain a smaller size, with the smallest cells being found in the most proximal 150 μm of the lateral lamina.

Correlations between cell size and growth rate

Visual comparison between areal growth rates (Fig 2B) with cell sizes (Fig 2E) suggested that regions with higher growth rates had smaller cell sizes. Plotting areal growth rates against log cell area confirmed this impression, revealing a negative correlation between growth rate and cell size (Fig 4B). Thus, rapidly growing regions tend to undergo more divisions. This relationship is reflected in the pattern of division competence: mean areal growth rates of competent cells in the lamina were higher than noncompetent cells, particularly at early stages (Fig 3I). However, there was no fixed threshold growth rate above which cells were competent, and for the midline region there was no clear difference between growth rates of competent and non-competent cells (Fig 3I). Plotting areal growth rates for competent and noncompetent cells showed considerable overlap (S6 Fig), with no obvious switch in growth rate when cells no longer divide (become noncompetent). Thus, high growth rate broadly correlates with division competence, but the relationship is not constant for different regions or times.

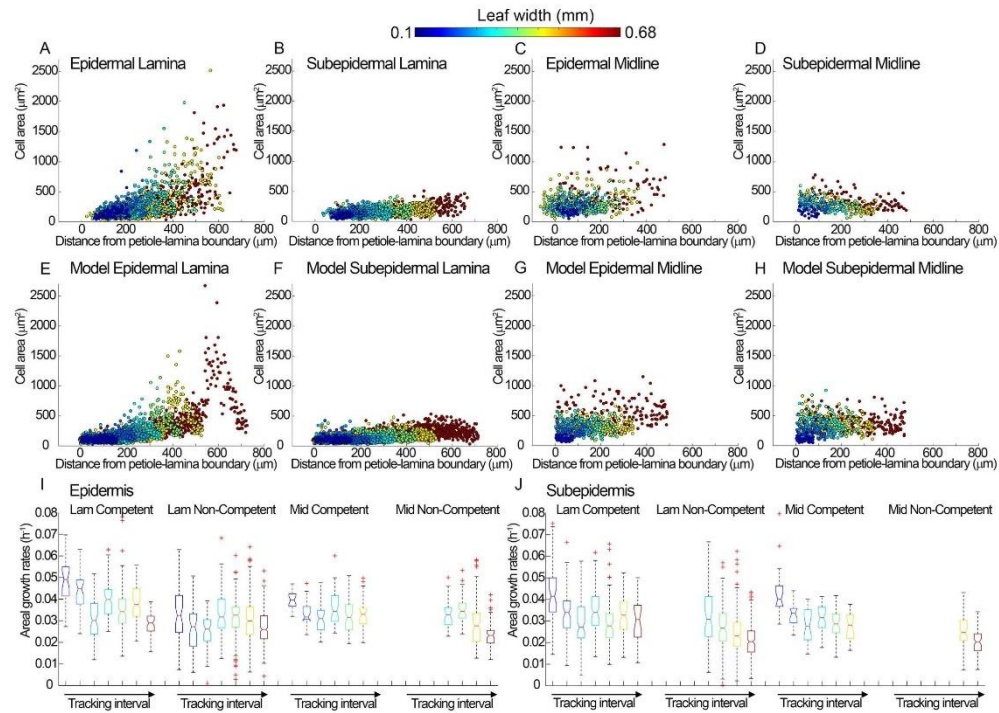


Fig 3. Quantification of cell areas and growth rates in epidermal and subepidermal data and models. (A–D) Data from cells amenable to tracking in the time-lapse experiment shown in Fig 1 and Fig 6. Data points are colour coded according to leaf width at the beginning of each time interval, as detailed in legend to Fig 1. (A) Epidermal cells in the lamina. (B) Subepidermal cells in the lamina. (C) Epidermal cells in the midline. (D) Subepidermal cells in the midline. (E–H) Output from epidermal and subepidermal models. (E) v-cells in the lamina of the epidermal model. (F) v-cells in the lamina of the subepidermal model. Model data points are colour coded according to leaf width at equivalent stages to the data. (G) v-cells in the midline of the epidermal model. (H) v-cells in the midline of the subepidermal model. (I–J) Areal growth rates of tracked cells in the lamina (Lam) and midline (Mid) regions, according to whether they were competent to divide or not competent to divide for the (I) epidermis and (J) subepidermis. Data are grouped according to tracking interval (as in Fig 1); colours represent leaf widths at the start of each interval (as for A–D). Boxes represent the central 50% of the data, with top and bottom at the 25% and 75% quantiles of the data. Central red lines represent the median of the data, and two medians are significantly different (at a 5% significance level) if their notches overlap. Outliers are shown as red crosses. Data with a sample size less than 15 are omitted. Source data are available from <https://figshare.com/s/b14c8e6cb1fc5135dd87>. Lam, lamina; Mid, midline; v-cell, virtual cell.

<https://doi.org/10.1371/journal.pbio.2005952.g003>

Subepidermal division rules can be decoupled from those of the overlying epidermis

To determine how the patterns and correlations observed for the epidermis compared to those in other tissues, we analysed growth and divisions in the subepidermis. The advantage of analysing an adjacent connected cell layer is that unless intercellular spaces become very large, the planar cellular growth rates will be very similar to those of the attached epidermis (because of tissue connectivity and lack of cell movement). Comparing the epidermal and subepidermal layers therefore provides a useful system for analysing division behaviours in a similar spatio-temporal growth context. Moreover, by using the *spch* mutant, one of the major distinctions in

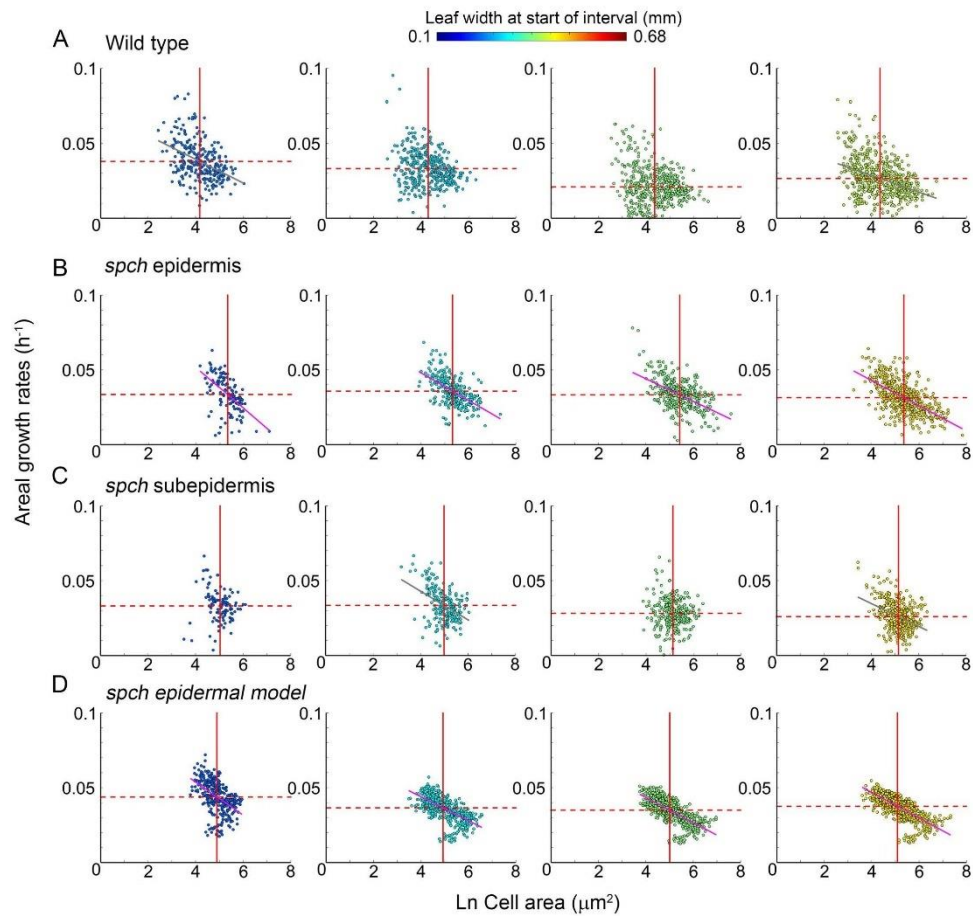


Fig 4. Correlations between growth rates and cell size. Areal cell growth rates against log cell area for time intervals at different developmental stages. Data points are colour coded according to leaf width at the start of the interval (colour scale is shown at the top). Solid red lines indicate mean cell areas (μ_a) and dashed red lines indicate mean growth rate (μ_k), with \pm ranges indicating $1.96 \times$ standard error of mean. Lines fitted for $R^2 > 0.2$ are shown in magenta; those with $R^2 < 0.2$ and > 0.1 are shown in grey (p -values are all less than 5.1×10^{-6} for line fits). (A) Wild type (from dataset shown in Fig 7B–7D, time intervals: 12–25 h, 25–37 h, 37–47 h, 47–57 h). From left to right, $\mu_a = \{4.2 \pm 0.08, 4.3 \pm 0.07, 4.4 \pm 0.07, 4.4 \pm 0.07\}$, $\mu_k = \{0.038 \pm 0.001, 0.033 \pm 0.001, 0.021 \pm 0.001, 0.026 \pm 0.001\}$, gradient $m = \{-0.008, -0.004, -0.002, -0.006\}$, and $R^2 = \{0.18, -, -, 0.14\}$. (B) *spch* epidermis (from dataset shown in Fig 1, time intervals: 14–24 h, 35–47 h, 47–58 h, 58–74 h), $\mu_a = \{5.3 \pm 0.08, 5.3 \pm 0.06, 5.4 \pm 0.06, 5.4 \pm 0.06\}$, $\mu_k = \{0.033 \pm 0.001, 0.036 \pm 0.001, 0.033 \pm 9 \times 10^{-4}, 0.031 \pm 8 \times 10^{-4}\}$, $m = \{-0.014, -0.009, -0.008, -0.008\}$, and $R^2 = \{0.31, 0.31, 0.27, 0.38\}$. (C) *spch* subepidermis (from dataset shown in Fig 6, time intervals: 14–24 h, 35–47 h, 47–58 h, 58–74 h), $\mu_a = \{5.0 \pm 0.09, 5.0 \pm 0.06, 5.1 \pm 0.05, 5.1 \pm 0.05\}$, $\mu_k = \{0.033 \pm 0.002, 0.033 \pm 0.001, 0.028 \pm 0.001, 0.026 \pm 9 \times 10^{-4}\}$, $m = \{-0.003, -0.010, -0.002, -0.008\}$, and $R^2 = \{-, 0.19, -, 0.15\}$. (D) *spch* epidermal model output at stages corresponding to leaf widths in (B), $\mu_a = \{4.9 \pm 0.05, 4.9 \pm 0.05, 5.0 \pm 0.04, 5.0 \pm 0.04\}$, $\mu_k = \{0.045 \pm 0.001, 0.037 \pm 5 \times 10^{-4}, 0.035 \pm 0.004, 0.038 \pm 1 \times 10^{-4}\}$, $m = \{-0.012, -0.008, -0.008, -0.009\}$, $R^2 = \{0.33, 0.42, 0.54, 0.59\}$. Source data are available from <https://figshare.com/s/b14c8e6cb1fc5135dd87>. Ln, natural logarithm; *spch*, *speechless*.

<https://doi.org/10.1371/journal.pbio.2005952.g004>

division properties between these layers (the presence of stomatal lineages in the epidermis) is eliminated.

Divisions in the abaxial subepidermis were tracked by digitally removing the overlying epidermal signal (the distalmost subepidermal cells could not be clearly resolved). As with the epidermis, 3D segmentation showed that cell areas were a good proxy for cell size, although average cell thickness was greater (S11 Fig, see also 'Analysis of cell size using 3D segmentation' in Materials and methods). Unlike the epidermis, intercellular spaces were observed for the subepidermis. As the tissue grew, subepidermal spaces grew and new spaces formed (Fig 5A–5D). Similar intercellular spaces were observed in subepidermal layers of wild-type leaves, showing they were not specific to *spch* mutants (S8 Fig).

Vertices and intercellular spaces in the subepidermis broadly maintained their spatial relationships with the epidermal vertices (Fig 5C, 5E and 5F). Comparing the cellular growth rates in the plane for a patch of subepidermis with the adjacent epidermis showed that they were similar (S9 Fig), although the subepidermal rates were slightly lower because of the intercellular spaces. This correlation is expected, because unless the intercellular spaces become very large, the areal growth rates of the epidermal and subepidermal layers are necessarily similar.

The most striking difference between subepidermal and epidermal datasets was the smaller size of the distal lamina cells of the subepidermis (compare Fig 6A with Fig 1E, and Fig 3A with Fig 3B). For the epidermis, these cells attain areas of about $1,000 \mu\text{m}^2$ at later stages, while for the subepidermis they remain below $500 \mu\text{m}^2$. This finding was consistent with the subepidermal division competence zone extending more distally (Fig 6B), reaching a distal limit of about $400 \mu\text{m}$ compared with $300 \mu\text{m}$ for the epidermis. A more distal limit for the subepidermis has also been observed for cell cycle gene expression in wild type [10]. Moreover, at early stages, divisions occurred throughout the subepidermis rather than being largely proximal, as observed in the epidermis, further contributing to the smaller size of distal subepidermal cells (S10 Fig). Despite these differences in cell size between layers, subepidermal cell areal growth rates showed similar spatiotemporal patterns to those of the overlying epidermis, as expected because of tissue connectivity (compare Fig 6C with Fig 1B). Consequently, correlations between growth rate and cell size were much lower for the subepidermis than for the epidermis (Fig 4B and 4C).

This difference in the relationship between growth and cell size in different cell layers was confirmed through analysis of cell division competence. In the subepidermis, at early stages there was no clear difference between mean growth rates for competent and noncompetent cells (Fig 3J cyan, green), in contrast to what is observed in the epidermis (Fig 3I cyan, green), while at later stages noncompetent cells had a slightly lower growth rate (Fig 3J yellow, red).

SPCH promotes division competence

To determine how the patterns of growth and division observed in *spch* related to those in wild type, we imaged a line generated by crossing a *spch* mutant rescued by a functional SPCH protein fusion (*pSPCH:SPCH-GFP*) to wild type expressing the *PIN3* auxin transporter (*PIN3:PIN3-GFP*), which marks cell membranes in the epidermis [23]. The resulting line allows stomatal lineage divisions to be discriminated from non-stomatal divisions (see below) in a *SPCH* context. At early stages, wild-type and *spch* leaves were not readily distinguishable based on cell size (S12 Fig). However, by the time leaf primordia attained a width of about $150 \mu\text{m}$, the number and size of cells differed dramatically. Cell areas in wild type were smaller in regions outside the midline region, compared with corresponding cells in *spch* (Fig 7A). Moreover, cell divisions in wild type were observed throughout the lamina that was amenable to tracking (Fig 7B, 0–12 h), rather than being largely proximal. Divisions were observed over the entire

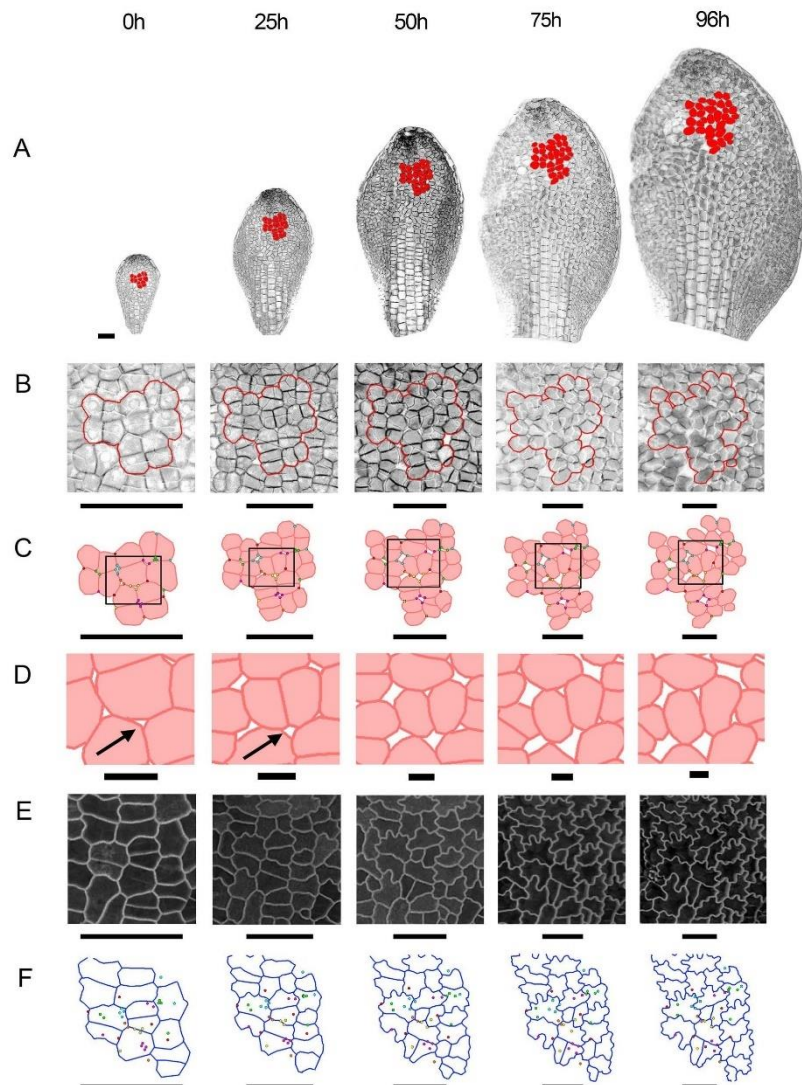


Fig 5. Subepidermal and epidermal cells in a *spch* leaf. (A) Projections of the subepidermal layer, imaged approximately every 24 h over 4 d (0–96 h). Cell divisions and growth for the epidermal layer of this leaf are shown in S3 Fig. Leaf widths (left to right) are 0.17, 0.27, 0.39, 0.50, and 0.58 mm. A patch of cells was tracked between intervals (cells coloured red). (B) Enlargement of the patch of cells in (A) (red outline). (C) Cells outlined in (B), showing individual cells (filled pink, outlined red) and vertices around some air spaces (coloured dots, also shown in F). (D) Enlargement of cells located in the black box of C, showing air spaces (white, examples

highlighted with black arrows). (E) Epidermal cells adjacent to the subepidermal patch (B). (F) Outlines of epidermal cells (blue) with vertices of subepidermal cells (coloured spots, also shown in C). Scale bars for A, B, C, E, F = 50 μm ; scale bar for D = 10 μm . See also S8 Fig and S9 Fig. Source data are available from <https://figshare.com/s/b14c8e6cb1fc5135dd87>. *spch*, *speechless*.

<https://doi.org/10.1371/journal.pbio.2005952.g005>

lamina for subsequent time intervals, including regions distal to 300 μm (Fig 7B, 12–57 h). These results indicate that SPCH can confer division competence in epidermal cells outside the proximal zone observed in *spch* mutants.

SPCH acts autonomously to reduce the cell area at which cells execute division

To further clarify how SPCH influences cell division, we used SPCH-GFP signal to classify wild-type cells into two types: (1) Stomatal lineage divisions, which include both amplifying divisions (cells express SPCH strongly around the time of division and retain expression in one of the daughter cells) (S1 Video, orange/yellow in Fig 7C) and guard mother cell divisions (SPCH expression is bright and diffuse during the first hours of the cycle, transiently switched on around time of division, and then switched off in both daughters). (2) Non-stomatal divisions, in which SPCH expression is much weaker, or only lasts <2 h, and switches off in both daughter cells (S2 Video, light/dark green in Fig 7C).

If cells with inactive SPCH behave in a similar way in wild-type or *spch* mutant contexts, we would expect non-stomatal divisions to show similar properties to divisions in the *spch* mutant. In the first time interval, non-stomatal divisions (green) were observed within the proximal 150 μm (Fig 7C, 0–12 h), similar to the extent of the competence zone in *spch* (Fig 1A, 0–14h). The zone of non-stomatal divisions then extended to about 250 μm and became restricted to the midline region. After leaf width was greater than 0.45 mm, we did not observe further non-stomatal divisions in the midline region, similar to the situation in *spch* leaves at a comparable width (Fig 1A, 58–74h, 0.48 mm). These results suggest that similar dynamics occur in the non-stomatal lineages of wild type and the *spch* mutant.

To determine how SPCH modulates division, we analysed stomatal and non-stomatal divisions in the lamina. Considerable variation was observed for both the area at which cells divide (25–400 μm^2) and cell cycle duration (8–50 h) (S13 Fig). The mean area at which cells execute division was greater for non-stomatal divisions (about $165 \pm 28 \mu\text{m}^2$ [1.96 \times standard error]) than stomatal divisions (about $80 \pm 6 \mu\text{m}^2$) (S13 Fig). Similarly, cell cycle durations were longer for non-stomatal divisions (about 25 ± 3 h) compared with stomatal divisions (about 18 ± 1 h). These results suggest that in addition to conferring division competence, SPCH acts cell autonomously to promote division at smaller cell sizes and/or for shorter cell cycle durations.

Wild type and *spch* can grow at similar rates despite different division patterns

Given the alteration in cell sizes and division patterns in wild type compared to *spch*, we wondered if these may reflect alterations in growth rates. When grown on agar plates, *spch* mutant leaves grow more slowly than wild-type leaves (S14A Fig). The slower growth of *spch* could reflect physiological limitations caused by the lack of stomata, or an effect of cell size on growth—larger cells in *spch* cause a slowing of growth. However, the tracking data and cell size analysis of *spch* and wild type described above were carried out on plants grown in a bio-imaging chamber in which nutrients were continually circulated around the leaves. Growth rates for wild type and *spch* leaves grown in these conditions were comparable for much of early development, and similar to those observed for wild type on plates (compare Fig 7D with Fig

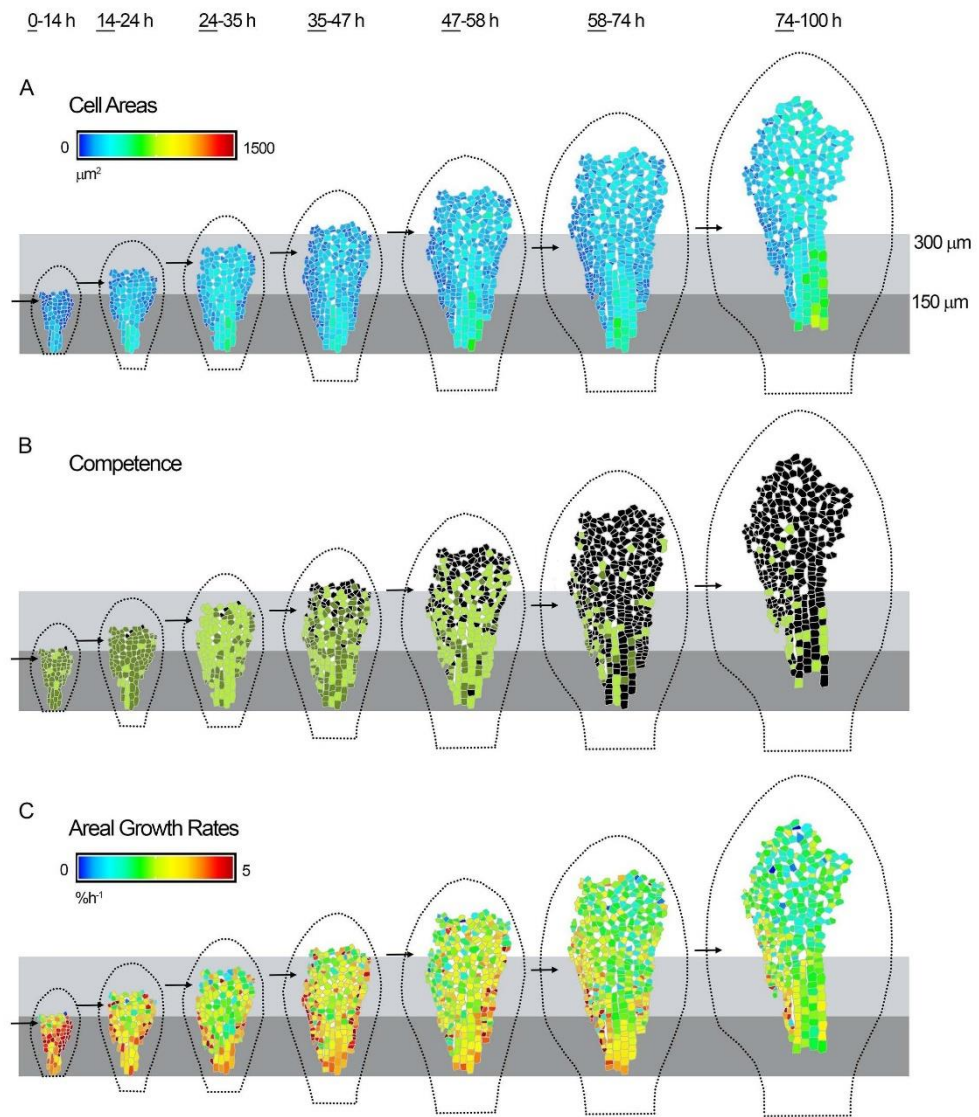


Fig 6. Dynamics of cell division and growth in the *spch* subepidermis. Cells amenable to tracking in the subepidermal layer of the *spch* leaf shown in Fig 1. Data shown on first time point (underlined) for each tracking interval. (A) Cell areas (heat map). (B) Cells that were competent to divide (green) and either executed

division during the interval (light green) or divided in a later interval (dark green). Cells that did not divide (black), intercellular air spaces (white). (C) Cellular areal growth rates (heat map). Leaf outline indicated by dotted black line. The petiole-lamina boundary was defined as described in Fig 1. Grey boxes are aligned to the petiole-lamina boundaries and extend to 150 or 300 μm . Black arrows indicate the distal boundary of the epidermal zone of division (as shown in Fig 1). Scale bar = 100 μm . See also S10 Fig and S11 Fig. Source data are available from <https://figshare.com/s/b14c8e6cb1fc5135dd87>. *spch*, *speechless*.

<https://doi.org/10.1371/journal.pbio.2005952.g006>

1B, S14 Fig). These results suggest that the reduced growth rates of *spch* compared with wild type at early stages on plates likely reflect physiological impairment caused by a lack of stomata rather than differences in cell size. As a further test of this hypothesis, we grew *fama* (basic helix-loop-helix transcription factor bHLH097) mutants, as these lack stomata but still undergo many stomatal lineage divisions [27]. We found that *fama* mutants attained a similar size to *spch* mutants on plates, consistent with the lack of stomata being the cause of reduced growth in these conditions (S14 Fig).

Plots of cell area against growth rates of tracked leaves grown in the chamber showed that, for similar growth rates, cells were about three times smaller in wild type compared with *spch* (compare Fig 4A with Fig 4B). Thus, the effects of *SPCH* on division can be uncoupled from effects on growth rate, at least at early stages of development.

At later stages (after leaves were about 1 mm wide), *spch* growth in the bio-imaging chamber slowed down compared with wild type, and leaves attained a smaller final size. This later difference in growth rate might be explained by physiological impairment of *spch* because of the lack of stomata, and/or by feedback of cell size on growth rates. This change in later behaviour may reflect the major developmental and transcriptional transition that occurs after cell proliferation ceases [9].

An integrated model of growth and division

The above results reveal that patterns of growth rate, cell division, and cell size and shape exhibit several features in *spch*: (1) a proximal corridor of cell division competence, with an approximately fixed distal limit relative to the petiole-lamina boundary; (2) the distal limit is greater for subepidermal (400 μm) than epidermal tissue (300 μm); (3) a further proximal restriction of division competence in the epidermis at early stages that extends with growth until the distal limit of the corridor (300 μm) is reached; (4) larger and narrower cells in the proximal midline region of the epidermis; (5) a proximodistal gradient in cell size in the epidermal lamina; (6) a negative correlation between cell size and growth rate that is stronger in the epidermis than subepidermis; (7) variation in both the size at which cells divide and cell cycle duration along both the proximodistal and mediolateral axes; and (8) variation in growth rates parallel or perpendicular to the leaf midline. In wild-type plants, these patterns are further modulated by the expression of *SPCH*, which leads to division execution at smaller cell sizes and extension of competence, without affecting growth rates at early stages. Thus, growth and division rates exhibit different relations in adjacent cell layers, even in *spch*, in which epidermal-specific stomatal lineages are eliminated, and division patterns can differ between genotypes (wild type and *spch*) without an associated change in growth rates.

These observations argue against spatiotemporal regulators acting solely on the execution of division, which then influences growth, as this would be expected to give conserved relations between division and growth. For the same reason, they argue against a single-point-of-control model in which spatiotemporal regulators act solely on growth, which then secondarily influences division. Instead, they suggest dual control, with spatiotemporal regulators acting on both growth and division components. With dual control, growth and division may still interact through cross-dependencies, but spatiotemporal regulation does not operate exclusively on one or the other.

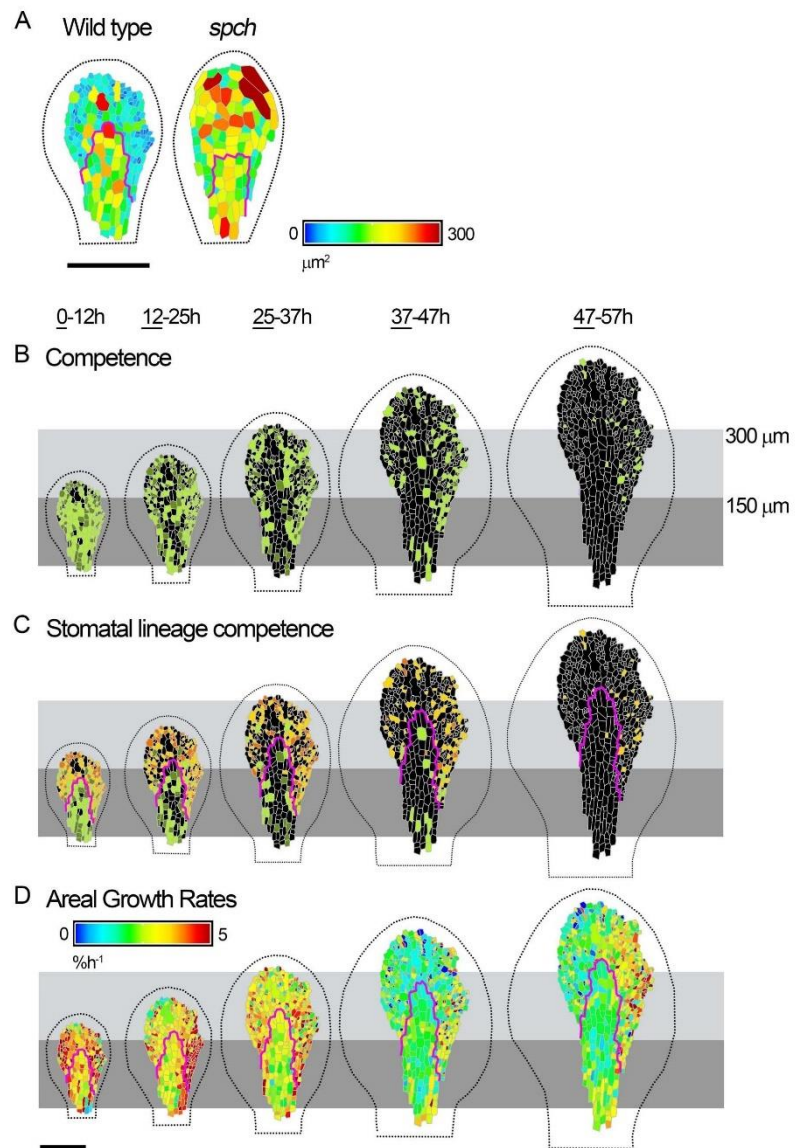


Fig 7. Dynamics of cell division and growth in the wild-type epidermis. (A) Cell areas (heat map) of wild-type (left) and *spch* (right) leaves at similar developmental stages. (B–D) Cells amenable to tracking from time-lapse imaging of a wild-type leaf (expressing *pSPCH:SPCH-GFP*, not shown) at approximately 1-h intervals over 2.5 d (0–57 h, last time point in series not shown). Data are visualised over about 12-h intervals and shown on first time point (underlined) for each interval. Leaf widths for first time point (left to right) are 0.17, 0.23, 0.28, 0.39, and 0.42 mm. (B) Cells amenable to tracking that were competent to divide (green) and either executed division during the interval (light green) or divided in a later interval (dark green). Cells that did not divide (black). (C) Non-stomatal divisions coloured as for (B). Stomatal lineage divisions that executed division during the interval (yellow) or divided in a later interval (orange). (D) Cellular areal growth rates (heat map) for each tracking interval. Leaf outline indicated by dotted black line. The petiole-lamina boundary was defined as described in Fig 1. Grey boxes are aligned to the petiole-lamina boundary and extend to 150 or 300 μm . Cells within the magenta lines were assigned as being destined to form the midline according to their position and shape in the final image. Scale bars = 100 μm . See also S12 Fig, S13 Fig, and S14 Fig. Source data are available from <https://figshare.com/s/b14c8e6cb1fc5135dd87>. GFP, green fluorescent protein; *spch*, speechless.

<https://doi.org/10.1371/journal.pbio.2005952.g007>

To determine how a hypothesis based on dual control may account for all the observations, we used computational modelling. We focussed on the epidermal and subepidermal layers of the *spch* mutant, as these lack the complications of stomatal lineages. For simplicity and clarity, spatiotemporal control was channelled through a limited set of components for growth and division (Fig 8A). There were two components for growth under spatiotemporal control: specified growth rates parallel and perpendicular to a proximodistal polarity field (K_{par} and K_{per} respectively) [16]. Together with mechanical constraints of tissue connectivity, these specified growth components lead to a pattern of resultant growth and organ shape change [28]. There were two components for cell division under spatiotemporal control: competence to divide (CDIV), and a threshold area for division execution that varies around a mean (\bar{A}). Controlling division execution by a threshold cell size (\bar{A}) introduces a cross-dependency between growth and division, as cells need to grow to attain the local threshold size before they can divide. The cross-dependency is indicated by the cyan arrow in Fig 8A, feeding information back from cell size (which depends on both growth and division) to division. An alternative to using \bar{A} as a component of division-control might be to use a mean cell cycle duration threshold. However, this would bring in an expected correlation between high growth rates and large cell sizes (for a given cell cycle duration, a faster-growing cell will become larger before cycle completion), which is the opposite trend of what is observed.

Spatiotemporal regulators of growth and division components can be of two types: those that become deformed together with the tissue as it grows (fixed to the tissue) and those that maintain their pattern to some extent despite deformation of the tissue by growth (requiring mobile or diffusible factors) [28]. In the previously published growth model, regulatory factors were assumed, for simplicity, to deform with the tissue as it grows [16]. These factors comprised a graded proximodistal factor (PGRAD), a mediolateral factor (MID), a factor distinguishing lamina from petiole (LAM), and a timing factor (LATE) (S15A and S15B Fig). However, such factors cannot readily account for domains with limits that remain at a constant distance from the petiole-lamina boundary, such as the observed corridors for division competence. This is because the boundary of a domain that is fixed to the tissue will extend with the tissue as it grows. We therefore introduced a mobile factor, proximal mobile factor (PMF), that was not fixed to the tissue to account for these behaviours. This motivation is similar to that employed by others [11–13]. PMF was generated at the petiole-lamina boundary and with appropriate diffusion and decay coefficients such that PMF initially filled the primordium and then showed a graded distribution as the primordium grew larger, maintaining a high concentration in the proximal region and decreasing towards the leaf tip (S15C and S15D Fig). This profile was maintained despite further growth, allowing thresholds to be used to define domains with relatively invariant distal limits. Further details of the growth model are given in Materials and methods, and the resultant growth rates are shown in S16 Fig (compare with Fig 1B and 1D).

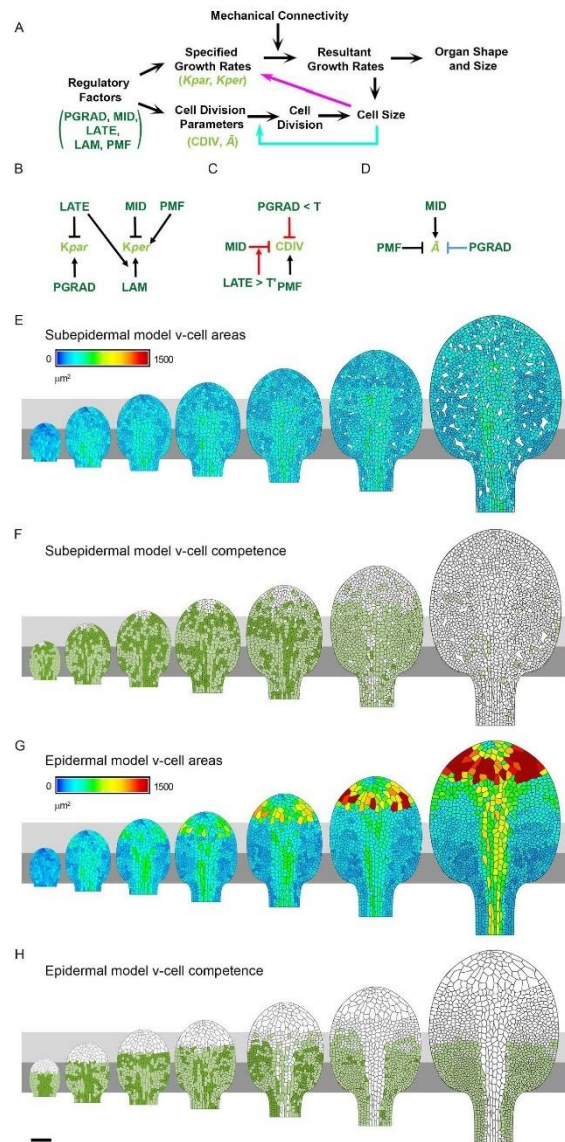


Fig 8. Model regulatory network and output. (A) Schematic showing how spatiotemporal regulatory factors (PGRAD, MID, LATE, LAM, PMF) act on components of specified growth (K_{par} , K_{per}) and cell division (CDIV and A)

to influence resultant growth, cell division, cell size, and organ shape and size. The magenta arrow shows an optional feedback on growth rate from cell size. The cyan arrow shows feedback from cell size to division. (B–D) Model regulatory networks for early stages of leaf development (124–182 h). (B) Growth regulatory network (KRN). Epidermal-specific interactions are denoted with red lines, subepidermal-specific interactions with light blue, and interactions common to both models with black. (C) The regulatory network for CDIV. (D) The division threshold (\bar{A}) regulatory network. (E–H) Model output leaves (left to right) at 115, 132, 140, 147, 156, 164, and 178 h for the (E–F) subepidermis model and (G–H) epidermis model. (E) Area and pattern of v-cells (heat map) with intercellular spaces (white). (F) v-cells that were competent to divide (green) and either executed division during the interval (light green) or divided in a later interval (dark green). Cells that did not divide (white). (G) Area and pattern of v-cells (heat map). (H) v-cells that were competent to divide (green) and either executed division during the interval (light green) or divided in a later interval (dark green). Cells that did not divide (white). Grey boxes are aligned to the petiole-lamina boundary and extend to 150 and 300 μm . Scale bar = 100 μm . See also S15 Fig and S16 Fig. Source data are available from <https://figshare.com/s/b14c86cb1fc5135dd87>. \bar{A} , threshold cell area for division execution; CDIV, competence to divide; K_{pm} , specified growth rate parallel to polarity axis; K_{pp} , specified growth rate perpendicular to polarity axis; KRN, growth regulatory network; LAM, a factor distinguishing lamina from petiole; LATE, a timing factor; MID, a mediolateral factor; PGRAD, a graded proximodistal factor; PMF, proximal mobile factor; v-cell, virtual cell.

<https://doi.org/10.1371/journal.pbio.2005952.g008>

Cells were incorporated by superimposing polygons on the initial tissue or canvas (S15A Fig, right). The sizes and geometries of these virtual cells (v-cells) were based on cells observed at corresponding stages in confocal images of leaf primordia [16]. The vertices of the v-cells were anchored to the canvas and displaced with it during growth. Cells divided according to Errera's rule: the shortest wall passing through the centre of the v-cell [29], with noise in positioning of this wall incorporated to capture variability. V-cells were competent to divide if they expressed factor CDIV, and executed division when reaching a mean cell target area, \bar{A} . As the observed area at time of division was not invariant (Fig 2F), we assumed the threshold area for division varied according to a standard deviation of $\sigma = 0.2\bar{A}$ around the mean. CDIV and \bar{A} are the two core components of division that are under the control of spatiotemporal regulators in the model (Fig 8A, 8C and 8D). Variation between epidermal and subepidermal patterns reflects different interactions controlling cell division (interactions colour coded red and blue, respectively, in Fig 8C and 8D).

We first modelled cell divisions in the subepidermis, as this layer shows a more uniform pattern of cell sizes (Fig 3B and Fig 6A). Formation of intercellular spaces was simulated by replacing a random selection of cell vertices with small empty equilateral triangles, which grew at a rate of $2.5\% \text{ h}^{-1}$, an average estimated from the tracking data. To account for the distribution of divisions and cell sizes, we assumed that v-cells were competent to divide (express CDIV) where PMF was above a threshold value. This value resulted in the competence zone extending to a distal limit of about 400 μm . To account for the proximodistal pattern of cell areas in the lamina (Fig 3B and Fig 6A) and larger cells in the midline (Fig 3D and Fig 6A), we assumed that \bar{A} was modulated by the levels of PMF, PGRAD, and MID (Fig 8D, black and blue). These interactions gave a pattern of average v-cell areas and division competence that broadly matched those observed (compare Fig 8E and 8F with Fig 6A and 6B, and Fig 3F and 3H with 3B and 3D, S3 Video).

For the epidermis, the zone of division competence was initially in the proximal region of the primordium and then extended with the tissue as it grew (Fig 1A). We therefore hypothesised that in addition to division being promoted by PMF, there was a further requirement for a proximal factor that extended with the tissue as it grew. We used PGRAD to achieve this additional level of control, assuming CDIV expression requires PGRAD to be above a threshold level (Fig 8C, red and black). V-cells with PGRAD below this threshold were not competent to divide, even in the presence of high PMF. Thus, at early stages, when PMF was high throughout the primordium, the PGRAD requirement restricted competence to the proximal region of the leaf (Fig 8H). At later stages, as the PGRAD domain above the threshold extended beyond 300 μm , PMF became limiting, preventing CDIV from extending beyond about 300

μm . To account for the earlier arrest of divisions in the midline region (Fig 1A), CDIV was inhibited by MID when LATE reached a threshold value (Fig 8C, red). As well as CDIV being regulated, the spatiotemporal pattern of \bar{A} was modulated by factors MID and PMF (Fig 8D black).

With these assumptions, the resulting pattern of epidermal divisions and v-cell sizes broadly matched those observed experimentally for the epidermis (compare Fig 8G with Fig 1E, S4 Video). In particular, the model accounted for the observed increases in cells sizes with distance from the petiole-lamina boundary, which arise because of the proximal restrictions in competence (compare Fig 3E and 3G with Fig 3A and 3C). The model also accounted for the elongated cell shapes observed in the midline region, which arise through the arrest of division combined with low specified growth rate perpendicular to the polarity. Moreover, the negative correlations between growth rates and cell size, not used in developing the model, were similar to those observed experimentally (Fig 4B and 4D). These correlations arise because both growth and division are promoted in proximal regions.

We also measured the cell topology generated by the epidermal model. It has previously been shown that the frequency of six-sided neighbours observed experimentally for the *spch* leaf epidermis is very low compared with that for other plant and animal tissues and also with that generated by a previous implementation of Errera's rule (S17 Fig) [30]. The topological distribution generated by the epidermal leaf model gave a six-sided frequency similar to that observed experimentally, falling two standard deviations away from the mean and thus close to a reasonable fit (S17 Fig). The increased similarity of the model output to the *spch* leaf epidermal topology, compared with a previous implementation of Errera's rule [31], may reflect the incorporation of anisotropic growth in our model. If polarity is removed from our model to render specified growth as isotropic (while preserving local areal growth rates), the frequency of six-sided neighbours increases, becoming more like the empirical data for the shoot apical meristem (S17 Fig). A further likely contribution to the lowering of six-sided neighbour frequency generated by our model is the use of random noise to displace the positioning of new walls, rather than positioning them always to pass precisely through the cell centre. Thus, our analysis shows how incorporating more realistic growth patterns can be valuable in evaluating division rules.

Taken together, the simulations show that the pattern of growth and division can be broadly accounted for by factors modulating specified growth rates (K_{par} and K_{per}) and cell division components (CDIV and \bar{A}). Variation between epidermal and subepidermal patterns generated by the models reflects different interactions controlling cell division (Fig 8C and 8D).

Modulation of model parameters leads to variation in leaf size, cell number, and cell size

Many mutants have been described that influence cell division and/or leaf size [32,33]. To gain a better understanding of such mutants, we explored how changes in key parameters in our model may alter leaf size, cell size, and cell number. As leaf size is normally measured at maturity, we first extended our analysis to later stages of development. Tracking *spch* to later stages of development showed that overall growth rates declined, on average, while remaining relatively high towards the proximal region of the lamina (S4B Fig), consistent with a previous study [18]. Cell divisions were not observed after the leaf reached a width of about 0.9 mm (S4A Fig, 96h). To capture arrest of division, we assumed that CDIV was switched off throughout the leaf after LATE reached a threshold value.

In the previously published growth model [16], the decline of growth rates with developmental time was captured through an inhibitory effect of LATE on growth. To extend the model to later stages and bring about eventual arrest of growth, we assumed that LATE increased exponentially after 189 h and inhibited both K_{per} and K_{par} thereafter. Parameters for growth inhibition were adjusted to give a final leaf width of about 3 mm, which was the final size attained for leaf 1 in *spch* mutants in the bio-imaging chamber. The v-cell sizes generated by the model broadly matched the patterns observed (Fig 9A and 9B, S5 Video). As epidermal divisions have ceased by the time the *spch* leaf is about 1 mm wide, all the growth depicted in Fig 9A and 9B occurs in the absence of division (i.e., cell expansion). However, a notable discrepancy between the model output and the experimental data was the generation of distal v-cells that exceeded the values observed (about 20,000 μm^2 compared with about 10,000 μm^2). A similar result was obtained if the model was tuned to match not only the final leaf width but also the reduced growth rate of *spch* in the growth chamber at later stages (S14B and S14C Fig). A better fit was obtained by inhibiting specified growth rates in distal regions at later stages. This inhibition was implemented by introducing inhibitory factors with levels that increased distally. The result was that distal v-cells remained at or below about 10,000 μm^2 (Fig 9C and S6 Video). We refer to this as the limit-free model. Another way of limiting the size of distal v-cells was to introduce feedback from cell size to growth, so that the specified growth rate decreased as v-cells approached upper size limits (Fig 9J and S7 Video). This feedback corresponds to introducing a further interaction in the regulatory pathway (Fig 8A, magenta). We refer to this as the limiting cell size model.

We varied parameters in both the limit-free model (Fig 9C) and the limiting cell size model (Fig 9J) to see how the parameters influence cell number, cell size, and final leaf size. Increasing \bar{A} by a constant amount did not change leaf size with the limit-free model but resulted in fewer, larger v-cells (Fig 9D). Reducing \bar{A} resulted in a leaf with more v-cells that were, on average, smaller but did not change leaf size (Fig 9E). With the limiting cell size model, increasing or decreasing \bar{A} had similar effects as with the limit-free model but also slightly reduced or increased leaf size (Fig 9K and 9L). Thus, it is possible to affect cell number and size without a major effect on organ size or growth.

To investigate how changing growth parameters influences cell numbers and areas, we reduced the specified growth rates (values for K_{par} and K_{per}) by 5%. For the limit-free model this resulted in a smaller leaf with both smaller and fewer v-cells (Fig 9F). There were fewer cells because they grew more slowly and thus took longer to reach \bar{A} , and cells were smaller because they grew at a slower rate after they had ceased dividing. Conversely, increasing specified growth rate by 5% led to larger leaves, with more v-cells that were, on average, larger (Fig 9G). The model with limiting cell size gave similar results (Fig 9M and 9N). Thus, modulating growth rates has consequences on organ size, cell size, and cell number. This may account for why many mutants with smaller organs have both fewer cells and smaller cells [34].

To examine the effect of changes in developmental timing, we altered the onset of LATE. Moving the onset earlier for the limit-free model led to smaller leaves because of the earlier decline in growth rate (Fig 9H). There were fewer v-cells because of the earlier arrest of division, and there was also a slight reduction in v-cell size. Delaying the onset of LATE had the opposite effect of increasing leaf size, cell number, and cell size (Fig 9I). The limiting cell size model gave similar results (Fig 9O and 9P). Thus, changes in developmental timing affected organ size and cell number, with a lesser effect on cell size. This is because changing LATE shifts both the onset of the growth rate decline and the time of division arrest (inactivation of CDIV).

A further application of the model is to explore the effects of the environment on leaf growth and division. To illustrate this possibility, we analysed data for the *spch* mutant grown

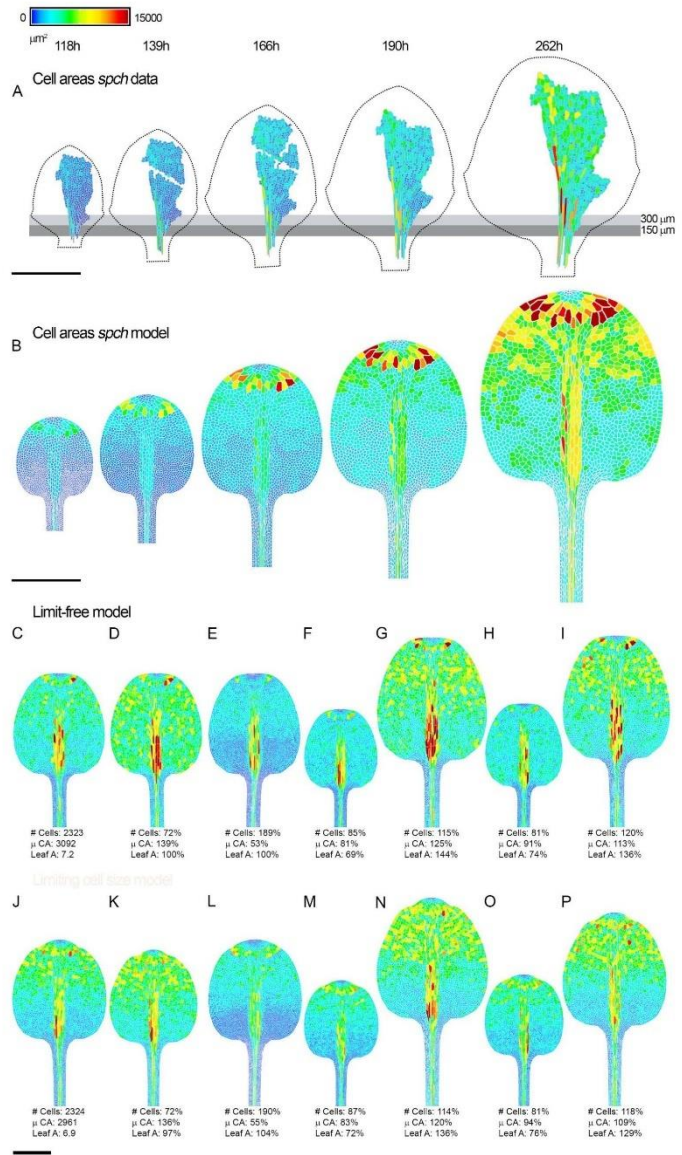


Fig 9. Cell areas, numbers, and leaf sizes at later developmental stages. (A) Cell areas for the *spch* leaf at later stages (earlier stages shown in S4 Fig). Leaf widths (left to right) are 1.1, 1.4, 1.8, 2.1, and 2.8 mm. Leaf outline is indicated by a dotted black line. Grey boxes are aligned to the petiole-lamina boundary and extend to 150 or 300 μm . (B) Model output at equivalent stages to experimental data (model times 201, 219, 243, 264, and 412 h). (C–I) Limit-free *spch* epidermal model outputs at maturity. (C) Wild type. (D) Cell division threshold increased by $85 \mu\text{m}^2$. (E) Cell division threshold decreased by $85 \mu\text{m}^2$. (F) Specified growth rate reduced by 5%. (G) Specified growth rate increased by 5%. (H) LATE comes on 6 h earlier. (I) LATE comes on 6 h later. (J–P) Limiting cell size *spch* epidermal model outputs at maturity. (J) Wild type. (K) Cell division threshold increased by $85 \mu\text{m}^2$. (L) Cell division threshold decreased by $85 \mu\text{m}^2$. (M) Specified growth rate reduced by 5%. (N) Specified growth increased by 5%. (O) LATE comes on 6 h earlier. (P) LATE comes on 6 h later. Number of cells (# Cells), average cell area (μCA) in μm^2 , and leaf area (Leaf A) in mm^2 are shown for each model. Percentage values for mutants show relative difference to limit-free (C) and limiting cell size (J) wild-type models. Scale bars = 1 mm. Source data are available from <https://figshare.com/s/b14c8e6cb1fc5135dd87>. # Cells, number of cells; μCA , average cell area; LATE, a timing factor; Leaf A, leaf area; *spch*, *speechless*.

<https://doi.org/10.1371/journal.pbio.2005952.g009>

on plates, which exhibits a greatly reduced growth rate compared with growth in the chamber (S14A and S14B Fig). A prediction of the model is that cell divisions should cease when the leaf is at a smaller size (i.e., the leaf will have grown less by the time the threshold value of LATE for division arrest is reached). In addition, as *spch* plants grown on plates have impaired general physiology, the rate of developmental progression (physiological time) may also be slowed down. We simulated these effects by modifying the model parameters such that the overall growth rate was reduced by 40% and physiological time reduced by 45%. This gave a growth curve matching that observed for *spch* grown on plates (blue line, S14A Fig). As expected, this model takes longer to attain a given leaf width (e.g., 0.5 mm) than the original model. The resulting cell areas are larger at the 0.5-mm leaf-width stage, particularly in proximal regions, because divisions arrest when the leaf is at a smaller size, so all subsequent cell growth occurs in the absence of division (Fig 10A and 10B and S18 Fig).

To test this prediction of enlarged cell size, we compared leaves when they had attained a width of about 0.5 mm (Fig 10C and 10D), which is just before divisions cease for *spch* grown in the chamber (Fig 1). Cells in the proximal lamina of the chamber-grown leaves were relatively small (mean = $123.3 \pm 6.4 \mu\text{m}^2$ for region shown in Fig 10I), typical of dividing cells (Fig 10C and 10G); whereas those of the plate-grown leaves were larger (mean = $199.8 \pm 17.3 \mu\text{m}^2$ for region shown in Fig 10J), indicating division arrest (Fig 10D and 10I and S18 Fig). Proximal lamina cells in plate-grown leaves also showed greater shape complexity, typical of pavement cells that have ceased division (Fig 10K–10N and S18 Fig). These results suggest that cell divisions in much of the lamina cease when the leaf is smaller for plate-grown compared to chamber-grown leaves, as predicted by the model. The sizes of midline cells for plate-grown leaves predicted by the model are larger than those observed (compare Fig 10B with Fig 10H), indicating that withdrawal of competence from this region, as implemented in the model, may be activated too early. Conversely, the most proximal lamina cells in the plate-grown leaves (dark blue cells, Fig 10H) are smaller than predicted (Fig 10B), suggesting that the uniform arrest of division when LATE reaches a threshold value is an oversimplification.

Discussion

Growth rates, cell division, and cell shapes and sizes in the growing first leaf of *Arabidopsis* exhibit complex spatiotemporal patterns. The main features observed in *spch* are (1) a proximal corridor of division competence with an approximately fixed distal limit; (2) the distal limit is greater for subepidermal compared to epidermal tissue; (3) a further proximal restriction of division competence in the epidermis at early stages that extends with growth until the distal limit is reached; (4) a proximodistal gradient in cell size in the epidermal lamina; (5) larger and narrower cells in the proximal midline region of the epidermis; (6) a negative

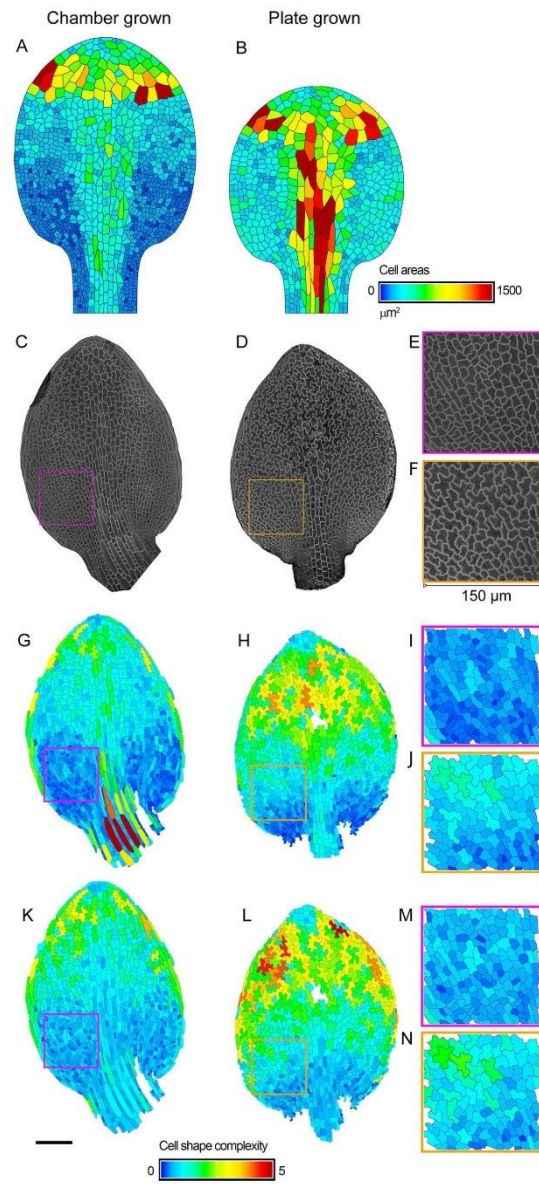


Fig 10. Comparison of *spch* epidermis grown in a bio-imaging chamber and on plates. (A, B) Model outputs when leaf has grown to a width of about 0.5 mm (see horizontal line in S14A Fig). (A) Epidermal model used to generate Fig 8G, corresponding to growth in a chamber. (B) Output from epidermal model tuned to match *spch* growth on plates (by slowing growth by 40% and physiological time by 45%). (C) Leaf grown in a bio-imaging chamber when width has attained 0.46 mm (8DAS). (D) Leaf grown on plates when width has attained 0.48 mm (13 DAS). (E) Enlargement of region indicated by magenta square in C. (F) Enlargement of region indicated by orange square in D. (G,H) Segmented cells from leaves shown in C,D. Cell area colour coded as heat map for A,B. (I) Enlargement of segmented region indicated by magenta square in G; average cell area $123.3 \pm 6.4 \mu\text{m}^2$ ($n = 184$). All cells with their centroid falling within the square were taken into account. (J) Enlargement of segmented region indicated by orange square in I; average cell area $199.8 \pm 17.3 \mu\text{m}^2$ ($n = 111$). (K,L) Cell complexity from leaves shown in C,D, quantified through the CD of the LOCO-EFA components of each individual cell's shape, normalised for cell area (see [Materials and methods](#)). Heat map range corresponds to zero for perfect circular or elliptical shapes, ranging to 5 as more LOCO-EFA harmonics are needed to describe the shape (dimensionless measure). (M) Enlargement of region indicated by magenta square in K. (N) Enlargement of region indicated by orange square in L. Scale bar = 100 μm . Source data are available from <https://figshare.com/s/b14c8e6cb1fc5135dd87>. CD, cumulative difference; DAS, days after stratification; LOCO-EFA, Lobe-Contribution Elliptic Fourier Analysis; *spch*, *speechless*.

<https://doi.org/10.1371/journal.pbio.2005952.g010>

correlation between cell size and growth rate that is stronger in the epidermis than in the subepidermis; (7) variation in both the size at which cells divide and cell cycle duration along both the proximodistal and mediolateral axes; (8) variation in growth rates parallel or perpendicular to the leaf midline. In wild-type plants these patterns are further modulated by expression of *SPCH*, which leads to division execution at smaller cell sizes and extension of competence, without affecting growth rates at early stages.

The observed varying relations between growth rates and division between tissue layers and genotypes argue against single-point-of-control models, in which spatiotemporal regulators act solely through either division or growth. Instead, they suggest dual control, in which spatiotemporal regulators act on both growth and division, with cross talk between them. We show that a model based on dual control can broadly account for the data. In this model, spatiotemporal control is channelled through two growth components (specified growth rates parallel and perpendicular to polarity) and two division components (competence and mean threshold size for division) (Fig 8A). The growth components reflect turgor and cell wall extensibility in different orientations, and the division components reflect regulatory mechanisms for partitioning cells. Orientation information is provided by a tissue-wide polarity field, for which direct evidence has recently been obtained in both wild-type and *spch* mutants [22,35]. The polarity field may be established through a biochemical mechanism as proposed here, likely involving tissue-level coordinated cell polarity [36]. Alternatively, information could be relayed through mechanical stresses [20,22,37]. The resulting patterns of growth and division determine the distribution of cell sizes and shapes and organ shape. The implications, limitations, and questions raised by this model are discussed below.

Growth, division, and cell size

Execution of leaf cell division does not occur at an unvarying cell size, even within a given region and developmental stage. Similar variability has been observed for cell divisions in apical meristems [21,38]. Variability may reflect experimental errors in estimation of cell size, stochasticity in the process of division, and/or mechanisms other than geometric size sensing that influence division execution (e.g., factors such as vacuole size, which is not monitored in our analysis). We model such variability by explicitly adding variation around a mean threshold size needed for division, \bar{A} . Controlling division execution by a threshold cell size (\bar{A}) introduces a cross-dependency between growth and division, as cells need to grow to attain the local threshold size before they can divide. An alternative to using \bar{A} would be to use a mean cell cycle duration threshold. However, this would bring in an expected correlation between

high growth rates and large cell sizes (for a given cell cycle duration, faster growing cells will become larger before cycle completion), which is the opposite of the correlation observed.

Role of tissue layers in growth

In contrast to the epidermal layer, intercellular spaces are observed in the subepidermis of wild-type and *spch* from early stages. The spaces may originate, in part, from a reduction in adhesion between subepidermal cells, allowing cell walls to become detached from each other. In addition to reduced adhesion, a further requirement for intercellular spaces is that cells are not too tightly packed against each other. Packing may be reduced if subepidermal cells have lower specified growth rates than the epidermis. Subepidermal cells could move away or be pulled apart from each other, as epidermal growth creates more space than they can fill through their own expansive growth. According to this view, the epidermis rather than the subepidermis provides the expansive force driving planar growth, in contrast to what has been described for other tissues, such as the stem [39]. A primary role for the epidermis in driving planar growth is also consistent with the observed developmental effects of epidermal gene activity [40]. However, it is possible that the subepidermis provides a restraint on growth, which could account for the effect of subepidermal tissue on leaf shape in some chimeras [41].

Spatiotemporal control

Spatiotemporal control of growth and division in the model of *spch* is established through combinatorial interactions between five factors: PGRAD, MID, LAM, LATE, and a mobile factor that allows proximal corridors with fixed distal limits to be established (PMF). PMF is similar to the previously proposed mobile growth factor [11], except that the effect of PMF on division does not have a consequential effect on growth. To account for the difference in distal limits of the division corridor between cell layers, PMF action extends more distally in the subepidermis compared with the epidermis, either because the competence threshold requirement for PMF is lower in the subepidermal layer, or because PMF levels are higher. A candidate factor for coordinating proliferation between layers is the transcriptional coactivator *ANGUSTI-FOLIA3* [42,43]. Candidates for LAM are *LEAFY PETIOLE* [44] and members of the *YABBY* gene family [45], which are expressed in the lamina and promote lateral outgrowth.

A fixed corridor for division has also been described for other systems such as the root, where a division zone is maintained at a distance of about 300–500 μm from the quiescent centre in *Arabidopsis* [46]. In contrast to the leaf, regions of highest growth rate in the root are outside the cell division zone, providing further support for a dual control mechanism. The spatial extent of the division zone in roots is maintained through auxin-cytokinin interactions [47]. Auxin-cytokinin interactions also influence leaf growth and division: temporal arrest of leaf growth depends on auxin-induced cytokinin breakdown [48]; increased cytokinin degradation in leaf primordia can accelerate termination of cell proliferation [49]; and accumulation of specific cytokinins may promote indeterminate leaf growth [50]. However, it is currently unclear whether auxin, cytokinin, and/or other molecular players underlie PMF.

A limitation of our model is that it does not consider modulation of growth or division near the leaf margin, creating serrations [51,52]. Serrations have previously been modelled by displacement of the leaf outline without modelling the tissue growth explicitly [52,53]. In terms of the modelling framework described here, they may reflect alterations in polarity and/or growth rates of tissue, and accounting for these behaviours would require the introduction of additional factors into the model, as illustrated by generation of winglike outgrowths in barley lemma mutants [54].

To account for the further proximal restriction of competence in the epidermis at early stages, PGRAD limits divisions in the epidermis until the distal limit set by PMF is reached. PMF also interacts with MID in the epidermis, accounting for larger cells in the midline region. The elongated shape of proximal midline cells is a result of early arrest of division combined with low specified growth rates perpendicular to the proximodistal polarity.

Divisions in the wild-type epidermis are also influenced by *SPCH*. We show that *SPCH* acts autonomously in the epidermis to confer competence, and has little impact in the proximal midline region, where its activity has previously been shown to be low [55]. The autonomous effect of *SPCH* on division competence contrasts with its nonautonomous effects at later stages of development, with regard to layer thickness and photosynthetic capacity [56]. This difference in autonomy may reflect primary and secondary consequences of *SPCH* activity. *SPCH* also promotes asymmetric divisions and divisions at smaller cell sizes or shorter cell cycle durations. The complex pattern of divisions in wild type epidermis observed here and elsewhere [9] would thus reflect the combined effect of PMF, PGRAD, MID, and *SPCH*, although the molecular basis of these interactions remains to be established.

In agreement with [24], we observed that mean cell cycle duration is relatively constant for wild type (about 20 h). However, cell cycle duration varies from 8 h to 50 h around the mean. Some of this variation depends on whether *SPCH* is active: epidermal cells that do not show high *SPCH* activity divide at a larger cell size and longer cell cycle duration. Moreover, the size at which cells with active *SPCH* divide is not fixed but becomes progressively smaller with successive divisions [23], indicating that cell cycle duration likely becomes shorter as well. Thus, the spatiotemporal variation in cell cycle duration may be the consequence of variation in growth rates (for a given threshold division size, cell cycle duration depends on growth rate) and/or direct control of cell cycle length.

Leaf size, cell size, and cell number

Most small-leaf mutants have both fewer and smaller cells [34]. Such outcomes can be generated with the model by reducing specified growth rates. The leaves end up smaller because of the lower growth rate, cells are smaller because they grow less after divisions have arrested, and there are fewer cells because they grow more slowly and thus take longer to reach \bar{A} . Thus, the observation that organ size, cell size, and cell number are commonly reduced together in mutants is a natural outcome of the model.

Change in developmental timing through factor LATE also leads to changes in leaf size, although this is mainly reflected in changes in cell number rather than cell size. This is because changing LATE shifts both the onset of growth rate decline and the time of division arrest (loss of division competence). Such variation in developmental timing could underlie mutants that change organ size with little or no effect on cell size, such as *kluh* and *big brother* [57,58].

Loss of expression of D-type cyclins leads to premature termination of cell division and fewer cells autonomously in each layer, without a major change in leaf size [59,60]. Such features can be captured by changing model parameters that are specific to cell division, such as the value of \bar{A} , in one or more layers (Fig 9D, 9E, 9K and 9L). This situation corresponds to compensation [61–63], as change in cell number is counterbalanced by a change in cell area (organ size is preserved). However, no dedicated mechanism for counterbalancing is needed, as division is under separate spatiotemporal control from growth in our model.

Although execution of division does not have an immediate effect on growth rates in our model, we explore the possibility of feedback from division on growth at later developmental stages. If growth slows down when cells approach an upper size limit, then cell division could postpone the slowing down of growth by reducing cell size. Such a mechanism would lead to

cell division extending the duration of growth, thus increasing leaf size. Mature leaves display an array of final cell sizes that correlate with levels of endoreduplication [64,65], suggesting that as cells approach a size limit, endocycles are induced that allow them to surpass the limit. If endoreduplication is impaired, these cell size limits may not be so easily overcome, leading to smaller leaves with smaller cells [66,67]. However, the extent to which endoreduplication is limited in wild type and thus may constrain final cell size and growth is unclear. Through modelling, we show that it is possible to account for the data with or without feedback from cell size on growth.

If endocycles are promoted as cells enlarge, then promoting division (e.g., by reducing \bar{A}) should lead to lower levels of endoreduplication (as cells will be smaller). This prediction is in accord with the effect of overexpressing D-type cyclins, which leads to smaller cells with lower levels of endoreduplication [68]. Conversely, inhibiting cell division (e.g., by increasing \bar{A}) should give larger cells and higher levels of endoreduplication, as observed with *cyd3* mutants [7]. However, if both division and the ability to endoreduplicate are impaired, cell size may eventually feedback to inhibit growth rate, giving smaller leaves and perhaps accounting for the phenotype of *ant* mutants, which have smaller organs with larger cells that do not endoreduplicate more than wild type [7,69].

A further application of the model is to explore the effects of different environments on leaf growth and division. As an illustration, we compared leaves of *spch* mutants grown in a bio-imaging chamber (in which nutrients were continually circulated around the leaves) with those grown on agar plates (in which growth rate is greatly reduced). Cell divisions arrested when leaves were at a smaller size in the slow-growing conditions, as predicted by the model in which division arrest depends on a timing mechanism (LATE). However, the growth and cell sizes observed suggests that the timing mechanisms are not based on external time but passage of physiological time, which may also be affected by altered growth conditions.

The model presented here identifies core components of growth and division that may be regulated and interact to generate the spatiotemporal patterns observed. Further integrative studies on growth and division at the subcellular, cellular, and tissue level in different genotypes and environments should help provide a deeper understanding of the mechanisms by which regulatory factors are established and control these core components.

Materials and methods

Plant material and growth conditions

For tracking growth of the *speechless* mutant, we used the previously published *Arabidopsis* line, *spch-1*, containing a fluorescently labelled plasma membrane marker [70]. To more precisely determine division execution times, we crossed the *spch* mutant to an *Arabidopsis* line containing fluorescently labelled nuclei, *HTA11-GFP* [71], and *PIN3:PIN3-GFP* [72], which labels plasma membranes in the epidermal layer only. For tracking growth in the wild-type background and to distinguish cells in the stomatal lineage, we used the previously published *Arabidopsis* line containing *pSPCH:SPCH-GFP* and *PIN3:PIN3-GFP* [23]. For measuring leaf widths in the *fama* mutant we used the previously published line *fama-1* (Ohashi-Ito and Bergmann, 2006).

Seeds were surface sterilised with 70% ethanol containing 0.05% Sodium Dodecyl Sulfate (SDS) for 10 min and then rinsed with 100% ethanol. Sterilised seeds were sown on petri dishes containing 25 mL of MS growth media {1× Murashige and Skoog salt mixture, 1% (w/v) sucrose, 100 mg/mL inositol, 1 mg/mL thiamine, 0.5 mg/mL pyridoxin, 0.5 mg/mL nicotinic acid, 0.5 mg/mL MES, 0.8% (w/v) agar, pH 5.7} and kept at 4 °C in the dark for 72 h

(stratification). Plates were then transferred to a controlled environment room (CER) at 20 °C in long-day conditions (16-h light/8-h dark cycles) for 5–8 d.

Time-lapse imaging

At 5–8 d after stratification, seedlings were transferred under sterile conditions into an autoclaved optical live-imaging chamber [16,73] and continuously supplied with 1/4 strength MS liquid growth medium, including sucrose to support growth. Time-lapse imaging was carried out at regular intervals using a Leica SP5 Confocal microscope, a Zeiss LSM 5 EXCITER confocal microscope, or a Zeiss LSM 780 confocal microscope. For experiments imaged with a high temporal resolution (intervals of 1–2 h), the chamber remained mounted on the microscope stage for the duration of the experiment, with room temperature and photoperiod set to be similar to that of the CER in which seedlings were germinated. For experiments with a longer interval between imaging (12–24 h), the chamber was returned to the CER between confocal imaging. Experiments were carried out on leaf 1 within the range of 0.15–2.75 mm width. Seedlings were positioned in the chamber such that the abaxial epidermis of the leaf was oriented approximately parallel and adjacent to the coverslip, although it curved away to some extent at the leaf margins. This curvature affected the leaf outline produced when projected images were made from confocal image stacks. Leaf outlines (indicated by dotted lines in Fig 1, Fig 2, Fig 6, Fig 7, Fig 9, S2 Fig, S3 Fig, S4 Fig, S6 Fig, and S9 Fig) reflect projections onto the imaging plane rather than being corrected for curvature and thus convey a shape that appears narrower than the actual leaf outline. Some regions could not be tracked because of occlusion by overlapping leaves (at early developmental stages) or because movement in the z-dimension caused parts of the leaf to go out of focus. Thus, some cell lineages could not be traced all the way back to the initial time point. Images are available from <https://figshare.com/s/b14c8e6cb1fc5135dd87>.

Image processing

To facilitate cell tracking, confocal image stacks were converted into 2D projections using either Volviewer [74] (<http://cmpdartsvr3.cmp.uea.ac.uk/wiki/BanghamLab/index.php/VolViewer>) or Fiji [75]. For early stages, when the leaf could be captured in a single scan, VolViewer was used to create a projection of the leaf surface. At later stages, when leaves were larger, multiple overlapping tiled scans were required to capture the entire leaf. In such cases, Fiji was used to create multiple 2D projections, which were merged together using Photoshop to create a single composite image. Leaf width was measured in 3D, when possible, using VolViewer. For later stages, leaf width was measured in 2D from merged projections using Fiji. Projections of the subepidermal layer were created in VolViewer using the ‘Depth-Peal Shader’ lighting editor. Several projections were created for each z-stack (using different parameters to reveal as many cells as possible in approximately the middle of the cell layer) and merged together using Photoshop to create a composite image.

Tracking growth and divisions

Projected confocal images were used to calculate growth rates and cell areas and monitor cell division dynamics in 2D by placing points around the vertices of individual cells using *PointTracker*, as described in [16]. A toolset (‘Track ‘n’ R’) was created for ImageJ (<https://imagej.nih.gov/ij/>) to facilitate access to ImageJ macros and offer improved visualisation of *PointTracker* data using R [76]. Track ‘n’ R was used to create leaf outlines, visualise the zone of cell division, and analyse cell lineages and to display cell cycle duration, cell area at division execution, and growth rates (source code and detailed instructions for Track’n’R and PointTracker

have been deposited at <https://github.com/fpantin/Track-n-R> and <https://figshare.com/s/b14c8e6cb1fc5135dd87> respectively).

Graphical outputs from Track 'n' R were reoriented so that the leaf tip pointed upwards. Cellular growth rates over a time interval t_1 – t_2 were calculated according to $\ln(A_{t_2}-A_{t_1})/(t_2-t_1)$, where A_{t_1} is cell area at t_1 and A_{t_2} is cell area at t_2 . If a cell divided in this interval, A_{t_2} was the area of the clone it gave rise to at time t_2 .

For each tracking experiment, the first row of nondividing cells was identified in the first time point and coloured orange by hand using Photoshop. These cells were identified in each subsequent image and also coloured orange (Fig 1A and S3 Fig and S4 Fig). The approximate location of the petiole-lamina boundary was identified based on the shape of the leaf outline in the last image available for each dataset. A cell was identified in the midline of this image, in line with the base of the leaf lamina. This cell was then traced back to through each image to its earliest ancestor in the first time point, thus identifying the location of the petiole-lamina boundary even when the leaf shape was less developed. Cells were identified as part of the midline region based on appearance (shape and location) in the last image of each tracking experiment. The lineage of these cells were traced back to the beginning of the experiment (S2 Fig). Cells that did not form part of the midline region were classed as lamina cells.

Analysis of cell size using 3D segmentation

For 3D segmentation and volume measurements, confocal image stacks were processed using Python scripts, as described [17], with additional scripts added to measure the external surfaces of epidermal cells in 3D and the corresponding 2D projections (source code and detailed instructions have been deposited at <https://figshare.com/s/b14c8e6cb1fc5135dd87>). Fiji macros [75] using the 3D Viewer and Point Picker plugins were used to visualise images and select cells during manual quality control.

For the epidermis, plotting projected segmentation-based area against vertex-based area gave a good linear fit ($R^2 = 0.87$) with a gradient of about 1, showing that vertex-based cell area is a good proxy for projected cell area (S5A Fig). Areas extracted from the cell surface plotted against vertex-based cell area also gave a good linear fit ($R^2 = 0.77$) with a gradient of about 1.2 (S5B Fig). The higher value for the gradient likely reflects curvature of the cell surface and the leaf, both of which increase area compared to projected values. Nevertheless, segmented surface area remains linearly related to vertex-based area. Plotting cell volume against segmentation-based cell surface area gave a linear fit, with $R^2 = 0.91$ and a gradient suggesting an approximately constant cell thickness of about $9 \mu\text{m}$ (S5C Fig). Variation in cell thickness is displayed by plotting cell volume divided by surface area as a heat map. Although a slight increase in cell thickness was observed in the proximal midline (about $15 \mu\text{m}$), cell thickness showed relatively little spatial variation for much of the lamina (S5D Fig), compared with the striking spatiotemporal variation in cell area (S5E Fig) and cell volume (S5F Fig). Thus, the major contribution to cell size variation derives from cell area rather than cell thickness. These results are also consistent with fixed leaf sections shown in [10], which have epidermal cells in the range of 8 – $15 \mu\text{m}$ thick (measured according to the scale in the published images).

For the subepidermal cell layer, fewer cells could be segmented in 3D because the bases of the cells were too deep within the tissue to be captured clearly by confocal imaging. However, around 13 cells could be segmented and plotting projected segmentation-based area against vertex-based cell area gave a good linear fit ($R^2 = 0.98$) with a gradient of about 1 (S11A Fig). Plotting the volume of these cells against projected segmentation-based cell areas showed that they had similar thickness to epidermal cells of the same area, except for cells in the proximal midline region, where subepidermal cells have a greater volume because of increased thickness

(S11B and S11C Fig). These results are also consistent with fixed leaf sections shown in [10], which have subepidermal cells in the range of 9–14 μm thick.

Analysis of cell shape complexity

To quantify cell shape complexity, we employed Lobe-Contribution Elliptic Fourier Analysis (LOCO-EFA), a method to decompose the outline of each cell into a list of biologically meaningful descriptors [77]. The LOCO-EFA decomposition was used to estimate a measure of cell shape complexity, coined the ‘cumulative difference’ (CD), which is the integral over all LOCO-EFA modes larger than 2 of the mismatch (Exclusive OR or XOR) between the original and reconstituted shape, yielding a scalar value representing the degree of shape complexity of each cell [77]. We used this measure normalised to cell area; hence, a small or large cell with the same shape will yield the same cell complexity measure (CD). It ranged from zero (low complexity, which describes perfectly circular or elongated cells) to higher values, as more LOCO-EFA harmonics are required to accurately describe the shape. The computer code was written in C and is available on a remote repository (Git repository), which is publicly available on Bitbucket (https://bitbucket.org/mareelab/LOCO_EFA).

Analysis of *spch* expression

The expression pattern of *pSPCH:SPCH-GFP* was analysed from time-lapse images to distinguish cells in the stomatal lineages from non-stomatal lineages. For each cell division, the duration of *SPCH* expression was determined from the time when *SPCH* first became visible in the nucleus of the mother cell to when it could no longer be seen in each daughter cell. [S1 Video](#) shows an example of cell division in the stomatal lineage. [S2 Video](#) shows an example cell division in a non-stomatal lineage.

Analysis of subepidermal cells in wild type

To facilitate imaging of the subepidermal cell layer in wild-type leaves, seedlings grown on plates were stained by the modified pseudo-Schiff propidium iodide (mPS-PI) method, as previously described [78]. After approximately 1 wk (for the mounting solution to set), leaf primordia were imaged using a Leica SP5 Confocal microscope. Projections of the subepidermal layer were created in VolViewer using the ‘Depth-Peak Shader’ lighting editor, as described above for *spch* in “Image processing”.

Modelling leaf growth

All models and GFT-box software used for modelling can be downloaded from <http://cmpdartsvr3.cmp.uea.ac.uk/wiki/BanghamLab/index.php/Software>.

Models are also downloadable from <https://figshare.com/s/b14c8e6cb1fc5135dd87>. To implement an integrated model of division and growth, we built on a previously published tissue-level model for wild-type leaf growth at early stages of development [16]. This model has two interconnected networks: the Polarity Regulatory Network specifies tissue polarity and hence specified orientations of growth, and the Growth Regulatory Network (KRN) determines how factors influence specified growth rates. Specified growth orientations are established in relation to a polarity field, determined by the local gradient of a factor determining polarity field (POL) that propagates through the tissue, termed the canvas. The resultant growth and shape depend on the specified growth rates parallel (K_{par}) and perpendicular (K_{per}) to the polarity, and the mechanical constraints arising from the connectedness of the tissue.

In the equations, factors are denoted by i subscripted with the factor name. For instance, the factor PGRAD is described by i_{pgrad} in the equations. Factors may promote growth rates through the linear function pro , defined as follows:

$$pro(p_f, i_f) = 1 + p_f i_f$$

where i_f is a factor, F , and p_f is a promotion coefficient for that factor. Factors may inhibit growth through the function inh , defined as follows:

$$inh(h_f, i_f) = 1/(1 + h_f i_f)$$

where h_f is an inhibition coefficient for factor F . All multiplications and divisions are elementwise.

The previously proposed tissue-level growth model [16] was based on tracking only a subset of cell vertices and therefore had a lower cellular resolution than the data presented in this paper. Based on the higher resolution cell fate map of the midline region of wild type and *spch* (S2 Fig), we widened the initial MID domain (S15 Fig) so that it gave a better match to the cellular data. Running the model with this change produced a narrower leaf, as MID inhibits K_{per} . To compensate for this effect and to account for the regions with high growth rate perpendicular to the midline (Fig 1D and S1B Fig), we promoted K_{per} with PMF.

S15 Fig—Model setup

The initial starting canvas for all models consists of 3,000 finite elements, which are not subdivided during the simulations, and model time is aligned with days after initiation (DAI), which is defined based on growth curves of leaf width [16]. To give finer resolution, times are given in hours (hours after initiation [HAI]). A list of growth parameter values is given in Table 1.

Specified growth rates are modulated by a set of overlapping regional factors, PGRAD, MID, and LAM, the concentrations of which are fixed to the canvas and deform with it during growth (S15A Fig). PGRAD declines distally and accounts for the proximodistal variation in growth rate parallel to the polarity. LAM is expressed highest in the presumptive lamina and at lower levels in the distal regions that will form the petiole. LAM promotes growth

Table 1. Model parameters.

Parameter	Description	Value
Polarity parameters		
b_{pol}	maximum POL levels	0.1
λ_{pol}	POL decay rate	0.1 h^{-1}
Growth parameters		
b_{pgrad}	minimum levels of PGRAD	0.195
g_{late}	increase in LATE over time	0.0048 h^{-1}
p_{pgrad}	K_{per} promotion by PGRAD	0.041 h^{-1}
p_{lam}	K_{per} promotion by LAM	0.0235 h^{-1}
p_{late}	K_{per} promotion by LATE	0.7
h_{late}	K_{per} inhibition by LATE	2.2
h_{mid}	K_{per} inhibition by MID	1.0
λ_{pmf}	PMF decay rate	0.3 h^{-1}
d_{pmf}	Diffusion rate of PMF	0.01
p_{pmf}	K_{per} promotion by PMF	0.9

<https://doi.org/10.1371/journal.pbio.2005952.t001>

perpendicular to polarity. MID is expressed in the midline region, as shown in S15A Fig, and inhibits growth perpendicular to the polarity. The maximum value of these factors is 1. Specified growth rates are also modulated by diffusible factor PMF, which is fixed to a value of 1 at the approximate position of the lamina-petiole boundary and allowed to diffuse through growth with a diffusion rate of d_{pmf} and a decay rate of μ_{pmf} giving the distribution shown in S15 Fig.

A temporally varying factor, LATE, is activated throughout the canvas to decrease growth at later stages. The value of LATE is initially 0 but rises linearly with time after 149 h:

$$i_{late} \begin{cases} 0 & \text{if } t < 148 \text{ h} \\ g_{late}(t - 148 \text{ h}) & \text{if } t \geq 148 \text{ h} \end{cases}$$

where g_{late} defines the increase of LATE with time. LATE inhibits specified growth rates with an inhibition coefficient of h_{late} .

Polarity regulatory network

Polarity is established using factor PROXORG, which is set to 1 at the base of the canvas and 0 elsewhere (S15A Fig). The value of POL is fixed at a value of b_{pol} where PROXORG is greater than zero. POL diffuses throughout the canvas with a diffusion rate of D_{pol} and a decay rate of μ_{pol} . POL distribution is allowed to establish during the setup phase for 20 time steps before the commencement of growth. Polarity is initially proximodistal and then deforms with the canvas as it grows to its final shape.

Fig 8E and 8F—*spch* subepidermis model

This is a model for *spch* subepidermis during early stages of development.

KRN. Specified growth rates parallel to the polarity field K_{par} are defined as follows:

$$K_{par} = p_{pgrad} \cdot i_{pgrad} \cdot inh(h_{late}, i_{late})$$

where p_{pgrad} is the promotion of growth by PGRAD.

Specified growth perpendicular to the polarity field K_{per} is defined as:

$$K_{per} = p_{lam} \cdot i_{lam} \cdot pro(p_{late}, i_{late}) \cdot inh(h_{mid}, i_{mid}) \cdot pro(p_{pmf}, i_{pmf})$$

where p_{lam} is the promotion of growth by LAM. The value of PMFTK is set to the value of PMF except where the value of PMF ≥ 0.295 , in which case the value PMFTK is capped at 0.295. The canvas grows for the period $87 \text{ h} < t < 178 \text{ h}$.

v-Cells

To incorporate cell divisions within our tissue-level model, we superimposed polygons on the initial canvas to represent cells (S15A Fig, right). The sizes and geometries of these v-cells are based on cells observed at corresponding stages in confocal images of leaf primordia [16]. The vertices of the v-cells are anchored to the canvas and displaced with it during growth. New vertices are introduced as v-cells divide, according to the shortest wall passing through the centre of the v-cell [29]. Calling this the nominal new wall, the actual new wall is chosen to be parallel to this, through a point that is randomly displaced from the midpoint of the nominal new wall. The displacement is a vector chosen uniformly at random from a disc centred on the

midpoint. The radius of this disc is 0.25 times the length of the nominal new wall. The length of the new wall is shortened slightly to give more realistic wall angles [79].

Cell divisions are determined through controlling competence and \bar{A} .

Competence. Competence was determined by factor CDIV. v-cells can only divide if $CDIV > 0$. Factor CDIV was set to a value of 1 in the zone in which v-cells are competent to divide. The value of CDIV was set to 1 where the value of PMF ≥ 0.184 , which corresponds to the value of PMF at about $400 \mu\text{m}^2$ from the petiole-lamina boundary. v-cells within the CDIV zone divide when they reach an area threshold, while v-cells outside the CDIV-expressing zone do not divide, regardless of their size. CDIV is turned off throughout the canvas when LA1E reaches a threshold value of 0.1680 at 183 h.

Control of \bar{A} . At cell birth, the cell is assigned a target area, A , equal to the mean target area \bar{A} plus a random variation with standard deviation $\sigma = 0.2\bar{A}$, in accordance with observed values of σ (Fig 2F). Before 114 h, we assume $\bar{A} = A_{min}$. After 114 h in the lamina, \bar{A} ranges from $150 \mu\text{m}^2$ to $300 \mu\text{m}^2$ according to the value of PMF. For PMF values above PMF_{max} , \bar{A} remains at A_{min} . As the value of PMF falls below PMF_{max} , \bar{A} rises linearly to A_{max} according to the formula:

$$\bar{A} \begin{cases} A_{min} & t < 114 \text{ h} \\ A_{min}(1 - \alpha) + A_{max} \alpha & t \geq 114 \text{ h} \end{cases}$$

where

$$\alpha = \frac{(PMF_{max} - i_{pmf})}{(PMF_{max} - PMF_{min})}$$

In the midline region,

$$\bar{A} \begin{cases} A_{min} & t < 114 \text{ h} \\ 1.5 A_{mid} i_{pgrad} & t \geq 114 \text{ h} \end{cases}$$

In the Fig 8E and 8F—*spch* subepidermis model, $PMF_{max} = 0.51$, $PMF_{min} = 0.184$, $A_{min} = 150 \mu\text{m}^2$, $A_{max} = 300 \mu\text{m}^2$, and $A_{mid} = 500 \mu\text{m}^2$.

Intercellular spaces. For the subepidermal model, formation of intercellular spaces was simulated by replacing a random selection of cell vertices with small empty equilateral triangles (with an initial area of $2 \mu\text{m}^2$). The number of initial intercellular spaces and the rate of additional spaces were calculated using the ratio of cells to intercellular spaces, in accordance with the experimental data. This resulted in 30 intercellular spaces being introduced at 120 h, and further replacements were made at a rate of 11 h^{-1} . The vertices of the intercellular spaces moved away from their centres at a rate of 1.25% of their length h^{-1} , equivalent to an areal growth rate of $2.5\% \text{ h}^{-1}$.

Fig 8G and 8H—*spch* epidermis model

This is a model for *spch* epidermis during early stages of development.

KRN. Specified growth rates parallel to the polarity field, K_{par} , and perpendicular to the polarity field, K_{per} , were defined as in “Fig 8E and 8F—*spch* subepidermis model”.

The canvas grew for the period $87 \text{ h} < t < 178 \text{ h}$.

v-Cells. v-cells were implemented as in “Fig 8E and 8F—*spch* subepidermis model,” but with the following modifications:

CDIV was set to 1 when the value of PMF $\geq PMF_{min} = 0.295$ (compared with $PMF_{min} = 0.184$ for the subepidermis model), which shifts the distal boundary from about $400 \mu\text{m}$ to

about 300 μm from the petiole-lamina boundary. Additionally, in order to model the initial restriction of cell division to proximal regions, CDIV was also set to 0 where PGRAD < 0.628.

\bar{A} in the lamina was set using the same equation as the Fig 8E and 8F—*spch* subepidermis model (but with $PMF_{min} = 0.295$, as described in the previous paragraph). In the midline region, \bar{A} was set to a constant value $A_{mid} = 500 \mu m^2$ and did not vary with PGRAD as in “Fig 8E and 8F—*spch* subepidermis model.”

$$\bar{A} \begin{cases} A_{min} & t < 114 \text{ h} \\ A_{mid} & t \geq 114 \text{ h} \end{cases}$$

Cells in the midline stopped dividing earlier than in the Fig 8E and 8F—*spch* subepidermis model and this was achieved in this model by reducing the LATE threshold in the midline to 0.0768 (compared with 0.1680).

Fig 9B—Later stage mature *spch* epidermis model

This model extends the Fig 8G and 8H—*spch* epidermis model to later stages of development.

A new factor, EARLYGROWTH, was introduced in the model setup and set to a value of 1 throughout the canvas. After 189 h, EARLYGROWTH decreases linearly by a value of 0.0417 h⁻¹ until it reaches a minimum value of 0.

$$i_{earlygrowth} \begin{cases} 1 & \text{if } t < 189 \text{ h} \\ i_{earlygrowth} - 0.0417 (t - 189) & \text{if } t \geq 189 \text{ h} \end{cases}$$

To arrest growth, we modified factor LATE to increase exponentially after 189 h:

$$i_{late} \begin{cases} 0 & \text{if } t < 148 \text{ h} \\ g_{late}(t - 148 \text{ h}) & \text{if } 189 \text{ h} < t \leq 148 \text{ h} \\ A e^{Bt} & \text{if } t \geq 189 \text{ h} \end{cases}$$

where $A = g_{late}(189 - 148) e^{-B \cdot 189}$ and $B = 1 / (189 - 148)$. This ensures i_{late} evaluates to $g_{late}(t - 148)$ at 189 h.

KRN. Changes relative to the Fig 8G and 8H—*spch* epidermis model are shown underlined.

Specified growth rate parallel to the polarity field K_{par} was modified with an additional term that led to inhibition after EARLYGROWTH starts to decline (at 189 h), as follows:

$$K_{par} = p_{grad} i_{grad} \cdot \text{inh}(h_{lat}, i_{late}) \cdot \text{inh}(0.2A, i_{late} \cdot (1 - i_{earlygrowth}))$$

Specified growth perpendicular to the polarity field K_{per} was modified with additional terms that led to loss of promotion by LATE and inhibition after EARLYGROWTH starts to decline (at 189 h), as follows:

$$K_{per} = p_{lam} i_{lam} \cdot \text{inh}(h_{mid}, i_{mid}) \cdot \text{pro}(p_{pmf}, i_{pmf}) \cdot \text{pro}(p_{late}, i_{late} \cdot i_{earlygrowth}) \cdot \text{inh}(2.8, i_{late} \cdot (1 - i_{earlygrowth}))$$

The canvas grows for the period 87 h < t < 412 h.

v-Cells. v-cells were defined as in “Fig 8G and 8H—*spch* epidermis model”.

Fig 9C—Later stage *spch* limit-free epidermis model

This model inhibits distal growth during later stages in order to reduce the size of distal cells. It does this by using the existing factors PGRAD and LAM.

KRN. Changes relative to the Fig 8G and 8H—*spch* epidermis model are shown underlined. Specified growth rates parallel to the polarity field K_{par} were modified by introducing inhibitory factors that increase distally. As both PGRAD and LAM values decrease distally from a maximum of 1, by subtracting their values from 1, we obtain factors that increase distally. These distally increasing factors inhibited growth as EARLYGROWTH decreased. As this introduces extra growth inhibition, this was compensated for by also inhibiting growth inhibition by LATE as EARLYGROWTH decreased:

$$K_{par} = P_{pgrad} i_{pgrad} \cdot \frac{\text{inh}(h_{late}, i_{late} \cdot \text{inh}(1.5, (1 - i_{earlygrowth})))}{\text{inh}(2, (1 - i_{lam}) \cdot (1 - i_{earlygrowth}))} \cdot \frac{\text{inh}(4, (1 - i_{pgrad}) \cdot (1 - i_{earlygrowth}))}{\text{inh}(4, (1 - i_{pgrad}) \cdot (1 - i_{earlygrowth}))}$$

Specified growth perpendicular to the polarity field K_{per} was modulated in a similar way as K_{par} described above:

$$K_{per} = P_{lam} i_{lam} \cdot \frac{\text{inh}(h_{mid}, i_{mid})}{\text{pro}(p_{pnf}, i_{pnfk})} \cdot \frac{\text{pro}(p_{hisc}, i_{hisc} \cdot i_{earlygrowth})}{\text{inh}(1.2, i_{late} \cdot (1 - i_{earlygrowth}))} \cdot \frac{\text{inh}(4, (1 - i_{pgrad}) \cdot (1 - i_{earlygrowth}))}{\text{inh}(4, (1 - i_{pgrad}) \cdot (1 - i_{earlygrowth}))}$$

The canvas grows for the period $87 \text{ h} < t < 412 \text{ h}$.

v-Cells. v-cells were implemented as in the Fig 8G and 8H—*spch* epidermis model.

Fig 9J—Later stage *spch* limiting cell size epidermis model

In this model, cell size can affect growth. This is an alternative way to limit the size of distal cells without having to use the factors PGRAD and LAM, as in the Fig 9C—Later stage *spch* limit-free epidermis model.

KRN. Specified growth rates were defined as in the Fig 9B—Later stage mature *spch* epidermis model, but with a v-cell size feedback on growth affecting K_{per} and K_{par} . When cell area, ca , exceeds a threshold size a_1 , specified growth rates (K_{par} and K_{per}) start to be reduced by ω in proportion to cell area until cell size reaches a_2 , after which specified growth rates are

set to zero.

$$K_{par} = \omega \cdot p_{pgrad} \cdot i_{pgrad} \cdot inh(h_{late}, i_{late}) \cdot inh(0.24, i_{late} \cdot (1 - i_{earlygrowth}))$$

$$K_{per} = \omega \cdot p_{lam} \cdot i_{lam} \cdot inh(h_{mid}, i_{mid}) \cdot pro(p_{prof}, i_{prof}) \cdot pro(p_{late}, i_{late} \cdot i_{earlygrowth}) \cdot inh(2.8, i_{late} \cdot (1 - i_{earlygrowth}))$$

where

$$\omega = \frac{a_2 - ca}{a_2 - a_1}$$

In the lamina region, $a_1 = 4,000 \mu\text{m}^2$ and $a_2 = 8,000 \mu\text{m}^2$, while in the midline region, $a_1 = 18,000 \mu\text{m}^2$ and $a_2 = 20,000 \mu\text{m}^2$.

All other v-cell properties were as in “Fig 9B—Later stage mature *spch* epidermis model.”

Fig 9D and 9E and 9K–9L—Cell division threshold mutant models

Cell division threshold models were developed for the Fig 9C—later stage *spch* limit-free epidermis model and Fig 9J—later stage *spch* limiting cell size epidermis model. Each of the cell division models was identical to its parent model, but the cell target area for division, \bar{A} , was increased by a constant a' for $t \geq 114$ h.

$$\bar{A} = (\bar{A}_{min}(1 - \alpha) + \bar{A}_{max} \alpha) + a'$$

In Fig 9D and 9K, $a' = 85 \mu\text{m}^2$, while in Fig 9E and 9L, $a' = -85 \mu\text{m}^2$.

Fig 9F and 9G and 9M–9N—Growth rate mutant models

Growth rate mutant models were developed for the Fig 9C—later stage *spch* limit-free epidermis model and the Fig 9J—later stage *spch* limiting cell size epidermis model. Each of the growth rate mutant models was identical to its parent model, but K_{per} and K_{par} were globally scaled by a factor k' . In Fig 9F and 9M, $k' = 0.95$, while in Fig 9G and 9N, $k' = 1.05$.

For the Fig 9C—later stage *spch* limit-free epidermis model:

$$K_{par} = k' \cdot p_{pgrad} \cdot i_{pgrad} \cdot inh(h_{late}, i_{late}) \cdot inh(1.5, (1 - i_{earlygrowth})) \cdot inh(2, (1 - i_{lam})) \cdot (1 - i_{earlygrowth}) \cdot inh(4, (1 - i_{pgrad})) \cdot (1 - i_{earlygrowth})$$

$$\begin{aligned}
 K_{per} = & \underline{k'} \\
 & \cdot P_{iam} \underline{i_{iam}} \\
 & \cdot \underline{inh}(h_{mid}, \underline{i_{mid}}) \\
 & \cdot \underline{pro}(P_{pmf}, \underline{i_{pmfk}}) \\
 & \cdot \underline{pro}(P_{late}, \underline{i_{late}} \cdot \underline{i_{earlygrowth}}) \\
 & \cdot \underline{inh}(1.2, \underline{i_{late}} \cdot (1 - \underline{i_{earlygrowth}})) \\
 & \cdot \underline{inh}(4, (1 - \underline{i_{grad}}) \cdot (1 - \underline{i_{earlygrowth}}))
 \end{aligned}$$

For the Fig 9J—later stage *spch* limiting cell size epidermis model:

$$K_{per} = \underline{k'} \cdot \underline{\omega} \cdot P_{grad} \underline{i_{grad}} \cdot \underline{inh}(h_{late}, \underline{i_{late}}) \cdot \underline{inh}(0.24, \underline{i_{late}} \cdot (1 - \underline{i_{earlygrowth}}))$$

$$\begin{aligned}
 K_{per} = & \underline{k'} \\
 & \cdot \underline{\omega} \\
 & \cdot P_{iam} \underline{i_{iam}} \\
 & \cdot \underline{inh}(h_{mid}, \underline{i_{mid}}) \\
 & \cdot \underline{pro}(P_{pmf}, \underline{i_{pmfk}}) \\
 & \cdot \underline{pro}(P_{late}, \underline{i_{late}} \cdot \underline{i_{earlygrowth}}) \\
 & \cdot \underline{inh}(2.8, \underline{i_{late}} \cdot (1 - \underline{i_{earlygrowth}}))
 \end{aligned}$$

Changes to models relative to those used to generate Fig 9C and Fig 9J are shown underlined.

Fig 9H, 9I, 9O and 9P—LATE mutant models

Models were developed for the Fig 9C—later stage *spch* limit-free epidermis model and Fig 9J—later stage *spch* limiting cell size epidermis model. Each of the LATE mutant models was identical to its parent model, but the activation of LATE and EARLYGROWTH was shifted by a constant number of hours, *t'*. In Fig 9H and 9O, *t'* = -6 h, while in Fig 9I and 9P, *t'* = 6 h.

$$i_{late} \begin{cases} 0 & \text{if } t < 148 \underline{h} + \underline{t'} \\ g_{late}(t - 148 \underline{h} + \underline{t'}) & \text{if } 189 \underline{h} + \underline{t'} > t \geq 148 \underline{h} + \underline{t'} \\ A e^{Bt} & \text{if } t \geq 189 \underline{h} + \underline{t'} \end{cases}$$

where $A = g_{late} \cdot (189 + \underline{t'} - 148 + \underline{t'})$, $e^{-B \cdot 189 + \underline{t'}}$ and $B = 1 / (189 + \underline{t'} - 148 + \underline{t'})$.

$$i_{earlygrowth} \begin{cases} 1 & \text{if } t < 189 \underline{h} + \underline{t'} \\ i_{earlygrowth} - 0.0417 \cdot (t - 189) & \text{if } t \geq 189 \underline{h} + \underline{t'} \end{cases}$$

Changes to models relative to those used to generate Fig 9C and Fig 9J are shown underlined.

Fig 10—Later stage mature *spch* epidermis model

In the above models, *t* refers to actual time. We modified the late stage *spch* epidermis model (as used for Fig 9B) by setting physiological time to be a constant fraction (physiological ratio)

of duration since the start of the simulation (when $t = 87$ h). Key transitions and growth rates were then set in relation to physiological time. Parameters describing physical processes such as diffusion were left unchanged. For the model for *spch* grown on plates, the physiological ratio was 0.55. In addition, the growth rates were globally scaled by a factor $k' = 0.6$. The net result of these two changes is that growth in actual time is slowed to 0.33 of normal. If this overall growth rate was matched purely by changing physiological time, the leaf on the plate would end up larger than observed at maturity. Conversely, if the growth rate was matched purely through changes in k' , the leaf would end up much smaller than observed for *spch* on plates at maturity. Thus, changes in both physiological time and k' are needed to match the observed growth curve.

S14C Fig—*spch* in chamber tuned to lower growth rate at later stages

The only change in relation to the late stage *spch* epidermis model (as used for Fig 9B) was that the physiological ratio (as defined above) was set to 0.75.

Supporting information

S1 Fig. Scatterplots of growth rates parallel and perpendicular to the midline in the *spch* epidermis. From the time-lapse imaging experiment shown in Fig 1. (A) Growth rates parallel to the midline ($K_{Midline}$) versus distance from the petiole-lamina boundary. (B) Growth rates perpendicular to the midline ($K_{PerMidline}$) versus distance from the centre of the midline. Data points are colour coded according to tracking interval (inset). Source data are available from <https://figshare.com/s/b14c8e6cb1fc5135dd87>. (TIF)

S2 Fig. Assignment of the midline and lamina regions. From the time-lapse imaging experiment shown in Fig 1. Lineages were traced from cells visible at the beginning of the experiment (0 h, left) through to the end (74 h, right) and were assigned an arbitrary colour, ensuring neighbours were coloured differently. Cells in the midline (within the black outline) were identified using the position and shape of clones (cells of the same lineage) in the final image, as was the approximate position of the distal end of the midline (dark grey). Cells outside the midline region were classified as being in the lamina. Scale bar = 100 μ m. (TIF)

S3 Fig. Dynamics of cell division and growth in the *spch* epidermis, additional dataset. Time-lapse imaging of a *spch* leaf at approximately 24-h intervals over 4 d (0–96 h, last time point in series not shown). Data shown on the first time point (underlined) for each tracking interval. Leaf widths for first time point (left to right) are 0.17, 0.27, 0.39, and 0.50 mm. (A) Cells amenable to tracking that were competent to divide (green) and either executed division during the interval (light green) or divided in a later interval (dark green). Cells that did not divide (black, first row in 0–25 h are coloured orange throughout). (B–D) Cellular growth rates (heat maps) for each tracking interval. Black line refers to orange cells in (A). (B) Areal growth rates. (C) Growth rates parallel to the midline (proximodistal). (D) Growth rates perpendicular to the midline (mediolateral). (E) Cell areas for the first time point of the interval. Leaf outline indicated by dotted black line. The petiole-lamina boundary was defined as described in Fig 1. Grey boxes are aligned to the petiole-lamina boundary and extend to 150 or 300 μ m. Black arrows indicate distal boundary of the zone of division. Scale bar = 100 μ m. Source data are available from <https://figshare.com/s/b14c8e6cb1fc5135dd87>. *spch*, *speechless*. (TIF)

S4 Fig. Dynamics of cell division and growth in the *spch* epidermis, additional dataset.

Time-lapse imaging of a *spch* leaf at approximately 24-h intervals over 5 d (0–118 h, last time point in series not shown). Data shown on first time point (underlined) for each tracking interval. Leaf widths for the first time point (left to right) are 0.23, 0.34, 0.48, 0.67, and 0.87 mm. (A) Cells amenable to tracking that were competent to divide (green) and either executed division during the interval (light green) or divided in a later interval (dark green). Cells that did not divide (black, first row in 0–23 h are coloured orange throughout). (B–D) Cellular growth rates (heat maps) for each tracking interval. Black line refers to orange cells in (A). (B) Areal growth rates. (C) Growth rates parallel to the midline (proximodistal). (D) Growth rates perpendicular to the midline (mediolateral). (E) Cell areas for the first time point of the interval. Leaf outline indicated by dotted black line. The petiole-lamina boundary was defined as described in Fig 1. Grey boxes are aligned to the petiole-lamina boundary and extend to 150 or 300 μm . Black arrows indicate distal boundary of the zone of division. Scale bar = 100 μm . Source data are available from <https://figshare.com/s/b14c8e6cb1fc5135dd87>. *spch*, *speechless*. (TIF)

S5 Fig. Analysis of epidermal cell size using 3D segmentation. (A,B)

Data from a sample of cells in the tracking experiment shown in S3 Fig, 96 h. (A) Segmentation-based projected cell area versus vertex-based cell area ($R^2 = 0.87$, slope = 1.03, intercept = 125, standard deviation along y-axis = 72). (B) Segmentation-based cell surface area versus vertex-based cell area ($R^2 = 0.77$, slope = 1.2, intercept = 145, standard deviation along y-axis = 115). (C–F) Data from a sample of cells in tracking experiment shown in Fig 1E, 58 h. (C) Cell volume versus segmentation-based cell surface area ($R^2 = 0.91$, slope = 8.93). (D) Cell volume divided by cell surface area (cell thickness). (E) Segmentation-based cell surface area. (F) Cell volume. Scale bar = 100 μm . For each heat map, the upper limit of the colour scale was set to 20-fold that of the lower limit. Source data are available from <https://figshare.com/s/b14c8e6cb1fc5135dd87>. (TIF)

S6 Fig. Cellular areal growth rates of dividing and nondividing cells in the *spch* epidermis.

Time-lapse imaging of a *spch* leaf shown in Fig 1. (A) Panel repeated from Fig 1A, for ease of comparison. Cells amenable to tracking that were competent to divide (green) and either executed division during the interval (light green) or divided in a later interval (dark green). Cells that did not divide (black, first row in 0–14 h are coloured orange throughout). For the last interval (74–100 h), cell divisions could only be tracked for a subset of cells because of missing data in the 100-h time point. (B–C) Cellular growth rates (heat maps) shown in Fig 1B, separated to show (B) areal growth rates of nondividing cells, coloured black in (A). (C) Areal growth rates of dividing cells, coloured green in (A). Leaf outline indicated by dotted black line. The petiole-lamina boundary was defined by selecting a cell from a later stage of development, where the lamina narrows, and then tracing its lineage back to all stages. Grey boxes are aligned to the petiole-lamina boundary and extend to 150 or 300 μm . Black arrows indicate distal boundary of the zone of division competence. Scale bar = 100 μm . *spch*, *speechless*. (TIF)

S7 Fig. Cell division dynamics of the epidermis at high temporal resolution.

Cells amenable to tracking from the time-lapse imaging experiment shown in Fig 2; data visualised over 24-h intervals, shown on the first image of the interval (underlined). (A) Cell cycle duration (heat map) for cells that were observed to complete a full cell cycle during the course of the experiment. Cells that did not divide or did not complete a full cell cycle are coloured black. (B) Cells that were competent to divide (green) and either executed division during the interval (light green) or divided in a later interval (dark green). Cells that did not divide (black). Leaf outline

indicated by dotted black line. The petiole-lamina boundary was defined as described in Fig 1. Grey boxes are aligned to the petiole-lamina boundary and extend to 150 or 300 μm . Scale bar = 100 μm .

(TIF)

S8 Fig. Subepidermal cells in wild-type leaves. (A) Projections of the subepidermal layer of four individual wild-type leaves, fixed and stained at developmental stages, similar to those of the tracked *spch* leaf in Fig 5. Leaf widths (left to right) are 0.14, 0.28, 0.40, and 0.53 mm. A patch of cells was coloured red and used to look in further detail. (B) Enlargement of the patch of cells in (A) (red outline). (C) Cells outlined in (B), showing spacing of individual cells (filled pink, outlined red). (D) Epidermal cells adjacent to the subepidermal patch (subepidermal cells filled and outlined red). (E) Epidermal cells without subepidermal patch outlined. Scale bars = 50 μm . Source data are available from <https://figshare.com/s/b14c8e6cb1fc5135dd87>. *spch*, *speechless*.

(TIF)

S9 Fig. Comparison of epidermal and subepidermal cell areal growth rates. A group of cells from the time-lapse imaging experiment shown in Fig 5, subepidermis (cells highlighted red), and adjacent epidermis (dynamics of the epidermis shown in full in S3 Fig). Average cell areal growth rates for each tracking interval are shown on the first image of each interval (time point underlined). (A) Epidermis, (B) subepidermis. The patch of cells is also shown enlarged for comparison. (C) Epidermis. (D) Subepidermis, showing increase in number of cells through division compared to the epidermis. Numbers refer to number of cells. Scale bars = 50 μm .

(TIF)

S10 Fig. Comparison of the zone of competence in epidermal and subepidermal layers.

Time-lapse imaging of a *spch* leaf at approximately 24-h intervals over 2 d (0–50 h); later time points of this experiment are shown in S3 Fig. Cells amenable to tracking are shown on the first time point (underlined). Cells that were competent to divide (green) and either executed division during the interval (light green) or divided in a later interval (dark green). Cells that did not divide (black). (A) Subepidermis. (B) Epidermis. Leaf outline indicated by dotted black line. Leaf widths from left to right are 0.17 and 0.27 mm. The petiole-lamina boundary was defined as described in Fig 1. Grey boxes are aligned to the petiole-lamina boundary and extend to 150 or 300 μm . Scale bar = 100 μm . *spch*, *speechless*.

(TIF)

S11 Fig. Analysis of subepidermal cell size using 3D segmentation. Analysis of a sample of abaxial subepidermal cells from the tracking experiment shown in Fig 6, 58 h. (A) Projected segmentation-based cell area versus vertex-based area ($R^2 = 0.98$, slope = 1.03, intercept = 46, standard deviation along y-axis = 20). (B) Cell volume versus projected segmentation-based cell area, subepidermal cells (blue, $R^2 = 0.94$, slope = 15.4), epidermal cells (red). (C) Cell volume divided by projected segmentation-based area (approximate cell thickness). (D) Projected segmentation-based area. (E) Cell volume. For each heat map, the upper limit was set to 8-fold that of the lower limit. (F) Orthogonal slice of confocal image, approximately through the mid-line of the leaf. Thickness of epidermal and subepidermal cells appears approximately uniform from leaf base (left) to leaf tip (right). Subepidermal cells close to the distal leaf tip are difficult to resolve. Scale bars = 100 μm . Source data are available from <https://figshare.com/s/b14c8e6cb1fc5135dd87>.

(TIF)

S12 Fig. Comparison of wild-type and *spch* primordia. Confocal images of an early wild-type leaf primordium (left) and a *spch* primordium (right) at similar developmental stages. The leaf primordia are partially obscured by the petioles of cotyledon leaves. Scale bar = 50 μm . *spch*, *speechless*. (TIF)

S13 Fig. Quantification of cell area at division execution in wild type. Data from cells amenable to tracking in the time-lapse experiment shown in Fig 7. (A,B) Area of lamina cells at the time of division execution versus distance from the petiole-lamina boundary. Mean cell area at the division for all cells is $87 \pm 6.0 \mu\text{m}^2$. (A) Cells classified as non-stomatal lineage (mean = $165 \pm 27.8 \mu\text{m}^2$). (B) Cells classified as stomatal lineage (mean = $81 \pm 5.7 \mu\text{m}^2$). (C,D) Cell cycle duration for all cells observed to complete a cell cycle. (C) Non-stomatal lineage cells (mean = $24.6 \pm 2.8 \text{ h}$). (D) Stomatal lineage cells (mean = $18.5 \pm 1.05 \text{ h}$). \pm ranges indicate $1.96 \times$ standard error of mean. Data points are colour coded according to time interval (inset in A). Source data are available from <https://figshare.com/s/b14c8e6cb1fc5135dd87>. (TIF)

S14 Fig. Comparison of wild-type and *spch* growth rates in leaf width. (A) Width measurements of leaf 1 from *spch*, wild-type, and *fama* seedlings grown in standard conditions on plates. The fitted growth curve of wild type (solid black line) was based on a logistic calculation [16]. Pink line shows output leaf widths for the model. Blue line shows output leaf widths for the model tuned to match *spch* growth on plates (by slowing growth by 40% and physiological time by 45%). Horizontal line shows leaf width at about 0.5 mm, corresponding to stages shown in Fig 10. (B) Width measurements of leaf 1 from seedlings grown in the bio-imaging chamber and scanned using confocal microscopy. Measurements are from six independent tracking experiments, two wild-type individuals, and four *spch* individuals (colour key). Because *spch* plants grown prior to moving into the chamber have much-reduced growth (shown in B), the initial data point from each tracking experiment was normalised to the wild-type logistic curve (solid black line) to enable subsequent growth rates to be compared. Pink line shows output leaf widths for the model. Blue line shows output for the leaf model tuned to match *spch* growth in the chamber at later stages (by slowing physiological time by 25%). (C) Outputs for the final stage comparing the model (left) with that tuned to match *spch* growth in chamber (right). Source data are available from <https://figshare.com/s/b14c8e6cb1fc5135dd87>. *spch*, *speechless*. (TIF)

S15 Fig. Model setup and regulatory factors. (A) Initial canvas distribution of regulatory factors, from left to right: PGRAD (greyscale), LAM (pink) and MID (purple), POL (blue, with arrows indicating gradient), and initial pattern of v-cells. (B) Time series showing accumulation of LATE at 115, 124, 153, and 182 h. (C) Time series of PMF levels at 115, 124, 153, and 182 h. (D) Sample plot of PMF concentration along the leaf midline. Note PMF concentration is fixed at 1 around the petiole-lamina boundary (dotted line). LAM, a factor distinguishing lamina from petiole; LATE, a timing factor; MID, a mediolateral factor; PGRAD, a graded proximodistal factor; PMF, proximal mobile factor; POL, factor determining polarity field; v-cell, virtual cell. (TIF)

S16 Fig. Resultant growth rates for model output at different developmental stages. Model output (from left to right) at 115, 132, 140, 147, 156, 164, and 178 h showing (A) resultant areal growth rates, (B) resultant growth rates parallel to the midline (proximodistal growth rates), and (C) resultant growth rates perpendicular to the midline (mediolateral growth rates). Grey

boxes are aligned to the petiole-lamina boundary and extend to 150 or 300 μm . Scale bar = 100 μm .

(TIF)

S17 Fig. Topological distributions (frequency of n -sided cells) from empirical data and different models. (A) Dark green line shows *Arabidopsis spch* epidermis with standard deviation between leaves for the fraction of n -sided cells indicated by a vertical line. Data are based on 42,901 cells from 99 *spch* leaves at different stages of development. The frequency of six-sided cells is 0.334 ± 0.019 (SD). Black line shows the result of the model of *spch* epidermis presented here. Grey line shows the model without polarity (isotropic specified growth). Light green line shows empirical data from the shoot apical meristem [31]. Orange line shows the model using the shortest path through the cell's centroid within an isotropically growing tissue [31]. Dark blue line shows a graph-model in which cells divide through the topological centre [30]. (B-D) Tissue topology with cells coloured according to their neighbourhood number, with six-sided cells in white, higher numbers in green, and lower numbers in brown, as shown in the colour scale. (B) Result for the model of *spch* epidermis presented here (black profile in A); (C) model without polarity, yielding an isotropically growing tissue (grey profile in A). (D) Example of *spch* leaf, as shown in S18D Fig. Source data are available from <https://figshare.com/s/b14c8e6cb1fc5135dd87>. *spch*, *speechless*.

(TIF)

S18 Fig. Additional comparisons between chamber- and plate-grown *spch* leaves. Supporting data for Fig 10; *spch* leaf grown in the chamber at 8 DAS (A-B) or grown on plates at 13 DAS (C-D) at similar leaf widths to leaves presented in Fig 10. (A, C) Confocal images of leaves, with segmentation outlines overlain in blue. (B, D) Analysis of segmentations in (A, C) showing (from left to right) neighbourhood numbers (following neighbourhood colour map used in S18B Fig); cell complexity based on the CD measure using LOCO-EFA (using complexity colour scale as in Fig 10K–10N); and absolute areas (using colour scale as in Fig 10A and 10B). Results are consistent with those described for Fig 10. Scale bars = 100 μm . Source data are available from <https://figshare.com/s/b14c8e6cb1fc5135dd87>. CD, cumulative difference; LOCO-EFA, Lobe-Contribution Elliptic Fourier Analysis; *spch*, *speechless*.

(TIF)

S1 Video. Cell division in the stomatal lineage. Magnification of a cell undergoing three rounds of amplifying divisions, from time-lapse imaging of a wild-type leaf (expressing *pSPCH:SPCH-GFP*, shown in Fig 7). Bright, nuclear-localised SPCH can be observed at the time of division and is retained in one daughter cell until the next division. Scale bar = 10 μm . Time interval, 1 h. Duration of video, 57 h. Images from time points 18–24 h are missing because of movement of the microscope stage. SPCH, SPEECHLESS.

(AVI)

S2 Video. Cell division not in the stomatal lineage. Time-lapse movie of a cell undergoing a single, non-stomatal division, from time-lapse imaging of a wild-type leaf (expressing *pSPCHII:SPCHII-GFP*, shown in Fig 7). Weak, nuclear-localised SPCHII can be observed at the time of division and disappears immediately after division in both daughter cells. Scale bar = 10 μm . Time interval, 1 h. Duration of video, 57 h. Images from time points 18–24 h are missing because of movement of the microscope stage. SPCHII, SPEECHLESS.

(AVI)

S3 Video. Subepidermal growth model. Stages of the model used to generate Fig 8E: growth and divisions of the subepidermal layer during early stages.
(MP4)

S4 Video. Epidermal growth model. Stages of the model used to generate Fig 8G: growth and divisions of the epidermal layer during early stages.
(MP4)

S5 Video. Epidermal growth model to maturity. Stages of the model used to generate Fig 9B: growth and divisions of the epidermal layer through to maturity.
(MP4)

S6 Video. Epidermal growth model to maturity, with limiting cell size. Stages of the model used to generate Fig 9J: growth and divisions of the epidermal layer through to maturity, with feedback of cell size limits on growth.
(MP4)

S7 Video. Epidermal growth model to maturity, limit-free. Stages of the model used to generate Fig 9C: growth and divisions of the epidermal layer through to maturity, with distal inhibition of growth.
(MP4)

Acknowledgments

We would like to thank Grant Calder for confocal microscopy support, Przemyslaw Prusinkiewicz for helpful discussions at early stages of the work, and Domonique Bergmann for providing *spch* and *fama* mutant seeds. We would also like to thank Des Bradley, Chris Whitewoods, Catherine Mansfield, Claire Bushell, and Beatriz Pinto-Goncalves for helpful discussions and comments on the manuscript. We thank Cindy Cooper for laboratory support.

Author Contributions

Conceptualization: Samantha Fox, Paul Southam, Florent Pantin, Sarah Robinson, J. Andrew Bangham, Enrico Coen.

Data curation: Samantha Fox, Paul Southam, Florent Pantin, Richard Kennaway.

Formal analysis: Samantha Fox, Paul Southam, Florent Pantin, Giulia Castorina, Robert Sablowski.

Funding acquisition: Enrico Coen.

Investigation: Samantha Fox, Sarah Robinson, Giulia Castorina, Yara E. Sánchez-Corrales.

Methodology: Samantha Fox, Paul Southam, Florent Pantin, Sarah Robinson, Enrico Coen.

Project administration: Enrico Coen.

Resources: Samantha Fox, Paul Southam, Florent Pantin, Richard Kennaway, Sarah Robinson, Jordi Chan.

Software: Paul Southam, Florent Pantin, Richard Kennaway.

Supervision: J. Andrew Bangham, Enrico Coen.

Validation: Samantha Fox, Paul Southam, Florent Pantin, Robert Sablowski.

Visualization: Samantha Fox, Paul Southam, Florent Pantin.

Writing – original draft: Samantha Fox, Paul Southam, Enrico Coen.

Writing – review & editing: Samantha Fox, Paul Southam, Florent Pantin, Sarah Robinson, Giulia Castorina, Yara E. Sánchez-Corrales, Robert Sablowski, Jordi Chan, Verónica Grieneisen, Athanasius F. M. Marée, Enrico Coen.

References

1. Harashima H, Schnittger A. The integration of cell division, growth and differentiation. *Curr Opin Plant Biol.* 2010; 13(1):66–74. <https://doi.org/10.1016/j.pbi.2009.11.001> PMID: 19963429.
2. Sablowski R, Carnier Dornelas M. Interplay between cell growth and cell cycle in plants. *J Exp Bot.* 2014; 65(10):2703–14. Epub 2013/11/13. <https://doi.org/10.1093/jxb/ert354> PMID: 24218325.
3. Lockhart JA. An analysis of irreversible plant cell elongation. *Journal of theoretical biology.* 1965; 8(2):264–75. Epub 1965/03/01. PMID: 5876240.
4. Moullia B, Fournier M. The power and control of gravitropic movements in plants: a biomechanical and systems biology view. *J Exp Bot.* 2009; 60(2):461–86. Epub 2009/03/07. <https://doi.org/10.1093/jxb/ern341> PMID: 19264759.
5. Coelho CM, Leevers SJ. Do growth and cell division rates determine cell size in multicellular organisms? *Journal of cell science.* 2000; 113 (Pt 17):2927–34. Epub 2000/08/10. PMID: 10934032.
6. Schmelzle T, Hall MN. TOR, a central controller of cell growth. *Cell.* 2000; 103(2):253–62. Epub 2000/11/01. PMID: 11057898.
7. Randall RS, Somay E, Dewitte W, Murray JA. AINTEGUMENTA and the D-type cyclin CYCD3;1 independently contribute to petal size control in Arabidopsis: evidence for organ size compensation being an emergent rather than a determined property. *J Exp Bot.* 2015; 66(13):3991–4000. Epub 2015/05/08. <https://doi.org/10.1093/jxb/erv200> PMID: 25948704; PubMed Central PMCID: PMC4473993.
8. Green PB. Growth and cell pattern formation on an axis: critique of concepts, terminology, and modes of study. *Bot Gaz.* 1976; 137(3):187–202.
9. Andriankaja M, Dhondt S, De Bodt S, Vanhaeren H, Coppens F, De Milde L, et al. Exit from Proliferation during Leaf Development in Arabidopsis thaliana: A Not-So-Gradual Process. *Developmental Cell.* 2012; 22(1):64–78. <https://doi.org/10.1016/j.devcel.2011.11.011> PMID: 22227310
10. Donnelly PM, Bonetta D, Tsukaya H, Dengler RE, Dengler NG. Cell cycling and cell enlargement in developing leaves of Arabidopsis. *Dev Biol.* 1999; 215(2):407–19. Epub 1999/11/05. <https://doi.org/10.1006/dbio.1999.9443> PMID: 10545247.
11. Kazama T, Ichihashi Y, Murata S, Tsukaya H. The Mechanism of Cell Cycle Arrest Front Progression Explained by a KLUH/CYP78A5-dependent Mobile Growth Factor in Developing Leaves of Arabidopsis thaliana. *Plant and Cell Physiology.* 2010; 51(6):1046–54. <https://doi.org/10.1093/pccp/pcq051> PubMed PMID: WOS:000279534200017. PMID: 20395288
12. Kuylen E, Beemster GT, Broeckhove J, De Vos D. Simulation of regulatory strategies in a morphogen based model of Arabidopsis leaf growth. *Procedia Computer Science.* 2017; 108C:139–48.
13. De Vos D, De Borger E, Broeckhove J, Beemster GT. Simulating leaf growth dynamics through Metropolis-Monte Carlo based energy minimization. *Journal of Computational Science.* 2015; 9:107–11.
14. Czesnick H, Lenhard M. Size control in plants—lessons from leaves and flowers. *Cold Spring Harb Perspect Biol.* 2015; 7(8):a019190. Epub 2015/08/05. <https://doi.org/10.1101/cshperspect.a019190> PMID: 26238357.
15. Tauriello G, Meyer HM, Smith RS, Koumoutsakos P, Roeder AH. Variability and constancy in cellular growth of Arabidopsis sepals. *Plant physiology.* 2015. Epub 2015/10/04. <https://doi.org/10.1104/pp.15.00839> PMID: 26432876.
16. Kuchen EE, Fox S, de Reuille PB, Kennaway R, Bensmihen S, Avondo J, et al. Generation of leaf shape through early patterns of growth and tissue polarity. *Science.* 2012; 335(6072):1092–6. Epub 2012/03/03. doi: 335/6072/1092 [pii] <https://doi.org/10.1126/science.1214678> PMID: 22383846.
17. Serrano-Mislata A, Schiesl K, Sablowski R. Active Control of Cell Size Generates Spatial Detail during Plant Organogenesis. *Current biology: CB.* 2015; 25(22):2991–6. Epub 2015/11/04. <https://doi.org/10.1016/j.cub.2015.10.008> PMID: 26526374.
18. Rolland-Lagan AG, Remmier L, Girard-Bock C. Quantifying Shape Changes and Tissue Deformation in Leaf Development. *Plant physiology.* 2014; 165(2):496–505. Epub 2014/04/09. <https://doi.org/10.1104/pp.113.231258> PMID: 24710066; PubMed Central PMCID: PMC4044856.

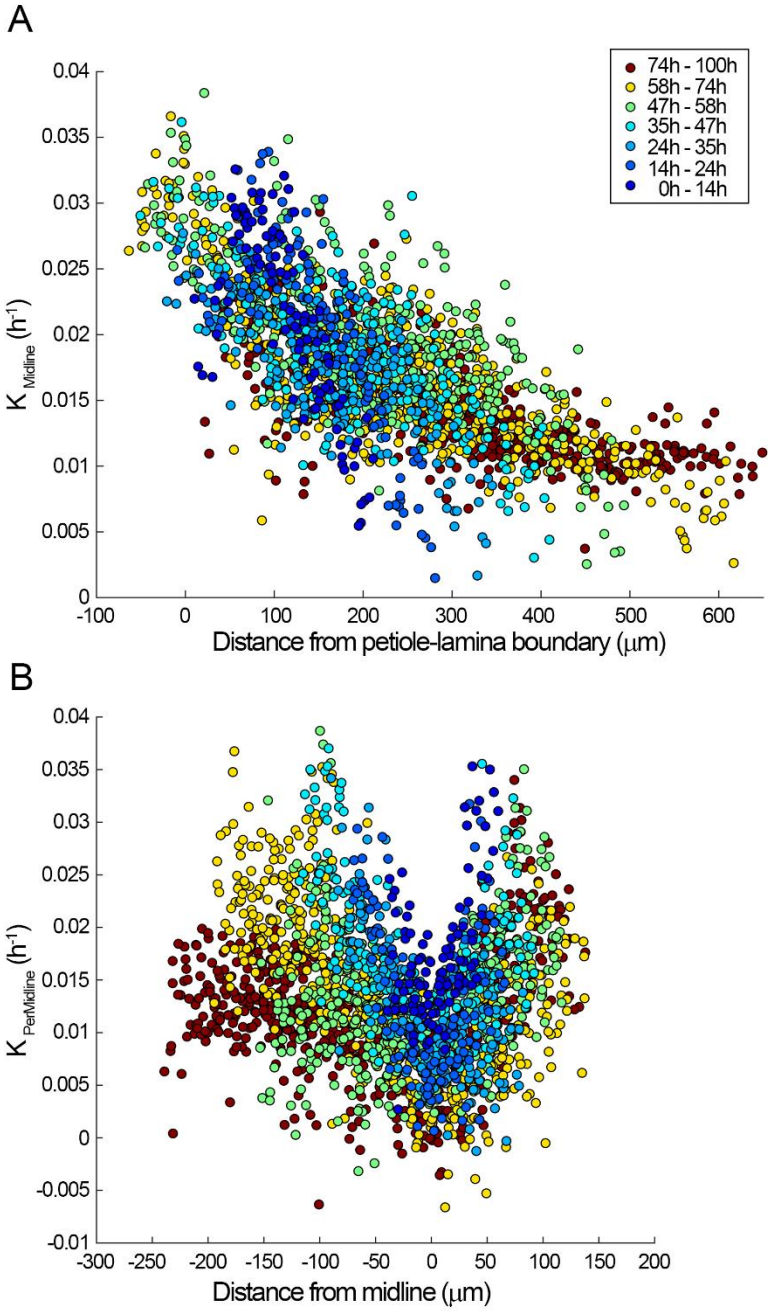
19. Vlad D, Kierzkowski D, Rast MI, Vuolo F, Dello Iorio R, Galinha C, et al. Leaf shape evolution through duplication, regulatory diversification, and loss of a homeobox gene. *Science*. 2014; 343(6172):780–3. Epub 2014/02/18. <https://doi.org/10.1126/science.1248384> PMID: 24531971.
20. Hervieux N, Dumond M, Sapala A, Routier-Kierzkowska AL, Kierzkowski D, Roeder AH, et al. A Mechanical Feedback Restricts Sepal Growth and Shape in Arabidopsis. *Current biology: CB*. 2016. Epub 2016/05/07. <https://doi.org/10.1016/j.cub.2016.03.004> PMID: 27151660.
21. Willis L, Refahi Y, Wightman R, Landrein B, Teles J, Huang KC, et al. Cell size and growth regulation in the Arabidopsis thaliana apical stem cell niche. *Proc Natl Acad Sci U S A*. 2016; 113(51):E8238–E46. <https://doi.org/10.1073/pnas.1616768113> PMID: 27930326; PubMed Central PMCID: PMC45187701.
22. Bringmann M, Bergmann DC. Tissue-wide Mechanical Forces Influence the Polarity of Stomatal Stem Cells in Arabidopsis. *Current biology: CB*. 2017; 27(6):877–83. Epub 2017/03/14. <https://doi.org/10.1016/j.cub.2017.01.059> PMID: 28285992.
23. Robinson S, Barbier de Reuille P, Chan J, Bergmann D, Prusinkiewicz P, Coen E. Generation of spatial patterns through cell polarity switching. *Science*. 2011; 333(6048):1436–40. Epub 2011/09/10. doi: 333/6048/1436 [pii] <https://doi.org/10.1126/science.1202185> PMID: 21903812.
24. Asl LK, Dhondt S, Boudolf V, Beemster GT, Beeckman T, Inze D, et al. Model-based analysis of Arabidopsis leaf epidermal cells reveals distinct division and expansion patterns for pavement and guard cells. *Plant physiology*. 2011; 156(4):2172–83. Epub 2011/06/23. <https://doi.org/10.1104/pp.111.181180> PMID: 21693673; PubMed Central PMCID: PMC3149966.
25. Goriely A. *The Mathematics and Mechanics of Biological Growth*. New York: Springer; 2017.
26. Alvarez JP, Furumizu C, Efroni I, Eshed Y, Bowman JL. Active suppression of a leaf meristem orchestrates determinate leaf growth. *eLife*. 2016; 5. <https://doi.org/10.7554/eLife.15023> PMID: 27710768; PubMed Central PMCID: PMC45096885.
27. Ohashi-Ito K, Bergmann DC. Arabidopsis FAMA controls the final proliferation/differentiation switch during stomatal development. *The Plant cell*. 2006; 18(10):2493–505. Epub 2006/11/08. <https://doi.org/10.1105/tpc.106.046136> PMID: 17088607; PubMed Central PMCID: PMC1626605.
28. Kennaway R, Coen E, Green A, Bangham A. Generation of diverse biological forms through combinatorial interactions between tissue polarity and growth. *PLoS Comput Biol*. 2011; 7(6):e1002071. Epub 2011/06/24. <https://doi.org/10.1371/journal.pcbi.1002071> PMID: 21698124; PubMed Central PMCID: PMC3116900.
29. Errera L. Sur une condition fondamentale d'équilibre des cellules vivantes. *CR Acad Sci* 1886; 103:822–4.
30. Carter R, Sanchez-Corrales YE, Hartley M, Grieneisen VA, Maree AFM. Pavement cells and the topology puzzle. *Development*. 2017; 144(23):4386–97. Epub 2017/11/01. <https://doi.org/10.1242/dev.157073> PMID: 29084800; PubMed Central PMCID: PMC5769637.
31. Sahlin P, Jonsson H. A modelling study on how cell division affects properties of epithelial tissues under isotropic growth. *PLoS ONE*. 2010; 5(7):e11750. Epub 2010/08/07. <https://doi.org/10.1371/journal.pone.0011750> PMID: 20689588; PubMed Central PMCID: PMC2912771.
32. Gonzalez N, De Bodd S, Sulpice R, Jikumaru Y, Chae E, Dhondt S, et al. Increased leaf size: different means to an end. *Plant physiology*. 2010; 153(3):1261–79. <https://doi.org/10.1104/pp.110.156018> PMID: 20460583; PubMed Central PMCID: PMC2899902.
33. Gonzalez N, Vanhaeren H, Inze D. Leaf size control: complex coordination of cell division and expansion. *Trends in plant science*. 2012; 17(6):332–40. <https://doi.org/10.1016/j.tplants.2012.02.003> PMID: 22401845.
34. Horiguchi G, Ferjani A, Fujikura U, Tsukaya H. Coordination of cell proliferation and cell expansion in the control of leaf size in Arabidopsis thaliana. *J Plant Res*. 2006; 119(1):37–42. Epub 2005/11/15. <https://doi.org/10.1007/s10265-005-0232-4> PMID: 16284709.
35. Mansfield C, Newman JL, Olsson TSG, Hartley M, Chan J, Coen E. Ectopic BASL reveals tissue cell polarity throughout leaf development in Arabidopsis thaliana *Current biology: CB*. 2018; in press.
36. Abley K, Barbier de Reuille P, Strutt D, Bangham A, Prusinkiewicz P, Marée A, et al. An intracellular partitioning-based framework for tissue cell polarity in plants and animals *Development (in press)*. 2013; 140. <https://doi.org/10.1242/dev.062984> PMID: 23633507
37. Heisler MG, Hamant O, Krupinski P, Uyttewaal M, Ohno C, Jonsson H, et al. Alignment between PIN1 polarity and microtubule orientation in the shoot apical meristem reveals a tight coupling between morphogenesis and auxin transport. *PLoS Biol*. 2010; 8(10):e1000516. Epub 2010/10/27. <https://doi.org/10.1371/journal.pbio.1000516> PMID: 20976043; PubMed Central PMCID: PMC2957402.
38. Jones AR, Forero-Vargas M, Withers SP, Smith RS, Traas J, Dewitte W, et al. Cell-size dependent progression of the cell cycle creates homeostasis and flexibility of plant cell size. *Nat Commun*. 2017;

- 8:15060. <https://doi.org/10.1038/ncomms15060> PMID: 28447614; PubMed Central PMCID: PMC5414177.
39. Kutschera U. The pacemaker of plant growth. *Trends in plant science*. 2008; 13(3):105–7. Epub 2008/02/12. <https://doi.org/10.1016/j.tplants.2007.12.002> PMID: 18261951.
 40. Savaldi-Goldstein S, Peto C, Chory J. The epidermis both drives and restricts plant shoot growth. *Nature*. 2007; 446(7132):199–202. Epub 2007/03/09. <https://doi.org/10.1038/nature05618> PMID: 17344852.
 41. Marcotrigiano M. Genetic Mosaics and the Analysis of Leaf Development. *International Journal of Plant Sciences*. 2001; 162(3):513–25.
 42. Kawade K, Tanimoto H, Horiguchi G, Tsukaya H. Spatially Different Tissue-Scale Diffusivity Shapes ANGUSTIFOLIA3 Gradient in Growing Leaves. *Biophys J*. 2017; 113(5):1109–20. <https://doi.org/10.1016/j.bpj.2017.06.072> PMID: 28877493.
 43. Kawade K, Horiguchi G, Usami T, Hirai MY, Tsukaya H. ANGUSTIFOLIA3 signaling coordinates proliferation between clonally distinct cells in leaves. *Current biology*. CB. 2013; 23(9):788–92. <https://doi.org/10.1016/j.cub.2013.03.044> PMID: 23602479.
 44. van der Graaff E, Dulk-Ras AD, Hooykaas PJ, Keller B. Activation tagging of the LEAFY PETIOLE gene affects leaf petiole development in *Arabidopsis thaliana*. *Development*. 2000; 127(22):4971–80. Epub 2000/10/25. PMID: 11044410.
 45. Sarojam R, Sappl PG, Goldshmidt A, Efroni I, Floyd SK, Eshed Y, et al. Differentiating *Arabidopsis* shoots from leaves by combined YABBY activities. *The Plant cell*. 2010; 22(7):2113–30. Epub 2010/07/16. <https://doi.org/10.1105/tpc.110.075853> PMID: 20628155; PubMed Central PMCID: PMC2929102.
 46. Beemster GT, Baskin TI. Analysis of cell division and elongation underlying the developmental acceleration of root growth in *Arabidopsis thaliana*. *Plant physiology*. 1998; 116(4):1515–26. Epub 1998/05/23. PMID: 9536070; PubMed Central PMCID: PMC35060.
 47. Di Mambro R, De Ruvo M, Pacifici E, Salvi E, Sozzani R, Benfey PN, et al. Auxin minimum triggers the developmental switch from cell division to cell differentiation in the *Arabidopsis* root. *Proc Natl Acad Sci U S A*. 2017; 114(36):E7641–E9. Epub 2017/08/24. <https://doi.org/10.1073/pnas.1705833114> PMID: 28831001; PubMed Central PMCID: PMC5594665.
 48. Carabelli M, Possenti M, Sessa G, Cioffi A, Sassi M, Morelli G, et al. Canopy shade causes a rapid and transient arrest in leaf development through auxin-induced cytokinin oxidase activity. *Genes & development*. 2007; 21(15):1863–8. Epub 2007/08/03. <https://doi.org/10.1101/gad.432607> PMID: 17671088; PubMed Central PMCID: PMC1935025.
 49. Holst K, Schmullig T, Werner T. Enhanced cytokinin degradation in leaf primordia of transgenic *Arabidopsis* plants reduces leaf size and shoot organ primordia formation. *J Plant Physiol*. 2011; 168(12):1328–34. Epub 2011/04/09. <https://doi.org/10.1016/j.jplph.2011.03.003> PMID: 21474200.
 50. Frugis G, Giannino D, Mele G, Nicolodi C, Chiappetta A, Bitonti MB, et al. Overexpression of KNAT1 in lettuce shifts leaf determinate growth to a shoot-like indeterminate growth associated with an accumulation of isopentenyl-type cytokinins. *Plant physiology*. 2001; 126(4):1370–80. Epub 2001/08/14. PMID: 11500537; PubMed Central PMCID: PMC17138.
 51. Nikovics K, Blein T, Peaucelle A, Ishida T, Morin H, Aida M, et al. The balance between the MIR164A and CUC2 genes controls leaf margin serration in *Arabidopsis*. *The Plant cell*. 2006; 18(11):2929–45. Epub 2006/11/14. <https://doi.org/10.1105/tpc.106.045617> PMID: 17098808; PubMed Central PMCID: PMC1693934.
 52. Billsborough GD, Runions A, Barkoulas M, Jenkins HW, Hasson A, Galinha C, et al. Model for the regulation of *Arabidopsis thaliana* leaf margin development. *Proc Natl Acad Sci U S A*. 2011; 108(8):3424–9. Epub 2011/02/09. <https://doi.org/10.1073/pnas.1015162108> PMID: 21300866; PubMed Central PMCID: PMC3044365.
 53. Runions A, Tsiantis M, Prusinkiewicz P. A common developmental program can produce diverse leaf shapes. *The New phytologist*. 2017; 216(2):401–18. Epub 2017/03/02. <https://doi.org/10.1111/nph.14449> PMID: 28248421; PubMed Central PMCID: PMC5638099.
 54. Richardson AE, Rebocho AB, Coen ES. Ectopic KNOX Expression Affects Plant Development by Altering Tissue Cell Polarity and Identity. *The Plant cell*. 2016. Epub 2016/08/25. <https://doi.org/10.1105/tpc.16.00284> PMID: 27553356; PubMed Central PMCID: PMC5059799.
 55. Pflitterer LJ, Sloan DB, Bogenschütz NL, Torii KU. Termination of asymmetric cell division and differentiation of stomata. *Nature*. 2007; 445(7127):501–5. <https://doi.org/10.1038/nature05467> PMID: 17183267.
 56. Dow GJ, Berry JA, Bergmann DC. Disruption of stomatal lineage signaling or transcriptional regulators has differential effects on mesophyll development, but maintains coordination of gas exchange. *The*

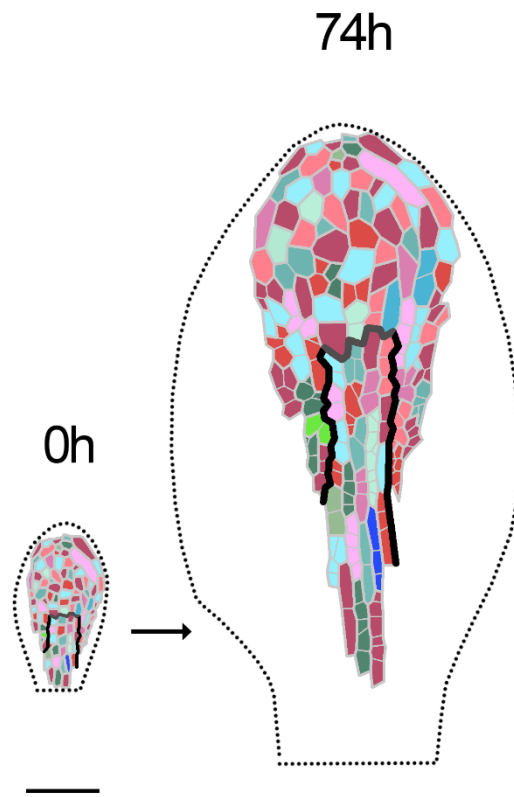
- New phytologist. 2017; 216(1):69–75. <https://doi.org/10.1111/nph.14746> PMID: 28833173; PubMed Central PMCID: PMC5601202.
57. Anastasiou E, Kenz S, Gerstung M, MacLean D, Timmer J, Fleck C, et al. Control of plant organ size by KLUH/CYP78A5-dependent intercellular signaling. *Dev Cell*. 2007; 13(6):843–56. Epub 2007/12/07. <https://doi.org/10.1016/j.devcel.2007.10.001> PMID: 18061566.
 58. Disch S, Anastasiou E, Sharma VK, Laux T, Fletcher JC, Lenhard M. The E3 ubiquitin ligase BIG BROTHER controls arabidopsis organ size in a dosage-dependent manner. *Current biology: CB*. 2006; 16(3):272–9. Epub 2006/02/08. <https://doi.org/10.1016/j.cub.2005.12.026> PMID: 16461280.
 59. Dewitte W, Scofield S, Alcasabas AA, Maughan SC, Menges M, Braun N, et al. Arabidopsis CYCD3 D-type cyclins link cell proliferation and endocycles and are rate-limiting for cytokinin responses. *Proc Natl Acad Sci U S A*. 2007; 104(36):14537–42. Epub 2007/08/30. <https://doi.org/10.1073/pnas.0704166104> PMID: 17726100; PubMed Central PMCID: PMC1964848.
 60. Bemis SM, Torii KU. Autonomy of cell proliferation and developmental programs during Arabidopsis aboveground organ morphogenesis. *Dev Biol*. 2007; 304(1):367–81. Epub 2007/01/30. <https://doi.org/10.1016/j.ydbio.2006.12.049> PMID: 17258192.
 61. Horiguchi G, Tsukaya H. Organ size regulation in plants: insights from compensation. *Frontiers in plant science*. 2011; 2:24. Epub 2011/01/01. <https://doi.org/10.3389/fpls.2011.00024> PMID: 22639585; PubMed Central PMCID: PMC3355714.
 62. Hisanaga T, Kawade K, Tsukaya H. Compensation: a key to clarifying the organ-level regulation of lateral organ size in plants. *J Exp Bot*. 2015; 66(4):1055–63. Epub 2015/01/31. <https://doi.org/10.1093/jxb/erv028> PMID: 25635111.
 63. Tsukaya H. Controlling size in multicellular organs: focus on the leaf. *PLoS Biol*. 2008; 6(7):e174. <https://doi.org/10.1371/journal.pbio.0060174> PMID: 18630989; PubMed Central PMCID: PMC2459211.
 64. Melaragno JE, Mehrotra B, Coleman AW. Relationship between Endopolyploidy and Cell Size in Epidermal Tissue of Arabidopsis. *The Plant cell*. 1993; 5(11):1661–8. Epub 1993/11/01. <https://doi.org/10.1105/tpc.5.11.1661> PMID: 12271050; PubMed Central PMCID: PMC160394.
 65. Roeder AH, Chickarmane V, Cunha A, Obara B, Manjunath BS, Meyerowitz EM. Variability in the control of cell division underlies sepal epidermal patterning in Arabidopsis thaliana. *PLoS Biol*. 2010; 8(5):e1000367. Epub 2010/05/21. <https://doi.org/10.1371/journal.pbio.1000367> PMID: 20485493; PubMed Central PMCID: PMC2867943.
 66. Sugimoto-Shirasu K, Stacey NJ, Corsar J, Roberts K, McCann MC. DNA topoisomerase VI is essential for endoreduplication in Arabidopsis. *Current biology: CB*. 2002; 12(20):1782–6. Epub 2002/10/29. PMID: 12401175.
 67. Noir S, Marocco K, Masoud K, Thomann A, Gusti A, Bitrian M, et al. The Control of Arabidopsis thaliana Growth by Cell Proliferation and Endoreplication Requires the F-Box Protein FBL17. *The Plant cell*. 2015; 27(5):1461–76. <https://doi.org/10.1105/tpc.114.135301> PMID: 25944099; PubMed Central PMCID: PMC4456641.
 68. Dewitte W, Riou-Khamlichi C, Scofield S, Healy JM, Jacqmar A, Kilby NJ, et al. Altered cell cycle distribution, hyperplasia, and inhibited differentiation in Arabidopsis caused by the D-type cyclin CYCD3. *The Plant cell*. 2003; 15(1):79–92. <https://doi.org/10.1105/tpc.004838> PMID: 12509523; PubMed Central PMCID: PMC143452.
 69. Mizukami Y, Fischer RL. Plant organ size control: ANTEGUMENTA regulates growth and cell numbers during organogenesis. *Proc Natl Acad Sci U S A*. 2000; 97(2):942–7. Epub 2000/01/19. PMID: 10639184; PubMed Central PMCID: PMC15435.
 70. MacAlister CA, Ohashi-Ito K, Bergmann DC. Transcription factor control of asymmetric cell divisions that establish the stomatal lineage. *Nature*. 2007; 445(7127):537–40. <https://doi.org/10.1038/nature05491> PubMed PMID: WOS:000243867300043. PMID: 17183265
 71. Kumar SV, Wigge PA. H2A.Z-Containing Nucleosomes Mediate the Thermosensory Response in Arabidopsis. *Cell*. 2010; 140(1):136–47. <https://doi.org/10.1016/j.cell.2009.11.006> PubMed PMID: WOS:000273391900021. PMID: 20079334
 72. Dello Ioio R, Nakamura K, Moubayidin L, Perilli S, Taniguchi M, Morita MT, et al. A Genetic Framework for the Control of Cell Division and Differentiation in the Root Meristem. *Science*. 2008; 322(5906):1380–4. <https://doi.org/10.1126/science.1164147> PubMed PMID: WOS:000261170600039. PMID: 19039136
 73. Calder G, Hindle C, Chan J, Shaw P. An optical imaging chamber for viewing living plant cells and tissues at high resolution for extended periods. *Plant Methods*. 2015; 11(1):22. <https://doi.org/10.1186/s13007-015-0065-7> PMID: 25806083
 74. Lee K, Avondo J, Morrison H, Blot L, Stark M, Sharpe J, et al. Visualizing plant development and gene expression in three dimensions using optical projection tomography. *The Plant cell*. 2006; 18(9):2145–

56. Epub 2006/08/15. <https://doi.org/10.1105/tpc.106.043042> PMID: 16905654; PubMed Central PMCID: PMC1560903.
75. Schindelin J, Arganda-Carreras I, Frise E, Kaynig V, Longair M, Pietzsch T, et al. Fiji: an open-source platform for biological-image analysis. *Nat Methods*. 2012; 9(7):676–82. <https://doi.org/10.1038/nmeth.2019> PubMed PMID: WOS:000305942200021. PMID: 22743772
76. R_Core_Team. A language and environment for statistical computing. Foundation for Statistical Computing, Vienna, Austria 2018 [cited 2018 Sep 20]. Available from: <http://www.R-project.org/>.
77. Sanchez-Corrales YE, Hartley M, van Rooij J, Maree AFM, Grieneisen VA. Morphometrics of complex cell shapes: lobe contribution elliptic Fourier analysis (LOCO-EFA). *Development*. 2018; 145(6). Epub 2018/02/16. <https://doi.org/10.1242/dev.156778> PMID: 29444894; PubMed Central PMCID: PMC5897594.
78. Truernit E, Bauby H, Dubreucq B, Grandjean O, Runions J, Barthelemy J, et al. High-resolution whole-mount imaging of three-dimensional tissue organization and gene expression enables the study of Phloem development and structure in *Arabidopsis*. *The Plant cell*. 2008; 20(6):1494–503. <https://doi.org/10.1105/tpc.107.056069> PMID: 18523061; PubMed Central PMCID: PMC2483377.
79. Nakielski J. Tensorial model for growth and cell division in the shoot apex. In: Carbone A, Gromov M, Prusinkiewicz P, editors. *Pattern Formation in Biology, Vision and Dynamics*. Singapore: World Scientific; 2000. p. 252–86.

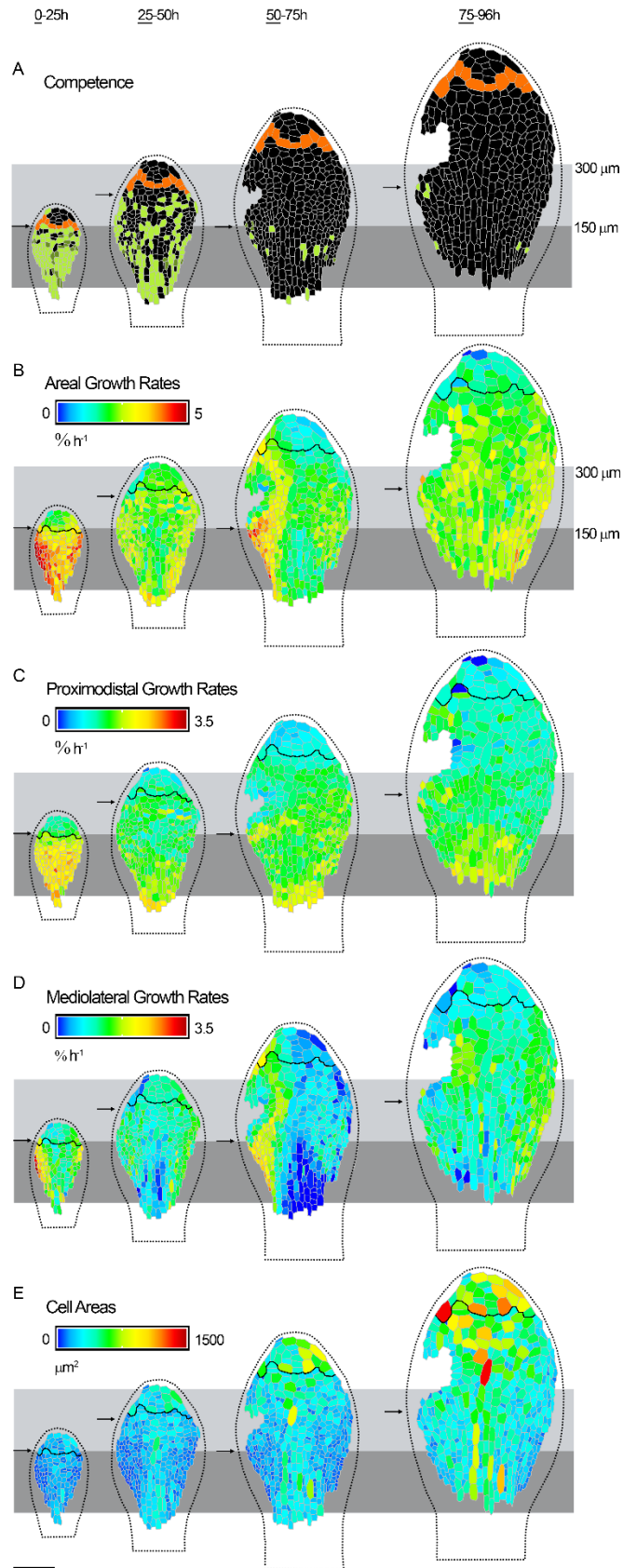
Supporting Figures



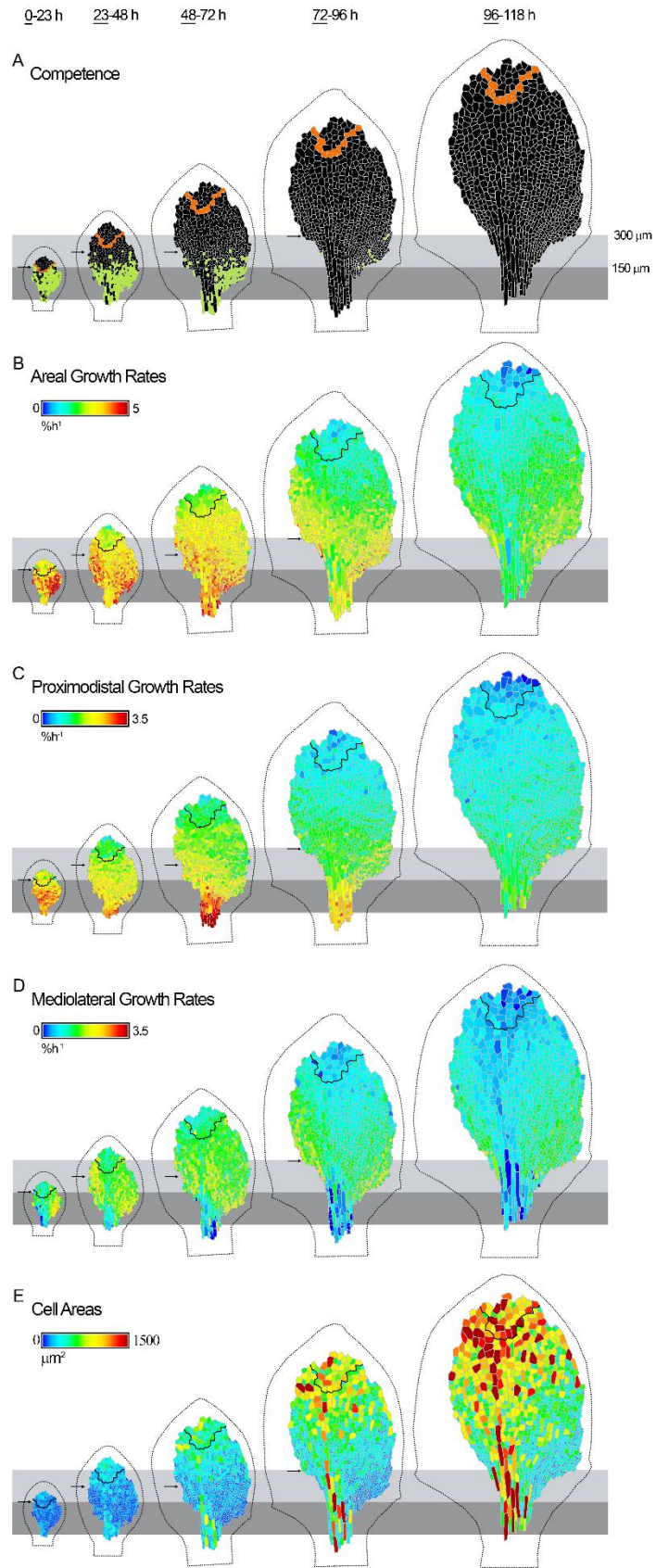
S1 Fig. Scatterplots of growth rates parallel and perpendicular to the midline in the *spch* epidermis



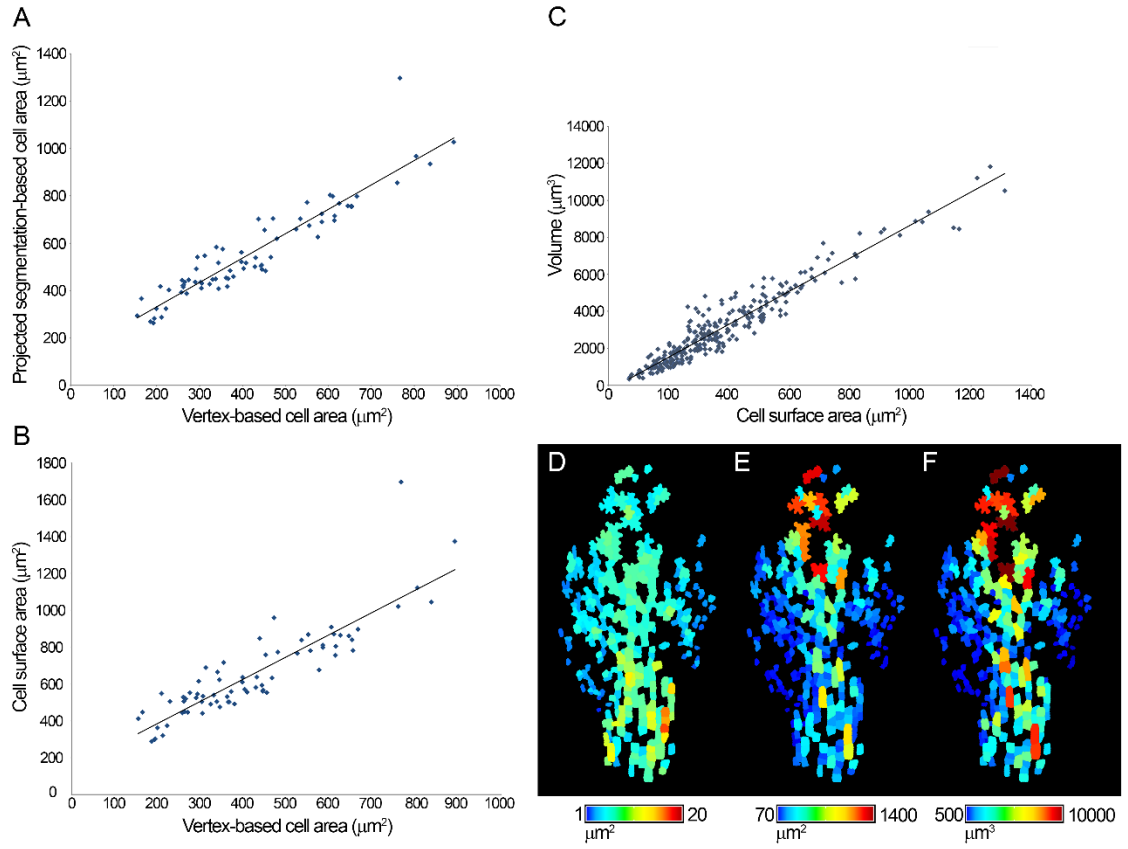
S2 Fig. Assignment of the midline and lamina regions



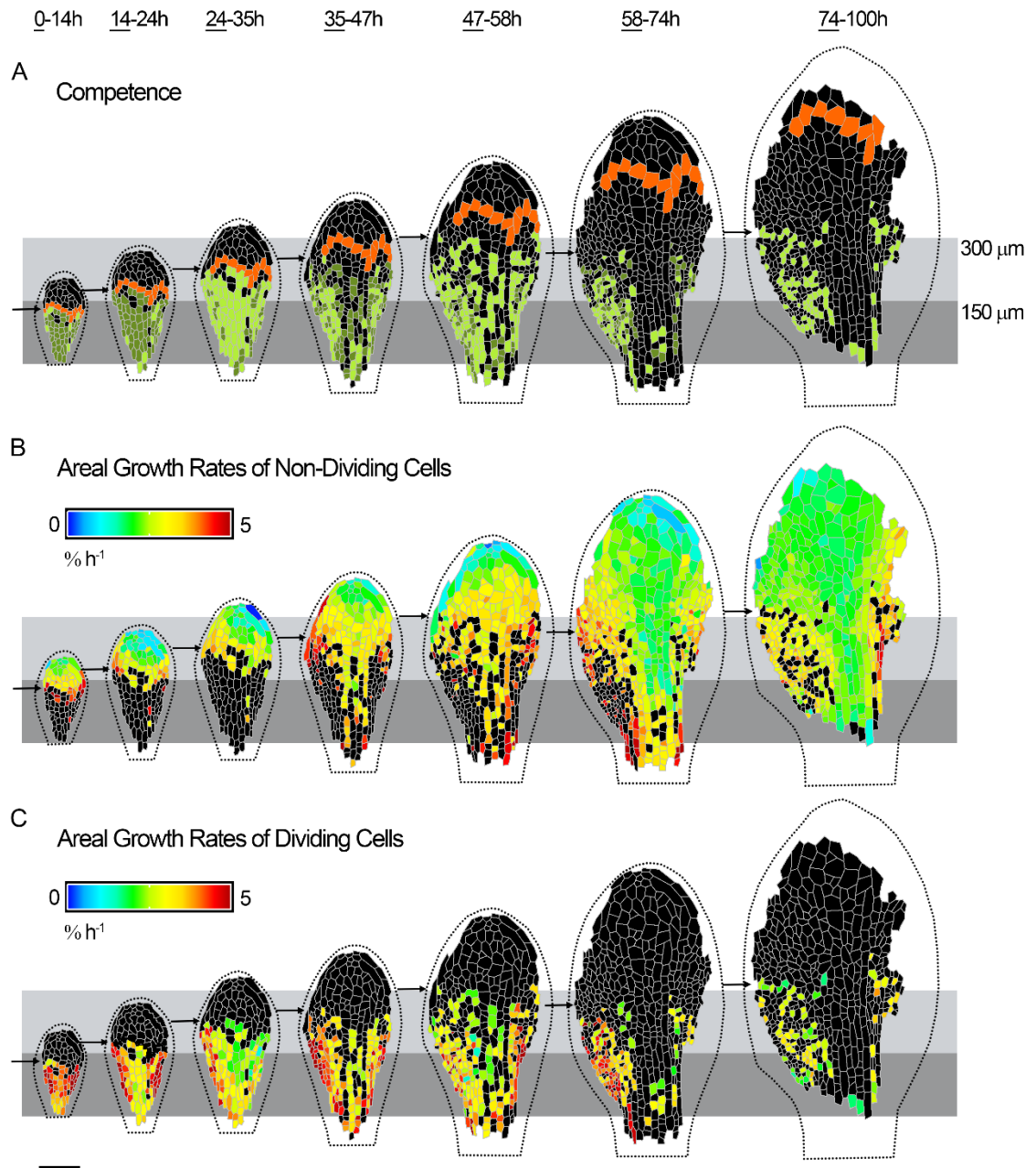
S3 Fig. Dynamics of cell division and growth in the *spch* epidermis, additional dataset.



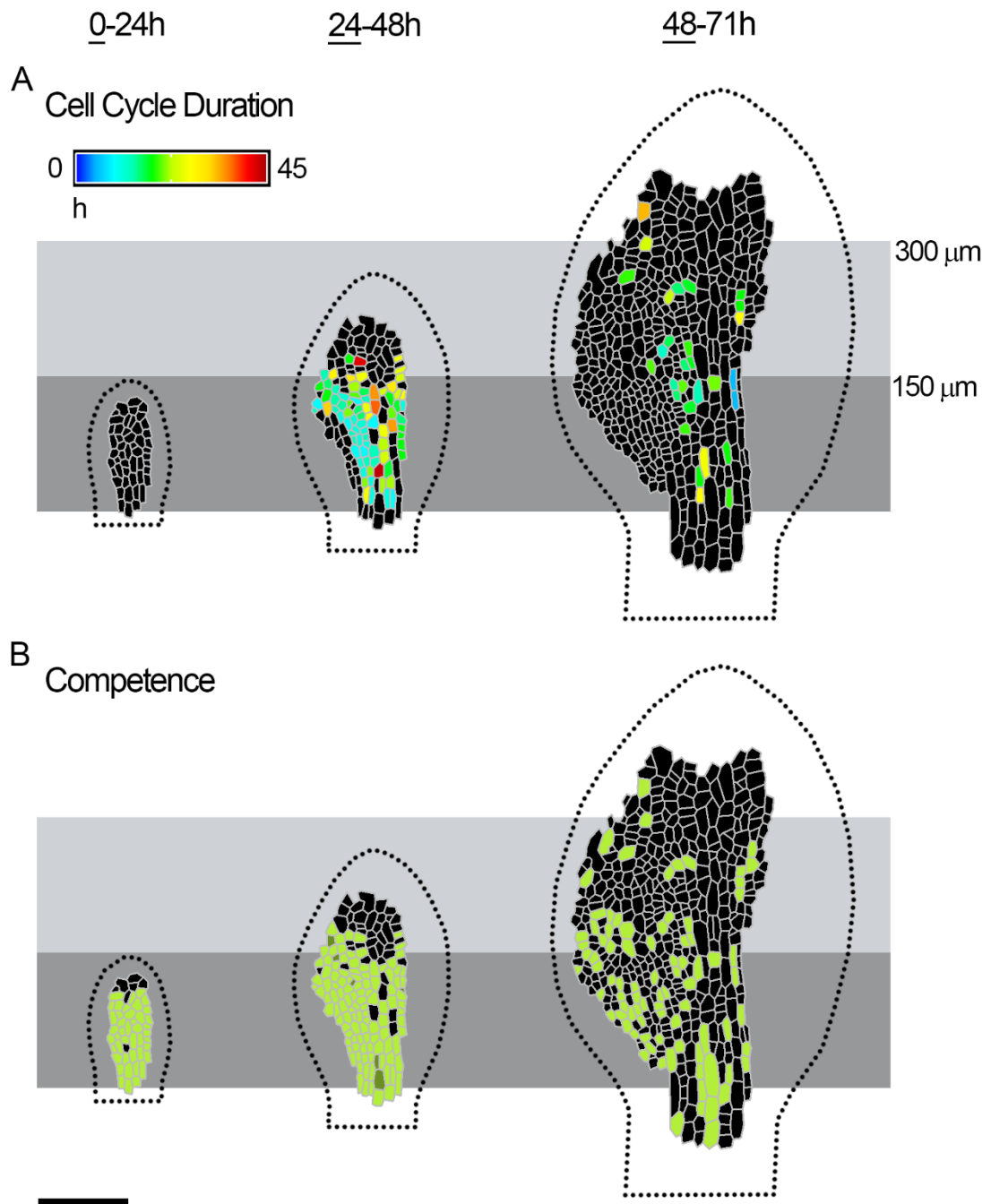
S4 Fig. Dynamics of cell division and growth in the *spch* epidermis, additional dataset.



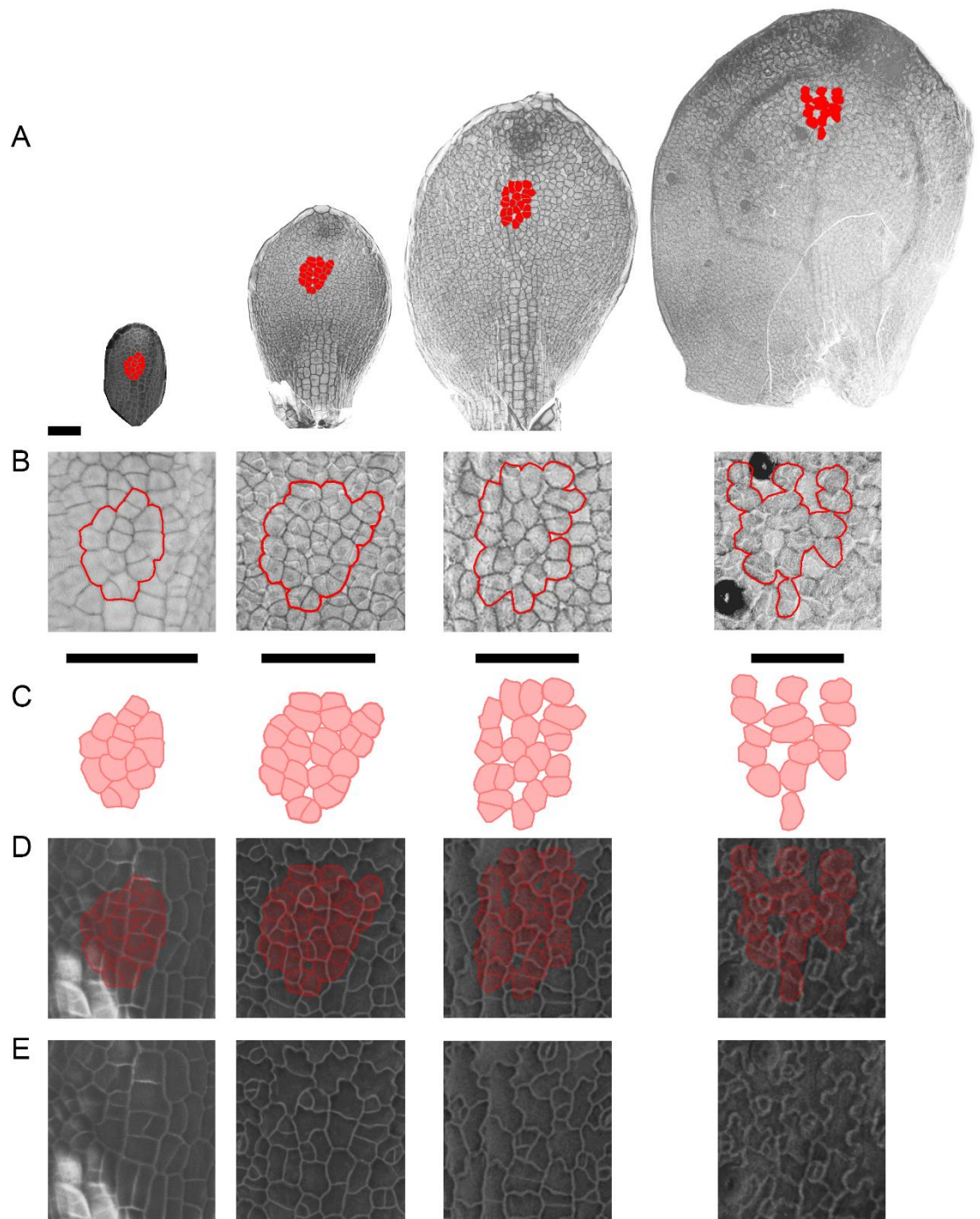
S5 Fig. Analysis of epidermal cell size using 3D segmentation.



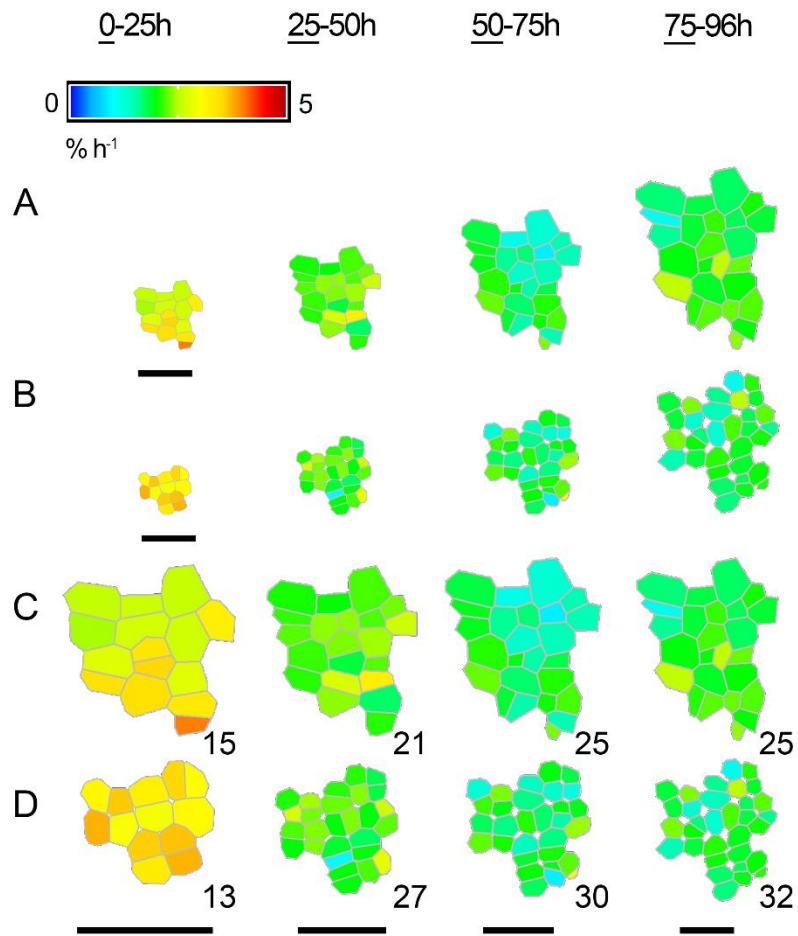
S6 Fig. Cellular areal growth rates of dividing and nondividing cells in the *spch* epidermis.



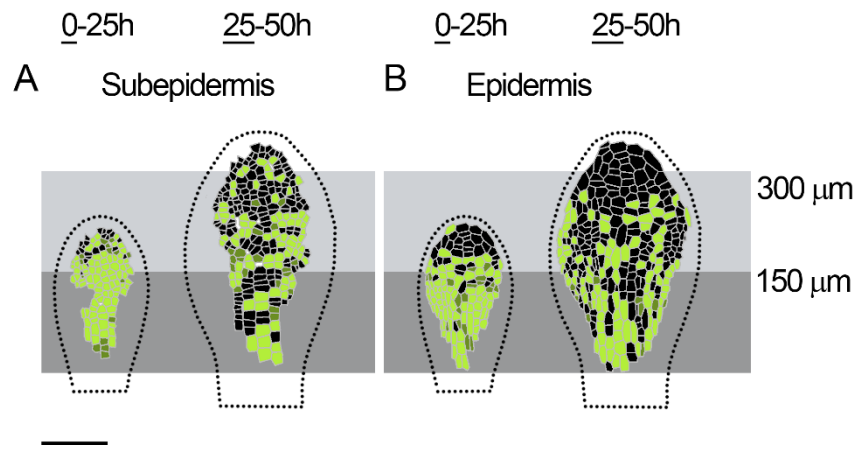
S7 Fig. Cell division dynamics of the epidermis at high temporal resolution.



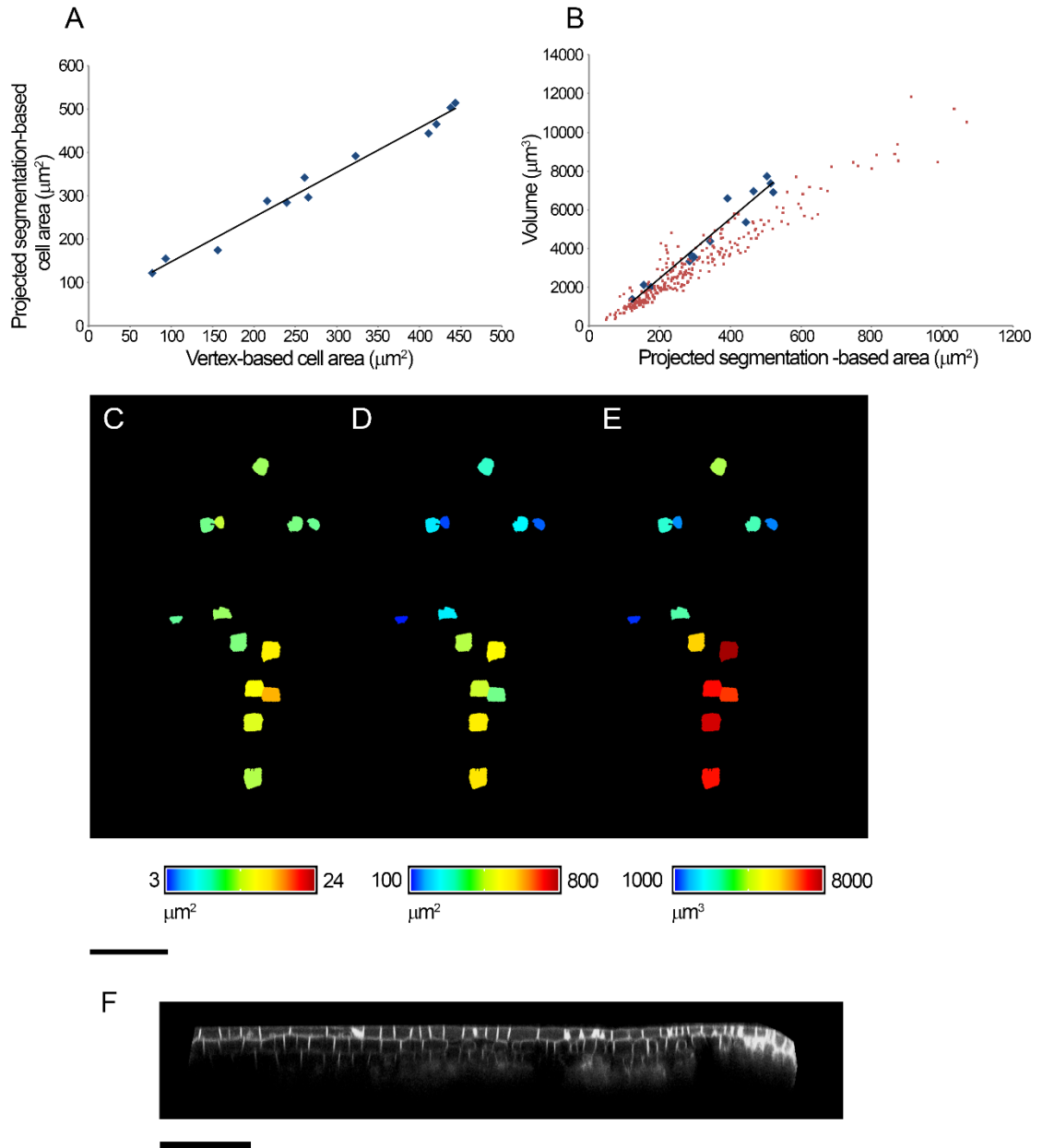
S8 Fig. Subepidermal cells in wild-type leaves.



S9 Fig. Comparison of epidermal and subepidermal cell areal growth rates.



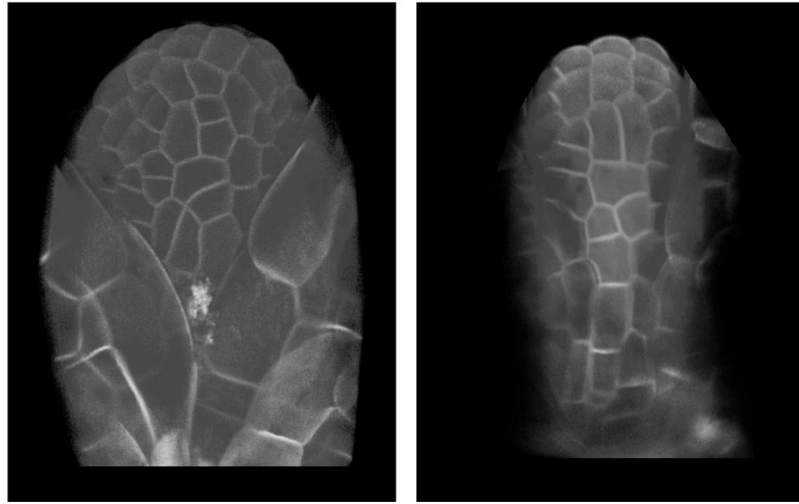
S10 Fig. Comparison of the zone of competence in epidermal and subepidermal layers.



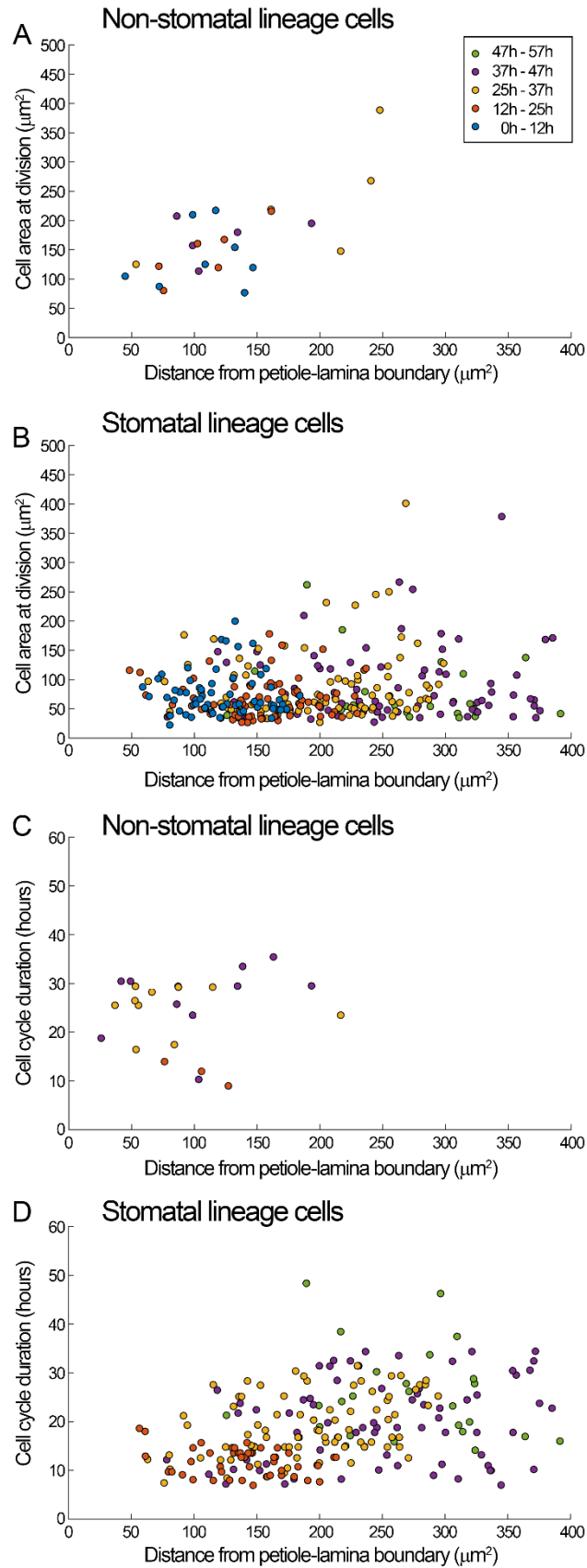
S11 Fig. Analysis of subepidermal cell size using 3D segmentation.

Wild type

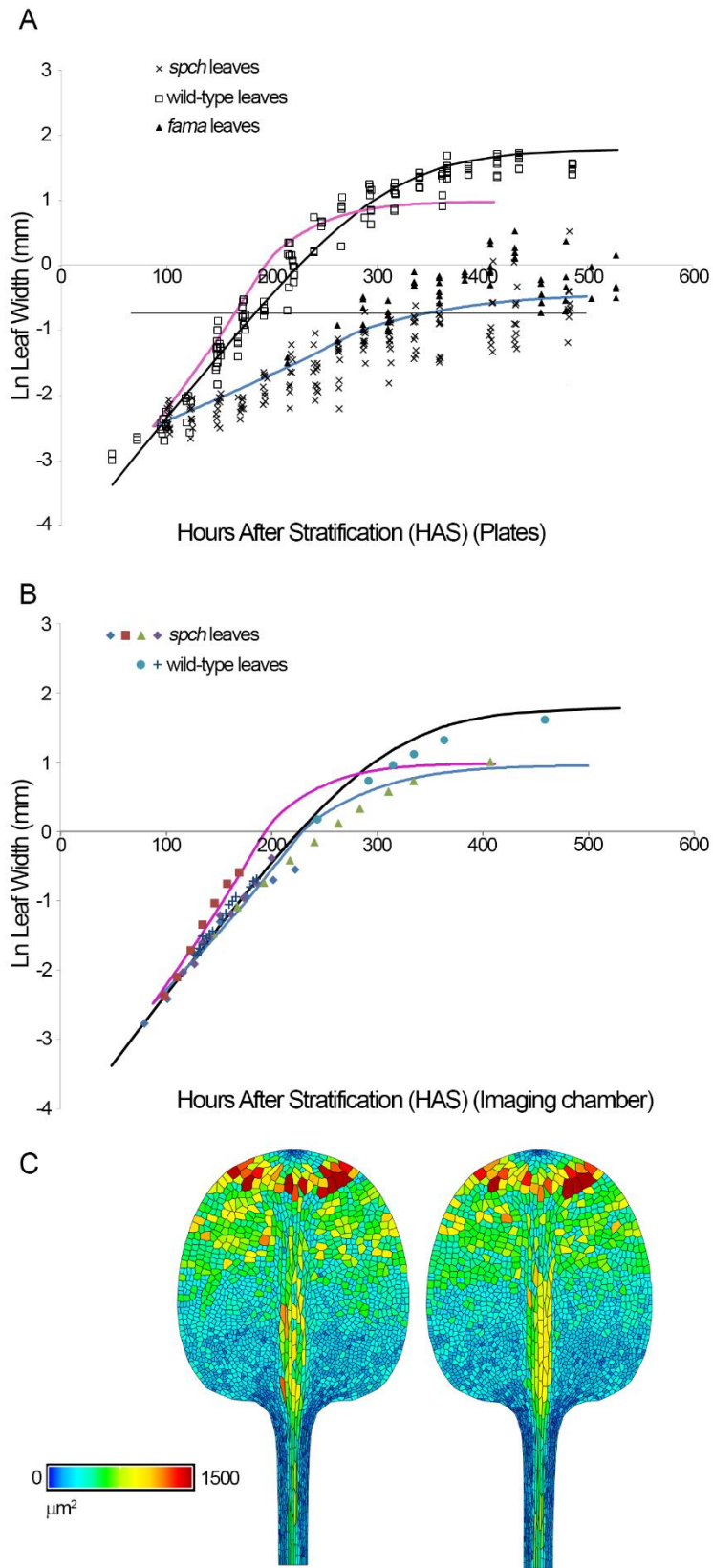
spch



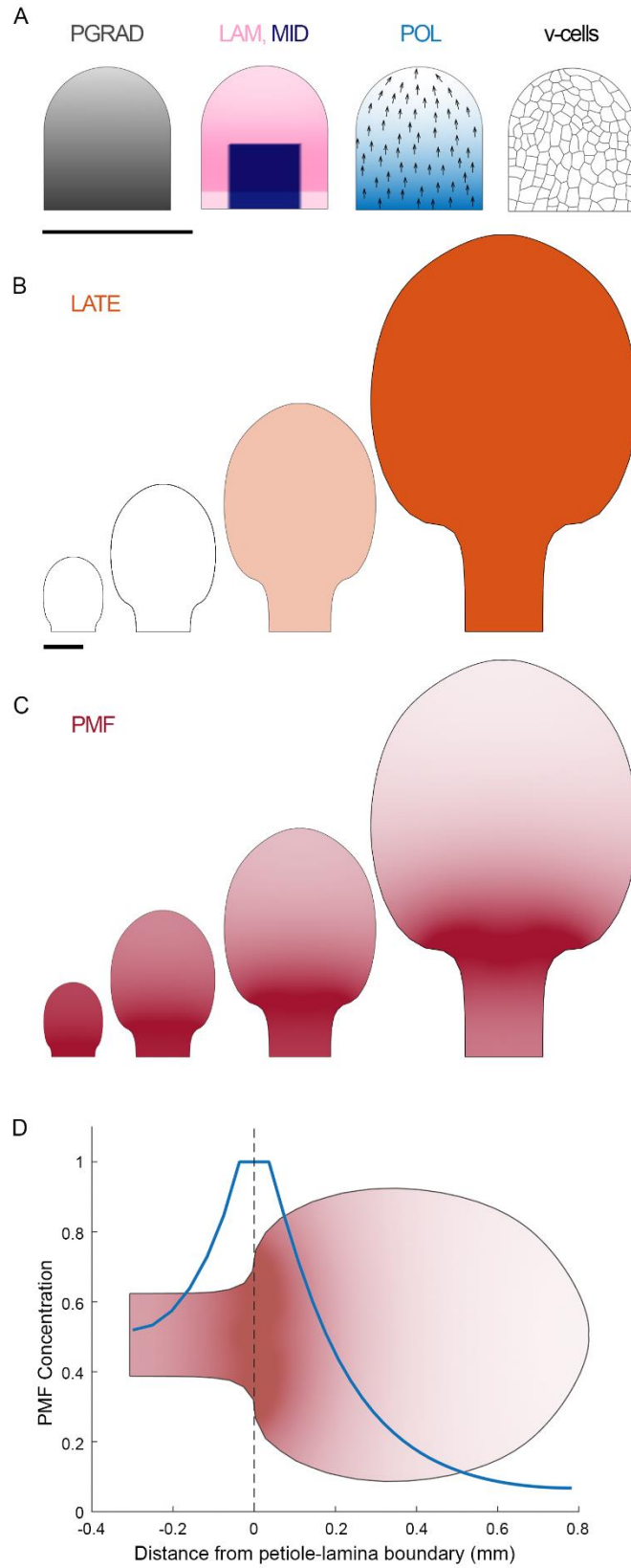
S12 Fig. Comparison of wild-type and *spch* primordia.



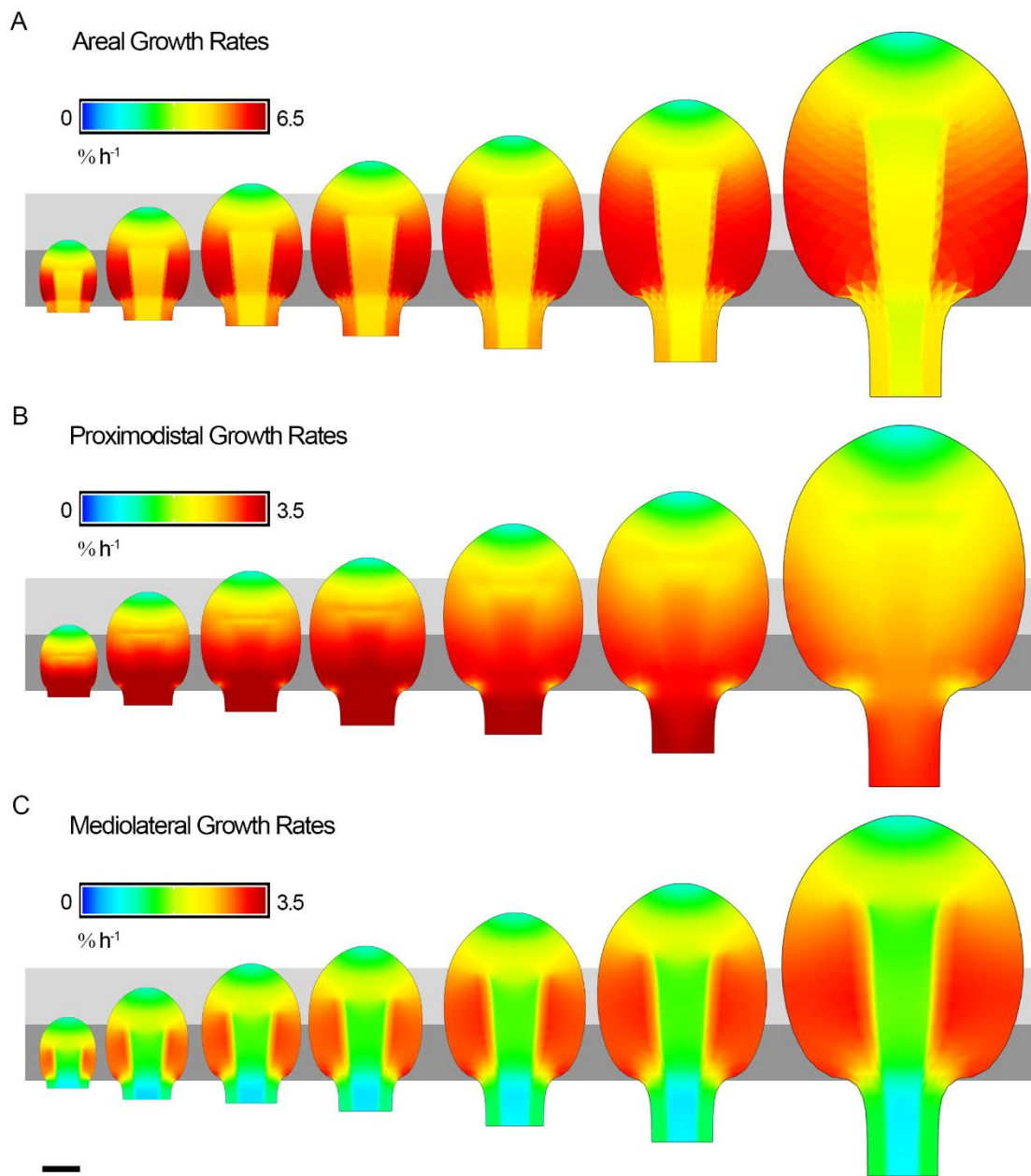
S13 Fig. Quantification of cell area at division execution in wild type.



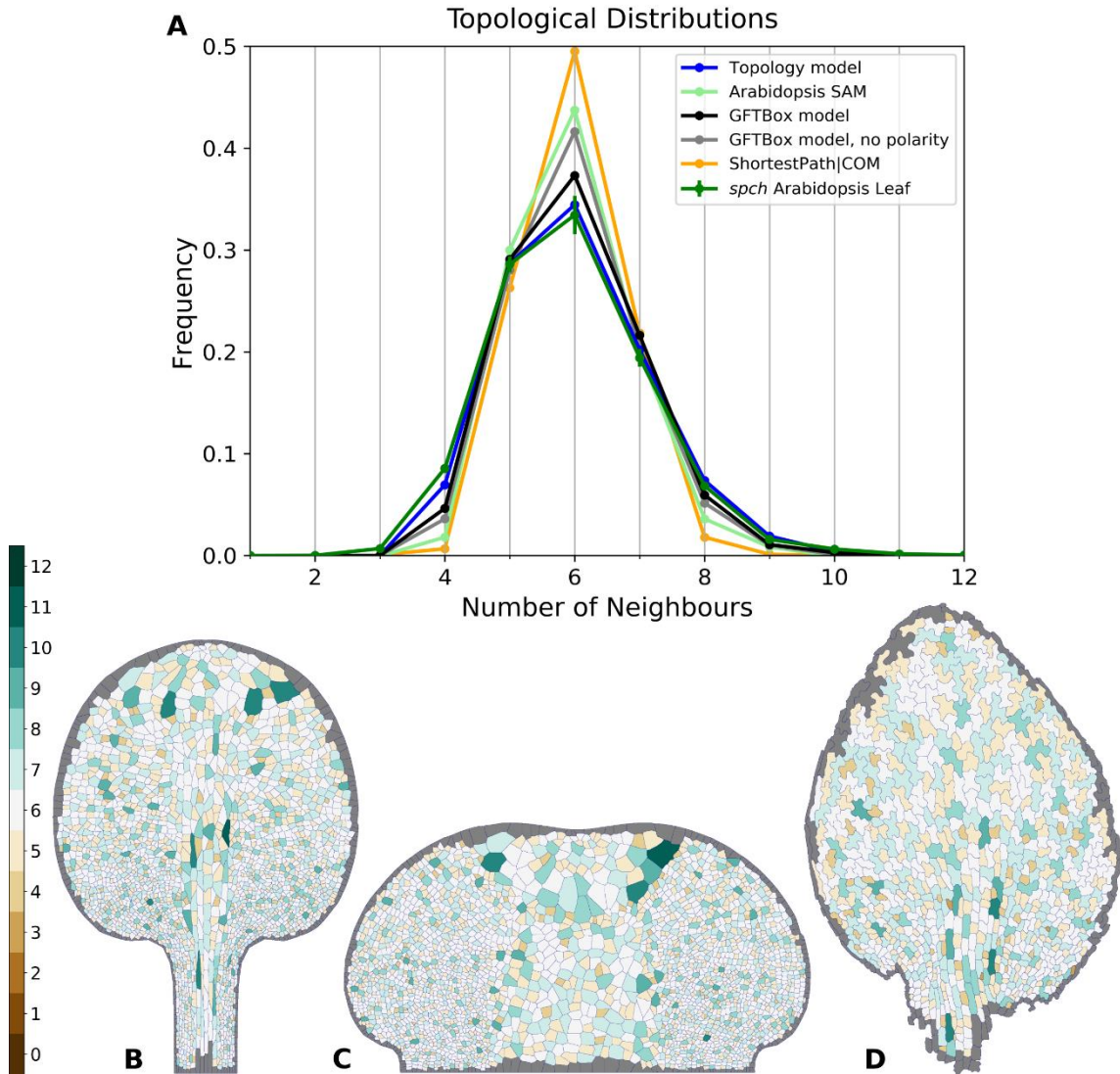
S14 Fig. Comparison of wild-type and *spch* growth rates in leaf width.



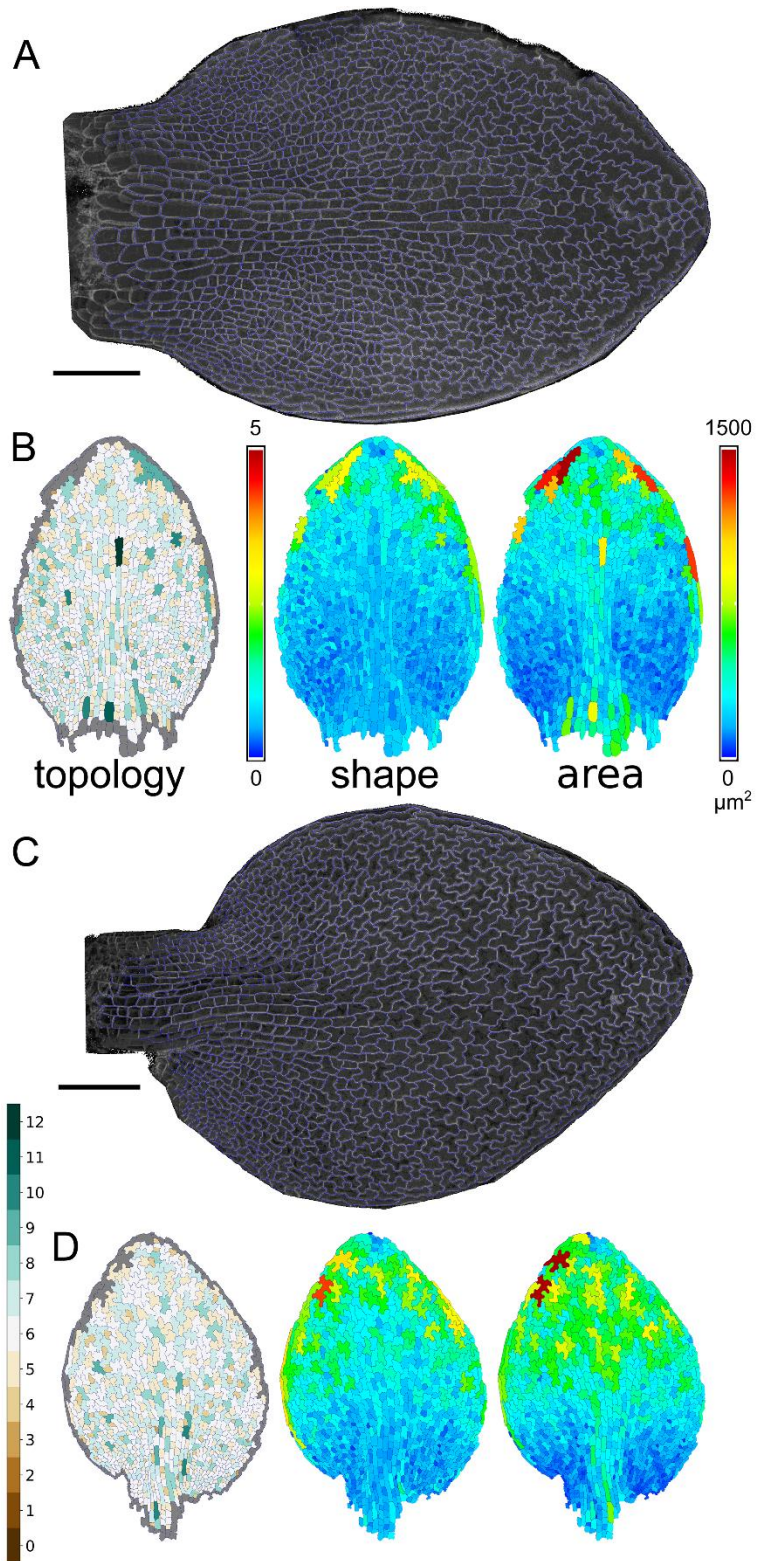
S15 Fig. Model setup and regulatory factors.



S16 Fig. Resultant growth rates for model output at different developmental stages.



S17 Fig. Topological distributions (frequency of n -sided cells) from empirical data and different models.



S18 Fig. Additional comparisons between chamber- and plate-grown *spch* leaves.



Generation of Leaf Shape Through Early Patterns of Growth and Tissue Polarity

Erika E. Kuchen, *et al.*
Science **335**, 1092 (2012);
DOI: 10.1126/science.1214678

This copy is for your personal, non-commercial use only.

If you wish to distribute this article to others, you can order high-quality copies for your colleagues, clients, or customers by [clicking here](#).

Permission to republish or repurpose articles or portions of articles can be obtained by following the guidelines [here](#).

The following resources related to this article are available online at www.sciencemag.org (this information is current as of March 9, 2012):

Updated information and services, including high-resolution figures, can be found in the online version of this article at:
<http://www.sciencemag.org/content/335/6072/1092.full.html>

Supporting Online Material can be found at:
<http://www.sciencemag.org/content/suppl/2012/02/29/335.6072.1092.DC1.html>

A list of selected additional articles on the Science Web sites **related to this article** can be found at:
<http://www.sciencemag.org/content/335/6072/1092.full.htm#related>

This article **cites 27 articles**, 9 of which can be accessed free:
<http://www.sciencemag.org/content/335/6072/1092.full.htm#ref-list-1>

This article appears in the following **subject collections**:
Botany
<http://www.sciencemag.org/cgi/collection/botany>

Downloaded from www.sciencemag.org on March 9, 2012

Science (print ISSN 0036-8075; online ISSN 1095-9203) is published weekly, except the last week in December, by the American Association for the Advancement of Science, 1200 New York Avenue NW, Washington, DC 20005. Copyright 2012 by the American Association for the Advancement of Science; all rights reserved. The title *Science* is a registered trademark of AAAS.

By measuring reinforcing selection acting on the dark flower color allele in *P. drummondii* under natural sympatric conditions and by quantifying selection in the absence of *P. cuspidata*, we were able to compare the relative strengths of direct selection by other environmental factors and by reinforcing selection on a trait conferring increased pre-mating isolation in a region of sympatry. The absence of detectable fitness differences among flower color genotypes in the absence of *P. cuspidata* indicates that another agent of selection is unlikely to be involved in flower color divergence in *P. drummondii*. Although we cannot rule out small, statistically undetectable differences in survival or reproductive success favoring these genotypes, such differences would be of minor importance compared with the strong reinforcing selection acting on the intensity locus.

Many plants have evolved pre-mating reproductive isolation by switching pollinator types (e.g., from bees to hummingbirds) (22–24). Our work suggests that increased reproductive isolation can also be achieved by a single pollinator species through constancy of individual pollinators. In particular, if pollinators transition between flowers with similar phenotypes more frequently than between flowers with unlike phenotypes, this will decrease gene flow between unlike flowers. Constancy is commonly studied in bumble bees but rarely investigated in butterfly pollinators (20, 25). That the primary pollinator *Battus philenor* exhibits this type of constancy is not surprising, given that females of this species exhibit constancy for leaf shape when searching for oviposition sites (21).

Theoretical models indicate that the likelihood of successful reinforcement is greater when selection is strong, because this will counteract gene flow and recombination, which tend to reduce pre-mating isolation (26–28). Our results indicate that, at least in some cases, very strong reinforcing selection may act on a single allele and lead to increased reproductive isolation.

Theory also indicates that reinforcement is more easily achieved by a one-allele mechanism (4, 29), but empirical assessment of this prediction has been difficult because the genetic basis of reinforcement is understood in few systems (7). Our current demonstration of reinforcing selection acting on the dark allele indicates that reinforcement in *P. drummondii* involves a two-allele reinforcement mechanism. The intensity locus causes reproductive isolation only if the dark allele is present in *P. drummondii* and the light allele is present in *P. cuspidata*. Consistent with theory, we find that strong selection and high levels of hybrid sterility cause the spread of the dark allele through sympatric *P. drummondii* populations. We suspect all reinforcement mechanisms involving different floral phenotypes to which pollination vectors must respond will be two-allele assortative mating mechanisms, because pollinators must be able to discriminate between the novel phenotype in one species and the ancestral phenotype in both species.

Although reinforcement has been studied primarily in animals (3, 7), our work indicates that it may also be an important contributor to speciation in plants. If so, this phenomenon may provide a partial explanation for the tremendous diversity of floral color, floral morphology, and inflorescence structure that characterize flowering plants.

References and Notes

1. R. Butlin, *Trends Ecol. Evol.* **2**, 8 (1987).
2. T. Dobzhansky, *Genetics and the Origin of Species* (Columbia Univ. Press, New York, 1937).
3. D. J. Howard, in *Hybrid Zones and the Evolutionary Process*, R. G. Harrison, Ed. (Oxford Univ. Press, New York, 1993), pp. 46–69.
4. M. R. Servedio, M. A. F. Noor, *Annu. Rev. Ecol. Syst.* **34**, 339 (2003).
5. A. R. Wallace, *Darwinism: An Exposition of the Theory of Natural Selection, with Some of Its Applications* (Macmillan, London, 1889).
6. M. Kirkpatrick, V. Ravigné, *Am. Nat.* **159** (suppl. 3), S22 (2002).
7. D. Ortiz-Barrientos, A. Gearty, P. Nosil, *Ann. N. Y. Acad. Sci.* **1168**, 156 (2009).
8. M. Kirkpatrick, *Proc. R. Soc. London Ser. B* **267**, 1649 (2000).
9. M. Kirkpatrick, M. R. Servedio, *Genetics* **151**, 865 (1999).
10. M. R. Servedio, *Evolution* **55**, 1909 (2001).
11. M. R. Servedio, *Evolution* **58**, 913 (2004).
12. A. Y. K. Albert, D. Schluter, *Evolution* **58**, 1099 (2004).
13. P. Nosil, B. J. Crespi, C. P. Sandava, *Proc. R. Soc. London Ser. B* **270**, 1911 (2003).
14. D. A. Levin, *Evolution* **39**, 1275 (1985).
15. R. Hopkins, D. A. Levin, M. D. Rausher, *Evolution* **66**, 469 (2012).
16. D. A. Levin, *Am. J. Bot.* **54**, 1122 (1967).
17. L. G. Ruane, K. Donohue, *Evol. Ecol.* **22**, 229 (2008).

18. R. Hopkins, M. D. Rausher, *Nature* **469**, 411 (2011).
19. Material and methods are available as supporting material on Science Online.
20. N. M. Waser, *Am. Nat.* **127**, 593 (1986).
21. M. D. Rausher, *Science* **200**, 1071 (1978).
22. H. D. Bradshaw Jr., D. W. Schemske, *Nature* **426**, 176 (2003).
23. D. R. Campbell, N. M. Waser, E. J. Melander-Ackerman, *Am. Nat.* **149**, 295 (1997).
24. M. E. Hobbalah et al., *Plant Cell* **19**, 779 (2007).
25. L. Chittka, J. D. Thomson, N. M. Waser, *Naturwissenschaften* **86**, 361 (1999).
26. M. Caisse, J. Antonovics, *Heredity* **40**, 371 (1978).
27. J. Felsenstein, *Evolution* **35**, 124 (1981).
28. L. W. Liou, T. D. Price, *Evolution* **48**, 1451 (1994).
29. M. R. Servedio, *Evolution* **54**, 21 (2000).

Acknowledgments: We thank M. Kirkpatrick, S. Otto, M. Whitlock, D. Des Marais, and members of the Rausher and Kirkpatrick laboratory group for advice on this manuscript and S. Scarpino for statistical consultation. We thank the University of Texas Stengel Research Station for field experiment support. This work was supported by NSF grant 0841521 to M.D.R. and a NSF Doctoral Dissertation Improvement Grant to R.H. and M.D.R. R.H. was supported by the NSF Graduate Research Fellowship Program. All data presented here are available in the supporting material.

Supporting Online Material

www.sciencemag.org/cgi/content/full/science.1215198/DC1
 Materials and Methods
 Figs. S1 and S2
 Tables S1 to S9
 References
 12 October 2011; accepted 12 January 2012
 Published online 2 February 2012;
 10.1126/science.1215198

Generation of Leaf Shape Through Early Patterns of Growth and Tissue Polarity

Erika E. Kuchen,^{1*} Samantha Fox,^{1*} Pierre Barbier de Reuille,² Richard Kennaway,² Sandra Bensmihen,¹ Jerome Avondo,¹ Grant M. Calder,¹ Paul Southam,² Sarah Robinson,¹ Andrew Bangham,²† Enrico Coen^{1†}

A major challenge in biology is to understand how buds comprising a few cells can give rise to complex plant and animal appendages like leaves or limbs. We address this problem through a combination of time-lapse imaging, clonal analysis, and computational modeling. We arrive at a model that shows how leaf shape can arise through feedback between early patterns of oriented growth and tissue deformation. Experimental tests through partial leaf ablation support this model and allow reevaluation of previous experimental studies. Our model allows a range of observed leaf shapes to be generated and predicts observed clone patterns in different species. Thus, our experimentally validated model may underlie the development and evolution of diverse organ shapes.

The shapes of many plant and animal appendages are thought to develop under the influence of orthogonal organizing

systems (i.e., systems with axes that intersect at right angles) (1–4). However, it is unclear how these orthogonal systems lead to changes in tissue shape and how shape changes may themselves feed back to deform the organizing systems. Consider a square piece of tissue that deforms during growth (Fig. 1A). The tissue has an initial linear orthogonal system that organizes the pattern of morphogenesis (Fig. 1B, arrows). We might en-

¹John Innes Centre, Norwich Research Park, Norwich, NR4 7UH, UK. ²School of Computing Sciences, University of East Anglia, Norwich Research Park, Norwich, NR4 7TJ, UK.

*These authors contributed equally to this work.
 †To whom correspondence should be addressed. E-mail: enrico.coen@jic.ac.uk (E.C.); a.bangham@uea.ac.uk (A.B.)

Downloaded from www.sciencemag.org on March 9, 2012

visage two extreme possibilities as the tissue deforms. One is that the organizing system retains its original arrangement despite the change in tissue shape (Fig. 1C). Another possibility is that the change in shape of the tissue feeds back to deform the organizing system during growth (Fig. 1D).

Here, we exploit live imaging of fluorescently marked *Arabidopsis* leaves to distinguish these possibilities. We concentrated on growth of leaf 1, from when the leaf primordium had a simple dome shape [3 days after initiation (DAI)] to the stage at which the characteristic leaf shape was evident (9 DAI) (fig. S1). We first determined areal growth rates for different regions of the leaf by tracking cell vertices over time. Areal growth rate is lower toward the distal tip of the leaf (Fig. 1J), consistent with previous tracking studies at later stages of growth (5–7). Areal growth rates also tend to be higher in lateral compared to medial domains (Fig. 1J).

To understand how the observed patterns of growth could be generated, we first considered growth rates in the proximodistal direction along the midline of the leaf lamina (Fig. 1, E to I). At early stages, growth rates parallel to the midline show an almost linear decrease from proximal to distal regions (Fig. 1, E and F). At later stages, the proximodistal gradient in growth rates becomes shallower throughout most of the leaf but maintains a steep decline near the tip (Fig. 1, G to I). To account for these observations, we used a one-dimensional (1D) model with a factor, PGRAD, that declines from proximal to distal positions with an initial linear gradient (fig. S2, A and B) and promotes specified growth rate K (Fig. 1P). PGRAD levels are maintained locally and deform with the tissue during growth. The output of this model is a gradient in growth rates that becomes shallower proximally because these regions extend more rapidly (Fig. 1, E to G, black lines; Fig. 1, H

and I, gray lines). Thus, the initial linear gradient is transformed into a curve that dips more steeply toward the distal end.

Although this model generates curves that match the data at early stages (Fig. 1, E to G), observed growth rates at later stages are lower than those predicted by the model (Fig. 1, H and I, gray lines). We therefore introduced a uniformly distributed factor into the model, LATE, that increases during later stages and inhibits the specified growth rates (Fig. 1P and fig. S2C). With this modification, the resulting proximodistal growth rates show a better match to the data (Fig. 1, H and I, black lines).

We next extended the model to 2D, using the growing polarized tissue framework (8), in which growth rates can be specified by a distribution of factors over a tissue. Regions of the tissue are mechanically connected, forming a canvas, allowing the deformation resulting from specified local growth patterns to be computed.

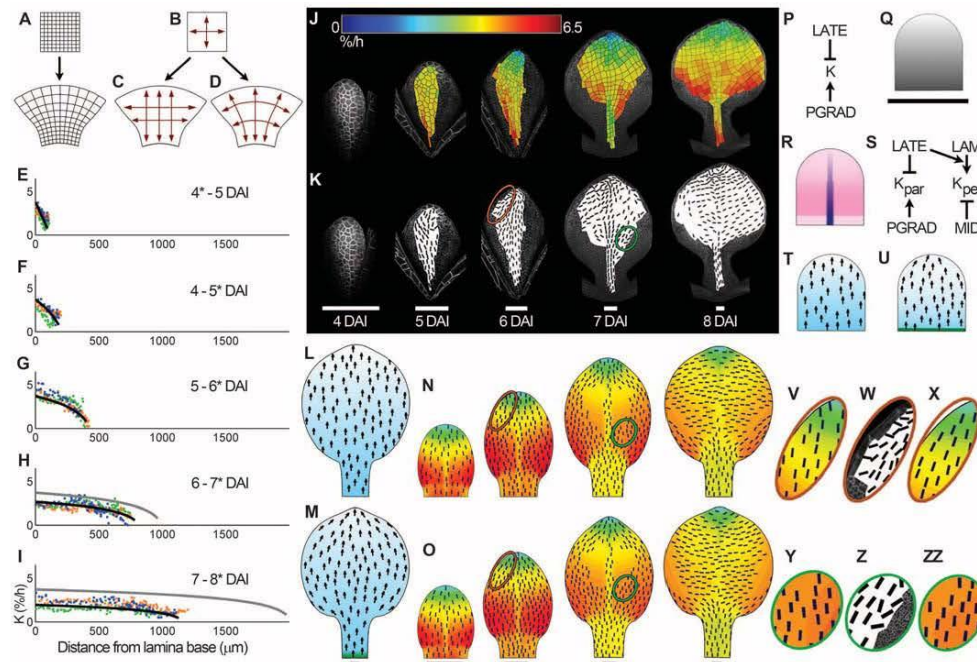
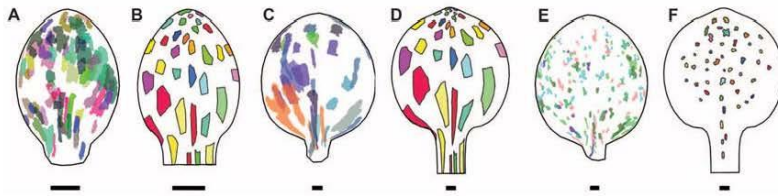


Fig. 1. Leaf growth analysis. (A) Tissue deforms through growth. (B) Orthogonal organizing system which (C) retains its original arrangement or (D) deforms during growth. (E to I) Midline proximodistal growth rates for three replicates (orange, green, and blue), and 1D models (black and gray lines). Distances from lamina base correspond to those on the day indicated by an asterisk. (J) Areal growth rates (heat map) and (K) principal directions of growth (black lines, where anisotropy > 10%) at the end of each period. (L) Resultant shape, POL levels and specified growth orientations (arrows) for nondeforming and (M) deforming (organizer-

based) models. (N) Resultant shapes, areal growth rates, and directions of growth (black lines, where anisotropy > 5%) for 2D nondeforming and (O) deforming (organizer-based) models. Heat map and staging as in (J). (P) 1D model regulatory network. (Q) 2D distribution of PGRAD (gray). (R) MID (blue) and LAM (magenta) distributions. (S) 2D model regulatory network. (T) Initial POL (cyan) distribution for nondeforming and (U) deforming models. PROXORG in green. (V to X) Enlargement of brown ellipses in (N), (K), and (O), respectively. (Y, Z, and ZZ) Enlargement of green ellipses in (N), (K), and (O), respectively. Scale bars, 100 μm .

Downloaded from www.sciencemag.org on March 9, 2012

Fig. 2. Clonal analysis. (A, C, and E) Clones induced at 3 DAI (A and C) or 6 DAI (E) and imaged at 6 DAI (A) or 9 DAI (C and E). Clones from several leaves are superimposed. (B, D, and F) Clonal patterns generated by the organizer-based model at stages corresponding to those shown on their left. Scale bars, 100 μ m.



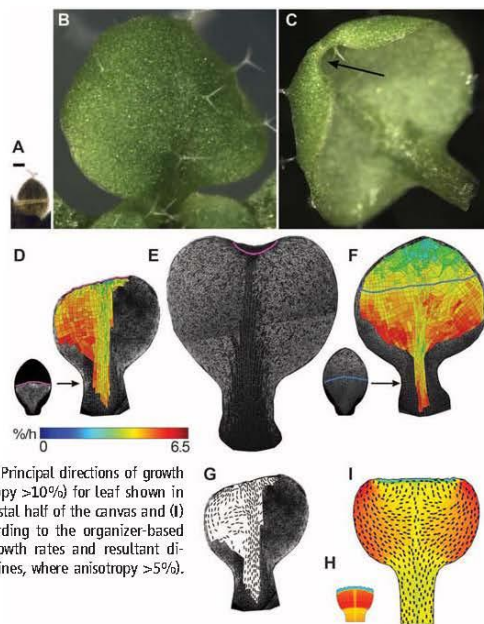
Each model has three components: (i) an initial canvas shape with distributed factors; (ii) a system for specifying polarity; and (iii) a growth regulatory network. The starting shape for the canvas is based on a simplified leaf primordium shape (Fig. 1Q and fig. S3). To account for the observed pattern of growth rates (Fig. 1J), the initial canvas has spatial domains defined by three factors: (i) PGRAD is expressed as a linear gradient along the proximodistal axis (as for the ID model); (ii) LAM is expressed everywhere but at a lower level in a narrow region at the base (which will form the petiole); and (iii) MID is expressed along the midline (Fig. 1, Q and R). For all these factors, levels are maintained locally and deform with the canvas during growth.

Growth orientations depend on a proximodistal gradient of a factor, POLARISER (POL), distributed throughout the canvas (Fig. 1T, arrows). The gradient of POL provides the axiality information needed to specify local growth orientations. We first assumed that growth orientations are specified according to a nondeforming system (Fig. 1C) with axes parallel (proximodistal axis) or perpendicular (mediolateral axis) to the midline (9, 10). This corresponds to keeping the POL gradient parallel to the midline throughout growth (Fig. 1L). There is thus no feedback between tissue deformation and specification of growth orientations. The growth regulatory network controls two specified growth rates: parallel (K_{par}) and perpendicular (K_{per}) to the POL gradient (fig. 1S). K_{par} is controlled by PGRAD and LATE as for the ID model (Fig. 1P). To account for the higher areal growth rates in the lateral domains, K_{per} is promoted by LAM and inhibited by MID. The extent to which LAM promotes K_{per} is further enhanced by LATE; otherwise, growth rates in the lamina drop below observed levels.

Running this nondeforming model leads to canvas shape changes and patterns of areal growth that are broadly similar to those observed experimentally (Fig. 1N). The principal orientations of resultant growth (Fig. 1N, black lines) switch from being mainly parallel to the midline at early stages to being mainly perpendicular to the midline in the lamina. The switch occurs because LATE enhances the effect of LAM on K_{per} (Fig. 1S).

The principal orientations of growth predicted by the nondeforming model of leaf development were compared with observed orientations,

Fig. 3. Distal leaf excision. (A) Excision of the distal half of leaf 1 lamina at 6 DAI. Distal region was removed after laser cut (pale line). (B) Leaf 1, 6 days after distal excision, viewed from the top and (C) from lower (abaxial) side, showing a curved indentation at the tip (arrow). (D) Leaf 1 cut at 6 DAI (left) and tracked until 9 DAI (right). Areal growth rates (heat map) calculated over the last 24 hours of tracking. Boundary of cut highlighted with magenta line. (E) Leaf after tracking growth for 5 days after distal excision. (F) Tracked uncut leaf with a blue line shown at a similar position to the cut in (D). (G) Principal directions of growth (black lines, where anisotropy >10%) for leaf shown in (D). (H) Excision of the distal half of the canvas and (I) output after growth according to the organizer-based model, showing areal growth rates and resultant directions of growth (black lines, where anisotropy >5%). Scale bar, 100 μ m.

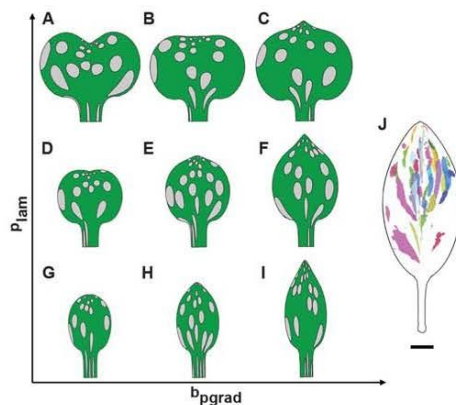


obtained from the measured displacement of cell vertices (11). The observed principal directions of growth are mainly oriented proximodistally at early stages and switch in the lamina toward a more mediolateral orientation during later stages of growth (Fig. 1K, N, V, and W, and fig. S4, A and B). Also, in the proximal lamina regions near the midvein, principal orientations of growth are oblique and diverge from the midline at later stages (green ellipses, Fig. 1, K and Z and fig. S4, C and D), in contrast to the largely parallel or perpendicular orientations predicted by the model (green ellipse, Fig. 1, N and Y).

We next considered an organizer-based model in which POL distribution arises by prop-

agation through the canvas and then deforms during growth. POL production is promoted at the base of the canvas through an identity factor PROXORG (proximal organizer) and is degraded everywhere at a constant rate (Fig. 1U). Propagation of POL through the canvas generates a proximodistal field of polarities that is initially parallel to the midline in the basal half of the canvas and converges toward the tip (Fig. 1U and fig. S5A) but then deforms (Fig. 1M and fig. S5B). The initial canvas, distribution of factors, and growth regulatory network are the same as in the nondeforming model (Fig. 1, Q to S). The resulting shape changes and growth patterns are also similar (Fig. 1O and fig. S5C). However, resultant growth orientations give a better match to the experimental data (table S1): Orientations converge toward the leaf tip (brown ellipse, Fig. 1, O and X) and have oblique orientations of growth that diverge from the midline at later

Fig. 4. Generation of diverse leaf shapes. (A to I) Morphospace generated from the organizer-based model, varying two growth parameters; the strength of promotion by LAM, p_{lam} , and the level of PGRAD at the distal end b_{pgrad} . *Arabidopsis* leaf 1 corresponds to (C). Clones induced as circles on day 3. (J) Clones on mature leaf (metamer 4) of *Antirrhinum*, induced when the leaf primordium is about 50 to 100 μm wide. Clones on the petiole were not recorded. Scale bar for *Antirrhinum* leaf, 1 cm.



stages due to deformation of the canvas (green ellipse, Fig. 1, O and Z).

An organizer-based model is also consistent with patterns of polarity observed in young leaf primordia. PIN1 (PIN-FORMED1) auxin transporters at this stage are oriented in a proximodistal pattern, with cell polarity pointing distally and converging toward the tip in the epidermis or pointing proximally in internal tissues (12). Both polarity patterns are consistent with an organizer-based model, because specifying growth orientation depends only on the axiality component of the polarity field, not the sense in which the polarity points (8). The mechanism determining PIN polarity is still unclear (13). One possibility is that auxin plays a primary role in establishing this pattern and would therefore be influenced by organizers of polarity. Alternatively, the PIN polarity pattern may be a read-out of a separate underlying polarity system.

The organizer-based model should account for growth patterns across the entire leaf as well as in regions accessible to tracking. This additional requirement was evaluated through clonal analysis. Clones were induced at 3 DAI (Fig. 2, A and C) or 6 DAI (Fig. 2E) using a heat shock-inducible Cre-Lox system (14). For regions accessible to tracking, the resulting clones were in good agreement with the fate of individually tracked cells (fig. S6). Clonal patterns were also compared with those generated by the organizer-based model. This was achieved by superimposing outlines of leaf cells on the canvas (fig. S3) and then growing the canvas to its final shape (Fig. 2, B, D, and F). The shapes and orientations of predicted and observed clones showed a good qualitative match: Clones diverge near the lamina base and converge toward the tip.

A key assumption of the above models is that the spatial pattern of growth rates is established at an early stage of leaf development. This assumption does not rule out modulations

in growth pattern at later stages but seems inconsistent with the claim that leaves regenerate after excision of the distal half at a time after patterning has been established according to our models (15). To investigate this discrepancy, we repeated the excision experiment by removing the distal half of the leaf at a similar developmental stage to that previously reported to give regeneration (6 DAI) (Fig. 3A and fig. S7A) (15). As with the previously published experiments, the cut edge was clearly evident after 2 days of growth but seemed to have disappeared after a further 4 days of growth when the leaf was viewed from above (Fig. 3B). However, examination of the underside of the leaf revealed a semicircular edge at the tip similar in length to the original cut, suggesting that regeneration from the cut edge may not have occurred (Fig. 3C). Tracking leaf development after distal excision revealed a similar spatial pattern of growth rates to a control uncut leaf, except for regions near the cut, where growth rates were reduced (Fig. 3, D and F). There was no evidence of tip regeneration (Fig. 3, D and E). The superficial resemblance to regeneration (Fig. 3B) is a consequence of the high contribution that proximal regions of the leaf primordium make to the mature leaf, and the reduced growth rate of the cut edge.

To determine whether the organizer-based model could account for the observed effects of distal excision, we grew the canvas until day 6 and then removed the distal half (Fig. 3H and fig. S2, D and E). Growth is assumed to be unaffected except at the cut margin, where growth is inhibited. The final shape and growth patterns generated by the model are broadly similar to that observed experimentally after distal excision (Fig. 3, G and I). Thus, distal excision validates the model rather than refuting it.

To determine whether the organizer-based model could account for leaf shapes other than leaf 1 in *Arabidopsis*, we varied each of the

model's growth parameters (fig. S8). The effect of varying b_{pgrad} (the level of PGRAD at the distal end) and p_{lam} (the strength of K_{per} promotion by LAM) in various combinations is shown in Fig. 4. The resulting morphospace includes many botanically described leaf shapes, such as obcordate (Fig. 4, A and D), ovate (Fig. 4F), and elliptic (Fig. 4, H and I) (16). Thus, the model may underlie a wide range of leaf forms.

As a further test of the model's generality, we compared the pattern of clones predicted to those observed in *Antirrhinum*, a species with an elliptic leaf shape amenable to clonal analysis (9). Clones were induced at an early stage of leaf development in *Antirrhinum*, using a temperature-sensitive transposon, and visualized in the mature leaf. The pattern of clones observed is in broad agreement with those generated by the model with low p_{lam} : Large narrow clones diverge outward from the lamina base, and small clones converge toward the tip (Fig. 4, H and J).

These results show that a relatively simple model can broadly account for the growth dynamics and shape changes observed during normal and perturbed growth of *Arabidopsis* and may also underlie a variety of other leaf shapes. The model assumes that growth orientations are specified through a tissue polarity system that deforms during growth and that a basic pattern of growth rates across the leaf is established from an early stage. This raises the question of how these features are specified at the cellular scale and what genes may underlie them. Candidate genes for LAM are *LEAFY PETIOLE* (17) and members of the *YABBY* family (18), which are expressed in the lamina and promote its lateral growth. Candidate organizers of tissue polarity are the *CUP-SHAPED COTYLEDON* (*CUC*) genes, which are expressed at the base of the leaf (19) and play a key role in leaf development (20, 21). Thus, our model provides a simple unifying framework for the control of organ shape that can be further tested experimentally, elaborated through the incorporation of genes and cellular properties, and extended to cover more complex leaf shapes.

References and Notes

1. L. I. Held, *Imaginal Discs: The Genetic and Cellular Logic of Pattern Formation* (Cambridge Univ. Press, Cambridge, 2002).
2. G. T. Kim, K. H. Cho, *Physiol. Plant.* **126**, 494 (2006).
3. G. F. Stopper, G. P. Wagner, *Dev. Biol.* **288**, 21 (2005).
4. L. Wolpert, C. Tickle, *Principles of Development* (Oxford Univ. Press, Oxford, ed. 4, 2011).
5. G. S. Avery, *Am. J. Bot.* **20**, 565 (1933).
6. D. Schmudt, M. Stitt, B. Jahne, U. Schurr, *Plant J.* **16**, 505 (1998).
7. S. O. Wolf, W. K. Silk, R. E. Plant, *Am. J. Bot.* **73**, 832 (1986).
8. R. Kennaway, E. Coen, A. Green, A. Bangham, *PLoS Comput. Biol.* **7**, e1002071 (2011).
9. A.-G. Rolland-Lagan, J. A. Bangham, E. Coen, *Nature* **422**, 161 (2003).
10. A. J. Fleming, *Plant Biol.* **5**, 341 (2003).
11. Z. Hejnowicz, J. A. Romberger, *J. Theor. Biol.* **110**, 93 (1984).

REPORTS

12. E. Scarpella, D. Marcos, J. Friml, T. Berleth, *Genes Dev.* **20**, 1015 (2006).
13. Y. Boutté, Y. Ikeda, M. Grebe, *Curr. Opin. Plant Biol.* **10**, 616 (2007).
14. J. L. Gallois, C. Woodward, G. V. Reddy, R. Sablowski, *Development* **129**, 3207 (2002).
15. G. Sena, X. Wang, H.-Y. Liu, H. Hofhuis, K. D. Birnbaum, *Nature* **457**, 1150 (2009).
16. F. Swink, G. Wilhelm, *Plants of the Chicago Region* (Indiana Academy of Science, Indianapolis, ed. **4**, 1994).
17. E. van der Graaff, A. D. Dulk-Ras, P. J. J. Hooykaas, B. Keller, *Development* **127**, 4971 (2000).
18. R. Sarojam *et al.*, *Plant Cell* **22**, 2113 (2010).
19. M. Aida, T. Ishida, M. Tasaka, *Development* **126**, 1563 (1999).
20. A. Hasson *et al.*, *Plant Cell* **23**, 54 (2011).
21. G. D. Bilsborough *et al.*, *Proc. Natl. Acad. Sci. U.S.A.* **108**, 3424 (2011).

Acknowledgments: This work was funded by the U.K. Biotechnology and Biological Sciences Research Council (BBSRC). We thank S. Sauret-Güeto, C. Hindle, and J. Chan for help in developing the tracking chamber; K. Lee for imaging cut leaves with OPT; and S. Grandson for mathematical support. The authors declare no competing financial interests.

Further information and software can be downloaded at www.uea.ac.uk/cmp/research/cmpbio/Giftbox.

Supporting Online Material

www.sciencemag.org/cgi/content/full/335/6072/1092/DC1

Materials and Methods

SOM Text

Figs. S1 to S8

Table S1

References (22–31)

30 September 2011; accepted 24 January 2012
10.1126/science.1214678



www.sciencemag.org/cgi/content/full/335/6072/1092/DC1

Supporting Online Material for

Generation of Leaf Shape Through Early Patterns of Growth and Tissue Polarity

Erika E. Kuchen, Samantha Fox, Pierre Barbier de Reuille, Richard Kennaway,
Sandra Bensmihen, Jerome Avondo, Grant M. Calder, Paul Southam,
Sarah Robinson, Andrew Bangham,* Enrico Coen*

*To whom correspondence should be addressed.

E-mail: enrico.coen@jic.ac.uk (E.C.); a.bangham@uea.ac.uk (A.B.)

Published 2 March 2012, *Science* **335**, 1092 (2012)
DOI: 10.1126/science.1214678

This PDF file includes:

- Materials and Methods
- SOM Text
- Figs. S1 to S8
- Table S1
- References

Materials and Methods

Plant Material

For tracking growth we used *Arabidopsis* lines pAR169 (*ATML1::mCitrine-RCI2A*) (22), or Lti6b (*35S::EGFP-LTI6b*) (23), which express fluorescently labelled plasma membrane markers and are in the Landsberg *erecta* background. For clonal analysis and calculating growth curves, we used lines carrying *35S::lox-uidA-loxGFP* and *hsp18.2::Cre* (14) in the Landsberg *erecta* background. Some of the cutting experiments used wild-type *Arabidopsis* in the Columbia background to ensure comparability with Sena *et al.* (15). *Arabidopsis* plants were grown in standard conditions (unless otherwise described): seeds were surface sterilised and sown on plates containing 25 ml of growth media [GM; 1x Murashige and Skoog salt mixture, 1 % (w/v) sucrose, 100 mg/ml inositol, 1 mg/ml thiamine, 0.5 mg/ml pyridoxin, 0.5 mg/ml nicotinic acid, 0.5 mg/ml MES, 0.8 % (w/v) agar, pH 5.7] then stratified at 4 °C for 3 days before being transferred to a controlled environment room at 20 °C in long day conditions (16 hours light/8 hours dark cycles). The unstable *Antirrhinum* line *pal-2* was grown on soil under continuous light at 25 °C except for short periods when plants were transferred to 15 °C to induce transposon excision (24).

Growth curves and staging

To generate growth curves (fig. S1), widths and lengths of leaf 1 were measured for multiple seedlings at various days after stratification (DAS). For early stages (2 to 6 DAS), leaves were imaged under the confocal microscope after staining with propidium iodide (25), and measurements were taken in 3D using VolViewer (<http://www.uea.ac.uk/cmp/research/cmpbio/VolViewer>). At later stages leaves were flattened, photographed and measurements taken from the 2D images using Fiji (<http://fiji.sc>). Logistic curves were fitted to the leaf width and length data:

$$y = -A/(1+\exp((t-t_m)k))+A$$

Where A is the upper asymptote, t is time (hours after stratification), k is the early exponential growth rate and t_m is the point of inflection, or time when y reaches $A/2$. For y = leaf width, parameter values were estimated to be: $A = 6$ mm, $k = 0.020$ h⁻¹ and $t_m = 306$ h. For y = leaf length, $A = 9.5$ mm, $k = 0.021$ h⁻¹ and $t_m = 310$ h.

The logistic function was used to estimate when the primordium has a width of 0.02 mm (~ two cells wide), which was taken as the time of leaf initiation. This time was about 1 DAS. Thus, days after leaf initiation (DAI) were calculated by subtracting 1 day from DAS.

Time-lapse imaging and analysis

Seedlings were grown in standard conditions before being transferred to a Growth-Tracking chamber (26) at 4 or 6 DAI. The chamber was mounted onto the stage of a Zeiss LSM 5 EXCITER Laser Scanning Microscope and the growing abaxial epidermis of leaves imaged at regular intervals over several days. The GFP or YFP probe was excited using the 488-nm line of an argon ion laser, and emitted light filtered through a 500-550-nm band-pass filter and imaged with either a 10x dry, or 20x dry, objective. The chamber was illuminated by a cold light source set to a long-day photoperiod. Room temperature was maintained at 20 °C. Widths of tracked leaves showed good agreement with the widths of leaf 1 grown under standard conditions.

Confocal z -stack images of time lapse data were processed using Merryproj (27) to create 2D projections of the leaf epidermis. Growth rates over 24 h intervals were extracted

using software called Point Tracker. The software is written in Python, uses NumPy and SciPy (28) for the data analysis and PyQt4 (<http://www.riverbankcomputing.co.uk/software/pyqt>) for the user interface. Cell vertices on the 2D projections were used as material points, which were linked to form regions (regions did not always correspond to biological cells). For each region, the growth tensor was estimated from the linear transformation that best approximated the deformation of the region (i.e. minimising the square error on the final vertex positions resulting from the transformation compared to the observed final positions). A polar decomposition allowed the rotation and scaling to be extracted from the transformation. From the scaling the strain tensor (I) was calculated. The scaling was further corrected to account for large time steps, with the assumption that the growth tensor is constant (i.e. the growth tensor is "attached" to the tissue and the tissue grows at a constant relative growth rate during the period covered, according to the Lagrangian formulation). The images shown in Fig. 1J and K, where growth is analysed over 5 days, are derived from two independent time lapse experiments

Growth in the direction of the midline (Fig. 1E to I) was calculated from the strain tensors of the cells in the midline region. The leaf midline axis was defined manually and the leaf rotated to align the midline axis with the y -axis. The position of each cell was recorded as the distance of its centroid from the petiole-lamina boundary along the y -axis. In cases where the midline was curved, it was divided into smaller segments, for each of which the midline axis was determined and aligned. Growth rate along the midline was calculated by projecting the midline unit vector onto the unit vectors defining the major and minor axis of growth for each cell.

Clonal analysis

Leaves were heat shocked at 3 or 6 DAI by submerging sealed plates containing seedlings into a water bath at 38 °C for 3 minutes. After 3 or 6 days of further growth in standard conditions, leaf 1 was removed, flattened and clones on the abaxial surface imaged on a Zeiss LSM 5 EXCITER Laser Scanning Confocal Microscope, or a Leica DM 6000 compound microscope. Leaves were imaged either at 6 DAI (leaf width ~ 0.34 mm), or 9 DAI (leaf width ~ 1.2 mm). For *Antirrhinum*, transposon excision was induced by moving plants from 25 °C to 15 °C for 24 hours, when metamer 4 (fourth node above the cotyledons) was ~ 50-100 µm wide. Mature metamer 4 leaves were flattened and photographed using a Kodak DCS Pro 14N camera. The Sector Analysis Toolbox (<http://www.uea.ac.uk/cmp/research/cmpbio/SectorAnalysisToolbox>) was used to analyse clonal patterns in *Arabidopsis* and *Antirrhinum* leaves. The program generates a virtual composite shape from the outline of individual leaves and the position and shape of their clones (Fig. 2, A, C and E, and Fig. 4J). Leaf outlines were captured by semi-automatic point placement and a mean leaf shape was calculated using Procrustes alignment (29), normalising for scale. Epidermal clones were segmented using a combination of automatic and manual segmentation. Each individual clone was warped onto the mean shape using a piecewise linear warp (30) in which the spatial transformations were maintained for each leaf. The Sector Analysis Toolbox was implemented in MATLAB. To simulate clones with the model, representative cell outlines were drawn on the canvas at the time of clone induction. The cell outlines were derived from confocal images of leaves at corresponding developmental stages. For the earliest stage (3 DAI) the curvature of the leaf surface precluded use of 2D projections for obtaining cell outlines. We therefore computed an approximation using a flattened curved section of the confocal image (fig. S3) using VolViewer (<http://www.uea.ac.uk/cmp/research/cmpbio/VolViewer>). The curved section was computed by first placing a 2D plane through the confocal image. The 2D plane was aligned to the leaf and discretised as a regular 2D (x, y) grid consisting of 64 x 64 vertices with connected

diagonals to form 8192 triangles. The 2D plane was made to curve independently along the x and y axis using two manually specified parameters. The parameters controlled the displacement along the z -axis at each vertex of the grid, using a sinusoid (sin) function. The parameters were adjusted until the curved section intersected the middle of the majority of the epidermal cells on the abaxial surface. To flatten the curved section image, the x , y -distances between the vertices were computed. The displacement along the z -axis was removed to flatten the curved section and the vertices were translated back to their computed x and y -distances in order to obtain a flattened image of the cell outlines.

Distal leaf excision

We repeated the leaf excision experiments in Sena *et al.* (15) as closely as possible by cutting leaf 3 of *Arabidopsis* accession Columbia-0 in half approximately perpendicular to the midvein (fig. S7) using Vannas micro-scissors (World Precision Instruments, 15 μm straight blades), as described by these authors. The excisions were carried out at 10 DAS, when leaf 3 width is ~ 0.2 mm. We found this to be the earliest stage that it was practical to cut the leaf using micro-scissors. We also repeated the excision experiments using leaf 1 of *Arabidopsis* Landsberg *erecta* at 6 DAI (leaf 1 width ~ 0.3 mm) and obtained the same results as for leaf 3 (no regeneration).

As the study by Sena *et al.* (15) shows that regeneration does not occur when leaves are cut at later stages (22 days after sowing), we wanted to ensure that our leaf cutting experiments had been done at a sufficiently early time point. We therefore compared the size of leaves 2 days and 5 days post cut to the published images by Sena *et al.* (15). In our experiments, leaf 3 was about 450 μm wide 2 days post cut, and 1.6 mm wide 5 days post cut. By contrast, in the experiments of Sena *et al.* (15), the leaf is 165 μm wide 2 days post cut, and 185 μm wide 5 days post cut, according to the scale bars in Fig. 4b and c of their paper. Thus it would seem that the leaves in the Sena *et al.* study are much smaller than ours and hardly grew during the 3 day period (the growth rate in width would be 0.16 %/h). However, closer inspection of their figure shows that the scale bar is most likely incorrect. The branches of mature *Arabidopsis* trichomes are about 250 μm long (31), yet according to the scale bars the trichome branches visible in Fig. 4b and c of Sena *et al.* (15) are about 20-25 μm long. Thus the scale bars seem to be out by a factor of about 10. Using the trichome branches for scaling, and assuming they are 200 μm long, we obtained estimated leaf widths of 1.25 mm for 2 days post cut, and 1.87 mm for 5 days post cut. These values are larger than those for leaves in our experiments, suggesting that our cuts had been carried out as early if not earlier than those of Sena *et al.* (15).

To improve the precision of leaf excision experiments, we used a Zeiss PALM laser dissecting microscope to cut the leaf. For these experiments we used leaf 1 as it is more accessible than leaf 3. Individual seedlings were placed on a drop of water on a glass slide and viewed using a 10x objective. The PALM software was then used to direct the laser beam to cut the lamina in half, perpendicular to the midvein. The laser was set to 100 % power and travelled at a speed of 5 mm/sec. The leaf tissue was severed completely (Fig. 3A) and the excised piece of leaf tissue removed using fine forceps. Seedlings were then returned to standard growing conditions for a further 3 or 6 days, and then imaged using a Leica MZ16 stereo microscope (Fig. 3, B and C). Alternatively, to track growth following excision, seedlings were mounted into a Growth-Tracking chamber immediately following laser cutting. The cut leaves were then imaged at regular intervals using a Zeiss LSM 5 EXCITER Laser Scanning Microscope (as described above). Cut edges grew in length by an average of

0.55 %/h in the tracking chamber, compared to 2.2 %/h for a corresponding region of an uncut leaf.

SOM Text

Supporting model description

1 Basic factors and functions

Growth patterns are determined by the pattern of factors distributed over the tissue, termed the canvas (8). Factors have one value for each segment or vertex of the canvas and are denoted by capital letters in the text. In the equations, factors that propagate through the canvas are denoted by the bold letter **s** subscripted with the factor name, while those that are fixed to the canvas are denoted by **i** subscripted with the factor name. For instance, the immobile factor PGRAD is described by i_{pgrad} in the equations.

Factors may promote growth rates through the linear function *pro*, defined as:

$$\text{pro}(p_f, \mathbf{x}_f) = 1 + p_f \mathbf{x}_f, \quad (1.1)$$

where \mathbf{x}_f is a factor, F, and \mathbf{x} denotes either **i** or **s**. p_f is a promotion coefficient for that factor. Factors may inhibit growth through the function *inh*, defined as:

$$\text{inh}(h_f, \mathbf{x}_f) = 1 / (1 + h_f \mathbf{x}_f), \quad (1.2)$$

where h_f is an inhibition coefficient for factor F. All multiplications and divisions are element-wise. Values of all coefficients are given in the tables below (section 2.2 for the 1D models and section 3.3 for the 2D models). All models run from $t = 87$ hours (end of day 3) to $t = 205$ hours (day 8 to 9).

2 1D models

Growth along the lamina midline (Fig. 1, E to G, black lines; Fig. 1, H and I, grey lines) was simulated using a one-dimensional model in MATLAB. An initial canvas comprises a line made up of multiple segments of equal length, L_0 , joined at vertices (fig. S2A). Each line segment grows according to:

$$L(t) = L_0 e^{Kt}, \quad (2.1)$$

where K is the growth rate and t is time in hours. The value of K is promoted by PGRAD according to:

$$K = p_{pgrad} i_{pgrad}, \quad (2.2)$$

where p_{pgrad} is the promotion of growth by PGRAD. PGRAD has a linear gradient across the canvas with the highest level of 0.94 at the base and lowest level of b_{pgrad} at the tip. Within each segment PGRAD levels are uniform (fig. S2B). The gradient in PGRAD forms

during setup (prior to the start of the growth simulation) and the value of PGRAD for each segment does not change as the line segments grow.

2.1 1D model with LATE

To decrease growth rates at later stages (Fig. 1, E to I, black lines), K is inhibited by LATE according to (Fig. 1P):

$$K = p_{pgrad} i_{pgrad} \cdot \text{inh}(h_{late}, i_{late}), \quad (2.3)$$

where h_{late} is the inhibition coefficient of LATE. The value of LATE is the same for each segment and increases linearly with time after 148 hours (end day 6, fig. S2C):

$$i_{late} \begin{cases} 0 & \text{if } t < 148 \text{ h} \\ g_{late}(t - 148 \text{ h}) & \text{if } t \geq 148 \text{ h} \end{cases} \quad (2.4)$$

where g_{late} defines the rate of increase of LATE with time.

2.2 1D models parameter list

Growth parameter	Description	Value
b_{pgrad}	minimum levels of PGRAD	0.195
p_{pgrad}	growth promotion by PGRAD	0.04 h^{-1}
g_{late}	increase in LATE over time	0.0048 h^{-1}
h_{late}	growth inhibition by LATE	4.5

3 2D models

2D leaf models were specified using the growing polarised tissue framework as implemented in the MATLAB application *Gfibox*. Full details of both are given in Kennaway *et al.* (8) and models can be downloaded with the *Gfibox* software from (<https://www.uea.ac.uk/cmp/research/cmpbio/Gfibox>). In this method an initial finite element mesh, also termed the canvas, is deformed during growth. The pattern of deformation depends on growth-modulating factors, whose initial distribution is established during setup. Factors have one value for each vertex and values between vertices are linearly interpolated across each finite element. In the models described here, the initial canvas is oriented with regard to the external xy -coordinate system such that the canvas base is parallel to the x -axis and the midline is parallel to the y -axis. Growth at the baseline is constrained to be parallel to the x -axis, reflecting the anchoring of the leaf to the stem. The initial canvas consists of 3000 elements. Elements are not subdivided during the simulations.

Each model has two interconnected networks: the Polarity Regulatory Network (PRN) specifies tissue polarity and hence specified orientations of growth, the Growth rate Regulatory Network (KRN) determines how factors influence specified growth rates. In total, growth interactions are specified by three equations, one for the PRN and two for the KRN. These networks determine the specified polarity and growth fields across the canvas. Due to the connectedness of the canvas this specified growth differs from the resultant growth by

which the system is deformed. The time step of each model corresponds to one hour of developmental time. Models take about 20 min to run on a dual core desktop computer.

3.1 Non-deforming model

This model involves growth orientations being held parallel to the midvein (y -axis) throughout growth (Fig. 1, L and T).

Setup

The initial canvas shape and distribution of factors are shown in Fig. 1Q and R. The PGRAD gradient is specified in the same way as in the 1D model, where PGRAD levels are 1 at the base and b_{pgrad} at the tip. PGRAD levels are calculated according to the initial y -coordinate of each vertex and interpolated across each element. LAM is highest in the proximal regions of the lamina with lower levels in the distal regions and in the proximal region that will form the petiole. MID is expressed along the midline and declines distally with a linear gradient. The value of all these factors at each vertex does not change during growth (they are fixed to the canvas). The maximum level of these factors is 1.

PRN

A proximodistal polarity field is specified as being oriented parallel to the midline throughout growth by the gradient of a polarity factor, POLARISER (POL, Fig. 1T). Similar to PGRAD, POL has a linear gradient across the canvas with highest levels, determined by b_{pol} , at the base and at level of 0 at the tip. POL levels are calculated according to the y -component of each vertex and interpolated across each element. To maintain polarity parallel to the y -axis throughout growth the POL gradient is re-established at every iteration and therefore does not deform with the canvas during growth (unlike PGRAD, LAM and MID).

KRN

Specified growth rate parallel to the polarity gradient, K_{par} , is defined in the same way as for the 1D model (Eqn. 2.3 and Fig. 1S):

$$K_{par} = P_{pgrad} \mathbf{i}_{pgrad} \cdot \text{inh}(h_{late}, \mathbf{i}_{late}) \quad (3.1)$$

Specified growth perpendicular to the polarity is promoted by LAM and LATE and inhibited by MID:

$$K_{per} = P_{lam} \mathbf{i}_{lam} \cdot \text{pro}(P_{late}, \mathbf{i}_{late}) \cdot \text{inh}(h_{mid}, \mathbf{i}_{mid}) \quad (3.2)$$

3.2 Organiser-based model (Deforming model)

These models involve growth orientations being established by POL propagation from an organiser, which was expressed at the canvas base. The gradient of POL defines the local polarity and hence local orientations of specified growth, which reorient with changes in the POL gradient. The KRN for all organiser model versions are the same as for the previous model (Eqn. 3.1 and Eqn. 3.2).

PRN

An identity factor, PROXORG, is expressed at a level of 1 along the base of the canvas and 0 elsewhere. The value of POL is fixed at a value of 0.1 (b_{pol}), where PROXORG is expressed (i.e. where PROXORG > 0). POL diffuses according to the equation:

$$\partial \mathbf{s}_{pol} / \partial t = D_{pol} \nabla^2 \mathbf{s}_{pol} - \mu_{pol} \mathbf{s}_{pol}, \quad (3.3)$$

where D_{pol} is the diffusion rate and μ_{pol} the decay rate of POL throughout the tissue. POL distribution is allowed to establish during the setup phase for 20 time steps before the commencement of growth.

The importance of POL propagation for the polarity field maintenance is explored using POL propagation rates at two extremes. At one extreme (fixed version), the local POL gradient is fixed to the initial canvas after setup and thus the gradient and polarity field deform with the canvas (Fig. 1, U and M). In the other version (dynamic), POL continues to propagate and the polarity field readjusts according to POL levels throughout growth (fig. S5, A and B; see 2D models parameter list). In the dynamic version, the polarity field deforms during growth because changes in tissue geometry affect the way POL becomes distributed. The patterns and orientations of resultant growth for the dynamic and fixed versions of the organiser-based model are very similar (Fig. 1O and fig. S5C) and match the data (Fig. 1, J and K). Thus, both versions of the organiser-based (deforming) model are compatible with our observations.

To confirm that the propagation rate in the dynamic model is high enough to polarise the tissue throughout growth and to explore the importance of canvas geometry on the polarity field, the polarity field is perturbed at 148 hours (fig. S5, D and E). POL levels are reduced 10-fold and spatially randomised everywhere, except at PROXORG, to give randomly orientated polarity. *De novo* production of POL at PROXORG and POL diffusion (Eqn. 3.3) restores the polarity pattern within 1 hour, with orientations diverging at the base and converging towards the tip (fig. S5F). Model shape and the polarity field are indistinguishable from an undisturbed run of the dynamic model (fig. S5, B and G).

3.2.1 Distal leaf excision

The above models assume that a basic pattern of growth rates is established early. This is verified by excising the distal half of the canvas (Fig. 3, H and I). During setup the distal part of the canvas is marked by DISTAL (fig. S2D). Regions expressing DISTAL are removed from the canvas at 148 hours (day 6), corresponding to the cuts performed experimentally. After deletion of the distal half, the remaining canvas grows to a time of 205 hours, but is inhibited at the cut edge by inhibitor induced by cut (INC), which is expressed after cutting along the cut edge (fig. S2E). INC is expressed at a level of 1 and inhibits K_{par} and K_{per} through an additional term to equations 3.1 and 3.2, giving the overall KRN equations:

$$K_{par} = p_{pgrad} \mathbf{i}_{pgrad} \cdot \text{inh}(h_{late}, \mathbf{i}_{late}) \cdot \text{inh}(h_{inc}, \mathbf{i}_{inc}) \quad (3.4)$$

$$K_{per} = p_{lam} \mathbf{i}_{lam} \cdot \text{pro}(p_{late}, \mathbf{i}_{late}) \cdot \text{inh}(h_{mid}, \mathbf{i}_{mid}) \cdot \text{inh}(h_{inc}, \mathbf{i}_{inc}) \quad (3.5)$$

3.3 2D models parameter list

For organiser-based models, the POL diffusion constant $D_{pol} = 0.0001 \text{ mm}^2\text{h}^{-1}$ in the fixed polarity version and $0.01 \text{ mm}^2\text{h}^{-1}$ in the dynamic polarity version. The other parameter values in all 2D models are:

Parameter	Description	Value
Polarity parameters		
b_{pol}	maximum POL levels	0.1
μ_{pol}	POL decay rate	0.1 h^{-1}
Growth parameters		
b_{pgrad}	minimum levels of PGRAD	0.195
g_{late}	increase in LATE over time	0.0048 h^{-1}
p_{pgrad}	K_{par} promotion by PGRAD	0.041 h^{-1}
p_{lam}	K_{per} promotion by LAM	0.0235 h^{-1}
p_{late}	K_{per} promotion by LATE	0.7
h_{late}	K_{par} inhibition by LATE	2.2
h_{mid}	K_{per} inhibition by MID	0.5
Excision parameters		
h_{inc}	growth inhibition by INC	5

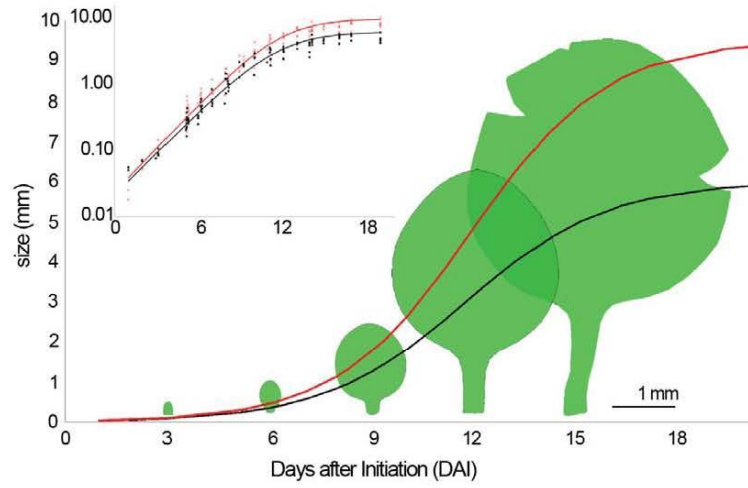


Fig. S1. Growth analysis of leaf 1.

Growth curves for leaf width (black) and length (red), with outlines of representative leaves. Several small cuts were made in the oldest leaf, allowing it to be flattened. Inset shows measurements on a logarithmic scale.

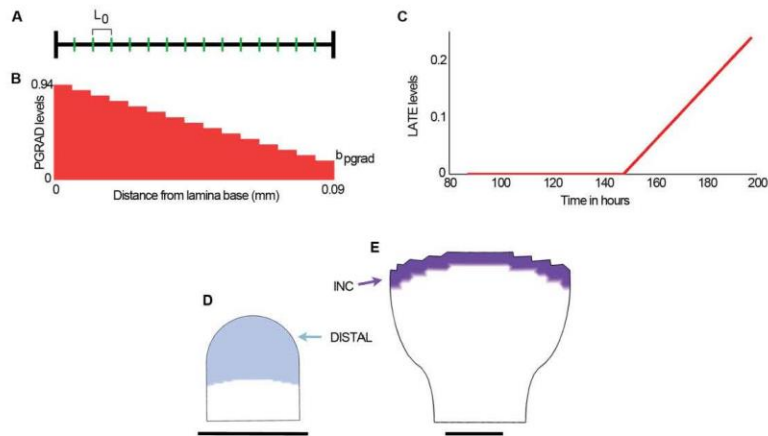


Fig. S2. Model methods.

(A) 1D example canvas with spatial discretisation. L_0 is the initial size of each segment. The canvas used in the 1D models consists of 1000 segments. (B) PGRAD levels along the 1D canvas. Levels are uniform in each segment. (C) LATE levels over time. (D) Canvas region to be excised at later stages was marked by DISTAL on the starting canvas (end of day 3). (E) Canvas shape just after cutting (day 6). Growth at the cut edge was inhibited by INC after excision of the DISTAL region. Scale bars for D and E, 100 μm .

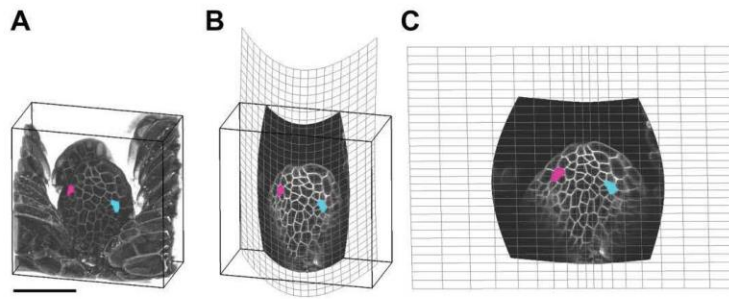


Fig. S3. Flattening the leaf using VolViewer.

(A) Volume rendering of leaf 1 at 3 DAI. (B) User-placed curved section through the abaxial epidermal layer. (C) Resulting flattened section image, which was used as the basis for the initial canvas shape for 2D models. Representative cells are highlighted. For clarity (in this figure) the grid resolution was reduced. Scale bar, 50 μm .

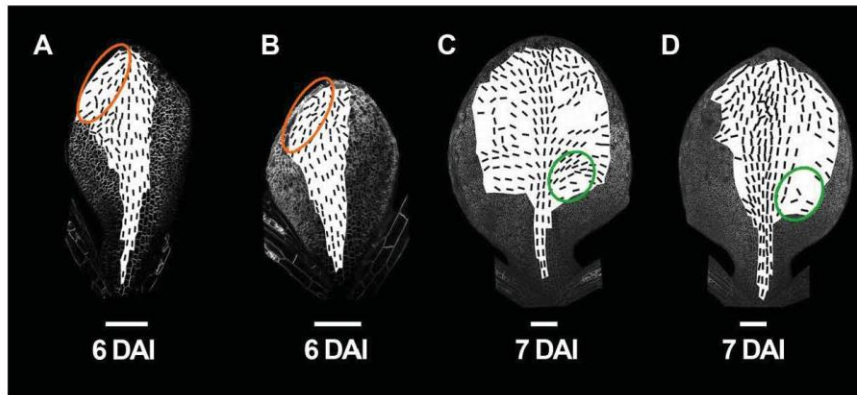


Fig. S4. Observed growth directions for additional images.

Principle directions of growth (black lines, calculated over 24 hour intervals and shown where anisotropy > 10%), from four different tracking experiments. Comparisons to the model were quantified for the tracked regions covered by ellipses. Scale bars, 100 μ m.

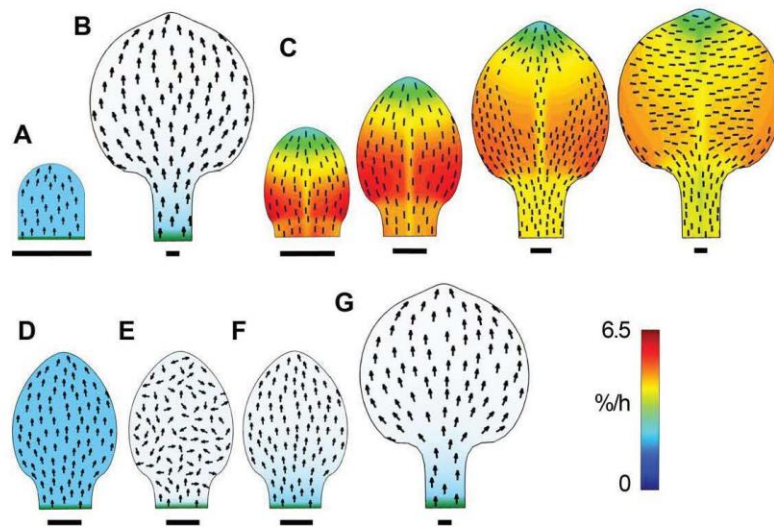


Fig. S5. Dynamic version of organiser-based model.

(**A and B**) Distribution of PROXORG (green) and polarity factor POL in the canvas for dynamic version of the organiser-based model (see section 3.2 of SOM text) at 3 days (**A**) and 8 days (**B**). (**C**) Resultant areal growth rates (heat map) and orientations of growth (black lines, shown where anisotropy $> 5\%$). (**D to G**) Transient POL reduction and redistribution. (**D**) Before POL reduction. (**E**) Immediately after POL reduction. (**F**) POL regains its initial distribution within one hour (one time step). (**G**) POL distribution and polarity field on day 8. Scale bars, 100 μm . POL (blue), polarity field (arrows).

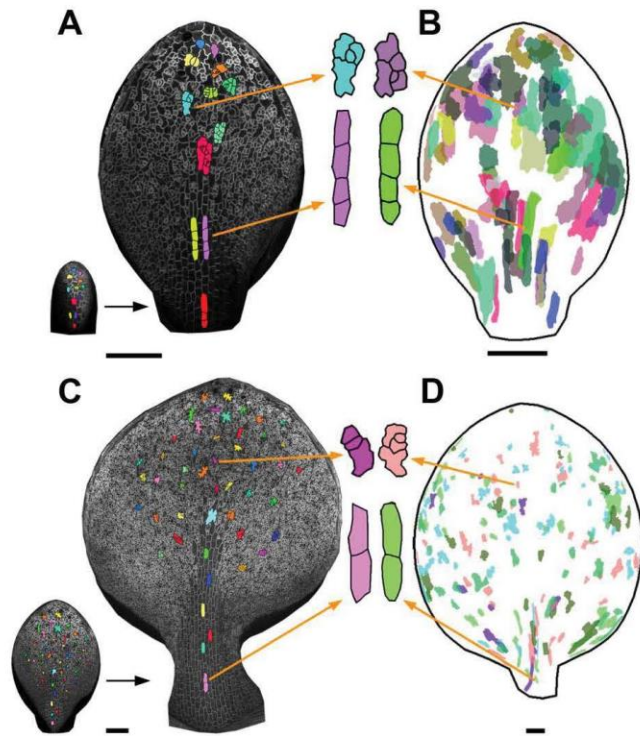


Fig. S6. Validation of direct tracking using clonal analysis.

(**A and C**) Cell fates from time-lapse imaging: (**A**) Cells tracked from 4 DAI (small leaf on left) to 6 DAI (right leaf) and (**C**) from 6 DAI (left leaf) to 8 DAI (right leaf). Examples of tracked clones are shown enlarged. (**B and D**) Clones induced at 3 DAI (**B**) or 6 DAI (**D**) and imaged at comparable developmental stages to (**A**) and (**B**) respectively (6 DAI and 9 DAI). Clones from several leaves have been superimposed. Scale bars, 100 μm .

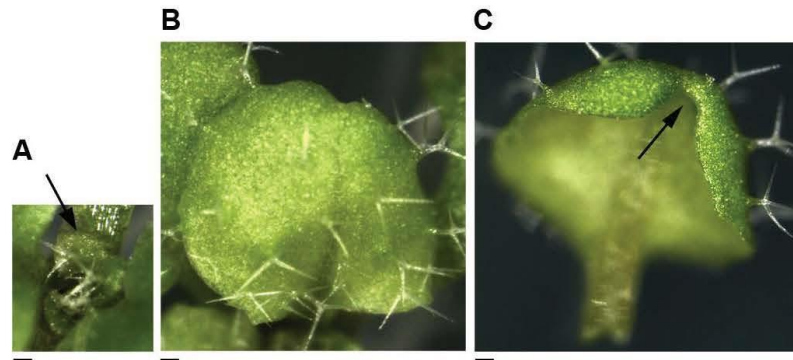


Fig. S7. Excision of leaf 3.

Excision of the distal half of the leaf 3 lamina at 10 DAS using micro-scissors. (A) Leaf shape after 2 days of growth, arrow points to cut. (B) Leaf viewed from the top after 5 days of growth, showing apparent regeneration of tip. (C) Same leaf as (B) viewed from lower (abaxial) side, showing curved indentation at tip (arrow). Scale bar, 100 μm .

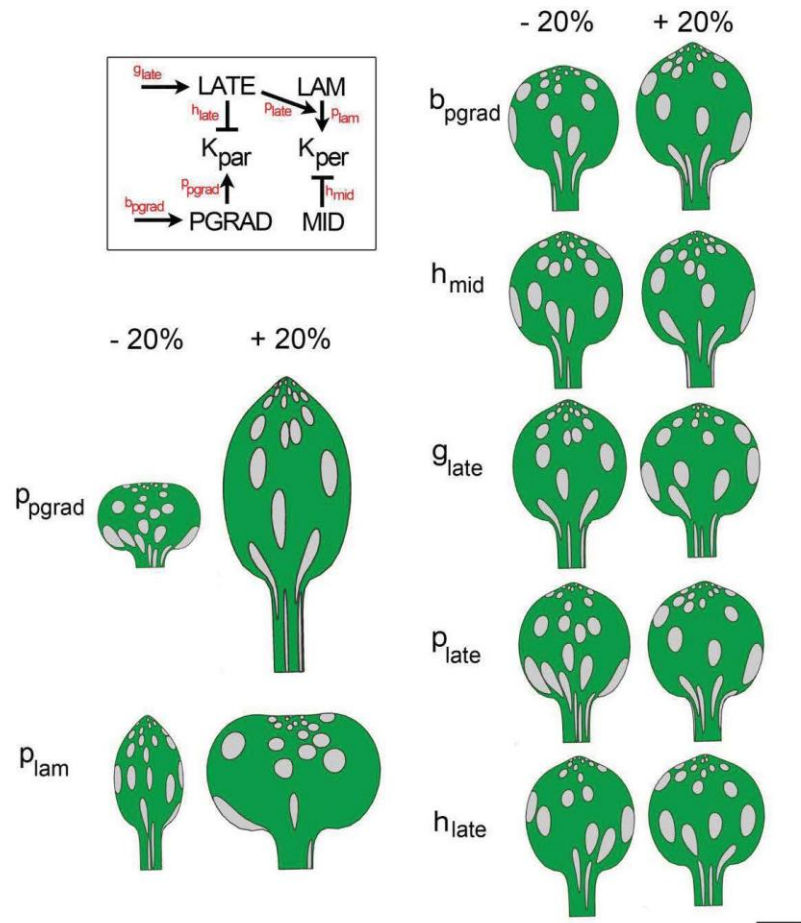


Fig. S8. Model sensitivity analysis.

Resultant canvas shapes and clones (circles on the initial canvas) with parameter values varied by +/- 20%. **Box**, Growth regulatory network of the 2D models with growth factors (black) and growth parameters (red). For explanation of growth parameters see section 3 of SOM text. Scale bar, 500 μ m.

Table S1. Quantitative comparisons between output from models and observed principal orientations of growth.

The results in Fig. 1K and fig. S4 provide 6 data sets for comparing observed orientations with those generated by the models. Comparisons were quantified by fitting the best matching growth tensor for the tracked regions covered by ellipses. The principal directions of growth were then determined, expressed as an angle in degrees clockwise from the midline. For the models, we performed the same computation, using the vertices of the finite element mesh instead of experimentally tracked points, at the times corresponding to the leaf observations. Model output and experimental data were scaled and aligned using reference points at the tip of the leaf and the base of the lamina. In all 6 cases the angles based on experimental data were positive (splaying outwards from the midline for green ellipses, and inwards towards the tip for the brown ellipses) as were those from the deforming (organiser-based) model. By contrast, the angles predicted by the non-deforming model were near zero or negative.

	Observed angle	Non-deforming model output	Deforming model output
Brown ellipse (Fig. 1K)	46 °	3 °	15 °
Brown ellipse (fig. S4A)	52 °	3 °	15 °
Brown ellipse (fig. S4B)	22 °	3 °	15 °
Green ellipse (Fig. 1K)	38 °	-4 °	6 °
Green ellipse (fig. S4C)	65 °	-4 °	6 °
Green ellipse (fig. S4D)	20 °	-4 °	6 °

References

1. L. I. Held, *Imaginal Discs: The Genetic and Cellular Logic of Pattern Formation* (Cambridge University Press, Cambridge, 2002).
2. G. T. Kim, K. H. Cho, Recent advances in the genetic regulation of the shape of simple leaves. *Physiol. Plant.* **126**, 494 (2006). [doi:10.1111/j.1399-3054.2006.00634.x](https://doi.org/10.1111/j.1399-3054.2006.00634.x)
3. G. F. Stopper, G. P. Wagner, Of chicken wings and frog legs: A smorgasbord of evolutionary variation in mechanisms of tetrapod limb development. *Dev. Biol.* **288**, 21 (2005). [doi:10.1016/j.ydbio.2005.09.010](https://doi.org/10.1016/j.ydbio.2005.09.010) [Medline](#)
4. L. Wolpert, C. Tickle, *Principles of Development* (Oxford Univ. Press, Oxford, ed. 4, 2011).
5. G. S. Avery, Structure and development of the tobacco leaf. *Am. J. Bot.* **20**, 565 (1933). [doi:10.2307/2436259](https://doi.org/10.2307/2436259)
6. D. Schmundt, M. Stitt, B. Jahne, U. Schurr, Quantitative analysis of the local rates of growth of dicot leaves at a high temporal and spatial resolution, using image sequence analysis. *Plant J.* **16**, 505 (1998). [doi:10.1046/j.1365-313x.1998.00314.x](https://doi.org/10.1046/j.1365-313x.1998.00314.x)
7. S. D. Wolf, W. K. Silk, R. E. Plant, Quantitative patterns of leaf expansion: Comparison of normal and malformed leaf growth in *Vitis vinifera* cv. Ruby Red. *Am. J. Bot.* **73**, 832 (1986). [doi:10.2307/2444294](https://doi.org/10.2307/2444294)
8. R. Kennaway, E. Coen, A. Green, A. Bangham, Generation of diverse biological forms through combinatorial interactions between tissue polarity and growth. *PLOS Comput. Biol.* **7**, e1002071 (2011). [doi:10.1371/journal.pcbi.1002071](https://doi.org/10.1371/journal.pcbi.1002071) [Medline](#)
9. A.-G. Rolland-Lagan, J. A. Bangham, E. Coen, Growth dynamics underlying petal shape and asymmetry. *Nature* **422**, 161 (2003). [doi:10.1038/nature01443](https://doi.org/10.1038/nature01443) [Medline](#)
10. A. J. Fleming, The molecular regulation of leaf form. *Plant Biol.* **5**, 341 (2003). [doi:10.1055/s-2003-42718](https://doi.org/10.1055/s-2003-42718)
11. Z. Hejnowicz, J. A. Romberger, Growth tensor of plant organs. *J. Theor. Biol.* **110**, 93 (1984). [doi:10.1016/S0022-5193\(84\)80017-X](https://doi.org/10.1016/S0022-5193(84)80017-X)
12. E. Scarpella, D. Marcos, J. Friml, T. Berleth, Control of leaf vascular patterning by polar auxin transport. *Genes Dev.* **20**, 1015 (2006). [doi:10.1101/gad.1402406](https://doi.org/10.1101/gad.1402406) [Medline](#)
13. Y. Boutté, Y. Ikeda, M. Grebe, Mechanisms of auxin-dependent cell and tissue polarity. *Curr. Opin. Plant Biol.* **10**, 616 (2007). [doi:10.1016/j.pbi.2007.07.008](https://doi.org/10.1016/j.pbi.2007.07.008) [Medline](#)
14. J. L. Gallois, C. Woodward, G. V. Reddy, R. Sablowski, Combined SHOOT MERISTEMLESS and WUSCHEL trigger ectopic organogenesis in *Arabidopsis*. *Development* **129**, 3207 (2002). [Medline](#)
15. G. Sena, X. Wang, H.-Y. Liu, H. Hofhuis, K. D. Birnbaum, Organ regeneration does not require a functional stem cell niche in plants. *Nature* **457**, 1150 (2009). [doi:10.1038/nature07597](https://doi.org/10.1038/nature07597) [Medline](#)
16. F. Swink, G. Wilhelm, *Plants of the Chicago Region* (Indiana Academy of Science, Indianapolis, ed. 4, 1994).
17. E. van der Graaff, A. D. Dulk-Ras, P. J. J. Hooykaas, B. Keller, Activation tagging of the LEAFY PETIOLE gene affects leaf petiole development in *Arabidopsis thaliana*. *Development* **127**, 4971 (2000). [Medline](#)

18. R. Sarojam *et al.*, Differentiating *Arabidopsis* shoots from leaves by combined YABBY activities. *Plant Cell* **22**, 2113 (2010). [doi:10.1105/tpc.110.075853](https://doi.org/10.1105/tpc.110.075853) [Medline](#)
19. M. Aida, T. Ishida, M. Tasaka, Shoot apical meristem and cotyledon formation during *Arabidopsis* embryogenesis: interaction among the CUP-SHAPED COTYLEDON and SHOOT MERISTEMLESS genes. *Development* **126**, 1563 (1999). [Medline](#)
20. A. Hasson *et al.*, Evolution and diverse roles of the CUP-SHAPED COTYLEDON genes in *Arabidopsis* leaf development. *Plant Cell* **23**, 54 (2011). [doi:10.1105/tpc.110.081448](https://doi.org/10.1105/tpc.110.081448) [Medline](#)
21. G. D. Bilsborough *et al.*, Model for the regulation of *Arabidopsis thaliana* leaf margin development. *Proc. Natl. Acad. Sci. U.S.A.* **108**, 3424 (2011). [doi:10.1073/pnas.1015162108](https://doi.org/10.1073/pnas.1015162108) [Medline](#)
22. A. H. K. Roeder *et al.*, Variability in the control of cell division underlies sepal epidermal patterning in *Arabidopsis thaliana*. *PLoS Biol.* **8**, e1000367 (2010). [doi:10.1371/journal.pbio.1000367](https://doi.org/10.1371/journal.pbio.1000367) [Medline](#)
23. S. Kurup *et al.*, Marking cell lineages in living tissues. *Plant J.* **42**, 444 (2005). [doi:10.1111/j.1365-313X.2005.02386.x](https://doi.org/10.1111/j.1365-313X.2005.02386.x) [Medline](#)
24. B. J. Harrison, J. R. S. Fincham, Instability at the Pal locus in *Antirrhinum majus*. *Heredity* **19**, 237 (1964). [doi:10.1038/hdy.1964.28](https://doi.org/10.1038/hdy.1964.28)
25. E. Truemit *et al.*, High-resolution whole-mount imaging of three-dimensional tissue organization and gene expression enables the study of Phloem development and structure in *Arabidopsis*. *Plant Cell* **20**, 1494 (2008). [doi:10.1105/tpc.107.056069](https://doi.org/10.1105/tpc.107.056069) [Medline](#)
26. S. Sauret-Güeto, G. Calder, N. P. Harberd, Transient gibberellin application promotes *Arabidopsis thaliana* hypocotyl cell elongation without maintaining transverse orientation of microtubules on the outer tangential wall of epidermal cells. *Plant J.* **69**, 628 (2012). [doi:10.1111/j.1365-313X.2011.04817.x](https://doi.org/10.1111/j.1365-313X.2011.04817.x) [Medline](#)
27. P. Barbier de Reuille, I. Bohn-Courseau, C. Godin, J. Traas, A protocol to analyse cellular dynamics during plant development. *Plant J.* **44**, 1045 (2005). [doi:10.1111/j.1365-313X.2005.02576.x](https://doi.org/10.1111/j.1365-313X.2005.02576.x) [Medline](#)
28. E. Jones, T. Oliphant, P. Peterson, SciPy: Open source scientific tools for Python (2001); www.scipy.org.
29. J. C. Gower, Generalized procrustes analysis. *Psychometrika* **40**, 33 (1975). [doi:10.1007/BF02291478](https://doi.org/10.1007/BF02291478)
30. A. Goshtasby, Piecewise linear mapping functions for image registration. *Pattern Recognit.* **19**, 459 (1986). [doi:10.1016/0031-3203\(86\)90044-0](https://doi.org/10.1016/0031-3203(86)90044-0)
31. X. Zhang, P. H. Grey, S. Krishnakumar, D. G. Oppenheimer, The IRREGULAR TRICHOME BRANCH loci regulate trichome elongation in *Arabidopsis*. *Plant Cell Physiol.* **46**, 1549 (2005). [doi:10.1093/pcp/pci168](https://doi.org/10.1093/pcp/pci168) [Medline](#)

Systems Biology Approach Pinpoints Minimum Requirements for Auxin Distribution during Fruit Opening

Xin-Ran Li^{1,6}, Renske M.A. Vroomans^{2,3,6}, Samantha Fox⁴, Verónica A. Grieneisen^{2,5}, Lars Østergaard^{1,*} and Athanasios F.M. Marée^{2,5,*}

¹Crop Genetics, John Innes Centre, Norwich NR4 7UH, UK

²Computational and Systems Biology, John Innes Centre, Norwich NR4 7UH, UK

³Centre of Excellence in Computational and Experimental Developmental Biology, Institute of Biotechnology, University of Helsinki, 00014 Helsinki, Finland

⁴Cell and Developmental Biology, John Innes Centre, Norwich NR4 7UH, UK

⁵School of Biosciences, Cardiff University, Cardiff CF10 3AX, Wales, UK

⁶These authors contributed equally

*Correspondence: Lars Østergaard (lars.ostergaard@jic.ac.uk), Athanasios F.M. Marée (marees@cardiff.ac.uk)

<https://doi.org/10.1016/j.molp.2019.05.003>

ABSTRACT

The phytohormone auxin is implied in steering various developmental decisions during plant morphogenesis in a concentration-dependent manner. Auxin maxima have been shown to maintain meristematic activity, for example, of the root apical meristem, and position new sites of outgrowth, such as during lateral root initiation and phyllotaxis. More recently, it has been demonstrated that sites of auxin minima also provide positional information. In the developing *Arabidopsis* fruit, auxin minima are required for correct differentiation of the valve margin. It remains unclear, however, how this auxin minimum is generated and maintained. Here, we employ a systems biology approach to model auxin transport based on experimental observations. This allows us to determine the minimal requirements for its establishment. Our simulations reveal that two alternative processes—which we coin “flux-barrier” and “flux-passage”—are both able to generate an auxin minimum, but under different parameter settings. Both models are in principle able to yield similar auxin profiles but present qualitatively distinct patterns of auxin flux. The models were tested by tissue-specific inducible ablation, revealing that the auxin minimum in the fruit is most likely generated by a flux-passage process. Model predictions were further supported through 3D PIN localization imaging and implementing experimentally observed transporter localization. Through such an experimental–modeling cycle, we predict how the auxin minimum gradually matures during fruit development to ensure timely fruit opening and seed dispersal.

Key words: auxin, mathematical modeling, polar auxin transport, fruit development, systems biology of patterning

Li X.-R., Vroomans R.M.A., Fox S., Grieneisen V.A., Østergaard L., and Marée A.F.M. (2019). Systems Biology Approach Pinpoints Minimum Requirements for Auxin Distribution during Fruit Opening. *Mol. Plant*. **12**, 863–878.

INTRODUCTION

Patterning through morphogens is considered one of the first triggers for correct tissue differentiation (Raspopovic et al., 2014; Wolpert, 2016). Cell differentiation hinges on the concept of genetic control, first elucidated for single cells by the pioneering work of Jacques Monod, an early advocate of a systems view of living cells (Ullmann, 2011). How the patterning of cell differentiation is controlled within a coordinated multicellular structure, however, leads us to go beyond “anything found to be true of *E. coli* must also be true of elephants, only more so” (Jacob and Philip, 1995). Alike elephants, plants are multicellular

organisms, but with a development that keeps continuously unfolding, never losing its capability to plastically alter in response to environmental cues. It is therefore insufficient to characterize the cells in isolation, mathematical modeling being required to study the entire tissue and explore its emerging properties and functionality (Grieneisen et al., 2012). In plants, tissue fates and their progressive differentiation are steered by phytohormones and their downstream genetic targets.

Published by the Molecular Plant Shanghai Editorial Office in association with Cell Press, an imprint of Elsevier Inc., on behalf of CSPB and IPPE, SIBS, CAS.

Molecular Plant 12, 863–878, June 2019 © The Author 2019. 863

This is an open access article under the CC BY license (<http://creativecommons.org/licenses/by/4.0/>).

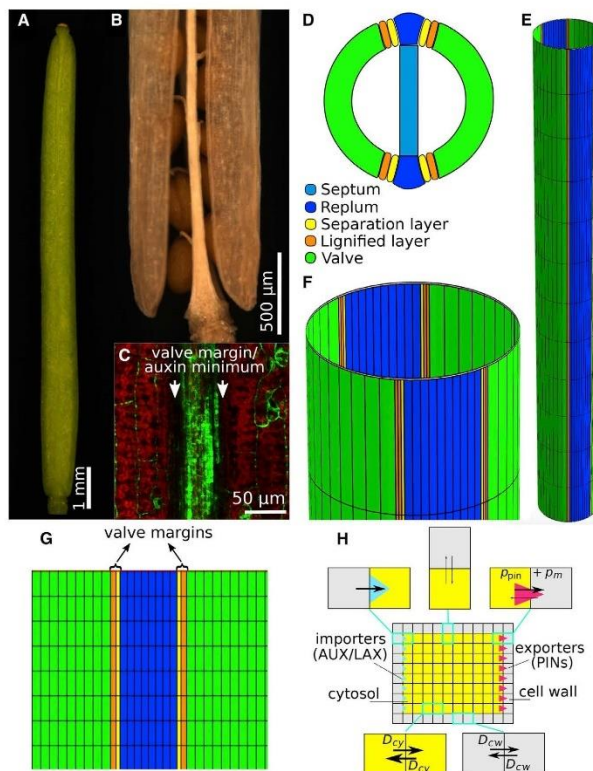


Figure 1. Modeling Auxin Transport in the Developing *Arabidopsis* Fruit.

(A) Silique at stage 17b. (B) Dehiscence along the valve margin (VM) (stage 19). (C) Auxin-signaling minimum at the VM, shown by DR5:GFP expression. (D) Schematic transversal cross-section of the bilaterally symmetric ovary, with tissues indicated, also showing the internal septum that we do not simulate within this modeling framework. (E) Schematic of the cylindrical model layout of the external fruit tissues, visualizing the topological connectedness. (F) Zoomed-in portion of (E), displaying approximately one cell row. (G) Schematic of the model layout of the longitudinal fruit, laid out in 2D, indicating all modeled tissue types through color coding. Note that here only half of the fruit tissue is displayed, whereas simulations were always done on the full, cylindrically connected tissue. (H) Within the model, auxin transport across plasma membrane as well as diffusion in cytosol and apoplast (cell wall) at subcellular resolution are taken into account.

role in the positioning and initiation of whole organs (Reinhardt et al., 2003), localized auxin maxima are also crucial for the correct spacing of serrations at the edge of leaves (Scarpella et al., 2006; Bilsborough et al., 2011), root hairs (Payne and Grierson, 2009), and xylem-phloem poles (el Showk et al., 2015).

Given the wide implications of auxin maxima to plant development, the existence of auxin minima has been largely eclipsed or simply regarded as inevitable concentration valleys intercalating maxima. However, functional significance of auxin minima and their modes of regulation that can be independent from maxima have been emerging within several contexts, ranging from phyllotaxis to root development. Extended regions of low auxin have been shown to be instructive for maintaining crevices between meristems in the SAM and between leaf indentations (Stoma et al., 2008; Heisler et al., 2010; Caggiano et al., 2017). Furthermore, the regulated formation and maintenance of an auxin minimum at the basal root meristem triggers cell differentiation (Di Mambro et al., 2017). The first evidence of a functional auxin minimum stems from *Arabidopsis* fruits, where depletion of auxin from narrow strips of cells is required for seed dispersal (Sorefan et al., 2009). In contrast to localized auxin maxima, the mechanistic basis of how such a distinct minimum can be established is less clear (Grieneisen et al., 2013) and has not been confirmed experimentally.

Distribution of the phytohormone auxin is facilitated by specialized proteins, such as PIN efflux transporters and influx transporters of the AUX1/LAX family (Swarup and Péret, 2012; Adamowski and Friml, 2015), with many additional transporters and processes capable of affecting auxin flows (Park et al., 2017). As a consequence of its rapid, and often polar, transport through plant tissues, auxin distribution can be quickly and drastically altered by modifications of the expression levels or cellular localization of these transport proteins (Grieneisen et al., 2012). In *Arabidopsis thaliana*, auxin has been implied in establishing and maintaining the root apical meristem through an auxin maximum at the stem cell niche (Sabatini et al., 1999), dynamically formed by means of an auxin reflux loop (Grieneisen et al., 2007). Dynamic auxin distribution is also involved in the phyllotactic patterning of the shoot apical meristem, where lateral organs emerge through auxin maxima that form as a consequence of neighboring PINs orienting toward these sites (Barbier de Reuille et al., 2006; Smith et al., 2006). Finally, auxin accumulation in root pericycle cells can trigger lateral root initiation sites (Benková et al., 2003; Dubrovsky et al., 2008), further amplified by the AUX1/LAX family (Marchant et al., 2002; Laskowski et al., 2008). In addition to its

Arabidopsis fruits develop into cylindrical siliques composed of two valves (seed pod walls) that are connected to a central replum (Figure 1A, 1B, and 1D). Internally, the replum is linked to the septum from which the seeds will develop (Figure 1D, light

blue). Specialized cell types differentiate at the border between the valves and the replum, called valve margin (VM) cells (Figure 1D and 1G). Late in development, the VM tissue differentiates into dehiscence zones where cells eventually undergo cell death, allowing the valves to separate from the replum and release the seeds in a process known as fruit dehiscence (Figure 1A and 1B) (Roeder and Yanofsky, 2006). Prior to formation of the dehiscence zone, the VM cells undergo a cell division event that leads to the formation of a lignified cell layer and a layer of cells that mediates the separation through secretion of cell-wall-degrading enzymes (Petersen et al., 1996; Spence et al., 1996).

The main tissues that compose the developing fruit are schematically outlined in Figure 1D–1G, with the lignifying and separation layer together forming the VM. INDEHISCENT (IND) is a bHLH-type transcription factor required for VM development (Liljegren et al., 2004). One of the functions of IND is to establish an auxin minimum at the VM prior to dehiscence (Sorefan et al., 2009). This is achieved at least in part by repressing the PINOID (PID) gene, which encodes a protein kinase involved in polar localization of PIN auxin transporter. The auxin minimum is located at the VM and was shown to be functionally important for dehiscence (Figure 1C), (Sorefan et al., 2009). It is clear that this functional auxin minimum requires an active process (rather than being the inevitable valley of low concentrations that has to exist between two regions containing maxima), because (i) it develops in a temporally regulated fashion, unlinked to specific auxin accumulation in the flanking regions; (ii) it is of a striking qualitative nature, with much lower auxin levels seen in the very narrow tissue region of the VM, but running longitudinally over the whole silique; and (iii) the quantitative and qualitative drop in auxin are directly linked to fruit maturation and dehiscence. It is thus a developmentally instructive minimum, which in that sense shares features with the auxin minimum that can be found at the transition zone in the root apical meristem, responsible for triggering the switch from dividing to elongating and differentiating cells. Also in the root, a qualitative and substantial drop in auxin can be found within a transversally confined region with developmental relevance; a pattern that is moreover spatio-temporally regulated and also cannot be explained as simply a manifestation resulting from neighboring maxima (Di Mambro et al., 2017). Here, we apply a systems biology approach to ask how the fruit is able to sustain the characteristic low auxin concentrations in tissues that are only two to three cell files wide but longitudinally run over the entire fruit length. Such a quasi-one-dimensional auxin minimum directly flanked by plateaus of higher auxin concentrations might be expected to readily homogenize with the neighboring tissue (Han et al., 2014), thus abolishing the minimum, except when active transport processes prevent this from happening. We therefore question what kind of auxin transporter patterns are required to form this auxin profile, what processes establish and maintain the minimum, and what this implies for the auxin fluxes through the tissue. Note that within this work, we do not study the dynamical auto-organization of transporter expression and polarity that would lead to the transporter patterns themselves.

We therefore combine computational and experimental approaches to identify the conditions required to maintain such a

distribution, and, by studying the flux patterns that ensue, generate novel predictions regarding plausible auxin transporter functionalities underpinning this process within a specific tissue context. Using computational modeling, we show that this system requires apolar auxin efflux in the VM cells combined with influx within the surrounding tissue to produce an auxin minimum at the VMs. Moreover, based on auxin flux predictions *in silico* and by perturbing auxin flux *in planta*, we show that directed efflux at the VM provides the primary driver for producing the VM auxin minimum. Interestingly, this process is fundamentally different from how minima were originally predicted to arise within the context of canalization models (Mitchison, 1980b, 1981).

RESULTS

Flower and fruit development in *Arabidopsis thaliana* has been intensely studied over decades. To facilitate this work, its flower development was divided into a series of stages based on the chronological occurrence of specific developmental events from the initial emergence of floral meristem to the final dispersal of the seeds (Smyth et al., 1990; Roeder and Yanofsky, 2006). In this work, we consider events that take place in development through stages 15–17b when fruit elongation takes place (15/16), the fruit fully matures, and the VM differentiates into a dehiscence zone (17b).

First, we used computational modeling to assess the auxin patterns that arise when taking into account known data regarding the tissue organization of the fruit and the polar localization and expression levels of the auxin transporters. These auxin transporter localization and expression patterns are not considered to alter during the course of the simulations. To this end, we captured the outermost epidermis of the fruit, with its different cell types, in a multicellular modeling description at a subcellular resolution (Figure 1D–1H). We display simulation results in a 2D flattened-out form (Figure 1G). In this description, we assumed an influx term of auxin from the topmost cells, representing auxin derived from the style tissue, capturing local apical auxin biosynthesis (Eklund et al., 2010; Kuusk et al., 2002; Cheng et al., 2006). In addition, low levels of biosynthesis and decay of auxin were homogeneously distributed over the whole tissue within all cells (see Methods and Supplemental Information for detailed model description, and Supplemental Tables 1 and 2 for parameter values). Auxin dynamics then result from those reaction terms, combined with diffusion in the cell wall and in the cytoplasm. We also took into account transport across cell membranes due to background influx and very low efflux permeability rates (reflecting the chemiosmotic nature of auxin transport), together with augmented influx and efflux contributed by the AUX1/LAXs and PINs (see Figure 1H, Methods, and Supplemental Information). Such an approach allows us to quantitatively distinguish between influx- and efflux-mediated contributions within this modeling framework. The model describes the characteristic polarity of these cells, without simulating the underlying dynamics of the intracellular partitioning itself (Abley et al., 2013; Grieneisen et al., 2013). Auxin was assumed to freely leave the fruit organ basally, capturing the connectedness of the fruit to the rest of the plant.

Two different reporters have been used to visualize the auxin minimum in the *Arabidopsis* fruit, namely DR5::GFP (Sorefan et al.,

2009) and DII-VENUS (van Gelderen et al., 2016). While the DR5 reporter monitors auxin response gene expression, DII-VENUS is considered an auxin sensor and is degraded in the presence of auxin in a TIR1/AFB-dependent manner (Brunoud et al., 2012). Hence, both report auxin signaling rather than auxin levels, and we therefore define an auxin minimum here as a region of low auxin signaling. The auxin minimum at the VM is most evident at developmental stage 17b (Figure 1C) (Sorefan et al., 2009; van Gelderen et al., 2016). At this stage, published distributions of PIN transporters have only reported the presence of PIN3 and only in the valve and replum cells, where it is localized basally (Sorefan et al., 2009; van Gelderen et al., 2016). Reflecting this consensus, we firstly considered the patterns that emerge when PIN3 is only expressed in the replum and the valve tissues, using the intensity and localization as observed, and without taking any additional importers into account. This was done by attributing higher permeability to specific polar cell membrane domains (Supplemental Figure 1), promoting auxin efflux. We call this setting the basic model (see Methods and Supplemental Information, and Supplemental Tables 1 and 2 for parameter values). Rather than becoming depleted from the VM, the resultant patterns showed that auxin would instead accumulate in both the separation and lignifying layers of the VM (Figure 2A). This indicates that currently reported transporter distributions are not able to account for the auxin minimum and raises the question what is needed to generate the observed auxin minimum.

Minimal Requirements for VM Minimum: Two Basic Modes

To determine the dynamic activities involved in auxin distribution at the VM, we next sought to identify the basic necessary conditions that could yield an auxin minimum in the VM in the most parsimonious manner. Firstly, the large differences in auxin concentration over a narrow region, within a tissue that also displays apical-basal auxin fluxes and large diffusion rates, excludes as a possible explanation classical reaction-diffusion models of morphogen patterning, such as those based upon production and decay. To confer this, we simulated such a production-breakdown mechanism, removing any differences in transporters between cell types (see Table 1), instead limiting auxin production to replum and valve and confining breakdown to the VM. These reaction-diffusion simulations show that for a noticeable auxin minimum to be formed and confined to the VM, the auxin breakdown in the VM has to be very fast, in fact, at least eight orders of magnitude larger than what is considered biologically reasonable (Supplemental Figure 3). Such an extremely fast breakdown would preclude any relevant non-local phytohormone signaling (Grieneisen et al., 2012), rendering a production-degradation mechanism non-viable.

In contrast, two other processes can be envisioned, which are instead based on modifications of polar auxin transport. The first possibility, the import-dependent model, is that all tissues, except for the VM, retain auxin through enhanced import, thereby sequestering auxin away from the VM; the second, the export-dependent model, is that the VM itself depletes auxin through active export as previously proposed (Sorefan et al., 2009). We tested this import-dependent model through simulations that assume all tissues, except for the VM, are endowed with high levels

of apolarly localized influx transporters (see Table 2 for transporter expression patterns). We found that at typical parameter values used for auxin influx (Grieneisen et al., 2012; Di Mambro et al., 2017), only a meagre reduction in auxin at the VM occurs, compared with the basic model (compare Figure 2A and 2B). In fact, auxin levels are still higher in the VM than within the other tissues (Figure 2B). To generate an auxin minimum within the VM in an import-dependent manner (Figure 2C), import permeability via the AUX1/LAX family importers needs to be at least 20 times larger than the background influx permeability. Moreover, even when these differences in permeability are extremely large (for example, more than 1000-fold), the auxin minimum still never becomes less than half the level found in the surrounding tissues. In contrast, when we ran the export-dependent model in the *in silico* fruit by introducing apolar PINs in the VM at reasonable permeability rates (such as previously reported, Grieneisen et al., 2012), we observed an immediate, striking drop in the auxin concentrations within the VM (Figure 2D). Thus, our model suggests that actively exporting auxin from the VM is a more efficient mechanism to establish an auxin minimum. Combining both scenarios (combined model), now using reasonable permeability values for the AUX1/LAX-driven auxin influx, synergistically generated an even more pronounced auxin minimum at the VM (Figure 2E). To quantitatively explore the difference between these models, we assessed the effect of the strength of the apolar exporter in the VM or the strength of the apolar importer in the valve and replum by calculating the resultant ratio between the auxin concentration in the separation layer and in the bordering replum cell (Figure 2F). This ratio determines the percentage auxin decrease within the VM and provides a good assessment of the magnitude of the auxin minimum. Moreover, we concomitantly analyzed the absolute auxin levels in both tissue types (Figure 2G). By performing a large parameter sweep, we found that a low level of apolar efflux activity in the VM (at 10% of the default permeability rate) is sufficient to generate a minimum. In contrast, only very strongly augmented import in the surrounding tissues (more than 200% of the default permeability rate) is able to generate an auxin minimum. Moreover, in the export-dependent model, apolar exporters in the VM acting at a strength of 70%, compared with the export permeability in the other tissues, yields a very well-defined minimum with a depth that the import-dependent model is unable to generate for any level of augmented import permeability (Figure 2F). This is partly because the import-based model is unable to substantially raise the auxin levels in the replum, whereas increasing efflux activity gave rise to a linear increase in the absolute concentrations in the replum (Figure 2G). Moreover, the export-dependent model greatly reduced the levels in the separation layer in a way that was much more responsive to alterations in its transporter activity than found for the import-dependent model (Figure 2G). This sensitivity analysis shows that local transport modifications in the VM, under the efflux-dependent scenario, can have spatially long-reaching effects in other tissues.

Experimental Confirmation of PIN Localization in the VM

Our simulations strongly suggested that apolar PIN localization in the VM cells is necessary and sufficient to generate an auxin minimum in the VM. This is in agreement with the findings of Sorefan

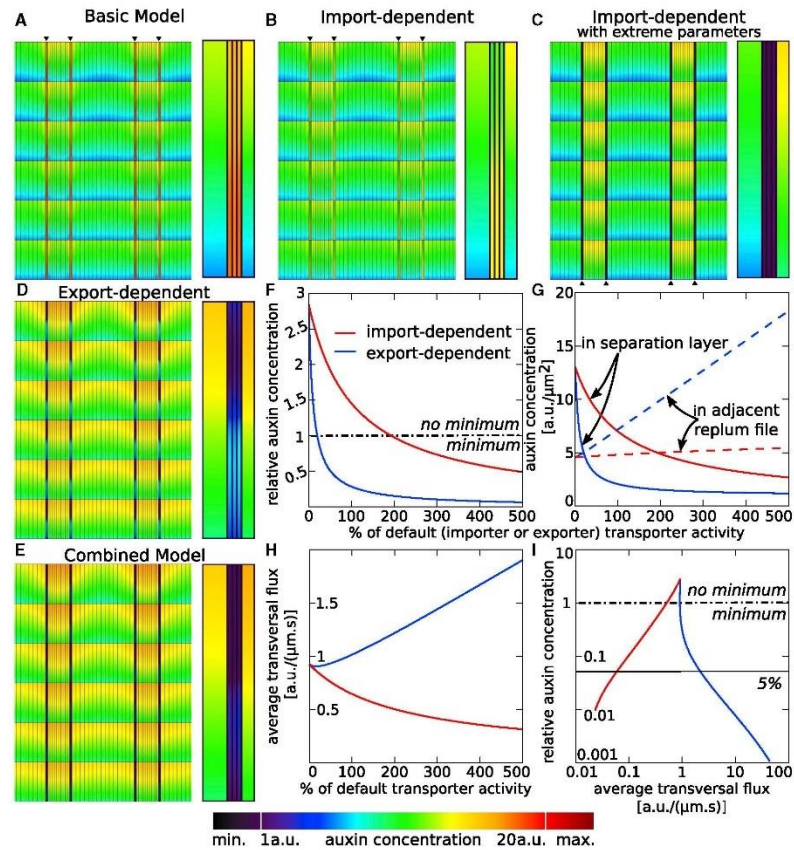


Figure 2. Minimal Requirements for Auxin Minimum at the VM.

(A) Basic model, based on currently published transporter expression, predicts an auxin maximum, rather than minimum, in the VM; right inset shows details of minimum, by showing a magnified, one-cell-high portion of the left VM, including an outer adjacent valve cell and an inner adjacent replum cell. (B and C) Import-dependent model shows that when all tissues except the VM have augmented influx activity, the minimum does not form under reasonable auxin importer transporter rates; as seen through right inset of magnified VM (B). In contrast, the minimum is only established under very high transporter rates (background influx set at $P_{VMH} = 5 \mu\text{m/s}$; augmented influx at $P_{LAX1} = 100 \mu\text{m/s}$) (C), with right inset showing corresponding VM minimum. (D) Export-dependent model reveals that the default rate of apolar efflux within the VM is sufficient to create an auxin minimum, as seen in detail in the right inset. (E) A combination of apolarly localized efflux transporters and VM-specific lack of influx transporters (combined model) strengthens the auxin minimum, as seen in detail in the right inset. (F and G) Both strengthening apolar exporters in the VM (blue line, export-dependent case) and apolar importers in the valve and replum (red line, import-dependent case) lead to a decrease in the ratio between the auxin concentration in the separation layer and in the bordering replum cell (F), as well as a decrease in the absolute auxin levels within the separation layer (G, solid lines). Auxin levels in the replum, however, increase with increasing transporter strength in the export-dependent model, but only marginally depend on the transporter strength in the import-dependent model (G, dashed lines). (H) Effect of those transporters on the total transversal fluxes crossing the VM (i.e., perpendicular to the VM). The x axes in (F–H) indicate the relative strength of either the VM-specific exporter (blue), or the augmented importer in the valve and replum (red), as a percentage of the default transport rates. (I) The fluxes crossing the VM transversally plotted against the VM minimum (as calculated in F), on a log-log scale. Details of parallel fluxes are shown in Supplemental Figure 2, and the description of average flux calculations is given in the Supplemental Information. Dashed-dotted lines indicate where the auxin level in the VM is equal to the surrounding tissue, i.e., below which an auxin minimum is formed; thin line indicates where the auxin level in the VM is 5% of the level in the surrounding tissue. Color bar indicates auxin concentrations in (A–E). Arrowheads in (A–C) indicate position of VM.

	Upper-outer	Upper-inner	Inner-upper	Inner-lower	Lower-inner	Lower-outer	Outer-lower	Outer-upper
Basic Model								
PIN3								
Replum	0	0	0	0.5	1	1	0.5	0
Valve	0	0	0	0.5	1	1	0.5	0
Import-Dependent								
PIN3								
Replum	0	0	0	0.5	1	1	0.5	0
Valve	0	0	0	0.5	1	1	0.5	0
LAX1								
Replum	1	1	1	1	1	1	1	1
Valve	1	1	1	1	1	1	1	1
Export-Dependent								
PIN3								
Replum	0	0	0	0.5	1	1	0.5	0
Separation layer	1	1	1	1	1	1	1	1
Lignifying layer	1	1	1	1	1	1	1	1
Valve	0	0	0	0.5	1	1	0.5	0
Combined								
PIN3								
Replum	0	0	0	0.5	1	1	0.5	0
Separation layer	1	1	1	1	1	1	1	1
Lignifying layer	1	1	1	1	1	1	1	1
Valve	0	0	0	0.5	1	1	0.5	0
LAX1								
Replum	1	1	1	1	1	1	1	1
Valve	1	1	1	1	1	1	1	1
Production Decay								
PIN3								
Replum	0	0	0	0.5	1	1	0.5	0
Separation layer	0	0	0	0.5	1	1	0.5	0
Lignifying layer	0	0	0	0.5	1	1	0.5	0
Valve	0	0	0	0.5	1	1	0.5	0

Table 1. Relative Auxin Importer and Exporter Strengths at the Different Facets along the Plasma Membrane, as Used in the Conceptual Models.

The facets are as depicted in Supplemental Figure 1, denoted as major-minor orientation. Values are only given for cell types that contain the specific transporter.

et al. (2009) who demonstrated that the VM-specific transcription factor INDEHISCENT (IND) is required for the minimum to form and is a repressor of the *PINOID* (*PID*) gene. *PID* encodes a protein kinase involved in the regulation of PIN polarization (Benjamins et al., 2001; Friml et al., 2004); however, whereas ectopically polarized PIN3-GFP was detected across all cell files in *ind* mutant fruits, no signal could be detected at the VM of wild-type fruits by the confocal microscopy setup used (Sorefan et al., 2009).

Therefore, to further test the prediction that enhanced auxin efflux occurs at the VM, we analyzed reporters of PIN expression and

localization during the late stages of fruit development. Confocal imaging confirmed previous observations that *PIN3* is expressed in the valves of the *Arabidopsis* fruit at stage 17b and that the PIN3-GFP protein is primarily localized at the basal side of the cells (Figure 3A and 3F) (Sorefan et al., 2009). Previous research suggested the existence of apolarly localized PIN efflux carriers in the VM, but was unable to detect this (Sorefan et al., 2009). Indeed, visualizing confocal Z stacks in 3D using VolViewer software (Lee et al., 2006) revealed low *PIN3::PIN3-GFP* expression at the VM with apolar localization of the PIN3-GFP protein (Figure 3I and 3J; Supplemental Video 1 for a clear

	Upper-outer	Upper-inner	Inner-upper	Inner-lower	Lower-inner	Lower-outer	Outer-lower	Outer-upper
Stage 17b								
PIN3								
Replum	0	0	0	0	0.8	0.8	0	0
Separation layer	0.2	0.2	0.2	0.2	0.2	0.2	0.2	0.2
Lignifying layer	0.2	0.2	0.2	0.2	0.2	0.2	0.2	0.2
Valve	0	0	0	0.4	1	1	0.4	0
PIN7								
Valve	0	0	0	0	1	1	0	0
LAX1								
Replum	1	1	1	1	1	1	1	1
Valve	0.2	0.2	0.2	0.2	0.2	0.2	0.2	0.2
Stage 16								
PIN3								
Replum	0.8	0.8	0.4	0.4	0.8	0.8	0.4	0.4
Separation layer	0.2	0.2	0.2	0.2	0.2	0.2	0.2	0.2
Lignifying layer	0.2	0.2	0.2	0.2	0.2	0.2	0.2	0.2
Valve	0	0	0	0.4	1	1	0.4	0
PIN7								
Replum	0	0	0	0	0.1	0.1	0	0
Valve	0	0	0.2	0.2	1	1	0.2	0.2
LAX1								
Replum	1	1	1	1	1	1	1	1
Valve	0.8	0.8	0.8	0.8	0.8	0.8	0.8	0.8
Stage 15								
PIN3								
Replum	0.8	0.8	0.4	0.4	0.8	0.8	0.4	0.4
Valve	0	0	0	0.4	1	1	0.4	0
PIN7								
Replum	0	0	0	0	0.1	0.1	0	0
Valve	0	0	0.2	0.2	1	1	0.2	0.2
LAX1								
Replum	1	1	1	1	1	1	1	1
Valve	0.8	0.8	0.8	0.8	0.8	0.8	0.8	0.8

Table 2. Relative Auxin Importer and Exporter Strengths at the Different Facets along the Plasma Membrane, as Used in the Detailed Models.

The facets are as depicted in [Supplemental Figure 1](#), denoted as major-minor orientation. Values are only given for cell types that contain the specific transporter. Matrixes for stage 17b and 16 are semi-quantitative approximations based upon careful (human) assessment of the microscopy images, as depicted in [Figures 3](#) and [5](#), respectively.

3D view). These data suggest that PIN3 contributes to auxin efflux from the VM into the surrounding tissues. Also a *PIN7::PIN7-GFP* reporter ([Billou et al., 2005](#)) was found to be expressed at this stage, specifically in the valve, albeit at lower levels than PIN3. No expression, however, could be detected in the VM ([Figure 3B](#) and [3G](#)). Finally, a *LAX1::LAX1-VENUS* reporter was found to be also expressed at this stage, in the valve and at particularly high levels in the replum, while—in agreement with

the computational model—expression was restricted from the VM domain ([Figure 3C](#) and [3H](#)). Interestingly, the LAX1 pattern mimics the expression pattern of the auxin-signaling reporter *DR5::GFP*, which also presents a high signal in the replum at this stage ([Figure 3D](#)). In addition to these reporters for *PIN3*, *PIN7*, and *LAX1*, we tested reporters for *PIN1*, *PIN4*, *AUX1*, *LAX2*, and *LAX3*, but were unable to detect their expression in the fruit at the developmental stages studied in this manuscript.

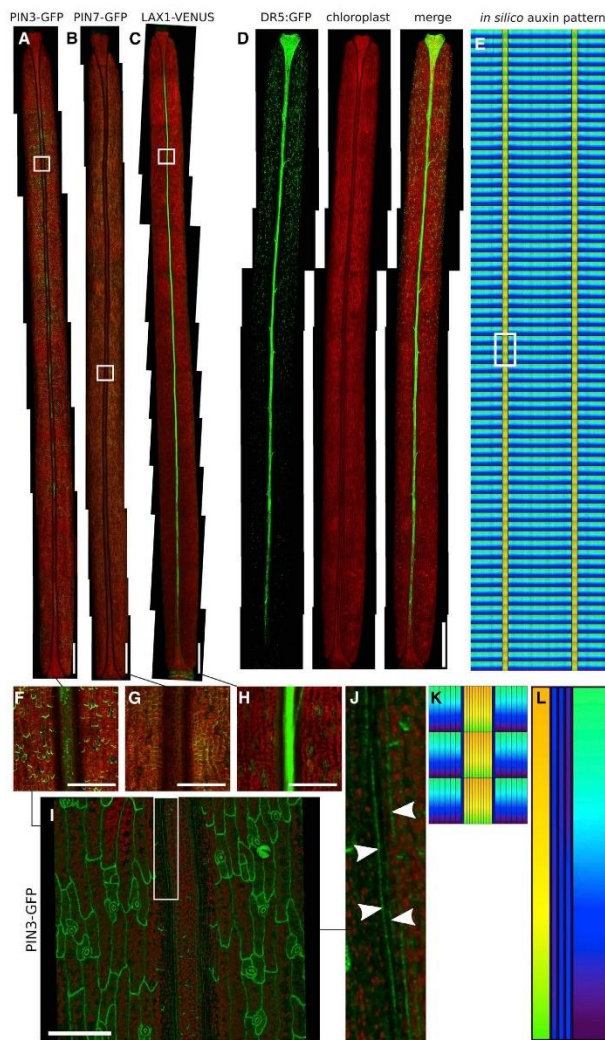


Figure 3. Detailed Analysis on Actual Transporter Localizations at Stage 17b

(A) *PIN3::PIN3-GFP*.
 (B) *PIN7::PIN7-GFP*.
 (C) *LAX1::LAX1-VENUS*.
 (D) *DR5::GFP*.
 (E) Simulation using imaged transporter localization and levels at stage 17b and tissue size and layout of that stage presents minimum at VM and elevated levels in the replum, in agreement with the experimentally observed auxin-signaling pattern.
 (F–H) Detailed insets from (A–C), as indicated.
 (I and J) (I) Detailed image showing apolar PIN3 localization, with (J) showing further magnification of PIN3 localization within a VM region indicated by a white rectangle in (I). Arrowheads indicate the position of lateral PIN3-GFP in the VM.
 (K) Inset from (E), as indicated.
 (L) Magnified right portion of the VM, indicating in detail the auxin minimum in (K).
 See Supplemental Figure 4 for further supporting experimental images. Scale bars: 1 mm for (A–D); 200 μ m for (F–H); 100 μ m for (I). Color coding of auxin levels as indicated in Figure 2.

transport permeability rates, for each combination of transporter, cellular polar domain (Supplemental Figure 1), and tissue (Figure 1E). Table 2 provides all the image-derived normalized permeability rates. For simplicity, we assumed a linear relationship between fluorescence levels and transport strength, ignoring potential saturation in transport, non-linearity in the relationship between fluorescence and protein levels, and transporter post-processing affecting transport strength. Highest overall observed fluorescence levels for each individual transporter were used to normalize the permeability rates. For the spatial simulation, we measured the typical width and height of individual cells belonging to a specific cell type from the experimental images, as well as the number of cell rows and cell files within each tissue. We then ran *in silico* simulations of auxin dynamics, incorporating the experimentally derived transporter patterns and intensities with the experimentally derived fruit layout (Figure 3E). Under these settings, the simulation resulted in an auxin pattern with a minimum matching that observed experimentally (Figure 3K and 3L). Furthermore, the simulation captured other aspects of the observed auxin pattern, in particular the significantly higher auxin levels in the replum compared with the valve. Note that the transporter quantification was done independently, before running the simulations, and not modified *a posteriori*, to prevent bias. We therefore conclude that the observed PIN3 levels, in conjunction with LAX1 levels, can account for the auxin minimum.

We next questioned whether the observed PIN3 and LAX1 levels and localization would also quantitatively be sufficient for generating the observed VM auxin minimum and patterning (Figures 3D and 3C). To answer this, we translated the experimentally observed fluorescence values of PIN3, PIN7, and LAX1 (Figure 3A–3C), which were captured using a fixed laser intensity into values ranging from 0 to 1, where 0 corresponds to no enhanced permeability and 1 corresponds to maximum

The VM: A Flux Passage or a Flux Barrier?

The models described above show that the VM minimum can be established through tissue-specific expression patterns of either influx carriers at high activity levels (Figure 2C) or efflux carriers (Figure 2D), or through an appropriate interplay of both (Figure 2E). When we subsequently sought to test these processes experimentally, we obtained evidence supporting both. Indeed, realistic simulations (Figure 3E) revealed that the experimentally observed transporter distributions are able to generate the auxin minimum as well (Figure 3K and 3L). It is difficult, however, to assess only by means of GFP transporter expression patterns what the relative contribution of the influx and efflux carriers are to the resultant pattern, i.e., which effective process/mechanism is predominantly being deployed. Moreover, single transporter mutants are notoriously difficult to interpret, due to redundancy and compensation (Blilou et al., 2005; Grieneisen and Scheres, 2009), rendering a systems biology approach to the problem necessary. Our initial parameter sweep suggested that an efflux-dependent process is primarily involved in producing the VM minimum, while the importer-based process only makes a minor contribution (Figure 2F and 2I). A putative candidate for the implementation of the efflux-dependent model is via PINs. However, an important confounding factor for the modeling is that fluorescence is not a direct indication of the actual permeability rate and a full-strength PIN3 permeability might therefore be very different from a full-strength LAX1 permeability. Therefore, even though our analysis (Figure 2F and 2G) showed that to produce a comparable auxin minimum, much higher augmented influx permeability rates are required (for example, via LAX1) than localized efflux rates (possibly, through PIN3), neither the experiments nor simulations presented can convincingly conclude that the efflux-based process is indeed the predominant process by which the minimum is established. Moreover, it is possible that other transporters, such as ABCBs (ATP-binding cassette transporters of the B subfamily) (Bandyopadhyay et al., 2007; Geisler et al., 2017), might be functionally present as well. In short, despite our finding that PIN3 localization at the VM is supportive of the active efflux-dependent model, the LAX1 expression observed in the surrounding tissues likewise supports the alternative hypothesis that sequestering auxin by the other tissues could be a driving process for generating the minimum. As both scenarios generate similar outcomes on the level of auxin distributions under appropriate parameter conditions, we sought an additional and alternative observable to distinguish between them.

We found that although both processes are able to generate qualitatively similar steady state auxin patterns, the auxin fluxes underlying them are both qualitatively and quantitatively very different (Figure 2F and 2H; Supplemental Figure 3). At the location of the auxin minimum, in the VM, the import-based process shows negligible auxin throughput over and along the VM (Supplemental Figure 3L and 3Q). In contrast, while still maintaining very low auxin levels at the VM, the efflux-based scenario yields considerably higher fluxes over the VM, transversally connecting the valve to the replum (Supplemental Figure 3M and 3R) through perpendicular fluxes across these cell files. Also the combined model would predict such transversal flows (Supplemental Figure 3N and 3S). To further quantify these patterns, we

calculated how the fluxes through the VM depend on the strength of the apolar exporter in the VM or on the strength of the apolar importer in the valve and replum. Interestingly, while the import-dependent scenario presents decreasing overall fluxes with decreasing auxin levels (Supplemental Figure 2C, for total flux magnitudes) with negligible and decreasing transversal fluxes across the VM, as would be the intuitive expectation, the efflux-dependent scenario in contrast presents increasing fluxes across (i.e., perpendicular to) the VM (Figure 2H) with decreasing auxin levels within the VM (Figure 2F, 2G and Supplemental Figure 2A and 2C). In short, the export-dependent scenario, by removing in all directions any auxin that enters these cells, generates an effective flux-passage-type process, allowing auxin to cross these files transversally. In contrast, the import-dependent case, preventing the entrance of auxin in the first place, generates a flux-barrier-type process, although a small level of parallel fluxes does linger (Supplemental Figure 2B). Plotting the relative strength of the minimum against the total fluxes that cross the minimum perpendicularly (Figure 2I) further illustrates this behavior: for a quantitatively similar minimum (e.g., of 5%, as indicated in the figure), the flux-barrier and the flux-passage processes present a 100-fold difference in regard to the resultant transversal auxin fluxes.

Note that also canalization models, as first proposed by Mitchison (1980a), predicted high auxin fluxes along veins containing lower auxin concentrations than the surrounding tissue. These models were based on the premise that fluxes effectively self-enhance themselves, triggering thereby a self-organized vasculature patterning. Subsequent experimental observations, however, showed that leaf veins actually have high auxin concentrations (Mattsson et al., 2003). Moreover, the nature of the fluxes as presented by the paradigmatic canalization mechanism are very different from the ones predicted by the flux-passage mechanism we report here. In our model, high fluxes occur across the quasi-1D structure of the VM and actually increase as transporter activity parameters strengthen the minimum; in contrast, the fluxes occurring along the VM do not increase as the minimum deepens (Supplemental Figure 2A and 2B). This contrasts to the behavior resulting from canalization models, where there are negligible fluxes crossing the veins perpendicularly, but large fluxes parallel to them.

While our computational model of auxin dynamics and patterning allows us to directly assess the underlying fluxes that result from any given transporter configuration, this is not possible experimentally. To overcome this, we hypothesized that physically blocking the auxin passage over the VM may allow for an indirect test of which flux mechanism is involved. In the case of a flux-passage process, blocking the VM should result in noticeable alterations in the auxin concentrations in the flanking tissues, while in the flux-barrier scenario, such a physical obstruction should only result in marginal differences in the auxin distribution within flanking tissues. Such differences, or lack of differences, in auxin concentration should be experimentally trackable through the DR5 auxin-signaling reporter and would allow us to assess whether the flux-passage process (PIN-mediated efflux from the VM) or flux-barrier process (LAX-mediated influx from surrounding tissue) predominates.

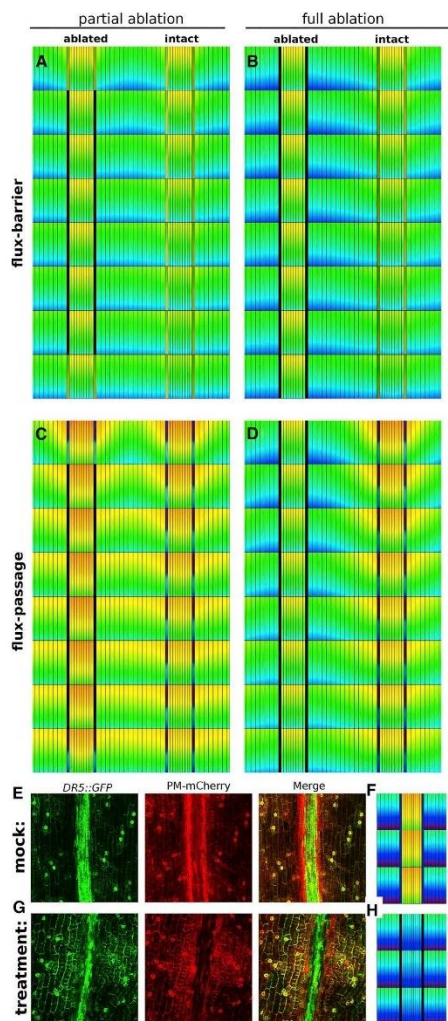


Figure 4. Interfering with the Auxin Fluxes through the VM.

(A and B) Modeling predicts that if the auxin minimum is solely due to lack of augmented influx activity in the VM, then partly (A) or fully (B) ablating the VM only slightly changes the auxin levels in the valve and replum.

(C and D) In contrast, if the auxin minimum were due to apolar PIN3 in the VM, then partly (C) or fully (D) ablating the VM strongly affects the auxin levels in those tissues. To better illustrate the impact, only the VMs flanking one of the repla are ablated.

(E and G) DR5:GFP in control treatment (E) and after DEX-induced VM ablation (G).

(F and H) Predicted auxin pattern using the full model for stage 17b (F) after VM ablation (H).

We first explored what effects ablating portions of the VM would yield in both contrasting scenarios. However, introducing a small *in silico* ablation at the VM in either the influx-dependent or efflux-dependent model (see Supplemental Information for modeling implementation) did not generate any noticeable changes in the auxin distributions (Supplemental Figure 5F–5I), despite them displaying distinct flux-barrier and flux-passage processes, respectively. Further *in silico* ablations revealed that only larger extents of VM obstruction cause noticeable changes in the auxin pattern (Figure 4C), with the model displaying the flux-passage process showing only a modest increase in the replum upon ablation, while the alternative model, the flux-barrier process, is unaffected (compare Figure 4A with 4C). Note that we assume for the *in silico* ablations that all domains maintain fixed PIN distributions and intensity, both before and after ablation. Hence, dynamical changes in auxin profiles and flux patterns that can be observed are solely due to VM ablation. (Although transporter reorientations might occur at longer timescales after ablation, we do not consider them within this modeling framework.)

We therefore realized that to experimentally verify the predicted distinction between the processes, only partially ablating the VM might not be sufficient. Indeed, small ablation extensions resulted only in minor effects (Supplemental Figure 5, Methods, and Supplemental Information for details). However, when ablating larger extents, changes in the auxin profile did occur, especially close to the VM, but in a very inconsistent and irreproducible manner (Supplemental Figure 5, and Dryad Repository for additional images). Although some ablation experiments provided support for the hypothesis that underlying fluxes are at play passing through the VM's auxin minimum, it also revealed the sensitivity of these experiments to the extent of the ablated region, and to possible wound damage responses in the surrounding tissues, given the large extent of tissue being laser ablated. Therefore, we sought an alternative method to test the model predictions.

From the simulations, it also became clear that even if a small region of the VM is kept intact after ablation, this will be sufficient to redistribute part of the auxin that would otherwise have accumulated alongside the VM, thereby obscuring the effect of the obstruction (compare for example, Figure 4C and 4D). In order to achieve the blockage of the whole VM, we therefore developed an inducible BARNASE system, for expression specifically at the VM. The BARNASE gene encodes a powerful toxin, which upon expression will stimulate cell death. In order to keep its toxic effect confined to the cell expressing it, the BARNASE gene is fused to its inhibitor, BARSTAR (Beals and Goldberg, 1997). In the two-component system employed here, the VM-specific *IND* promoter drives the expression of the LhGR transcription factor (LhG4 transcription factor fused to the Glucocorticoid Receptor), while the BARNASE-BARSTAR gene is under control of the pOp promoter recognized by the LhGR protein. Upon treatment by dexamethasone (DEX), the LhGR protein produced in the VM will enter the nucleus and

(F and H) Predicted auxin pattern using the full model for stage 17b (F) after VM ablation (H).

Scale bar: 200 μ m for (E and G). Color coding of auxin levels as indicated in Figure 2.

induce expression of the toxin. The effect of inducing the *IND>GR>BARNASE-BARSTAR* system can be seen after 3–9 days of treatment (see *Methods*), with scanning electron micrographs showing the damaged VM cells (*Supplemental Figure 7*). Importantly, the effect is highly local, as the wound-induced reporter line *WIND1::GUS* is only expressed in the VM cells (*Supplemental Figure 7*). The genetic ablation of the VM cells was verified using an mCherry marker for the plasma membrane (PM) (Nelson et al., 2007). Without DEX treatment, this line clearly marks the VM cells, whereas the PM of these cells has disappeared in the presence of DEX (*Figure 4E* and *4G*). Therefore, this system allows us to induce cell death of the entire VM in a temporally controlled manner, without causing collateral damage to the surrounding tissues. In contrast to the control treatment (*Figure 4E*), such a chemically induced obstruction of the VM, at stage 17b, resulted in a consistent and significant drop of auxin in the replum cells directly flanking the VM, as well as a rise in auxin in the valve cells (*Figure 4G*). The observed pattern closely corresponded to the pattern predicted by modeling full ablation in the situation in which differences in efflux carriers yield the flux-passage process (*Figure 4D*, with the VMs flanking the left replum being ablated while the ones flanking the right replum stay intact, for straightforward comparison). In our ablation simulations, only cell death (total impermeability) of the VM tissue was taken into account, using the assumption that no changes in transporter intensity and localization in the adjacent tissues occurred. To establish if this is a reasonable assumption, we crossed *PIN3::PIN3-GFP* with the *IND>RG>BARNASE-BARSTAR* line to be able to observe *PIN3* intensity and localization after chemical ablation of the VM at 9 days after the initialization of DEX treatment. No noticeable changes in *PIN3* intensity or localization were observed in the replum or valve after chemical ablation of the VM, supporting the modeling assumption of unaltered transporter patterning (*Supplemental Figure 8*). The dynamic effect of VM ablation on auxin levels (*Figure 4E–4H*) therefore indicates that transversal auxin fluxes are taking place at the VM at stage 17b even though the auxin levels themselves are low. Taken together, these results predict that the auxin minimum predominantly involves active efflux across the VM, with lower influx possibly contributing to the depth of the minimum. In addition, our combined modeling and experimental data suggest that differences in transporter patterns within the valve and replum underlie the constant flux over the VM.

The auxin minimum at the VM plays a well-defined developmental role in maintaining the position and regulating the temporal timing of dehiscence. We therefore next analyzed the temporal regulation of the minimum.

Efflux: Digging Deeper into the Minimum

The results described above from experimentally induced tissue perturbations support the notion that auxin efflux at the VM plays a central role in the auxin minimum formation. Based on imaging, *PIN3* may be a key factor in this process, although we cannot exclude the action of yet unknown auxin exporters in this region. Thus far, our analysis was confined to a single developmental stage, 17b (*Figure 5A* and *5B*). If the expression patterns that we took into account to explain that specific developmental time points are indeed determining the auxin and flux patterns,

we would expect that observed differences in transporter expression at other stages should roughly correlate with the predicted auxin patterns at those different stages as well. With this in mind, we extended our analysis to an earlier developmental stage, 16, and generated a detailed map of relative permeability rates based on *PIN3*, *PIN7*, and *LAX1* localization and intensity patterns (*Figure 5C* and *Supplemental Figure 9*, and *Table 2*). The main developmental difference considered between stages 17b and 16 is that at stage 16, *PIN3* is more abundant in the replum, while *PIN7* is slightly more abundant in the valve, as is *LAX1*. Running the model generated auxin distributions that matched observed auxin-signaling patterns of *DR5::GFP* (*Figure 5D* and *5E*). Notably, the auxin minimum in the early stages was not as prominent as during later stages (when comparing stage 16 and 17b) (*Figure 5A*, *5D*, *5B*, and *5E*), as reported previously (Sorefan et al., 2009; van Gelderen et al., 2016).

We extrapolated these insights to an even earlier developmental time point, around stages 14–15, based upon recently published data regarding this stage (van Gelderen et al., 2016). We captured this earlier stage by reducing the strength of *PIN3* in the VM. Moreover, the number of cell files was reduced taking into account that the VM at stage 15 has not yet undergone the asymmetric cell division that specifies the separation and lignified cell layers (*Supplemental Figure 6F* and *6H*) (Wu et al., 2006). The resultant auxin pattern for this early stage reveals higher auxin levels at the VM (*Figure 5F*) compared to stage 16 (*Figure 5D*). Thus, when VM-localized efflux is lower, auxin levels are predicted to be substantially higher, suggesting that the fruit ripens by gradually transitioning from an initial auxin maximum at the VM to an auxin minimum later in development. These high auxin levels result from the fact that VM cells at early stages have a higher perimeter-to-area ratio, thereby gaining more auxin through the chemiosmotically biased influx (*Supplemental Figure 6B* and *6F*), as well as from reduced auxin efflux activity (*Supplemental Figure 6C* and *6G*). The sequence of *DR5* expression patterns therefore matches the auxin pattern predicted by the model in a qualitatively temporal fashion (van Gelderen et al., 2016).

DISCUSSION

Auxin maxima have been studied extensively for a wide set of plant systems, and different modes of auxin maximum formation have been inferred (Grieneisen and Scheres, 2009; Grieneisen et al., 2012). The relative role of importers and exporters for auxin accumulation has been theoretically explored, showing that interplay between export and import can be critical (Kramer, 2004; Band et al., 2014). However, for such quantitative evaluation to be made, *in silico* plant models require the cell-wall compartment to be taken into account explicitly, as was done here. Only when this apoplastic compartment is explicitly treated can correct units of permeability for the exporters/importers be used, their functional role be separated, and hence their quantitative contributions be assessed (see also Kramer, 2004; Abley et al., 2013; el Showk et al., 2015). Hence, for a systems biology approach to reveal the processes of auxin transport underlying developmental patterning, one must treat the multi-scale nature of the transport phenomena, as done here.

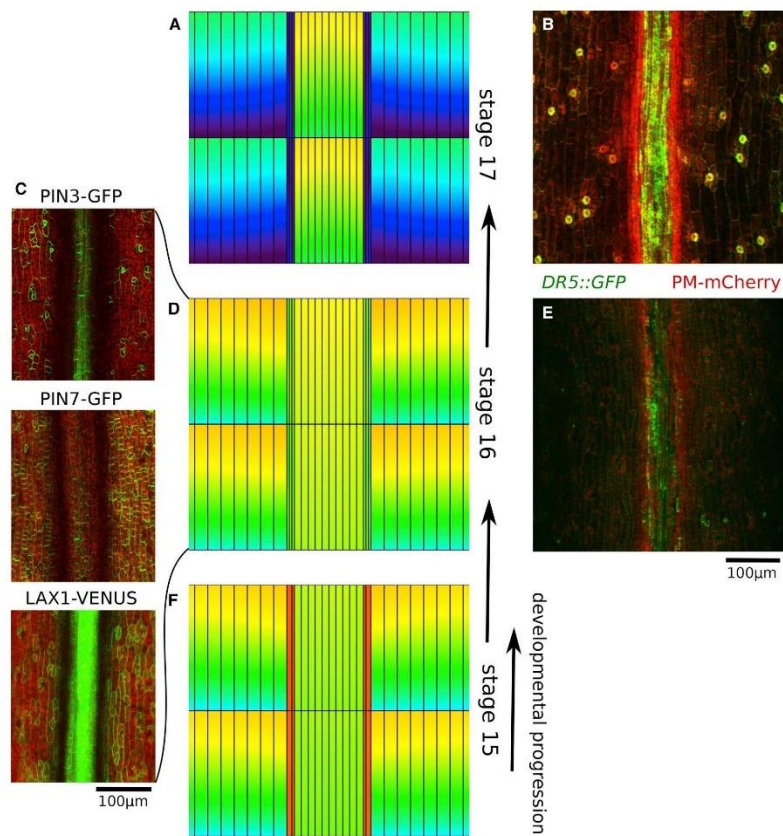


Figure 5. Temporal Development of the VM Minimum.

(A and B) Auxin patterning as predicted by the model **(A)** and experimentally observed **(B)** during stage 17b.

(C–E) **(C)** PIN3:PIN3-GFP (top); PIN7:PIN7-GFP (middle); LAX1:LAX1-VENUS (bottom) at stage 16, with **(D and E)** auxin patterns as predicted by the model **(D)** and experimentally observed **(E)**.

(F) Predicted auxin patterns using the full model for stage 15. **(A, D, and F)** illustrate the formation of the auxin minimum in the VM and build-up of auxin in the replum over time. Scale bars as indicated. Color coding of auxin levels as indicated in Figure 2.

Moreover, the mechanisms underlying instructive auxin minima, defined as regulated and biologically functional regions of lower auxin signaling, have not yet been mechanistically analyzed to the same extent as maxima. It was recently established that the regulated maintenance of an auxin minimum at the basal root meristem triggers cell differentiation (Di Mambro et al., 2017). This work provided a mechanistic and genetic explanation for how another important phytohormone, cytokinin, controls and positions this minimum through auxin degradation and alterations in polar auxin transport. In the root system, as a consequence of the continuous growth of the root tip accompanied by a continuous spatial translocation of the

phytohormone patterning, cells rapidly transit through that auxin minimum, triggering swift auxin variations within each cell. In contrast, the auxin minimum in the silique is much more constrained, extending over the whole longitudinal dimension of the fruit while being only two to three cell files wide. Moreover, cells are confined to this pattern, suggesting a very different mechanism for auxin minimum formation and information processing. Indeed, here we show, combining spatial modeling and experiments in a systems biology approach, that there are two contrasting processes that could account for the stripes of auxin minimum observed at the VM of the *Arabidopsis* fruit. Those processes are indistinguishable at the level of relative

auxin distributions. Our modeling indicates that the efflux-dependent “flux-passage” process, relying on active apolar exporter activity at the VM, is more robust than the “flux-barrier” process, which relies on augmented influx into the surrounding tissues. Moreover, the flux-passage process also appears more likely, given its convincing performance within a reasonable permeability range. Visualization of microscopy images in 3D confirmed that *PIN3* is co-expressed with the auxin minimum and that the *PIN3* protein is apolarly localized, providing support for the flux-passage process. We therefore propose that a rise in *PIN3* levels may be associated with a gradual transition of the fruit from presenting an auxin maximum in the VM at early stages (stage 15; van Gelderen et al., 2016) to displaying an actual minimum at stage 17b. This process is correlated with the ripening of the fruit.

Interestingly, we found that the auxin minimum in the VM at stage 17b is obtained and maintained despite significant transversal fluxes across that tissue. Obstructing the VM tissue both *in silico* and *in vivo* over its entire longitudinal extension resulted in similar changes in the auxin distribution to emerge, confirming the somewhat counterintuitive notion that the VM, although presenting stable low auxin levels, is nevertheless presenting a rich auxin flux pattern. The *in silico* results were built upon the assumption that transporters' intensity and localization in the replum and valve did not alter, which was experimentally verified for *PIN3*. *PIN3* is expressed in the valve and is the only *PIN* transporter found to be expressed in the replum tissue during fruit development. However, we cannot ascertain that other transporters (besides *PIN3*) might have been altered due to the chemical ablation, underlying the observed auxin alterations. Nevertheless, even if other transporter patterns did change, this would not negate the flux-passage model *per se* as a likely cause, for such a (non-observed and hypothetical) response would likely be the changes in the auxin patterning or fluxes themselves, and such changes after ablation are only predicted to be triggered within the flux-passage model. We acknowledge that the development of additional crosses between the *IND>GR>BARNASE-BARSTAR* system and GFP-tagged transporters would be beneficial, since following these inducible lines on a fine-grained timescale would determine exactly if and how changes in auxin and auxin fluxes might unleash transporter modifications, in their turn further affecting the auxin levels and fluxes. Taken together, these results already demonstrate that the flux-passage process is most likely the predominant process, while the flux-barrier process plays a minor role. Such an inverted relationship between low concentrations and high fluxes may be counterintuitive, and can be easily overlooked as a plausible mechanism for patterning.

To our knowledge, the only other instance in which similar correlations have been drawn between low concentrations and high fluxes are the canalization models to describe vein formation (Mitchison, 1980a, b, 1981; Sachs, 1975, 1981, 1991a,b; Feugier et al., 2005). In those models, “with-the-flow” assumptions link *PIN* positioning to fluxes, yielding low concentrations within veins. Although the thinking behind these models has played a huge part in developing plant systems biology as a discipline, the models themselves incorrectly predicted low auxin levels in the veins, in contrast to the experimentally revealed high auxin concentrations (Mattsson

et al., 2003). Here, for the *Arabidopsis* fruit, we support a high flux-low concentration scenario also experimentally. Secondly, canalization models are based on heuristic rules regarding *PIN* auxin feedbacks, in which it is assumed that cells respond to measuring devices that are not yet supported by known molecular processes, as pointed out by Mitchison (1980a, 1980b, 1981), Feugier et al. (2005) and others (Bennett et al., 2014). In contrast, we built our model using observed and analyzed molecular biological data. Thirdly, even when not considering the mismatch between actual leaf data and canalization predictions, it remains that the resultant fluxes within these models solely form along the vein/minimum, not across it (Feugier et al., 2005). Hence, the directionality of the fluxes in relation to the orientation of the minimum is an important predictor to distinguish between the processes. We demonstrated empirically that relevant perpendicular fluxes under the low concentration fields through our ablation interferences, driven by a systems understanding of the auxin minimum formation.

Finally, we have shown that to realistically enable the flux-passage process, an exporter-based scenario is far more robust and likely, for which the inclusion of the cell-wall compartment is essential (Kramer, 2004; el Showk et al., 2015); Grieneisen and Scheres (2009). Interestingly, we here find that a flux-passage process is not only more robust over parameter space but displays additional intriguing behavior, such as effectively connecting tissues over larger domains through fluxes while being separated by a concentration minimum. While it is well established that auxin is developmentally instructive through local concentrations within cells, it has been shown that the auxin fluxes themselves can also be informative (Prusinkiewicz et al., 2009; Bennett et al., 2014; Cieslak et al., 2015). If concentrations and fluxes can indeed be perceived independently by cells, then the decoupling of concentration and flux patterns shown here may help explain some of the amazing versatility of responses to the phytohormone auxin.

METHODS

Plant Material and Growth Conditions

Plants were grown under long-day conditions (16-h light/8-h dark) at 22°C. Reporter lines of *DR5::GFP* (Friml et al., 2003), *PIN3::PIN3::GFP* (Žádníková et al., 2010), *PIN7::PIN7::GFP* (Billou et al., 2005), *LAX1::LAX1::VENUS* (Robert et al., 2015), *WIND1::GUS* (Iwase et al., 2011), and *PM-mCherry* (Nelson et al., 2007) were in Col-0 background. Plants were grown in small individual cells in a glasshouse (maintained at approximately 21°C) in *Arabidopsis* soil mixture (ratio of Levington F2 600 L peat:100 L 4 mm grit:196 g Exemptor (chloronicotyl insecticide)).

Construct of *IND::GR>>Barnase-Barstar*

A 2.5 kb *IND* promoter was amplified from *Arabidopsis* genomic DNA and cloned into the Gateway donor vector pDONR207, then recombined into the vector pBIN-LR-LhGR2 (Craft et al., 2005) to produce *INDp-LhGR2*. The *Barnase-Barstar* coding sequence was cloned into the Gateway donor vector pDONR201, then recombined into the vector pOp6 (Craft et al., 2005), which contains pOp6 promoter to produce pOp6-Barnase-Barstar. Finally, the *INDp-LhGR2* fusion fragment was digested by *AscI* and inserted into the vector of pOp6-Barnase-Barstar to generate *INDp-LhGR2-pOp6-Barnase-Barstar* (*IND::GR>>Barnase-Barstar*). The construct was introduced into *Agrobacterium tumefaciens* strain AGL1 for transformation into Col-0 plants.

Molecular Plant

Minimum Requirements for Auxin Distribution during Fruit Opening

Dexamethasone Treatment

Inflorescence and siliques were dipped in the solutions containing 10 μ M DEX (Sigma-Aldrich) and 0.015% Silwet L-77 for 5 s and treated every 2 days. Relatively mild doses were used to prevent that the ensuing cell death would also cause mechanical separation and disintegration of the fruit tissue, which could be observed at higher doses. At the treatment intensity used, it took several days to a week to obtain complete cell death of the VM. Hence, images of stage 16 fruits (floral organs withering and falling from the fruits) were obtained at 3 days after the first treatment and images of stage 17b fruits (fully elongated and expanded fruits) were taken at 9 days after the first treatment.

Confocal Microscopy

Fluorescent images were taken on a Zeiss LSM 780 confocal microscope. GFP and chloroplast autofluorescence were excited by 488-nm excitation and mCherry was excited by 514-nm excitation. GFP emission spectra were collected between 499 and 526 nm, autofluorescence was collected between 626 and 695 nm and mCherry was collected between 561 and 602 nm. The images were processed using ImageJ (Schneider et al., 2012).

GUS Assay

Fruits at stage 17b were collected in Eppendorf tubes containing X-Gluc solution (1 mg/ml X-Gluc (5-bromo-4-chloro-3-indolyl glucuronide; Melford) dissolved in DMSO, 100 mM sodium phosphate buffer, 10 mM EDTA, 0.5 mM $K_3Fe(CN)_6$, 3 mM $K_4Fe(CN)_6$, 0.1% Triton X-100) and vacuum infiltrated for 30 s, and then incubated at 37°C in the dark for 16 h. The fruits were then treated in 70% ethanol to destain for 2–3 days before taking images on a Leica M205 FA stereo microscope.

Scanning Electron Microscopy

Fruits were fixed in FAA (50% ethanol, 5% glacial acetic, and 3.7% formaldehyde) for 4 h at room temperature and overnight at 4°C. Samples were then dehydrated through an ethanol series (30 min each in 50%, 60%, 70%, 80%, 90%, 95%, 100%, 100%, and dry ethanol). After critical point drying, samples were coated with gold and examined using a Zeiss Supra 55VP field emission scanning electron microscope.

Laser Ablation

Tissue ablations were conducted using a Zeiss PLAM MicroBeam microscope, with an inverted 10x objective, a cutting speed of 20 μ m/s, and laser power of 65%. These settings were found through trial and error to be the optimum for cutting a single layer of cells while causing minimal damage to the surrounding tissue. Experiments were conducted on individual fruits of the inflorescence meristem, at a stage when the main stem was about 10 cm long. Mature siliques, open flowers, and young buds were removed from the inflorescence, leaving only flowers around stage 15. Prior to ablation, the sepals, petals, and anthers of each flower were removed to reveal the fruit.

For each sample, the inflorescence was placed onto a dry microscope slide, and the rest of the plant was balanced horizontally across the microscope stage. The main stem was adhered to the microscope slide using double-sided sticky tape to hold the gynoecium in the correct orientation. This technique permitted the positioning of the replum roughly perpendicular to the microscope objective. If necessary, an additional microscope slide was placed on top of the gynoecium to hold it in place. Samples were visualized using bright-field illumination. The Zeiss PALM software was used to draw target cutting lines in the location of the VM, which guided the laser path during ablation. Tissue damage was immediately and clearly visualized in the region of ablation as the cells broke open. Samples were imaged (with bright-field illumination) immediately after ablation to confirm the location of the cut site before the plants were returned to the glasshouse to continue growing.

876 Molecular Plant 12, 863–878, June 2019 © The Author 2019.

Fruits were removed for imaging at 5 or 6 days after cutting. Double-sided sticky tape was used to mount fruits onto a microscope slide with a drop of 0.1% Silwet L-77 solution (to facilitate imaging through the waxy coating) and topped with a coverslip. Samples were imaged using bright-field illumination on a Leica DM6000 upright light microscope or a Leica SP5 laser confocal scanning microscope, using a 20x immersion objective.

Video

The confocal Z stack was converted to individual .png files for each slice using ImageJ (Schneider et al., 2012). The converted stack was opened using the 3D visualization software VolViewer (<http://cmpdartsvr3.cmp.uea.ac.uk/wiki/BanghamLab/index.php/VolViewer>, Lee et al., 2006), and a transfer function was applied to optimize levels. This tool was used to create a series of images, which were saved and then animated using virtual dub (<http://virtuallab.sourceforge.net/>) before being saved as an .avi file.

DATA AND SOFTWARE AVAILABILITY

All simulations were performed using computer code written in C developed in-house. A remote repository (Git repository) has been used for the code as well as for the scripts that generated all simulation outputs (graphs and images) that are presented and discussed in the main text and figures and supplemental figures. Details of the computational model are given in the Supplemental Information. Access to the repository is available through Bitbucket after acceptance (<https://bitbucket.org/mareelab/FruitMin/>).

SUPPLEMENTAL INFORMATION

Supplemental Information is available at *Molecular Plant Online*.

FUNDING

This work was supported by the Institute Strategic Programme grants (BB/J004588/1 and BB/P013511/1) from the Biotechnology and Biological Sciences Research Council (BBSRC) to the John Innes Centre and by grant BB/M018164/1 to L.Ø. from the FACCE ERA-NET+ and BBSRC.

AUTHOR CONTRIBUTIONS

X.-R.L., S.F., V.A.G., A.F.M.M., and L.Ø. planned experiments; X.-R.L. and S.F. performed experiments; V.A.G. and A.F.M.M. planned simulations; R.M.A.V. and A.F.M.M. performed simulations; R.M.A.V., V.A.G., and A.F.M.M. developed the code for simulations; S.F. performed ablation experiments; X.-R.L. developed lines for induction of tissue-specific cell death and performed the experiment; X.-R.L., S.F., and L.Ø. generated microscopy images; X.-R.L., V.A.G., L.Ø., and A.F.M.M. interpreted tissue polarity from data; V.A.G., L.Ø., and A.F.M.M. interpreted all results and wrote the paper; X.-R.L., R.M.A.V., and S.F. edited paper, A.F.M.M., L.Ø., and V.A.G. conceived the research.

ACKNOWLEDGMENTS

We are grateful to Heather Bland, Yang Dong, Laila Moubaydin, and Tongbing Su for comments and discussion on the manuscript, and Enrico Coen, John Fozard, and José Feijó for helpful discussions. We also thank Luis Canás Clemente for providing materials for the BARNASE/BARSTAR system and Keiko Sugimoto for the WIND1::GUS line. No conflict of interest declared.

Received: December 14, 2018

Revised: May 1, 2019

Accepted: May 3, 2019

Published: May 22, 2019

REFERENCES

Abley, K., Barbier de Reuille, P., Strutt, D., Bangham, A., Prusinkiewicz, P., Marée, A.F.M., Grieneisen, V.A., and Coen, E. (2013). An intracellular partitioning-based framework for tissue cell polarity in plants and animals. *Development* 140:2061–2074.

- Adamowski, M., and Friml, J. (2015). PIN-dependent auxin transport: action, regulation, and evolution. *Plant Cell* **27**:20–32.
- Band, L.R., Wells, D.M., Fozard, J.A., Ghetiu, T., French, A.P., Pound, M.P., Wilson, M.H., Yu, L., Li, W., Hijazi, H.I., et al. (2014). Systems analysis of auxin transport in the *Arabidopsis* root apex. *Plant Cell* **26**:862–875.
- Bandyopadhyay, A., Blakeslee, J.J., Lee, O.R., Mravec, J., Sauer, M., Titapiwatanakun, B., Makam, S.N., Bouchard, R., Geisler, M., Martinola, E., et al. (2007). Interactions of PIN and GGP auxin transport mechanisms. *Biochem. Soc. Trans.* **35**:137–141.
- Barbier de Reuille, P., Bohn-Courseau, I., Ljung, K., Morin, H., Carraro, N., Godin, C., and Traas, J. (2006). Computer simulations reveal properties of the cell-cell signaling network at the shoot apex in *Arabidopsis*. *Proc. Natl. Acad. Sci. U S A* **103**:1627–1632.
- Beals, T.P., and Goldberg, R.B. (1997). A novel cell ablation strategy blocks tobacco anther dehiscence. *Plant Cell* **9**:1527–1545.
- Benjamins, R., Quint, A., Weijers, D., Hooykaas, P., and Offringa, R. (2001). The PINOID protein kinase regulates organ development in *Arabidopsis* by enhancing polar auxin transport. *Development* **128**:4057–4067.
- Benková, E., Michniewicz, M., Sauer, M., Teichmann, T., Seifertová, D., Jürgens, G., and Friml, J. (2003). Local, efflux-dependent auxin gradients as a common module for plant organ formation. *Cell* **115**:591–602.
- Bennett, T., Hines, G., and Leyser, O. (2014). Canalization: what the flux? *Trends Genet.* **30**:41–48.
- Bilsborough, G.D., Runions, A., Barkoulas, M., Jenkins, H.W., Hasson, A., Gallinha, C., Laufs, P., Hay, A., Prusinkiewicz, P., and Tsiantis, M. (2011). Model for the regulation of *Arabidopsis thaliana* leaf margin development. *Proc. Natl. Acad. Sci. U S A* **108**:3424–3429.
- Billou, I., Xu, J., Wildwater, M., Willemsen, V., Paponov, I., Friml, J., Heidstra, R., Aida, M., Palme, K., and Scheres, B. (2005). The PIN auxin efflux facilitator network controls growth and patterning in *Arabidopsis* roots. *Nature* **433**:39–44.
- Brunoud, G., Wells, D.M., Oliva, M., Larrieu, A., Mirabet, V., Burrow, A.H., Beeckman, T., Kepinski, S., Traas, J., Bennett, M.J., et al. (2012). A novel sensor to map auxin response and distribution at high spatio-temporal resolution. *Nature* **482**:103–106.
- Caggiano, M.P., Yu, X., Bhatia, N., Larsson, A., Ram, H., Ohno, C.K., Sappl, P., Meyerowitz, E.M., Jönsson, H., and Heisler, M.G. (2017). Cell type boundaries organize plant development. *Elife* **6**:e27421.
- Cheng, Y., Dai, X., and Zhao, Y. (2006). Auxin biosynthesis by the YUCCA flavin monooxygenases controls the formation of floral organs and vascular tissues in *Arabidopsis*. *Genes Dev.* **20**:1790–1799.
- Cieslak, M., Runions, A., and Prusinkiewicz, P. (2015). Auxin-driven patterning with unidirectional fluxes. *J. Exp. Bot.* **66**:5083–5102.
- Craft, J., Samalova, M., Baroux, C., Townley, H., Martinez, A., Jepson, I., Tsiantis, M., and Moore, I. (2005). New pOp/LhG4 vectors for stringent glucocorticoid-dependent transgene expression in *Arabidopsis*. *Plant J.* **41**:899–918.
- Dubrovsky, J.G., Sauer, M., Napsucialy-Mendivil, S., Ivanchenko, M.G., Friml, J., Shishkova, S., Celenza, J., and Benková, E. (2008). Auxin acts as a local morphogenetic trigger to specify lateral root founder cells. *Proc. Natl. Acad. Sci. U S A* **105**:8790–8794.
- Eklund, D.M., Ståldal, V., Valsecchi, I., Cierlik, I., Eriksson, C., Hiratsu, K., Ohme-Takagi, M., Sundström, J.F., Thelander, M., Ezcurra, I., et al. (2010). The *Arabidopsis thaliana* STYLISH1 protein acts as a transcriptional activator regulating auxin biosynthesis. *Plant Cell* **22**:349–363.
- Feugier, F.G., Mochizuki, A., and Iwasa, Y. (2005). Self-organization of the vascular system in plant leaves: inter-dependent dynamics of auxin flux and carrier proteins. *J. Theor. Biol.* **236**:365–375.
- Friml, J., Vieten, A., Sauer, M., Weijers, D., Schwarz, H., Hamann, T., Offringa, R., and Jürgens, G. (2003). Efflux-dependent auxin gradients establish the apical-basal axis of *Arabidopsis*. *Nature* **426**:147–153.
- Friml, J., Yang, X., Michniewicz, M., Weijers, D., Quint, A., Tietz, O., Benjamins, R., Ouwerkerk, P.B., Ljung, K., Sandberg, G., et al. (2004). A PINOID-dependent binary switch in apical-basal PIN polar targeting directs auxin efflux. *Science* **306**:862–865.
- Geisler, M., Aryal, B., di Donato, M., and Hao, P. (2017). A critical view on ABC transporters and their interacting partners in auxin transport. *Plant Cell Physiol.* **58**:1601–1614.
- van Gelderen, K., van Rongen, M., Liu, A., Otten, A., and Offringa, R. (2016). An INDEHISCENT-controlled auxin response specifies the separation layer in early *Arabidopsis* fruit. *Mol. Plant* **9**:857–869.
- Grieneisen, V.A., and Scheres, B. (2009). Back to the future: evolution of computational models in plant morphogenesis. *Curr. Opin. Plant Biol.* **12**:606–614.
- Grieneisen, V.A., Xu, J., Marée, A.F.M., Hogeweg, P., and Scheres, B. (2007). Auxin transport is sufficient to generate a maximum and gradient guiding root growth. *Nature* **449**:1008–1013.
- Grieneisen, V.A., Scheres, B., Hogeweg, P., and Marée, A.F.M. (2012). Morphogenetic roots: comparing mechanisms of morphogen gradient formation. *BMC Syst. Biol.* **6**:37.
- Grieneisen, V.A., Marée, A.F.M., and Østergaard, L. (2013). Juicy stories on female reproductive tissue development: coordinating the hormone flows. *J. Integr. Plant Biol.* **55**:847–863.
- Han, X., Hyun, T.K., Zhang, M., Kumar, R., Koh, E.J., Kang, B.H., Lucas, W.J., and Kim, J.Y. (2014). Auxin-callose-mediated plasmodesmal gating is essential for tropic auxin gradient formation and signaling. *Dev. Cell* **28**:132–146.
- Heisler, M.G., Hamant, O., Krupinski, P., Uyttewaald, M., Ohno, C., Jönsson, H., Traas, J., and Meyerowitz, E.M. (2010). Alignment between PIN1 polarity and microtubule orientation in the shoot apical meristem reveals a tight coupling between morphogenesis and auxin transport. *PLoS Biol.* **8**:e1000516.
- Iwase, A., Mitsuda, N., Koyama, T., Hiratsu, K., Kojima, M., Arai, T., Inoue, Y., Seki, M., Sakakibara, H., Sugimoto, K., et al. (2011). The AP2/ERF transcription factor WIND1 controls cell dedifferentiation in *Arabidopsis*. *Curr. Biol.* **21**:508–514.
- Jacob, F., and Phillip, F. (1995). *The Statue within: An Autobiography* (Cold Spring Harbor, NY: Cold Spring Harbor Press).
- Kramer, E.M. (2004). PIN and AUX/LAX proteins: their role in auxin accumulation. *Trends Plant Sci.* **9**:578–582.
- Kuusk, S., Sohlberg, J.J., Long, J.A., Fridborg, I., and Sundberg, E. (2002). STY1 and STY2 promote the formation of apical tissues during *Arabidopsis* gynoecium development. *Development* **129**:4707–4717.
- Laskowski, M., Grieneisen, V.A., Hoffhuis, H., ten Hove, C.A., Hogeweg, P., Marée, A.F.M., and Scheres, B. (2008). Root system architecture from coupling cell shape to auxin transport. *PLoS Biol.* **6**:e307.
- Lee, K., Avondo, J., Morrison, H., Blot, L., Stark, M., Sharpe, J., Bangham, A., and Coen, E. (2006). Visualizing plant development and gene expression in three dimensions using optical projection tomography. *Plant Cell* **18**:2145–2156.
- Liljegren, S.J., Roeder, A.H.K., Kempin, S.A., Gremski, K., Østergaard, L., Guimil, S., Reyes, D.K., and Yanofsky, M.F. (2004). Control of fruit patterning in *Arabidopsis* by INDEHISCENT. *Cell* **116**:843–853.

Molecular Plant

Minimum Requirements for Auxin Distribution during Fruit Opening

- Di Mambro, R., De Ruvo, M., Pacifici, E., Salvi, E., Sozzani, R., Benfey, P.N., Busch, W., Novak, O., Ljung, K., Di Paola, L., et al.** (2017). Auxin minimum triggers the developmental switch from cell division to cell differentiation in the *Arabidopsis* root. *Proc. Natl. Acad. Sci. U S A* **114**:E7641–E7649.
- Marchant, A., Bhalerao, R., Casimiro, I., Eklöf, J., Casero, P.J., Bennett, M., and Sandberg, G.** (2002). AUX1 promotes lateral root formation by facilitating indole-3-acetic acid distribution between sink and source tissues in the *Arabidopsis* seedling. *Plant Cell* **14**:589–597.
- Mattsson, J., Ckurshumova, W., and Berleth, T.** (2003). Auxin signaling in *Arabidopsis* leaf vascular development. *Plant Physiol.* **131**:1327–1339.
- Mitchison, G.J.** (1980a). The dynamics of auxin transport. *Proc. R. Soc. Lond. B* **209**:489–511.
- Mitchison, G.J.** (1980b). A model for vein formation in higher plants. *Proc. R. Soc. Lond. B* **207**:79–109.
- Mitchison, G.J.** (1981). The polar transport of auxin and vein patterns in plants. *Philos. Trans. R. Soc. Lond. B* **295**:461–471.
- Nelson, B.K., Cai, X., and Nebenführ, A.** (2007). A multicolored set of *in vivo* organelle markers for co-localization studies in *Arabidopsis* and other plants. *Plant J.* **51**:1126–1136.
- Park, J., Lee, Y., Martinoia, E., and Geisler, M.** (2017). Plant hormone transporters: what we know and what we would like to know. *BMC Biol.* **15**:93.
- Payne, R.J.H., and Grierson, C.S.** (2009). A theoretical model for ROP localisation by auxin in *Arabidopsis* root hair cells. *PLoS One* **4**:e8337.
- Petersen, M., Sander, L., Child, R., van Onckelen, H., Ulvskov, P., and Borkhardt, B.** (1996). Isolation and characterisation of a pod dehiscence zone-specific polygalacturonase from *Brassica napus*. *Plant Mol. Biol.* **31**:517–527.
- Prusinkiewicz, P., Crawford, S., Smith, R.S., Ljung, K., Bennett, T., Ongaro, V., and Leyser, O.** (2009). Control of bud activation by an auxin transport switch. *Proc. Natl. Acad. Sci. U S A* **106**:17431–17436.
- Raspopovic, J., Marcon, L., Russo, L., and Sharpe, J.** (2014). Modeling digits. Digit patterning is controlled by a Bmp-Sox9-Wnt Turing network modulated by morphogen gradients. *Science* **345**:566–570.
- Reinhardt, D., Pesce, E.R., Stieger, P., Mandel, T., Baltensperger, K., Bennett, M., Traas, J., Friml, J., and Kuhlemeier, C.** (2003). Regulation of phyllotaxis by polar auxin transport. *Nature* **426**:255–260.
- Robert, H.S., Grunewald, W., Sauer, M., Cannoot, B., Soriano, M., Swarup, R., Weijers, D., Bennett, M., Boutilier, K., and Friml, J.** (2015). Plant embryogenesis requires AUX/LAX-mediated auxin influx. *Development* **142**:702–711.
- Roeder, A.H.K., and Yanofsky, M.F.** (2006). Fruit development in *Arabidopsis*. *Arabidopsis Book* **4**:e0075.
- Sabatini, S., Beis, D., Wolkenfelt, H., Murfett, J., Guilfoyle, T., Malamy, J., Benfey, P., Leyser, O., Bechtold, N., Weisbeek, P., et al.** (1999). An auxin-dependent distal organizer of pattern and polarity in the *Arabidopsis* root. *Cell* **99**:463–472.
- Sachs, T.** (1975). The control of the differentiation of vascular networks. *Ann. Bot.* **39**:197–204.
- Sachs, T.** (1981). The control of the patterned differentiation of vascular tissues. *Adv. Bot. Res.* **9**:151–262.
- Sachs, T.** (1991a). Cell polarity and tissue patterning in plants. *Development* **113**:83–93.
- Sachs, T.** (1991b). *Pattern Formation in Plant Tissues* (Cambridge: Cambridge University Press).
- Scarpella, E., Marcos, D., Friml, J., and Berleth, T.** (2006). Control of leaf vascular patterning by polar auxin transport. *Genes Dev.* **20**:1015–1027.
- Schneider, C.A., Rasband, W.S., and Eliceiri, K.W.** (2012). NIH Image to ImageJ: 25 years of image analysis. *Nat. Methods* **9**:671–675.
- el Showk, S., Help-Rinta-Rahko, H., Blomster, T., Siligato, R., Marée, A.F.M., Mähönen, A.P., and Grieneisen, V.A.** (2015). Parsimonious model of vascular patterning links transverse hormone fluxes to lateral root initiation: auxin leads the way, while cytokinin levels out. *PLoS Comput. Biol.* **11**:e1004450.
- Smith, R.S., Guyomarc'h, S., Mandel, T., Reinhardt, D., Kuhlemeier, C., and Prusinkiewicz, P.** (2006). A plausible model of phyllotaxis. *Proc. Natl. Acad. Sci. U S A* **103**:1301–1306.
- Smyth, D.R., Bowman, J.L., and Meyerowitz, E.M.** (1990). Early flower development in *Arabidopsis*. *Plant Cell* **2**:755–767.
- Sorefan, K., Girin, T., Liljegren, S.J., Ljung, K., Robles, P., Galván-Ampudia, C.S., Offringa, R., Friml, J., Yanofsky, M.F., and Østergaard, L.** (2009). A regulated auxin minimum is required for seed dispersal in *Arabidopsis*. *Nature* **459**:583–586.
- Spence, J., Vercher, Y., Gates, P., and Harris, N.** (1996). 'Pod shatter' in *Arabidopsis thaliana*, *Brassica napus* and *B. juncea*. *J. Microsc.* **181**:195–203.
- Stoma, S., Lucas, M., Chopard, J., Schaedel, M., Traas, J., and Godin, C.** (2008). Flux-based transport enhancement as a plausible unifying mechanism for auxin transport in meristem development. *PLoS Comput. Biol.* **4**:e1000207.
- Swarup, R., and Péret, B.** (2012). AUX/LAX family of auxin influx carriers – an overview. *Front. Plant Sci.* **3**:225.
- Ullmann, A.** (2011). In memoriam: Jacques Monod (1910–1976). *Genome Biol. Evol.* **3**:1025–1033.
- Wolpert, L.** (2016). Positional information and pattern formation. *Curr. Top. Dev. Biol.* **117**:597–608.
- Wu, H., Mori, A., Jlang, X., Wang, Y., and Yang, M.** (2006). The INDEHISCENT protein regulates unequal cell divisions in *Arabidopsis* fruit. *Planta* **224**:971–979.
- Zádníková, P., Petrásek, J., Marhavý, P., Raz, V., Vandenbussche, F., Ding, Z., Schwarzerová, K., Morita, M.T., Tasaka, M., Hejátko, J., et al.** (2010). Role of PIN-mediated auxin efflux in apical hook development of *Arabidopsis thaliana*. *Development* **137**:607–617.

RESEARCH ARTICLE

Open Access

A novel role for *STOMATAL CARPENTER 1* in stomata patterning



Giulia Castorina¹, Samantha Fox², Chiara Tonelli¹, Massimo Galbiati^{1*} and Lucio Conti^{1*}

Abstract

Background: Guard cells (GCs) are specialised cells within the plant epidermis which form stomatal pores, through which gas exchange can occur. The GCs derive through a specialised lineage of cell divisions which is specified by the transcription factor *SPEECHLESS (SPCH)*, the expression of which can be detected in undifferentiated epidermal cells prior to asymmetric division. Other transcription factors may act before GC specification and be required for correct GC patterning. Previously, the DOF transcription factor *STOMATAL CARPENTER 1 (SCAP1)* was shown to be involved in GC function, by activating a set of GC-specific genes required for GC maturation and activity. It is thus far unknown whether *SCAP1* can also affect stomatal development.

Results: Here we show that *SCAP1* expression can also be observed in young leaf primordia, before any GC differentiation occurs. The study of transgenic plants carrying a *proSCAP1:GUS-GFP* transcriptional fusion, coupled with qPCR analyses, indicate that *SCAP1* expression peaks in a temporal window which is coincident with expression of stomatal patterning genes. Independent *scap1* loss-of-function mutants have a reduced number of GCs whilst *SCAP1* over expression lines have an increased number of GCs, in addition to altered GC distribution and spacing patterns. The study of early markers for stomatal cell lineage in a background carrying gain-of-function alleles of *SCAP1* revealed that, compared to the wild type, an increased number of protodermal cells are recruited in the GC lineage, which is reflected in an increased number of meristemoids.

Conclusions: Our results suggest an early role for *SCAP1* in GC differentiation. We propose that a function of *SCAP1* is to integrate different aspects of GC biology including specification, spacing, maturation and function.

Keywords: Arabidopsis, *SCAP1* (AT5G65590), Guard Cells development, DOF-type transcription factors, *SPCH* (AT5G53210), *AtMYB60* (AT1G08810)

Background

Guard cells (GCs) are specialised epidermal cells which form stomatal pores, through which gas exchange can occur. Since transpiration is linked to plant growth and survival, control of GC number, distribution and activity is tightly regulated. Mature GC pairs form in the epidermal cell layer and originate from a single undifferentiated protodermal cell (PDC). Each PDC undergoes a series of cell divisions and successive cell-state transitions. These transitional states are characterized by changes in cell morphology and are associated with alterations in the transcriptomic signature [1–3]. A subset of PDCs, termed meristemoid mother cells – MMCs –, become

competent to initiate the stomatal cell lineage. The MMCs divide asymmetrically to produce a small triangular cell, the meristemoid, which serves as precursor of stomata guard cells and a larger cell referred to as the stomatal lineage ground cell (SLGC). The SLGC has the potential to directly differentiate into a lobed pavement cell or alternatively, to divide again asymmetrically to produce satellite meristemoids. All new meristemoids are oriented at least one cell away from an existing meristemoid according to the one-cell-spacing rule [3–7]. After up to three rounds of amplifying divisions, meristemoids mature into guard mother cells (GMC) acquiring the distinct rounded shape. A GMC divides symmetrically to generate two paired guard cells, which form the stomata pore. The genes responsible for GC specification and development have been characterised: the bHLH-type transcription factors (TFs) *SPEECHLESS (SPCH)*, *MUTE*,

* Correspondence: massimo.galbiati@unimi.it; lucio.conti@unimi.it
¹Dipartimento di Bioscienze, Università degli studi di Milano, Via Celoria 26, 20133 Milan, Italy
Full list of author information is available at the end of the article



© 2016 The Author(s). **Open Access** This article is distributed under the terms of the Creative Commons Attribution 4.0 International License (<http://creativecommons.org/licenses/by/4.0/>), which permits unrestricted use, distribution, and reproduction in any medium, provided you give appropriate credit to the original author(s) and the source, provide a link to the Creative Commons license, and indicate if changes were made. The Creative Commons Public Domain Dedication waiver (<http://creativecommons.org/publicdomain/zero/1.0/>) applies to the data made available in this article, unless otherwise stated.

and *FAMA* act sequentially to regulate formation of meristemoids, GMCs and GCs, respectively [8–10]. Alongside the afore-mentioned genes, another class of bHLH-type TFs, *SCREAM/ICE1* and *SCREAM2* redundantly affect the activities of *SPCH*, *MUTE* and *FAMA* through heterodimerization [11]. Previous studies have shown that *SPCH* is required for cells to enter the stomatal cell lineage and to promote the amplifying divisions of the meristemoids [9, 10, 12]. Experiments utilising *SPCH* promoter-reporter transcriptional fusions revealed that *SPCH* is expressed in the developing leaf epidermis and persists in GMC and GCs throughout the lineage. However, the *SPCH* protein has only been detected in undifferentiated PDCs, MMCs and in young meristemoids, suggesting that *SPCH* is regulated at the post-transcriptional level [9]. The activity of *SPCH* protein is negatively regulated by a signalling cascade, which includes secreted peptides EPIDERMAL PATTERNING FACTORS 1 and 2 (*EPF1/2*), leucine-rich repeat (LRR) receptor-like kinases *ERECTA* and *TOO MANY MOUTHS (TMM)* [3–5, 7, 13, 14]. The *MITOGEN ACTIVATED KINASE (MAPK)* genes act downstream of the LRR receptors and include *YODA*, *MKK4/MKK5* and *MPK3/MPK6* [15–17]. Stimulation of MAPK results in *SPCH* phosphorylation and inactivation by proteasomal degradation [1–3, 15, 18].

Several signals converge to regulate the stability of *SPCH* protein, including the phytohormone Brassinosteroid and CO_2 [19, 20]. *SPCH* protein stabilization in protodermal cells is critical to trigger its transcriptional activity and consequent GC lineage entry. Among the direct targets of *SPCH* is the *EPF2* gene which encodes a peptide that activates a regulatory feed back loop that promotes *SPCH* protein destabilization [21]. Therefore modulation of *SPCH* activity translates multiple environmental and endogenous developmental signals into different GC patterns [8–10, 22].

Besides bHLHs, other transcription factors may play an important role in GC specification. The DNA BINDING WITH ONE FINGER (DOF) proteins are an important class of transcriptional regulators in *Arabidopsis thaliana* comprising 37 members [11, 23]. These proteins have been shown to be involved in several aspects of plant development including growth, germination and abiotic stress response [9, 10, 12, 24]. Also, DOF-type factors are implicated in cell cycle control [9, 25]. In stomata development, DOFs have been hypothesized to play a role in GC maturation [3–5, 7, 13, 14, 26, 27]. Recently the DOF transcription factor *STOMATAL CARPENTER 1 (SCAP1)* has been shown to directly regulate essential processes related to guard cell maturation and function. Mutants of *scap1* display altered levels of transcripts of multiple genes directly involved in stomatal movement and furthermore are defective in some mechanical properties of the GC cell wall [28]. The potential role of *SCAP1* in stomata

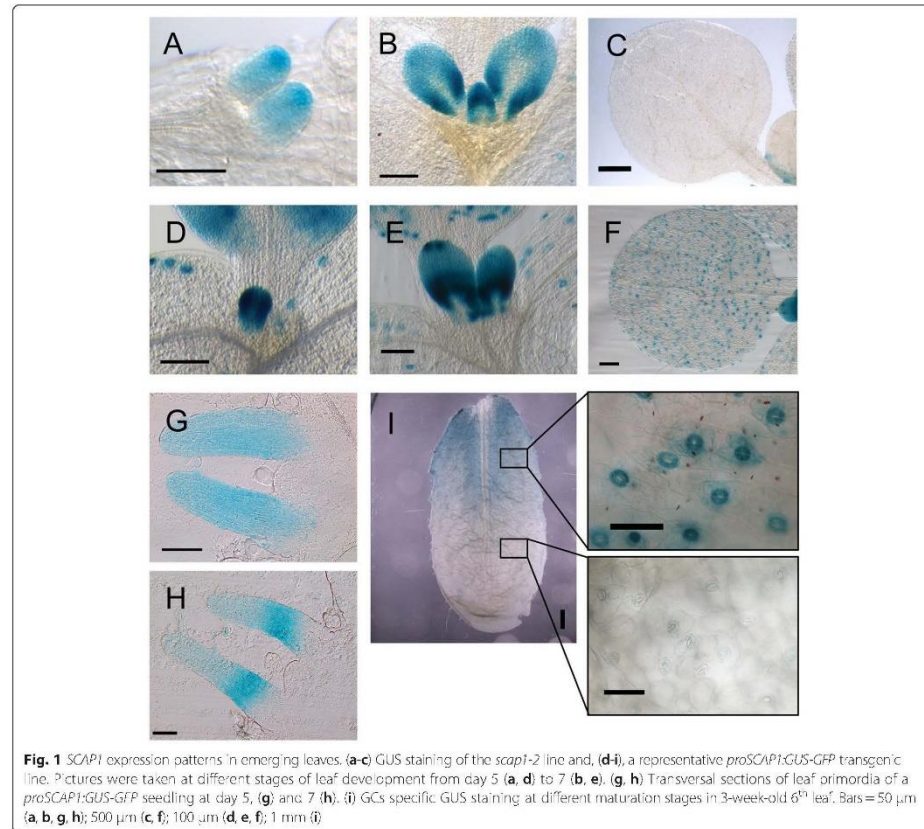
patterning has not previously been investigated. In this study we provide evidence that *SCAP1* plays a key role in GC patterning, in a manner that is temporally and spatially distinct from its role in GC maturation. We observed *SCAP1* expression throughout the leaf lamina at early developmental stages, when primordia consist of only undifferentiated cells. Mutants of *scap1* had significantly reduced stomatal density and stomatal index compared with wild type. Conversely, over expression of *SCAP1* resulted in increased stomatal density and stomatal index. Furthermore *SCAP1* expression temporarily overlapped with the expression of several other genes that regulate stomatal patterning, consistent with *SCAP1* playing a role in stomata patterning. Induction of *SCAP1* activity using a glucocorticoid-based system resulted in repression of several early stomatal patterning genes including *SPCH*, *MUTE* and *EPF2*, and the ectopic production of GCs with altered spacing and morphology. In accordance with these phenotypes, detailed confocal microscopic analysis of marker lines on expanding leaf primordia revealed that high levels of *SCAP1* correlated with an increase in the population of meristemoids as well as the number of undifferentiated PDCs. Our work thus provides evidence for a novel role for *SCAP1* in stomatal patterning

Results

SCAP1 expression in leaf precedes GC specification

To further elucidate the role of *SCAP1* in stomatal development we characterised a *scap1* transposon insertion mutant publicly available in the Cold Spring Harbour collection. This allele (dubbed *scap1-2*) carries a gene trap construct, which permits endogenous patterns of expression of the trapped gene to be visualised via GUS staining. We characterised *scap1-2* plants at different developmental stages and revealed two distinct patterns of gene expression during leaf development (Fig. 1). At early developmental stages (preceding GC formation) GUS staining was present throughout the emerging leaf primordia (Fig. 1a). At later developmental stages of primordia, levels of GUS staining were highest at the flanks of the lamina and much reduced in the midvein region (Fig. 1b). In mature organs (i.e. leaves and cotyledons) the GUS signal was mainly confined to maturing GCs (Fig. 1c). GC-specific *SCAP1* expression was very faint in *scap1-2* mutants compared with transgenic *proSCAP1:GUS-GFP* lines (Fig. 1f) (see below).

The *scap1-2* mutant carries a *GUS* reporter gene in antisense orientation with respect to the *SCAP1* open reading frame (Additional file 1). To verify that the GUS pattern observed in the *scap1-2* allele reflects endogenous *SCAP1* promoter activity we fused a 2977 base pairs genomic region upstream of the *SCAP1* coding sequence to *GUS* and *GFP* and generated independent *Arabidopsis*



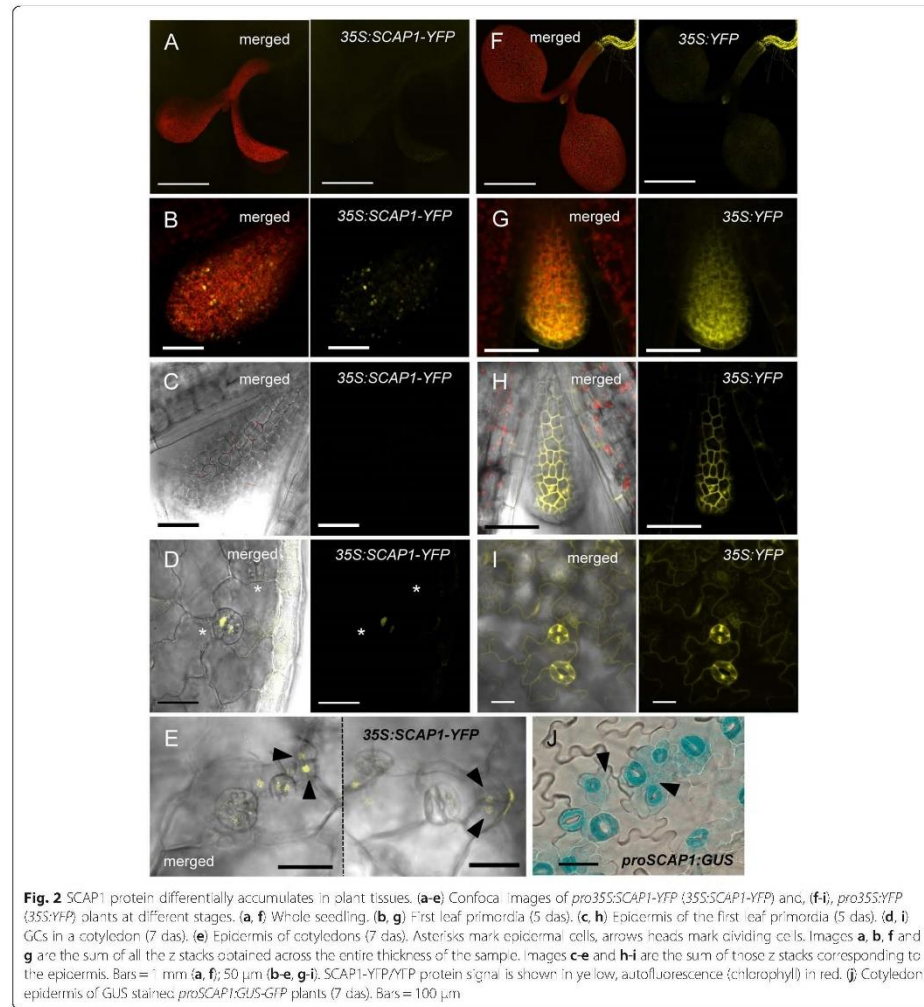
stable transformants. These transgenic plants (*proSCAP1:GUS-GFP*) displayed GUS activity in young leaf primordia which was similar to that observed in *scap1-2* plants (Fig. 1d, e, f). At later stages of development, the pattern of GUS accumulation in the *proSCAP1:GUS-GFP* lines was broadly similar with that observed in *scap1-2*. Coincident with the expansion of leaf primordia, GUS staining gradually disappeared in the midvein region (Fig. 1e). In young leaf primordia, *SCAP1* promoter activity appeared stronger in the proximal region of the leaf lamina. This observation was confirmed by analysing transverse sections of GUS stained *proSCAP1:GUS-GFP* plants. At early stages of primordium differentiation, the *SCAP1* promoter was uniformly active in the mesophyll and the epidermis of leaf primordia (Fig. 1g). Subsequently we observed a sharp proximodistal gradient of GUS accumulation, with

increased signal in the proximal part of the leaf primordium (Fig. 1h). *SCAP1* expression was initially strong in GCs but tended to decrease in a distal to proximal gradient coincident with the maturation of GCs (Fig. 1i). These data reveal a previously undisclosed pattern of *SCAP1* expression in early leaf development, which could suggest an additional role for *SCAP1* alongside its already known function in GC maturation and function.

To gain insights in *SCAP1* protein cellular localization we generated lines of Arabidopsis overexpressing *SCAP1* ($n = 15$). The *SCAP1* coding sequence was fused to the *YELLOW FLUORESCENT PROTEIN (YFP)* gene under the control of the constitutive promoter *CaMV35S (pro35S:SCAP1-YFP)*. We anticipated that this construct would generate ectopic expression of *SCAP1* throughout all plant tissues, however we were only able to observe

YFP in a subset of plant tissues. The SCAP1-YFP protein-derived signal was absent in roots (Fig. 2a) whereas control plants overexpressing soluble YFP showed an ectopic signal in all tissues (Fig. 2f-i). We observed SCAP1-YFP accumulation in nuclei of mesophyll cells in young leaf primordia (Fig. 2b), while very little, if any SCAP1-YFP signal was observed in adjacent epidermal cells (Fig. 2c).

At later stages we observed SCAP1-YFP in GCs, which is consistent with the known function of SCAP1 in GC maturation (Fig. 2d). Detailed analysis of the epidermal layer of *pro35S:SCAP1-YFP* cotyledons revealed low levels of nuclear SCAP1-YFP protein in dividing (or recently divided) epidermal cells adjacent to differentiated GCs (Fig. 2e). In summary, the expression of SCAP1-YFP appeared restricted to the sub-epidermal layer in early



leaf primordia and only at later stages of leaf development the expression become visible in mature GCs and adjacent cells. The pattern of SCAP1 protein accumulation at later stages is similar to the domain where the SCAP1 promoter was transcriptionally active as shown by GUS staining of cotyledons of *proSCAP1:GUS-GFP* plants (Fig. 2j). We conclude that the SCAP1 protein is subject to a strong post-transcriptional regulation and that the site of SCAP1 protein accumulation only partially overlaps with the pattern of SCAP1 gene expression.

SCAP1 regulates GC development

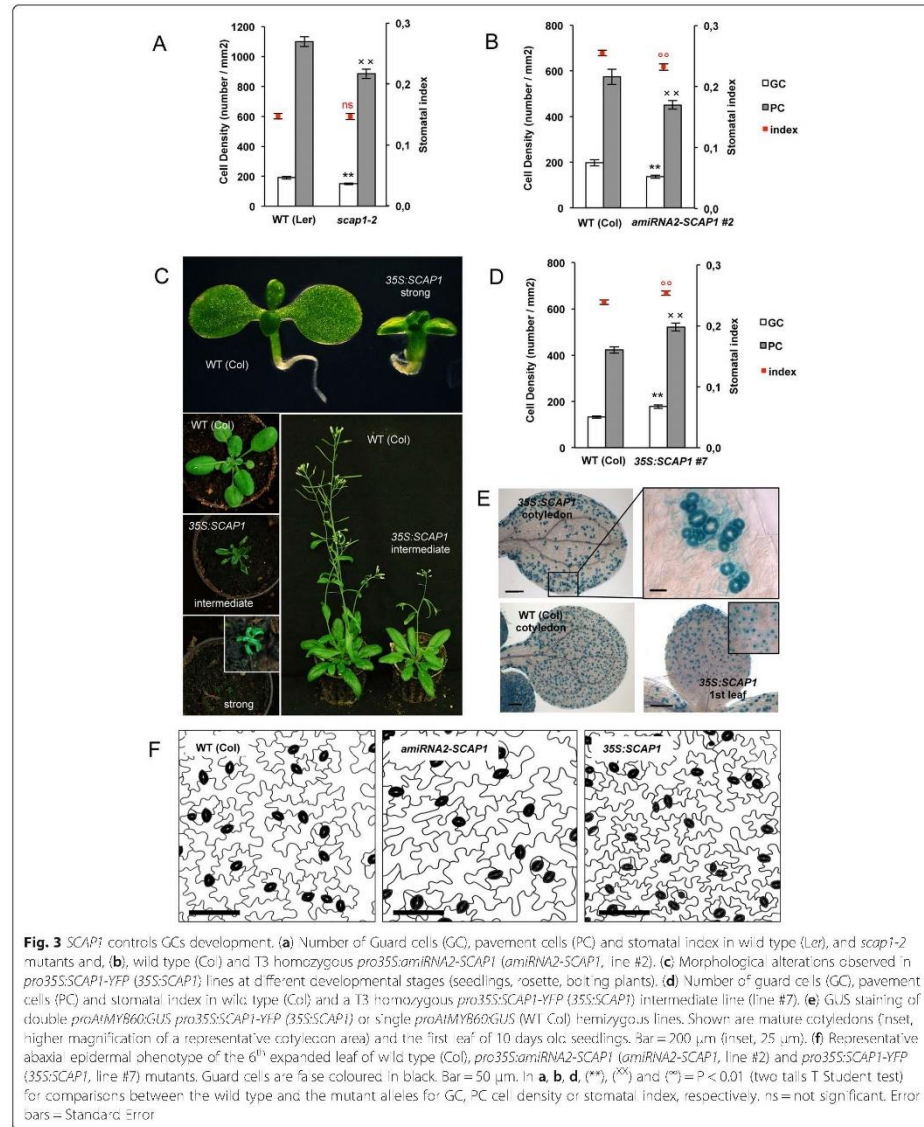
The *scap1-2* allele was likely a null since it did not produce any detectable full-length SCAP1 transcript (Additional file 1). To further investigate the role of SCAP1 in stomatal development we compared the number of GCs in adult leaves of *scap1-2* mutants with that of wild type (ecotype Landsberg, *Ler*). In *scap1-2* stomatal density is reduced (Fig. 3a) but this was not reflected in a reduction of stomatal index since *scap1-2* plants also have a significant reduction in pavement cells compared to wild type (Fig. 3a, Additional file 2). To confirm these observations we generated two independent artificial microRNA (amiRNA1 and 2) constructs specifically targeting SCAP1 in wild type (ecotype Columbia, Col). We isolated sixteen and fourteen independent T1 lines for *amiRNA1-SCAP1* and *amiRNA2-SCAP1*, respectively and confirmed that T2 lines had reduced levels of SCAP1 transcript compared to wild type (Additional file 2). Downregulation of SCAP1 did not produce any obvious phenotypic effects on overall plant morphology, similar to *scap1-2* plants. Closer observations revealed that leaves of segregating T2 *amiRNA-SCAP1* knock-down independent lines produced significantly fewer GCs than wild type (Additional file 2). In homozygous T3 *amiRNA-SCAP1* lines we observed a general reduction in cell density, analogous to the result observed in *scap1-2*, and also a reduction in stomatal index. Taken together these results suggest that SCAP1 plays a role in GCs specification in addition to its role in cell division (Fig. 3b, f).

To determine whether overexpression of SCAP1 is sufficient to alter GC development we analysed the phenotypes of the aforementioned *pro35S:SCAP1-YFP* lines. We observed T1 individuals with altered phenotypes ranging in severity from strong to mild (Fig. 3c). Plants classified as strong over-expressors of SCAP1 (60 %) exhibited numerous developmental defects including reduced germination, slow and stunted growth, upward-curling leaves and sterility. A second phenotypic class (40 %) displayed a less severe phenotype, exhibiting reduced growth compared to wild type at the seedling stage. In transgenic lines with intermediate phenotype, defects appeared to recover at later stages of development so that these lines were eventually comparable in final size and leaf area to wild type.

Given the strong phenotypic abnormalities in strong SCAP1-YFP overexpressing lines, we carried out our analyses on intermediate lines, which are more comparable to wild type in terms of plant morphology. Lines with intermediate levels of *pro35S:SCAP1-YFP* had an increased number of both GCs and PCs in true leaves compared to wild type and this was accompanied by an overall increase in stomatal index (Fig. 3d, f and Additional file 2). The epidermal phenotype of *pro35S:SCAP1-YFP* plants was characterised in more detail by crossing to a GC-specific reporter line carrying *proAtMYB60:GUS* [29] which allowed us to detect subtler GC patterning defects. The cotyledons of *pro35S:SCAP1-YFP* showed gross alterations in stomata spacing as shown by the presence of massive clusters of GCs which were located at the edges of the cotyledon, especially on the adaxial surface (Fig. 3e). Interestingly, no clusters of GCs were detectable in true leaves of *pro35S:SCAP1-YFP* plants. Furthermore, based on GUS detection, over expression of SCAP1 did not confer guard cell identity to every cell type, nor was it able to induce stomata production in the cotyledon mesophyll cells (Fig. 3e). Thus, SCAP1 also plays an important role in determining GC spacing, at least in cotyledons.

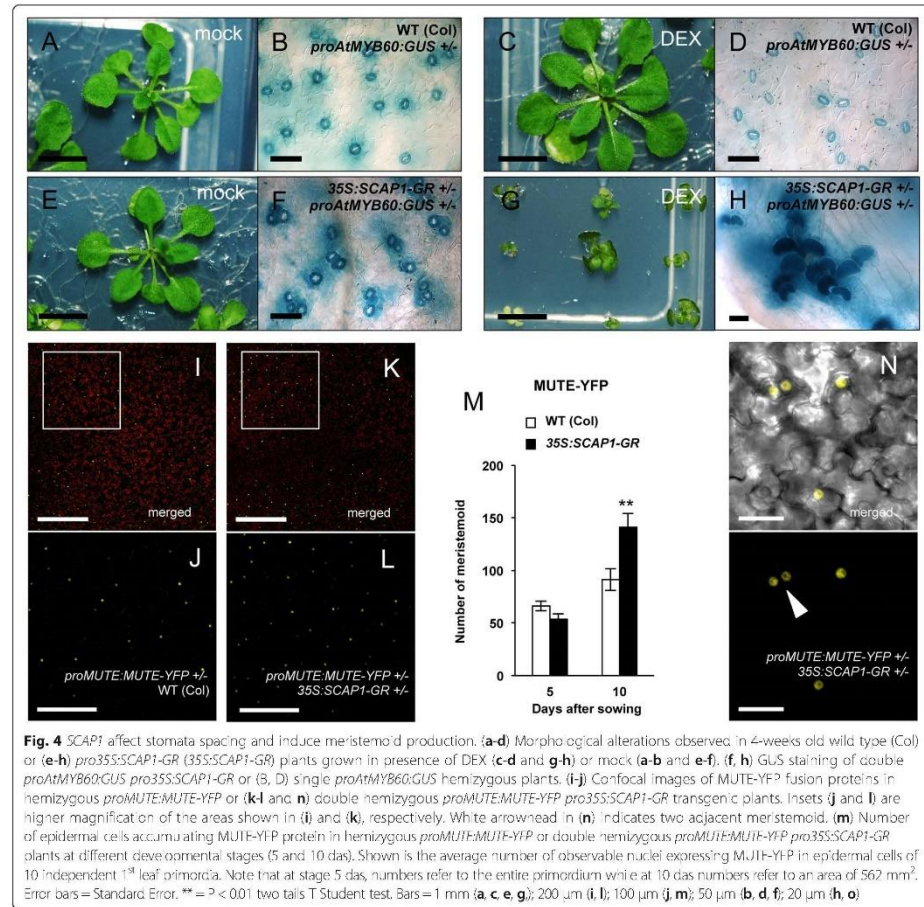
To confirm these observations we generated a second gain-of-function allele of SCAP1 in which constitutively expressed SCAP1 is fused to the *GLUCOCORTICOID RECEPTOR* (*pro35S:SCAP1-GR*) [30]. In this inducible system the fusion protein is normally localised in the cytosol but can shuttle to the nucleus upon application of DEXAMETHASONE (DEX) to trigger a rapid SCAP1-dependent transcriptional activation [30]. Prior to induction, plants of *pro35S:SCAP1-GR* were phenotypically indistinguishable from the wild type (Fig. 4e), despite accumulating high levels of SCAP1-GR transcript (Additional file 3). *pro35S:SCAP1-GR* seeds did not germinate on media supplemented with DEX, suggesting high levels of SCAP1 could inhibit germination. Therefore we grew *pro35S:SCAP1-GR* seeds on DEX-free media and transferred seedlings 5 days after sowing on media supplemented with DEX or a mock solution. Twenty days following transfer to DEX *pro35S:SCAP1-GR* plants produced similar morphological alterations previously observed in strong *pro35S:SCAP1-YFP* transgenic plants (Fig. 4g). In contrast, DEX treatment had no significant morphological effects in control plants (Fig. 4c).

To further investigate the epidermal phenotype of SCAP1-GR plants we analysed the pattern of GUS distribution in *pro35S:SCAP1-GR proAtMYB60:GUS* double hemizygous plants. Microscopic analysis of untreated *pro35S:SCAP1-GR proAtMYB60:GUS* plants revealed GCs cluster in both cotyledons and leaves although these clusters were generally made of few GCs (Fig. 4f and Additional file 3). Also, *pro35S:SCAP1-GR proAtMYB60:GUS* plants frequently presented unpaired GCs as well as



clusters of meristemoid cells adjacent to GCs (Fig. 4f and Additional file 3). DEX treated *pro35S:SCAP1-GR proAtMYB60:GUS* plants, showed an even stronger

phenotype in stomata patterning compared with the untreated control as we observed an overproduction of GCs in true leaves, which were grouped in extensive



clusters (Fig. 4h). Also in this case, GUS detection revealed that clusters were frequently made of unpaired GCs (Fig. 4h).

To identify whether the altered stomata patterning of *pro35S:SCAP1-GR* could depend on increased number of cells entering the stomatal lineage we generated double hemizygous *proMUTE:MUTE-YFP pro35S:SCAP1-GR* plants which allowed us to visualise meristemoid cells. Even in the absence of DEX, at the later stages of primordium development *pro35S:SCAP1-GR proMUTE:MUTE-YFP* plants displayed an increased number of meristemoids compared to control hemizygous *proMUTE:MUTE-YFP* plants (Fig. 4i to l). A closer inspection of the

epidermis revealed that in *pro35S:SCAP1-GR proMUTE:MUTE-YFP* meristemoid cells often did not follow the correct spacing and were close to each other (Fig. 4n). Taken together *SCAP1* appears to regulate different aspects of stomata development, including stomata number, distribution and spacing.

Effects of *SCAP1* on stomatal patterning gene expression

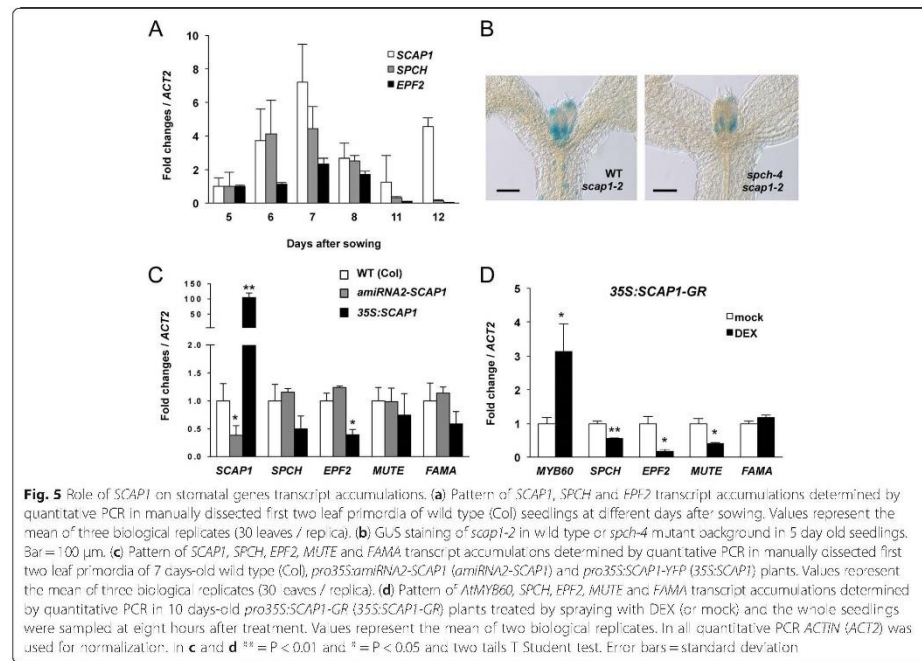
The early activation of *SCAP1* in leaf primordia coupled with its role in stomata development led us to hypothesise a genetic interaction between *SCAP1* and genes that regulate stomatal patterning. Two genes, *SPCH* and *EPF2* that are required for early stomatal patterning are

expressed in the protodermal cells of leaf primordia. To determine the timing of *SCAP1* activation with respect to stomata early patterning genes we sampled primordia of leaves one and two from seedlings at different time points, representative of different stages of leaf development. Transcript abundance of *SCAP1*, *SPCH* and *EPF2* peaked at 7 days after sowing and subsequently decreased during the next 3 days (Fig. 5a). At around 12 days after sowing, *SCAP1* expression levels reactivated, presumably in relation to GC formation in the maturing leaf (Fig. 5a). To test if *SCAP1* expression is dependent on *SPCH*, we crossed *scap1-2* (*Ler*) with *spch-4* (*Col*) mutants to obtain homozygous *spch* mutants carrying a transposon tagged version of *SCAP1*. Of 26 *spch* homozygous plants, two displayed GUS staining that was similar in terms of pattern of expression to wild type *SPCH* plants. The reduced frequency of this genotype could be due to genetic linkage since *SPCH* and *SCAP1* are physically close on chromosome 5. *SPCH* is thus not required for the early *SCAP1* activation (Fig. 5b), consistent with previous studies indicating that *SCAP1* was not a high-confidence *SPCH* target [21].

We next measured transcript accumulation of early stomatal patterning genes in plants with different dosage

of *SCAP1*. Transcript levels of *SPCH*, *EPF2*, *MUTE* and *FAMA* were analysed at 7 DAS when levels of *SCAP1*, *SPCH* and *EPF2* expression are at their peak in the wild type (Fig. 5a). In loss-of-function *scap1* mutant plants we detected no significant changes in transcript levels of any of the genes analysed compared with the wild type (Fig. 5c and additional file 4). If *SPCH* and *SCAP1* genetically interact we might predict that increased GC production in *pro35S:SCAP1-YFP* plants would be reflected in an increased level and/or activity of positive regulators of stomatal production, or alternatively down regulation of negative regulators. To determine if this is the case we analysed transcript levels of *SPCH*, *EPF2*, *MUTE* and *FAMA* in the *pro35S:SCAP1-YFP* over expression line. Our analysis confirmed that this transgene conferred around 100-fold increase in *SCAP1* transcript accumulation when compared to wild type (Fig. 5c). Analysis at 7 DAS revealed no significant difference in transcript levels of either *MUTE* or *FAMA* compared to wild type (Fig. 5c). However, we noticed a down regulation of *EPF2* and, marginally, *SPCH* as compared to the wild type (Fig. 5c).

To confirm these observations we analysed the stomatal patterning genes in *pro35S:SCAP1-GR* plants after a short DEX induction. We first tested the ability of *SCAP1:GR*



protein to activate expression of its known target gene *AtMYB60* [28]. Indeed, *scap1* loss of function mutants displayed reduced levels of *AtMYB60* accumulation compared with wild type (Additional file 3). Conversely, compared to wild type plants, *pro35S:SCAP1-GR* plants showed up-regulation of *AtMYB60* after DEX treatment (Fig. 5d and Additional file 3). These data indicate that *SCAP1-GR* protein retains its biochemical function in the context of transcriptional regulation.

Under similar conditions, eight hours after induction we observed a strong downregulation of the negative stomatal regulator *EPF2* (Fig. 5d and Additional file 4). Such *EPF2* downregulation became detectable in DEX treated compared to mock treated plants after four hours and was maintained throughout our experiment (Additional file 4). Besides *EPF2* we also observed a general downregulation of *SPCH* transcript levels and its direct target gene *MUTE*, but not *FAMA* (Fig. 5d). As a control, DEX treatment on wild type plants had no effects in altering stomata patterning genes (Additional file 4). *SCAP1* can therefore act both as a positive and negative transcriptional regulator. However as these experiments were performed on whole seedlings, they may not entirely reveal the mode of action of *SCAP1* during the early stages of leaf development.

SCAP1 affects SPCH protein accumulation

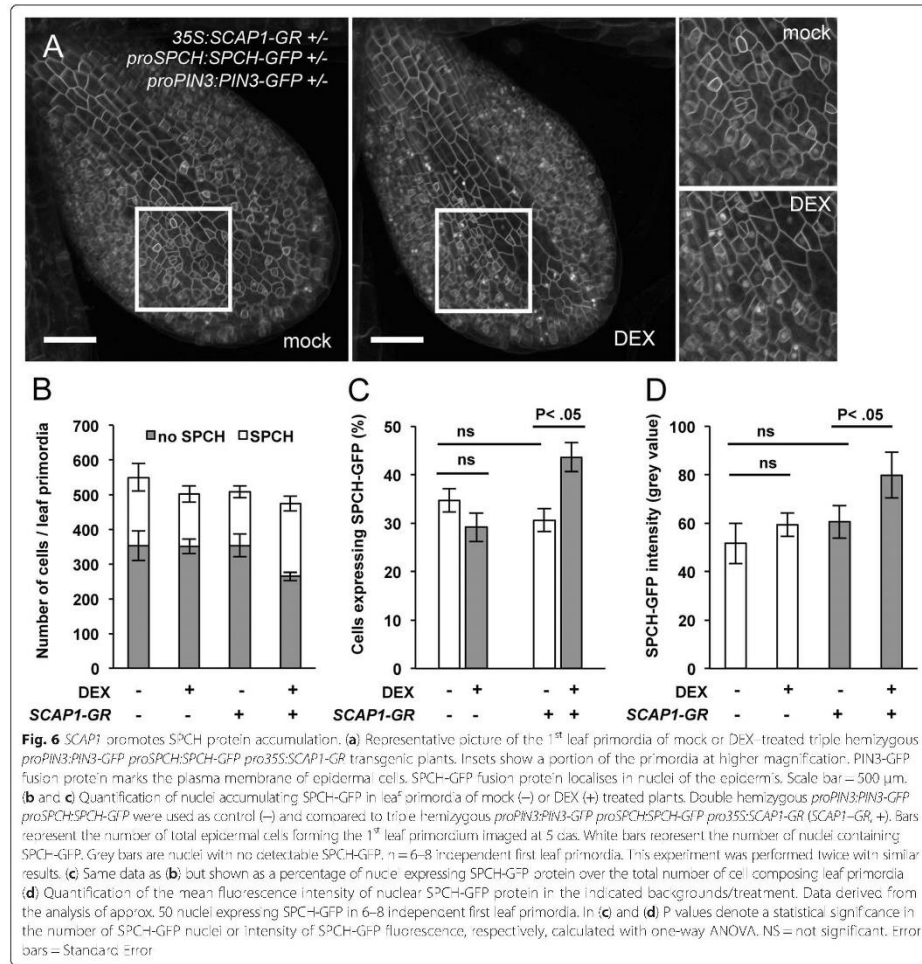
Constitutive expression of *SCAP1* resulted in several developmental abnormalities, which could indirectly alter GC development. To avoid this potential problem, we analysed the effect of *SCAP1* after rapid activation by DEX using the *pro35S:SCAP1-GR* line. We studied the pattern *SPCH-GFP* fusion protein accumulation in the primordia of the first leaf (5 das) through microscope confocal analysis by visualizing nuclear fluorescence of GREEN FLUORESCENT PROTEIN (GFP) in a *proSPCH:SPCH-GFP* line. At 5 das, we did not detect variations in the number of meristemoids, suggesting that *SCAP1-GR* expression did not yet produce detectable effects at this particular stage (Fig. 4m). We reasoned that by providing a short pulse of *SCAP1* (through DEX applications) we could influence the competence of cells entering the stomata lineage (as estimated by the number of cells expressing *SPCH*). We generated hemizygous *proSPCH:SPCH-GFP proPIN3:PIN3-GFP pro35S:SCAP1-GR* or hemizygous *proSPCH:SPCH-GFP proPIN3:PIN3-GFP* in a wild type Col background. The *PIN3-GFP* fusion protein was used as plasma membrane marker and allowed us to identify individual epidermal cells. In control double hemizygous *proSPCH:SPCH-GFP proPIN3:PIN3-GFP* plants no significant differences were found in the number of *SPCH-GFP* expressing cells following DEX treatment (Fig. 6b and c). Also, DEX treatment did not alter the average intensity of nuclear *SPCH-GFP*

fluorescence, which rules out a general effect of DEX on *SPCH-GFP* protein accumulation (Fig. 6d). *proSPCH:SPCH-GFP proPIN3:PIN3-GFP pro35S:SCAP1-GR* hemizygous lines showed no apparent defects in *SPCH-GFP* accumulation at this developmental stage (Fig. 6a to d). At 6 hours following DEX treatment, *proSPCH:SPCH-GFP proPIN3:PIN3-GFP pro35S:SCAP1-GR* plants showed a significant increase in the proportion of nuclei expressing *SPCH-GFP* protein (Fig. 6a, b and c). Furthermore, this was accompanied with a general increase in the mean nuclear GFP fluorescence intensity ($n > 50$ nuclei / 1st leaf primordia for each genotype/treatment combination) (Fig. 6a, d). It is most likely that the increased nuclear GFP signals reflected increased *SPCH-GFP* protein since neither DEX treatment or *SCAP1-GR* alone caused variations in nuclear GFP accumulations (e.g. as a result of detachment of GFP from the membrane marker *PIN3* or *SPCH*). Increased *SPCH* stabilisation in protodermal cells may thus contribute to stomata patterning alterations in *SCAP1* over expressing plants.

Discussion

Previously *SCAP1* was shown to control GC morphology and activity, a role coherent with its expression in developing and fully mature stomata [28]. Here we report an in-depth analysis of the spatio-temporal control of *SCAP1* expression throughout leaf development. Our results indicate an early activation of *SCAP1* expression in leaf primordia coinciding with the expression of genes controlling stomatal cell lineage and thus before GC differentiation [6, 7, 10, 31]. This pattern of *SCAP1* gene expression is maintained in *spch* mutants demonstrating that *SCAP1* early expression is independent of GC lineage specification. Besides transcriptional regulation, *SCAP1* is regulated at the post-transcriptional level, as constitutively expressed *SCAP1-YFP* fusion did not accumulate in all plant tissues, despite high levels of expression. In leaf primordia where *SCAP1* promoter is active in both epidermis and mesophyll, *SCAP1-YFP* protein was mainly observed in the mesophyll and in GCs. This observation may either suggest that the role of *SCAP1* in GC development is indirect (e.g. to promote signals from the mesophyll cells to the epidermis [32–35] or that the activity of *SCAP1* in the epidermis is tightly regulated as a result of rapid protein turn over. Therefore, *SCAP1* protein may accumulate in the epidermis in some cell types or at certain stages. Future experiments involving the use of tissue/cell specific promoters to drive *SCAP1* expression may help elucidate the precise cell/tissue-specific pattern of *SCAP1* stabilization and provide clues as to the mode of action of *SCAP1* in GC patterning.

A question emerging from our study is whether the role of *SCAP1* in stomata patterning is direct or indirect. For example, changes in CO₂ perceived by one leaf affect



the patterning of GCs in subsequent leaves, implying the existence of a signalling network to optimize GC number and patterning according to environmental conditions [36–38]. Since *scap1* mutants are impaired in GC function one could hypothesise that such alterations in stomata activity may affect global GC development. Although we cannot exclude this possibility, we also showed that *SCAP1* overexpressing plants had GC alterations in embryonic tissues such as cotyledons (where we observed GCs cluster). *SCAP1-GR* plants also had increased stomata cells density in true leaves arguing in

favour of a direct role of *SCAP1* in stomata patterning. Furthermore, a detailed analysis of *SCAP1-GR* plants revealed a role of *SCAP1* in both promoting GCs production and directing the spacing of meristemoid at the very early stages of stomatal cell lineage specification (Fig. 4i to n). These observations are indicative of a role of *SCAP1* in GC patterning which is independent of its general function in GC maturation. The accumulation of *SCAP1* transcript in young leaf primordia is consistent with an early role for *SCAP1* in controlling GC development. *SCAP1* could also play an additional role in the

specification of GCs at later stages of leaf development, for example by controlling satellite meristemoid cells, since *SCAP1* expression can be transiently detected in dividing (or recently divided) epidermal cells adjacent to differentiated GCs in older tissue (Fig. 2e).

The overall increased cell density of *SCAP1* overexpressing plants is reminiscent of *SPCH* overexpression or *epf2* mutant plants [6, 7, 9, 15]. Ectopic expression of *SCAP1* could not initiate GCs development in the interior layers of cotyledons or leaves, suggesting that *SCAP1* affects GCs production in conjunction with the known elements of stomatal cell lineage pathway (e.g. *SPCH*, *MUTE* and *FAMA*). Therefore, one attractive hypothesis arising from these observations is that *SCAP1* participates in the same genetic pathway of GC development controlled by *SPCH* and its regulators. Some evidence for this was provided by experiments which showed expression of *SPCH*, *EPF2* and *SCAP1* temporarily overlapping during development. Mutants of *scap1* are not defective in global *SPCH* or *EPF2* gene expression levels, although we have not tested the possibility that the spatial distribution of *SPCH* or *EPF2* genes might be altered in *scap1* mutant plants. Furthermore, the relatively weak epidermal phenotype of *scap1* mutants might be masked by a yet unknown *SCAP1*-like function.

Not only did *SCAP1* affect stomata number but also stomata spacing. Clusters of GCs were present in post-embryonic tissues in *pro35S:SCAP1-GR* plants, a phenotype which was even further exacerbated upon DEX application. Surprisingly, this phenotype was not observed in *pro35S:SCAP1-YFP* plants (in which this spacing defects were confined to the cotyledons). The reasons why the *SCAP1-GR* fusion is more active than *SCAP1-YFP* is currently unknown. As *SCAP1* accumulation is tightly controlled at the posttranscriptional levels, one possibility is that the GR moiety protects it from degradation.

SCAP1 overexpression caused *EPF2* downregulation, which could account for spacing defects. The signalling peptides *EPF2* acts early in the stomatal lineage controlling asymmetric cell division and thus regulating stomatal density [7]. Previously, comparably similar defects in stomata density and spacing were described in mutants of *epf2*, *epf1* and *tmm* [3, 5–7, 31], or in transgenic plants overexpressing *SPCH*, *MUTE* or *FAMA* [8, 9, 15]. The *SPCH* protein directly binds and positively regulates the transcription of several stomatal patterning genes including *EPF2*, *MUTE* and *TMM* as well as its own transcription [21]. Our data indicates that some of the direct targets of *SPCH* are negatively regulated by *SCAP1*, suggesting a competition between *SPCH* and *SCAP1* for the regulation of these genes at transcriptional level. In this model, *SCAP1* promotes stomata production and boosts cell divisions by enhancing *SPCH* protein accumulation possibly as a result of down regulation of *EPF2*

transcript. Whether this competition occurs in the same cell and/or is direct should be elucidated by further experiments.

Conclusions

Our results highlight a previously unappreciated role for *SCAP1* in stomata development. We propose that *SCAP1* is an essential component of a genetic pathway to fine-tune stomatal production in *Arabidopsis*. A key control mechanism of this loop could involve a *SCAP1*-mediated downregulation of *EPF2* counteracting the previously demonstrated *SPCH*-mediated activation of *EPF2* [21]. DOF-type factors have been proposed to play an important role in GC maturation and function based on an enrichment of a DOF binding motif in GC specific genes [26, 27]. It would be interesting to test whether this observation can also be extended to genes involved in the early events of GC lineage specification. In this sense, *SCAP1* may link GC patterning and function.

Methods

Plant material and growth conditions

In this study we used *Arabidopsis thaliana* ecotypes Columbia (Col) and Landsberg *erecta* (*Ler*). Seeds were germinated and plants grown in a controlled-environment cabinet at a temperature of 20 °C to 23 °C, 65 % relative humidity, under long day conditions (16 h of light/8 h of dark). Light was cool-white fluorescent tubes (Osram; Sylvania) at a fluency of 120 to 150 μE (photosynthetically active radiation). The *scap1-2* allele is a transposon insertion (line GT-23689, *Ler* background) obtained from the Cold Spring Harbour gene trap collection (<http://genetraps.cshl.edu>). The *spch-4* knock out allele and the *proSPCH:SPCH-GFP proPIN3:PIN3-GFP* and *proMUTE:MUTE-YFP* lines were previously detailed [9, 12, 39]. The *proAtMYB60:GUS* line (Col background) was previously described [29]. The *proSCAP1:GUS-GFP*, *pro35S:amiRNA-SCAP1*, *pro35S:SCAP1-YFP* and *pro35S:SCAP1-GR* lines were generated in this study in wild-type Col background except for the *proSCAP1:GUS-GFP* which was in the *Ler* background. Transgenic lines were obtained using the floral dipping method [40]. Transgenic seedlings were selected on Murashige and Skoog (MS) media with kanamycin (50 μg/ml) (*pro35S:SCAP1-GR*) or Basta (25 μM) (*proSCAP1:GUS-GFP*, *pro35S:amiRNA-SCAP1*, *pro35S:SCAP1-YFP* and *pro35S:SCAP1-GR*). For each construct several T1 independent lines were generated and single insertion transgenic plants were isolated based on the segregation of resistance genes. Independent homozygous T3 lines analysed in this study are: *pro35S:SCAP1-YFP* (#4 and #7), *pro35S:amiRNA-SCAP1* (amiRNA1-2, amiRNA2-2 and amiRNA2-5), *proSCAP1:GUS-GFP* (#8 and #2), *pro35S:SCAP1-GR* (#34 and #26).

Glucocorticoid applications were done by administering a solution of DEX (13 μ M DEX, 0.01 % (v/v) Tween 20) either by spraying (for expression analysis) or by soaking seedlings in a MS medium containing DEX (for confocal and GUS experiments). Stratified *pro35S:SCAP1-GR* seeds were germinated on MS plates for 5 to 7 days before spraying with DEX or mock treated or transferred in phytatray (Sigma–Aldrich) on MS media containing DEX for prolonged glucocorticoid treatment.

Molecular cloning

To generate the *proSCAP1:GLIS-GFP* construct a 2977 bp region upstream of the *SCAP1* start codon was amplified from genomic DNA by PCR with oligos attB1-*SCAP1* and attB2-*SCAP1* which contain the *AttB* adaptors for Gateway-mediated cloning. The PCR product was cloned into *pDONR207* and subsequently transferred to *pBGWFS7* destination vector [41] according to the guidelines detailed in the Gateway protocol (Life Technologies). The *pro35S:amiRNA-SCAP1* constructs were engineered as detailed in <http://wmd3.weigelworld.org> [42] with primers I, II, III and IV. The PCR products containing *SCAP1*-specific amiRNA were cloned in the pENTR-DTOPO vector (Life Technologies) and transferred to the destination vector pEarleyGate 100 [43] via LR-mediated recombination. To generate the *pro35S:SCAP1-YFP*, the *SCAP1* open reading frame (without stop codon) was amplified by PCR from Arabidopsis DNA, with primers *SCAP1-Fw*, *SCAP1-Re2* and cloned into the pENTR-DTOPO vector (Life Technologies) and recombined with the Gateway destination vector pEarleyGate 101 [43]. The DEX-inducible *SCAP1* construct (*pro35S:SCAP1-GR*) was kindly provided by the RIKEN Plant Functional Genomic Minami Matsui lab. Sequences of the primers are detailed in Additional file 5.

Genotyping and transcript analysis

Sequences of the primers used for genotyping are provided in Additional file 5. Total RNA was extracted with TRIzol reagent following the manufacturer's instructions (Life Technologies). The first-strand cDNA was synthesized with 500 ng of total RNA using SuperScript VILO Reverse Transcriptase kit (Life Technologies). Quantitative real-time PCR was performed with Fast SYBR Green Master Mix (Applied Biosystems), and amplification was real-time monitored on a 7900 HT Fast Real-Time PCR system (Applied Biosystems). Changes in gene expression were calculated relative to *ACT2* using the $\Delta\Delta C_t$ method [44]. The qPCR primers to detect *SCAP1*, *AtMYB60*, *SPCH*, *EPF2*, *MUTE*, *FAMA* and *ACTIN* transcripts are detailed in Additional file 5.

β -glucuronidase (GUS) histochemical assay and Histological procedures

GUS staining was performed as previously described [26]. Depending on the experiment, incubation time was for 4 to 12 h at 37 °C. For detection of GUS staining in thin resin sections, after staining, samples were dehydrated in 70 % (v/v) ethanol, post-fixed over night at 4 °C in FAE (50 % [v/v] ethanol, 5 % [v/v] formaldehyde, 10 % [v/v] acetic acid), and further dehydrated in a series of 85 %, 95 % and 100 % (v/v) EtOH and embedded in Technovit 7100 resin according to the manufacturer's instructions (Heraeus Kulzer). Samples were sectioned with a microtome fitted with a stainless steel blade to a 7 μ M thickness.

Microscopy and quantitative analysis of fluorescence emission

For analysis of the stomatal pattern, the 6th expanded leaves of one-month-old plants (displaying an inflorescence of about 3–4 cm) were incubated in 70 % ethanol. The epidermis of the abaxial side was peeled and examined under a transmission light microscope (DM2500, Leica). For determining the mean stomatal index and density, one square area (0.2 mm²) of a leaf region was microphotographed and scored for cell parameters. Care was used to select a similar leaf region from the 6th leaf from at least 12 independent plants for each genotype in independent experiments. For confocal laser scanning microscopy, the abaxial side of first leaf primordia of 5-day-old seedlings expressing GFP- or YFP-tagged proteins were analysed under a Leica TCS SP5 confocal microscope. Fluorochromes were excited using an Argon laser (488 nm and 514 nm excitation for GFP and YFP, respectively) and emission collected at a 500 – 570 nm and 525 – 600 nm for the GFP and YFP, respectively. When comparing independent samples, the acquisition parameters (including z-step size) were maintained constant to enable measurement of GFP intensity in different primordia and different treatments. Fluorescence intensity of nuclear SPCH-GFP protein was analysed with ImageJ software (<http://imagej.nih.gov/ij/>). GFP fluorescence intensity was measured from individual nuclei (at least 50 for each primordium). A region of interest (ROI) tool was superimposed to selected nuclei so to include the largest possible nuclear area in single optical plane (z stack). An identical ROI size was used to process all the images so to minimise detection of background fluorescence.

Additional files

Additional file 1: Characterisation of the *scap1* mutant allele. (A) Schematic representation of the *SCAP1* loci. Grey boxes represent amiRNAs target regions and triangles represent transposon genomic insertion points for *scap1-2*. (B) Reverse Transcriptase-PCR analysis of *SCAP1* in wild type

(*Ler*) and *scap1-2* plants. Total RNA was isolated from 2-week-old seedlings and PCR was conducted for 35 cycles. Actin was used as a positive control and amplified for 25 cycles. (JPG 97 kb)

Additional file 2: *SCAP1* affects GCs development. (A) Representative abaxial epidermal phenotype of a 6th expanded leaf of wild type (*Ler*) and *scap1-2* mutants. Guard cells are false coloured in black. Scale bar = 50 μ m. (B) Pattern of *SCAP1* transcript accumulation determined by quantitative PCR in mature leaves in independent T1 BASTA resistant *pro35S:amiRNA-SCAP1* (*amiRNA-SCAP1*) transgenic lines, compared with wild type (Col-0). *ACTIN* (*ACT2*) was used for normalization. Values represent the mean of two technical replicates. Error bars = standard deviation. (C) Number of Guard cells (GC), pavement cells (PC) and stomatal index in wild type (Col) or BASTA selected T2 *pro35S:amiRNA-SCAP1* (*amiRNA-SCAP1*) lines. A transgenic line transformed with empty vector (vector) was used as a further control to account for BASTA treatment. Lines tested in this experiment are labelled in (B) with a filled arrowhead. Line #2, white arrowhead in (B), was not included in this particular experiment. (D) Number of Guard cells (GC), pavement cells (PC) and stomatal index in wild type (Col) or BASTA selected T2 *pro35S:SCAP1-YFP* (*35S:SCAP1*) lines. In C and D (**), (***) and (*) = $P < 0.01$ (two tails T Student test) for comparisons between the wild type and the mutant alleles for GC, PC cell density or stomatal index, respectively. ns = not significant. Values of PC in (C) are all not significantly different compared with the wild type or vector. Error bars = Standard Error. (JPG 382 kb)

Additional file 3: *SCAP1* regulates *AtMYB60* expression. (A) *AtMYB60* accumulation determined by quantitative PCR in manually dissected first two-leaf primordia of wild type (WT) *scap1-2* and *pro35S:amiRNA-SCAP1* (*amiRNA2-SCAP1*) seedlings at different time points. Values represent the mean of three biological replicates (30 leaves / replica). (B) *SCAP1* transcript accumulations determined by RT-PCR in *pro35S:SCAP1-GR* T1 lines. Total RNA was isolated from 2-week-old seedlings and PCR was conducted for 30 cycles. Actin was used as a positive control and amplified for 25 cycles. (C) Transcript accumulation of *AtMYB60* determined by quantitative PCR in DEX (or mock) treated wild type (Col) and *pro35S:SCAP1-GR* (*35S:SCAP1-GR*) transgenic plants at different time points. Values represent the mean of two biological replicates. In all quantitative PCR *ACTIN* (*ACT2*) was used for normalization. In A and C, ** = $P < 0.01$ and * = $P < 0.05$ and two tails T Student test. Error bars = standard deviation. (D) Morphological alterations of stomata in cotyledons of GUS stained 4-weeks old single *proAtMYB60:GUS* WT (Col) or double *proAtMYB60:GUS pro35S:SCAP1-GR* (*35S:SCAP1-GR*) hemizygous plants. Bar = 20 μ m. (E) Close up of GCs surrounded by clusters of meristemoids with altered spacing in cotyledons of DEX treated double *proAtMYB60:GUS pro35S:SCAP1-GR* (*35S:SCAP1-GR*) hemizygous plants (this plant was not subject to GUS staining) Bar = 10 μ m. (JPG 370 kb)

Additional file 4: Role of *SCAP1* on stomatal genes transcript accumulations. (A) Transcript accumulation of stomatal markers *SPCH*, *EPF2*, *MUTE* and *FAMA* genes determined by quantitative PCR in manually dissected first two leaf primordia of 7 days-old wild type (*Ler*) and *scap1-2* plants. Values represent the mean of three biological replicates (30 leaves/ replica). (B-E) Transcript accumulation of stomatal markers *EPF2*, *SPCH*, *MUTE* and *FAMA* genes determined by quantitative PCR in 10 days-old DEX (or mock) treated wild type (Col) and (F-I) *pro35S:SCAP1-GR* (*35S:SCAP1-GR*) transgenic plants at different time point after treatment. Values represent the mean of two biological replicates. In all quantitative PCR *ACTIN* (*ACT2*) was used for normalization. Error bars = standard deviation. ** = $P < 0.01$ and * = $P < 0.05$ and two tails T Student test. Values in (A) are all not significantly different compared with the wild type. (JPG 348 kb)

Additional file 5: Primers used in this study. (PDF 1736 kb)

Abbreviations

DEX, Dexamethasone; DOF, DNA Binding With One Finger; GC, Guard cell; GMC, guard mother cell; GR, Glucocorticoid Receptor; MMC, meristemoid mother cell; PC, Pavement cell; PDC, protodermal cell; SLGC, stomatal lineage ground cell; TF, Transcription Factor.

Acknowledgements

We would like to thank Prof. Enrico Coen for suggestions, the Nottingham Arabidopsis and the Cold Spring Harbour stock centres for providing T-DNA and Transposon tagged lines, Dr. Matsui (RIKEN Plant Functional Genomic)

for the gift of the *pro35S:SCAP1-GR* construct. All the authors have no conflict of interest to declare.

Funding

GC was supported by a PhD fellowship from the University of Milan and, in part, by an Erasmus Student Placement Scheme. This work was supported by the Fondazione Umberto Veronesi, Milan (project AGRISOST) and in part by a MIUR PRIN project (2010–2011 prot. 2010HEBB88_006) (to MG and CT).

Availability of data and materials

All supporting data are included as additional files. Transgenic lines, mutants and constructs described in this work are available upon request.

Authors' contributions

GC carried out the construction of transgenic plants, plant transformation and expression studies. GC and SF performed confocal studies. CT, MG, and LC conceived the study, participated in its design and coordination. GC, CT, MG and LC wrote the manuscript. All authors read and approved the final manuscript.

Competing interests

The authors declare that they have no competing interests.

Consent for publication

Not applicable.

Ethics approval and consent to participate

Not applicable.

Author details

¹Dipartimento di Bioscienze, Università degli studi di Milano, Via Celoria 26, 20133 Milan, Italy. ²Department of Cell and Developmental Biology, John Innes Centre, Norwich NR4 7UH, UK

Received: 15 March 2016 Accepted: 8 July 2016

Published online: 02 August 2016

References

- Dong J, MacAllister CA, Bergmann DC. BASL controls asymmetric cell division in Arabidopsis. *Cell*. 2009;137:1320–30.
- Pillitteri LJ, Dong J. Stomatal development in Arabidopsis. *Arabidopsis Book*. 2013;11:e0162.
- Gelsler M, Nadeau J, Sack FD. Oriented asymmetric divisions that generate the stomatal spacing pattern in Arabidopsis are disrupted by the too many mouths mutation. *Plant Cell*. 2000;12:2075–86.
- Shpak ED, McAbee JM, Pillitteri LJ, Torii KU. Stomatal patterning and differentiation by synergistic interactions of receptor kinases. *Science*. 2005;309:290–3.
- Hara K, Kajita R, Torii KU, Bergmann DC, Kakimoto T. The secretory peptide gene EPF1 enforces the stomatal one-cell-spacing rule. *Genes Dev*. 2007;21:1720–5.
- Hara K, Yokoo T, Kajita R, Onishi T, Yahara S, Peterson KM, Torii KU, Kakimoto T. Epidermal cell density is autoregulated via a secretory peptide, EPIDERMAL PATTERNING FACTOR 2 in Arabidopsis leaves. *Plant Cell Physiol*. 2009;50:1019–31.
- Hunt L, Gray JE. The signaling peptide EPF2 controls asymmetric cell divisions during stomatal development. *Curr Biol*. 2009;19:864–9.
- Ohashi-ito K, Bergmann DC. Arabidopsis FAMA controls the final proliferation/differentiation switch during stomatal development. *Plant Cell*. 2006;18:2493–505.
- MacAllister CA, Ohashi-ito K, Bergmann DC. Transcription factor control of asymmetric cell divisions that establish the stomatal lineage. *Nature*. 2007;445:537–40.
- Pillitteri LJ, Sloan DB, Bogenschutz NL, Torii KU. Termination of asymmetric cell division and differentiation of stomata. *Nature*. 2007;445:501–5.
- Kanaoka MM, Pillitteri LJ, Fujii H, Yoshida Y, Bogenschutz NL, Takabayashi J, Zhu J-K, Torii KU. SCREAM/ICE1 and SCREAM2 specify three cell-state transitional steps leading to Arabidopsis stomatal differentiation. *Plant Cell*. 2008;20:1775–85.
- Robinson S, Barbier de Reuille P, Chan J, Bergmann D, Prusinkiewicz P, Coen E. Generation of spatial patterns through cell polarity switching. *Science*. 2011;333:1436–40.

13. Hunt L, Bailey KJ, Gray JE. The signalling peptide EPFL9 is a positive regulator of stomatal development. *New Phytol.* 2010;186:609–14.
14. Lee JS, Kuroha T, Hnilova M, Khatayevich D, Kanaoka MM, McAbee JM, Sarikaya M, Tamerler C, Torii KU. Direct interaction of ligand-receptor pairs specifying stomatal patterning. *Genes Dev.* 2012;26:126–36.
15. Lampard GR, MacAlister CA, Bergmann DC. Arabidopsis stomatal initiation is controlled by MAPK-mediated regulation of the bHLH SPEECHLESS. *Science.* 2008;322:1113–6.
16. Lampard GR, Lukowitz W, Ellis BE, Bergmann DC. Novel and expanded roles for MAPK signaling in Arabidopsis stomatal cell fate revealed by cell type-specific manipulations. *Plant Cell.* 2009;21:3506–17.
17. Bergmann DC, Lukowitz W, Somerville CR. Stomatal development and pattern controlled by a MAPKK kinase. *Science.* 2004;304:1494–7.
18. Jewaria PK, Hara T, Tanaka H, KONDO T, Betsuyaku S, Sawa S, Sakagami Y, Aimoto S, KAKIMOTO T. Differential effects of the peptides Stomagen, EPF1 and EPF2 on activation of MAP kinase MPK6 and the SPCH protein level. *Plant Cell Physiol.* 2013;54:1253–62.
19. Gudesbiat GE, Schneider-Pizzo J, Betti C, Mayerhofer J, Vanhoutte I, van Dongen W, Boeren S, Zhiponova M, de Vries S, Jonak C, Russinova E. SPEECHLESS integrates brassinosteroid and stomata signalling pathways. *Nature Cell Biol.* 2012;14:548–54.
20. Engineer CB, Ghassemlan M, Anderson JC, Peck SC, Hu H, Schroeder JL. Carbonic anhydrases, EPF2 and a novel protease mediate CO₂ control of stomatal development. *Nature.* 2014;513:246–50.
21. Lau OS, Davies KA, Chang J, Adrian J, Rowe MH, Ballenger CE, Bergmann DC. Direct roles of SPEECHLESS in the specification of stomatal self-renewing cells. *Science.* 2014;345:1605–9.
22. Wang H, Ngwenyama N, Liu Y, Walker JC, Zhang S. Stomatal development and patterning are regulated by environmentally responsive mitogen-activated protein kinases in Arabidopsis. *Plant Cell.* 2007;19:63–73.
23. Riechmann JL, Heard J, Martin G, Reuber L, Keddie J, Adam L, Pineda O, Ratcliffe OJ, Samaha RR, Creelman R. Arabidopsis transcription factors: genome-wide comparative analysis among eukaryotes. *Science.* 2000;290:2105–10.
24. Yanagisawa S. The Dof family of plant transcription factors. *Trends Plant Sci.* 2002;7:555–60.
25. Skiryicz A, Radziejewski A, Busch W, Hannah MA, Czeszejko J, Kwaśniewski M, Zanor M-I, Lohmann JU, De Veylder L, Witt I, Mueller-Roeber B. The DOF transcription factor OBP1 is involved in cell cycle regulation in Arabidopsis thaliana. *Plant J.* 2008;56:779–92.
26. Galbiati M, Simoni L, Pavesi G, Cominelli E, Francia P, Vavasseur A, Nelson T, Bevan M, Tonelli C. Gene trap lines identify Arabidopsis genes expressed in stomatal guard cells. *Plant J.* 2008;53:750–62.
27. Cominelli E, Galbiati M, Albertini A, Fomara F, Conti L, Coupland G, Tonelli C. DOF-binding sites additively contribute to guard cell-specificity of AtMYB60 promoter. *BMC Plant Biol.* 2011;11:162.
28. Negi J, Moriwaki K, Konishi M, Yokoyama R, Nakano T, Kusurni K, Hashimoto-Sugimoto M, Schroeder JI, Nishitani K, Yanagisawa S, Iba K. A DoF Transcription Factor, SCAP1, is Essential for the Development of Functional Stomata in Arabidopsis. *Curr Biol.* 2013;23:479–84.
29. Cominelli E, Galbiati M, Vavasseur A, Conti L, Sala T, Vuylsteke M, Leonhardt N, Dellaporta SL, Tonelli C. A guard-cell-specific MYB transcription factor regulates stomatal movements and plant drought tolerance. *Curr Biol.* 2005;15:1196–200.
30. Aoyama T, Chua NH. A glucocorticoid-mediated transcriptional induction system in transgenic plants. *Plant J.* 1997;11:605–12.
31. Nadeau JA, Sack FD. Control of stomatal distribution on the Arabidopsis leaf surface. *Science.* 2002;296:1697–700.
32. Kondo T, Kajita R, Miyazaki A, Hokoyama M, Nakamura-Miura T, Mizuno S, Masuda Y, Irie K, Tanaka Y, Takada S, KAKIMOTO T, Sakagami Y. Stomatal density is controlled by a mesophyll-derived signaling molecule. *Plant Cell Physiol.* 2010;51:1–8.
33. Sugano SS, Shimada T, Imai Y, Okawa K, Tamai A, Mori M, Hara-Nishimura I. Stomagen positively regulates stomatal density in Arabidopsis. *Nature.* 2010;463:241–4.
34. Abrash EB, Bergmann DC. Regional specification of stomatal production by the putative ligand CHALLAH. *Development.* 2010;137:447–55.
35. Lee JS, Hnilova M, Maes M, Lin Y-CL, Putafunjan A, Han S-K, Avila J, Torii KU. Competitive binding of antagonistic peptides fine-tunes stomatal patterning. *Nature.* 2015;522:439–43.
36. Lake JA, Quick WP, Beerling DJ, Woodward FI. Plant development: signals from mature to new leaves. *Nature.* 2001;411:154–154.
37. Lake JA, Woodward FI, Quick WP. Long-distance CO₂ signalling in plants. *J Exp Bot.* 2002;53:183–93.
38. Coupe SA, Palmer BG, Lake JA, Overy SA, Oxborough K, Woodward FI, Gray JE, Quick WP. Systemic signalling of environmental cues in Arabidopsis leaves. *J Exp Bot.* 2006;57:329–41.
39. Davies KA, Bergmann DC. Functional specialization of stomatal bHLHs through modification of DNA-binding and phosphoregulation potential. *Proc Natl Acad Sci U S A.* 2014;111(43):15585–90.
40. Clough SJ, Bent AF. Floral dip: a simplified method for Agrobacterium-mediated transformation of Arabidopsis thaliana. *Plant J.* 1998;16:735–43.
41. Karimi M, Inzé D, Depicker A. GATEWAY™ vectors for Agrobacterium-mediated plant transformation. *Trends Plant Sci.* 2002;7:193–5.
42. Ossowski S, Schwab R, Weigel D. Gene silencing in plants using artificial microRNAs and other small RNAs. *Plant J.* 2008;53:674–90.
43. Earley KW, Haag JR, Pontes O, Opper K, Juehne T, Song K, Pikaard CS. Gateway-compatible vectors for plant functional genomics and proteomics. *Plant J.* 2006;45:616–29.
44. Livak KJ, Schmittgen TD. Analysis of relative gene expression data using real-time quantitative PCR and the 2^{-ΔΔC_T} Method. *Methods.* 2001;25:402–8.

Submit your next manuscript to BioMed Central and we will help you at every step:

- We accept pre-submission inquiries
- Our selector tool helps you to find the most relevant journal
- We provide round the clock customer support
- Convenient online submission
- Thorough peer review
- Inclusion in PubMed and all major indexing services
- Maximum visibility for your research

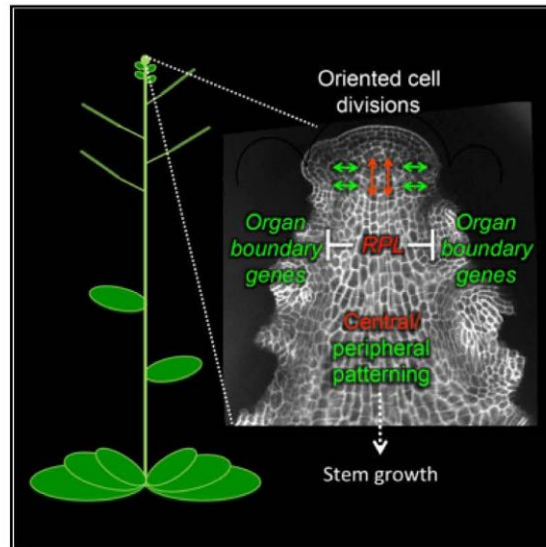
Submit your manuscript at
www.biomedcentral.com/submit



Developmental Cell

Control of Oriented Tissue Growth through Repression of Organ Boundary Genes Promotes Stem Morphogenesis

Graphical Abstract



Authors

Stefano Bencivenga,
Antonio Serrano-Mislata, Max Bush,
Samantha Fox, Robert Sablowski

Correspondence

robert.sablowski@jic.ac.uk

In Brief

The origin of the stem is a major gap in our understanding of plant development. Bencivenga et al. show that during stem initiation in *Arabidopsis*, the regulatory gene *REPLUMLESS* controls three-dimensional patterns of cell division and growth through repression of organ boundary genes.

Highlights

- Image and sector analysis revealed 3D growth patterns in early stem development
- *Arabidopsis* *RPL* controls oriented cell division and growth in the rib meristem
- *RPL* interacts with many of the key genes that regulate shoot organogenesis
- *RPL* controls oriented growth by directly repressing organ boundary genes

Accession Numbers

GSE78727
GSE78511



Bencivenga et al., 2016, *Developmental Cell* 39, 198–208
October 24, 2016 © 2016 The Author(s). Published by Elsevier Inc.
<http://dx.doi.org/10.1016/j.devcel.2016.08.013>

CellPress

Control of Oriented Tissue Growth through Repression of Organ Boundary Genes Promotes Stem Morphogenesis

Stefano Bencivenga,¹ Antonio Serrano-Mislata,¹ Max Bush,¹ Samantha Fox,¹ and Robert Sablowski^{1,2,*}

¹Cell and Developmental Biology Department, John Innes Centre, Norwich Research Park, Norwich NR4 7UH, UK

²Lead Contact

*Correspondence: robert.sablowski@jic.ac.uk

<http://dx.doi.org/10.1016/j.devcel.2016.08.013>

SUMMARY

The origin of the stem is a major but poorly understood aspect of plant development, partly because the stem initiates in a relatively inaccessible region of the shoot apical meristem called the rib zone (RZ). We developed quantitative 3D image analysis and clonal analysis tools, which revealed that the *Arabidopsis* homeodomain protein REPLUMLESS (RPL) establishes distinct patterns of oriented cell division and growth in the central and peripheral regions of the RZ. A genome-wide screen for target genes connected RPL directly to many of the key shoot development pathways, including the development of organ boundaries; accordingly, mutation of the organ boundary gene *LIGHT-SENSITIVE HYPOCOTYL 4* restored RZ function and stem growth in the *rpl* mutant. Our work opens the way to study a developmental process of importance to crop improvement and highlights how apparently simple changes in 3D organ growth can reflect more complex internal changes in oriented cell activities.

INTRODUCTION

Virtually all plant growth is sustained by stem cell populations located within the apical meristems (Aichinger et al., 2012). Decades of intense study have revealed much about how the meristems form roots, leaves, and floral buds. In contrast, little is known about how the stem is initiated in the subapical region of the shoot meristem and how regulatory genes that function in this region influence stem size and shape. The origin of the stem is not only a major aspect of plant development that has been relatively neglected, but is also of great importance in crop improvement: genes that modify stem development have played a key role in yield increases in the last 50 years (Khush, 2001), but the developmental basis for their effects on plant architecture remains unclear.

The shoot apical meristem, which produces leaves, flowers, and the stem, has distinct zones with different functions (Fletcher, 2002) (Figure 1F). Leaves and floral buds are initiated in the peripheral zone (PZ), while long-term progenitors in the

central zone (CZ) constantly replenish the PZ. The underlying rib zone (RZ) gives rise to the stem and includes a central region called the rib meristem (named after its distinct pattern of transverse cell divisions), which gives rise to the pith, and a peripheral region that appears continuous with the overlying PZ and gives rise to the epidermis, cortex, and vascular tissues of the stem (Sachs, 1965; Sanchez et al., 2012). Superimposed on this functional zonation, the shoot meristem has a layered structure; in angiosperms such as *Arabidopsis*, the cells in the outermost two to three layers divide mostly anticlinally (perpendicular to the meristem surface), so their descendants generally remain in the same layer (Fletcher, 2002). Growth of the different meristem regions can be controlled differentially: during the vegetative stage in *Arabidopsis*, the CZ and PZ sustain leaf production but the RZ is inhibited, whereas at the transition to flowering, activation of the RZ leads to rapid stem elongation while the CZ and PZ start to produce floral buds.

Parallels can be drawn between activation of stem growth at the shoot apex and the well-studied control of root growth at the opposite end of the plant's main axis (Aichinger et al., 2012), but there are important differences. In the root, terminal growth mostly precedes the emergence of lateral roots and the vast majority of cell growth and division is aligned with the main root axis, so growth rate is proportional to root meristem size and to the overall rate of cell proliferation (Beemster and Baskin, 1998). In contrast, development of the stem occurs simultaneously with that of lateral structures such as flower buds, and cell files in the RZ appear much less organized than in the root. The more complex structure of the RZ requires three-dimensional (3D) analysis of cell behavior and overall organ growth. A further complication is the relative inaccessibility of the RZ in comparison with the root meristem. Thus RZ growth and early stem development remain considerably less well understood than the root system, and illustrate the general challenge of describing and understanding the regulation of tissue growth in 3D structures with no obvious internal landmarks.

In *Arabidopsis*, one of the master regulators of stem growth is most often named *PENNYWISE* (*PNY*) (Smith and Hake, 2003), *REPLUMLESS* (*RPL*) (Roeder et al., 2003), and *BELLRINGER* (*BLR*) (Byrne et al., 2003); we used *rpl* mutant alleles and therefore adopted *RPL* for simplicity. *RPL* encodes a BEL1-like TALE homeodomain (BLH) transcription factor that controls multiple aspects of meristem and floral development, including meristem maintenance, the distribution of lateral organs around the meristem (phyllotaxis), the transition to flowering and the

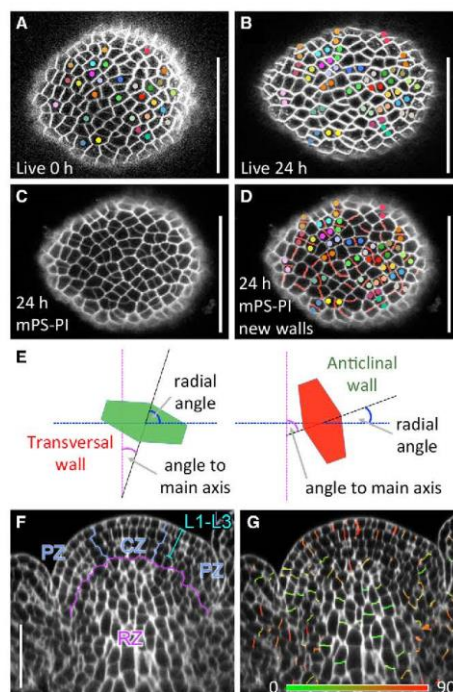


Figure 1. Automated Detection of the 3D Orientation of Cell Divisions in the Shoot Apex

(A and B) Confocal sections through the outer layers of a live *Arabidopsis* (*L-er*) inflorescence meristem stained with FM4-64 at 0 hr (A) and 24 hr later (B). When cell divisions occurred, mother cells in (A) and their corresponding daughter cells in (B) were manually marked with dots of the same color.

(C) Confocal section of the same meristem as in (B), after staining by modified pseudo-Schiff propidium iodide (mPS-PI), showing variable intensity of cell-wall signals.

(D) Same section as in (C), overlaid with an image of segmented cell facets detected as new walls (red lines); colored dots mark recent divisions corresponding to (B). Note that new walls were correctly attributed for most of the recent divisions (27 out of 29), in addition to low-intensity walls that likely correspond to divisions completed more than 24 hr earlier.

(E) Scheme of how the orientation of new walls was measured. Walls are represented by colored hexagons, with a line normal to their best-fitting plane shown in black; the magenta line is parallel to the main axis of the stem; the blue line is perpendicular to the to the main axis of the stem and passes through the wall's center of mass; angles to the main axis and radial angles are indicated by the magenta and blue arcs, respectively; the red and green walls correspond to transversal and anticlinal walls, as frequently seen in the RZ and in the outer meristem layers, respectively; anticlinal walls can have small to large radial angles, depending on whether they face the central axis or not.

(F and G) Longitudinal slice through a stack of confocal images of mPS-PI-stained inflorescence apex, with (F) the outer meristem layers (L1–L3), central zone (CZ), peripheral zone (PZ), and rib zone (RZ) indicated. (G) Image cor-

responding to (F), overlaid with an image of cell facets detected as new walls and colored according to the angle to the main axis of the stem. Scale bars, 50 μ m. See also Figure S1.

associated activation of stem development, and subsequently floral organ patterning (Byrne et al., 2003; Roeder et al., 2003; Smith and Hake, 2003; Arnaud et al., 2011). Based on its expression in the shoot meristem, extending into the RZ (Smith and Hake, 2003; Andrés et al., 2015), *RPL* likely affects stem growth by regulating the earliest steps in stem development, but the molecular and cellular processes controlled by *RPL* in the RZ are virtually unknown.

Here, we used quantitative 3D imaging and clonal analysis to reveal how *RPL* controls early stem development. Our findings indicate that *RPL* controls RZ function through oriented cell activities rather than local rates of cell proliferation. We also show that *RPL* directly interacts with many of the key regulatory genes in shoot organogenesis and that interaction with genes involved in organ boundary development are particularly important for the role of *RPL* in the RZ.

RESULTS

RPL Is Required for Oriented Tissue Growth in the RZ

If *RPL* controls morphogenesis in the RZ, it would be expected to modify rates or orientations of tissue growth, or a combination of both. To verify this we would require new imaging and analysis methods, because tracking cells by live imaging (Serrano-Mislata et al., 2015) is not feasible in the deeper layers of the shoot meristem, whereas high-resolution 3D images of fixed apices (Schiessl et al., 2012) cannot provide temporal information. Instead, we exploited the fact that new cell walls are placed perpendicular to the mitotic spindle (Smith, 2001), thus retaining information about the orientation of recent cell divisions. To detect recent cell divisions, we cross-linked wall polysaccharides to propidium iodide (PI) (Truernit et al., 2008), which would be expected to produce lower fluorescence for thinner, more recently synthesized walls. After 3D segmentation the PI signal was measured in all facets between cells, and individual facets were identified as new walls if they had the weakest signal density for both adjacent cells (details in Supplemental Experimental Procedures and annotated source code in Data S1). This method accurately detected cell divisions identified by time-lapse imaging in both outer and inner meristem layers, and correctly detected the predominance of anticlinal divisions in the outer meristem layers and of transversal divisions in the RZ (Figures 1 and S1). Thus information about 3D patterns of oriented cell divisions can be extracted from single-time-point images of fixed shoot apices.

We next used the method to compare shoot apices of wild-type and *rpl-1* mutant plants. The RZ of the wild-type apex showed a well-defined rib meristem with cell divisions perpendicular to the main stem axis, while the peripheral region was enriched for radial cell divisions, which potentially increase RZ width and may contribute to elongating the basal region of floral pedicels (Figure 2A). In contrast, *rpl-1* appeared to have a less organized RZ and the difference between the central and peripheral regions was less obvious (Figure 2B).

responding to (F), overlaid with an image of cell facets detected as new walls and colored according to the angle to the main axis of the stem.

Scale bars, 50 μ m. See also Figure S1.

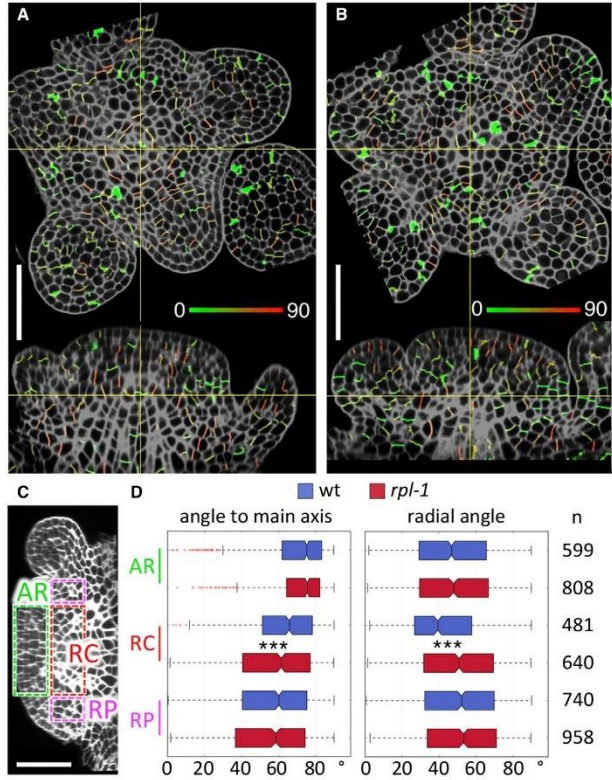


Figure 2. *rpl-1* Disrupts the Orientation of Cell Divisions in the RZ

(A and B) Orthogonal views of confocal image stacks of wild-type (wt) (*L-er*) (A) and *rpl-1* (B) inflorescence apices stained by mPS-PI, overlaid with images of segmented cell facets detected as new walls, and colored according to their radial orientation (see Figure 1E). In each image, the yellow cross-hairs mark the same point in the top and side views; note the less organized RZ in *rpl-1* and the high frequency of radially oriented divisions in the periphery of the wild-type RZ, but not in the mutant.

(C and D) Measurement of oriented divisions in wild-type and *rpl-1*. (C) Regions where new wall angles were measured (AR, apical region; RC, rib meristem core; RP, rib meristem periphery). (D) Boxplots show the distribution of new wall angles to the main stem axis or radial angles (see Figure 1E). n indicates the number of new walls in each set (combined data from four apices for each genotype); asterisks indicate statistically significant differences (***) $p < 0.001$, Mann-Whitney test). In the boxplots, the box extends from the lower to upper quartile values with a line at the median; whiskers extend to 1.5 times the interquartile range, and outlier points beyond the whiskers are shown in red. Scale bars, 50 μ m. See also Figure S2.

ented divisions corresponded to directions of tissue growth and to obtain information about growth rates, we used a *Cre-loxP* recombination system (Gallois et al., 2004) to mark individual cells with GFP expression and track their descendants in the shoot apex (Figure 3A). To overlap marked sectors from multiple apices and analyze them in 3D, we landmarked cells within each sector manually and used custom scripts to align the images and measure the position, size, and orientation of the main axis for each sector (details in Supplemental Experimental Procedures and annotated source code in Data S1). As expected from the anticlinal cell divisions in the outer layers of the meristem, sectors in these layers were oriented tangentially to the meristem surface (Figures 3B and 3C). The wild-type sectors also confirmed the expectation that the RP originates from the overlying PZ of the meristem, where lateral organs are also initiated. Sectors in the RC grew vertically and more slowly than in the surrounding region, and based on their orientation appeared to originate from a region below the CZ progenitors that sustain the initiation of lateral organs (Aichinger et al., 2012) (Figure 3C). Based on cell number and length of sectors, growth rates were not significantly different between wild-type and *rpl-1*; in contrast, the orientation of *rpl-1* sectors was different from the wild-type specifically within the RC, and as seen in the analysis of recent cell walls, was more similar to the pattern seen in the RP region (Figures 3E–3H).

Based on the combined analyses of new cell walls and marked clones, we conclude that *RPL* regulates oriented tissue growth

To quantify the differences between wild-type and *rpl-1*, we compared the orientation of recent cell walls in the region where the rib meristem originates (“RM core” [RC], within 30–60 μ m of the meristem summit and 0–40 μ m of the main axis), in the overlying CZ and PZ cells (“apical region” [AR], within 30 μ m of the meristem summit and within 40 μ m of the shoot main axis), and in the PZ surrounding the RM (“RM periphery” [RP], within 30–60 μ m of the summit and 40–50 μ m of the main axis) (Figures 2C and 2D). Significant differences were detected in the RC, where *rpl-1* showed a pattern more similar to that in the RP, with more variable angles to the main axis and more radially oriented divisions; these differences were seen not only in data from combined apices but also across individual apices (Figure S2).

The orientation of cell divisions can respond to cell geometry, which reflects principal directions of growth, or to the direction of mechanical stress, which can accumulate during growth of interconnected cells, and these physical signals can also be overruled by chemical signals (Kwiatkowska, 2004; Besson and Dumais, 2011; Yoshida et al., 2014). To test whether ori-

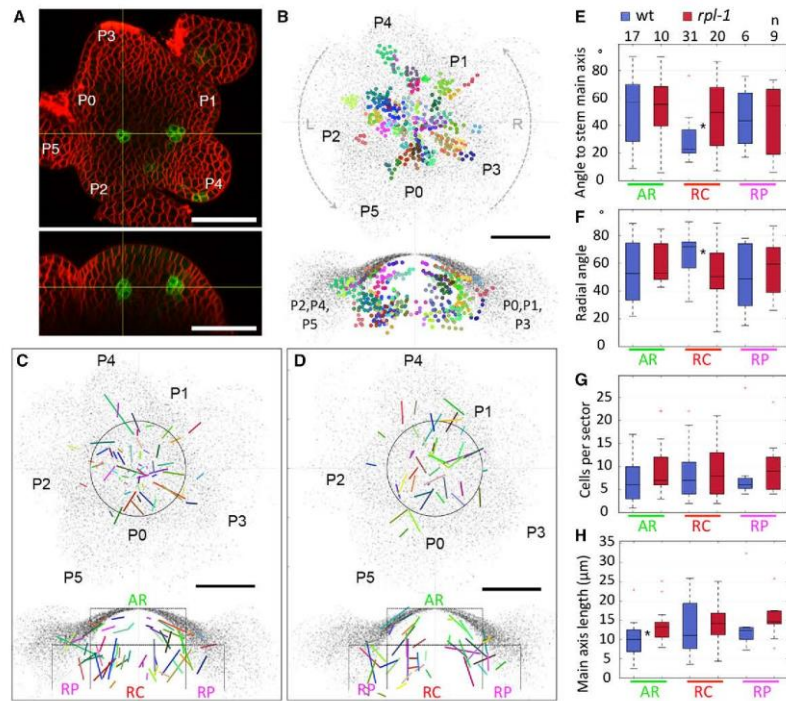


Figure 3. Clonal Analysis Shows that RPL Controls Orientation, but Not Rates of Growth, in the Central Region of the RZ
 (A) Orthogonal views of a confocal images stack of a wild-type inflorescence apex with two mGFP5-ER-marked clones (green), 3 days after Cre-catalyzed recombination. P1 to P5 mark the positions of successive floral bud primordia.
 (B) Vertical (top) and radial (bottom) projections of superimposed GFP-marked clones from 15 wild-type apices. Each clone is marked in a different color, with the position of individual cells indicated by dots. Each clone was projected onto a plane containing its center of mass and the stem main axis to produce the radial projection. Clones on the right and left sides of the vertical projection (arrows marked R and L) are shown, on the right and left sides of the radial projection.
 (C) Vertical (top) and radial (bottom) projections of the main axes of clones shown in (B). On the radial projection, the AR, RC, and RP regions are defined as in Figure 2C.
 (D) Projections of the main axes of clones from 15 superimposed *rpl-1* apices, produced as described for the wild-type clones in (B) and (C).
 (E–H) Boxplots showing the vertical angles of the main axes of clones (relative to the stem main axis) (E), radial angles (relative to the shortest line between the clone's center of mass and the stem main axis) (F), number of cells per clone (G), and length of the clone main axes (H). AR, RC, and RP correspond to the regions shown in (C) and (D); n indicates the number of sectors in each region; asterisks indicate statistically significant differences (* $p < 0.01$, Mann-Whitney test). In the boxplots, the box extends from the lower to upper quartile values with a line at the median; whiskers extend to 1.5 times the interquartile range, and outlier points beyond the whiskers are shown in red. Scale bars, 50 μm .

and establishes distinct growth patterns in the central and peripheral regions of the RZ.

RPL Directly Binds to Key Genes that Regulate Meristem Function, Organ Patterning, and Growth

As a transcriptional regulator, *RPL* is expected to affect patterns of growth indirectly through its downstream target genes. To reveal genes and processes regulated by *RPL* in the RZ, we first used chromatin immunoprecipitation (ChIP)

sequencing (ChIP-seq) to detect loci bound by *RPL* within the inflorescence apex. As internal controls, we used genes previously reported to interact with *RPL* genetically or by ChIP, including close partners or repressors of *RPL* function, such as *BREVIPEDICELLUS* (*BP*), *FOUND-FOOLISH* (*PNF*), *ARABIDOPSIS THALIANA HOMEBOX GENE 1* (*ATH1*), *KNOTTED1-LIKE HOMEBOX GENE 6* (*KNAT6*), *BLADE ON PETIOLE 1* (*BOP1*), and *BOP2* (Smith and Hake, 2003; Smith et al., 2004; Khan et al., 2012, 2015; Ragni et al., 2008; Khan

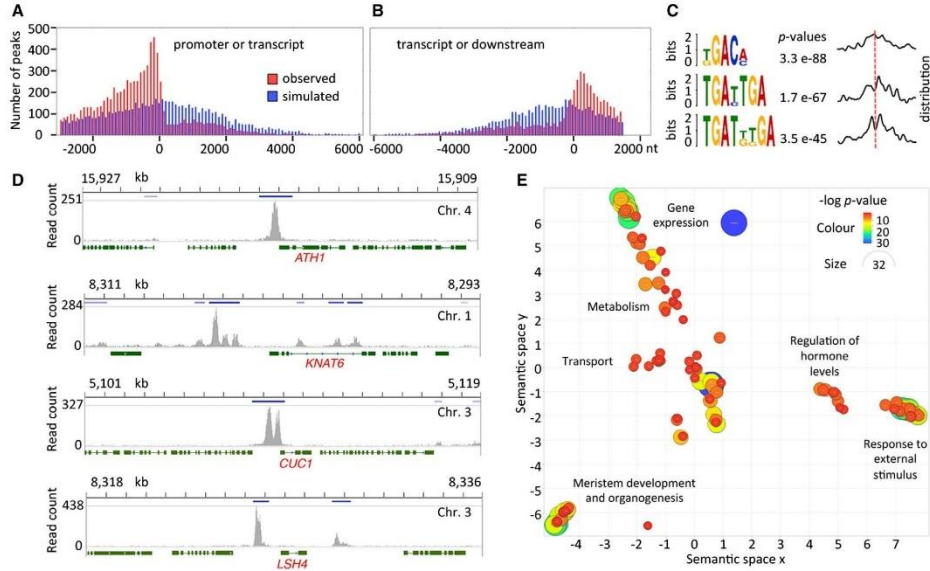


Figure 4. Genome-wide RPL Targets Identified by ChIP-Seq
 (A and B) Enrichment of RPL binding sites within promoter regions (A) and downstream regions (B) compared with transcribed regions, for the 2,917 high-confidence RPL candidate targets (Table S1). Red bars show the frequency of peak regions (overlap of peaks from three ChIP-seq replicates) centered at the indicated nucleotide positions relative to transcript start (A) or end (B); blue bars show how simulated peaks at random genome positions were distributed within the set of high-confidence RPL targets. Based on 10,000 simulations, the observed RPL binding sites were significantly enriched ($p < 10^{-4}$) in both promoter and downstream regions compared with transcribed regions.
 (C) Enrichment for sequence motifs within 75 nt of the RPL binding sites analyzed in (A) and (B), detected using the MEME Suite (Bailey et al., 2009). Curves on the right show the frequency distribution of enriched motifs, relative to the center of the peak region (red line).
 (D) Representative raw ChIP-seq peaks (replicate 1 only) for control genes (*ATH1*, *KNAT6*) and two key organ boundary genes (*CUC1*, *LSH4*). Dark-blue bars show regions of overlap between peaks detected in three replicates (peak regions mentioned in A–C); green bars and lines are exons and introns, respectively; numbers above each graph show chromosome position in kilobases. All genes are oriented 5' (left) to 3' (right).
 (E) Semantic clustering (Supek et al., 2011) of GO categories enriched in the set of 2,917 candidate RPL targets (Table S2). The diameter and color of each circle reflect the p value for individual GO terms within the cluster; the broad terms used to describe each cluster are attributed to specific GO terms in Table S2. See also Figure S3; Tables S1 and S2.

et al., 2015), as well as genes that interact with *RPL* during flowering, floral organ, and fruit development, such as *LEAFY* (*LFY*), *AGAMOUS* (*AG*), *APETALA 1* (*AP1*), *SEPALLATA 3* (*SEP3*), *APETALA 2* (*AP2*), *SHATTERPROOF 1* (*SHP1*), *SHP2*, *FRUITFULL* (*FUL*), and *MIR156A*, *C*, and *E* (Lal et al., 2011; Roeder et al., 2003; Smaczniak et al., 2012; Andrés et al., 2015). Anti-GFP antibodies were used to pull down DNA bound by RPL-GFP expressed as a genomic fusion (*pRPL:RPL-GFP*) that mirrored the endogenous *RPL* expression and complemented the *rpl-1* mutant (Figure S1). ChIP-seq peaks with a false discovery rate of less than 0.001 and consistently detected in three RPL-GFP replicates but not in wild-type replicates were selected and associated with genes that contained a peak within 3 kb upstream and 1.5 kb downstream of their coding sequences (see examples in Figure 4D). From the list of genes that satisfied these conditions, we selected a set of 2,917 high-confidence candidates (Table

S1) that showed a peak enrichment at least as high as the positive control gene with the lowest enrichment (*APETALA2*). Within the high-confidence targets set, ChIP-seq peaks were depleted in transcribed regions but enriched in the immediately adjacent regions, as expected for the role of RPL as a transcriptional regulator (Figures 4A, 4B, and 4D). BLH proteins function with a KNOX homeodomain partner (Bellaoui et al., 2001), which is BP in the case of RPL (Smith and Hake, 2003). Accordingly, sequences in the vicinity of the peak summits were significantly enriched for short motifs containing TGAC/T (Figure 4C), similar to the binding sites previously described for BLH and KNOX proteins (Smith et al., 2002). Gene ontology (GO) analysis (Falcon and Gentleman, 2007) followed by semantic clustering (Supek et al., 2011) revealed clusters of highly enriched functional categories (Figure 4E and Table S2). As for other master regulatory genes (Kaufmann et al., 2009; Schiessl et al., 2014), the most highly enriched

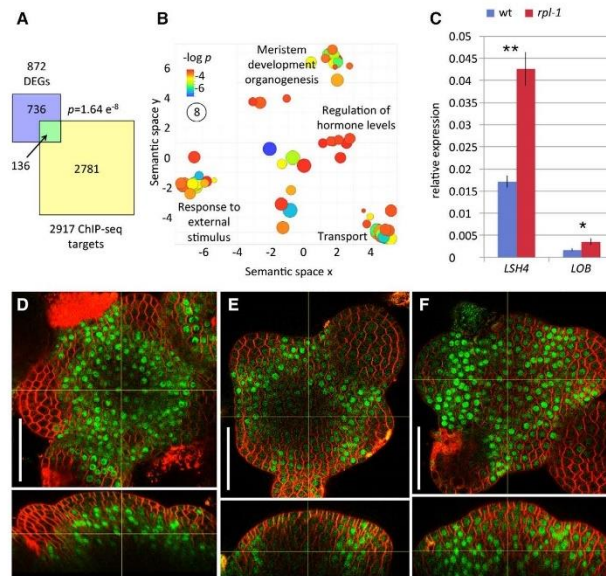


Figure 5. Genes Regulated by RPL Include the Boundary Gene *LSH4*

(A) Overlap between ChIP-seq results and genes that were differentially expressed (DEGs) in wild-type and *rpl-1* inflorescence apices (Table S3). The overlap of both sets was larger than expected by chance ($p = 1.64 \times 10^{-8}$, Fisher's exact test).

(B) Semantic clustering (Supek et al., 2011) of GO categories enriched in the set of 136 direct RPL target genes. The diameter and color of each circle reflect the p value for individual GO terms within the cluster; broad terms used to describe each cluster are attributed to specific GO terms in Table S4.

(C) qRT-PCR measurement of *LSH4* and *LOB* expression levels in wild-type and *rpl-1* inflorescence apices. Bars and lines show means and SD (three biological replicates), with asterisks indicating significant difference (Student's t test; *LSH4*: ** $p < 0.01$, *LOB*: * $p < 0.05$).

(D–F) orthogonal views of confocal image stacks of inflorescence apices showing the expression pattern of *pRPL-RPL-GFP* (D), *pLSH4:LSH4-GFP* in wild-type (E), and *pLSH4:LSH4-GFP* in *rpl-1* (F). In each image, the yellow cross-hairs mark the same point in the top and side views. Scale bars, 50 μm . See also Tables S3 and S4.

terms were related to transcriptional control (Table S1). The second most highly enriched cluster of GO terms corresponded to meristem functions, early organogenesis, and reproductive development, as detailed below. Additional sets of enriched terms were related to hormone metabolism and responses (particularly involving auxin, gibberellin, and jasmonic acid), ion and sugar transport, and responses to external stimuli (e.g., pathogens and light) (Figure 4E).

Genes in the "meristem development and organogenesis" cluster revealed direct links to many well-known players in shoot development. Reflecting the role of *RPL* in meristem establishment, its targets included genes involved in maintaining the stem cell niche: *SHOOT MERISTEMLESS*, *CLAVATA 1*, *A-TYPE RESPONSE REGULATOR 7* (*ARR7*), *ARR15*, and *ARGONAUTE 10* (Aichinger et al., 2012). Based on its antagonism with *ATH1*, *BOP1*, *BOP2*, and *KNAT6*, which are expressed at the boundary between lateral organs the stem, *RPL* has been proposed to oppose organ boundary development (Khan et al., 2015); accordingly, *RPL* interacted directly with the majority of known organ boundary genes, including *CUP-SHAPED COTYLEDONS 1* (*CUC1*), *CUC3*, *CUC*-repressing microRNAs (*miR164B* and *miR164C*), known downstream components of the *CUC* pathway *LATERAL ORGAN FUSION 1* (*LOF1*), *LOF2*, *LIGHT-DEPENDENT SHORT HYPOCOTYL 3* (*LSH3*), *LSH4*, and multiple members of the *LATERAL ORGAN BOUNDARIES* (*LOB*) *DOMAIN* family, including *LOB* and *JAGGED LATERAL ORGANS* (Žádníková and Simon, 2014; Hepworth and Pautot, 2015). Furthermore, the ChIP-seq results revealed links between *RPL* and a large number of genes involved in shoot organogen-

esis, including genes that control abaxial/adaxial identity, organ growth, cell cycle, cell-wall functions, and vascular development (Table S1). In summary, the ChIP-seq results placed *RPL* in a central hub connecting many of the key regulatory pathways in shoot development.

RPL Promotes Rib Meristem Function by Antagonizing the Organ Boundary Gene *LSH4*

Many of the target genes mentioned above are likely regulated by both *RPL* and its close homolog *PNF*, since these two genes function redundantly in meristem establishment and in the control of the floral transition. To narrow down the list of genes that could mediate the role of *RPL* in the RZ, we took advantage of the fact that some processes, such as stem elongation and fruit development, are preferentially affected in the *rpl* single mutant (Smith and Hake, 2003; Roeder et al., 2003; Byrne et al., 2003). To filter the ChIP-seq data for genes relevant to stem development, we looked for transcriptome changes in dissected inflorescence apices of *rpl-1* compared with the wild-type (Table S3). Although the majority of differences in mRNA abundance were expected to result from indirect, steady-state effects of *RPL*, the set of differentially expressed genes (DEGs) was significantly enriched for direct RPL targets based on ChIP-seq ($p = 1.64 \times 10^{-8}$, Fisher's exact test; Figure 5A). The 136 directly regulated targets included approximately equal numbers of upregulated (67) and downregulated genes (69) (Table S3), indicating that *RPL* can function as both a transcriptional activator and repressor. GO analysis of these genes showed clusters similar to those in the ChIP-seq experiments, highlighting meristem development and organogenesis, regulation of hormone levels, responses to hormones and external stimuli, and transport of ions and sugar (Figure 5B and

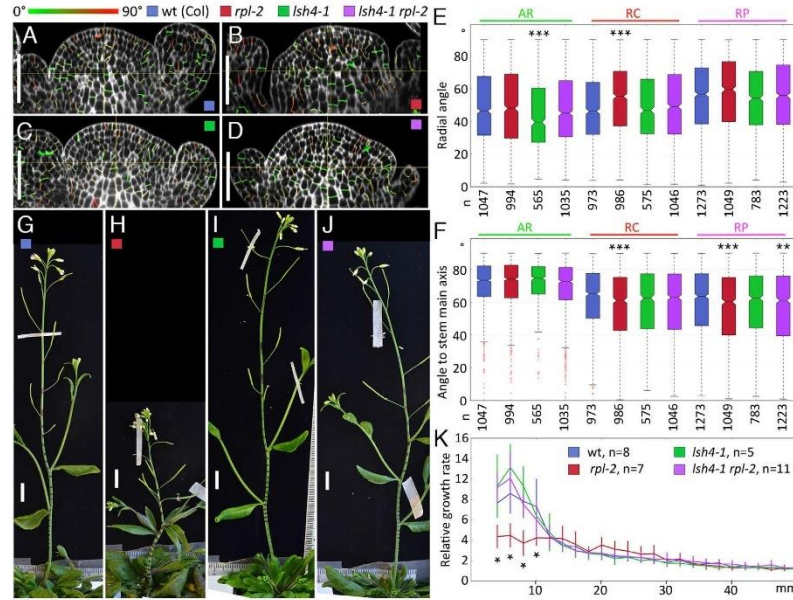


Figure 6. *LSH4* Expression Causes the *rpl* Defects in RZ Development and Stem Growth

(A–D) Longitudinal sections through confocal image stacks of inflorescence apices stained by mPS-PI, overlaid with images of segmented cell facets detected as new walls and colored (color scale above A) according to their radial orientation as in Figure 2A. (A) Wild-type (Columbia); (B) *rpl-2*; (C) *lsh4-1*; (D) *rpl-2 lsh4-1*. (E and F) Boxplots showing the distribution of new wall radial angles (E) or angles to the main stem axis (F). Colors correspond to the genotypes indicated above (A and B). n indicates the number of new walls in each set (combined data from four apices for each genotype); asterisks indicate statistically significant differences (** $p < 0.01$, *** $p < 0.001$, Mann-Whitney test).

(G–J) Inflorescences of wild-type Columbia (G), *rpl-2* (H), *lsh4-1* (I), and *lsh4-1 rpl-2* (J), 4 days after the first flower self-pollinated and black marks were placed on the stem at 2-mm intervals to track growth rates.

(K) Relative growth of different stem regions, measured by tracking landmarks placed on the stem as in (G)–(J). The graph shows mean and SD; the number of replicates is indicated on the color legend for each genotype; asterisks indicate statistically significant differences relative to the wild-type (* $p < 0.01$, Student's t test). The horizontal axis shows the original distance of landmarks to the apex, before growth. In the boxplots, the box extends from the lower to upper quartile values with a line at the median; whiskers extend to 1.5 times the interquartile range, and outlier points beyond the whiskers are shown in red. Scale bars, 50 μ m (A–D) and 1 cm (G–J). See also Figure S6.

Table S4). The meristem and organogenesis cluster included components of the core RPL regulatory module (*ATH1*, *KNAT6*), genes that regulate meristem function (*STM*, *ARR7*, *AGO10*, *HAM3*), and genes implicated in organ boundary development (*LSH4*, *LOB*) (Table S3).

Of the known regulators of shoot development present in the set of directly regulated targets, *LSH4* showed the most significant differential expression (Table S3). We next focused on this gene, considering that *LSH4* functions downstream of *CUC* genes, which control not only organ boundary development but also stem development (Vroemen et al., 2003; Hibara et al., 2006). The higher expression of *LSH4* in the mutant, seen in the transcriptome profiling, was verified by RT-PCR, and similar results were obtained for *LOB* (Figure 5C). To determine the spatial localization of *LSH4*, we used a genomic fusion with GFP (*pLSH4:LSH4-GFP*) to visualize the expression pattern in

apical meristems. In wild-type apices we observed GFP around the base of floral buds and in the peripheral region of the RZ (Figure 5D), similar to the previously described expression pattern for *LSH4* (Takeda et al., 2011). In contrast, in the *rpl-1* mutant, the region of *pLSH4:LSH4-GFP* expression extended into the central region of the RZ (Figure 5E). Comparable results were obtained with the *pCUC1:CUC1-GFP* organ boundary reporter (Baker et al., 2005), confirming that *RPL* represses a suite of organ boundary genes in the RZ (Figure S4).

To test the functional relevance of *LSH4* repression by *RPL*, we crossed the *rpl-2* and *lsh4-1* mutants (both strong alleles in the Columbia accession) (Takeda et al., 2011; Roeder et al., 2003). Similar to our observations for *rpl-1*, cells in the RZ appeared less ordered in *rpl-2* than in wild-type apices (Figures 6A and 6B), with significant differences in the orientation of new walls in the central region (RC), relative to both the radial

axes (Figure 6E) and the stem main axis (Figure 6F). We did not observe differences in the RC of the *lsh4-1* single mutant compared with the wild-type, although the mutant did show an increase in radially oriented divisions in the AR of the meristem (Figure 6E). In the double mutant *rpl-2 lsh4-1*, the RC was visibly more ordered than in *rpl-2* (Figure 6D) and the orientation of cell divisions was restored to the wild-type pattern in the RC, although not in the surrounding RP (Figures 6E and 6F). The defect in stem elongation of *rpl-2* was also suppressed in *rpl-2 lsh4-1* due to restoration of elongation rates close to the inflorescence apex (Figures 6G–6K), while defects in fruit development were not suppressed in the double mutant (Figure S5).

In conclusion, ectopic *LSH4* expression caused most of the defects in RZ function and stem growth seen in the *rpl* mutant. Mutations in *BOP1*, *BOP2*, *ATH1*, and *KNAT6* have been shown to restore all wild-type functions in the *rpl* mutant, including flowering time and fruit development, indicating that these genes function within the same central regulatory node as *RPL* (Khan et al., 2012, 2015; Ragni et al., 2008; Khan et al., 2015). In contrast, *lsh4-1* suppressed a subset of the *rpl-2* phenotypes, suggesting a more specialized role for organ boundary functions in the control of stem growth by *RPL*. In accordance with a role for *LSH4* downstream of the *BOP1/BOP2/ATH1/KNAT6* module, suppression of the *rpl-2* defects by *knat6-2* included restoration of *LSH4* repression and rescue of oriented divisions in the RZ (Figure S6). At the same time, the almost complete rescue of RZ function and stem growth in the *rpl lsh4* double mutant (Figure 6) suggests that if additional organ boundary genes are relevant to the control of RZ function by *RPL*, these genes function within a module that requires *LSH4* activity.

DISCUSSION

Our results provide insight into the 3D patterns of growth and cell division in the deep layers of the shoot apical meristem, a region crucial for the development of new stem tissues. We reveal that *RPL* controls RZ function not through the rate of cell growth and proliferation but by repressing organ boundary genes to allow the establishment of central and peripheral regions, which have characteristic patterns of oriented cell division.

Organ boundaries are considered regions of reduced growth (Hepworth and Pautot, 2015), so activation of boundary genes in the RZ could be expected to inhibit tissue growth (Žádníková and Simon, 2014; Hepworth and Pautot, 2015). However, our clonal analysis did not reveal reduced growth rates in tissues that expressed *LSH4*, i.e., in the RP region in the wild-type and *rpl-1*, or in the RC region of *rpl-1* (Figure 6). Instead, the most obvious change caused by *LSH4* was in the orientation of cell divisions. Ectopic *LSH4* expression in the *rpl* mutant may have narrowed the rib meristem because of the lower frequency of radial divisions observed in the RC region, where the rib meristem is initiated (Figures 2 and 6), or may have induced inappropriate radial divisions during subsequent growth of the rib meristem. Either way, within the region of the developing stem that overlaps the *RPL* expression domain (Smith and Hake, 2003) (Figure S3), the primary consequence of losing *RPL* function was not a reduction in overall growth, but a defect in establishing distinct central and peripheral regions. The reduced stem growth seen within a few millimeters of the apex in the *rpl* mutant is likely an

indirect consequence of the early RZ defects. One possibility is that an abnormal or displaced boundary between the central and peripheral RZ might affect development of the stem vasculature and interfascicular fibers, which form at this boundary, are affected in the *rpl* mutant, and have been proposed to mechanically constrain stem elongation (Muñiz et al., 2008; Mele et al., 2003; Smith and Hake, 2003).

An important question is by which mechanism *RPL* and *LSH4* could affect oriented cell growth and division. Mechanical stress during tissue growth feeds back to influence the orientation of microtubule arrays and cell division (Hamant et al., 2008), so a possible mechanism would be that the visibly thicker cell walls of the rib meristem (e.g., Figures 2A and 6C) could impose mechanical constraints on the surrounding tissues. Alternatively, *RPL* and *LSH4* could modulate auxin signaling or transport. The orientation of cell divisions responds to auxin (Yoshida et al., 2014), perhaps through regulation of the molecular mechanism that orients the mitotic spindle, or perhaps indirectly by setting the direction of cell growth (Sassi and Traas, 2015). Furthermore, auxin transport is regulated at organ boundaries to create a low-auxin environment (Heisler et al., 2010; Wang et al., 2014; Hepworth and Pautot, 2015). A role in regulating auxin functions is also suggested by our ChIP-seq results showing direct interaction between *RPL* and multiple genes involved in auxin transport and signaling (Vanneste and Friml, 2009), e.g., *PIN-FORMED 5* (*PIN5*), *PIN6*, *LIKE AUXIN 1* (*LAX1*), *LAX3*, *AUXIN RESPONSIVE FACTOR 4* (*ARF4*), *ARF6*, *ARF8*, *ARF10*, *ARF11*, and *ARF17* (Table S1).

At first sight it could be expected that the rate of stem elongation would simply reflect the rate of cell growth and proliferation in the RZ, just as root elongation reflects the rate at which new cells are produced by the root meristem (Beemster and Baskin, 1998). Contrary to this expectation, our results emphasize the regulation of axial growth through orientation, rather than rates of cell growth and division. In an analogous way, it has been assumed that elongation of the vertebrate limb results from a proximodistal gradient of cell proliferation, but recent 3D imaging and mathematical modeling highlighted the role of oriented cell activities (Boehm et al., 2010). In addition to providing insight into the internal cell behavior required for growth of a 3D structure, our work opens the way to study and modify a developmental process that influences plant traits with key practical importance.

EXPERIMENTAL PROCEDURES

Plant Material

Plants were grown on JIC *Arabidopsis* Soil Mix at 16°C under continuous light (100 μE). *Arabidopsis thaliana* Landsberg-erecta (*L-er*) and Columbia (*Col*) were used as wild-types; *rpl-1* (Roeder et al., 2003), *rpl-2* (Roeder et al., 2003), *lsh4-1* (Takeda et al., 2011), *knat6-2* (Ragni et al., 2008), *pCUC1:CUC1-GFP* (Baker et al., 2005), and *hsp18.2:Cre* (Sieburth et al., 1998) have been described. Transgenic lines were generated by floral dip transformation (Clough and Bent, 1998).

PCR primers used to create DNA constructs are listed in Supplemental Experimental Procedures. For construction of *pRPL:RPL-GFP*, *RPL* was amplified from *Col* genomic DNA and fused in-frame with sGFP(S65T) (Chiu et al., 1996), and cloned into pZP222 (Hajdukiewicz et al., 1994). For construction of *pLSH4:LSH4-GFP*, *LSH4* was amplified from *Col* genomic DNA and the sGFP(S65T) cDNA was inserted in-frame at the end of the *LSH4* coding sequence before assembly into pCambia 1300 (CAMBIA). The

35S:*loxCFPloxGFP* was created by Golden Gate cloning in the vector pAGM4723 (Addgene #48015) as described by Weber et al. (2011), using synthesized DNA (Lifetech) for the 35S promoter, *loxP* reverse, CFP-ER, 35S terminator, *loxP* reverse, GFP-ER, and the actin terminator (see Supplemental Experimental Procedures for sequences).

Imaging and Image Analysis

Dissection and live imaging of inflorescence apices, including time-lapse experiments, and imaging of apices stained by the modified pseudo-Schiff protidum iodide (mPS-Pi) method were performed as described previously (Serrano-Mislata et al., 2015; Truemit and Haseloff, 2008). For generation of Cre-*loxP* sectors, plants hemizygous for *hsp18.2:Cre* and 35S:*loxCFPloxGFP* were heat-shocked by immersing their inflorescence apices in a water bath at 38.5°C for 70 s and returned to standard growth conditions for 3 days before dissection and live imaging.

For 3D segmentation, cell measurements, and matching cells at different time points, 3D_meristem_analysis was used (Serrano-Mislata et al., 2015), with additional scripts added to detect and analyze the 3D orientation of new cell walls, to landmark, align, and measure Cre-*loxP* sectors from different apices (Data S1).

Chromatin Immunoprecipitation/High-Throughput Sequencing and Data Analysis

ChIP was performed on dissected inflorescence apices as described by Schiesl et al. (2014) (details in Supplemental Experimental Procedures). Six Illumina TruSeq ChIP-seq libraries (three *pRPL:RPL-GFP* replicates and three wild-type controls) were produced as described by Kaufmann et al. (2009) and sequenced (50-bp single-end reads) using a HiSeq 2500 (Rapid-Run mode) as described by the manufacturer (Illumina). Reads from three replicate treatments and three replicate controls were aligned against the TAIR10 Col-0 reference sequence with Bowtie2 (v2.2.1.0; Langmead and Salzberg, 2012), data were sorted and indexed with SAMtools (Li et al., 2009), and MACS 2.0.10 (Feng et al., 2012) was used to call peaks and calculate fold enrichments and q values, comparing the combined replicates with combined controls. For selection of peaks that were consistently detected across replicates, peak calling with MACS 2.0.10 was applied to individual replicates and overlapping peak regions were accepted if they had q values of 10^{-3} or lower in each *RPL:RPL-GFP* replicate, were not detected in any of the negative controls, and the overlapping region was at least 50 nt long. After this filtering step, peaks were attributed to gene models within 3 kb upstream or 1.5 kb downstream of the corresponding coding sequence, without intervening coding sequences. For peak overlaps and association to gene models, the script `Overlap_MACS2_files.py` was used (details in annotated source code, associated gene models, and annotation tables in Data S2). ChIP-seq data were visualized using the Integrative Genomics Viewer (Robinson et al., 2011).

To analyze the distribution of peaks within genes we used the script `peak_statistics.py`, which also includes details of the Monte Carlo method used to estimate the p value for the hypothesis that these frequencies correspond to a random distribution of peaks within genes (Data S2). For detection of enrichment for sequence motifs, MEME-ChIP (<http://meme-suite.org/tools/meme-chip>) (Bailey et al., 2009) was used in discriminative mode, comparing the sequences around observed peaks with a control set of sequences around a 10-fold larger number of random peaks; both sets were produced with script `peak_sequences.py` (Data S2). To test for overrepresented GO terms, we used the hypergeometric test of the GOstats package (Falcon and Gentleman, 2007) with the org.At.tair.cb annotation package (Gentleman et al., 2004), and Revigo (Supek et al., 2011) was used to cluster enriched terms.

Raw and processed data have been deposited in the NCBI Gene Expression Omnibus (Edgar et al., 2002) under accession number GEO: GSE78727.

Transcriptome Analysis

Ten micrograms of RNA was extracted from inflorescence apices of wild-type Ler and *rpl-1* (three replicates each) with Trizol (Sigma) and purified using Qiagen RNeasy columns (Qiagen) according to the manufacturer's instructions. AGRONOMICS1 arrays (Affymetrix) were hybridized with labeled cDNA following the manufacturer's instructions. To detect DEGs, we used the affymGUI package (<http://bioinf.wehi.edu.au/affymGUI/about.html>) to run LIMMA (Linear Models for MicroArray data) (Smyth, 2005) using a chip

description format (CDF) file for the AGRONOMICS1 array and TAIR10 (Müller et al., 2012). Raw and processed data have been deposited in the NCBI Gene Expression Omnibus (Edgar et al., 2002) under accession number GEO: GSE78511.

qPCR

qRT-PCR was performed as published by Schiesl et al. (2012) (details in Supplemental Experimental Procedures).

Measurements of Stem Growth

Plants were grown as described above; when the first flower self-pollinated, ink dots were manually placed on the stem at 2-mm intervals and photographed next to a ruler. After a further 4 days of growth, the stems were photographed again. The ink marks and positions on the ruler were landmarked manually on the images using the Point Picker plugin of Fiji (Schindelin et al., 2012). Distances between landmark coordinates were measured, graphs were plotted, and Mann-Whitney U tests and Student's t tests were performed using standard functions in matplotlib (<http://matplotlib.org>), Python 2.7, and Scientific Python (<http://www.scipy.org>).

ACCESSION NUMBERS

Raw and processed data have been deposited in the NCBI Gene Expression Omnibus under accession numbers GEO: GSE78727 and GSE78511.

SUPPLEMENTAL INFORMATION

Supplemental Information includes Supplemental Experimental Procedures, six figures, four tables, and two data files and can be found with this article online at <http://dx.doi.org/10.1016/j.devcel.2016.08.013>.

AUTHOR CONTRIBUTIONS

Conceptualization, S.B. and R.S.; Investigation, S.B., A.S.-M., and M.B.; Resources, S.F.; Software, Formal Analysis, and Data Curation, R.S.; Writing – Original Draft, R.S.; Writing – Review & Editing, S.B., S.F., A.S.-M., M.B., and R.S.; Funding Acquisition, R.S.; Supervision, R.S.

ACKNOWLEDGMENTS

We thank Mitsuhiro Aida (Nara Institute of Science and Technology, Japan) for *lsh4-1* seeds, Shelley Hepworth (Carleton University, Canada) for *kna6-2 rpl-2* seeds, Martin Trick for help with the initial ChIP-seq analysis, and Katharina Schiesl, Bihai Shi, Vishmita Sethi, and Lars Østergaard for critical comments. The work was supported by BBSRC grants BB/J007056/1 and BB/J004588/1.

Received: March 3, 2016

Revised: April 14, 2016

Accepted: August 24, 2016

Published: September 22, 2016

REFERENCES

- Aichinger, E., Komet, N., Friedrich, T., and Laux, T. (2012). Plant stem cell niches. *Annu. Rev. Plant Biol.* 63, 615–636.
- Andrés, F., Romera-Branchat, M., Martínez-Gallegos, R., Patel, V., Schneeberger, K., Jang, S., Altmüller, J., Nürnberg, P., and Coupland, G. (2015). Floral induction in *Arabidopsis* by FLOWERING LOCUS T requires direct repression of BLADE-ON-PETIOLE genes by the homeodomain protein PENNYWISE. *Plant Physiol.* 169, 2187–2199.
- Amaud, N., Lawrenson, T., Østergaard, L., and Sablowski, R. (2011). The same regulatory point mutation changed seed-dispersal structures in evolution and domestication. *Curr. Biol.* 21, 1215–1219.
- Bailey, T.L., Boden, M., Buske, F.A., Frith, M., Grant, C.E., Clementi, L., Ren, J., Li, W.W., and Noble, W.S. (2009). MEME suite: tools for motif discovery and searching. *Nucleic Acids Res.* 37, W202.

- Baker, C.C., Sieber, P., Wellmer, F., and Meyerowitz, E.M. (2005). The early extra petals1 mutant uncovers a role for microRNA miR164c in regulating petal number in *Arabidopsis*. *Curr. Biol.* **15**, 303–315.
- Beemster, G., and Baskin, T. (1998). Analysis of cell division and elongation underlying the developmental acceleration of root growth in *Arabidopsis thaliana*. *Plant Physiol.* **116**, 1515–1526.
- Bellaoui, M., Plickowich, M.S., Samach, A., Kushalappa, K., Kohalmi, S.E., Modrusan, Z., Crosby, W.L., and Haughn, G.W. (2001). The *Arabidopsis* BELL1 and KNOX TALE homeodomain proteins interact through a domain conserved between plants and animals. *Plant Cell* **13**, 2455–2470.
- Besson, S., and Dumais, J. (2011). Universal rule for the symmetric division of plant cells. *Proc. Natl. Acad. Sci. USA* **108**, 6294–6299.
- Boehm, B., Westerberg, H., Lesnicar-Pucko, G., Raja, S., Rautschka, M., Cotterell, J., Swoger, J., and Sharpe, J. (2010). The role of spatially controlled cell proliferation in limb bud morphogenesis. *PLoS Biol.* **8**, e1000420.
- Byrne, M.E., Groover, A.T., Fontana, J.R., and Martienssen, R.A. (2003). Phylotactic pattern and stem cell fate are determined by the *Arabidopsis* homeobox gene BELLRINGER. *Development* **130**, 3941–3950.
- Chiu, W., Niwa, Y., Zeng, W., Hirano, T., Kobayashi, H., and Sheen, J. (1996). Engineered GFP as a vital reporter in plants. *Curr. Biol.* **6**, 325–330.
- Clough, S.J., and Bent, A.F. (1998). Floral dip: a simplified method for *Agrobacterium*-mediated transformation of *Arabidopsis thaliana*. *Plant J.* **16**, 735–743.
- Edgar, R., Domrachev, M., and Lash, A.E. (2002). Gene Expression Omnibus: NCBI gene expression and hybridization array data repository. *Nucleic Acids Res.* **30**, 207–210.
- Falcon, S., and Gentleman, R. (2007). Using GOstats to test gene lists for GO term association. *Bioinformatics* **23**, 257–268.
- Feng, J., Liu, T., Qin, B., Zhang, Y., and Liu, X.S. (2012). Identifying ChIP-seq enrichment using MACS. *Nat. Protoc.* **7**, 1728–1740.
- Fletcher, J.C. (2002). Shoot and floral meristem maintenance in *Arabidopsis*. *Annu. Rev. Plant Biol.* **53**, 45–66.
- Gallois, J.L., Nora, F.R., Mizukami, Y., and Sablowski, R. (2004). WUSCHEL induces shoot stem cell activity and developmental plasticity in the root meristem. *Genes Dev.* **18**, 375.
- Gentleman, R.C., Carey, V.J., Bates, D.M., Bolstad, B., Detting, M., Dudoit, S., Ellis, B., Gautier, L., Ge, Y., and Gentry, J. (2004). Bioconductor: open software development for computational biology and bioinformatics. *Genome Biol.* **5**, R80.
- Hajdukiewicz, P., Svab, Z., and Maliga, P. (1994). The small, versatile pPZP family of *Agrobacterium* binary vectors for plant transformation. *Plant Mol. Biol.* **25**, 989–994.
- Hamant, O., Heisler, M., Jonsson, H., Krupinski, P., Uyttewaal, M., Bokov, P., Corson, F., Sahlin, P., Boudaoud, A., Meyerowitz, E., et al. (2008). Developmental patterning by mechanical signals in *Arabidopsis*. *Science* **322**, 1650–1655.
- Heisler, M.G., Hamant, O., Krupinski, P., Uyttewaal, M., Ohno, C., Jonsson, H., Traas, J., and Meyerowitz, E.M. (2010). Alignment between PIN1 polarity and microtubule orientation in the shoot apical meristem reveals a tight coupling between morphogenesis and auxin transport. *PLoS Biol.* **8**, e1000516.
- Hepworth, S., and Pautot, V. (2015). Beyond the divide: boundaries for patterning and stem cell regulation in plants. *Front. Plant Sci.* **6**, 1052.
- Hibara, K.-I., Karim, M.R., Takada, S., Taoka, K.-I., Furutani, M., Aida, M., and Tasaka, M. (2006). *Arabidopsis* CUP-SHAPED COTYLEDON3 regulates postembryonic shoot meristem and organ boundary formation. *Plant Cell* **18**, 2946–2957.
- Kaufmann, K., Muñio, J.M., Jauregui, R., Airoldi, C.A., Smaczniak, C., Krajewski, P., and Angenent, G.C. (2009). Target genes of the MADS transcription factor SEPALLATA3: integration of developmental and hormonal pathways in the *Arabidopsis* flower. *PLoS Biol.* **7**, e90.
- Khan, M., Xu, M., Mumu, J., Tabb, P., Liu, Y., Storey, K., Mckim, S.M., Douglas, C.J., and Hepworth, S.R. (2012). Antagonistic interaction of BLADE-on-PETIOLE1 and 2 with BREVIPEDICELLUS and PENNYWISE regulates *Arabidopsis* inflorescence architecture. *Plant Physiol.* **158**, 946–960.
- Khan, M., Ragni, L., Tabb, P., Salasini, B.C., Chatfield, S., Datta, R., Lock, J., Kuai, X., Després, C., and Proveniers, M. (2015). Repression of lateral organ boundary genes by PENNYWISE and POUND-FOOLISH is essential for meristem maintenance and flowering in *Arabidopsis*. *Plant Physiol.* **169**, 2166–2186.
- Khush, G.S. (2001). Green revolution: the way forward. *Nat. Rev. Genet.* **2**, 815–822.
- Kwiatkowska, D. (2004). Structural integration at the shoot apical meristem: models, measurements, and experiments. *Am. J. Bot.* **91**, 1277–1293.
- Lai, S., Pacis, L.B., and Smith, H.M. (2011). Regulation of the SQUAMOSA PROMOTER-BINDING PROTEIN-LIKE genes/microRNA156 module by the homeodomain proteins PENNYWISE and POUND-FOOLISH in *Arabidopsis*. *Mol. Plant* **4**, 1123–1132.
- Langmead, B., and Salzberg, S.L. (2012). Fast gapped-read alignment with Bowtie 2. *Nat. Methods* **9**, 357–359.
- Li, H., Handsaker, B., Wysoker, A., Fennell, T., Ruan, J., Homer, N., Marth, G., Abecasis, G., and Durbin, R. (2009). The sequence alignment/map format and SAMtools. *Bioinformatics* **25**, 2078–2079.
- Mele, G., Ori, N., Sato, Y., and Hake, S. (2003). The knotted1-like homeobox gene BREVIPEDICELLUS regulates cell differentiation by modulating metabolic pathways. *Genes Dev.* **17**, 2088–2093.
- Müller, M., Patrignani, A., Rehauer, H., Gruissem, W., and Hennig, L. (2012). Evaluation of alternative RNA labeling protocols for transcript profiling with *Arabidopsis* AGRONOM/C51 tiling arrays. *Plant Methods* **8**, 1.
- Muñiz, L., Minguet, E.G., Singh, S.K., Pesquet, E., Vera-Sirera, F., Moreau-Courtois, C.L., Carbonell, J., Blázquez, M.A., and Tuominen, H. (2008). ACAULUS5 controls *Arabidopsis* xylem specification through the prevention of premature cell death. *Development* **135**, 2573–2582.
- Ragni, L., Belles-Boix, E., Günl, M., and Pautot, V. (2008). Interaction of KNAT6 and KNAT2 with BREVIPEDICELLUS and PENNYWISE in *Arabidopsis* inflorescences. *Plant Cell* **20**, 888–900.
- Robinson, J.T., Thorvaldsdóttir, H., Winckler, W., Guttman, M., Lander, E.S., Getz, G., and Mesirov, J.P. (2011). Integrative genomics viewer. *Nat. Biotechnol.* **29**, 24–26.
- Roeder, A.H.K., Ferrandiz, C., and Yanofsky, M.F. (2003). The role of the REPLUMLESS homeodomain protein in patterning the *Arabidopsis* fruit. *Curr. Biol.* **13**, 1630–1635.
- Sachs, R.M. (1965). Stem elongation. *Annu. Rev. Plant Physiol.* **16**, 73–95.
- Sanchez, P., Nehlin, L., and Greb, T. (2012). From thin to thick: major transitions during stem development. *Trends Plant Sci.* **17**, 113–121.
- Sassi, M., and Traas, J. (2015). When biochemistry meets mechanics: a systems view of growth control in plants. *Curr. Opin. Plant Biol.* **28**, 137–143.
- Schiessl, K., Kausika, S., Southam, P., Bush, M., and Sablowski, R. (2012). JAGGED controls growth anisotropy and coordination between cell size and cell cycle during plant organogenesis. *Curr. Biol.* **22**, 1739–1746.
- Schiessl, K., Muñio, J.M., and Sablowski, R. (2014). *Arabidopsis* JAGGED links floral organ patterning to tissue growth by repressing Kip-related cell cycle inhibitors. *Proc. Natl. Acad. Sci. USA* **111**, 2830–2835.
- Schindelin, J., Arganda-Carreras, J., Frise, E., Kaynig, V., Longair, M., Pietzsch, T., Preibisch, S., Rueden, C., Saalfeld, S., and Schmid, B. (2012). Fiji: an open-source platform for biological-image analysis. *Nat. Methods* **9**, 676–682.
- Serrano-Mislata, A., Schiessl, K., and Sablowski, R. (2015). Active control of cell size generates spatial detail during plant organogenesis. *Curr. Biol.* **25**, 2991–2996.
- Sieburth, L.E., Drews, G.N., and Meyerowitz, E.M. (1998). Non-autonomy of AGAMOUS function in flower development: use of a Cre/loxP method for mosaic analysis in *Arabidopsis*. *Development* **125**, 4303–4312.
- Smaczniak, C., Immink, R.G., Muñio, J.M., Blanvillain, R., Busscher, M., Busscher-Lange, J., Dinh, Q.P., Liu, S., Westphal, A.H., Boeren, S., et al. (2012). Characterization of MADS-domain transcription factor complexes in *Arabidopsis* flower development. *Proc. Natl. Acad. Sci. USA* **109**, 1560–1565.
- Smith, L.G. (2001). Plant cell division: building walls in the right places. *Nat. Rev. Mol. Cell Biol.* **2**, 33–39.

- Smith, H.M.S., and Hake, S. (2003). The interaction of two homeobox genes, *BREVIPEDICELLUS* and *PENNYWISE*, regulates internode patterning in the *Arabidopsis* inflorescence. *Plant Cell* **15**, 1717–1727.
- Smith, H.M.S., Boschke, I., and Hake, S. (2002). Selective interaction of plant homeodomain proteins mediates high DNA-binding affinity. *Proc. Natl. Acad. Sci. USA* **99**, 9579–9584.
- Smith, H.M.S., Campbell, B.C., and Hake, S. (2004). Competence to respond to floral inductive signals requires the homeobox genes *PENNYWISE* and *POUND-FOOLISH*. *Curr. Biol.* **14**, 812–817.
- Smyth, G.K. (2005). Limma: linear models for microarray data. In *Bioinformatics and Computational Biology Solutions Using R and Bioconductor*, R. Gentleman, V. Carey, S. Dudoit, R. Irizarry, and W. Huber, eds. (New York: Springer), pp. 397–420.
- Supek, F., Bošnjak, M., Škunca, N., and Smuc, T. (2011). Revigo summarizes and visualizes long lists of gene ontology terms. *PLoS One* **6**, e21800.
- Takeda, S., Hanano, K., Kariya, A., Shimizu, S., Zhao, L., Matsui, M., Tasaka, M., and Aida, M. (2011). *CUP-SHAPED COTYLEDON1* transcription factor activates the expression of *LSH4* and *LSH3*, two members of the *ALOG* gene family, in shoot organ boundary cells. *Plant J.* **66**, 1066–1077.
- Truernit, E., and Haseloff, J. (2008). A simple way to identify non-viable cells within living plant tissue using confocal microscopy. *Plant Methods* **4**, 15.
- Truernit, E., Bauby, H., Dubreucq, B., Grandjean, O., Runions, J., Barthelemy, J., and Palauqui, J.-C. (2008). High-resolution whole-mount imaging of three-dimensional tissue organization and gene expression enables the study of phloem development and structure in *Arabidopsis*. *Plant Cell* **20**, 1494–1503.
- Vanneste, S., and Friml, J. (2009). Auxin: a trigger for change in plant development. *Cell* **136**, 1005–1016.
- Vroemen, C.W., Mordhorst, A.P., Albrecht, C., Kwaaitaal, M.A., and De Vries, S.C. (2003). The *CUP-SHAPED COTYLEDON3* gene is required for boundary and shoot meristem formation in *Arabidopsis*. *Plant Cell* **15**, 1563–1577.
- Wang, Y., Wang, J., Shi, B., Yu, T., Qi, J., Meyerowitz, E.M., and Jiao, Y. (2014). The stem cell niche in leaf axils is established by auxin and cytokinin in *Arabidopsis*. *Plant Cell* **26**, 2055–2067.
- Weber, E., Engler, C., Gruetzner, R., Werner, S., and Marillonnet, S. (2011). A modular cloning system for standardized assembly of multigene constructs. *PLoS One* **6**, e16765.
- Yoshida, S., De Reuille, P.B., Lane, B., Bassel, G.W., Prusinkiewicz, P., Smith, R.S., and Weijers, D. (2014). Genetic control of plant development by overriding a geometric division rule. *Dev. Cell* **29**, 75–87.
- Zádníková, P., and Simon, R. (2014). How boundaries control plant development. *Curr. Opin. Plant Biol.* **17**, 116–125.

Viewpoints

Standards for plant synthetic biology: a common syntax for exchange of DNA parts

Summary

Inventors in the field of mechanical and electronic engineering can access multitudes of components and, thanks to standardization, parts from different manufacturers can be used in combination with each other. The introduction of BioBrick standards for the assembly of characterized DNA sequences was a landmark in microbial engineering, shaping the field of synthetic biology. Here, we describe a standard for Type IIS restriction endonuclease-mediated assembly, defining a common syntax of 12 fusion sites to enable the facile assembly of eukaryotic transcriptional units. This standard has been developed and agreed by representatives and leaders of the international plant science and synthetic biology communities, including inventors, developers and adopters of Type IIS cloning methods. Our vision is of an extensive catalogue of standardized, characterized DNA parts that will accelerate plant bioengineering.

Introduction

The World Bank estimates that almost 40% of land mass is used for cultivation of crop, pasture or forage plants (World Development Indicators, The World Bank 1960–2014). Plants also underpin production of building and packing materials, medicines, paper and decorations, as well as food and fuel. Plant synthetic biology offers the means and opportunity to engineer plants and algae for new roles in our environment, to produce therapeutic compounds and to address global problems such as food insecurity and the contamination of ecosystems with agrochemicals and macronutrients. The adoption of assembly standards will greatly accelerate the pathway from product design to market, enabling the full potential of plant synthetic biology to be realized.

The standardization of components, from screw threads to printed circuit boards, drives both the speed of innovation and the economy of production in mechanical and electronic engineering. Products as diverse as ink-jet printers and airplanes are designed and constructed from component parts and devices. Many of these components can be selected from libraries and catalogues of standard parts in which specifications and performance characteristics are described. The agreement and implementation of assembly standards that allow parts, even those from multiple

manufacturers, to be assembled together has underpinned invention in these fields.

This conceptual model is the basis of synthetic biology, with the same ideal being applied to biological parts (DNA fragments) for the engineering of biological systems. The first widely-adopted biological standard was the BioBrick, for which sequences and performance data are stored in the Registry of Standard Biological Parts (Knight, 2003). BioBrick assembly standard 10 (BBF RFC 10) was the first biological assembly standard to be introduced. Its key feature is that the assembly reactions are idempotent: each reaction retains the key structural elements of the constituent parts so that resulting assemblies can be used as input in identical assembly processes (Knight, 2003; Shetty *et al.*, 2008). Over the years, several other BioBrick assembly standards have been developed that diminish some of the limitations of standard 10 (Phillips & Silver, 2006; Anderson *et al.*, 2010). Additionally, several alternative technologies have been developed that confer the ability to assemble multiple parts in a single reaction (Engler *et al.*, 2008; Gibson *et al.*, 2009; Quan & Tian, 2009; Li & Elledge, 2012; Kok *et al.*, 2014).

While overlap-dependent methods are powerful and generally result in 'scarless' assemblies, their lack of idempotency and the requirement for custom oligonucleotides and amplification of even well characterized standard parts for each new assembly are considerable drawbacks (Ellis *et al.*, 2011; Liu *et al.*, 2013; Patron, 2014). Assembly methods based on Type IIS restriction enzymes, known widely as Golden Gate cloning, are founded on standard parts that can be characterized, exchanged and assembled cheaply, easily, and in an automatable way without proprietary tools and reagents (Engler *et al.*, 2009, 2014; Sarrion-Perdigones *et al.*, 2011; Werner *et al.*, 2012).

Type IIS assembly methods have been widely adopted in plant research laboratories with many commonly used sequences being adapted for Type IIS assembly and subsequently published and shared through public plasmid repositories such as AddGene (Sarrion-Perdigones *et al.*, 2011; Weber *et al.*, 2011; Emami *et al.*, 2013; Lampropoulos *et al.*, 2013; Binder *et al.*, 2014; Engler *et al.*, 2014; Vafaei *et al.*, 2014). Type IIS assembly systems have also been adopted for the engineering of fungi (Terfrüchte *et al.*, 2014) and 'IP-Free' host expression systems have been developed for bacteria, mammals and yeast (Whitman *et al.*, 2013).

To reap the benefits of the exponential increase in genomic information and DNA assembly technologies, bioengineers require assembly standards to be agreed for multicellular eukaryotes. A standard for plants must be applicable to the diverse taxa that comprise Archaeplastida and also be capable of retaining the features that minimize the need to reinvent common steps such as transferring genetic material into plant genomes. In this Viewpoint article, the authors of which include inventors, developers and

adopters of Golden Gate cloning methods from multiple international institutions, we define a Type IIS genetic grammar for plants, extendible to all eukaryotes. This sets a consensus for establishing a common language across the plant field, putting in place the framework for a sequence and data repository for plant parts.

Golden Gate cloning

Golden Gate cloning is based on Type IIS restriction enzymes and enables parallel assembly of multiple DNA parts in a one-pot, one-step reaction. Contrary to Type II restriction enzymes, Type IIS restriction enzymes recognize nonpalindromic sequence motifs and cleave outside of their recognition site (Fig. 1a). These features enable the production of user-defined overhangs on either strand, which in turn allow multiple parts to be assembled in a predetermined order and orientation using only one restriction enzyme. Parts are released from their original plasmids and assembled into a new plasmid backbone in the same reaction, bypassing time-consuming steps such as custom primer design, PCR amplification and gel purification (Fig. 1b).

The one-step digestion–ligation reaction can be performed with any collection of plasmid vectors and parts providing that:

(1) Parts are housed in plasmids flanked by a convergent pair of Type IIS recognition sequences;

(2) The accepting plasmid has a divergent pair of recognition sequences for the same enzyme, between which the part or parts will be assembled;

(3) The parts themselves, and all plasmid backbones, are otherwise free of recognition sites for this enzyme;

(4) None of the parts are housed in a plasmid backbone with the same antibiotic resistance as the accepting plasmid into which parts will be assembled;

(5) The overhangs created by digestion with the Type IIS restriction enzymes are unique and nonpalindromic.

To date, several laboratories have converted ‘in-house’ and previously published plasmids for use with Golden Gate cloning and have assigned compatible overhangs to standard elements such as promoters, coding sequences and terminators found in eukaryotic genes (Sarrion-Perdigones *et al.*, 2011; Weber *et al.*, 2011; Emami *et al.*, 2013; Lampropoulos *et al.*, 2013; Binder *et al.*, 2014; Engler *et al.*, 2014). The GoldenBraid2.0 (GB2.0) and Golden Gate Modular Cloning (MoClo) assembly standards, the main features of which are described later, are both widely used having been adopted by large communities of plant research laboratories such as the European Cooperation in Science and Technology (COST) network for plant metabolic engineering, the Engineering Nitrogen Symbiosis for Africa (ENSA) project, the C₄ Rice project and the Realizing Increased Photosynthetic Activity (RIPE) project. MoClo and GB2.0 are largely, though not entirely,

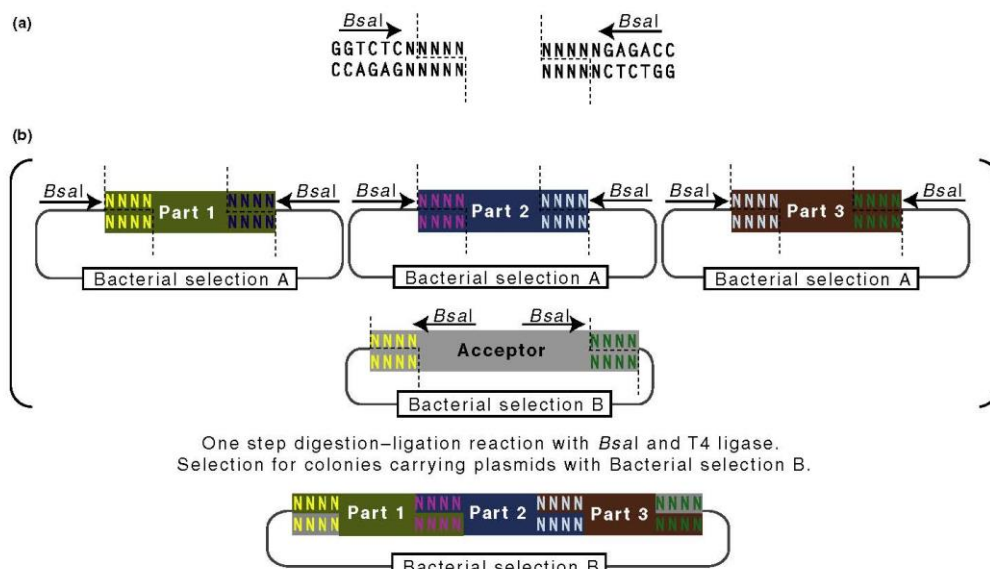


Fig. 1 (a) Type IIS restriction enzymes such as *BsaI* are directional, cleaving outside of their nonpalindromic recognition sequences. (b) Providing compatible overhangs are produced on digestion, standard parts cloned in plasmid backbones flanked by a pair of convergent Type IIS restriction enzyme recognition sites can be assembled in a single digestion–ligation reaction into an acceptor plasmid with divergent Type IIS restriction enzyme recognition sites and a unique bacterial selection cassette.

syntax bounded by an adjacent pair of adjacent fusion sites. However, when the full level of complexity is unnecessary, or if particular functional elements such as amino (N)- or carboxyl (C)-terminal tags are not required, standard parts can comprise sequences that span multiple fusion sites (Fig. 3).

The sequences that comprise the fusion sites have been selected both for maximum compatibility in the one-step digestion–ligation reaction and to maximize biological functionality. The 5' nontranscribed region is separated into core, proximal and distal promoter sequences, with the core region containing the transcriptional start site (TSS). The transcribed region is separated into coding parts and 5' and 3' untranslated parts. For maximum flexibility, an ATG codon for methionine is wholly or partially encoded into two fusion sites. The translated region, therefore, may be divided into three or four parts. The 3' nontranscribed region is followed by the 3' untranslated region, which contains the polyadenylation sequence (PAS). Amino acids coded by fusion sites within the coding region have been rationally selected: neutral, nonpolar amino acids, methionine and alanine, are encoded in the 3' overhangs of parts that may be used to house signal and transit peptides in order to prevent interference with recognition and cleavage. An alternative overhang, encoding a glycine, is also included to give greater flexibility for the fusion of noncleaved coding parts. Serine, a small amino acid commonly used to link peptide and reporter tags, is encoded in the overhang that will fuse C-terminal tag parts to coding sequences.

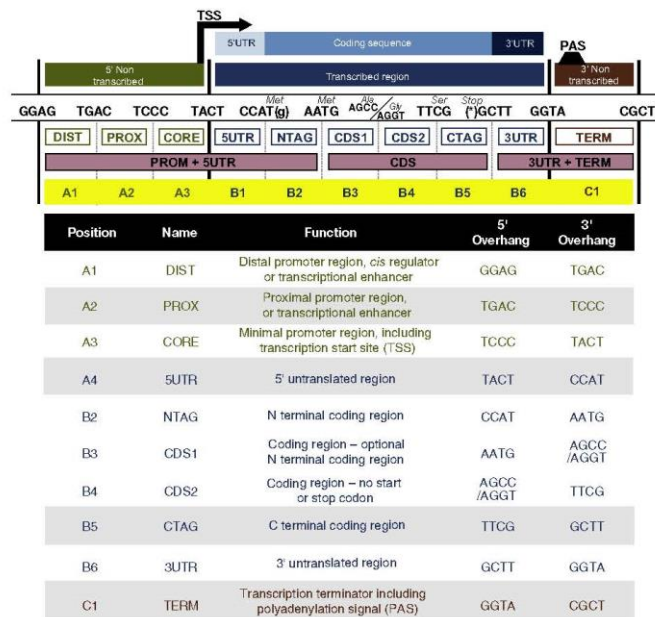


Fig. 3 Twelve fusion sites have been defined. These sites allow a multitude of standard parts to be generated. Standard parts comprise any portion of a gene cloned into a plasmid flanked by a convergent pair of *Bsal* recognition sequences. Parts can comprise the region between an adjacent pair of adjacent fusion sites. Alternatively, to reduce complexity or when a particular functional element is not required, parts can span multiple fusion sites (examples in pink boxes).

Universal acceptor plasmids (UAPs)

Universal acceptor plasmids (UAPs) allow the conversion of any sequence to a standard part in a single step (Fig. 4). This is achieved by PCR amplification of desired sequences as a single fragment or, if restriction sites need to be domesticated, as multiple fragments (Fig. 4). The oligonucleotide primers used for amplification add 5' sequences to allow cloning into the UAP, add the standard fusion sites that the sequence will be flanked with when released from the UAP as a standard part with *Bsal* and can also introduce mutations (Fig. 4). Two UAPs, pUPD2 (<https://gbclooning.org/feature/GB0307/>) and pUAP1 (AddGene no. 63674) can be used to create new standard parts in the chloramphenicol resistant pSB1C3 backbone, in which the majority of BioBricks housed at the Registry of Standard Parts are cloned. A spectinomycin resistant UAP, pAGM9121 has been published previously (AddGene no. 51833; Engler *et al.*, 2014).

Compatibility with multigene assembly systems

Standard parts are assembled into transcriptional units in plasmid vectors that contain the features and sequences required for delivery to the cell, for example Left border (LB) and Right border (RB) sequences and an origin of replication for *Agrobacterium*-mediated delivery. Subsequently, transcriptional units can be assembled into multigene constructs in plasmid acceptors that also contain these features. It is important that a standard Type IIS syntax be

compatible with the plasmid vector systems that are in common use such as GB2.0 and MoClo while also allowing space for further innovation in Type IIS-mediated multigene assembly methodologies and the development of plasmid vectors with features required for delivery to other species and by other delivery methods. The definition of a standard Type IIS syntax for plants is therefore timely and will allow the growing plant synthetic biology community access to an already large library of standard parts.

Conclusions

Synthetic biology aims to simplify the process of designing, constructing and modifying complex biological systems. Plants provide an ideal chassis for synthetic biology, are amenable to genetic engineering and have relatively simple requirements for growth (Cook *et al.*, 2014; Fesenko & Edwards, 2014). However, their eukaryotic gene structure and the methods commonly used for transferring DNA to their genomes demand specific plasmid vectors and a tailored assembly standard. Here, we have defined a

Type IIS genetic syntax that employs the principles of part reusability and standardization. The standard has also been submitted as a Request for Comments (BBF RFC 106) (Rutten *et al.*, 2015) at the BioBrick Foundation to facilitate iGEM teams working on plant chassis. Using the standards described here, new standard parts for plants can be produced and exchanged between laboratories enabling the facile construction of transcriptional units. We invite the plant science and synthetic biology communities to build on this work by adopting this standard to create a large repository of characterized standard parts for plants.

Acknowledgements

This work was supported by the UK Biotechnological and Biological Sciences Research Council (BBSRC) Synthetic Biology Research Centre 'OpenPlant' award (BB/L014130/1), BBSRC grant no. BB/K005952/1 (A.O. and A.L.), BBSRC grant no. BB/L02182X/1 (A.A.R.W.), the Spanish MINECO grant no. BIO2013-42193-R (D.O.), the BBSRC Institute Strategic

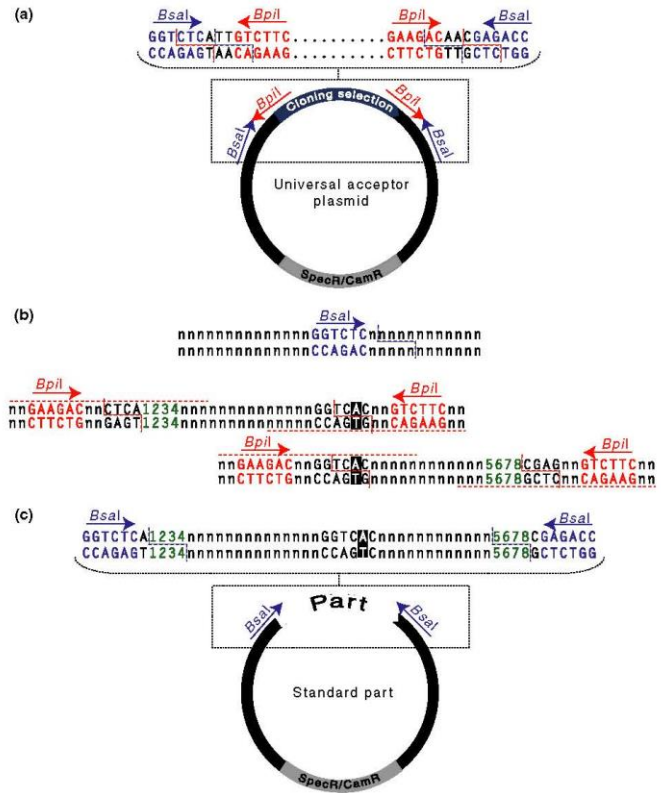


Fig. 4 (a) Universal acceptor plasmids (UAPs) comprise a small plasmid backbone conferring resistance to spectinomycin or chloramphenicol in bacteria. They contain a cloning site consisting of a pair of divergent Type IIS recognition sequences (e.g. *Bpil*, as depicted, or *BsmBI*) flanked by overlapping convergent *Bsal* recognition sequences. (b) A sequence containing an illegal *Bsal* recognition sequence can be amplified in two fragments using oligonucleotide primers with 5' overhangs (red dashed lines) that (i) introduce a mutation to destroy the illegal site (reversed type), (ii) add Type IIS recognition sequences (e.g. *Bpil*, as depicted, or *BsmBI*) and fusion sites to allow one step digestion–ligation into the universal acceptor, and (iii) add the desired fusion sites (green numbers) that will define the type of standard part and that will flank the part when rereleased from the backbone with *Bsal*. (c) When the resulting amplicons are cloned into a UAP, the new standard part will be flanked by a pair of convergent *Bsal* recognition sequences capable of releasing the part with the desired fusion sites (green numbers).

Programme Grants 'Understanding and exploiting plant and microbial metabolism' and 'Biotic interactions for crop productivity', the John Innes Foundation and the Gatsby Foundation. Supported by the Engineering Nitrogen Symbiosis for Africa (ENSA) project, through a grant to the John Innes Centre from The Bill & Melinda Gates Foundation, the DOE Early Career Award and the DOE Joint BioEnergy Institute supported by the US Department of Energy, Office of Biological and Environmental through contract DE-AC02-05CH1123. The authors also acknowledge the support of COST Action FA1006, PlantEngine.

Nicola J. Patron^{1,2*}, Diego Orzaez³, Sylvestre Marillonnet⁴, Heribert Warzecha⁵, Colette Matthewman^{2,6}, Mark Youles¹, Oleg Raitskin^{1,2}, Aymeric Leveau⁶, Gemma Farré⁶, Christian Rogers⁶, Alison Smith^{2,7}, Julian Hibberd^{2,7}, Alex A. R. Webb^{2,7}, James Locke^{2,8}, Sebastian Schornack^{2,8}, Jim Ajioka^{2,9}, David C. Baulcombe^{2,7}, Cyril Zipfel¹, Sophien Kamoun¹, Jonathan D. G. Jones¹, Hannah Kuhn¹, Silke Robatzek¹, H. Peter Van Esse¹, Dale Sanders^{2,6}, Giles Oldroyd^{2,6}, Cathie Martin^{2,6}, Rob Field^{2,6}, Sarah O'Connor^{2,6}, Samantha Fox⁶, Brande Wulff⁶, Ben Miller⁶, Andy Breakspear⁶, Guru Radhakrishnan⁶, Pierre-Marc Delaux⁶, Dominique Loque^{10,11}, Antonio Grandell³, Alain Tissier⁴, Patrick Shih¹⁰, Thomas P. Brutnell¹², W. Paul Quick¹³, Heiko Rischer¹⁴, Paul D. Fraser¹⁵, Asaph Aharoni¹⁶, Christine Raines¹⁷, Paul F. South¹⁸, Jean-Michel Añe¹⁹, Björn R. Hamberger²⁰, Jane Langdale²¹, Jens Stougaard²², Harro Bouwmeester²³, Michael Udvardi²⁴, James A. H. Murray²⁵, Vardis Ntoukakis²⁶, Patrick Schäfer²⁶, Katherine Denby²⁶, Keith J. Edwards²⁷, Anne Osbourn^{2,6} and Jim Haseloff^{2,7}

¹The Sainsbury Laboratory, Norwich Research Park, Norwich, NR4 7RG, UK;

²OpenPlant Consortium: The University of Cambridge, The John Innes Centre and The Sainsbury Laboratory, Norwich, NR4 7UH, UK;

³Instituto de Biología Molecular y Celular de Plantas (IBMCP), Consejo Superior de Investigaciones Científicas, Universidad Politécnica de Valencia, Avda Tarongers SN, Valencia, Spain;

⁴Leibniz-Institut für Pflanzenbiochemie, Weinberg 3, 06120, Halle (Saale), Germany;

⁵Plant Biotechnology and Metabolic Engineering, Technische Universität Darmstadt, Schnittspahnstrasse 4, Darmstadt 64287, Germany;

⁶The John Innes Centre, Norwich Research Park, Norwich, NR4 7UH, UK;

⁷Department of Plant Sciences, University of Cambridge, Downing Street, Cambridge, CB2 3EA, UK;

⁸The Sainsbury Laboratory, Cambridge University, Bateman Street, Cambridge, CB2 1LR, UK;

⁹Department of Pathology, University of Cambridge, Tennis Court Road, Cambridge, CB2 1QP, UK;

¹⁰Physical Biosciences Division, Lawrence Berkeley National Laboratory, Berkeley, CA 94720, USA;

¹¹Joint BioEnergy Institute, EmeryStation East, 5885 Hollis St,

4th Floor, Emeryville, CA 94608, USA;

¹²The Donald Danforth Plant Science Center, St Louis, MO 63132, USA;

¹³Department of Animal and Plant Sciences, University of Sheffield, Sheffield, S10 2TN, UK;

¹⁴VTT Technical Research Centre of Finland, Espoo 02044, Finland;

¹⁵School of Biological Sciences, Royal Holloway, University of London, Egham Hill, Egham, TW20 0EX, UK;

¹⁶Department of Plant Sciences, Weizmann Institute of Science, Rehovot 76100, Israel;

¹⁷School of Biological Sciences, University of Essex, Colchester, CO4 3SQ, UK;

¹⁸United States Department of Agriculture, Global Change and Photosynthesis Research Unit, ARS 1206 West Gregory Drive, Urbana, IL 61801, USA;

¹⁹Departments of Bacteriology and Agronomy, University of Wisconsin, 1575 Linden Drive, Madison, WI 53706, USA;

²⁰Biochemistry Laboratory, Department of Plant and Environmental Sciences, University of Copenhagen, Thorvaldsensvej 40, Frederiksberg C, Denmark;

²¹Department of Plant Sciences, University of Oxford, Oxford, OX1 3RB, UK;

²²Centre for Carbohydrate Recognition and Signalling, Department of Molecular Biology and Genetics, Aarhus University, Gustav Wiedes Vej 10C, Aarhus, Denmark;

²³Wageningen UR, Wageningen University, Wageningen 6700 AA, the Netherlands;

²⁴Plant Biology Division, The Samuel Roberts Noble Foundation, 2510 Sam Noble Parkway, Ardmore, OK 73401, USA;

²⁵School of Biosciences, Sir Martin Evans Building, Cardiff University, Museum Avenue, Cardiff, CF10 3AX, UK;

²⁶Warwick Integrative Synthetic Biology Centre and School of Life Sciences, University of Warwick, Coventry, CV4 7AL, UK;

²⁷BrisSynBio, Life Sciences Building, University of Bristol, Tyndall Avenue, Bristol, BS8 1TQ, UK

(* Author for correspondence: tel +44 1603 450527; email nicola.patron@tsl.ac.uk)

References

- Anderson JC, Duerber JE, Leguia M, Wu GC, Goler JA, Arkin AP, Keasling JD. 2010. BglBricks: a flexible standard for biological part assembly. *Journal of Biological Engineering* 4: e88218.
- Binder A, Lambert J, Morbitzer R, Popp C, Ott T, Lahaye T, Parniske M. 2014. A modular plasmid assembly kit for multigene expression, gene silencing and silencing rescue in plants. *PLoS ONE* 9: e88218.
- Cook C, Bastow R, Martin L. 2014. *Developing plant synthetic biology in the UK – challenges and opportunities*. Report from the 2013 GARNet meeting 'An introduction to opportunities in plant synthetic biology'. Cardiff, UK: GarNET.
- Ellis T, Adie T, Baldwin GS. 2011. DNA assembly for synthetic biology: from parts to pathways and beyond. *Integrative Biology* 3: 109–118.
- Emami S, Yee M-C, Dimeny JR. 2013. A robust family of Golden Gate *Agrobacterium* vectors for plant synthetic biology. *Frontiers in Plant Science* 4: 339.
- Engler C, Gruetzner R, Kandzia R, Marillonnet S. 2009. Golden Gate shuffling: a one-pot DNA shuffling method based on type II restriction enzymes. *PLoS ONE* 4: e5553.

- Engler C, Kandzia R, Marillonnet S. 2008. A one pot, one step, precision cloning method with high throughput capability. *PLoS ONE* 3: e3647.
- Engler C, Youles M, Gruetzner R, Ehnert T-M, Werner S, Jones JDG, Patron NJ, Marillonnet S. 2014. A Golden Gate modular cloning toolbox for plants. *ACS Synthetic Biology* 3: 839–843.
- Fesenko E, Edwards R. 2014. Plant synthetic biology: a new platform for industrial biotechnology. *Journal of Experimental Botany* 65: 1927–1937.
- Gibson D, Young L, Chuang R, Venter C, Hutchison CA III, Smith H. 2009. Enzymatic assembly of DNA molecules up to several hundred kilobases. *Nature Methods* 6: 343–345.
- Knight T. 2003. *Idempotent vector design for standard assembly of BioBricks*. Boston, MA, USA: MIT Synthetic Biology Working Group, MIT Artificial Intelligence Laboratory.
- Kok S, Stanton L, Slaby T. 2014. Rapid and reliable DNA assembly via ligase cycling reaction. *ACS Synthetic Biology* 3: 97–106.
- Lampropoulos A, Sutikovic Z, Wenzl C, Maegele I, Lohmann JU, Forner J. 2013. GreenGate – a novel, versatile, and efficient cloning system for plant transgenesis. *PLoS ONE* 8: e83043.
- Li MZ, Elledge SJ. 2012. SLIC: a method for sequence- and ligation-independent cloning. In: Peccoud J, ed. *Methods in molecular biology*. Totowa, NJ, USA: Humana Press, 51–59.
- Liu W, Yuan JS, Stewart CN. 2013. Advanced genetic tools for plant biotechnology. *Nature Reviews Genetics* 14: 781–793.
- Patron NJ. 2014. DNA assembly for plant biology: techniques and tools. *Current Opinion in Plant Biology* 19C: 14–19.
- Phillips I, Silver P. 2006. *BBF RFC 23: a new BioBrick assembly strategy designed for facile protein engineering*. [WWW document] URL <http://hdl.handle.net/1721.1/32535> [accessed 16 June 2015].
- Quan J, Tian J. 2009. Circular polymerase extension cloning of complex gene libraries and pathways. *PLoS ONE* 4: e6441.
- Rutten V, Munabi A, Riche F, Lewy G, Wilson H, Papan M, Bhatte S, Nghiem T-A, Kaufhold W. 2015. *BBF RFC 106: a standard Type IIS syntax for plants*. [WWW document] URL <http://hdl.handle.net/1721.1/96069> [accessed 16 June 2015].
- Sarrion-Perdigones A, Falconi EE, Zandalinas SI, Juárez P, Fernández-del-Carmen A, Granell A, Orzaez D. 2011. GoldenBraid: an iterative cloning system for standardized assembly of reusable genetic modules. *PLoS ONE* 6: e21622.
- Sarrion-Perdigones A, Vazquez-Vilar M, Palací J, Castelijns B, Forment J, Ziarosolo P, Blanca J, Granell A, Orzaez D. 2013. GoldenBraid2.0: a comprehensive DNA assembly framework for plant synthetic biology. *Plant Physiology* 62: 1618–1631.
- Shetty RP, Endy D, Knight TF. 2008. Engineering BioBrick vectors from BioBrick parts. *Journal of Biological Engineering* 2: 5.
- Terfruchte M, Joehnk B, Fajardo-Somera R, Braus GH, Riquelme M, Schipper K, Feldbrugge M. 2014. Establishing a versatile Golden Gate cloning system for genetic engineering in fungi. *Fungal Genetics and Biology* 62: 1–10.
- Vafaei Y, Staniek A, Mancheno-Solano M, Warzecha H. 2014. A modular cloning toolbox for the generation of chloroplast transformation vectors. *PLoS ONE* 9: e110222.
- Weber E, Engler C, Gruetzner R, Werner S, Marillonnet S. 2011. A modular cloning system for standardized assembly of multigene constructs. *PLoS ONE* 6: e16765.
- Werner S, Engler C, Weber E, Gruetzner R, Marillonnet S. 2012. Fast track assembly of multigene constructs using Golden Gate cloning and the MoClo system. *Bioengineered Bugs* 3: 38–43.
- Whitman L, Gore M, Ness J, Theodorou E, Gustafsson C, Minshull J. 2013. Rapid, scarless cloning of gene fragments using the Electra Vector System™. *Genetic Engineering and Biotechnology News* 76: 42.

Key words: cloning, DNA assembly, genetic syntax, GoldenGate, synthetic biology, Type IIS restriction endonucleases.



About New Phytologist

- **New Phytologist** is an electronic (online-only) journal owned by the New Phytologist Trust, a **not-for-profit organization** dedicated to the promotion of plant science, facilitating projects from symposia to free access for our Tansley reviews.
- Regular papers, Letters, Research reviews, Rapid reports and both Modelling/Theory and Methods papers are encouraged. We are committed to rapid processing, from online submission through to publication 'as ready' via *Early View* – our average time to decision is <27 days. There are **no page or colour charges** and a PDF version will be provided for each article.
- The journal is available online at Wiley Online Library. Visit www.newphytologist.com to search the articles and register for table of contents email alerts.
- If you have any questions, do get in touch with Central Office (np-centraloffice@lancaster.ac.uk) or, if it is more convenient, our USA Office (np-usaoffice@lancaster.ac.uk)
- For submission instructions, subscription and all the latest information visit www.newphytologist.com

Cortical microtubule arrays undergo rotary movements in *Arabidopsis* hypocotyl epidermal cells

Jordi Chan^{1,2}, Grant Calder¹, Samantha Fox¹ and Clive Lloyd¹

Plant-cell expansion is controlled by cellulose microfibrils in the wall¹ with microtubules providing tracks for cellulose synthesizing enzymes². Microtubules can be reoriented experimentally^{3–11} and are hypothesized to reorient cyclically in aerial organs^{12–14}, but the mechanism is unclear. Here, *Arabidopsis* hypocotyl microtubules were labelled with ATEB1a-GFP (*Arabidopsis* microtubule end-binding protein 1a) or GFP-TUA6 (*Arabidopsis* α -tubulin 6) to record long cycles of reorientation. This revealed microtubules undergoing previously unseen clockwise or counter-clockwise rotations. Existing models emphasize selective shrinkage and regrowth¹⁵ or the outcome of individual microtubule encounters to explain realignment¹⁶. Our higher-order view emphasizes microtubule group behaviour over time. Successive microtubules move in the same direction along self-sustaining tracks. Significantly, the tracks themselves migrate, always in the direction of the individual fast-growing ends, but twentyfold slower. Spontaneous sorting of tracks into groups with common polarities generates a mosaic of domains. Domains slowly migrate around the cell in skewed paths, generating rotations whose progressive nature is interrupted when one domain is displaced by collision with another. Rotary movements could explain how the angle of cellulose microfibrils can change from layer to layer in the polylamellate cell wall.

Cortical microtubules form tracks for cellulose-synthesizing complexes that move along the surface of the plasma membrane. The orientation of the cellulose microfibrils is then thought to constrain the direction of turgor-driven cell expansion¹. In elongating root cells¹⁷, microtubules tend to be perpendicular to the growth axis but orientation is more variable in light-grown aerial organs of a variety of species^{3–8}, including *Arabidopsis* hypocotyls^{18–20}. This greater angular dispersion, observed in fixed cells of shoots, has led to suggestions that such microtubules may be undergoing regular reorientation based on endogenous rhythms^{12–14}. Plant microtubules are highly dynamic²¹ and translocate by hybrid treadmilling, in which the front end polymerizes more quickly than the back end depolymerises²². At the whole-cell level, however, little is known

about how the entire array reorients, as it has not been possible to follow living cells for long periods nor, importantly, to determine microtubule polarity during reorientation.

Here, *Arabidopsis* seedlings were grown in chambers²³ and placed under a spinning disk confocal microscope so that epidermal cells of hypocotyls could be followed for long periods as they elongate. Seedlings expressing the microtubule plus end-binding protein, ATEB1a-GFP²³ were phenotypically indistinguishable from wild type and were used to follow polarity in microtubule reorientation.

ATEB1a-GFP forms 'comets' at the growing ends of microtubules, enabling the polarity of individual microtubules to be followed by live-cell imaging^{24–26}. However, to monitor longer-term behaviour, 2-day-old seedlings expressing ATEB1a-GFP were used and successive 6 min time-lapse movies were collected every 20 min for up to 24 h. To ensure that the cortex was always sampled, each time-lapse movie was collected by z-scanning a depth of at least 15 μ m with a temporal resolution of 20 s, allowing the polarity of microtubule growth to be discerned (see Supplementary Information, Movie 1). Only those frames including the upper epidermal face were projected to trace the trajectories of growing microtubules and build an overall pattern of the array (Fig. 1). Then, successive time-lapse movies were projected to form a movie showing how the microtubule array changes with time (see below).

Microtubule alignment varies from cell to cell in light-grown *Arabidopsis* hypocotyls^{18–20}, probably reflecting the slower growth in the light²⁷. Movies of 2–3-day-old seedlings (see Supplementary Information, Movies 2 and 3) reveal these patterns are not static as the entire microtubule array undergoes striking reorientations, in some cases seeming to rotate through 360°. Such movements, which were consistently observed in all plants expressing ATEB1-GFP (10 plants), were also observed in seedlings expressing GFP-TUA6 (10 plants) and were therefore unrelated to labelling by ATEB1a-GFP (see Supplementary Information, Movie 4). Similar reorientations were also observed whether the seedling was placed horizontally on the microscope stage or vertically on a rotated microscope (see Supplementary Information, Movie 5).

In these slow-growing hypocotyls the pattern of re-orientation differed between cells. For instance, the time taken for the array to reorientate through 360° varied from 200–800 min, whereas some arrays

¹Department of Cell and Developmental Biology, John Innes Centre, Norwich NR4 7UH, UK.

²Correspondence should be addressed to J.C. (e-mail: jordi.chan@bbsrc.ac.uk.)

Received 03 November 2006; accepted 25 November 2006; published online 14 January 2007; DOI: 10.1038/ncb1533

LETTERS

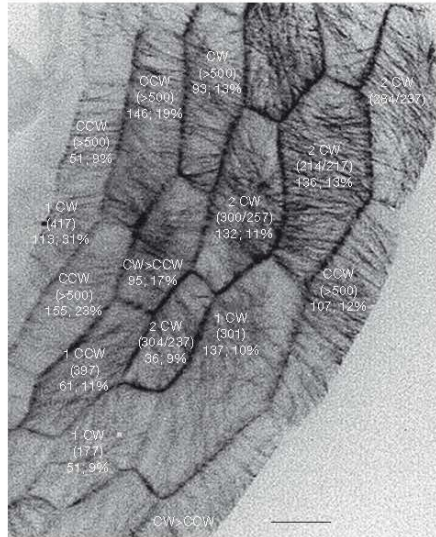


Figure 1 *Arabidopsis* hypocotyl epidermal cells expressing AtEB1a-GFP display rotatory microtubule reorientations. This four-dimensional (x , y , z and t ; time) projection, taken over a 6 min period, summarizes the durations and directions of the rotatory movements observed in the cells shown in the Supplementary Information, Movie 1 (covering a 500-min period of growth). Microtubule arrays rotate in clockwise or counter-clockwise directions and adjacent cells can rotate in opposite directions and the direction can reverse. CW and CCW refer to the number of clockwise or counter-clockwise rotations observed in a cell over the 8 h period, respectively. Numbers in brackets refer to the time taken for each rotation (min). The lower figures refer to the area in μm^2 gained in 500 min and the percentage refers to the cell's relative growth over the same period (for example, 51.9%). The scale bar represents 20 μm .

never underwent a complete cycle. Reorientation could be clockwise and counter-clockwise in adjacent cells, even changing direction within a cell (Fig. 1 and see Supplementary Information, Movies 2 and 3). Our analysis (see Supplementary Information, Fig. S1) confirmed that reorientation occurs in light-grown cells that are still elongating (average $0.88 \pm 0.36 \mu\text{m h}^{-1}$, 30 cells from 3 plants). When cells stopped elongating, microtubules came to rest in steeply pitched oblique and/or longitudinal patterns (see Supplementary Information, Movie 6), showing that rotation only occurred during growth. Plus-end growth rates were similar for both growing and non-growing states (see below).

Reorientation was insensitive to the anti-actin drug, latrunculin B, despite the inhibition of cytoplasmic streaming (see Supplementary Information, Movie 7). Also, the inhibitor of cellulose biosynthesis, 2,6-dichlorobenzonitrile, did not stop reorientation despite the cells becoming swollen, suggesting that neither the deposition of cellulose nor the biophysical restraints maintaining cell shape affect the reorientation of the microtubule array (see Supplementary Information, Movie 8). In contrast, reorientation was arrested by the microtubule-stabilizing drug, taxol (see Supplementary Information, Movie 9), consistent with hybrid treadmilling²² providing the motive force. Taxol also deformed cell shape after several days of incubation, suggesting that microtubule dynamics are required to maintain cell polarity.

Longer-term time-lapse movies revealed groups of microtubules displaying higher-order behaviours that may account for the rotatory movement. Microtubules grow along common trajectories or tracks that often display strong polarity^{22,24,25} (see Supplementary Information, Fig. S1), with a succession of plus-end comets running in a single direction. Electron microscopic studies showed cortical microtubules forming small groups (bundles) of stabilized, parallel microtubules⁴, but movies show bundles as dynamic, self-replenishing tracks in which polarized microtubules grow alongside one another in a telescopic manner. This suggests bundles or tracks are the basic unit of array behaviour. To quantify the polarity of tracks during microtubule reorientation, individual frames of successive time-lapse movies were analysed (four cells, each undergoing 360° reorientations, totaling over seventy 6-min movies; see Supplementary Information, Fig. S2). This showed that tracks themselves migrate, more slowly (see below) than the individual AtEB1a-GFP comets moving along them, but in the same plus end direction (Fig. 2). Moreover, groups of tracks can be identified in which microtubules predominantly move over the cell surface in the same direction — we named these groups 'polarized domains' (see Supplementary Information, Fig. S2). Polarized domains are constantly evolving structures as movement of domains through each other, in opposite directions, generates areas of mixed polarity. Fig. 2B shows a mosaic of several such domains migrating in different directions. Importantly, although individual microtubules grow in straight lines, over the longer period the tracks themselves move in curved paths, as illustrated by the progressive rotation of the arrows marked in the green and yellow sectors in Fig. 2B. Hence, although the array may seem to rotate like the hands of a clock around a fixed point, the reorientation is actually the sum of the curved migratory paths of several domains at different parts of the cell surface. In Fig. 2, this curved migration of tracks is progressive, giving the appearance of a smooth, overall rotation. However, such progressive rotation can be broken by 'jumps'¹⁴ or discontinuities in the migratory path (for example, from longitudinal to net transverse arrays or from left-handed to right-handed oblique arrays). Jumps had been deduced from aldehyde-fixed sunflower cells¹⁴ and our movies show they are introduced by the appearance onto the cell surface of discordant domains of differently-angled tracks. Fig. 2A and B, i–l, illustrate a discordant domain whose tracks move transversely from the right-hand edge of the cell, displacing the existing domain without going through an intermediate oblique stage.

Key features of discontinuous rearrangements are summarized in Fig. 2: first, discordant domains invariably advance in the direction of their plus end comets; second, where one domain collides with the flank of another domain, a curved collision site is formed (indicated by arrow) that moves ahead of the incoming domain; third, instead of disappearing from the collision site, the incoming domain slowly advances into the adjacent domain, without changing orientation. One model^{16, 26} for microtubule encounters suggests that 60% of individual microtubules depolymerize when they collide with another at a steep angle. However, our observations on the longer-term outcome of interactions between tracks indicate that incoming discordant domains tend not to be lost, but succeed in migrating into the adjacent area. Calculations show that curved collision fronts move more slowly ($0.3 \mu\text{m min}^{-1}$, s.d. ± 0.08 ; $n = 10$) than individual microtubule plus ends, whose movement remains fairly constant during reorientation (transverse = $5.64 \mu\text{m min}^{-1}$, s.d. ± 0.88 , $n = 42$; left-handed oblique = $5.62 \mu\text{m min}^{-1}$, s.d. ± 1.09 , $n = 42$; right-handed oblique = $5.53 \mu\text{m min}^{-1}$, s.d. ± 0.90 , $n = 42$;

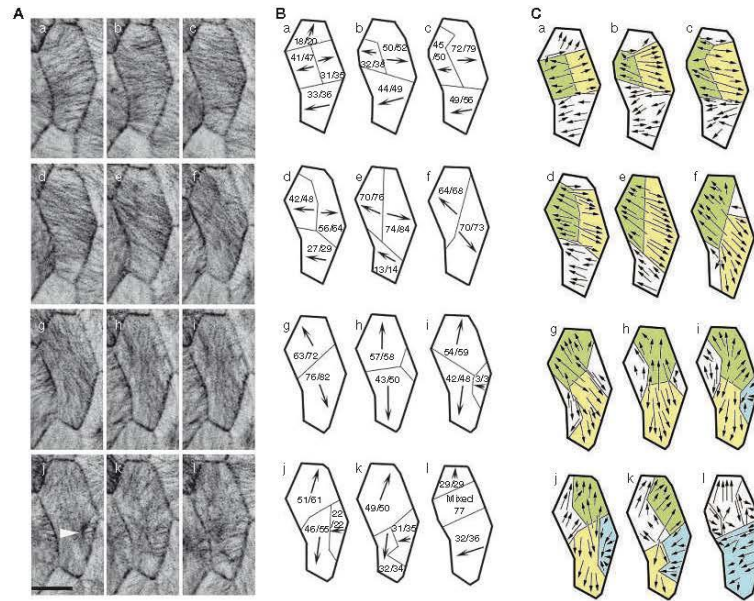


Figure 2 Microtubules moving as a mosaic of polarized domains. **(A)** ATEB1 a-GFP time-projections (each covering 6 min, taken at 20-min intervals) follows microtubule reorientation within a single cell over a 4-h period and shows that microtubules follow persistent tracks that themselves migrate. **(B)** Quantification of the polarity of ATEB1 a-GFP comets during reorientation shows the presence of domains consisting of tracks in which 83–100% of microtubules grow, and tracks migrate, in a common direction. **(C)** The colour-coding shows that domains move in skewed paths generating shifts in array patterning and polarity. In this example, domains are displaced in a clockwise direction (for example, green domain). Panels I–I show that

reorientation can occur in a discontinuous manner, with a 'discordant' domain of transversely-moving microtubules (blue) colliding with and displacing the yellow domain moving vertically down the page. Arrows in **B** and **C** indicate the direction of plus end growth (ATEB1 a-GFP comets) along tracks. The numbers in **B** indicate the numbers of microtubules moving in the assigned direction versus the total number observed. Mixed indicates area with no overall polarity in which number represents the total number of microtubules observed. Polarity was scored from kymographs (see Supplementary Information, Fig. S2). The arrowhead in **A** marks a collision front. Frames were taken at 20-min intervals. The scale bar represents 19 μm .

longitudinal = $6.30 \mu\text{m min}^{-1}$; s.d. ± 0.86 , $n = 42$). The slower movement of the collision front is more similar to the rate of minus-end depolymerization^{23,24} than of plus end growth, suggesting that the net movement of the array may be limited by microtubule depolymerization from the treadmilling minus end, perhaps required for generating space into which other microtubules migrate. Comigration of nucleation sites with the tracks²⁴ would explain the successive flow of microtubules along a track (that is, their self-sustaining nature) and the persistence of collision fronts. The curvature of these collision fronts indicates that the incoming domain is likely to be exerting a pushing force.

By aligning sequential frames in a kymograph it is possible to reconstruct a panoramic view of the cortical array as it migrates over the outer surface (Fig. 3) and show that their component domains are greater than the width of the cell. This indicates that domains are likely to move around the entire cell. In support of this, in tilted cells, we have observed comets moving around the radial walls and have also observed reorientations on the inner epidermal wall (data not shown), demonstrating that movement occurs on all faces of the cell.

The paths in which tracks migrate are intriguing. Fig. 3B shows one polarized domain of tracks (red arrows) moving from right-to-left, while another domain (yellow arrows) moves from left-to-right.

Depending on the direction of movement, individual microtubules grow either into (red arrows, Fig. 3C) or away from (yellow arrows, Fig. 3D) adjacent tracks. Bipolar tracks arise when microtubules join tracks of opposite polarity, but when tracks of common polarity join (see Fig. 3C), the persistence of branch-points shows that tracks do not inevitably merge to form giant bundles — as might be expected if crossbridging were the only outcome of microtubule–microtubule interaction.

In summary, the array can be visualized as a global system of interconnected tracks. Within the tracks the microtubules are growing fast, although the tracks themselves are moving slowly around the cell. Different regions can move together as polarized domains, or through each other, or can collide to cause fronts that slowly resolve.

In long-term reconstructions (for example, 8 h) these migratory movements can be observed to generate various undulatory patterns passing over the outer epidermal wall (Fig. 4). The speed at which the array moves ($0.3 \mu\text{m min}^{-1}$) is similar to that of the rate of movement reported for cellulose synthase ($0.33 \mu\text{m min}^{-1}$)². As microtubules can guide the movement of cellulose synthases⁶, rotation of the microtubular template could account for a spectrum of cell wall patterns, including consecutive wall layers with different orientations as reported for slow-growing *Arabidopsis* hypocotyls²⁸.

LETTERS

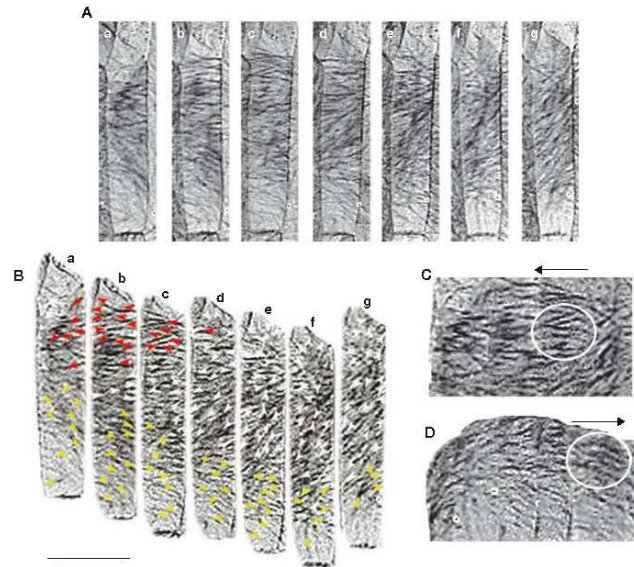


Figure 3 Reconstruction of polarized domains. **(A, B)** Time-projections of ATEB1a-GFP comets (each covering 6 min, taken at 20-min intervals) over a 2 h period **(A)** can be joined according to their track polarities (see red, yellow and white arrows, **B**). Tracks (red arrows) are moving from right-to-left across the surface; yellow tracks move in the opposite direction; white arrows mark tracks moving independently of the red and yellow domains. **(C, D)** Polarized domains are wider than the outer cell face **(C, red domain;**

D, yellow domain; arrows denote direction of ATEB1a-GFP comet movement along tracks). Alignment also reveals that the cortical array is a system of interconnected tracks along which microtubules circulate. Circle in **C** highlights microtubules that grow into adjacent tracks; circle in **D** shows microtubules branching away from tracks. The scale bars represent 28 μm for **A** and **B** and 16 μm for **C** and **D**. Frames were taken at 20-min intervals.

METHODS

Plant material and drug treatments. *Arabidopsis thaliana* plants expressing 35S: ATEB1a-GFP and 35S:GFP-TUA6 have previously been described^{22,29}. Drugs were added to 2-day-old seedlings. Taxol (Sigma-Aldrich, Poole, UK), Latrunculin B (Sigma) and 2,6-dichlorobenzonitrile (DCB, Maybridge, UK) were used at concentrations of 4 μM , 200 nM and 2 μM , respectively.

Time-lapse microscopy. Cold-treated seeds were placed on filter paper soaked with sterile water. A chamber was constructed from a hollow square of double-sided adhesive tape stuck to a large coverslip. Seed and paper were then inserted into the chamber and covered with a gas-permeable membrane (bioPOLIE; VivaScience, Göttingen, Germany). The chamber was then placed over a 1-cm hole drilled into a plastic slide and the edges of the sandwich sealed with tape.

Chambers were placed vertically in the growth room for 2 days then imaged using a VisiTech spinning disc confocal microscope fitted with a 40 \times /1.3NA oil objective lens. Alternatively, slides were imaged on a Bio-Rad 1024 confocal laser scanning microscope in a vertical position on a purpose-built horizontal z-axis microscope as previously described³⁰. GFP was excited using the 488-nm line of an argon ion laser and emitted light filtered through a 500–550-nm band-pass filter. Fluorescence was detected using a Hamamatsu Orca ER cooled CCD camera with 1–4 \times binning, set at 0.7–1.0 s exposure time. Four-dimensional time-lapse was collected and projected (max) using the MetaMorph Imaging System. A z-stack of images (with 1–2 μm z-step intervals) was acquired every 20 s for 6 min and then repeated every 20 min. Long-term movies of growing hypocotyls were projected using nd-Stack Builder (F. Cordelières, Institut Curie, Orsay,

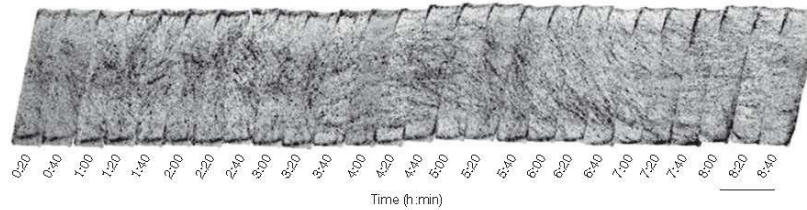


Figure 4 The long-term migratory pattern of ATEB1a-GFP comets over the outer cell surface. Time projections (each covering 6 min) taken at 20-min intervals were placed in a montage, plotting the movement of microtubule tracks for

more than 8 h. Over the first 3 h, tracks are variably oriented, but subsequently resolve into a more homogeneous, undulating pattern due to alternate counter-clockwise and clockwise rotations. The scale bar represents 19 μm .

France; <http://rsb.info.nih.gov/ij/plugins/track/builder.html>) and aligned using Stackreg (P. Thévenaz, Swiss Federal Institute of Technology, Lausanne, Switzerland; <http://bigwww.epfl.ch/thevenaz/stackreg/>) plug-ins of ImageJ (<http://rsb.info.nih.gov/ij/>). Movies were edited using the brightness/contrast tool of imageJ and the time-stamper plug-in (W. Rasband, NIH, MD; <http://rsb.info.nih.gov/ij/plugins/stamper.html>). Microtubule growth rates and the polarity of domains were calculated from kymographs constructed using the re-slice tool. Cell area was calculated using CellFinder³¹.

Note: Supplementary Information is available on the Nature Cell Biology website.

ACKNOWLEDGEMENTS

We are grateful to E. Coen for useful discussions, H. Jones for technical support, I. Rothe for assistance with time-lapse montages and A. Mackie for assistance with vertical imaging. The work was funded by a grant-in-aid to the John Innes Centre by the Biotechnology and Biological Sciences Research Council.

AUTHOR CONTRIBUTIONS

J.C. contributed to project planning, collection of experimental data, data analysis, supervision and writing. G.C. contributed to the collection of experimental data and data analysis. S.F. produced the AtEB1-GFP lines. C.L. was responsible for supervision and writing.

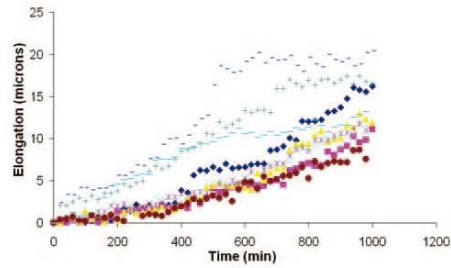
COMPETING FINANCIAL INTERESTS

The authors declare that they have no competing financial interests.

Published online at <http://www.nature.com/naturecellbiology/>

Reprints and permissions information is available online at <http://npg.nature.com/reprintsandpermissions/>

- Giddings, T. H. & Staehelin, A. Microtubule-mediated control of microfibril deposition: A re-examination of the hypothesis (ed. Lloyd, C. W.) (Academic Press Ltd., London, 1991).
- Paredes, A. R., Somerville, C. R. & Ehrhardt, D. W. Visualization of cellulose synthase demonstrates functional association with microtubules. *Science* **312**, 1491–1495 (2006).
- Iwata, T. & Hogetsu, T. The effect of light irradiation on the orientation of microtubules in seedlings of *Avena sativa* L. *Plant Cell Physiol.* **30**, 1011–1016 (1989).
- Nick, P., Bargfeld, R., Schäfer, E. & Schopfer, P. Unilateral reorientation of microtubules at the outer epidermal wall during photo- and gravitropic curvature of maize coleoptiles and sunflower hypocotyls. *Planta* **181**, 162–168 (1990).
- Laskowski, M. Microtubule orientation in pea stem cells: a change in orientation follows the initiation of growth rate decline. *Planta* **181**, 44–52 (1990).
- Ishida, K. & Katsumi, M. Immunofluorescence microscopical observation of cortical microtubule arrangement as affected by gibberellin d_6 mutant of *Zea mays* L. *Plant Cell Physiol.* **32**, 409–417 (1991).
- Ishida, K. & Katsumi, M. Effects of gibberellin and abscisic acid on the cortical microtubule orientation in hypocotyls of light-grown cucumber seedlings. *Int. J. Plant Sci.* **153**, 155–163 (1992).
- Zandomeni, K. & Schopfer, P. Reorientation of microtubules at the outer epidermal wall of maize coleoptiles by phytochrome, by blue-light photoreceptor and auxin. *Protoplasma* **173**, 103–112 (1993).
- Yuan, M., Shaw, P. J., Warn, R. M. & Lloyd, C. W. Dynamic reorientation of cortical microtubules, from transverse to longitudinal, in living plant cells. *Proc. Natl Acad. Sci. USA* **91**, 6050–6053 (1994).
- Lloyd, C. W., Shaw, P. J., Warn, R. M. & Yuan, M. Gibberellin acid-induced reorientation of cortical microtubules in living plant cells. *J. Microsc.* **181**, 140–144 (1996).
- Ueda, K. & Matsuyama, T. Rearrangement of cortical microtubules from transverse to oblique or longitudinal in living cells of transgenic *Arabidopsis thaliana*. *Protoplasma* **213**, 28–38 (2000).
- Mayumi, K. & Shibaoka, H. The cyclic reorientation of cortical microtubules on walls with a crossed polyamellate structure: effects of plant hormones and an inhibitor of protein kinases on the progression of the cycle. *Protoplasma* **195**, 112–122 (1996).
- Takesue, K. & Shibaoka, H. The cyclic reorientation of cortical microtubules in epidermal cells of azuki bean epicotyls: the role of actin filaments in the progression of the cycle. *Planta* **205**, 539–546 (1998).
- Hejnowicz, Z. Autonomous changes in the orientation of cortical microtubules underlying the helical cell wall of the sunflower hypocotyl epidermis: spatial variation translated into temporal changes. *Protoplasma* **225**, 243–256 (2005).
- Yuan, M., Warn, R. M., Shaw, P. J. & Lloyd, C. W. Dynamic microtubules under the radial and outer tangential walls of microinjected pea epidermal cells observed by computer reconstruction. *Plant J.* **7**, 17–23 (1995).
- Dixit, R. & Cyr, R. Encounters between dynamic cortical microtubules promote ordering of the cortical array through angle-dependent modifications of microtubule behavior. *Plant Cell* **16**, 3274–3284 (2004).
- Sugimoto, K., Willamson, R. E. & Wasteneys, G. O. New techniques enable comparative analysis of microtubule orientation, wall texture, and growth rate in intact roots of *Arabidopsis*. *Plant Physiol.* **124**, 1493–1506 (2000).
- Buschmann, H. et al. Helical growth of the *Arabidopsis* mutant tortifolia reveals a plant-specific microtubule-associated protein. *Curr. Biol.* **14**, 1515–1521 (2004).
- Le, J., Vandenbussche, F., De Cnodder, T., Van Der Straeten, D. & Verbelen, J.-P. Cell elongation and microtubule behavior in the *Arabidopsis* hypocotyl: responses to ethylene and auxin. *J. Plant Growth Regul.* **24**, 166–178 (2005).
- Nakajima, K., Kawamura, T. & Hashimoto, T. Role of the SPIRAL I gene family in anisotropic growth of *Arabidopsis thaliana*. *Plant Cell Physiol.* **47**, 513–522 (2006).
- Hush, J. M., Wadsworth, P., Callahan, D. A. & Hepler, P. K. Quantification of microtubule dynamics in living plant cells using fluorescence redistribution after photobleaching. *J. Cell Sci.* **107**, 775–784 (1994).
- Shaw, S. L., Kamyar, R. & Ehrhardt, D. W. Sustained microtubule treadmilling in *Arabidopsis* cortical arrays. *Science* **300**, 1715–1718 (2003).
- Chan, J., Calder, G., Fox, S. & Lloyd, C. W. Localization of the end-binding protein EB1 reveals alternative pathways of spindle development in *Arabidopsis* suspension cells. *Plant Cell* **17**, 1737–1748 (2005).
- Chan, J., Calder, G. M., Doonan, J. H. & Lloyd, C. W. EB1 reveals mobile microtubule nucleation sites in *Arabidopsis*. *Nature Cell Biol.* **5**, 967–971 (2003).
- Dhonukshe, P., Mathur, J., Hulskamp, M. & Gadelia, T. W., Jr. Microtubule plus-ends reveal essential links between intracellular polarization and localized modulation of endocytosis during division-plane establishment in plant cells. *BMC Biol.* **3**, 11 (2005).
- Dixit, R., Chang, E. & Cyr, R. Establishment of polarity during organization of the acerosomal plant cortical microtubule array. *Mol. Biol. Cell.* **17**, 1298–1305 (2006).
- Gendreau, E. et al. Cellular basis of hypocotyl growth in *Arabidopsis thaliana*. *Plant Physiol.* **114**, 295–305 (1997).
- Refrégier, G., Pelletier, S., Jaillard, D. & Höfte, H. Interaction between wall deposition and cell elongation in dark-grown hypocotyl cells in *Arabidopsis*. *Plant Physiol.* **135**, 1–10 (2004).
- Ueda, K., Matsuyama, T. & Hashimoto, T. Visualization of microtubules in living cells of transgenic *Arabidopsis thaliana*. *Protoplasma* **206**, 201–206 (1999).
- Penfold, R., Watson, A. D., Mackie, A. R. & Hibberd, D. J. Quantitative imaging of aggregated emulsions. *Langmuir* **22**, 2005–2015 (2006).
- Costa, M. M., Fox, S., Hanna, A. I., Baxter, C. & Coen, E. Evolution of regulatory interactions controlling floral asymmetry. *Development* **132**, 5093–5101 (2005).



Supplementary Graph 1. Growth kinetics of hypocotyl cells The graph shows that hypocotyl cells display slow elongation (e.g. brown circles/ pink squares) during microscopic observation. Several cells, however, cease to elongate during imaging (e.g. blue dashed lines). In these cases, microtubules adopted steeply pitched oblique/longitudinal patterns (also see suppl. movie 6) underlining the relationship between microtubule rotation and growth. 9

hypocotyl cells from 3 different plants are shown. Plants were imaged 2-days after incubation in the growth room. Cell length was measured between the midpoints of end walls using the line tool of ImageJ. Small oscillations in length are due to small changes in the plane of viewing or changes in the fluorescent intensity of the end walls.

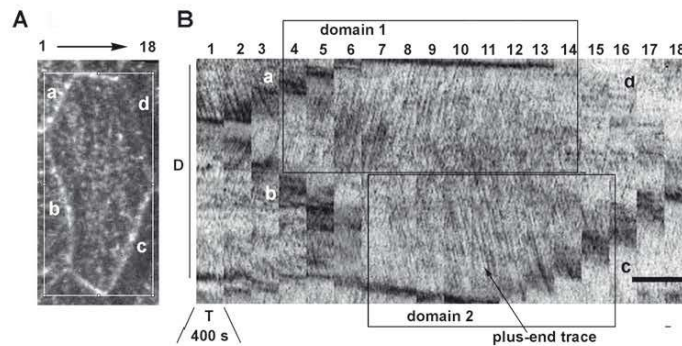


Supplementary Figure 1. Cortical microtubules grow along tracks.

The movement of EB1-GFP comets along a single line of a time-lapse movie (i.e. the width of a pixel: e.g. 0.326 μ m [camera bin2, x40 magnification]) is displayed as a kymograph. The kymograph sequentially (frame-by-frame) stacks the information along that line and projects the images one on top of the other to make a montage of distance (length of the line) versus time (depending on the number of frames). Comets moving along the axis of

the line produce linear traces, the gradient of the traces describe the rate of movement and their orientation describes the direction of movement. The kymograph was projected from a line traversing the longitudinal axis of the cell highlighted [**] in movie 1 and records EB1 comets over a 6 min period. This kymograph encompasses two different growth paths (or tracks) with comets moving towards opposite ends of the cell.

SUPPLEMENTARY INFORMATION



Supplementary Figure 2. Tracks form polarised domains. Microtubule movements within entire regions of a cell were monitored by sequentially recording kymographs (line-by-line) through the selected region. This generates a movie of kymographs which can be projected in blocks of 5-10 slices (1.63-3.26 μm) and aligned to form a montage. Panel B shows a montage of 18 kymographs which corresponds to the area depicted by the rectangular box in panel A (a single frame from a time-lapse experiment). Each kymograph covers a width of 1.63 μm and projects the movement of EB1-GFP comets travelling along the longitudinal axis of the cell (i.e.

parallel to the growth trajectories of the microtubules) over 400 sec. Here, the cortical array can be seen to be composed of two domains of polarised tracks in which traces share common orientations: microtubules overwhelmingly (92%) grow towards the top of the cell in domain 1 or towards the bottom of the cell in domain 2 (88%). The orientations of the traces were scored from such montages to quantify the polarity of the domains shown in Figure 2.A, b, c, d mark corresponding sides of the cell; D = distance, T = time; bar = 1.4 μm in panel A and 13 μm in panel B.

Supplementary movie 1. Dynamic behaviour of microtubule ends labelled by AtEB1-GFP in Arabidopsis hypocotyl cells.

This time-lapse movie collected over 6 minutes shows AtEB1-GFP forms comet-like streaks at the growing ends of microtubules. EB1 comets move along polarised tracks (bundles). Tracks often form domains with common polarity (see arrows). Within longitudinal arrays (see *) polarised tracks extend towards the cell ends. Frames were taken at 20 sec intervals. Bar = 20 μm .

Supplementary movie 2 and 3. Long-term behaviour of microtubules labelled by AtEB1-GFP in elongating hypocotyl cells.

Successive 6-min time-lapse movies of Arabidopsis hypocotyls expressing AtEB1-GFP were projected and compiled into movies to see the long-term behaviour of microtubules in elongating cells. This reveals that microtubules (tracks) of epidermal cells undergo dramatic reorientations – sometimes appearing to rotate 360° (*). Neighbouring cells display variable patterns of microtubule re-orientation. Each frame is derived from a time projection of EB1 comets collected over a 6 min period; frames were taken at 20 min intervals. Bar = 20 μm .

Supplementary movie 4. Behaviour of microtubules labelled by GFP-tubulin in elongating hypocotyl cells.

This time-lapse movie confirms that rotary-like reorientations also occur in Arabidopsis hypocotyl cells expressing GFP-tubulin (see *). In addition to microtubules, the streaming of fluorescently-labelled cytoplasm can be seen in these GFP-tubulin plants (for comparison, in movie 9, streaming can be observed in the absence of microtubule reorientation). Each frame is derived from a z-series projection; frames were taken at 15 min intervals. Bar = 20 μm .

Supplementary movie 5. Vertical imaging of elongating hypocotyl cells expressing GFP-tubulin.

This time-series shows that rotary-like microtubule reorientations are also characteristic of hypocotyl cells imaged vertically on a horizontal z-axis microscope. The hypocotyl cells are expressing GFP-tubulin; each frame is derived from a z-series projection; frames were taken at 15 min intervals. Bar = 20 μm .

Supplementary movie 6. Behaviour of microtubules in non-elongating hypocotyl cells expressing AtEB1-GFP.

Microtubules rest in oblique to longitudinal arrays when cells cease to elongate. The asterisk marks the same cell highlighted in suppl. movie 2, except filmed 24 hours later as growth is ceasing. Each frame is derived from a time projection of EB1 comets collected over a 6 min period; frames were taken at 20 min intervals. Bar = 20 μm .

Supplementary movie 7. Re-orientation is insensitive to latrunculin B.

This time-lapse movie shows that microtubule reorientation is insensitive to the actin-depolymerising drug, latrunculin B. Accumulations of cytoplasm gather at the cell ends in the absence of streaming. The hypocotyl cells are expressing GFP-tubulin; each frame is derived from a z-series projection; frames were taken at 15 min intervals. Bar = 20 μm .

Supplementary movie 8. Re-orientation is insensitive to DCB.

This time-lapse movie shows that microtubule reorientation is also insensitive to the drug DCB, an inhibitor of cellulose synthesis. Cells swell and eventually grow out of the focal plane of the microscope. The hypocotyl cells are expressing GFP-tubulin; each frame is derived from a z-series projection; frames were taken at 15 min intervals. Bar = 20 μm .

Supplementary movie 9. Re-orientation is sensitive to taxol.

This time-lapse movie shows that microtubule re-orientation ceases in the presence of taxol, a drug that stabilises microtubules. Cytoplasmic streaming, however, continues. The hypocotyl cells are expressing GFP-tubulin; each frame is derived from a z-series projection; frames were taken at 15 min intervals. Bar = 20 μm .

REFERENCES

1. Giddings, T. H. & Staehelin, A. *Microtubule-mediated control of microfibril deposition: A re-examination of the hypothesis* (ed. Lloyd, C. W.) (Academic Press Ltd, London, 1991).
2. Paredez, A. R., Somerville, C. R. & Ehrhardt, D. W. Visualization of Cellulose Synthase Demonstrates Functional Association with Microtubules. *Science* **312**, 1491-1495 (2006).
3. Iwata, T. & Hogetsu, T. The effect of light irradiation on the orientation of microtubules in seedlings of *Avena sativa* L. *Plant Cell Physiol.* **30**, 1011-1016 (1989).
4. Nick, P., Bergfeld, R., Schafer, E. & Schopfer, P. Unilateral reorientation of microtubules at the outer epidermal wall during photo- and gravitropic curvature of maize coleoptiles and sunflower hypocotyls. *Planta* **181**, 162-168 (1990).
5. Laskowski, M. Microtubule orientation in pea stem cells: a change in orientation follows the initiation of growth rate decline. *Planta* **181**, 44-52 (1990).
6. Ishida, K. & Katsumi, M. Immunofluorescence microscopical observation of cortical microtubule arrangement as affected by gibberellin d_5 mutant of *Zea mays* L. *Plant Cell Physiol.* **32**, 409-417 (1991).
7. Ishida, K. & Katsumi, M. Effects of gibberellin and abscisic acid on the cortical microtubule orientation in hypocotyls of light-grown cucumber seedlings. *Int. J. Plant Sci.* **153**, 155-163 (1992).
8. Zandomeni, K. & Schopfer, P. Reorientation of microtubules at the outer epidermal wall of maize coleoptiles by phytochrome, by blue-light photoreceptor and auxin. *Protoplasma* **173**, 103-112 (1993).
9. Yuan, M., Shaw, P. J., Warn, R. M. & Lloyd, C. W. Dynamic reorientation of cortical microtubules, from transverse to longitudinal, in living plant cells. *Proc Natl Acad Sci U S A* **91**, 6050-3 (1994).
10. Lloyd, C. W., Shaw, P. J., Warn, R. M. & Yuan, M. Gibberellic acid-induced reorientation of cortical microtubules in living plant cells. *Journal of Microscopy* **181**, 140-144 (1996).
11. Ueda, K. & Matsuyama, T. Rearrangement of cortical microtubules from transverse to oblique or longitudinal in living cells of transgenic *Arabidopsis thaliana*. *Protoplasma* **213**, 28-38 (2000).
12. Mayumi, K. & Shibaoka, H. The cyclic reorientation of cortical microtubules on walls with a crossed polylamellate structure: effects of plant hormones and an inhibitor of protein kinases on the progression of the cycle. *Protoplasma* **195**, 112-122 (1996).
13. Takesue, K. & Shibaoka, H. The cyclic reorientation of cortical microtubules in epidermal cells of azuki bean epicotyls: the role of actin filaments in the progression of the cycle. *Planta* **205**, 539-46 (1998).
14. Hejnowicz, Z. Autonomous changes in the orientation of cortical microtubules underlying the helicoidal cell wall of the sunflower hypocotyl epidermis: spatial variation translated into temporal changes. *Protoplasma* **225**, 243-56 (2005).
15. Yuan, M., Warn, R. M., Shaw, P. J. & Lloyd, C. W. Dynamic microtubules under the radial and outer tangential walls of microinjected pea epidermal cells observed by computer reconstruction. *Plant J.* **7**(1), 17-23 (1995).
16. Dixit, R. & Cyr, R. Encounters between dynamic cortical microtubules promote ordering of the cortical array through angle-dependent modifications of microtubule behavior. *Plant Cell* **16**, 3274-84 (2004).
17. Sugimoto, K., Willamson, R.E. & Wasteneys, G.O. New techniques enable comparative analysis of microtubule orientation, wall texture, and growth rate in intact roots of *Arabidopsis*. *Plant Physiol.* **124**, 1493-1506 (2000).
18. Buschmann, H., Fabri, C.O., Hauptmann, M., Hutzler, P., Laux, T., Lloyd, C.W. & Schaffner, A.R. Helical growth of the *Arabidopsis* mutant *tortifolia1* reveals a plant-specific microtubule-associated protein. *Current Biol.* **14**, 1515-1521 (2004).
19. Le, J., Vandenbussche, F., De Cnodder, T., Van Der Straeten, D. & Verbelen, J-P. Cell elongation and microtubule behavior in the *Arabidopsis* hypocotyl: responses to ethylene and auxin. *J. Plant Growth Regul.* **24**, 166-178 (2005).
20. Nakajima, K., Kawamura, T. & Hashimoto, T. Role of the *SPIRAL1* gene family in anisotropic growth of *Arabidopsis thaliana*. *Plant Cell Physiol.* **47**, 513-522 (2006).
21. Hush, J. M., Wadsworth, P., Callahan, D. A. & Hepler, P. K. Quantification of microtubule dynamics in living plant cells using fluorescence redistribution after photobleaching. *J Cell Sci* **107**, 775-84 (1994).
22. Shaw, S. L., Kamyar, R. & Ehrhardt, D. W. Sustained microtubule treadmill in *Arabidopsis* cortical arrays. *Science* **300**, 1715-8 (2003).
23. Chan, J., Calder, G., Fox, S. & Lloyd, C. Localization of the end-binding protein EB1 reveals alternative pathways of spindle development in *Arabidopsis* suspension cells. *Plant Cell* **17**, 1737-1748 (2005).
24. Chan, J., Calder, G. M., Doonan, J. H. & Lloyd, C. W. EB1 reveals mobile microtubule nucleation sites in *Arabidopsis*. *Nat Cell Biol* **5**, 967-71 (2003).
25. Dhonukshe, P., Mathur, J., Hulskamp, M. & Gadella, T. W., Jr. Microtubule plus-ends reveal essential links between intracellular polarization and localized modulation of endocytosis during division-plane establishment in plant cells. *BMC Biol* **3**, 11 (2005).
26. Dixit, R., Chang, E. & Cyr, R. Establishment of Polarity during Organization of the Acentrosomal Plant Cortical Microtubule Array. *Mol Biol Cell* **17**, 1298-305 (2006).
27. Gendreau, E., Traas, J., Desnos, T., Grandjean, O., Caboche, M. & Höfte, H. Cellular basis of hypocotyl growth in *Arabidopsis thaliana*. *Plant Physiol.* **114**, 295-305 (1997).
28. Refrégier, G., Pelletire, S., Jaillard, D. & Höfte, H. Interaction between Wall Deposition and Cell Elongation in Dark-Grown Hypocotyl Cells in *Arabidopsis*. *Plant physiol.* **135**, 1-10 (2004).
29. Ueda, K., Matsuyama, T. & Hashimoto, T. Visualization of microtubules in living cells of transgenic *Arabidopsis thaliana*. *Protoplasma* **206**, 201-206 (1999).
30. Penfold, R., Watson, A.D., Mackie, A.R. & Hibberd, D.J. Quantitative imaging of aggregated emulsions. *Langmuir* **22**, 2005-2015 (2006).
31. Costa, M.M., Fox, S., Hanna, A.I., Baxter, C. & Coen, E. Evolution of regulatory interactions controlling floral asymmetry. *Development* **132**, 5093-101 (2005).

Evolution of regulatory interactions controlling floral asymmetry

Maria Manuela R. Costa, Samantha Fox, Andy I. Hanna, Catherine Baxter and Enrico Coen*

Department of Cell and Developmental Biology, John Innes Centre, Norwich NR4 7UH, UK

*Author for correspondence (e-mail: enrico.coen@bbsrc.ac.uk)

Accepted 9 September 2005

Development 132, 5093–5101
Published by The Company of Biologists 2005
doi:10.1242/dev.02085

Summary

A key challenge in evolutionary biology is to understand how new morphologies can arise through changes in gene regulatory networks. For example, floral asymmetry is thought to have evolved many times independently from a radially symmetrical ancestral condition, yet the molecular changes underlying this innovation are unknown. Here, we address this problem by investigating the action of a key regulator of floral asymmetry, *CYCLOIDEA* (*CYC*), in species with asymmetric and symmetric flowers. We show that *CYC* encodes a DNA-binding protein that recognises sites in a downstream target gene *RADIALIS* (*RAD*) in *Antirrhinum*. The interaction between *CYC* and *RAD* can be reconstituted in *Arabidopsis*, which has radially symmetrical flowers. Overexpression of *CYC* in *Arabidopsis* modifies petal and leaf development, through

changes in cell proliferation and expansion at various stages of development. This indicates that developmental target processes are influenced by *CYC* in *Arabidopsis*, similar to the situation in *Antirrhinum*. However, endogenous *RAD*-like genes are not activated by *CYC* in *Arabidopsis*, suggesting that co-option of *RAD* may have occurred specifically in the *Antirrhinum* lineage. Taken together, our results indicate that floral asymmetry may have arisen through evolutionary tinkering with the strengths and pattern of connections at several points in a gene regulatory network.

Key words: Cycloidea, Radialis, Dorsoventral, Gene networks, Atavism, *Arabidopsis*, *Antirrhinum*

Introduction

One approach to studying the evolution of novel traits is to analyse mutants that eliminate the trait. Such mutants have been termed *atavistic* as they give phenotypes resembling the presumed ancestral condition (Cantu and Ruiz, 1985; Hall, 1995). The genes identified by atavistic mutations can provide a convenient starting point for analysing how changes in gene interactions can lead to phenotypic novelty (Babu et al., 2004; Gibson and Honeycutt, 2002; Tautz, 2000). By comparing the network of interactions in species with and without the relevant trait, it should be possible to pinpoint some of the key steps underlying evolutionary change. Here, we adopt this approach for the case of dorsoventral asymmetry in flowers, a trait that is thought to have arisen many times independently during evolution (Donoghue et al., 1998; Endress, 1999; Stebbins, 1974) and for which key regulatory genes giving atavistic mutant phenotypes have been identified.

Several genes controlling floral asymmetry have been identified in *Antirrhinum majus*. *Antirrhinum* flowers are asymmetric along their dorsoventral axis, having distinct dorsal, lateral and ventral organ types. Asymmetry is most evident in the petal and stamen whorls and depends on the action of the duplicate genes *CYCLOIDEA* (*CYC*) and *DICHOTOMA* (*DICH*). *CYC* and *DICH* are both expressed in the dorsal domain of the flower meristem and continue to be expressed at later stages in dorsal floral organs, although expression of *CYC* occurs in a wider region than that of *DICH* (Almeida et al., 1997; Luo et al., 1999; Luo et al., 1996). *cyc dich* double mutants have radially symmetric ventralised

flowers, while single *cyc* or *dich* mutants have partially ventralised flowers, consistent with sub-functionalisation of paralogs following the *CYC-DICH* duplication (Gubitz et al., 2003; Hileman and Baum, 2003). Developmental analysis of single and double mutants has shown that *CYC* and *DICH* can enhance or repress organ growth, depending on developmental stage and organ type, with *CYC* having a stronger phenotypic effect than *DICH* (Almeida et al., 1997; Luo et al., 1999; Luo et al., 1996).

CYC and *DICH* encode transcription factors belonging to the TCP family, many members of which influence patterns of plant cell growth and proliferation (Almeida et al., 1997; Crawford et al., 2004; Kosugi and Ohashi, 1997; Kosugi and Ohashi, 2002; Kosugi et al., 1995; Luo et al., 1999; Luo et al., 1996; Nath et al., 2003; Palatnik et al., 2003; Tremousaygue et al., 2003). Members of this family can be grouped into two classes, I and II, based on sequence similarity in the TCP domain and the consensus DNA-binding sequence. A good candidate for a direct target of *CYC* and *DICH* is *RADIALIS* (*RAD*). *RAD* is expressed in the dorsal domain of floral meristems, in a manner that depends on *CYC* and *DICH*. Plants mutant for *RAD* have almost fully ventralised flowers, retaining only slight dorsal identity in their uppermost regions, suggesting that many of the effects of *CYC* and *DICH* are mediated through *RAD*. *RAD* acts antagonistically to *DIVARICATA* (*DIV*), which promotes ventral identity (Almeida et al., 1997; Corley et al., 2005; Galego and Almeida, 2002). *RAD* and *DIV* encode related MYB-like proteins that are thought to compete for common protein or DNA targets.

Unlike *Antirrhinum*, *Arabidopsis* has radially symmetrical flowers. The *TCPI* gene of *Arabidopsis* is the closest homologue to *CYC/DICH* and is expressed asymmetrically in the dorsal domain of young flower meristems and axillary meristems (Cubas et al., 2001). This indicates that the common ancestor of *Antirrhinum* and *Arabidopsis* had a *CYC/TCPI*-related gene that was asymmetrically expressed even though the flowers were presumably radially symmetric. In contrast to *CYC* and *DICH*, *TCPI* is only transiently expressed at very early stages of flower development.

To understand the evolution of asymmetry, we analysed how *CYC* acts in *Antirrhinum* and *Arabidopsis*. We show that *CYC* binds to DNA, and use random binding site selection to define the consensus binding site. Sequences matching this site are found in the *RAD* promoter and intron, and are bound by *CYC*, indicating that *RAD* may be a direct target of *CYC*. *CYC* is also able to activate the *RAD* gene of *Antirrhinum* in the context of *Arabidopsis* but is unable to activate endogenous *RAD*-like genes of *Arabidopsis*, which lack sequences identical to the consensus binding site. *CYC* is nevertheless able to act in *Arabidopsis*, reducing leaf and increasing petal size, through changes in cell proliferation and expansion. By activating *CYC* protein at specific times, we show that *CYC* can act at various stages of *Arabidopsis* organ growth. Taken together, our results suggest that ancestral *TCPI/CYC*-like genes played a role in regulating a network of target genes involved in growth and development. Some of these interactions could have been retained in both *Antirrhinum* and *Arabidopsis*, accounting for the common developmental effects of *CYC* expression in both species. In addition, an interaction between *CYC* and *RAD* was established or preserved specifically in the *Antirrhinum* lineage.

Materials and methods

Plant material and growth conditions

Arabidopsis seeds were sterilised and grown on growth media [GM; 1× Murashige and Skoog salt mixture, 1% (w/v) sucrose, 100 µg/ml inositol, 1 µg/ml thiamine, 0.5 µg/ml pyridoxin, 0.5 µg/ml nicotinic acid, 0.5 mg/ml MES, 0.8% (w/v) agar, pH 5.7] with or without 50 µM kanamycin (Kan). The media was supplemented with 10 µM dexamethasone (DEX; stock solution 25 mM in ethanol) or ethanol 0.04% (v/v) as a control. Plants were grown on a mix of John Innes Potting Compost No 1, vermiculite and grit in the ratio 1.5:1:1 (by volume) at 20°C with 16 hour light/8 hour dark cycles. All *Arabidopsis* transgenic lines (35S::CYC:GR, RAD::RAD) were in the Columbia background, which was also used as the wild-type control.

Production of recombinant CYC protein and electrophoretic mobility shift assays (EMSAs)

The pRSET-b vector (Invitrogen) was used for production of recombinant *CYC* protein in *E. coli* (plasmid pJAM2093). BL21(DE3) SBET pLysE (Schenk et al., 1995; Studier and Moffatt, 1986) *E. coli* cells were transformed with the construct and the recombinant His-CYC fusion protein was expressed under the control of the T7 promoter and purified from the soluble fraction or from inclusion bodies produced in bacteria, as described previously (Kosugi and Ohashi, 1997; Kosugi and Ohashi, 2002). The conditions for the DNA-binding reaction and electrophoresis, and the DNA probes used were as described (Kosugi and Ohashi, 2002). For the EMSA with the *RAD* promoter and intron, the DNA probes were obtained by PCR using the primer combinations 5733/5734 and 5735/5736 with the plasmid pJAM2283, respectively (5733, 5'-

ACCGTAGAACATTATAGACAACA-3'; 5734, 5'-CACCAACAA-AACCTTCCACATAG-3'; 5735, 5'-GCTATAACGTCGATGTGTCTC-3'; 5736, 5'-ATTCTAAAAACCACGAGAGTCC-3'). For the EMSA with the *RAD* promoter and intron, the primer combinations 5733-5734 and 5735-5736 were used, respectively.

Random binding site selection

Random binding site selection for the His-CYC protein was performed using the oligonucleotide BS18N, as described previously (Kosugi and Ohashi, 1997; Kosugi and Ohashi, 2002). The DNA-protein complex was separated by polyacrylamide gel electrophoresis and the DNA recovered from the gel was amplified by PCR. After the fifth round of selection, the DNA amplified by PCR was cloned into pGEMT-easy vector (Promega) for sequencing.

Plasmid construction

The binary plasmid coding for the *CYC* protein fused to the rat glucocorticoid receptor (GR) (Lloyd et al., 1994) under the control of cauliflower mosaic virus (CaMV) 35S promoter was obtained as follows. The *CYC* open reading frame was amplified by PCR using the primers 5'-*CYC* (5'-CGGGATCCATGTTGGGAAG-3') and 3'-*CYC* (5'-GAAGATCTTTGATGAACCTTGTGCT-3') from plasmid pJAM2095. The forward primer introduced a Kozac sequence and a *Bam*HI site before the start codon and the reverse primer removed the *CYC* stop codon and created a *Bgl*II restriction site at the C terminus. This PCR fragment was digested with *Bam*HI and *Bgl*II and cloned into the *Bam*HI restriction site of the plasmid GR-pBlueScript (pRS020) (Sablowski and Meyerowitz, 1998) resulting in an in-frame translational fusion at the C terminus of *CYC* with the rat glucocorticoid hormone-binding domain (pJAM2387). The *CYC* cDNA was sequenced to check for PCR errors and to check if the protein was in frame with the *GR* sequence. This fusion was called *CYC:GR*. The double CaMV 35S promoter and 35S polyadenylation signal from CaMV were isolated as a 1.56 kb *Kpn*I/*Eco*RV fragment from pJIT60 (Guerineau, 1993) and cloned into a *Sac*I filled in/*Kpn*I sites in pGreenII 0029 (plasmid pJAM2388). A 1.7 kb *Xba*I/*Bam*HI fragment containing the *CYC:GR* fusion was isolated from plasmid pJAM2387 and the ends filled in. This fragment was cloned into the *Sma*I dephosphorylated site of plasmid pJAM2388, adjacent to the double 35S promoter and the orientation was checked by restriction mapping. This construct was called 35S::CYC:GR (plasmid pJAM2389).

Transformation of Arabidopsis

Arabidopsis plants were transformed with the 35S::CYC:GR construct by floral dipping (Clough and Bent, 1998). The *Agrobacterium* strain used was C58CI pGV101 pMP90. Kan-resistant transformants (T1 generation) were selected on GM plates. Approximately, two thirds of T2 plants (segregating 3:1 on Kan) showed a phenotype when also germinated on DEX. T3 progeny of plants that showed a phenotype on DEX-containing media were hemizygous, whereas the progeny of plants that did not show a phenotype were homozygous. 35S::CYC:GR homozygous plants were crossed to other homozygous independent lines and to wild type. Double hemizygous plants never showed a phenotype when grown in DEX-containing media, whereas the hemizygous lines obtained from the cross with wild type showed the phenotype.

Analysis of expression by northern blot and by RT-PCR

For Northern-blot analysis, total RNA was extracted with TRI-Reagent (Sigma), according to the manufacturer's instructions, from 35S::CYC:GR T2 seedlings grown on Kan and DEX, with and without a phenotype. The RNA was blotted onto Hybond N+ (Amersham) according to the manufacturer's instructions and probed with *CYC* or *NPTII* (neomycin phosphotransferase II) probe.

For RT-PCR analysis, RNA was extracted using RNeasy Plant mini kit (Qiagen), from duplicate samples of tissue from 21-day-old 35S::CYC:GR RAD::RAD plants grown on GM media, 6, 18 and 48

hours after transfer to 10 μ M DEX plates. cDNA was prepared from 2 μ g of total RNA using Thermoscript RT-PCR system (Invitrogen). Aliquots of the cDNA were used as template for PCR with gene-specific primers.

Phenotypic analysis

Scanning electron microscopy (SEM) analysis was carried out on '2-Ton' epoxy (Devcon) replicas of *Arabidopsis* petals and leaves as previously described (Carpenter et al., 1995; Green and Linstead, 1990). These replicas were sputter coated with gold palladium, analysed and photographed with a Philips XL 30 FEG SEM. Petal and leaf areas were calculated using a program written in MatLab called CellFinder. Medians were obtained by analysis of variance. The analyses were carried out using the statistical package GenStat for Windows 7th Edition (VSN International, Oxford, UK).

Results

CYC binds to TCP class I binding-sites

To determine whether CYC would bind to the consensus DNA-binding sequences for TCP proteins (Kosugi and Ohashi, 1997; Kosugi and Ohashi, 2002), the *CYC* open reading frame was fused in-frame with a HIS-Tag epitope and the recombinant protein purified from *E. coli* extracts using a metal affinity resin. The protein was present in both the insoluble and soluble fractions. Electrophoretic mobility shift assays (EMSA) were

carried out using a 21 bp double-stranded oligonucleotide probe that contained the overlapping consensus binding sites for both class I and class II TCP proteins (GTGGTCCCAC) (Kosugi and Ohashi, 2002). Incubation of the probe with CYC protein from the soluble fraction showed band retardation (Fig. 1A, lane 1), indicating that CYC protein can bind to these DNA sequences. Mutations in the core of the oligonucleotide abolished binding (Fig. 1A, lanes 2 and 3), indicating that these nucleotides were important for interaction with CYC. According to the sequence of the TCP domain, CYC belongs to the class II subfamily of TCP proteins (Kosugi and Ohashi, 2002) and should therefore bind preferentially to a class II binding site GTGGNCCC. However, when various mutations were introduced in the oligonucleotide to test this, the DNA-binding behaviour of CYC protein was more similar to class I than class II proteins (Fig. 1A, lanes 4 and 5). In particular, mutations that disrupt class II binding did not disrupt CYC binding (Fig. 1A, lane 4). It was only when mutations that affect class I binding were introduced that CYC binding was affected, suggesting that despite sequence similarity to class II proteins, CYC DNA-binding specificity resembles that of class I proteins (Fig. 1A, lane 5). To determine the optimal sequence specificity for the binding of CYC protein, we conducted a random binding site selection analysis using CYC recombinant protein. After five rounds of selection, the program MEME (meme.sdsc.edu) was used to align the sequences of the selected oligonucleotides and the consensus binding site GGNCCCNC was obtained (Fig. 1B), confirming that the CYC binding site is more similar to that of TCP class I than class II proteins.

In *Antirrhinum*, genetic analysis has suggested that *RAD* could be a potential target gene of CYC (Corley et al., 2005). To investigate whether this interaction could be direct, the *RAD* promoter and intron were screened for CYC-binding sites. Two sites matching the CYC consensus were found 1.5 kb upstream of the start codon of the *RAD* open reading frame, within 24 bp of each other (Fig. 2A). A third matching site was found in the intron. PCR fragments containing promoter and intron putative binding-sites were amplified and used as probes in an EMSA with recombinant CYC protein (Fig. 2B). CYC was able to bind to these sequences, supporting the idea that *RAD* is a direct target of CYC.

CYC affects growth of *Arabidopsis*

To investigate whether CYC expression could affect growth in *Arabidopsis*, the coding region of CYC was fused to that of the rat glucocorticoid receptor and expressed under the control of the 35S promoter (35S::CYC:GR). Sixteen transformants were obtained, of which 10 had a clear developmental phenotype when grown on the glucocorticoid inducer dexamethasone (DEX). Northern-blot analysis on three independent transformants segregating for the construct showed that the severity of the phenotype correlated with the level of CYC mRNA accumulation (Fig. 3). Curiously, only plants hemizygous for the construct showed strong expression, indicating that expression was silenced in homozygotes. To check whether this was a consequence of transgene dosage or allelic suppression, 35S::CYC:GR homozygotes were crossed to other independent homozygous lines and to wild type. Double hemizygous plants did not show a phenotype when grown in DEX media, whereas the hemizygous lines obtained

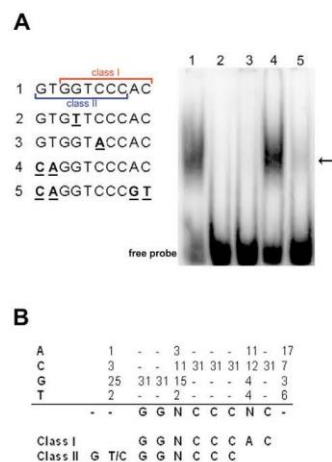


Fig. 1. CYC protein binds to DNA. (A) Specificity of CYC recombinant protein binding to class I and class II TCP consensus binding sites. Oligonucleotide probes contain a shared consensus binding site for class I GGNCCCAC (red) and class II GTGGNCCC (blue) to which CYC protein binds (arrow; lane 1). Bold underlined nucleotides indicate mutations introduced that affect both class I and II binding (lanes 2 and 3) or specifically only class II (lane 4) or class I (lane 5). (B) Consensus DNA-binding sequence for CYC protein obtained by a random binding site selection method. After five rounds of selection, a total of 31 binding sites of CYC were piled up using MEME (meme.sdsc.edu) and a consensus sequence generated. Nucleotides that were not occupied by a specific residue are indicated by N.

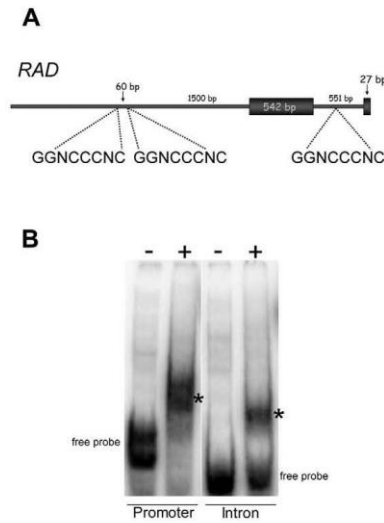


Fig. 2. Interaction of CYC recombinant protein with *RAD* promoter and intron. (A) *RAD* genomic region showing three potential CYC-binding sites in the promoter and intron. (B) PCR fragments of promoter and intron sequences with putative CYC-binding sites were amplified and used as probes in an EMSA with recombinant CYC protein. + or – indicates the presence or absence of CYC protein; asterisks indicate retardation of the mobility of CYC-DNA binding complex.

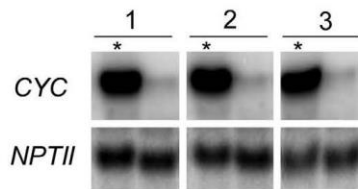


Fig. 3. Northern blot of RNA from 35S::CYC:GR DEX-grown T2 plants derived from three independent transformants, probed with *CYC* (top) or *NPTII* as control (bottom). For each transformant, seedlings were grouped according to whether they had a strong (*) or a wild-type phenotype. Progeny testing showed that in all cases, plants with the strong phenotype were hemizygous, whereas plants with wild-type phenotypes were homozygous for the construct.

from the cross with wild type showed the phenotype. These results indicate that two doses of the transgene result in gene silencing, a phenomenon that has been recorded previously for some transgenes (de Carvalho et al., 1992).

CYC promotes petal expansion in *Arabidopsis*

One aspect of the phenotype of DEX-induced 35S::CYC:GR plants was that the petals were bigger than those of wild type

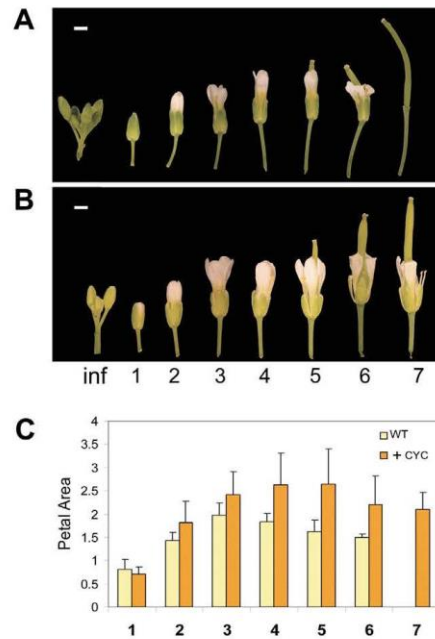


Fig. 4. Effect of CYC in the growth of the petals of *Arabidopsis*. Flowers along the inflorescence of (A) wild-type and (B) 35S::CYC:GR plants grown in DEX. (C) Petal area (mm²) of consecutive flowers in the inflorescence. Flowers are numbered from the first flower with visible petals (flower 1). The inflorescence remaining after removal of flowers equal or older than stage 1 is labelled 'inf'. Error bars indicate standard deviations. Number of petals measured for each stage was between five and eight. Yellow bars indicate wild-type and orange bars indicate 35S::CYC:GR plants (+CYC) grown with DEX. Scale bars: 1 mm.

(Fig. 4). To determine the stage at which this size change became evident, flowers were staged according to the number of nodes below the first flower with visible petals, termed flower 1 (Butenko et al., 2003; Patterson, 2001). Petals from 35S::CYC:GR flowers became larger than wild-type petals after flower 2 (Fig. 4A-C). Measurements of surface area of mature petals (Fig. 4C) showed that 35S::CYC:GR petals were about 1.5 times larger in area for all four petals. In addition, floral organ senescence was delayed as petals remained attached to the silique for a prolonged period, in contrast to wild-type organs, which abscise at flower 5 or 6. To investigate the correlation between petal area and senescence further, we measured petal areas in two mutants with delayed or deficient abscission: *inflorescence deficient in abscission (ida)*, in which floral organs remain attached to the plant body after the shedding of mature seeds (Butenko et al., 2003); and *ethylene-response gene (etr1-1)*, an ethylene response mutant that shows delayed floral organ abscission (Bleecker et al., 1988; Bleecker

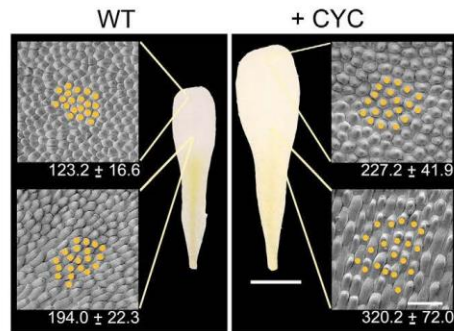


Fig. 5. Effect of *CYC* on *Arabidopsis* petal cell size. SEM images of the tip and middle areas of wild-type and 35S::CYC:GR petals show that the increase in petal area when *CYC* is active is due to an increase in cell size. In each SEM image, the same number of cells are highlighted in orange. Numbers indicate cell size ($\mu\text{m}^2 \pm \text{s.e.m.}$) in the tip and middle regions of the petals, determined using the CellFinder programme. On average between 200 and 500 cells were measured per image and five petals were used to obtain the average cell size in the different petal areas. Left panel shows wild-type and right panel shows 35S::CYC:GR plants (+CYC) grown with DEX. Scale bar: 50 μm on the SEM images; 1 cm on the whole petals.

and Patterson, 1997; Patterson and Bleeker, 2004). In neither of these mutants was petal size affected to the same degree as 35S::CYC:GR plants, although there may have been a slight increase in size for *etr1-1* (data not shown).

To determine whether the increase in petal area reflected changes in cell proliferation or expansion, the adaxial epidermal layer of mature petals was analysed by SEM (Fig. 5). The average cell area from the tip and middle regions of the petal epidermis was determined. This showed that the cells of 35S::CYC:GR petals were about 1.6 (middle region) or 1.8 (tip region) times bigger than the epidermal cells of wild-type petals. These values are comparable with the overall increase in petal area (1.5 times), indicating that the effect of *CYC* on petal area could be largely accounted for by increased cell expansion.

To determine the developmental stage at which *CYC* exerts its effects on petal development in *Arabidopsis*, 35S::CYC:GR plants were transferred to DEX after bolting, when the first two flowers had opened in the main inflorescence. The inflorescence was then allowed to develop further. All flowers showed delayed senescence and abscission, indicating that *CYC* can have an effect late in development even after the flowers have opened.

CYC represses growth of *Arabidopsis* leaves

35S::CYC:GR plants grown in DEX-containing media, were dwarfed and exhibited small oval-shaped leaves (Figs 6, 7, 8). Mature leaves of 35S::CYC:GR plants were on average eight times smaller in surface area than those of wild type (Fig. 7A,C). To investigate whether the difference in leaf size was due to a difference in cell size or in cell number, the adaxial epidermal layer of leaf 4 was analysed by SEM at different

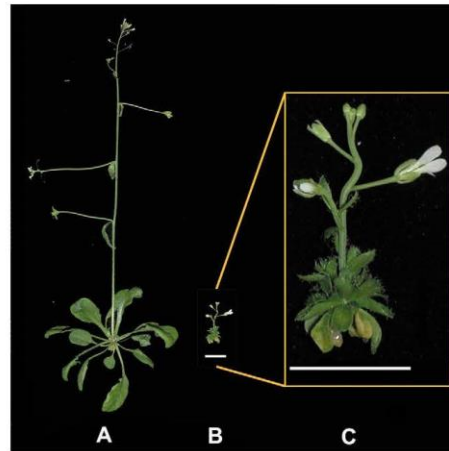


Fig. 6. Effect of overexpressing *CYC* in *Arabidopsis*. 35S::CYC:GR plants have smaller leaves and bigger petals. (A) Wild type; (B) 35S::CYC:GR plants grown on DEX; (C) higher magnification of B ($\sim 6\times$). Scale bars: 1 cm.

stages of development (Fig. 7B,D). At maturity, cells of 35S::CYC:GR leaves were about four times smaller than those in wild-type plants, suggesting that contrary to what was observed in the petals, *CYC* has a role in repressing cell expansion in the leaves. However, if reduced cell size was solely responsible for the reduction in overall leaf size, the leaves of 35S::CYC:GR plants should be four times smaller rather than observed value of eight times. This indicates that 35S::CYC:GR leaves also had about half the number of cells of wild type. To determine whether this reflected an early arrest of cell proliferation, epidermal cells of younger leaves were analysed. At day 14, cells of 35S::CYC:GR leaves were larger than those of wild type, suggesting that cell division had arrested early and the cells were starting to differentiate (Fig. 7B,D). Moreover, evidence of recent cell divisions could be seen in the epidermal cells of wild-type leaves (formation of new stomata), whereas in 35S::CYC:GR leaves no such events could be seen. Thus, *CYC* reduces both cell proliferation (by promoting early arrest of cell division) and cell expansion in leaves.

To determine the developmental stages at which *CYC* can affect leaf growth, 35S::CYC:GR plants were grown in media with DEX and transferred to media without DEX at day 10 and left to grow to maturity (Fig. 8B). At the time of transfer, the first two rosette leaves were about 2 mm wide and the third leaf was 0.5 mm wide. Analysis of consecutive rosette leaves of mature plants showed that from the third leaf onwards, the leaves increasingly resembled leaves of plants grown continually in the absence of DEX (compare Fig. 8A with 8B).

This showed that removal of *CYC* could restore leaf growth at early stages of development, before they were about 0.5 mm wide. Moreover, the effect was greater the earlier that *CYC* was removed.

Conversely, when plants were grown without DEX and moved onto DEX at day 10 (Fig. 8C), growth repression was first detected for leaves 3–4 and became progressively more pronounced in later leaves (compare Fig. 8C with 8D). These results suggest that activation of CYC can influence leaf development at early stages, before leaves are 0.5 mm wide, leading to a reduction in final leaf size.

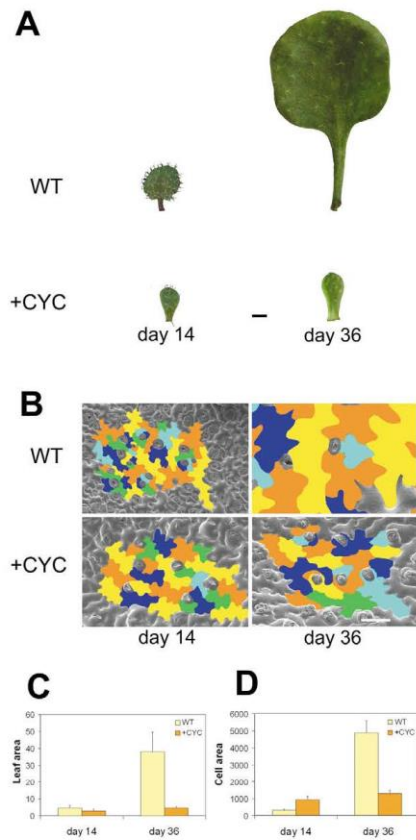


Fig. 7. CYC represses leaf growth in *Arabidopsis*. (A) Leaves from wild-type and 35S::CYC:GR plants grown on DEX (+CYC), at early (day 14; left) and late (day 36; right) developmental stages. In all cases, the fourth rosette leaf was measured. Scale bar: 1 mm. (B) SEM images of adaxial epidermal cells from leaves at the same developmental stage as in A with individual cells highlighted in diverse colours. Scale bar: 50 µm. (C) Measurements of leaf area (mm²) and (D) epidermal cell area (µm²) show that CYC reduces leaf surface area by a reducing cell proliferation and cell expansion. Three to five leaves were measured and the area of 19–87 cells in each leaf was obtained. Error bars indicate standard deviations.

CYC activates *Antirrhinum* RAD in *Arabidopsis* but not endogenous RAD-like genes

The *Arabidopsis* genome contains six *RAD*-like genes none of which containing the consensus CYC binding-site within 2 kb upstream or downstream of the coding regions (C.B., M.M.R.C. and E.C.). To investigate whether the effects of CYC in *Arabidopsis* might nevertheless involve activation of these genes, RT-PCR was performed on 35S::CYC:GR plants 6, 24 and 48 hours after being transferred to DEX-containing media. No increase in expression of the *RAD*-like genes was observed, suggesting that CYC does not affect expression of any of these genes.

To test whether CYC could activate the *Antirrhinum* *RAD* gene in the context of *Arabidopsis*, 35S::CYC:GR *Arabidopsis* plants were crossed to transgenic plants containing *RAD* under the control of its own promoter (*RAD*::*RAD*) (C.B., M.M.R.C. and E.C.). When plants with both transgenes were grown in DEX, they showed the same phenotype as 35S::CYC:GR plants. The double transgenics were also grown without DEX and transferred, at 21 days after germination, to media containing DEX. Fig. 9 shows that *RAD* expression was upregulated 6 hours after the induction of CYC, confirming that CYC can bind to the *RAD* promoter in vivo, and showing that this interaction can be reconstituted in *Arabidopsis*.

Discussion

We have shown that CYC most likely acts as a transcription factor that binds to the *RAD* target gene. The interaction

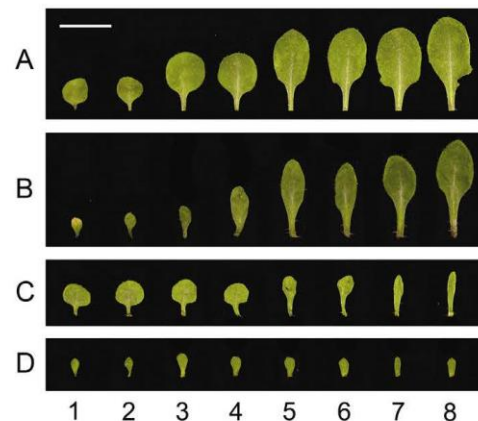


Fig. 8. Effect of CYC activation or inactivation on the growth of *Arabidopsis* leaves. (A,B) 35S::CYC:GR plants were grown in media without DEX (A) or with DEX (B) and left to grow to maturity. (C,D) Alternatively, 10 day after germination, seedlings in which leaf 3 was less than 0.5 mm wide were transferred from media without DEX to media with DEX (C) or from media containing DEX to media without DEX (B). Numbers correspond to consecutive rosette leaves in the mature plants. Scale bar: 1 cm.

between *CYC* and *RAD* can be reconstituted in *Arabidopsis*, as induction of *CYC* leads to increased expression of the *Antirrhinum RAD* gene in *Arabidopsis*. Moreover, *CYC* expression affects growth and development of leaves and petals in *Arabidopsis*, indicating that it is able to influence developmental target genes in this species, as well as in *Antirrhinum*. In the case of leaves, *CYC* acts from an early stage in development to inhibit cell proliferation and at a later stage to reduce cell expansion, resulting in an overall reduction in leaf size. In petals, *CYC* acts at a late stage to promote cell expansion, leading to an increase in size of all petals.

In contrast to the situation in *Antirrhinum*, endogenous *RAD*-like genes are not activated by *CYC* in *Arabidopsis*. This suggests that although *CYC* can exert effects in *Arabidopsis*, the network of interactions involving *CYC* has changed since the *Antirrhinum* and *Arabidopsis* lineages diverged. The most recent common ancestor of *Arabidopsis* and *Antirrhinum* most likely had a *TCPI/CYC* gene that was asymmetrically expressed in axillary meristems (Cubas et al., 2001). How might the network of interactions have diverged in the lineages derived from this common ancestor?

In considering the evolutionary changes in a regulatory network, it is convenient to distinguish between two types of target process influenced by a transcription factor. One is the set of potential targets that could be influenced by expression of the transcription factor at any developmental stage and in any part of the plant. This class of targets can be revealed through constitutive expression of the transcription factor. Evolutionary changes in potential targets may occur, for example, through changes in the structure of the transcription factor (i.e. binding site) or changes in the promoters of target genes. The other type of target process is the set of actual targets that are influenced only where and when the transcription factor is normally active. Given a set of potential targets, changes in the expression pattern of the transcription factor can lead to modifications to the defined subset of actual targets.

The ability of *CYC* to influence both *Antirrhinum* and *Arabidopsis* development suggests that a range of potential developmental targets were present in their common ancestor. A subset of these would have been the ancestral actual targets in the dorsal regions of axillary meristems. Although these actual targets are unknown, they are unlikely to have involved

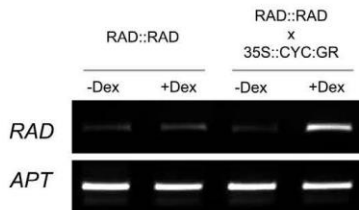


Fig. 9. *CYC* upregulates *RAD* expression in *Arabidopsis*. RT-PCR analysis of *RAD* transcript in 35S::CYC:GR RAD::RAD plants transferred to DEX. RNA was extracted after 6 hours after transfer. *APT* (adenosine phosphotransferase) was used as a constitutive control.

morphological asymmetry of the flower as the ancestral condition is thought to have been radial symmetry.

A key step in the lineage leading to *Antirrhinum* may have been co-option of *RAD* into the network of potential targets (Fig. 10, step a). This could have arisen through mutations in the *RAD* promoter or intron, bringing *RAD* under the control of *CYC*. This would account for why over-expression of *CYC* in *Arabidopsis* does not lead to activation of *RAD*-like genes (as they lack appropriate recognition sites) even though it can activate the *Antirrhinum RAD* gene. It is also consistent with the more restricted role of *RAD* in floral symmetry compared with *CYC* and *DICH*.

In addition to co-option of *RAD*, other alterations in the regulatory interactions may also have occurred in the *Antirrhinum* lineage. For example, *CYC* has developmental effects on stamen arrest as well as a slight effect on petal lobe asymmetry independent of *RAD*. These effects may have arisen through divergence in some of the target processes influenced by *CYC* (Fig. 10, step b). It is also possible that the target sequence recognised by *CYC* diverged to some extent (the *CYC* consensus binding site is not typical of type II TCP proteins).

Another evolutionary change may have involved persistent expression of *CYC* in the dorsal domain of *Antirrhinum* floral meristems [in contrast to transient expression of *TCPI* in *Arabidopsis* (Cubas et al., 2001)], leading to a change in expression or range of actual targets. Given the phenotypic effects of *CYC* on petal size in *Arabidopsis*, it is possible that such persistence could create an asymmetric *Arabidopsis* flower with larger dorsal petals. Persistence in the *Antirrhinum* lineage may have arisen through evolution of an auto-regulatory loop (Fig. 10, step c), as *CYC* contains promoter sequences matching the consensus *CYC*-binding site (the

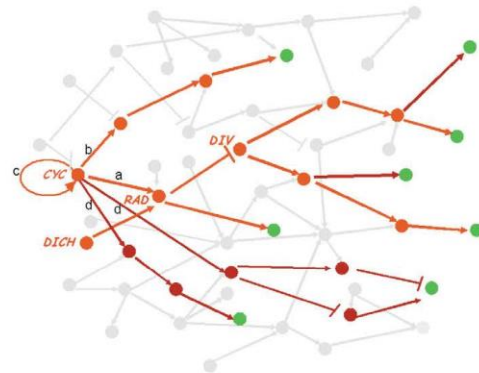


Fig. 10. Schematic representation of evolution of gene interactions in the *Antirrhinum* lineage controlling flower dorsoventral asymmetry. Potential direct and indirect targets of *CYC* are highlighted in orange and red, with the subset of actual targets indicated in orange. Downstream targets regulating growth are in green and the rest of the regulatory network in which *CYC* interactions are embedded is shown in grey. Steps where divergence involving *CYC* interactions are lettered a-d (see text for explanation).

TCPI promoter does not contain such sites). However, persistent expression could also have arisen through interaction with other factors that are not directly dependent on *CYC*. In addition, we cannot rule out the possibility that the ancestral *CYC/TCPI* gene was persistently expressed in dorsal floral meristems and that expression became transient in the lineage leading to *Arabidopsis*.

Compared with *CYC*, little is known about the role of *TCPI* and its downstream targets in *Arabidopsis*. Nevertheless, it seems that some of the potential target processes influenced by *CYC* may be conserved in *Arabidopsis*. Expression of *CYC* in leaf primordia influences both cell division and expansion. Moreover, this effect is cumulative with increased duration of *CYC* expression. This is comparable with the effects of *CYC* on organ development in *Antirrhinum*, consistent with some overlap between potential target processes influenced by *CYC* in the two species but also some divergence (Fig. 10, step d).

Expression of *CYC* also influences petal development in *Arabidopsis*. All petals are equally affected, reflecting ectopic expression of *CYC* all around the developing flower. The effect of *CYC* largely involves cell expansion late in development, in contrast to *CYC* in *Antirrhinum*, which also has early developmental effects. Moreover, *CYC* expression does not affect stamen development in *Arabidopsis*, unlike the situation in *Antirrhinum*. Thus, the potential developmental targets in floral organs have probably diverged, consistent with the inability of *CYC* to switch on *RAD*-like genes in *Arabidopsis*.

Taken together, our results indicate that interactions involving *CYC* have changed in many ways since the separation of the *Antirrhinum* and *Arabidopsis* lineages. These changes may themselves represent a subset of the changes that have occurred in the whole regulatory network in which *CYC* is embedded. Nevertheless, some elements of the network have been preserved, such as the initial asymmetric expression pattern and the modification of developmental target gene activity. Thus, floral asymmetry has most likely arisen through a process of tinkering (Jacob, 1977; Jacob, 2001) with the strengths and pattern of connections in a regulatory network, in which some common elements may still be discernable.

We thank Shunichi Kosugi for providing the oligonucleotides with the TCP class I and II binding sequences and for technical help. We are grateful to Robert Sablowski for providing the plasmid pRS20 containing the glucocorticoid receptor sequence, Mark Chadwick for making the pRSET-CYC construct and Reidunn Aalen for providing the *ida* seeds. This work was funded by a grant from the BBSRC.

References

- Almeida, J., Rocheta, M. and Galego, L. (1997). Genetic control of flower shape in *Antirrhinum majus*. *Development* **124**, 1387-1392.
- Babu, M. M., Luscombe, N. M., Aravind, L., Gerstein, M. and Teichmann, S. A. (2004). Structure and evolution of transcriptional regulatory networks. *Curr. Opin. Struct. Biol.* **14**, 283-291.
- Bleecker, A. B. and Patterson, S. E. (1997). Last exit: senescence, abscission, and meristem arrest in *Arabidopsis*. *Plant Cell* **9**, 1169-1179.
- Bleecker, A. B., Estelle, M. A., Somerville, C. and Kende, H. (1988). Insensitivity to ethylene conferred by a dominant mutation in *Arabidopsis thaliana*. *Science* **241**, 1086-1089.
- Butenko, M. A., Patterson, S. E., Grini, P. E., Stenvik, G. E., Amundsen, S. S., Mandal, A. and Aalen, R. B. (2003). Inflorescence deficient in abscission controls floral organ abscission in *Arabidopsis* and identifies a novel family of putative ligands in plants. *Plant Cell* **15**, 2296-2307.
- Cantu, J. and Ruiz, C. (1985). On atavisms and atavistic genes. *Annu. Genet.* **28**, 141-142.
- Carpenter, R., Copsey, L., Vincent, C., Doyle, S., Magrath, R. and Coen, E. (1995). Control of flower development and phyllotaxy by meristem identity genes in *antirrhinum*. *Plant Cell* **7**, 2001-2011.
- Clough, S. J. and Bent, A. F. (1998). Floral dip: a simplified method for *Agrobacterium*-mediated transformation of *Arabidopsis thaliana*. *Plant J.* **16**, 735-743.
- Corley, S. B., Carpenter, R., Copsey, L. and Coen, E. (2005). Floral asymmetry involves an interplay between TCP and MYB transcription factors in *Antirrhinum*. *Proc. Natl. Acad. Sci. USA* **102**, 5068-5073.
- Crawford, B. C., Nath, U., Carpenter, R. and Coen, E. S. (2004). CINCINNATA controls both cell differentiation and growth in petal lobes and leaves of *Antirrhinum*. *Plant Physiol.* **135**, 244-253.
- Cubas, P., Coen, E. and Zapater, J. M. (2001). Ancient asymmetries in the evolution of flowers. *Curr. Biol.* **11**, 1050-1052.
- de Carvalho, F., Gheysen, G., Kushnir, S., Van Montagu, M., Inze, D. and Castresana, C. (1992). Suppression of beta-1,3-glucanase transgene expression in homozygous plants. *EMBO J.* **11**, 2595-2602.
- Donoghue, M. J., Ree, R. and Baum, D. A. (1998). Phylogeny and the evolution of flower symmetry in the Asteridae. *Trends Plant Sci.* **3**, 311-317.
- Endress, P. K. (1999). Symmetry in flowers: diversity and evolution. *Int. J. Plant Sci.* **160**, S3-S23.
- Galego, L. and Almeida, J. (2002). Role of DIVARICATA in the control of dorsoventral asymmetry in *Antirrhinum* flowers. *Genes Dev.* **16**, 880-891.
- Gibson, G. and Honeycutt, E. (2002). The evolution of developmental regulatory pathways. *Curr. Opin. Genet. Dev.* **12**, 695-700.
- Green, P. B. and Linstead, P. (1990). A procedure for SEM of complex shoot structures applied to the inflorescence of snapdragon (*Antirrhinum*). *Protoplasma* **158**, 33-38.
- Gubitz, T., Caldwell, A. and Hudson, A. (2003). Rapid molecular evolution of CYCLOIDEA-like genes in *antirrhinum* and its relatives. *Mol. Biol. Evol.* **20**, 1537-1544.
- Guerineau, F. and Mullineaux, P. M. (1993). Plant transformation and expression vectors. In *Plant Molecular Biology Labfax* (ed. R. R. D. Croy), pp. 121-148. London: BIOS Scientific Publishers.
- Hall, B. (1995). Atavisms and atavistic mutations. *Nat. Genet.* **10**, 126-127.
- Hileman, L. C. and Baum, D. A. (2003). Why do paralogs persist? Molecular evolution of CYCLOIDEA and related floral symmetry genes in *Antirrhineae* (Veronicaaceae). *Mol. Biol. Evol.* **20**, 591-600.
- Jacob, F. (1977). Evolution and tinkering. *Science* **196**, 1161-1166.
- Jacob, F. (2001). Complexity and tinkering. *Annu. New York Acad. Sci.* **929**, 71-73.
- Kosugi, S. and Ohashi, Y. (1997). PCF1 and PCF2 specifically bind to cis elements in the rice proliferating cell nuclear antigen gene. *Plant Cell* **9**, 1607-1619.
- Kosugi, S. and Ohashi, Y. (2002). DNA binding and dimerization specificity and potential targets for the TCP protein family. *Plant J.* **30**, 337-348.
- Kosugi, S., Suzuki, I. and Ohashi, Y. (1995). Two of three promoter elements identified in a rice gene for proliferating cell nuclear antigen are essential for meristematic tissue-specific expression. *Plant J.* **7**, 877-886.
- Lloyd, A. M., Schena, M., Walbot, V. and Davis, R. W. (1994). Epidermal cell fate determination in *Arabidopsis*: patterns defined by a steroid-inducible regulator. *Science* **266**, 436-439.
- Luo, D., Carpenter, R., Vincent, C., Copsey, L. and Coen, E. (1996). Origin of floral asymmetry in *Antirrhinum*. *Nature* **383**, 794-799.
- Luo, D., Carpenter, R., Copsey, L., Vincent, C., Clark, J. and Coen, E. (1999). Control of organ asymmetry in flowers of *Antirrhinum*. *Cell* **99**, 367-376.
- Nath, U., Crawford, B. C., Carpenter, R. and Coen, E. (2003). Genetic control of surface curvature. *Science* **299**, 1404-1407.
- Palatnik, J. F., Allen, E., Wu, X., Schommer, C., Schwab, R., Carrington, J. C. and Weigel, D. (2003). Control of leaf morphogenesis by microRNAs. *Nature* **425**, 257-263.
- Patterson, S. E. (2001). Cutting loose: Abscission and dehiscence in *Arabidopsis*. *Plant Physiol.* **126**, 494-500.
- Patterson, S. E. and Bleecker, A. B. (2004). Ethylene-dependent and -independent processes associated with floral organ abscission in *Arabidopsis*. *Plant Physiol.* **134**, 194-203.
- Sablowski, R. W. and Meyerowitz, E. M. (1998). Temperature-sensitive splicing in the floral homeotic mutant *apelta3-1*. *Plant Cell* **10**, 1453-1463.
- Schenk, P. M., Baumann, S., Mattes, R. and Steinbiss, H. H. (1995). Improved high-level expression system for eukaryotic genes in *Escherichia*

- coli using T7 RNA polymerase and rare ArgRNAs. *Biotechniques* **19**, 196-198, 200.
- Stebbins, G. L.** (1974). *Flowering Plants: Evolution Above the Species Level*. Cambridge, MA: Harvard University Press.
- Studier, F. W. and Moffatt, B. A.** (1986). Use of bacteriophage T7 RNA polymerase to direct selective high-level expression of cloned genes. *J. Mol. Biol.* **189**, 113-130.
- Tautz, D.** (2000). Evolution of transcriptional regulation. *Curr. Opin. Genet. Dev.* **10**, 575-579.
- Tremousaygue, D., Garnier, L., Bardet, C., Dabos, P., Herve, C. and Lescure, B.** (2003). Internal telomeric repeats and 'TCP domain' protein-binding sites co-operate to regulate gene expression in *Arabidopsis thaliana* cycling cells. *Plant J.* **33**, 957-966.

Localization of the Microtubule End Binding Protein EB1 Reveals Alternative Pathways of Spindle Development in Arabidopsis Suspension Cells^W

Jordi Chan,^{1,2} Grant Calder,¹ Samantha Fox, and Clive Lloyd

Department of Cell and Developmental Biology, John Innes Centre, Norwich NR 4 7UH, United Kingdom

In a previous study on *Arabidopsis thaliana* suspension cells transiently infected with the microtubule end binding protein ATEB1a–green fluorescent protein (GFP), we reported that interphase microtubules grow from multiple sites dispersed over the cortex, with plus ends forming the characteristic comet-like pattern. In this study, ATEB1a-GFP was used to study the transitions of microtubule arrays throughout the division cycle of cells lacking a defined centrosome. During division, the dispersed origin of microtubules was replaced by a more focused pattern with the plus end comets growing away from sites associated with the nuclear periphery. The mitotic spindle then evolved in two quite distinct ways depending on the presence or absence of the preprophase band (PPB): the cells displaying outside-in as well as inside-out mitotic pathways. In those cells possessing a PPB, the fusion protein labeled material at the nuclear periphery that segregated into two polar caps, perpendicular to the PPB, before nuclear envelope breakdown (NEBD). These polar caps then marked the spindle poles upon NEBD. However, in the population of cells without PPBs, there was no prepolarization of material at the nuclear envelope before NEBD, and the bipolar spindle only emerged clearly after NEBD. Such cells had variable spindle orientations and enhanced phragmoplast mobility, suggesting that the PPB is involved in a polarization event that promotes early spindle pole morphogenesis and subsequent positional stability during division. Astral-like microtubules are not usually prominent in plant cells, but they are clearly seen in these Arabidopsis cells, and we hypothesize that they may be involved in orienting the division plane, particularly where the plane is not determined before division.

INTRODUCTION

In higher plant cells, the origins of the different microtubule arrays are not always clear because these cells do not contain an obvious microtubule organizing center, like the animal centrosome. Higher plant cells form four different microtubule arrays that succeed each other during the cell cycle: the interphase cortical array, the preprophase band (PPB), the mitotic spindle, and the cytokinetic phragmoplast. During interphase, microtubules are diffusely distributed at the cell cortex, where they associate with the plasma membrane and form parallel groups. At the plasma membrane, cortical microtubules are motile, exhibiting a hybrid form of dynamic instability and treadmilling (Shaw et al., 2003), and we recently showed that microtubules grow and shrink from multiple foci that can be tagged with *Arabidopsis thaliana* end binding protein 1a–green fluorescent protein (ATEB1a-GFP) (Chan et al., 2003).

During preprophase, the PPB develops from the selective stabilization and destabilization of cortical microtubules (Dhonukshe

and Gadella, 2003), which gives rise to a band of cortical microtubules that encircles the nucleus. The directionality of EB1 comets shows that the PPB, like the cortical array, is composed of microtubules of mixed polarity (Chan et al., 2003). Despite appearing before mitosis, the PPB has a connection with cytokinesis in that it marks the plane of cell division (Mineyuki, 1999). In addition to the cortical band that somehow marks the division plane, the microtubules radiating from the preprophase nuclear surface have also been suggested to play roles in premitotic nuclear positioning, spindle orientation, and spindle pole morphogenesis (Lloyd, 1991; Mineyuki, 1999; Granger and Cyr, 2000). The fact that microtubules radiate from the nuclear envelope during preprophase (also in the early postcytokinetic period) has led to the nuclear periphery being one of the accepted sites for microtubule nucleation in plants (Erhardt et al., 2002; Schmit, 2002).

The next transition concerns the formation of the spindle. At prophase, a cage of microtubules develops around the nucleus, forming the prophase spindle which, by metaphase, consists of two half sets of microtubules with opposite polarity. The plus ends of the microtubules for each half set lie in the equatorial plane (Euteneuer et al., 1982). The spindle poles are not as tightly focused as in animal cells for there may be multiple minipoles that frequently give rise to broad poles. At anaphase, after the chromosomes have separated, the microtubules of the spindle midzone give way to a column comprised of two sets of interdigitating microtubules; in the conventional cytokinesis of somatic cells, these remnants of the central spindle are considered to initiate the cytokinetic apparatus (Staehelein and Hepler, 1996;

¹These authors contributed equally to this work.

²To whom correspondence should be addressed. E-mail jordi.chan@bbsrc.ac.uk; fax 44-1603-450022.

The authors responsible for distribution of materials integral to the findings presented in this article in accordance with the policy described in the Instructions for Authors (www.plantcell.org) are: Jordi Chan (jordi.chan@bbsrc.ac.uk) and Clive Lloyd (clive.lloyd@bbsrc.ac.uk).

^WOnline version contains Web-only data.

Article, publication date, and citation information can be found at www.plantcell.org/cgi/doi/10.1105/tpc.105.032615.

Otegui and Staehelin, 2000). This, the phragmoplast, then grows out centrifugally, opening up as a ring that deposits the cell plate in its center. Microtubule hook decoration studies have shown that phragmoplast microtubules share the same polarity as those of the spindle, with the plus ends overlapping in the equatorial plane (Euteneuer and McIntosh, 1980). Drug and molecular biological studies indicate that phragmoplast expansion is dependent upon continuous microtubule depolymerization and repolymerization, during which microtubule disassembly is tightly coupled to cell plate expansion (Yasuhara et al., 1993; Nishihama and Machida, 2001).

Throughout this cyclic formation of different microtubule arrays, the absence of a centriole-containing centrosome as an unambiguous marker of microtubule nucleation has led to uncertainty about the origin of, and continuity between, the various microtubule arrays. For instance, the absence of centrosomes from the plant cell's spindle poles has been taken as support for the idea that spindles form by an inside-out mechanism in which microtubules first associate with the chromosomes before being sorted and drawn by microtubule motors into an antiparallel array in which the minus ends only latterly become organized into poles (reviewed in Compton, 2000). The origins and sites of microtubule nucleation during phragmoplast expansion are also unclear. In somatic cells, the phragmoplast appears to evolve out of spindle remnants (Zhang et al., 1990; Otegui and Staehelin, 2000), whereas in endosperm, the phragmoplast microtubules are nucleated from the surfaces of the daughter nuclei with the cell plate being deposited where microtubules overlap at the periphery of the various nuclear-cytoplasmic domains (Vaughn and Harper, 1998; Brown and Lemmon, 2001). However, in somatic cells, once the phragmoplast grows out beyond the internuclear corridor, it is not apparent where new microtubules originate, and the idea that microtubule plus ends overlap at the midline is not universally agreed upon: the possibility has been raised that nucleating material becomes deposited in the midline, resulting in a reversal of microtubule polarity (Schmit, 2002). Markers for the plus or the minus ends of microtubules should help us to understand the origin of the arrays.

Although higher land plants do not have centrioles as part of their life cycle, it is possible that they possess some of the antigens that constitute the amorphous pericentriolar material from which spindle and cytoplasmic microtubules emerge. γ -Tubulin is an important constituent of animal centrosomes, forming ring complexes that act as templates for new microtubule growth (Zheng et al., 1995). However, in plants, γ -tubulin is found in variously sized complexes (Drykova et al., 2003): it decorates the entire length of microtubules, not just the minus ends, and has consequently not proved a good marker for nucleation sites (Joshi and Palevitz, 1996).

An alternative marker for microtubule ends is the end binding protein EB1, a member of a conserved family of microtubule-associated proteins that in other eukaryotic cells is known to bind the plus ends of microtubules. At the plus end of microtubules, EB1 regulates microtubule dynamics by acting as an anticatastrophe factor (Rogers et al., 2002; Tirnauer et al., 2002) and promotes the end-on-attachment of microtubules to different subcellular targets (Korinek et al., 2000). However, EB1 has also been shown to accumulate at the minus ends of microtubules

(Bu and Su, 2001; Morrison and Askham, 2001; Askham et al., 2002; Rehberg and Gráf, 2002; Rogers et al., 2002; Tirnauer et al., 2002, 2004; Louie et al., 2004; Piehl et al., 2004) in organisms as diverse as fungi (Straube et al., 2003) to vertebrates (Piehl et al., 2004). A plausible explanation is that the minus end EB1 acts as a repository for the material that grows out with the plus end (Rehberg and Gráf, 2002).

Recently, we reported on the distribution of an Arabidopsis homolog of EB1 (AtEB1a) transiently expressed as a C-terminal GFP fusion in Arabidopsis suspension cells (Chan et al., 2003). We demonstrated that AtEB1a-GFP marks the plus ends of microtubules with the familiar comet-like pattern (see also, Mathur et al., 2003; van Damme et al., 2004). Using time-lapse microscopy, we also showed that AtEB1a-GFP marked foci at the minus ends from which microtubules (sometimes more than one) were observed to grow and shrink back (Chan et al., 2003).

Now, using AtEB1a-GFP as a directional marker, we report on the origin and continuity of the microtubule structures involved in division, showing the existence of alternative pathways for spindle pole and phragmoplast expansion in Arabidopsis suspension cells.

RESULTS

Time-lapse microscopy was used to follow the direction of plus end comet growth and the general staining pattern of AtEB1a-GFP around the cell cycle. A brief overview of the changing patterns of fluorescence is presented before focusing on phases of particular interest.

As previously shown (Chan et al., 2003), during interphase, plus end comets arose at multiple dispersed sites around the cortex, but with the onset of division, the nuclear periphery became a prominent site for microtubule outgrowth. Plus end comets were observed to grow out from the perinuclear region toward the cell cortex (see Supplemental Movie 1 online) to form a radial array, in contrast with the interphase array in which the microtubule ends are dispersed over the cortex. Prophase cells were also readily distinguishable from interphase cells by accumulations of AtEB1a-GFP around the periphery of their nuclear envelopes (Figures 1A and 1B).

Metaphase spindles were characterized by general labeling of the microtubules with heavy concentrations of AtEB1a-GFP at their spindle poles (Figures 1C and 1D). Double labeling with antitubulin confirmed that the GFP signal was concentrated at the spindle poles (Figures 2A to 2E), forming annular structures in favorably presented spindles (Figure 2E). Time-lapse movies showed that the dynamic ends of spindle microtubules were distal to these accumulations of AtEB1a-GFP at spindle poles (data not shown).

During telophase and cytokinesis, AtEB1a-GFP accumulated in two main locations: around the daughter nuclei and in the midzone of the phragmoplast (Figures 1E and 1F). The relationship of these locations to microtubules was confirmed by double labeling fixed cells with antitubulin antibodies (Figures 2F to 2Q). Time-lapse movies established that plus end comets grow away from the opposing faces of the daughter nuclei during telophase (see Supplemental Movie 2 online) and cytokinesis

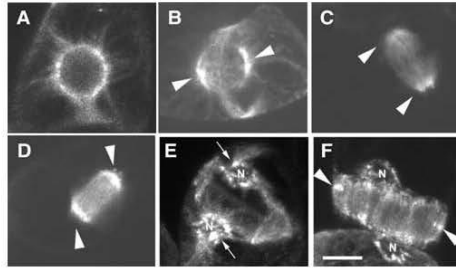


Figure 1. Subcellular Distribution of AtEB1a-GFP in Dividing Suspension Cells of Arabidopsis.

Distribution of AtEB1a-GFP in living suspension cells of Arabidopsis [(A) to (F)] at prophase/preprophase [(A) and (B)], metaphase (C), anaphase (D), and cytokinesis [(E) and (F)]. Arrowheads indicate accumulations of AtEB1a-GFP at spindle poles [(B) to (D)]. Arrows in (E) indicate accumulations around the nucleus. Arrowheads in (F) indicate accumulated label in the midline of the phragmoplast. Bar = 7 μ m.

(see Supplemental Movie 3 online). This places the plus ends of microtubules at the midline of the phragmoplast, distal to the forming nuclear surfaces, in agreement with the hook decoration studies of Euteneuer and McIntosh (1980). In favorably presented cells, the comets appeared to originate from foci of AtEB1a-GFP

at the nuclear periphery (Figure 3, focus 1)—often multiple comets emerged from a single focus (see foci 2 and 5). These foci were also highly dynamic, capable of circumferential and radial movement at the nuclear periphery, concomitant with the microtubule polymerization events (foci 2 and 3). In some cases, the foci exhibited a reduced intensity of fluorescence (focus number 5) or disappeared (focus number 1) after the emergence of the comets.

Time-lapse movies of anaphase and cytokinesis also showed that the plus end comets contribute to the midline location of AtEB1a-GFP at the phragmoplast. Supplemental Movie 2 online demonstrates that this labeling arose from the plus end comets of microtubules that grew from the opposing faces of the daughter nuclei, meeting at the midline. In actively expanding cells, this midline labeling was limited to the leading edge of the phragmoplast (Figures 4A to 4F), resulting in a ring-shaped labeling pattern during symmetrical growth of the phragmoplast (Figure 4F); however, less regular patterns were formed during polarized forms of phragmoplast growth (e.g., Figure 1F). No evidence was found for the contrary outgrowth of microtubules from the phragmoplast midline toward the daughter nuclei. These data therefore indicate that the plus ends of growing microtubules are orientated toward the midzone of the phragmoplast.

Different Mechanisms of Plant Mitosis

By observing microtubule arrays in dividing Arabidopsis cells, we were able to identify a subpopulation of cells that divided without

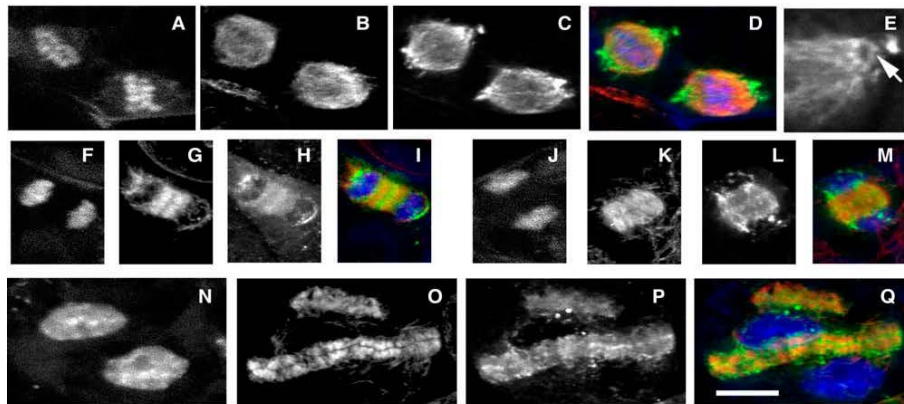


Figure 2. Triple Staining of Dividing Cells Transformed with AtEB1a-GFP.

Transformed Arabidopsis suspension cells were fixed and stained with anti-GFP antibodies (green), antitubulin antibodies (red), and 4',6-diamidino-2-phenylindole (DAPI) (blue).

(A) to (E) Metaphase/anaphase cells expressing AtEB1a-GFP:DAPI (A), antitubulin (B), anti-GFP (C), and merge (D). A magnified image of the top, right-hand spindle pole in (C) is shown in (E). The arrow indicates the presence of an annular structure found at the pole.

(F) to (Q) Cells expressing AtEB1a-GFP during cytokinesis: DAPI [(F), (J), and (N)], antitubulin [(G), (K), and (O)], anti-GFP [(H), (L), and (P)], and merge [(I), (M), and (Q)].

Bar = 14 μ m in (A) to (D), 5 μ m in (E), 13 μ m in (F) to (I), and 11 μ m in (J) to (M) and (N) to (Q).

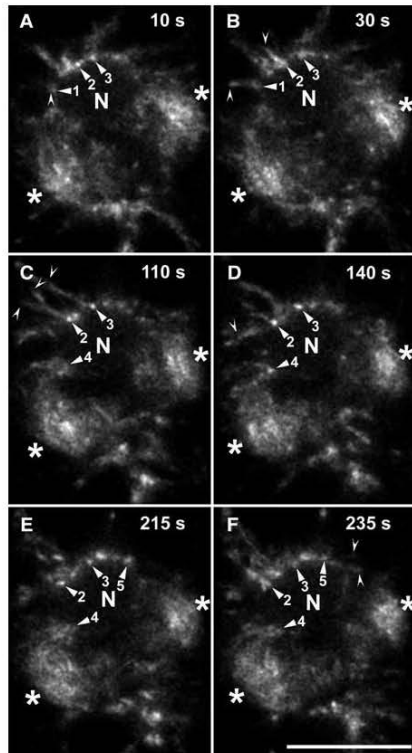


Figure 3. Plus End Comets Emerge from Foci of AtEB1a-GFP at the Periphery of the Nuclear Envelope during Cytokinesis.

AtEB1a-GFP marks foci at the nuclear envelope (arrowheads 1 to 5) from which plus end comets of AtEB1a-GFP (small arrowheads) can be seen to grow toward the cell cortex or phragmoplast. Focus 1 (10 s; [A]) disappears (frame 110 s; [C]) after the emergence of a plus end comet in frame 30 s (B)—microtubule growth then ceases from this spot. Foci 2 and 3 display mobility at the circumference of the nucleus concomitant with microtubule nucleation events—two plus end comets can be seen to emerge from focus 2 and split at different angles in frame 110 s (C). Focus 4 appears in frame 110 s (C) and demonstrates microtubule growth toward the phragmoplast. Focus 5 (frame 215 s; [E]) demonstrates that the brightness of foci decreases after comet growth; similar to focus 2, two comets emerge from focus 5 and grow at divergent angles (frame 235 s; [F]). Note that AtEB1a-GFP is absent from the lower face of the daughter nucleus where no microtubule growth can be detected.

T, time (s); arrowheads, minus end foci of AtEB1a-GFP; small arrowheads, plus end comets; asterisks, outer edges of the phragmoplast; N, upper nucleus of daughter pair. Bar = 10 μ m.

a PPB. Despite the absence of the predictive band of microtubules, the accumulation of label around the nuclear envelope (e.g., Figure 1A) marked these cells as premitotic and allowed them to be followed as they entered mitosis.

Time-lapse studies revealed that there were two pathways for spindle pole development depending on whether a PPB was present or not. In this cell line, \sim 70% of cells in prophase did not have a PPB even after the images were contrast stretched using an inverted grayscale image to visualize the cortex more clearly (Figure 5A, T0). All images presented in subsequent parts of the study were taken from cells that were tracked successfully through division (prophase cells representing 0.17% of transformed cells).

In cells without a PPB, the premitotic nucleus was associated with radial microtubule arrays. An important characteristic of mitosis in such cells was that spindle bipolarity always developed during prometaphase, after nuclear envelope breakdown (NEBD). This is exemplified in Figures 5A to 5D, where it can be seen that AtEB1a-GFP became diffusely distributed in the vicinity of the condensed chromosomes upon NEBD (Figure 5C). Spindle bipolarity was then expressed during prometaphase, with AtEB1a-GFP becoming concentrated at the spindle poles by metaphase/anaphase (Figure 5D). These data therefore show that cells proceeding into cell division without a PPB did not exhibit distinct, bipolar staining patterns of AtEB1-GFP until the bipolar axis of the spindle had been established after NEBD.

By contrast, in those cells that did display a PPB, spindle bipolarity was established much earlier, at preprophase/prophase (Figures 5E to 5H). In these cases, spindle poles developed from sites at opposite sides of the premitotic nucleus so that the interpolar axis was perpendicular to the PPB (Figure 5G). This polar arrangement of AtEB1-GFP at prophase differed

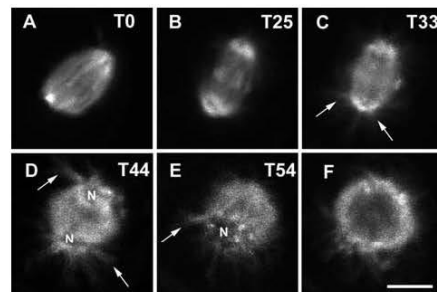


Figure 4. AtEB1a-GFP Accumulates at the Midline of the Phragmoplast.

Time-lapse confocal laser scanning microscopy images of the anaphase-telephase transition in a single cell show that AtEB1-GFP is present at the midzone of the phragmoplast throughout its morphogenesis ([A] to [F]). Selected stacks highlighting the nucleus (N) are shown in (E). Selected stacks from (D) showing the outer ring staining of the growing phragmoplast, which has rotated, are shown in (F). Arrows indicate nucleus-associated microtubules that interact with the cell cortex. T, time (min). Bar = 6.4 μ m in (A) to (F).

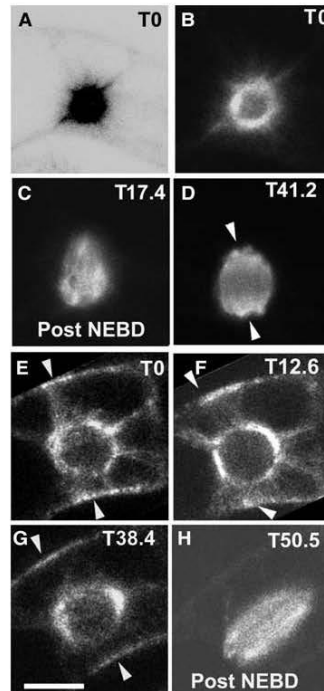


Figure 5. AtEB1a-GFP during Spindle Morphogenesis: Alternative Routes to Pole Formation, with and without a PPB.

Arabidopsis suspension cells undergoing spindle morphogenesis in either the absence ([A] to [D]) or presence of a PPB ([E] to [H]). In the absence of a PPB, spindle poles develop during prometaphase after NEBD and redistribution of AtEB1a-GFP around the condensed chromosomes ([C] and [D]). Accumulations of AtEB1a-GFP at spindle poles then become evident at metaphase/anaphase ([D], arrowheads). In the absence of a PPB, the bipolar axis of the spindle is variable, in this case forming perpendicular to the cell's long axis ([A]; the inverted image [T0] highlights the cell's outline). By contrast, when cells display a PPB ([E] to [H]), the bipolar axis of the spindle forms at prophase (G) before NEBD and the mixing of AtEB1a-GFP with the condensed chromosomes. During this process, AtEB1-GFP labels polar caps (G) that mark the poles of the prometaphase spindle after NEBD (H). In cells with a PPB, the bipolar axis of the spindle always forms parallel to the cell's long axis. The arrowheads ([E] to [H]) indicate cortical microtubules of the PPB. Post NEBD indicates that the nuclear envelope has broken down. T, time (min). Bar = 6.1 μm in (A) (9.6 μm in the inverted grayscale image), 7 μm in (B) to (D), and 7.9 μm in (E) to (H).

significantly from the nonpolarized form seen in cells without a PPB (cf. Figures 1A with 1B). The fact that polar caps of AtEB1a-GFP coexisted with the PPB suggested that the nuclear envelope was still intact during spindle morphogenesis. This was confirmed in Arabidopsis suspension cells expressing HDEL-yellow fluorescent protein (YFP) and immunostained with antitubulin antibodies (see Supplemental Figure 1 online). This showed that the nuclear envelope was intact when the PPB was present, indicating that the development of spindle bipolarity is flexible, in that it can occur both before and after NEBD.

In addition to differences in spindle pole development, we also found that the orientations of spindles were different in the two subpopulations of cells. In all of the seven cells with a PPB that were tracked through division, the spindle formed in a predictable orientation, perpendicular to the long axis of the cell. This differed significantly to mitosis in the absence of a PPB, in which the premitotic nucleus was asymmetrically disposed and the equatorial plane of the spindle was variable. Of the 11 prophase cells observed by time lapse to undergo spindle formation in the absence of a PPB, eight spindles formed with equatorial planes parallel to the cell's long axis (as shown in Figures 5A to 5D) and two formed with equatorial planes perpendicular to the cell's long axis. The orientation of the remaining spindle was unknown because the cell was spherical in shape. It would therefore appear that in the absence of a PPB, the orientation of the spindle is indeterminate.

Variable Forms of Phragmoplast Expansion

Although two forms of early mitosis were seen in Arabidopsis suspension cells, the genesis of the phragmoplast proceeded by a single route—always occurring from the central spindle region. During the anaphase-telophase transition, the pronounced labeling at the poles declined, and AtEB1a-GFP relocated diffusely to the region of the central spindle and then became more focused again around the reformed nuclei (Figure 6).

As demonstrated in the movies of telophase cells (see Supplemental Movies 2 and 3 online), we observed microtubule outgrowth to occur from the nuclear periphery during the early stages of phragmoplast morphogenesis. During later stages, when the phragmoplast was expanding, we observed (Figure 6) that nucleus-associated strands of cytoplasm continued to contribute to the growing edge of the cytokinetic apparatus (T10.70 to T12.88). However, in some cells, the nucleus becomes less tightly associated with the phragmoplast and its growing front, with the cytokinetic apparatus appearing to break away during subsequent stages. This can be seen by comparing the relative positions of the lower nucleus in panel T10.70 with T12.83 of Figure 6. In this case, a GFP-labeled locus forms independently of the nuclear surface, with filaments radiating from it toward the midzone of the leading edge of the phragmoplast (Figure 6, panels T14.22 to T15.91); this could provide a potential means of expanding the phragmoplast as it grows beyond the corridor between the daughter nuclei.

The process of centrifugal outgrowth also showed some variability in its behavior. We were able to follow by time lapse both symmetrical (11 cells, e.g., see Figures 3A to 3F) and

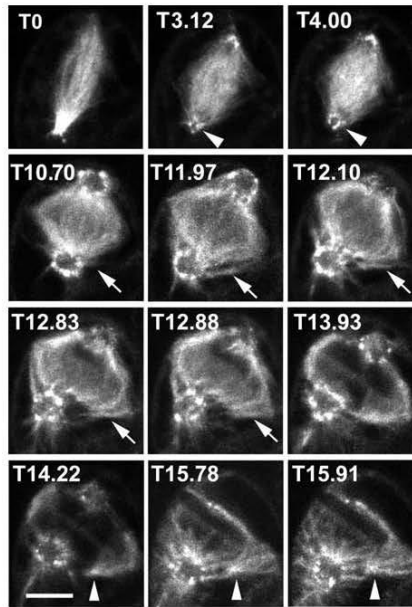


Figure 6. AtEB1a-GFP during Phragmoplast Morphogenesis.

Time-lapse confocal laser scanning microscopy images of AtEB1a-GFP during the transition between metaphase and telophase in *Arabidopsis* suspension cells. The phragmoplast develops from the center of the spindle. Arrowheads (T3.12 to T4.00) indicate the presence of an annular structure at the spindle pole. AtEB1a-GFP then concentrates in the vicinity of the daughter nuclei after their reconstitution in telophase. The arrow shows the development of a cytoplasmic strand emanating from the nucleus and then incorporating into the growing face of the phragmoplast. The arrowheads (T14.22 to T15.91) indicate the formation of a new site in the outer margin of the phragmoplast. T, time (min). Bar = 8 μ m.

polarized (five cells, where the phragmoplast contacts one mother wall first, see Cutler and Ehrhardt, 2002) forms of expansion in *Arabidopsis* suspension cells. The daughter nuclei of these *Arabidopsis* suspension cells often remained stationary during cytokinesis (e.g., see Figure 6). By contrast, we encountered cases where the nuclei moved. Figure 7 shows a different kind of polarized cytokinesis in which phragmoplast expansion began symmetrically (T0 min) but switched to polarized growth after contact of the cell plate with one side of the cell cortex (T9.46 min). Instead of remaining static, the daughter nuclei then migrated toward the opposite side of the cell in the wake of the outgrowing phragmoplast (T24.0 to T59.21 min). Microtubular fluorescence was then diminished at the side of the phragmoplast that had made first contact with the cell wall and became biased toward the leading edge of the phragmoplast, giving rise

to a C-shaped array of microtubules (T24.0 to T59.21 min; note the loss of microtubules from the left-hand sides of both nuclei).

The final positioning of the cell plate also involved phragmoplast reorientation. Figure 8 (using an inverted grayscale image to visualize the cortex more clearly) shows an actively expanding phragmoplast rotate through 90° before selection of the division plane. Note that this rotation occurred in the same cell as illustrated in Figures 5A to 5D, underlining the fact that phragmoplast rotations (three cells) were only observed in cells undergoing mitosis in the absence of a PPB. In these cases, the phragmoplast reorientation resulted in division occurring along the shortest axis of the cell (Supplemental Movies 5 and 6 online show spindle and phragmoplast morphogenesis in the presence and absence of a PPB, respectively).

Astral-Like Microtubules

As shown in Figure 8 (but better seen in Supplemental Movies 2 and 3 online), a general and notable feature of mobile daughter nuclei was a subset of microtubules that emanated from polar caps of AtEB1a-GFP around the nuclear surfaces distal to the phragmoplast (see arrows in Figures 4, 7, and 8). These microtubules interacted with the cell cortex (see Supplemental Movie 2 online). The appearance of these microtubules, which were reminiscent of the astral microtubules of animal cell division, was cell cycle regulated. They gradually increased in length and number as cells progressed from metaphase (where a few, short microtubules emanated from spindle poles) to anaphase and telophase, during which numerous microtubules were observed radiating from the outer surfaces of the reforming daughter nuclei (see Figure 4). Like astral microtubules (Timauer et al., 2004), the average growth rate of these nucleus-associated microtubules was faster than reported for interphase rates of cortical

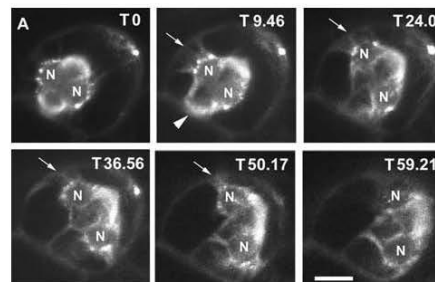


Figure 7. Polarized Cytokinesis.

Time-lapse confocal laser scanning microscopy images of a novel form of polarized cytokinesis. Selected stacks show the mobility of the daughter nuclei during phragmoplast expansion. Phragmoplast expansion begins symmetrically (T0 to T9.46) but switches to a polarized form (T24.0 to T59.21) after contact of the cell plate with one side of the cell cortex (arrowhead). Arrows indicate nucleus-associated microtubules that interact with the cell cortex. N, daughter nuclei, which have accumulated AtEB1a-GFP along their surfaces; T, time (min). Bar = 8.3 μ m.

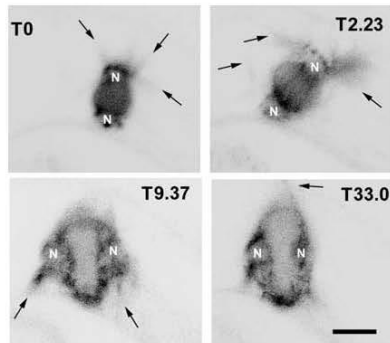


Figure 8. Phragmoplast Rotations.

Time-lapse confocal laser scanning microscopy images (inverted gray-scale) showing an actively growing phragmoplast rotate through 90°. This data set was collected from the same cell shown in Figure 5A, which was used to demonstrate mitosis in the absence of a PPB. Arrows indicate nucleus-associated microtubules that interact with the cell cortex. N, nucleus; T, time (min). Bar = 8.3 μ m.

microtubule polymerization (6.12 ± 0.29 μ m/min; 52 microtubules versus 3.53 ± 0.26 μ m/min; Chan et al., 2003).

DISCUSSION

The Distribution of AtEB1a around the Cell Cycle

EB1 is a well-established microtubule binding protein that preferentially attaches to the growing plus end of microtubules in animals (Morrison et al., 1998; Mimori-Kiyosue et al., 2000) and fungi (Straube et al., 2003). This was also recently found to apply to cortical microtubules in *Arabidopsis* suspension cells, with AtEB1a labeling the fast-growing ends of cortical microtubules in a comet-like pattern (Chan et al., 2003; Mathur et al., 2003; van Damme et al., 2004). Previously, we used this labeling pattern to show that microtubules of the cortical array are of mixed polarity and that comets arise from multiple dispersed sites around the cell cortex (Chan et al., 2003).

In this study, the nuclear periphery becomes active as a site for microtubule outgrowth and is particularly obvious in those cells without a PPB where the microtubules form a radial array. This is consistent with the association of nucleating material with the perinuclear region at specific stages of the cell cycle, as reviewed by Vaughn and Harper (1998). During preprophase/prophase, comets were observed to grow away from the nuclear periphery toward the cell cortex. Comets were difficult to detect during metaphase, but during anaphase they could be seen to grow from the poles toward the equator of the spindle. During telophase, comets grew from the outward-facing side of the daughter nucleus toward the cell cortex or from the inward-facing side

to the equator of the phragmoplast. In all cases, it can be deduced from the fact that plus end comets grow away from the nuclear periphery that the minus ends are located at the poles or the nuclear surface. This is consistent with hook decoration studies that place the minus ends at the spindle poles in mitosis (Euteneuer et al., 1982) and in the vicinity of the nuclear envelope during cytokinesis (Euteneuer and McIntosh, 1980)—in both cases with plus ends meeting at the midline.

It is intriguing that in all of these loci where it can be inferred that minus ends are directed, AtEB1a-GFP is also accumulated. Although microtubules arise during mitosis in the general region of the nucleus, the association is not tight, for we observe both circumferential and radial movements of the minus end foci at the nuclear periphery. Also, we observe nucleation to occur during anaphase when the nuclear envelope is not completely reformed. For these reasons, it does not seem that the minus end loci are exclusively associated with the nuclear envelope but may be associated, for example, with other components of the endomembrane system such as the endoplasmic reticulum that is known to aggregate at spindle poles upon breakdown of the nuclear envelope (Hepler, 1980; Zachariadis et al., 2001).

The minus end localization of AtEB1a-GFP is consistent with findings from diverse organisms, ranging from yeast to vertebrates, that plus end tracking EB1 also gathers at the minus ends of microtubules (Bu and Su, 2001; Morrison and Askham, 2001; Askham et al., 2002; Rehberg and Gräf, 2002; Rogers et al., 2002; Timmer et al., 2002, 2004; Straube et al., 2003; Louie et al., 2004; Piehl et al., 2004). It is also consistent with our previous study on *Arabidopsis* cells, which showed that AtEB1a-GFP labeled foci at the minus ends of cortical microtubules from which microtubules could be seen to grow or shrink (Chan et al., 2003). This initial targeting of AtEB1a-GFP to the minus end can be explained by the idea that it acts as a repository for the EB1 required during plus end growth (Rehberg and Gräf, 2002). The fact that EB1 accumulates at the poles in suspension cells appears to be related to the elevated levels of expression under the 35S promoter of *Cauliflower mosaic virus* and the transient-expression system where spindle fluorescence was 16.7 (mean of 35) times brighter than in *Arabidopsis* plants under the native promoter. By contrast, polar accumulations were only occasionally seen in *Arabidopsis* plants transformed under the 35S promoter (2.5, mean of 9) and never seen in plants transformed with the native promoter nor has it been observed in stable tobacco (*Nicotiana tabacum*) BY-2 lines expressing AtEB1a-GFP (van Damme et al., 2004). We observed that the minus end labeling was less prominent in those cells displaying rapid plus end dynamics with the comet-like pattern (see Supplemental Movie 3 online) and that the fluorescence intensity of perinuclear foci was reduced or disappeared after the emergence of comets. We therefore suggest that the higher levels of overexpression obtained in *Arabidopsis* suspension cells with the 35S promoter of *Cauliflower mosaic virus* allow for AtEB1a-GFP to persist at the minus ends at levels that are less readily depleted by microtubule outgrowth.

Whatever the explanation, the ability of AtEB1a-GFP to mark sites at the nuclear periphery has allowed the identification of a subpopulation of premitotic cells that divide without a PPB,

allowing us to compare their behavior with cells that divide in a more conventional manner.

Alternative Mechanisms for Spindle Pole Morphogenesis

The time-lapse studies showed that two mechanisms for mitosis exist side by side in a suspension culture, much as has been reported for cultured and embryonic *Drosophila melanogaster* cells (Goshima and Vale, 2003). In *Arabidopsis* suspension cells where there is a PPB, perinuclear AtEB1a-GFP is sorted into two polar caps perpendicular to the PPB before NEBD. This is reminiscent of the redistribution of γ -tubulin into bipolar caps in preprophase onion (*Allium cepa*) root tip cells (Liu et al., 1993). These premitotic bipolar caps of AtEB1-GFP transform seamlessly to locate to the spindle poles after NEBD. In most of the cells, however, there is no PPB, AtEB1a-GFP is not prepolarized into caps, and the bipolar spindle is formed after NEBD. This suggests that in these cells the polar accumulations only become focused upon the assembly of the spindle in what would appear to be a microtubule-dependent process.

Recent reviews of spindle development have focused on an inside-out mechanism for plant cells and meiotic animal cells that possess no centrioles/centrosomes. In this mechanism, microtubules first associate with chromosomes before being self-organized into bipolar arrays by motor proteins (for review, see Compton, 2000). Using beads coated with bacterial DNA, incubated in centrosome-free extracts of *Xenopus*, Heald et al. (1996) showed that this method accounted for spindle development in the absence of centrosomes and kinetochores. In this mechanism, microtubules are nucleated in the vicinity of chromatin and then sorted by plus end-directed BIM C kinesins into two antiparallel sets with plus ends overlapping at the midline. Then, the distal minus ends are focused into poles by the action of minus end motors that could convey materials such as AtEB1a-GFP to the poles as spindle bipolarity develops.

In the alternative outside-in or search and capture mechanism (Compton, 2000), centrosomes are the dominant centers of microtubule nucleation and they determine the number and position of the spindle poles. Thus, spindle bipolarity in such cells relies on both the proper duplication and separation of the centrosomes. This situation would seem to be analogous to the process we observe in cells possessing a PPB, where AtEB1a-GFP labels two polar caps before NEBD; that is, before the microtubules and the chromatin mix. During the premitotic period in such cells, the three-dimensional arrangement of cytoplasmic strands that radiates from, and suspends, the nucleus is reorganized to form a two-dimensional division plane—the phragmosome with the PPB at its perimeter (Lloyd, 1991). The fact that the perinuclear AtEB1a-GFP does not separate into two polar caps in those cells without PPBs implies that this premitotic cytoplasmic reorganization may be necessary for bipolar cap formation. In this scenario, AtEB1a-GFP is moved to opposite poles of the premitotic nucleus as part of the process that draws most of the cytoplasmic strands into the PPB/phragmosomal plane and leaves polar strands to radiate from the nucleus perpendicular to the division plane. This premitotic polarization involves actin as well as microtubules, and destruction of the polar strands can cause the spindle axis to be misaligned (Lloyd

and Traas, 1988). The formation of a tight PPB and the defining of the spindle poles (and, by extension, polar caps) in premitosis may also be connected and has been observed in other studies. For instance, Granger and Cyr (2001) showed that nuclei not overlapped by a PPB do not form distinct spindle poles (see Figure 9 of their study). Abnormal PPB and spindle pole formation has also been observed in *Arabidopsis* plants deficient in the kinesin, *KatA*, where the PPB did not narrow to the same degree as wild-type cells (Marcus et al., 2003). Consequently, microtubules formed symmetrically around the nucleus, without clearing to form distinct spindle poles.

In early models, the opposite outside-in mechanism was predicted from the existence of the prophase spindle (e.g., Wick and Duniec, 1983; Baskin and Cande, 1990; Lambert et al., 1991). However, the recent application of the inside-out mechanism to plants (Compton, 2000) overlooks the existence of polar caps and the prophase spindle. These observations underline the inadequacy of equating plant cells with meiotic animal cells because plant cell division can be brought about by both inside-out and outside-in mechanisms and that the latter can function in the absence of centrioles.

In a recent study by Goshima and Vale (2003), spindle pole development in somatic animal cells was similarly demonstrated to proceed via outside-in as well as inside-out mechanisms—the latter being activated when one of the poles lacks a centrosome, as in the centrosome ablation studies of Khodjakov et al. (2000). However, rather than thinking of the inside-out mechanism as a backup, Gadde and Heald (2004) have suggested that this model, which was once thought not to apply to somatic animal cells with centrosomes, may in fact operate in such cells, reflecting a natural redundancy. In plants, such a redundancy would be important for endosperm and meiotic cells that do not display PPBs and which, without the premitotic cytoplasmic reorganization that this implies, would divide by the inside-out route. It is unclear why this phenomenon is so prevalent in the *Arabidopsis* culture. This phenomenon is not seen in our tobacco BY-2 cell line that is grown alongside the *Arabidopsis* culture under similar conditions. The fact that the latter tends to divide in an undifferentiated mass instead of forming regular chains of cells like BY-2 does suggest that aspects of cytoplasmic polarization (of which PPB formation is an indicator) have been lost during culture.

Variable Phragmoplast Growth and Astral Microtubules

Variations in cytokinesis have been reported before (Venverloo and Libbenga, 1981), and Cutler and Ehrhardt (2002) used the term polarized cytokinesis to describe the situation observed in *Arabidopsis* plants where the phragmoplast contacts one wall first and subsequently expands as a crescent, not a ring. In their study, Venverloo and Libbenga (1981) showed that the nucleus remained anchored to the first-contacted wall throughout subsequent cytokinesis. Another form of polarized cytokinesis was observed in this study in which the daughter nuclei do not remain anchored relative to the first-contacted wall but move with the cell plate to the opposite side of the cell. By this means, the AtEB1a-decorated nuclei move with the leading edge of the phragmoplast. In this case, microtubules would seem to persist

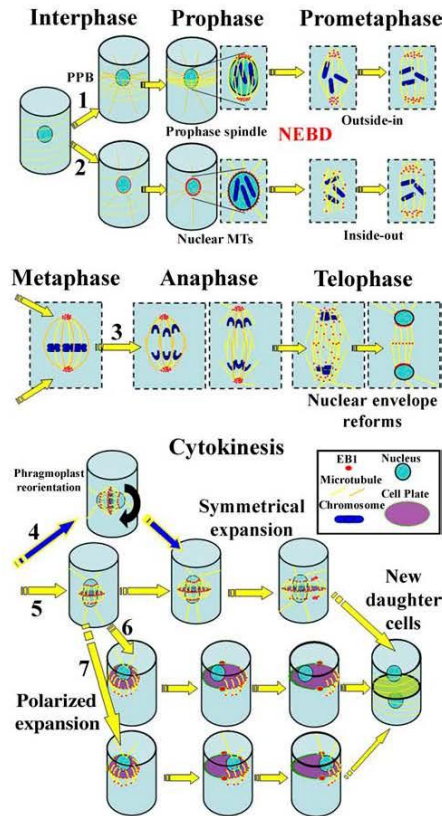


Figure 9. Model Showing Pathways of Spindle and Phragmoplast Morphogenesis in Higher Plants.

Cells undergo alternative pathways of spindle pole development depending upon the presence or absence of a PPB. In its presence (follow arrow 1), spindle poles form during prophase before NEBD in a manner consistent with outside-in (Compton, 2000) spindle assembly. By contrast, in cells without a PPB (follow arrow 2), spindle poles form during prometaphase in a manner consistent with inside-out spindle assembly pathway. Phragmoplast morphogenesis occurs via a single pathway (follow arrow 3) from remnants of microtubules present in the spindle midzone region in somatic cells. The subsequent stages of phragmoplast expansion, however, are flexible and can occur either symmetrically (follow arrow 5) or are polarized after contact of the cell plate with one side of the cell cortex (follow arrows 6 and 7). Polarized cytokinesis can occur with either stationary nuclei (follow arrow 6) or with nuclei that migrate with the growing front of the phragmoplast (follow arrow 7). Nuclear migrations can also contribute to the outgrowth of the phragmoplast (follow arrow 6) and to the final position of the cell plate in the absence of a PPB, where the orientation of the spindle is indeterminate

with the nucleus rather than redistributing away from it as shown in Figure 6. Because Cutler and Ehrhardt (2002) have shown that both central and polarized cytokinesis can occur a few cells apart in *Arabidopsis* roots, it is likely that the different mechanisms we observe similarly reflect a natural phenomenon rather than an abnormality of cultured cells.

Actively growing phragmoplasts, together with their nuclei, often rotated during cytokinesis before selection of the final division plane. This behavior was observed in cells that divided without a PPB, indicating that the PPB (when present) promotes the positional stability of these structures during cell division, as suggested by Gimenez-Abian et al. (1998). This could mean that the division site, which is somehow marked during preprophase, provides a reference point for cytoplasmic elements (e.g., cytoplasmic strands) to be used later during phragmoplast outgrowth.

An interesting feature of the phragmoplast reorientations observed in this study was the aster-like polar microtubules that extended from the upper surfaces of the daughter nuclei toward the cell cortex, moving around the circumference of the cell as the daughter nuclei and phragmoplast migrated. Astral microtubules are rarely mentioned in plants and have been suggested to be remnants of the nucleus-associated radial microtubules of the preceding interphase (for review, see Baskin and Cande, 1990). However, like the astral microtubules of animal cells (Morrison and Askham, 2001; Tirnauer et al., 2002), these nucleus-associated plant microtubules appear to be cell cycle regulated: their growth rate was almost twice as fast as interphase microtubules and they became more prominent from anaphase to telophase.

In animals and yeast, forces generated by growing astral microtubules are thought to push against the cortex; alternatively, cortically bound motor complexes reel in the astral microtubules (Kusch et al., 2002), thereby helping to orientate the spindle axis. In plants, these astral-like microtubules could assist with nuclear migration, helping to orientate the nuclei (and/or phragmoplast) relative to the plane of cell division and providing support for the growing edge of the phragmoplast as it moves across the vacuole. However, phragmoplast expansion probably involves more than microtubules, and there are indications that actin filaments may be involved in spindle rotation as well as in the centrifugal guidance and proper orientation of the new cell plate (Lloyd, 1991).

In conclusion, this study has shown that both spindle development and phragmoplast expansion can occur in different ways that may be related to the variable degrees of premitotic cytoplasmic reorganization according to the presence or absence of a PPB. Some of these behaviors, including the inside-out spindle development pathway and mobility of the daughter nuclei (phragmoplast reorientations), may therefore serve as alternative mechanisms to rescue cell division in the absence of premitotic cues that predict the plane of cell division (Figure 9). This would be consistent with the fact that sex cells and endosperm divide without a PPB and appear to erect a spindle

(arrow 4). Red dots indicate the cell cycle distribution of AtEB1a-GFP, which, apart from labeling at the midline of the phragmoplast, marks the location of microtubule minus ends.

by the inside-out mechanism (Smirnova and Bajer, 1992). Division is not confined to small meristematic cells but can occur adventitiously in large highly vacuolated cells under a variety of natural and experimental conditions. Alternative pathways provide the flexibility for plants to adapt to varying circumstances.

METHODS

Plant Material

Suspension cultures of *Arabidopsis thaliana* (Columbia) were maintained as described in Chan et al. (2003). *Arabidopsis* seedlings were grown on plates containing 3% (w/v) phytigel, 0.5% (w/v) sucrose, and 0.43% (w/v) MS powdered medium, with macro- and micro-elements (Duchefa, Haarlem, The Netherlands). Plates were incubated for 2 d at 4°C and then transferred to the growth room at 22°C under continuous lighting. Seedlings were used for confocal microscopy after 3 to 5 d.

Transient Transformation of Arabidopsis Suspension Cultures

Cells were transformed with either AtEB1a-GFP or HDEL-YFP as described by Chan et al. (2003), except that 200 μ L of the *Agrobacterium tumefaciens* suspension was used to transform cells and that suspension cultures were supplemented with 50 μ g/mL of acetosyringone before transformation. Expression of AtEB1-GFP was visible within 2 d, after which cells were subcultured to encourage division. The HDEL-YFP construct was obtained from Chris Hawes (Oxford Brookes University, Oxford, UK).

Preparation of the Native Promoter:AtEB1-GFP Construct and Preparation of Stable Lines

The *AtEB1a* gene (introns and exons) plus 1 kb of sequence upstream of the open reading frame was amplified from genomic DNA and inserted into the pGEM-T-Easy vector (Promega, Southampton, UK) according to the manufacturer's instructions. The primers used for the PCR reaction were as follows: 5'-AAGGTACCTAACCGATTAGACTTGCAGG-3' (AtEB1-3-kpn1) and 5'-TTGTGACTTGGCTTGAGTCTTTCTTC-3', which amplified a product of 3263 bp. These primers also flanked the genomic DNA fragment with *Sal*I and *Kpn*I restriction enzyme sites. These sites were then used to cut the PCR product from the pGEM-T-Easy vector and ligate it into the pGR4 plasmid (provided by Gethin Roberts, John Innes Centre, Norwich, UK), which contains a C-terminal GFP tag. The native promoter:AtEB1a-GFP construct was checked by sequencing and transformed into *Arabidopsis* plants by transformation with *Agrobacterium* (strain gv3101) using the floral dip technique (Bechtold et al., 1993). To select for transformants, T1 generation seeds were harvested and sown on MS powdered medium containing 50 μ g/mL of kanamycin. Resistant seedlings were transplanted to soil and the T2 seeds analyzed for the segregation of kanamycin resistance. The χ^2 test was used to predict lines containing a single copy of the transgene. Homozygous lines were then identified in the T3 generation and used for microscopic analysis of GFP expression. The 35S:AtEB1a-GFP construct was transformed into plants as described above.

Immunofluorescence

Transformed cells were fixed for 1 h in PME buffer (50 mM piperazine-*N,N'*-bis-[2-ethanesulphonic acid], 5 mM magnesium sulphate, and 5 mM ethylene-glycol-bis[β -aminoethylether]*N,N'*-tetracetic acid) plus 0.025 M sorbitol (PMES), containing 4% (w/v) formaldehyde and 0.1% (v/v) glutaraldehyde. After three washes in PMES, the cells were stuck to poly-L-Lys-coated slides and extracted in PMES containing 0.5%

(w/v) Onozuka R-10 cellulase (Yakult, Tokyo, Japan), 0.05% (w/v) Pectolase Y-23 (Yakult), and 0.05% (v/v) Triton X-100. Cells were labeled with rat antitubulin (YOL 1/34; Harlan Sera-Lab, Loughborough, UK; 1:50) and rabbit anti-GFP (Molecular Probes, Eugene, OR; 1:100) diluted in PMES containing 1% (w/v) BSA. Primary antibody binding was then detected, after three washes in PMES, by applying anti-rabbit fluorescein isothiocyanate-conjugated (DAKO, Glostrup, Denmark; 1:200) and anti-rat CY3-conjugated antibodies (Amersham Biosciences, Little Chalfont, UK; 1:500) diluted as described above. The cells were washed four more times, stained with 4',6-diamidino-2-phenylindole (DAPI; 3 μ g/mL), and then mounted in Citifluor antifade mountant (City University Chemistry Department, London, UK).

DAPI Staining of Cells

DNA was visualized by adding 25 μ L of Triton X-100 (10% [v/v] stock; 0.25% [v/v] final concentration) and 5 μ L of DAPI (3 μ g/mL stock; 0.015 μ g/mL final concentration) to 1 mL of suspension cells.

Confocal Microscopy and Image Analysis

Images were acquired using a Bio-Rad MRC 1024 confocal microscope (Hercules, CA). Cells were maintained in a modified chamber fitted with a gas-permeable membrane (bioFOLIE; VivaScience, Goettingen, Germany). Images were taken at 5- to 600-s intervals. Both EB1-GFP and HDEL-YFP were excited at 488 nm and visualized using a 515-nm long-pass filter. Microtubule growth rates were measured in the time-lapse images using the line and reslice tools of ImageJ (<http://reb.info.nih.gov/ij/>).

Quantification of Fluorescence Levels in Spindles of Transgenic Plants and Suspension Cultures by Confocal Microscopy

For quantification experiments, single transgenic lines of AtEB1a-GFP under control of either 35S or native promoter were selected. In both cases, AtEB1a-GFP was uniformly expressed, and cells were phenotypically indistinguishable from those in control plants. Nonsaturated images of spindles labeled by AtEB1a-GFP were collected using a VisiTech spinning disc confocal microscope (Sunderland, UK) fitted with a \times 60/1.4 oil objective lens. GFP was excited using the 488-nm line of an argon ion laser and the emitted light filtered through a 500- to 550-nm band-pass filter. Spindle fluorescence was detected using a Hamamatsu Orca ER cooled CCD camera (Hamamatsu City, Japan) with 4 \times binning, set at 1-s exposure time and 1- μ m z-step intervals. Images were analyzed using ImageJ, z-sections were projected (max), and the average intensities of entire spindles calculated using the measure tool. Max z-projections ensured that the calculations were performed on complete spindles.

Sequence data from this article have been deposited with the EMBL/GenBank data libraries under accession numbers At3g47690 (AtEB1-a), At5g62500 (AtEB1-b), and At5g67270 (AtEB1-c).

ACKNOWLEDGMENTS

We thank Gethin Roberts, Pascale Rossignol, Hannah Jones, and Nuno Geraldo for assistance in molecular biology and Guoie Mao for useful discussions. We also thank Chris Hawes for supplying the HDEL-YFP construct. G.C. and J.C. would like to dedicate this paper to the memory of Dagon Prince.

Received March 10, 2005; revised April 13, 2005; accepted April 14, 2005, published May 6, 2005.

REFERENCES

- Askham, J.M., Vaughan, K.T., Goodson, H.V., and Morrison, E.E. (2002). Evidence that an interaction between EB1 and p150(Glued) is required for the formation and maintenance of a radial microtubule array anchored at the centrosome. *Mol. Biol. Cell* **13**, 3627–3645.
- Baskin, T.I., and Cande, W.Z. (1990). The structure and function of the mitotic spindle in flowering plants. *Annu. Rev. Plant Physiol. Plant Mol. Biol.* **41**, 277–315.
- Bechtold, N., Ellis, J., and Pelletier, G. (1993). In planta Agrobacterium-mediated gene transfer by infiltration of *Arabidopsis thaliana* plants. *C. R. Acad. Sci. III* **316**, 1194–1199.
- Brown, R.C., and Lemmon, B.E. (2001). The cytoskeleton and spatial control of cytokinesis in the plant life cycle. *Protoplasma* **215**, 335–349.
- Bu, W., and Su, L.K. (2001). Regulation of microtubule assembly by human EB1 family proteins. *Oncogene* **20**, 3185–3192.
- Chan, J., Calder, G.M., Doonan, J.H., and Lloyd, C.W. (2003). EB1 reveals mobile microtubule nucleation sites in *Arabidopsis*. *Nat. Cell Biol.* **5**, 967–971.
- Compton, D.A. (2000). Spindle assembly in animal cells. *Annu. Rev. Biochem.* **69**, 95–114.
- Cutler, S.R., and Ehrhardt, D.W. (2002). Polarized cytokinesis in vacuolate cells of *Arabidopsis*. *Proc. Natl. Acad. Sci. USA* **99**, 2812–2817.
- Dhonukshe, P., and Gadella, T.W., Jr. (2003). Alteration of microtubule dynamic instability during preprophase band formation revealed by yellow fluorescent protein-CLIP170 microtubule plus-end labeling. *Plant Cell* **15**, 597–611.
- Drykova, D., Cenklova, V., Sulimenko, V., Volc, J., Draber, P., and Binarova, P. (2003). Plant gamma-tubulin interacts with alphabeta-tubulin dimers and forms membrane-associated complexes. *Plant Cell* **15**, 465–480.
- Ehardt, M., Stoppin-Mellet, V., Campagne, S., Canaday, J., Mutterer, J., Fabian, T., Sauter, M., Muller, T., Peter, C., Lambert, A.M., and Schmit, A.C. (2002). The plant Spc88p homologue colocalizes with gamma-tubulin at microtubule nucleation sites and is required for microtubule nucleation. *J. Cell Sci.* **115**, 2423–2431.
- Euteneuer, U., Jackson, W.T., and McIntosh, J.R. (1982). Polarity of spindle microtubules in *Haemaphysalis endosperm*. *J. Cell Biol.* **94**, 644–653.
- Euteneuer, U., and McIntosh, J.R. (1980). Polarity of midbody and phragmoplast microtubules. *J. Cell Biol.* **87**, 509–515.
- Gadde, S., and Heald, R. (2004). Mechanism and molecules of the mitotic spindle. *Curr. Biol.* **14**, R797–R805.
- Gimenez-Abian, M.I., Utrilla, L., Canovas, J.L., Gimenez-Martin, G., Navarrete, M.H., and De la Torre, C. (1998). The positional control of mitosis and cytokinesis in higher-plant cells. *Planta* **204**, 37–43.
- Goshima, G., and Vale, R.D. (2003). The roles of microtubule-based motor proteins in mitosis: Comprehensive RNAi analysis in the *Drosophila* S2 cell line. *J. Cell Biol.* **162**, 1003–1016.
- Granger, C., and Cyr, R. (2001). Use of abnormal preprophase bands to decipher division plane determination. *J. Cell Sci.* **114**, 599–607.
- Granger, C.L., and Cyr, R.J. (2000). Microtubule reorganization in tobacco BY-2 cells stably expressing GFP-MBD. *Planta* **210**, 502–509.
- Heald, R., Tournéize, R., Blank, T., Sandaltzopoulos, R., Becker, P., Hyman, A., and Karsenti, E. (1996). Self-organization of microtubules into bipolar spindles around artificial chromosomes in *Xenopus* egg extracts. *Nature* **382**, 420–425.
- Hepler, P.K. (1980). Membranes in the mitotic apparatus of barley cells. *J. Cell Biol.* **86**, 490–499.
- Joshi, H.C., and Palevitz, B.A. (1996). Gamma-tubulin and microtubule organization in plants. *Trends Cell Biol.* **6**, 41–44.
- Khodjakov, A., Cole, R.W., Oakley, B.R., and Rieder, C.L. (2000). Centrosome-independent mitotic spindle formation in vertebrates. *Curr. Biol.* **10**, 59–67.
- Korinek, W.S., Copeland, M.J., Chaudhuri, A., and Chant, J. (2000). Molecular linkage underlying microtubule orientation toward cortical sites in yeast. *Science* **287**, 2257–2259.
- Kusch, J., Meyer, A., Snyder, M.P., and Barral, Y. (2002). Microtubule capture by the cleavage apparatus is required for proper spindle positioning in yeast. *Genes Dev.* **16**, 1627–1639.
- Lambert, A.-M., Vantard, M., Schmit, A.-C., and Stoeckel, H. (1991). Mitosis in plants. In *The Cytoskeletal Basis of Plant Growth and Form*, C.W. Lloyd, ed (London: Academic Press), pp. 199–208.
- Liu, B., Marc, J., Joshi, H.C., and Palevitz, B.A. (1993). A gamma-tubulin-related protein associated with the microtubule arrays of higher plants in a cell cycle-dependent manner. *J. Cell Sci.* **104**, 1217–1228.
- Lloyd, C.W., and Traas, J.A. (1988). The role of F-actin in determining the division plane of carrot suspension cells. *Drug studies. Development* **102**, 211–221.
- Lloyd, C.W. (1991). Cytoskeletal elements of the phragmosome establish the division plane in vacuolated higher plant cells. In *The Cytoskeletal Basis of Plant Growth and Form*, C.W. Lloyd, ed (London: Academic Press), pp. 245–257.
- Louie, R.K., Bahmanyar, S., Siemers, K.A., Votin, V., Chang, P., Stearns, T., Nelson, W.J., and Barth, A.I. (2004). Adenomatous polyposis coli and EB1 localize in close proximity of the mother centriole and EB1 is a functional component of centrosomes. *J. Cell Sci.* **117**, 1117–1128.
- Marcus, A.J., Li, W., Ma, H., and Cyr, R.J. (2003). A kinesin mutant with an atypical bipolar spindle undergoes normal mitosis. *Mol. Biol. Cell* **14**, 1717–1726.
- Mathur, J., Mathur, N., Kernebeck, B., Srinivas, B.P., and Hulskamp, M. (2003). A novel localization pattern for an EB1-like protein links microtubule dynamics to endomembrane organization. *Curr. Biol.* **13**, 1991–1997.
- Mimori-Kiyosue, Y., Shiina, N., and Tsukita, S. (2000). The dynamic behavior of the APC-binding protein EB1 on the distal ends of microtubules. *Curr. Biol.* **10**, 865–868.
- Mineyuki, Y. (1999). The preprophase band of microtubules: Its function as a cytokinetic apparatus in higher plants. *Int. Rev. Cytol.* **187**, 1–49.
- Morrison, E.E., and Askham, J.M. (2001). EB1 immunofluorescence reveals an increase in growing astral microtubule length and number during anaphase in NRK-52E cells. *Eur. J. Cell Biol.* **80**, 749–753.
- Morrison, E.E., Wardleworth, B.N., Askham, J.M., Markham, A.F., and Meredith, D.M. (1998). EB1, a protein which interacts with the APC tumour suppressor, is associated with the microtubule cytoskeleton throughout the cell cycle. *Oncogene* **17**, 3471–3477.
- Nishihama, R., and Machida, Y. (2001). Expansion of the phragmoplast during plant cytokinesis: A MAPK pathway may MAP it out. *Curr. Opin. Plant Biol.* **4**, 507–512.
- Otegui, M., and Staehelin, L.A. (2000). Cytokinesis in flowering plants: More than one way to divide a cell. *Curr. Opin. Plant Biol.* **3**, 493–502.
- Piehl, M., Tulu, U.S., Wadsworth, P., and Cassimeris, L. (2004). Centrosome maturation: Measurement of microtubule nucleation throughout the cell cycle by using GFP-tagged EB1. *Proc. Natl. Acad. Sci. USA* **101**, 1584–1588.
- Rehberg, M., and Gräf, R. (2002). Dictyostelium EB1 is a genuine centrosomal component required for proper spindle formation. *Mol. Biol. Cell* **13**, 2301–2310.

- Rogers, S.L., Rogers, G.C., Sharp, D.J., and Vale, R.D.** (2002). *Drosophila* EB1 is important for proper assembly, dynamics, and positioning of the mitotic spindle. *J. Cell Biol.* **158**, 873–884.
- Schmit, A.C.** (2002). Acentrosomal microtubule nucleation in higher plants. *Int. Rev. Cytol.* **220**, 257–289.
- Shaw, S.L., Kamyar, R., and Ehrhardt, D.W.** (2003). Sustained microtubule treadmilling in *Arabidopsis* cortical arrays. *Science* **300**, 1715–1718.
- Smirnova, E.A., and Bajer, A.S.** (1992). Spindle poles in higher plant mitosis. *Cell Motil. Cytoskeleton* **23**, 1–7.
- Staehelein, L.A., and Hepler, P.K.** (1996). Cytokinesis in higher plants. *Cell* **84**, 821–824.
- Straube, A., Brill, M., Oakley, B.R., Horio, T., and Steinberg, G.** (2003). Microtubule organization requires cell cycle-dependent nucleation at dispersed cytoplasmic sites: Polar and perinuclear microtubule organizing centers in the plant pathogen *Ustilago maydis*. *Mol. Biol. Cell* **14**, 642–657.
- Tirnauer, J.S., Grego, S., Salmon, E.D., and Mitchison, T.J.** (2002). EB1-microtubule interactions in *Xenopus* egg extracts: Role of EB1 in microtubule stabilization and mechanisms of targeting to microtubules. *Mol. Biol. Cell* **13**, 3614–3626.
- Tirnauer, J.S., Salmon, E.D., and Mitchison, T.J.** (2004). Microtubule plus-end dynamics in *Xenopus* egg extract spindles. *Mol. Biol. Cell* **15**, 1776–1784.
- van Damme, D., Bouget, F.Y., van Poucke, K., Inze, D., and Geelen, D.** (2004). Molecular dissection of plant cytokinesis and phragmoplast structure: A survey of GFP-tagged proteins. *Plant J.* **40**, 386–398.
- Vaughn, K.C., and Harper, J.D.** (1998). Microtubule-organizing centers and nucleating sites in land plants. *Int. Rev. Cytol.* **181**, 75–149.
- Venverloo, C.J., and Libbenga, K.R.** (1981). Cell division in *Nautilocalyx* explants. II. Duration of cytokinesis and velocity of cell-plate growth in large, highly vacuolated cells. *Z. Pflanzenphysiol.* **102**, 267–284.
- Wick, S.M., and Duniec, J.** (1983). Immunofluorescence microscopy of tubulin and microtubule arrays in plant cells. I. Preprophase band development and concomitant appearance of nuclear envelope-associated tubulin. *J. Cell Biol.* **97**, 235–243.
- Yasuhara, H., Sonobe, S., and Shibaoka, H.** (1993). Effects of taxol on the development of the cell plate and of the phragmoplast in tobacco BY-2 cells. *Plant Cell Physiol.* **34**, 21–29.
- Zachariadis, M., Quader, H., Galatis, B., and Apostolakos, P.** (2001). Endoplasmic reticulum preprophase band in dividing root-tip cells of *Pinus brutia*. *Planta* **213**, 824–827.
- Zhang, D., Wadsworth, P., and Hepler, P.K.** (1990). Microtubule dynamics in living dividing plant cells: Confocal imaging of microinjected fluorescent brain tubulin. *Proc. Natl. Acad. Sci. USA* **87**, 8820–8824.
- Zheng, Y., Wong, M.L., Alberts, B., and Mitchison, T.** (1995). Nucleation of microtubule assembly by a gamma-tubulin-containing ring complex. *Nature* **378**, 578–583.